NOVEL ISOTOPE SYSTEMS AND BIOGEOCHEMICAL CYCLING DURING CRYOSPHERIC WEATHERING IN POLAR ENVIRONMENTS

EDITED BY: Katharine Rosemary Hendry, Melissa Jean Murphy and
Sophie Opfergelt
PUBLISHED IN: Frontiers in Earth Science

frontiers Research Topics

ISSN 1664-8714
ISBN 978-2-88966-724-6
DOI 10.3389/978-2-88966-724-6

About Frontiers

Frontiers is more than just an open-access publisher of scholarly articles: it is a pioneering approach to the world of academia, radically improving the way scholarly research is managed. The grand vision of Frontiers is a world where all people have an equal opportunity to seek, share and generate knowledge. Frontiers provides immediate and permanent online open access to all its publications, but this alone is not enough to realize our grand goals.

Frontiers Journal Series

The Frontiers Journal Series is a multi-tier and interdisciplinary set of open-access, online journals, promising a paradigm shift from the current review, selection and dissemination processes in academic publishing. All Frontiers journals are driven by researchers for researchers; therefore, they constitute a service to the scholarly community. At the same time, the Frontiers Journal Series operates on a revolutionary invention, the tiered publishing system, initially addressing specific communities of scholars, and gradually climbing up to broader public understanding, thus serving the interests of the lay society, too.

Dedication to Quality

Each Frontiers article is a landmark of the highest quality, thanks to genuinely collaborative interactions between authors and review editors, who include some of the world's best academicians. Research must be certified by peers before entering a stream of knowledge that may eventually reach the public - and shape society; therefore, Frontiers only applies the most rigorous and unbiased reviews.
Frontiers revolutionizes research publishing by freely delivering the most outstanding research, evaluated with no bias from both the academic and social point of view. By applying the most advanced information technologies, Frontiers is catapulting scholarly publishing into a new generation.

What are Frontiers Research Topics?

Frontiers Research Topics are very popular trademarks of the Frontiers Journals Series: they are collections of at least ten articles, all centered on a particular subject. With their unique mix of varied contributions from Original Research to Review Articles, Frontiers Research Topics unify the most influential researchers, the latest key findings and historical advances in a hot research area! Find out more on how to host your own Frontiers Research Topic or contribute to one as an author by contacting the Frontiers Editorial Office: frontiersin.org/about/contact

NOVEL ISOTOPE SYSTEMS AND BIOGEOCHEMICAL CYCLING DURING CRYOSPHERIC WEATHERING IN POLAR ENVIRONMENTS

Topic Editors:
Katharine Rosemary Hendry, University of Bristol, United Kingdom
Melissa Jean Murphy, University of Copenhagen, Denmark
Sophie Opfergelt, Catholic University of Louvain, Belgium

Citation: Hendry, K. R., Murphy, M. J., Opfergelt, S., eds. (2021). Novel Isotope Systems and Biogeochemical Cycling During Cryospheric Weathering in Polar Environments. Lausanne: Frontiers Media SA. doi: 10.3389/978-2-88966-724-6

Table of Contents

frontiers in Earth Science

EDITORIAL
published: 11 March 2021
doi: 10.3389/feart.2021.660333

Editorial: Novel Isotope Systems and Biogeochemical Cycling During Cryospheric Weathering in Polar Environments

Melissa J. Murphy[1], *Katharine Hendry*[2]* *and Sophie Opfergelt*[3]

[1]Department of Geosciences and Natural Resource Management, Center for Permafrost (CENPERM), University of Copenhagen, Copenhagen, Denmark, [2]School of Earth Sciences, University of Bristol, Bristol, United Kingdom, [3]Earth and Life Institute, Environmental Sciences, Université Catholique de Louvain, Louvain-la-Neuve, Belgium

Keywords: cryosphere, isotope, permafrost, glacier, geochemistry

Editorial on the Research Topic

Novel Isotope Systems and Biogeochemical Cycling During Cryospheric Weathering in Polar Environments

Cryospheric weathering processes in permafrost and glaciated environments play an essential role in carbon cycling within the Earth system. Chemical weathering of silicate, carbonate and sulfide-bearing rocks releases cations and anions that can consume (or release) atmospheric carbon dioxide (CO_2), as well as biologically important nutrients such as phosphorous, iron and silicon, which can impact downstream ecosystems (**Figure 1**). How these cryospheric weathering processes will respond to future climate-driven changes in permafrost thaw and glacial melt is difficult to predict due to the role of complex forcing mechanisms and feedbacks.

Isotope geochemistry utilizes changes in the relative abundance of different isotopes due to physical, chemical and biological reactions, allowing some of the complexities of cryospheric weathering processes to be unpicked. In recent years, there has been an explosion in the range of stable and radiogenic isotope systems used for the study of high-latitude environments, including isotopes of major elements such as carbon, oxygen, and silicon (e.g., Opfergelt et al., 2013; Kutscher et al., 2017), and trace metal isotopes such as strontium (Hindshaw et al., 2014), lithium (Murphy et al., 2019), iron (Zhang et al., 2015), uranium-series (e.g., Arendt et al., 2018) and rare earth elements (e.g., Clinger et al., 2016). This research topic explores some of the developments in high-latitude field and experimental studies that utilize such geochemical tools to trace the degree and nature of weathering reactions that play a critical role in carbon cycling. The nine contributions to the research topic involve the analysis of traditional (C, N, S, O) and non-traditional (Mg, Li, Si, Ge) isotopes from different samples types such as river waters, lake waters, rocks, sediments, or mineral separates from locations both in the Northern (Greenland, Iceland, Canada, Svalbard) and Southern Hemisphere (Patagonia, Antarctica).

Two papers use isotope geochemistry to explore organic and inorganic carbon cycling within permafrost and active layer soils. Jones et al. show that biogeochemical processes and decomposition pathways of organic carbon in ice-wedge polygons in Svalbard are dependent upon water and organic carbon content. Sulfur ($\delta^{34}S$) and oxygen ($\delta^{18}O$) isotopes show that iron and sulfate reduction processes dominate in water saturated, high organic carbon environments, whereas sulfide oxidation dominates in drier areas with less organic carbon. Zolkos and Tank use an experimental approach in combination with stable carbon isotopes ($\delta^{13}CO_2$) to show that carbonate weathering coupled with sulfide oxidation in recently or previously unthawed Canadian permafrost sediments is a net source of inorganic CO_2 to the atmosphere, albeit partly counterbalanced by carbonate buffering.

Edited and reviewed by:
Martyn Tranter,
Aarhus University, Denmark

***Correspondence:**
Katharine Hendry
K.Hendry@bristol.ac.uk

Specialty section:
This article was submitted to Geochemistry,
a section of the journal Frontiers in Earth Science

Received: *29 January 2021*
Accepted: *02 February 2021*
Published: *11 March 2021*

Citation:
Murphy MJ, Hendry K and Opfergelt S (2021) Editorial: Novel Isotope Systems and Biogeochemical Cycling During Cryospheric Weathering in Polar Environments.
Front. Earth Sci. 9:660333.
doi: 10.3389/feart.2021.660333

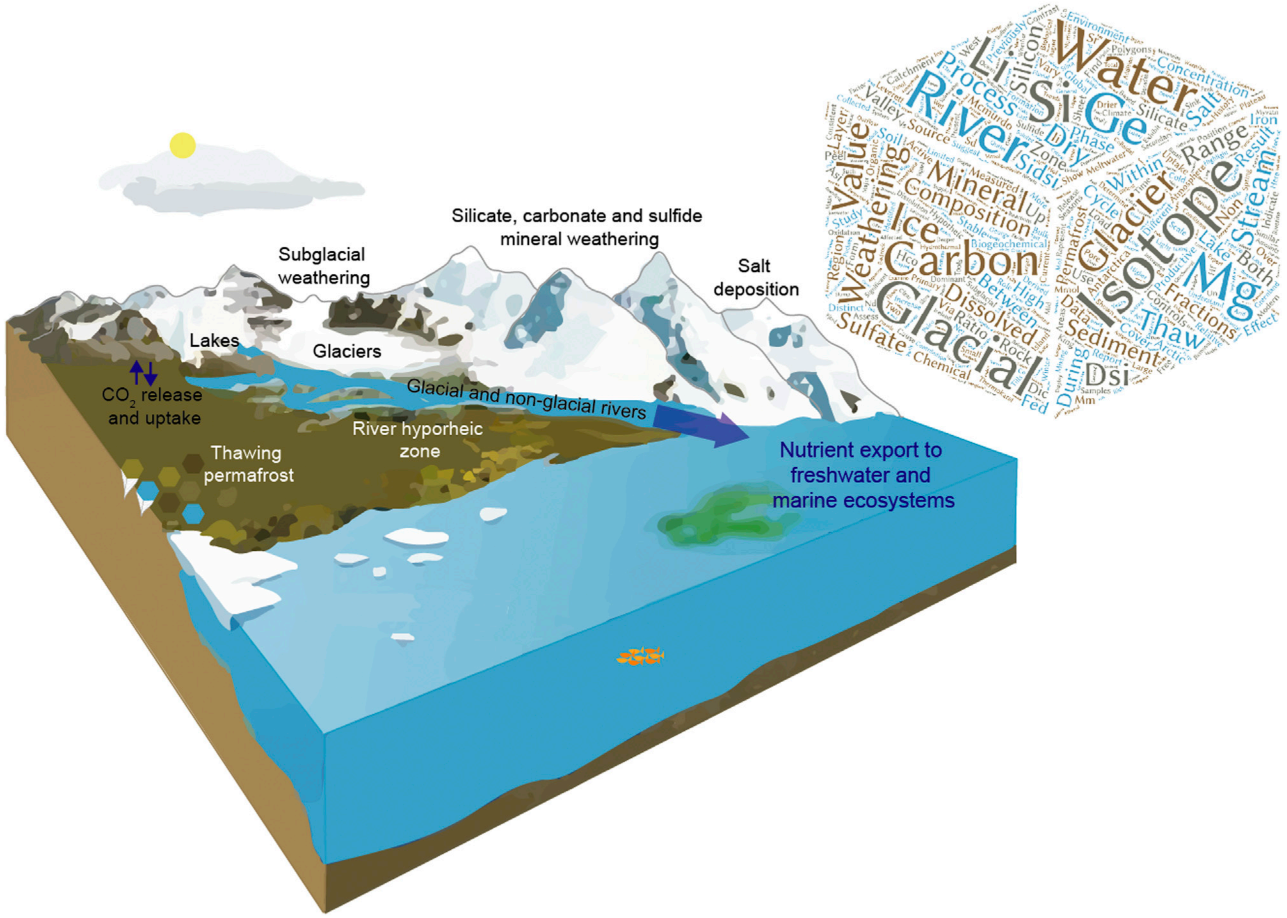

FIGURE 1 | Schematic showing the key cryospheric weathering processes that were investigated in this research topic (Modified from AMAP, 2017). The wordcloud shows the key concepts explored across the contributions, proportionally resized to the number of times word was used throughout titles and abstracts.

Two papers add to the growing body of work combining different isotope systems to understand subglacial weathering processes under the Greenland Ice Sheet. New measurements of magnesium (δ^{26}Mg) and lithium (δ^{7}Li) isotopes by Hindshaw et al. (2014) from the Leverett Glacier catchment, together with a number of radiogenic isotope systems, highlight the importance of the preferential dissolution of silicate and carbonate phases on chemical weathering and carbon cycling in meltwaters. Baronas et al. present new germanium isotope (Δ^{74}Ge) measurements of glacial meltwaters from the Watson River catchment, which - together with batch dissolution experiments - reveal that meltwaters are isotopically light and contrasting germanium fractionation mechanisms occur during subglacial dissolution-precipitation weathering reactions when compared to its "geochemical twin," silicon.

Previous studies have shown that stable silicon isotopes (δ^{30}Si) are isotopically lighter in glacial rivers compared to non-glacial counterparts as a result of subglacial physical crushing and/or precipitation-dissolution reactions involving amorphous silica phases (Hatton et al., 2019). To date, these studies have only focused on Arctic glacial and river systems. Pryer et al. detail the first δ^{30}Si measurements across a climate gradient from non-glaciated to glaciated catchments from Chilean Patagonia. Using careful filtration methods, a colloidal-size silica phase comprised predominantly of feldspars was identified in isotopically light, glacial-fed rivers. Not only does this add another mechanism for explaining variation in silica export and isotope mass balance in Arctic glaciated environments, but likely has consequences for other isotope systems.

Glacial meltwaters in the McMurdo Dry Valleys (MDVs) in Antarctica originate from cold-based glaciers in one of the driest places on Earth. Combined δ^{30}Si and Ge/Si measurements from Crescent Stream in MDVs (Hirst et al.) reflect the formation of amorphous silica phases and secondary clays in an extensive hyporheic zone during freeze-thaw cycles. Interestingly, these data highlight that rivers draining cold-based glaciers have higher δ^{30}Si compositions than rivers draining polythermal-based glaciers and similar δ^{30}Si compositions to rivers draining permafrost in the Arctic. Hatton et al. present δ^{30}Si measurements from Commonwealth Stream in MDVs that show the opposite relationship with dissolved silicon concentrations to that observed in rivers draining polythermal glaciers in the Arctic or Antarctic. Such contrasting behavior highlights the different origins of meltwater, with cold-based glaciers characterized by a higher proportion of supraglacial relative to subglacial melt, and dominance of in-stream weathering.

The MDVs are also explored by Diaz et al., who use stable isotopes of carbon, nitrogen and sulfur to investigate the transport of salts from the Central Transantarctic Mountains to the highly saline soils in the MDVs. Their findings show that regional variations in stable isotopes reflect both water availability and different atmospheric inputs of sulfates and nitrates, and evaporation-precipitation of carbonates.

Polar lakes are key sites of further chemical alteration of cryospheric weathering products, biological productivity and nutrient uptake. Pogge von Strandmann et al. present δ^{26}Mg records from a groundwater-fed Icelandic lake, fed by both cold and hot springs. Magnesium isotopes are fractionated by changes in lake temperature, as well as a strong seasonal signal due to biogenic calcium carbonate production in summer.

This research topic highlights the important role that isotope geochemistry plays in understanding the mechanistic links between cryospheric processes and climate-weathering feedbacks. Looking to the future, combining multiple isotopic systems with inter-disciplinary approaches will provide insight on the different aspects of the weathering processes occurring under and around ice sheets, and within permafrost. Furthermore, encouraging wider collaborations and standardized field sampling and experimental methodologies (e.g., Bouchard et al., 2020), will allow the geochemical community to better use the large number of existing and complementary datasets from the high-latitude regions to understand cryospheric weathering in polar environments.

AUTHOR CONTRIBUTIONS

All authors listed have made a substantial, direct, and intellectual contribution to the work and approved it for publication.

REFERENCES

AMAP (2017). *Snow, water, ice and permafrost in the arctic (SWIPA) 2017*. Oslo, Norway: Arctic Monitoring and Assessment Programme (AMAP), 269.

Arendt, C. A., Aciego, S. M., Sims, K. W., Das, S. B., Sheik, C., and Stevenson, E. I. (2018). Influence of glacial meltwater on global seawater δ234U. *Geochimica Cosmochimica Acta* 225, 102–115. doi:10.1016/j.gca.2018.01.007

Bouchard, F., Agnan, Y., Bröder, L., Fouché, J., Hirst, C., Sjöberg, Y., et al. (2020). The SPLASH action group – towards standardized sampling strategies in permafrost science. *Adv. Polar Sci.* 31 (3). doi:10.13679/j.advps.2020.0009

Clinger, A. E., Aciego, S. M., Stevenson, E. I., Arendt, C. A., and Robbins, M. J. (2016). Implications for post-comminution processes in subglacial suspended sediment using coupled radiogenic strontium and neodymium isotopes. *Geomorphology.* 259, 134–144. doi:10.1016/j.geomorph.2016.02.006

Hatton, J. E., Hendry, K. R., Hawkings, J. R., Wadham, J. L., Opfergelt, S., Kohler, T. J., et al. (2019). Silicon isotopes in Arctic and sub-Arctic glacial meltwaters: the role of subglacial weathering in the silicon cycle. *Proc. R. Soc. A.* 475 (2228), 20190098. doi:10.1098/rspa.2019.0098

Hindshaw, R. S., Rickli, J., Leuthold, J., Wadham, J., and Bourdon, B. (2014). Identifying weathering sources and processes in an outlet glacier of the Greenland Ice Sheet using Ca and Sr isotope ratios. *Geochimica Cosmochimica Acta* 145, 50–71. doi:10.1016/j.gca.2014.09.016

Kutscher, L., Mörth, C.-M., Porcelli, D., Hirst, C., Maximov, T. C., Petrov, R. E., et al. (2017). Spatial variation in concentration and sources of organic carbon in the Lena River, Siberia. *J. Geophys. Res. Biogeosci.* 122, 1999–2016. doi:10.1002/2017JG003858

Murphy, M. J., Porcelli, D., Pogge von Strandmann, P. A. E., Hirst, C. A., Kutscher, L., Katchinoff, J. A., et al. (2019). Tracing silicate weathering processes in the permafrost-dominated Lena River watershed using lithium isotopes. *Geochimica Cosmochimica Acta* 245, 154–171. doi:10.1016/j.gca.2018.10.024

Opfergelt, S., Burton, K. W., Pogge von Strandmann, P. A. E., Gislason, S. R., and Halliday, A. N. (2013). Riverine silicon isotope variations in glaciated basaltic terrains: implications for the si delivery to the ocean over glacial–interglacial intervals. *Earth Planet. Sci. Lett.* 369, 211–219. doi:10.1016/j.epsl.2013.03.025

Zhang, R., John, S. G., Zhang, J., Ren, J., Wu, Y., Zhu, Z., et al. (2015). Transport and reaction of iron and iron stable isotopes in glacial meltwaters on svalbard near kongsfjorden: from rivers to estuary to ocean. *Earth Planet. Sci. Lett.* 424, 201–211. doi:10.1016/j.epsl.2015.05.031

Conflict of Interest: The authors declare that the research was conducted in the absence of any commercial or financial relationships that could be construed as a potential conflict of interest.

The handling editor declared a shared affiliation with one of the authors, KRH at time of review.

frontiers in Earth Science

ORIGINAL RESEARCH
published: 29 November 2019
doi: 10.3389/feart.2019.00316

Mg and Li Stable Isotope Ratios of Rocks, Minerals, and Water in an Outlet Glacier of the Greenland Ice Sheet

Ruth S. Hindshaw[1]*, **Jörg Rickli**[2] **and Julien Leuthold**[2]

[1] Department of Earth Sciences, University of Cambridge, Cambridge, United Kingdom, [2] Department of Earth Sciences, Institute of Geochemistry and Petrology, ETH Zurich, Zurich, Switzerland

Magnesium and lithium stable isotope ratios (δ^{26}Mg and δ^{7}Li) have shown promise as tools to elucidate biogeochemical processes both at catchment scales and in deciphering global climate processes. Nevertheless, the controls on riverine Mg and Li isotope ratios are often difficult to determine as a myriad of factors can cause fractionation from bulk rock values such as secondary mineral formation and preferential weathering of isotopically distinct mineral phases. Quantifying the relative contribution from carbonate and silicate minerals to the dissolved load of glacierized catchments is particularly crucial for determining the role of chemical weathering in modulating the carbon cycle over glacial-interglacial periods. In this study we report Mg and Li isotope data for water, river sediment, rock, and mineral separates from the Leverett Glacier catchment, West Greenland. We assess whether the silicate mineral contributions to the dissolved load, previously determined using radiogenic Sr, Ca, Nd, and Hf isotopes, are consistent with dissolved Mg and Li isotope data, or whether a carbonate contribution is required as inferred previously for this region. For δ^{7}Li, the average dissolved river water value (+19.2 ± 2.5‰, 2SD) was higher than bedrock, river sediment, and mineral δ^{7}Li values, implying a fractionation process. For δ^{26}Mg, the average dissolved river water value (−0.30 ± 0.14‰, 2SD) was within error of bedrock and river sediment and within the range of mineral δ^{26}Mg values (−1.63 to +0.06‰). The river δ^{26}Mg values are consistent with the mixing of Mg derived from the same mineral phases previously identified from radiogenic isotope measurements as controlling the dissolved load chemistry. Glacier fed rivers previously measured in this region had δ^{26}Mg values ~0.80‰ lower than those measured in the Leverett River which could be caused by a larger contribution from garnet (−1.63‰) dissolution compared to Leverett. This study highlights that dissolved Mg and Li isotope ratios in the Leverett River are affected by different processes (mixing and fractionation), and that since variations in silicate mineral δ^{26}Mg values exist, preferential weathering of individual silicate minerals should be considered in addition to carbonate when interpreting dissolved δ^{26}Mg values.

Keywords: chemical weathering, Leverett glacier, mineral separates, silicate, Li isotopes, Mg isotopes

Edited by:
Sophie Opfergelt,
Catholic University of Louvain,
Belgium

Reviewed by:
Anne-Sophie Bouvier,
Université de Lausanne, Switzerland
Jacob Clement Yde,
Western Norway University of Applied
Sciences, Norway
Christopher Robert Pearce,
University of Southampton,
United Kingdom

***Correspondence:**
Ruth S. Hindshaw
ruth.hindshaw@gmail.com

Specialty section:
This article was submitted to
Geochemistry,
a section of the journal
Frontiers in Earth Science

Received: 18 August 2019
Accepted: 14 November 2019
Published: 29 November 2019

Citation:
Hindshaw RS, Rickli J and Leuthold J
(2019) Mg and Li Stable Isotope
Ratios of Rocks, Minerals, and Water
in an Outlet Glacier of the Greenland
Ice Sheet. Front. Earth Sci. 7:316.
doi: 10.3389/feart.2019.00316

1. INTRODUCTION

Chemical weathering in glacierized regions results in water with a chemical composition distinct to that originating from non-glacierized regions (e.g., Tranter, 2003). Glacial erosion produces fine grained sediments that, combined with high discharge conditions during the melt season, leads to the preferential weathering of mineral phases such as calcite, sulfide, and biotite, resulting in elevated Ca and K concentrations (Anderson et al., 1997; Blum and Erel, 1997; Tranter et al., 2002). Glacial runoff can contain elevated concentrations of key nutrients such as iron (Raiswell et al., 2006; Bhatia et al., 2013; Hawkings et al., 2014), phosphorus (Hawkings et al., 2016), and silica (Meire et al., 2016; Hawkings et al., 2017) and therefore has a direct impact on the adjacent fjord environment (Wehrmann et al., 2014; Hopwood et al., 2015) and potentially the wider ocean.

Understanding how glaciation alters chemical fluxes and the underlying chemical weathering reactions is important for understanding how weathering reactions changed during glacial-interglacial cycles (Vance et al., 2009; AMAP, 2017; Hawkings et al., 2017). If calcite and sulfide weathering dominate fluxes in glacial catchments, as concluded from studies of alpine glaciers, then these areas would not contribute to long-term removal of CO_2, and may even be a source (Sharp et al., 1995; Torres et al., 2017). However, recent studies of ice sheets, in particular from outlet glaciers of the Greenland Ice Sheet, indicate that silicate weathering is dominant (Graly et al., 2014; Hindshaw et al., 2014; Andrews and Jacobson, 2018) and therefore large-scale glaciation could contribute to the drawdown of atmospheric CO_2 over geological timescales (Walker et al., 1981; Berner et al., 1983).

A first estimate of the relative contributions of carbonate and silicate weathering to dissolved fluxes can be done by applying an end-member mixing analysis to major ion concentrations, utilizing "ideal" end-members (e.g., Gaillardet et al., 1999). However, this method is particularly problematic in glacierized catchments due to weathering incongruency (net effect of dissolution and precipitation/adsorprtion reactions both with respect to bulk rock and with respect to individual minerals), ion exchange and adsorption reactions which occur in glacial streams characterized by high sediment loads and dilute solute concentrations (e.g., Tranter, 2003). For example, the use of end-member ion ratios such as Ca/Na to calculate the relative proportions of carbonate and silicate weathering could overestimate the carbonate contribution if the preferential release of Ca from individual silicate minerals is not accounted for (Oliva et al., 2004; Hindshaw et al., 2011). Isotope tracers (stable and radiogenic) have been developed in recent decades to refine the apportioning of carbonate and silicate weathering in catchment studies (e.g., Blum et al., 1994; Bullen and Bailey, 2005; Nezat et al., 2010; Sullivan et al., 2016).

Magnesium (Mg) and lithium (Li) isotopes have shown promise at tracing weathering sources and processes (Tomascak et al., 2016; Teng, 2017) and have both been applied to study glacial weathering in the Kangerlussuaq area of West Greenland (**Figure 1**, Wimpenny et al., 2010, 2011). Magnesium is the 5th most abundant element in the continental crust (MgO = 3.7 wt.%, Wedepohl, 1995) and it is intimately coupled to the carbon cycle through the formation of magnesium carbonates (Berner et al., 1983). Carbonate δ^{26}Mg values (−6 to 0‰) tend to be lower than silicate rocks (−1 to +2‰) potentially enabling the partitioning of carbonate and silicate weathering (Teng, 2017). However, Mg isotopes are also fractionated during secondary clay formation and biological processes (Tomascak et al., 2016). Lithium is a trace element predominantly hosted in silicate rocks (Huh et al., 1998) and as a consequence, Li isotopes have the potential to be a tracer of silicate weathering (e.g., Misra and Froelich, 2012). In natural systems secondary mineral formation and/or adsorption onto particles imparts a large (often >10‰) fractionation and biological processes have minimal impact (e.g., Pistiner and Henderson, 2003; Vigier et al., 2008; Clergue et al., 2015). It is therefore hypothesized that the Li isotopic composition of rivers provides information on the balance between dissolution of primary (silicate) minerals and secondary mineral formation occurring in a catchment (e.g., Dellinger et al., 2015). Waters draining from the Greenland ice sheet were found to have lower δ^{26}Mg values compared to suspended sediment and this was attributed to disseminated carbonate weathering (Wimpenny et al., 2011). The δ^{7}Li values were higher than suspended sediment and the authors concluded this was due to adsorption to subglacially formed amorphous iron hydroxides (Wimpenny et al., 2010). Nevertheless, mineral separates to constrain local end-members were not analyzed, which leads to an element of uncertainty in source apportionment.

Research on the δ^{26}Mg values of mineral separates has demonstrated variation in δ^{26}Mg values which in some cases overlaps with the δ^{26}Mg range in carbonate rocks (−5.57 to −0.38‰, Teng, 2017), e.g., biotite (−0.40 to +0.44‰, Shen et al., 2009; Liu S.-A. et al., 2010; Ryu et al., 2011), chlorite (−1.82 to +0.40‰, Ryu et al., 2011; Pogge von Strandmann et al., 2015; Chapela Lara et al., 2017), clinopyroxene (−0.62 to +0.43‰, Pogge von Strandmann et al., 2011; Wang et al., 2012, 2014; Hu et al., 2016; Li et al., 2016; Chen et al., 2018; Stracke et al., 2018), and garnet (−1.96 to −0.37‰, Wang et al., 2012, 2014; Pogge von Strandmann et al., 2015; Hu et al., 2016; Li et al., 2016; Stracke et al., 2018). Within single rock samples, resolvable variation has also been observed e.g., 1.5‰ between chlorite and hornblende in granite (Ryu et al., 2011). This silicate mineral source variation in δ^{26}Mg has only recently begun to be acknowledged as a source of variation in river δ^{26}Mg values (Chapela Lara et al., 2017; Kimmig et al., 2018). Given that recent studies of chemical weathering in the Kangerlussuaq area of West Greenland have stressed the role of silicate weathering (Wimpenny et al., 2011; Andrews and Jacobson, 2018), we wanted to test whether silicate mineral variation in δ^{26}Mg values could also account for low δ^{26}Mg values in river samples from this area. There is less data on Li isotope variation between minerals (Teng et al., 2006; Pogge von Strandmann et al., 2011; Penniston-Dorland et al., 2017; Neukampf et al., 2019) but variation has been reported where there is a difference in coordination number (∼3‰, Wunder et al., 2007) and in field sites with a history of magmatic differentiation (−8 to +17‰, Marks et al., 2007). Dissolved δ^{7}Li values may therefore also be impacted by variations in silicate mineral isotopic compositions, particularly when the geology of the catchment is heterogeneous.

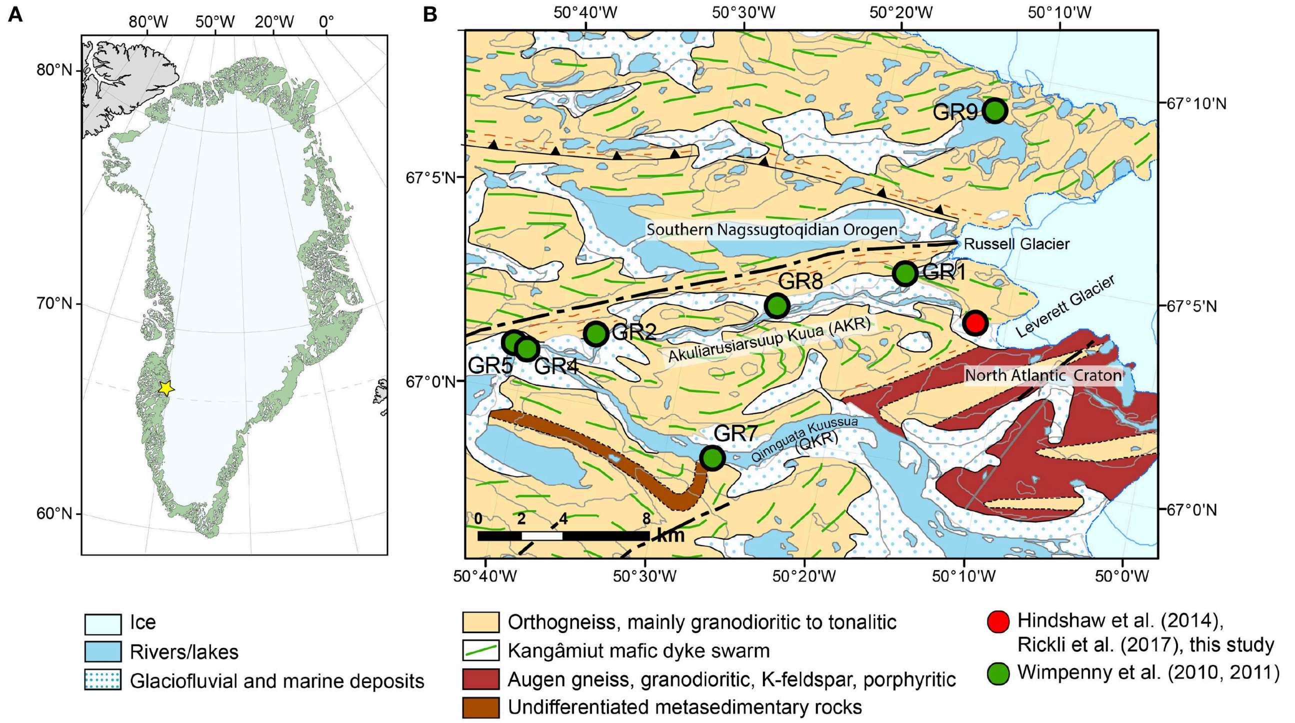

FIGURE 1 | (A) The study site is indicated by a yellow star. **(B)** Geological map of the Kangerlussuaq area of West Greenland. The location of the time series of water samples from the river draining Leverett Glacier analyzed in this study is marked as a red circle. River sediment and rock samples were also collected at this location. The water samples with a glacier contribution, bedload, suspended sediment, and bedrock samples analyzed by Wimpenny et al. (2010, 2011) are marked as green circles together with their sample names (GR1–GR9). Watson River refers to the river after the confluence of the Qinnguata Kuussua and Akuliarusiarsuup Kuua rivers. Geological basemap from Geological Survey of Denmark and Greenland, and Ministry of Mineral Resources under the Government of Greenland. Datum and projection: WGS84 UTM Zone 24N.

Previous work on water draining the Leverett Glacier, an outlet glacier in the Kangerlussuaq area (**Figure 1**), used Ca, Sr, Nd, and Hf data of water, rock, and mineral separates to constrain chemical weathering reactions contributing to the dissolved load (Hindshaw et al., 2014; Rickli et al., 2017). Our aim in this study was to analyse mineral separates, bulk rock samples, sediments, and water samples for δ^{26}Mg and δ^{7}Li in order to test whether the dissolution of silicate minerals previously identified as controlling the dissolved load composition in this catchment were consistent with dissolved δ^{26}Mg and δ^{7}Li values from this region or whether a carbonate contribution to dissolved δ^{26}Mg is indeed required.

2. FIELD SITE

Leverett Glacier is a land-terminating outlet glacier of the Greenland Ice Sheet situated on the west coast of Greenland ∼ 25 km east of Kangerlussuaq (Søndre Strømfjord, **Figure 1**). Together with Russell Glacier to the north these two glaciers form one of three subcatchments of the Watson River with a combined area of 900 km^2 (Lindbäck et al., 2015). Bartholomew et al. (2011) estimated the hydrological catchment of Leverett Glacier to be 600 km^2. The largest subcatchment (11,100 km^2) is the Ørkendalen subcatchment to the south containing the Qinnguata Kuussua River (QKR). The third subcatchment (Point 660) lies to the north of Russell Glacier and has an area of 40 km^2. Water draining Point 660 catchment feeds into water draining Russell Glacier. Approximately 19 km upstream from Kangerlussuaq this water merges with the Leverett River to form the Akuliarusiarsuup Kuua River (AKR). Unlike Leverett River, which has a single subglacial portal, the river draining past Russell Glacier has several inputs of water sourced from both non-glacial lakes and sub-glacial sources (Rennermalm et al., 2012). The watershed areas referred to above are the maximum summer extent as the catchment area grows and shrinks each melt-season in line with the expansion and contraction of the subglacial drainage network (Chandler et al., 2013). In addition, there is water piracy where the catchment areas and positions change with subglacial water pressure (Lindbäck et al., 2015). In 2009, the melt season was ∼115 days long at Leverett and a peak discharge of 317 m^3 s^{-1} was measured on 16th July (Bartholomew et al., 2011).

Leverett Glacier drains distinct tectonic units of Precambrian age (**Figure 1**). To the north of Leverett is the Southern Nagssugtoqidian Orogen, which is composed of re-worked epidote amphibolite to amphibolite facies basement tonalitic to granodioritic orthogneiss (Escher, 1971; Van Gool et al., 2002).

The orthogneisses were intruded by the 2.04 Ga Kangâmiut mafic dyke swarm (Cadman et al., 2001), now forming amphibolite lenses, with deformation increasing toward the north (Van Gool et al., 2002; Engström and Klint, 2014). To the south of Leverett is the North Atlantic Craton, composed of granulite-facies granodioritic augen orthogneiss and paragneiss locally (Escher et al., 1976; Henriksen et al., 2000). The augen orthogneiss was intruded by late Archaean felsic intrusions (45 km south of the Leverett Glacier) related to the Qôrqut granite (ca. 2.5 Ga, Escher et al., 1976; Nutman et al., 2010). See Brown et al. (1981) for a petrographic description of the Qôrqut granite. The exact boundary between the above-described tectonic units underneath the Greenland ice sheet is unknown.

The area experiences an Arctic climate with a mean annual temperature (2001–2011) of −3.9°C (Hanna et al., 2012). There are strong seasonal variations in temperature: the mean temperatures in winter and summer are −16.1 and +10.3°C, respectively (Hanna et al., 2012). The region receives relatively little precipitation [258 ± 63 mm (2001–2012), (Mernild et al., 2015)] and annual evapotranspiration exceeds annual precipitation (Johansson et al., 2015). In the non-glacierized area, permafrost is continuous with an active layer thickness of 0.1–2.5 m (Van Tatenhove, 1996).

3. METHODS

3.1. Water Samples

The Leverett River was sampled twice a day from 5 July to 1 August 2009 at 67°03.755′N, 50°11.874′W. The sampling location was ∼1 km downstream from the glacier front (**Figure 1**). At this location there was no braiding in the river channel and the water was turbulent. Therefore, we assume that the river was well-mixed and samples taken at the edge of the river are representative of bulk river water chemistry. Temperature and pH were measured *in situ* (Hanna HI 98160 pH meter). Water samples were collected in a bucket previously rinsed with river water and filtered on the day of collection through 0.2 μm nylon filters using a Nalgene filtration unit connected to a hand pump. Filtered samples were stored in pre-cleaned HDPE bottles and acidified to pH 2 with single-distilled concentrated HNO_3. Discharge was measured as described in Bartholomew et al. (2011). In terms of the number of days, the sampling campaign covered 24% of the 2009 melt-season and in terms of water flux it covered 45% of the total of that year.

The hydrology and chemistry of the Leverett River during the 2009 melt-season have previously been reported (Bartholomew et al., 2011; Hindshaw et al., 2014; Rickli et al., 2017) and the main results are summarized here. The hydrology was typical for a glacierized catchment with strong seasonal variation. Before June discharge was <6 m^3/s and rapidly increased to a maximum of 317 m^3/s on 16 July before decreasing again (Bartholomew et al., 2011). The sampling season was divided into three periods based on changes in hydrochemistry (Hindshaw et al., 2014). Immediately prior to the sampling period there was a spike in discharge linked to the sudden drainage of supraglacial lakes (**Figure 2**, Bartholomew et al., 2011). This pulse of water coincided with high pH, suspended sediment and ion concentrations. The first period (P1) was defined as the period from the start of measurements to the end of the marked decrease in element (**Figure 2**) and suspended sediment concentrations. The second period (P2) was characterized by increasing discharge and decreasing $^{87}Sr/^{86}Sr$ values. During this period the subglacial drainage system was expanding. The third period (P3) was characterized by decreasing discharge with a diurnal cycle. During P2 and P3 element concentrations were relatively stable (**Figure 2**). High radiogenic Sr and Ca isotope ratios at the start of the sampling period were interpreted to reflect flushed out water stored over winter with ions derived from chlorite and feldspar weathering. As the melt-season progressed and the subglacial drainage system expanded, the relative contribution of unradiogenic trace minerals such as epidote was inferred to increase as water-rock residence time decreased, resulting in the observed decrease in radiogenic Sr and Ca isotope ratios (Hindshaw et al., 2014). For this study a subset of ten samples were selected for isotope analyses covering all three hydrological periods (**Figure 2**). Samples were selected to coincide with those already measured for Ca and Sr isotopes. We focussed in particular on P2 where the subglacial drainage system expands and where a decrease in $^{87}Sr/^{86}Sr$ from 0.745 to 0.741 was interpreted to represent a change in the relative contribution of different mineral weathering reactions to the dissolved load (Hindshaw et al., 2014).

Wimpenny et al. (2010, 2011) collected their glacial samples between 11 and 14 July 2006 but discharge data was not reported. Discharge data from the Watson River at Kangerlussuaq shows that during this period discharge was increasing and comparable to the form of the hydrograph in 2009 for the same time period (van As et al., 2017). Both years had similar total water flux: 5.4 ± 2.9 km^3 in 2006 and 4.9 ± 0.9 km^3 in 2009, and peak flux: 1,690 ± 1,190 $m^3\ s^{-1}$ in 2006 and 1,430 ± 210 $m^3\ s^{-1}$ in 2009 (van As et al., 2017). Therefore, these samples were likely collected when discharge conditions resembled those of P2 and we can assume that the hydrological conditions during the two studies are comparable.

3.2. Rock, Sediment, and Mineral Separates

Four rock samples representing the dominant rocks types on the north side of Leverett Glacier (Southern Nagssugtoqidian Orogen, **Figure 1**) were collected and described in Hindshaw et al. (2014) and Rickli et al. (2017). These rock samples were two orthogneisses and two amphibolites and were located within 1 km of where the water samples were taken. In addition, two bulk samples of river sediment were analyzed. These samples were analyzed in this study for Mg and Li isotopes.

A sample of augen gneiss from the North Atlantic Craton (**Figure 1**) collected 20 km southwest of Leverett (50.338066 W, 66.894928 N) by the Geological Survey of Denmark and Greenland (GEUS) was analyzed in Rickli et al. (2017) where this sample was referred to as "Archaean granite." Rickli et al. (2017) concluded, based on Nd isotope data, that the contribution of gneiss from the North Atlantic Craton to the dissolved load of Leverett River was negligible and therefore this rock was

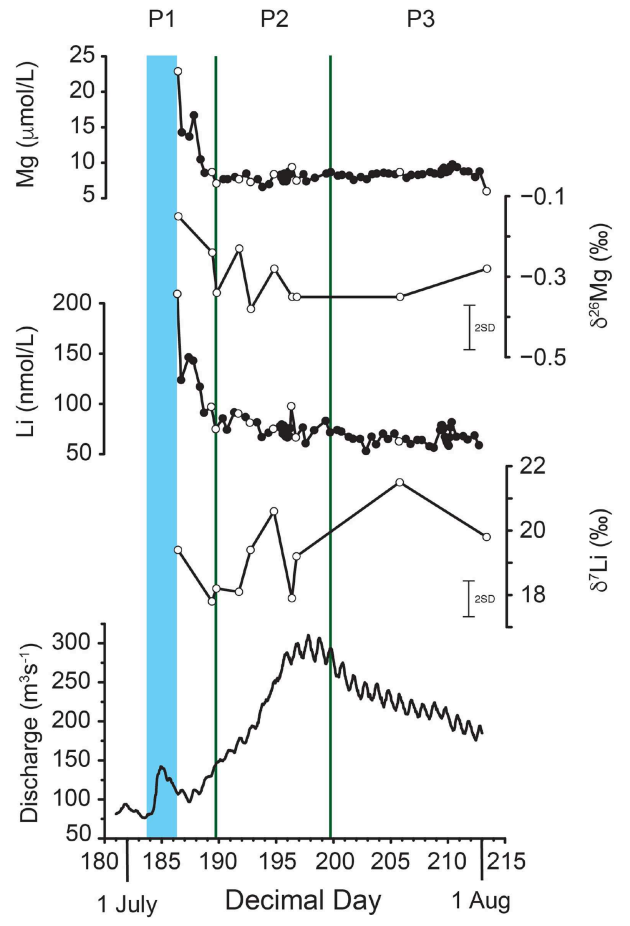

FIGURE 2 | Time series. From top to bottom: Mg concentration, δ^{26}Mg, Li concentration, δ^7Li and discharge. White circles are samples analyzed for this study and black circles are time series data from Hindshaw et al. (2014). The blue band marks the fourth outburst event of 2009 which coincided with the drainage of a supraglacial lake (Bartholomew et al., 2011). The green lines mark indicate divisions between three hydrological periods (P1, P2, and P3) identified by Hindshaw et al. (2014) based on changes in hydrochemistry. P1 is influenced by the outburst event, P2 is the rising limb of the hydrograph, and P3 the falling limb.

not analyzed for Li and Mg isotopes (see further discussion in section 5.3).

Rock samples were washed, weathered surfaces removed with a diamond saw and crushed using a jaw crusher. A portion of each rock sample and all of the other solid samples were ground to a fine powder using a rotary disc mill with an agate grinding set for further analysis. The remainder of the rock samples were ground to <1,000 μm and mineral separates were obtained from the <425 μm fraction using heavy liquids, magnetic separation and hand-picking.

Two river sediments (Sed1 and Sed2, **Table 1**) were collected from the riverbank, and can therefore be considered comparable to the bedload samples reported in Wimpenny et al. (2010, 2011).

Mineral abundances were obtained by point counting on thin section (rock samples) and EPOXY mounts (sediments) microphotographs combined with scanning electron microscope (SEM) back-scattered images (Hitachi S-3500N microscope equipped with Thermo Noran energy dispersive spectrometer at the University of Bristol) and element maps.

The primary rock forming minerals in the orthogneiss samples (Ro2 and Ro4) are K-feldspar (24–43 wt.%), plagioclase (21–49 wt.%), and quartz (22–27 wt.%). These rocks also contain chlorite (2–7 wt.%) and minor (<3 wt.%) epidote, titanite, zircon, hornblende, and apatite (Rickli et al., 2017). In both orthogneisses, chlorite and epidote replaced biotite during green schist metamorphism. The garnet amphibolite rock sample Ro1 is primarily composed of hornblende (71 wt.%), plagioclase (11 wt.%), and quartz (8 wt.%) together with lesser amounts of garnet (5 wt.%), titanite (3 wt.%), and magnetite (2 wt.%) (Rickli et al., 2017). Amphibolite Ro3 contains hornblende (47 wt.%), clinopyroxene (24 wt.%), plagioclase (15 wt.%), and scapolite (10 wt.%) and trace minerals are epidote (3 wt.%) and titanite (<1 wt.%) (Rickli et al., 2017). Although the alteration of plagioclase to Ca-rich carbonate was observed in the orthogneiss samples (Ro2 and Ro4, Hindshaw et al., 2014) through saussuritization, the presence of Mg-bearing carbonate minerals was not detected in SEM chemical maps of the Leverett catchment rocks and sediments. For this study minerals with high Mg concentration were selected for analysis: garnet, hornblende, clinopyroxene, and chlorite.

The mineralogy of sediment samples reflected a mixture of gneiss and amphibolite and contained plagioclase (39–44%), quartz (33–37%), K-feldspar (7–16%), hornblende (7–11%), garnet (2–4%), clinopyroxene (<3%), and minor (<2%) apatite, biotite, chlorite, epidote, ilmenite, orthopyroxene, magnetite, titanite, and zircon (Rickli et al., 2017).

Approximately 0.2 g of each rock powder or sediment sample and 0.02 g of each mineral were digested in a mixture of concentrated, single-distilled HNO_3, HCl, and HF. The solution was repeatedly dried down and redissolved until clear and was finally redissolved in 2% HNO_3 for cation analysis.

3.3. Concentration Analysis

Magnesium concentrations in water, rock, and mineral separate samples were measured by inductively-coupled plasma optical emission spectrometry (ICP-OES, Vista-MPX, Varian Inc., USA at ETH Zurich) as described and reported in Hindshaw et al. (2014). The Mg concentration of the water standard SLRS-4 (National Research Council Canada) was 1,686 ± 40 μg L^{-1} (2SD, $n = 7$) compared to a recommended value of 1,600 μg L^{-1} (Yeghicheyan et al., 2007). Magnesium concentrations of minerals in rocks were additionally determined using a Cameca SX100 electron microprobe analyser (EMPA) at University of Bristol and a JEOL JXA-8200 EPMA at ETH Zurich, with a 15 kV accelerating voltage and a beam current of 20 nA. Natural and synthetic silicates and oxides were used as standards and the error on concentration measurements was typically less than 2%. Lithium concentrations were measured by ICP-OES. The Li concentration of the water standard SLRS-4 (National Research Council Canada) was 0.56 ± 0.03 μg L^{-1} (2SD, $n = 6$) compared to a recommended value of 0.54 μg L^{-1} (Yeghicheyan et al., 2007).

TABLE 1 | Magnesium and lithium concentrations and isotope ratios of rocks, mineral separates, and river sediment samples.

Name	Abundance wt.%	Mg[a] g/kg	Mg[b] g/kg	Fraction[c] Mg	δ^{25}Mg ‰	2SD	δ^{26}Mg ‰	2SD	Li mg/kg	Fraction[d] Li	δ^{7}Li ‰	2SD
Ro1 - Garnet Amphibolite		48.5			–0.10	0.05	–0.20	0.06	5.2		6.8	0.7
Garnet	5	11.2	10.9	0.02	–0.84	0.04	–1.63	0.06	5.3	0.01	6.6	1.3
Hornblende	71	41.9	46.2	0.98	–0.08	0.10	–0.16	0.11	46.4	0.96	6.9	0.4
Ro3 - Amphibolite		47.0			0.04	0.08	0.09	0.13	9.19		8.3	0.1
Clinopyroxene	24	70.0	70.3	0.37	–0.07	0.03	–0.14	0.11	44.3	0.43	6.5	0.3
Hornblende	47	62.4	59.1	0.63	0.03	0.04	0.06	0.08	26.4	0.50	12.1	0.2
Ro2 - Orthogneiss		6.5			–0.04	0.06	–0.08	0.09	5.4		6.3	0.9
Chlorite	2	76.3	72.7	0.86	–0.11	0.05	–0.21	0.11	59.2	0.36	3.4	0.2
K-feldspar	24	0.9	0.0	0.11	n.m.	n.m.	n.m.	n.m.	10.0	0.64	n.m.	n.m.
Plagioclase	49	0.1	0.3	0.03	n.m.	n.m.	n.m.	n.m.	0.0	0.00	n.m.	n.m.
Ro4 - Orthogneiss		10.8			–0.09	0.02	–0.20	0.02	6.3		5.0	0.8
Chlorite	7	32.5	82.7	0.96	–0.15	0.02	–0.29	0.05	117.9	0.66	3.2	2.0
Hornblende	<1	38.1	n.m.	0.00	–0.15	0.05	–0.28	0.08	n.m.	0.00	n.m.	n.m.
Epidote	3	1.5	0.6	0.02	n.m.	n.m.	n.m.	n.m.	12	0.03	n.m.	n.m.
Feldspar[e]	64	0.1	0.1	0.03	n.m.	n.m.	n.m.	n.m.	6	0.31	n.m.	n.m.
Feldspar+Epidote[f]	67	*0.7*		0.04					*6.4*	0.34	*8.5*	*2.1*
Other solid samples												
Sed1		20.9			–0.18	0.14	–0.33	0.16	n.m.		4.9	0.4
Sed2		12.4			–0.26	0.07	–0.48	0.15	81.2		n.m.	n.m.

*Rock samples are all from the Southern Nagssugtoqidian Orogen (**Figure 1**). Mineral abundances and Mg concentrations are from Hindshaw et al. (2014).*
n.m., not measured.
[a] *Measured by ICP-OES.*
[b] *Measured by microprobe.*
[c] *Calculated using ICP-OES concentrations.*
[d] *Plagioclase and epidote account for the rest of the Li fraction in Ro1 and Ro3.*
[e] *Feldspar = Plagioclase and K-feldspar.*
[f] *Values in italics are calculated by mass balance using the fraction and concentrations of Mg and Li reported for the respective minerals.*

3.4. Isotope Analysis

An aliquot of each sample, corresponding to ∼ 15 ng Li was dried down in a teflon beaker. The solid residue was re-dissolved in concentrated HNO_3, dried down again and re-dissolved in 0.4 M HCl for column chemistry. The first column contained 1 mL Bio-Rad AG 50W-X12 200-400 mesh resin. In the first column the sample was eluted in 0.4 M HCl and the first 15 of 50 mL containing Li and Na were collected. The Mg cut was then collected in 15 mL 1 M HCl. For rocks and mineral samples, a 0.5 M HF step was inserted prior to the 0.4 M HCl elution step in order to elute Al, Ti, and Zr (Tipper et al., 2008). The Mg cut from the first column pass was passed through the column a second time and Mg was collected in a small volume of 6 M HCl in order to minimize procedural blanks (Tipper et al., 2008). Lithium was purified from the Li-Na cut using a column containing 3 mL Bio-Rad AG 50W-X12 200–400 mesh resin, eluting with 0.2 M HCl (James and Palmer, 2000; Hindshaw et al., 2018). Standards were processed in an identical manner to samples.

Both isotope systems were measured on a Neptune Plus MC-ICP-MS (Thermo, University of Cambridge) using an APEX sample introduction system. Magnesium isotopes were run at 100 ppb and Li at 5 ppb. Magnesium and Li were standard-sample bracketed to DSM3 and L-SVEC (NIST RM 8545), respectively. For each isotope system mono-elemental secondary standards were analyzed: ^{6}Li-N and ^{7}Li-N for Li, and “Cambridge1” and “Zurich1” for Mg. The values obtained for these standards are reported in **Table 2** and are in agreement with previously reported values (Tipper et al., 2006, 2012b; Carignan et al., 2007; Millot et al., 2010; Wimpenny et al., 2014). Seawater (OSIL IAPSO batch P157) was processed identically to the water samples and gave values of δ^{26}Mg = –0.81 ± 0.11 (2SD, $n = 5$) and δ^{7}Li = +31.4 ± 0.4 (2SD, $n = 3$), in agreement with both our long-term values for this standard (δ^{26}Mg = –0.80 ± 0.11, 2SD, $n = 25$; δ^{7}Li = +30.8 ± 1.1, 2SD, $n = 45$) and literature values (δ^{26}Mg = –0.83‰, Teng et al., 2015; δ^{7}Li = +30.8‰, Rosner et al., 2007). The synthetic water standard CCS2 (Tipper et al., 2008) and USGS granite G-2 were measured for Mg isotopes giving values of −2.70 ± 0.14 (2SD, $n = 13$) and −0.05 ± 0.13 (2SD, $n = 5$) compared to the respective literature values of −2.71 ± 0.07‰ (Tipper et al., 2008) and −0.15 ± 0.07‰ (Teng et al., 2015). Lithium isotope measurements of USGS granite G-2 were +0.9 ± 1.0‰ (2SD, $n = 6$) compared to literature values of +0.1 ± 1.8‰ (Barnes et al., 2012), +0.1 ± 0.8‰ (Phan et al., 2016), and +0.3 ± 1.9‰ (Liu X.-M. et al., 2010). The long-term 2SD values from measurements of seawater standards (δ^{7}Li = ±1.1‰, δ^{26}Mg = ±0.11‰) are used as a measure of the overall uncertainty of the analytical procedure and is indicated on all figures.

TABLE 2 | Major cation (Hindshaw et al., 2014) and isotopic composition of Leverett River water samples in 2009.

Sample name	Local time	Runoff (m/s)	pH	Ca μmol/L	Mg μmol/L	Na μmol/L	K μmol/L	Li nmol/L	δ^7Li ‰	2SD	δ^{25}Mg ‰	2SD	δ^{26}Mg ‰	2SD
0705a.m.	09:10	108	9.32	67.7	22.9	110.1	58.4	192.5	19.4	0.9	–0.07	0.04	-0.15	0.09
0708a.m.	08:25	130	8.48	34.0	8.7	48.4	32.1	98.4	17.8	0.2	–0.12	0.07	–0.24	0.12
0708p.m.	17:45	145	8.02	26.6	7.1	35.9	25.2	78.1	18.2	0.2	–0.18	0.04	–0.34	0.07
0710p.m.	17:00	175	7.68	30.0	7.7	38.9	39.4	87.4	18.1	0.4	–0.12	0.04	–0.23	0.09
0711p.m.	17:15	191	8.28	28.6	7.3	36.4	25.3	83.0	19.4	0.1	–0.19	0.02	–0.38	0.06
0713p.m.	18:20	249	8.07	28.4	8.4	32.9	27.3	78.3	20.6	0.3	–0.14	0.00	–0.28	0.06
0715a.m.	08:00	274	8.25	38.8	9.4	39.4	28.4	109.7	17.9	0.3	–0.19	0.13	–0.35	0.16
0715p.m.	17:35	299	7.96	29.2	7.5	33.3	22.0	87.3	19.2	0.4	–0.18	0.10	–0.35	0.15
0724p.m.	17:50	235	7.88	33.5	8.7	36.7	23.9	77.9	21.5	0.3	–0.18	0.01	–0.35	0.02
0801a.m.	08:00	172	7.88	20.8	6.0	35.0	21.5		19.8	0.1	–0.14	0.01	–0.28	0.00
Mono-elemental standards														
^{6}Li-N ($n = 59$)									–8.1	0.9				
^{7}Li-N ($n = 50$)									30.2	0.9				
Cambridge1 ($n = 29$)											–1.35	0.06	–2.61	0.12
Zurich1 ($n = 21$)											–1.73	0.10	–3.35	0.20

4. RESULTS

4.1. Rock and Mineral Separates

The range in isotope values of the four bulk rock samples is δ^{26}Mg = –0.20 to +0.09‰ and δ^7Li = +5.0 to +8.3‰ (**Table 1**). The isotopic compositions of the amphibolite samples (Ro1 and Ro3) overlap with those of the orthogneiss samples (Ro2 and Ro4) for δ^7Li and δ^{26}Mg. For Li, the range in bulk rock δ^7Li values agrees with the range measured by Wimpenny et al. (2010) for rocks from the Southern Nagssugtoqidian Orogen in the Kangerlussuaq region (+5.8 to +10.4‰, **Figure 1**, **3**).

The river sediment sample Sed1 has a δ^7Li value of +4.9‰ (**Table 1**) which is at the lower end of the range measured in bulk rock samples from this study and bedload samples (+4.8 to +6.9‰) measured by Wimpenny et al. (2010) (**Figure 3**). For Mg, the δ^{26}Mg values of the river sediment samples (–0.33 and –0.48‰, **Table 1**) are in the same range as bedload samples reported in Wimpenny et al. (2011) (–0.43 to –0.53‰), but are lower than the rock samples from this study (**Figure 3**). Based on the major element composition and plagioclase chemistry of the river sediment samples, it was determined that of the two observed orthogneiss varieties (pink and gray), gray orthogneisses like Ro4 have a dominant contribution to the sediment load (Hindshaw et al., 2014). This conclusion is supported by the fact that for both Li and Mg, rock Ro4 is closest in isotope composition to the river sediment (**Figure 3**). The lower δ^{26}Mg value of the river sediment samples compared to Ro4 is likely due to the contribution of garnet (2–4%, Rickli et al., 2017) which is not present in Ro4 and is derived from the amphibolite rocks.

The measured Mg concentrations in the minerals obtained by ICP-OES agree well with the analysis of those same minerals by microprobe (**Table 1**). Two exceptions are K-feldspar in Ro2, where the Mg concentration obtained by ICP-OES is over ten times greater than the microprobe measurement and chlorite in Ro4, where the Mg concentration obtained by ICP-OES is half the microprobe measurement. We note that the isotope and concentration values reported by ICP-OES are unlikely to reflect the pure mineral phase as they will also include a contribution from inclusions and/or trace amounts of other minerals not removed during hand-picking. Both discrepancies are likely caused by the alteration of K-feldspar to chlorite (Garrels and Howard, 1957) making it difficult to separate these minerals during hand-picking. Based on a mass balance calculation, nearly all the Mg and Li in Ro1 is contained in hornblende (>96%) whereas in Ro3 both clinopyroxene and hornblende host these elements (**Table 1**). In the orthogneiss samples the largest fraction of Mg and Li in Ro4 is in chlorite (96 and 66%, respectively) and chlorite is also the primary host of Mg in Ro2 (86%). Lithium in Ro2 is mainly contained in K-feldspar (including any potential inclusions) (64%, **Table 1**) and the remaining Li is in chlorite (36%, **Table 1**).

The mineral separates display a large range in δ^{26}Mg from –1.63‰ in garnet (Ro1) to +0.06‰ in hornblende (Ro3, **Table 1**). The range in δ^{26}Mg is comparable to that found within mineral separates from a granodiorite from Boulder Creek, USA (1.53‰, Ryu et al., 2011). Taking all the mineral separates together, hornblende has higher δ^{26}Mg values compared to chlorite (**Figure 3**), consistent with mineral separate data reported by Ryu et al. (2011) but in contrast to Chapela Lara et al. (2017) who observed that chlorite had higher δ^{26}Mg values than both pyroxene (by ∼0.2‰) and amphibole (by ∼0.5‰), though they note that the amphiboles were heavily altered. Garnet had lower δ^{26}Mg values compared to clinopyroxene (**Figure 3**), consistent with previous studies (Wang et al., 2012, 2014; Hu et al., 2016; Li et al., 2016). A large inter-mineral range is also observed in δ^7Li values from +3.2‰ in chlorite (Ro4) to +12.1‰ in hornblende (Ro3, **Table 1**). As for Mg isotopes, hornblende mineral separates have higher δ^7Li values compared to chlorite mineral separates (**Figure 3**), in agreement with Marks et al. (2007).

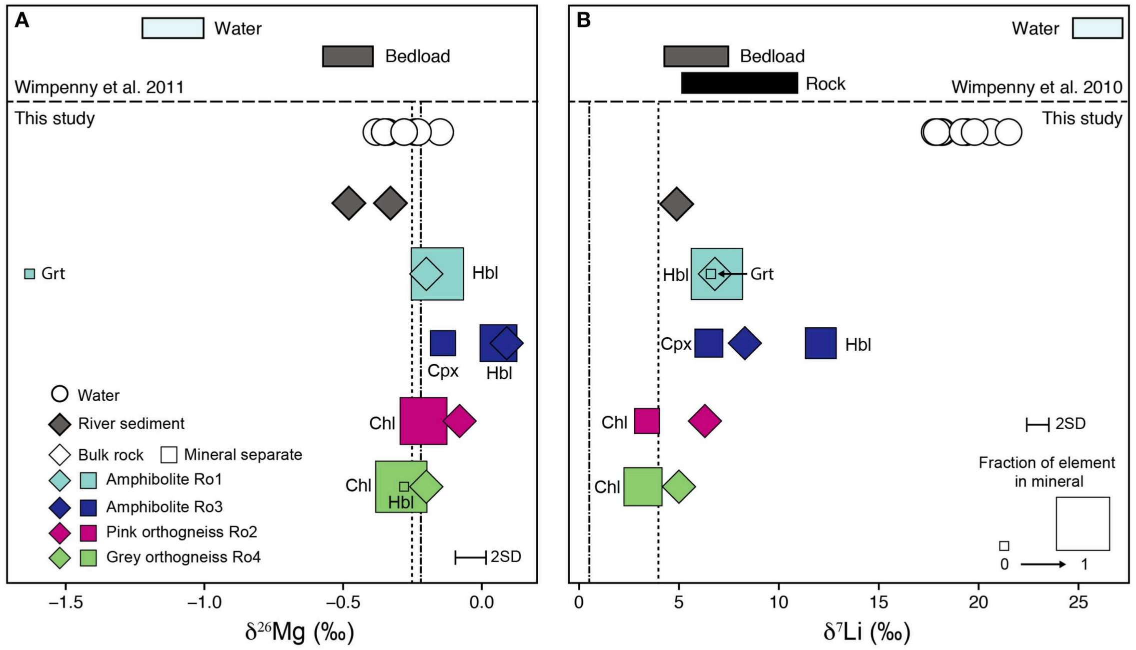

FIGURE 3 | Range of magnesium **(A)** and lithium **(B)** isotope values measured in the rocks, mineral separates, and river water of the Leverett Glacier catchment. Mineral abbreviations are: Grt, garnet; Hbl, hornblende; Chl, chlorite; Cpx, clinopyroxene. The fraction of the element contained in each mineral (**Table 1**) is indicated by the size of the square. Also shown are data from Wimpenny et al. (2010, 2011) which were collected in the same region, but not the same outlet glacier (**Figure 1**). The vertical dotted lines depict the normal mantle value for Mg (–0.25‰, Teng et al., 2010) and the upper mantle value for Li (+4‰, Teng et al., 2004). The dash-dot lines indicate average upper continental crust values for Mg (–0.22‰, Li et al., 2010) and Li (+0.6‰, Sauzéat et al., 2015).

4.2. Hydrochemistry

Similar to Ca and Sr concentrations, Mg and Li concentrations are highest at the start of the sampling period (Mg 0.6 mg/L and Li 1.3 μg/L) and rapidly decrease over a period of 4 days (**Figure 2**, Hindshaw et al., 2014). After the initial decrease, concentrations are stable (Mg ~0.2 mg/L and Li ~0.6 μg/L) with a diurnal cycle (**Table 2**). The stable isotope values of the water samples range from δ^{26}Mg = –0.15 to –0.38‰ and δ^{7}Li = +17.8 to +21.5‰ and no obvious temporal trend is observed in either Li or Mg isotope values despite the aforementioned changes in concentrations and subglacial drainage conditions (**Figure 2**, **Table 2**). Despite the proximity of Leverett Glacier to the sampling locations in Wimpenny et al. (2010, 2011) (**Figure 1**), the Li and Mg isotope values for the water samples in this study are distinct, having lower δ^{7}Li and higher δ^{26}Mg values (**Figure 3**).

5. DISCUSSION

5.1. Inter-mineral Isotope Variation

The range in δ^{26}Mg and δ^{7}Li between all the mineral separates measured in the four rock samples is 1.69 and 8.8‰ respectively. Inter-mineral variations in isotope values have been attributed to equilibrium fractionation (Schauble, 2004, 2011; Wunder et al., 2007; Liu et al., 2018). Coordination number is the first order control: heavy isotopes are preferentially incorporated into sites with a low coordination number (CN) (Oi et al., 1989). Excluding garnet (see later), there is a statistically significant correlation between the δ^{26}Mg and δ^{7}Li values of the measured minerals and bulk rock samples (R^2 = 0.67, $p < 0.01$, **Figure 4**). This trend is consistent with the similar chemical radii of the two elements such that Li can readily substitute for Mg and both elements will therefore likely experience similar bonding environments in a given mineral.

Based on equilibrium fractionation models at a range of temperatures relevant to weathering and igneous processes (273–2,000 K), the δ^{26}Mg and δ^{7}Li values of garnet (CN = 8) are predicted to be lower (Schauble, 2011; Huang et al., 2013) compared to hornblende (CN = 6/5, Wunder et al., 2007) and for Mg isotopes this is what we observe (**Figure 3**). In contrast, the δ^{7}Li value of garnet is not markedly lower than the other minerals as would be predicted if Li was in the dodecahedral site (e.g., Yang et al., 2009). Studies of lithium-rich synthetic garnets have demonstrated that Li can be contained in sites with CNs of 4 and 6 (Mazza, 1988; O'Callaghan et al., 2008; Cussen, 2010; Rettenwander et al., 2016). If this were true for natural garnets then the Li CN may be less than 8 accounting for the δ^{7}Li value that is indistinguishable from the hornblende separate in the same rock (Ro1, **Figure 4**). The low δ^{26}Mg value of garnet, 1.34‰ lower than the δ^{26}Mg values for the other minerals (**Figure 3**), is consistent with data from clinopyroxene-garnet pairs where garnet always has lower δ^{26}Mg values compared to clinopyroxene (Huang et al., 2013; Stracke et al., 2018). The magnitude of the difference increases as metamorphism temperature decreases (Huang et al., 2013; Stracke et al., 2018). Therefore, the relatively large difference between garnet and clinopyroxene observed in

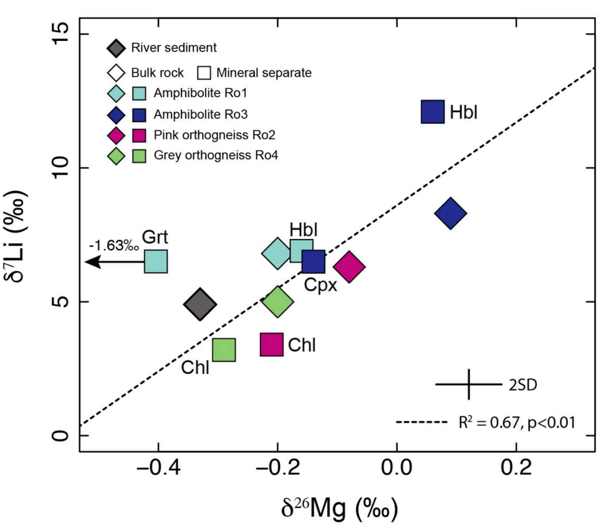

FIGURE 4 | Excluding garnet, where Li and Mg may be held in sites with different coordination numbers, a positive relationship is observed between the δ^{26}Mg and δ^{7}Li values of the rocks (diamonds) and mineral separates (squares). Mineral abbreviations are: Grt, garnet; Hbl, hornblende; Chl, chlorite; Cpx, clinopyroxene.

this study is consistent with the relatively low temperatures of amphibolite facies metamorphism experienced by rocks of the Southern Nagssugtoqidian Orogen (Henriksen et al., 2000).

5.2. Assessment of External Inputs to the Dissolved Load

As the river emanates directly from the mouth of the glacier we consider vegetation (which in the wider field setting is sparse) to have negligible impact on biogeochemical processes at this field site and no vegetation samples were analyzed. In addition to water derived from subglacial weathering reactions, solutes could be derived from surficial inputs such as dust deposition and meteorological precipitation. It neither rained nor snowed during the duration of the sampling campaign. However, information on atmospheric deposition could be gained from supraglacial streams which are assumed to be the water source most likely to be influenced by atmospheric deposition (melting snow/ice and dust). Five supraglacial streams were sampled in Hindshaw et al. (2014) and were combined for analysis. The Mg concentration was <0.05 μmol L^{-1} and the Li concentration was below the detection limit. The low concentration of Li and Mg in supraglacial streams implies that precipitation and dust are unlikely to affect subglacial river concentrations and isotope ratios. The effect of meteorological precipitation on Mg and Li isotope ratios can further be assessed by assuming that all Cl in the river is derived from seawater and correcting the isotope ratios according to the following equation:

$$\delta X^{*} = \frac{\delta X_r \cdot X_r - ((X/Cl)_{sw} \cdot Cl_r) \cdot \delta X_{sw}}{X_r - (X/Cl)_{sw} \cdot Cl_r} \qquad (1)$$

where subscripts *r* and *sw* stand for “river” and “seawater,” respectively and X is either Mg or Li. The corrected ratios are within experimental uncertainty of the uncorrected ratios (<0.04‰ and <0.05‰ difference for δ^{26}Mg and δ^{7}Li, respectively). The negligible impact of meteorological precipitation is in agreement with Ca and Sr isotope data for this region (Hindshaw et al., 2014; Andrews and Jacobson, 2018). We therefore assume that the dominant solute source to the river is subglacial weathering reactions and as a result data was not corrected for additional precipitation inputs, consistent with Wimpenny et al. (2010, 2011).

5.3. Mineral Source Control on River Water Isotope Ratios

The Mg and Li stable isotope ratios of the dissolved load can reflect mixing between distinct solute sources and/or fractionation processes. We will examine each of these in turn.

Mixing between Mg derived from isotopically distinct silicate mineral sources has been observed in a variety of catchments (Chapela Lara et al., 2017; Kimmig et al., 2018). For Mg, the δ^{26}Mg isotope ratios of the Leverett River water samples are intermediate between the garnet (–1.63‰) and hornblende (+0.06‰). The δ^{26}Mg values measured in the river could therefore reflect mixing between different mineral sources. Previous work utilizing Ca and Sr isotope ratios concluded that for these elements, the primary mineral sources contributing to the dissolved load were minerals from orthogneiss Ro4: feldspar, chlorite, and epidote (Hindshaw et al., 2014). In addition, the weathering of garnet, titanite, hornblende, and apatite from Ro4 and other rocks was invoked to explain the radiogenic Hf and Nd isotope compositions in river water (Rickli et al., 2017).

In orthogneiss Ro4, Mg is primarily hosted in chlorite and the δ^{26}Mg value of this mineral separate (–0.29‰) is identical within error of the average river water (–0.30 ± 0.14‰, 2SD). However, the weathering of chlorite only is inconsistent with the ^{87}Sr/^{86}Sr river water data which indicate mixing with unradiogenic feldspar and epidote (Hindshaw et al., 2014). We have not measured the δ^{26}Mg values of feldspar and epidote from Ro4. We can estimate the δ^{26}Mg value of a combined feldspar-epidote fraction based on mass balance, but since the bulk rock δ^{26}Mg value (–0.20 ± 0.11‰) is within analytical uncertainty of the chlorite separate (–0.29 ± 0.11‰, **Table 1**), this calculation is poorly constrained. However, based on the observation that inter-mineral variation between minerals is minor when Mg is octahedrally coordinated (∼0.06‰, Liu S.-A. et al., 2010), we infer that the Mg isotope composition of a combined epidote-feldspar fraction is close to that of chlorite and we assume the bulk rock value of –0.20‰ for this fraction. A mixing line in δ^{26}Mg vs. ^{87}Sr/^{86}Sr space between chlorite and “feldspar-epidote” passes through the river water sample points (**Figure 5**). Therefore, similar to radiogenic Sr and Ca (Hindshaw et al., 2014), the dissolved δ^{26}Mg values would be consistent with the dissolution of this group of minerals. However, we emphasize that the fraction of Mg hosted in plagioclase and epidote is low (4%, **Table 1**), and therefore these two minerals are expected to have a minor contribution to dissolved Mg.

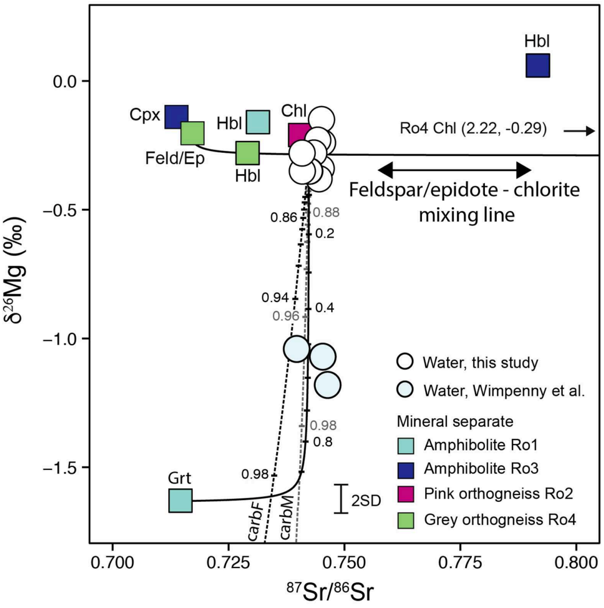

FIGURE 5 | δ^{26}Mg vs. ^{87}Sr/^{86}Sr. Previous work demonstrated the dominance of orthogneiss Ro4, in particular chlorite, feldspar, and epidote, to the dissolved and sediment load of the Leverett River (Hindshaw et al., 2014; Rickli et al., 2017). The mixing line between chlorite and feldspar/epidote in Ro4 is shown. The point where this line has the same ^{87}Sr/^{86}Sr value as the average of the river water samples (0.742435, Hindshaw et al., 2014) is defined as "Ro4-Leverett." The garnet end-member is defined in **Table 1**. Two carbonate end-members are defined based on acetic acid leaches of a felsic (carbF) and a mafic (carbM) rock from Akuliarusiarsuup Kuua River (AKR) (Andrews and Jacobson, 2018) and a δ^{26}Mg carbonate value of −3.2‰(Wimpenny et al., 2011). Mixing lines between Ro4-Leverett and carbonate (dashed lines) and Ro4-Leverett and garnet (solid line) are shown and assume congruent dissolution of each end-member. The numbers indicate the mass fraction of the garnet or carbonate end-member. Mineral abbreviations: Hbl, Hornblende; Chl, Chlorite; Cpx, Clinopyroxene; Grt, Garnet; Feld/Ep, K-feldspar, plagioclase, epidote mixture.

Further contributions from hornblende to the Mg budget in the river are likely based on the high fraction of Mg hosted in this mineral in the amphibolite rock samples (**Table 1**), high abundances of hornblende in catchment sediments (up to 9.5 vol.%, Rickli et al., 2017) and dissolved riverine Hf and Nd isotope compositions (Rickli et al., 2017). A contribution from hornblende would also be consistent with dissolved δ^{26}Mg and ^{87}Sr/^{86}Sr values since the range of δ^{26}Mg and ^{87}Sr/^{86}Sr values measured in hornblende separates encompasses those measured in the dissolved load (**Figure 5**).

Minerals derived from augen gneiss (**Figure 1**) could also contribute to dissolved Mg and Li in the Leverett River. Mg- and Li-rich minerals in the augen gneiss sample analyzed by Rickli et al. (2017) are biotite and hornblende (both 3 wt.%). Biotite was inferred to contribute to the dissolved load chemistry of the Russell Glacier river (Andrews and Jacobson, 2018; Auqué et al., 2019) and is found in river sediments from the Leverett catchment (<1.4 wt.%, Rickli et al., 2017). Mineral separates of the augen gneiss were not obtained and given the spread of δ^{7}Li and δ^{26}Mg in minerals from different rock samples is quite large (**Figure 4**), it is difficult to predict what the δ^{7}Li and δ^{26}Mg values of the Mg- and Li- rich augen gneiss minerals would be. Therefore, an accurate assessment of their contribution to the dissolved Mg and Li load in Leverett must await further data. We note though that Andrews and Jacobson (2018) concluded, based on ^{87}Sr/^{86}Sr and major element data, that the waters draining Point 660 catchment [where Auqué et al. (2019) collected their samples] drained a distinctly different lithology to Leverett, with a greater proportion of K-feldspar and/or biotite weathering compared to plagioclase weathering. Therefore, the contribution of biotite weathering to the dissolved load of Leverett River is expected to be lower compared to Russell.

The δ^{26}Mg values of river water samples previously measured in this region (**Figure 1**) were also explained as arising from a mixture of different mineral sources (Wimpenny et al., 2011). In the following discussion this sample set will be referred to as "Wimpenny's samples." In their study the authors suggested that low δ^{26}Mg values were arising from the presence of finely disseminated secondary carbonate in the catchment rocks. The presence of carbonate was not directly confirmed but was supported by elevated Ca/Na (up to 3.9 mol/mol) and Ca/Mg (up to 3.5 mol/mol) ratios in those water samples compared to a pure silicate end-member (Ca/Na = 0.5; Ca/Mg = 1.3, Wimpenny et al., 2011). Further, calcite has recently been detected in a glacier borehole sample from the AKR catchment (**Figure 1**, Harper et al., 2016) and the presence of disseminated calcite was inferred from element ratios of the fine fraction of till samples from north of Russell Glacier (Auqué et al., 2019). The estimated contribution of carbonate weathering to dissolved Mg was 2–7% (Wimpenny et al., 2011) and this estimate is consistent with other studies conducted in this region (Graly et al., 2014; Yde et al., 2014; Andrews and Jacobson, 2018).

We observe that the δ^{26}Mg values of Leverett River are ∼0.82‰ higher compared to Wimpenny's samples. This offset could be due to a difference in the contribution of carbonate weathering to dissolved Mg. In the Leverett River samples the molar Ca/Na ratios in river water (0.59 to 0.98, **Table 2**) are lower than those reported by Wimpenny et al. (2011) (1.07–3.88). This together with the lack of Mg-carbonate phases detected in the Leverett catchment rock and sediment samples could suggest that the contribution of carbonate weathering is lower in Leverett compared to the surrounding region. Since carbonate has low δ^{26}Mg values (–5.57 to –0.38‰, Teng, 2017) compared to the silicate rocks in this study (–0.20 to +0.09‰, **Table 1**), a smaller carbonate contribution in Leverett compared to Wimpenny's samples would result in higher dissolved δ^{26}Mg values, as observed.

In addition to carbonate, garnet also has lower δ^{26}Mg values compared to bulk silicate rocks and all the water samples (**Figure 3**, **Table 1**). The weathering rate of garnet (almandine) is predicted to be about two orders of magnitude faster than epidote and chlorite at the pH of the river waters (Palandri and Kharaka, 2004, and references therein) and therefore it is plausible that the dissolution of this mineral could impact on the dissolved load Mg isotopic composition. The higher Ca/Na ratios in Wimpenny's samples could similarly be explained by increased weathering from silicate minerals with high Ca/Na ratios, such as garnet

(Ca/Na molar ratio = 300), which are more abundant in the amphibolites compared to the orthogneisses (**Table 1**). Spatial differences in the relative contribution of garnet weathering may therefore also account for the difference in δ^{26}Mg values between the two datasets.

In order to test these two hypothesis (garnet and carbonate) we utilize ^{87}Sr/^{86}Sr ratios to assess if mixing between the proposed mineral sources fits the ^{87}Sr/^{86}Sr and δ^{26}Mg isotope data from the water samples (**Figure 5**). Wimpenny et al. (2011) did not analyse their samples for ^{87}Sr/^{86}Sr ratios, however data from similar sample sites along the AKR are available for 2014 and 2015 (Andrews and Jacobson, 2018). Compared to 2009, annual total and peak discharge were higher in 2014 and lower in 2015 (van As et al., 2017). No statistically significant change in ^{87}Sr/^{86}Sr ratios was observed during either melt season or between 2014 and 2015 at each site despite variations in discharge. Therefore, for the three sites common to both studies [GR1, GR2, GR8 in Wimpenny et al. (2011) and E, B, D in Andrews and Jacobson (2018)], we use the site-specific average ^{87}Sr/^{86}Sr value from 2014 and 2015. We assume that dissolved ^{87}Sr/^{86}Sr in Wimpenny's samples is controlled by the same reactions as inferred for Leverett, where minerals from orthogneiss Ro4 (chlorite, feldspar and epidote) appear to control the dissolved load composition. This assumption is supported by the overlapping range in ^{87}Sr/^{86}Sr ratios of AKR (0.7395–0.7462, sites E, B, D, Andrews and Jacobson, 2018) and Leverett water samples (0.7406–0.7455, **Figure 5**, Hindshaw et al., 2014).

We define one end-member (Ro4-Leverett) as the point where the feldspar/epidote—chlorite mixing line is at the average Leverett River ^{87}Sr/^{86}Sr ratio (0.742435, Hindshaw et al., 2014). We then assess the impact of mixing between Ro4-Leverett and solute sources with low δ^{26}Mg values: carbonate and garnet. There are no direct measurements of carbonate from this region, however Andrews and Jacobson (2018) performed an acetic acid leach of two rock samples (R05F and R05M) from the AKR catchment targeting carbonate. One sample was from a felsic rock (carbF, [Mg] =141 mg/kg, [Sr] = 3.1 mg/kg, ^{87}Sr/^{86}Sr = 0.71558) and the other from a mafic rock (carbM, [Mg] = 107 mg/kg, [Sr] = 0.7 mg/kg, ^{87}Sr/^{86}Sr = 0.72240). No δ^{26}Mg values exist for these samples and we therefore apply the same δ^{26}Mg value (–3.2‰) that (Wimpenny et al., 2011) assumed for carbonate. The mixing lines indicate that additional weathering of either carbonate or garnet could account for the lower δ^{26}Mg values observed in Wimpenny's samples compared to Leverett (**Figure 5**). For mixing between Ro4-Leverett and carbonate, the dissolved δ^{26}Mg values would require that carbonate weathering dominates in the AKR catchment (∼95 wt.% of the weathering substrate, **Figure 5**), which contradicts previous conclusions (Wimpenny et al., 2011; Andrews and Jacobson, 2018). In terms of garnet weathering, Rickli et al. (2017) estimated that, based on Nd and Hf isotopes, the contribution of garnet in Leverett was 2%. The δ^{26}Mg values measured in Leverett correspond to 0–6% garnet contribution, which is broadly consistent with the proposed mixing model for Nd and Hd isotope data. For Wimpenny's samples, the garnet mass fraction is ∼0.55 (**Figure 5**). Compared to Leverett, suspended sediments in AKR, QKR, and Watson River collected by Wimpenny et al. (2010) had higher Hf isotopic compositions (εHf = –38.12 ± 1.2, 1SD) compared to Leverett (εHf = –45.2 ± 1.2, 1SD) which was interpreted to reflect a combination of more garnet and less zircon in those suspended sediments (Rickli et al., 2017). Assuming that the suspended sediments provide a measure of the average lithology drained, the Hf isotope data would support the hypothesis that the lower δ^{26}Mg values in Wimpenny's samples could, at least in part, be caused by increased garnet weathering. However, the inferred difference in garnet abundance was estimated to be <1 wt.% and therefore unlikely to result in such a large difference in garnet contribution to the dissolved load as implied by the mixing proportions from **Figure 5**.

In summary, we cannot conclusively identify the origin of the offset between δ^{26}Mg values in Wimpenny's samples and Leverett River. Both increased garnet and carbonate weathering compared to Leverett may play a role, but neither on its own is consistent with constraints from mineral abundances and other geochemical data. However, there may be differences in lithology between Leverett and the other catchments (**Figure 1**), invalidating the assumption that the dissolution of orthogneiss Ro4 is the primary solute source to the dissolved load in Wimpenny's samples. Further data from bulk rock and mineral separate samples from the area where Wimpenny et al. (2011) collected their samples would be required to provide additional constraints on plausible weathering sources.

5.4. Fractionation Control on River Water Isotope Ratios

The δ^{7}Li values of Leverett River water samples cannot be reconciled with mixing between isotopically distinct mineral end-members (**Figure 6**). A fractionation process must therefore control river δ^{7}Li values and could also impact on δ^{26}Mg values.

The difference in the magnitude of fractionation ($\Delta^{7}\text{Li}_{water-sed}$) between the samples measured by Wimpenny et al. (2010) (∼20.4‰) and this study (∼14.3‰) could be due to a difference in lithology or the relative amount of Li lost from solution due to processes such as secondary mineral formation and adsorption. In the first scenario, the $\Delta^{7}\text{Li}_{water-sed}$ value would be constant but if the starting rock composition for Wimpenny's samples had a higher δ^{7}Li value compared to Leverett then the δ^{7}Li of the water samples would be correspondingly higher. There is only a minor difference in the δ^{7}Li values of the amphibolite (+6.8 to +8.3‰) and orthogneiss samples (+5.0 to +6.3‰, **Figure 3**). Similarly the range in rock δ^{7}Li values from this study (+5.0 to +8.3‰) overlaps with the range reported by Wimpenny et al. (2010) (+5.8 to +10.4‰). Theoretically, a hornblende with a high δ^{7}Li value such as that measured in Ro3 (+12.1‰) could dominate the dissolved load of the Wimpenny et al. (2010) samples, but that would be inconsistent with the Mg, Ca, and Sr isotope data (**Figure 5**, Hindshaw et al., 2014). As such it is unlikely that differences in the Li isotopic composition of the source rocks and minerals can account for the ∼6‰ difference in the δ^{7}Li values of the two sets of river water samples.

It is therefore more likely that the degree of fractionation between the two sample sets differs. Fractionation of Li isotopes

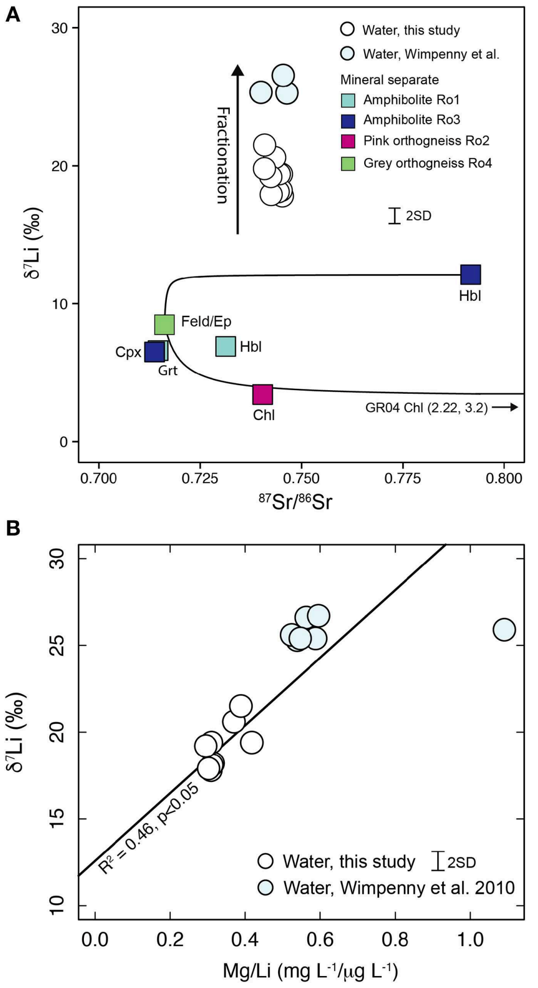

FIGURE 6 | (A) Mixing between the minerals of Ro4 (feldspar, epidote, and chlorite) cannot explain the δ^7Li values of water. Hornblende, the mineral with the highest δ^7Li values, also cannot account for the water δ^7Li values, even if it dominated the dissolved Li budget. Therefore, although some variation may be attributable to mineral source heterogeneity a fractionation process must also be occurring. Mineral abbreviations: Hbl, Hornblende; Chl, Chlorite; Cpx, Clinopyroxene; Grt, Garnet; Feld/Ep, K-feldspar, plagioclase, epidote mixture. Note that a change in the relative proportion of garnet weathering will have a negligible effect on δ^7Li ratios. **(B)** The water samples measured in this study have lower δ^7Li and Mg/Li values compared to Wimpenny et al. (2010). The lower Mg/Li values would be consistent either with a lower relative loss of Li compared to Mg or with a decreased contribution from garnet weathering (Mg/Li garnet = 2.1, **Figure 5B**). The solid line is the regression through Leverett River samples.

is attributed to two main processes: adsorption and secondary mineral formation (Huh et al., 2001; Pistiner and Henderson, 2003; Vigier et al., 2008). Both of these processes lead to an enrichment of ^{7}Li in the fluid. In high latitude environments adsorption rather than clay mineral formation likely controls dissolved Li isotopic compositions (Millot et al., 2010; Wimpenny et al., 2010). Evidence for the role of adsorption in glacierized catchments comes from the low δ^7Li values measured in a leach targeting Fe-oxyhydroxide phases in sediments from West Greenland (Wimpenny et al., 2010). Ilmenite ($FeTiO_3$) and magnetite (Fe_3O_4) are present in the Leverett River sediments and Phreeqc calculations indicate that water samples from the region are over-saturated in amorphous and crystalline iron oxide phases (Wimpenny et al., 2010; Hindshaw et al., 2014). Adsorption of metal cations (e.g., Li) onto these phases could therefore occur, particularly as adsorption is favored at basic pH due to a more negative surface charge compared to at neutral pH (Stumm and Morgan, 1996). Although Wimpenny et al. (2010) and Auqué et al. (2019) considered the formation of secondary clay minerals unlikely, smectite has been detected in sediments retrieved from glacier boreholes in this region (Graly et al., 2016). Smectite may originate from overridden soils (Yde et al., 2014; Carrivick et al., 2018) and adsorption onto the clay surface could also induce isotope fractionation (Pistiner and Henderson, 2003; Chan and Hein, 2007). Mineralogical and isotopic analysis of the clay-sized fraction of river sediment would be required to assess the role of clay minerals on dissolved δ^{26}Mg and δ^7Li.

The Mg/Li ratio is commonly used to assess the relative loss of Li in water samples (Dellinger et al., 2015). The Mg/Li mass ratios of the Wimpenny et al. (2010) samples are higher (0.6) compared to Leverett (0.3) potentially indicating increased loss of Li (**Figure 6B**). However, the Mg/Li ratio is also dependent on the relative proportion of garnet (Mg/Li = 2.1) weathering in these samples. The difference in lithology inferred from δ^{26}Mg values (**Figure 5**) implies that a common initial ion ratio cannot be assumed for all the water samples in this region and that the Mg/Li ratio is not a reliable measure of relative Li loss. Nevertheless, if we assume a single lithological source in the Leverett catchment, higher Mg/Li ratios are associated with higher δ^7Li values (**Figure 6B**), consistent with fractionation accompanying removal of Li from solution. We therefore consider it likely that the trend observed between δ^7Li and Mg/Li in the Leverett samples (**Figure 6B**) arises due to increased loss of Li. By extension, the higher δ^7Li values observed in the Wimpenny et al. (2010) samples are most likely due to greater fractionation (greater proportion of Li lost) rather than source differences.

If Li isotope fractionation in this region is caused by adsorption, as proposed by Wimpenny et al. (2010), then the difference in mineralogy of suspended sediments may impact the identity and availability of adsorption sites. Suspended sediments measured by Wimpenny et al. (2010) had Fe (3.68–5.07 wt.%) and Li (21.5–35.4 mg/kg) concentrations higher than those measured in Leverett (Fe = 3.46–3.92 wt.%; Li = 4.9–8.3 mg/kg, n = 6). The lower Fe and Li concentrations in Leverett suspended sediment may indicate fewer Fe oxides and a lower proportion of Li adsorbed, resulting in reduced fractionation compared to Wimpenny's samples.

The inferred fractionation of Li as a result of adsorption could imply that Mg isotopes are affected by the same process. Coupled Mg and Li isotope behavior has been observed in the Mackenzie River basin linked to secondary fractionation processes involving clay minerals (Tipper et al., 2012a). However, the range of dissolved δ^{26}Mg values in Leverett (−0.38 to −0.15‰) overlaps with those of the river sediments (−0.33 to −0.48, **Table 1**) suggesting negligible process-related fractionation. Rather, the Mg isotope data in Leverett can be adequately explained by mixing between different mineral sources (**Figure 5**). Although the Mg isotope data in Wimpenny's samples is not fully compatible with mixing between mineral sources inferred for Leverett (section 5.3) we consider it unlikely that fractionation of Mg would occur in one catchment and not the other.

The samples collected downstream of the confluence of rivers draining Russell and Leverett glaciers would be expected to represent a mixture of water draining those glaciers. Transects of water samples from AKR show an increase in dissolved $^{87}Sr/^{86}Sr$ ratios downstream of the confluence with Leverett River (average increase = 0.006678, Andrews and Jacobson, 2018). This increase was attributed to the mixing of two end-members draining areas with different geology. We would therefore also expect the δ^7Li and $\delta^{26}Mg$ values downstream of the confluence (GR2 and GR8) to reflect a mixture between Leverett ($\delta^{26}Mg = -0.29‰$, $\delta^7Li = +19.2‰$) and GR1 ($\delta^{26}Mg = -1.04‰$, $\delta^7Li = +25.4‰$) (**Figure 1**). Yet, this is not what is observed. Rather the downstream $\delta^{26}Mg$ and δ^7Li values are within error of GR1 (Wimpenny et al., 2010, 2011). We do not have a good explanation for why the mixing signal for dissolved Li and Mg isotope values is absent. One source of uncertainty is that we are comparing water samples collected in different years (2006 and 2009) and the subglacial drainage pathways may not be identical from year to year (Lindbäck et al., 2015), potentially resulting in inter-annual variations in the dominant lithology being weathered for each glacier sub-catchment. For example, one year could have a higher proportion of solutes derived from mafic dykes compared to another year. Simultaneous measurements of water chemistry from both glaciers in the same melt-season would be needed to test this hypothesis.

6. CONCLUSIONS

Lithium and magnesium stable isotope ratios measured in a time series of water samples from Leverett Glacier display no systematic temporal variation and are affected by different processes. The Li isotope values of water samples are higher than bedrock, river sediment, and mineral separate measurements, implying a fractionation processes. A previous study concluded that dissolved lithium isotope values in this region were controlled by adsorption onto iron oxyhydroxide minerals (Wimpenny et al., 2010) and the same process is likely occurring in this catchment. In contrast, the $\delta^{26}Mg$ values of the dissolved load are within error of bedrock and river sediment measurements and would be consistent with the mixing of Mg derived from minerals contained in orthogneiss (chlorite, feldspar, and epidote), previously identified by radiogenic Ca and Sr measurements as being key sources to the dissolved load (Hindshaw et al., 2014). In addition there are likely contributions from garnet and hornblende. A previous study in this region (Qinnguata Kuussua (QKR) and Akuliarusiarsuup Kuua (AKR) rivers, Wimpenny et al., 2011), reported dissolved $\delta^{26}Mg$ values ~0.80‰ lower than those we measured in Leverett and concluded that there was a carbonate ($\delta^{26}Mg$ = –1 to –5‰) contribution to Mg in the dissolved load. However, garnet also has low $\delta^{26}Mg$ value (–1.63‰), and could also contribute to dissolved Mg in these samples. Mixing calculations between a "Leverett" end-member and either carbonate or garnet suggest that whilst the weathering of both minerals could account for the difference in $\delta^{26}Mg$ values between the two data sets, the inferred mixing proportions are incompatible with other geochemical data. It is likely that the mineral data from Leverett does not capture all mineral sources for the AQR and QKR catchments due to small differences in lithology.

In the context of the carbon cycle it is crucial to determine whether Mg (and Ca) derive from carbonate or silicate weathering. This study highlights that certain silicate minerals can have $\delta^{26}Mg$ values in the same range as carbonate minerals, emphasizing that source rock mineral characterization is an essential step in the interpretation of dissolved stable isotope ratios.

DATA AVAILABILITY STATEMENT

All datasets generated for this study are included in the manuscript or are available in the referenced companion manuscripts.

AUTHOR CONTRIBUTIONS

RH designed the project and conducted the fieldwork together with JR. JL collected element and abundance data on mineral separates and RH analyzed samples for Li and Mg isotope ratios. All authors contributed to the interpretation of the results and the writing of the article.

FUNDING

This work was funded by a SNF fellowship (127764) and Marie-Curie Fellowship (Project No. 253117) to JR and an ETH Research Grant (no. 04/06-3) and NERC Standard Grant (NE/M001865/1) to RH. JL acknowledges support from a Swiss National Science Foundation (SNSF) Ambizione grant.

REFERENCES

AMAP (2017). *Snow, Water, Ice and Permafrost in the Arctic (SWIPA) 2017.* Oslo: Arctic Monitoring and Assessment Programme (AMAP).

Anderson, S. P., Drever, J. I., and Humphrey, N. F. (1997). Chemical weathering in glacial environments. *Geology* 25, 399–402. doi: 10.1130/0091-7613(1997)025<0399:CWIGE>2.3.CO;2

Andrews, M. G., and Jacobson, A. D. (2018). Controls on the solute geochemistry of subglacial discharge from the Russell Glacier, Greenland Ice Sheet determined by radiogenic and stable Sr isotope ratios. *Geochim. Cosmochim. Acta* 239, 312–329. doi: 10.1016/j.gca.2018.08.004

Auqué, L. F., Puigdomenech, I., Tullborg, E.-L., Gimeno, M. J., Grodzinsky, K., and Hogmalm, K. J. (2019). Chemical weathering in a moraine at the ice sheet margin at Kangerlussuaq, western Greenland. *Arct. Antarct. Alp. Res.* 51, 440–459. doi: 10.1080/15230430.2019.1660125

Barnes, E. M., Weis, D., and Groat, L. A. (2012). Significant Li isotope fractionation in geochemically evolved rare element-bearing pegmatites from the Little Nahanni Pegmatite Group, NWT, Canada. *Lithos* 132–133, 21–36. doi: 10.1016/j.lithos.2011.11.014

Bartholomew, I., Nienow, P., Sole, A., Mair, D., Cowton, T., Palmer, S., et al. (2011). Supraglacial forcing of subglacial drainage in the ablation zone of the Greenland ice sheet. *Geophys. Res. Lett.* 38:L08502. doi: 10.1029/2011GL047063

Berner, R. A., Lasaga, A. C., and Garrels, R. M. (1983). The carbonate-silicate geochemical cycle and its effect on atmospheric carbon dioxide over the past 100 million years. *Am. J. Sci.* 283, 641–683. doi: 10.2475/ajs.283.7.641

Bhatia, M. P., Das, S. B., Xu, L., Charette, M. A., Wadham, J. L., and Kujawinski, E. B. (2013). Organic carbon export from the Greenland ice sheet. *Geochim. Cosmochim. Acta* 109, 329–344. doi: 10.1016/j.gca.2013.02.006

Blum, J. D., and Erel, Y. (1997). Rb-Sr isotope systematics of a granitic soil chronosequence: the importance of biotite weathering. *Geochim. Cosmochim. Acta* 61, 3193–3204. doi: 10.1016/S0016-7037(97)00148-8

Blum, J. D., Erel, Y., and Brown, K. (1994). ^{87}Sr/^{86}Sr ratios of Sierra Nevada stream waters: implications for relative mineral weathering rates. *Geochim. Cosmochim. Acta* 58, 5019–5025. doi: 10.1016/S0016-7037(05)80014-6

Brown, M., Friend, C. R. L., McGregor, V. R., and Perkins, W. T. (1981). The late Archaean Qôrqut granite complex of Southern West Greenland. *J. Geophys. Res.* 86, 10617–10632. doi: 10.1029/JB086iB11p10617

Bullen, T. D., and Bailey, S. W. (2005). Identifying calcium sources at an acid deposition-impacted spruce forest: a strontium isotope, alkaline earth element multi-tracer approach. *Biogeochemistry* 74, 63–99. doi: 10.1007/s10533-004-2619-z

Cadman, A. C., Tarney, J., Bridgewater, D., Mengel, F., Whitehouse, M. J., and Windley, B. F. (2001). The petrogenesis of the Kangâmiut dyke swarm, W. Greenland. *Precambrian Res.* 105, 183–203. doi: 10.1016/S0301-9268(00)00111-X

Carignan, J., Vigier, N., and Millot, R. (2007). Three secondary reference materials for lithium isotope measurements: Li7-N, Li6-N and LiCl-N solutions. *Geostand. Geoanal. Res.* 31, 7–12. doi: 10.1111/j.1751-908X.2007.00833.x

Carrivick, J. L., Yde, J. C., Knudsen, N. T., and Kronborg, C. (2018). Ice-dammed lake and ice-margin evolution during the Holocene in the Kangerlussuaq area of west Greenland. *Arct. Antarct. Alp. Res.* 50:e1420854. doi: 10.1080/15230430.2017.1420854

Chan, L.-H., and Hein, J. R. (2007). Lithium contents and isotopic compositions of ferromanganese deposits from the global ocean. *Deep Sea Res. II* 54, 1147–1162. doi: 10.1016/j.dsr2.2007.04.003

Chandler, D. M., Wadham, J. L., Lis, G. P., Cowton, T., Sole, A., Bartholomew, I., et al. (2013). Evolution of the subglacial drainage system beneath the Greenland Ice Sheet revealed by tracers. *Nat. Geosci.* 6, 195–198. doi: 10.1038/ngeo1737

Chapela Lara, M., Buss, H. L., Pogge von Strandmann, P. A. E., Schuessler, J., and Moore, O. W. (2017). The influence of critical zone processes on the Mg isotope budget in a tropical, highly weathered andesitic catchment. *Geochim. Cosmochim. Acta* 202, 77–100. doi: 10.1016/j.gca.2016.12.032

Chen, L.-M., Teng, F. Z., Song, X.-Y., Hu, R.-Z., Yu, S.-Y., Zhu, D., et al. (2018). Magnesium isotopic evidence for chemical disequilibrium among cumulus minerals in layered mafic intrusion. *Earth Planet. Sci. Lett.* 487, 74–83. doi: 10.1016/j.epsl.2018.01.036

Clergue, C., Dellinger, M., Buss, H. L., Gaillardet, J., Benedetti, M. F., and Dessert, C. (2015). Influence of atmospheric deposits and secondary minerals on Li isotopes budget in a highly weathered catchment, Guadeloupe (Lesser Antilles). *Chem. Geol.* 414, 28–41. doi: 10.1016/j.chemgeo.2015.08.015

Cussen, E. J. (2010). Structure and ionic conductivity in lithium garnets. *J. Mater. Chem.* 20, 5167–5173. doi: 10.1039/b925553b

Dellinger, M., Gaillardet, J., Bouchez, J., Calmels, D., Louvat, P., Dosseto, A., et al. (2015). Riverine Li isotope fractionation in the Amazon River basin controlled by the weathering regimes. *Geochim. Cosmochim. Acta* 164, 71–93. doi: 10.1016/j.gca.2015.04.042

Engström, J., and Klint, K. E. S. (2014). Continental collision structures and post-orogenic geological histroy of the Kangerlussuaq are in the southern part of the Nagssugtoqidian Orogen, Central West Greenland. *Geosciences* 4, 316–334. doi: 10.3390/geosciences4040316

Escher, A. (1971). *Geological Map of Greenland, 1:500 000, Søndre Strømfjord - Nûgssuaq, Sheet 3*. Copenhagen: Geological Survey of Greenland.

Escher, A., Sørensen, K., and Zeck, H. P. (1976). "Nagssugtoqidian mobile belt in West Greenland," in *Geology of Greenland*, eds A. Escher and W. S. Watt (Copenhagen: Grønlands Geologiske Undersøgelse), 76–95.

Gaillardet, J., Dupré, B., Louvat, P., and Allègre, C. J. (1999). Gobal silicate weathering and CO_2 consumption rates deduced from the chemistry of large rivers. *Chem. Geol.* 159, 3–30. doi: 10.1016/S0009-2541(99)00031-5

Garrels, R. M., and Howard, P. (1957). Reactions of feldspar and mica with water at low temperature and pressure. *Clay Clay Miner.* 6, 68–88.

Graly, J. A., Humphrey, N. F., and Harper, J. T. (2016). Chemical depletion of sediment under the Greenland Ice Sheet. *Earth Surf. Process. Landforms* 41, 1922–1936. doi: 10.1002/esp.3960

Graly, J. A., Humphrey, N. F., Landowski, C. M., and Harper, J. (2014). Chemical weathering under the Greenland Ice Sheet. *Geology* 42, 551–554. doi: 10.1130/G35370.1

Hanna, E., Mernild, S. H., Cappelen, J., and Steffen, K. (2012). Recent warming in Greenland in a long-term instrumental (1881-2012) climatic context: I. evalulation of surface air temperature records. *Environ. Res. Lett.* 7:045404. doi: 10.1088/1748-9326/7/4/045404

Harper, J., Hubbard, A., Ruskeeniemi, T., Claesson Liljedahl, L., Kontula, A., Hobbs, M., et al. (2016). *The Greenland Analogue Project: Data and Processes*. Tech. Rep. R-14-13, Svensk Kärnbränslehantering AB, Stockholm.

Hawkings, J., Wadham, J., Tranter, M., Telling, J., Bagshaw, E., Beaton, A., et al. (2016). The Greenland Ice Sheet as a hotspot of phosphorus weathering and export in the Arctic. *Glob. Biogeochem. Cycles* 30, 191–210. doi: 10.1002/2015GB005237

Hawkings, J. R., Wadham, J. L., Benning, L. G., Hendry, K. R., Tranter, M., Tedstone, A., et al. (2017). Ice sheets as a missing source of silica to the polar oceans. *Nat. Commun.* 8:4198. doi: 10.1038/ncomms14198

Hawkings, J. R., Wadham, J. L., Tranter, M., Raiswell, R., Benning, L. G., Statham, P. J., et al. (2014). Ice sheets as a significant source of highly reactive nanoparticulate iron to the oceans. *Nat. Commun.* 5:3929. doi: 10.1038/ncomms4929

Henriksen, N., Higgins, A. K., Kalsbeek, F., and Pulvertaft, T. C. R. (2000). Greenland from Archaean to quaternary: descriptive text to the geological map of Greenland, 1:2 500 000. *Geol. Greenland Surv. Bull.* 185, 1–126. Available online at: https://eng.geus.dk/products-services-facilities/publications/geus-bulletin/geology-of-greenland-survey-bulletin/bulletin-185/

Hindshaw, R. S., Aciego, S. M., and Tipper, E. T. (2018). Li and U isotopes as a potential tool for monitoring active layer deepening in permafrost dominated catchments. *Front. Earth Sci.* 6:102. doi: 10.3389/feart.2018.00102

Hindshaw, R. S., Rickli, J., Leuthold, J., Wadham, J., and Bourdon, B. (2014). Identifying weathering sources and processes in an outlet glacier of the Greenland Ice Sheet using Ca and Sr isotope ratios. *Geochim. Cosmochim. Acta* 145, 50–71. doi: 10.1016/j.gca.2014.09.016

Hindshaw, R. S., Tipper, E. T., Reynolds, B. C., Lemarchand, E., Wiederhold, J. G., Magnusson, J., et al. (2011). Hydrological control of stream water chemistry in a glacial catchment (Damma Glacier, Switzerland). *Chem. Geol.* 285, 215–230. doi: 10.1016/j.chemgeo.2011.04.012

Hopwood, M. J., Bacon, S., Arendt, K., Connelly, D. P., and Statham, P. J. (2015). Glacial meltwater from Greeland is not likely to be an important source of Fe to the North Atlantic. *Biogeochemistry* 124, 1–11. doi: 10.1007/s10533-015-0091-6

Hu, Y., Teng, F. Z., Zhang, H.-F., Xiao, Y., and Su, B.-X. (2016). Metasomatism-induced mantle magnesium isotopic heterogeneity: evidence from pyroxenites. *Geochim. Cosmochim. Acta* 185, 88–111. doi: 10.1016/j.gca.2015.11.001

Huang, F., Chen, L., Wu, Z., and Wang, W. (2013). First-principles calculations of equilibrium Mg isotope fractionations between garnet, clinopyroxene, orthopyroxene, and olivine: implications for Mg isotope thermometry. *Earth Planet. Sci. Lett.* 367, 61–70. doi: 10.1016/j.epsl.2013.02.025

Huh, Y., Chan, L.-H., and Edmond, J. M. (2001). Lithium isotopes as a probe of weathering processes: Orinoco river. *Earth Planet. Sci. Lett.* 194, 189–199. doi: 10.1016/S0012-821X(01)00523-4

Huh, Y., Panteleyev, G., Babich, D., Zaitsev, A., and Edmond, J. M. (1998). The fluvial geochemistry of the rivers of Eastern Siberia: II. Tributaries of the Lena, Omoloy, Yana, Indigirka, Kolyma, and Anadyr draining the collisional/accretionary zone of the Verkhoyansk and Cherskiy ranges. *Geochim. Cosmochim. Acta* 62, 2053–2075. doi: 10.1016/S0016-7037(98)00127-6

James, R. H., and Palmer, M. R. (2000). The lithium isotope composition of international rock standards. *Chem. Geol.* 166, 319–326. doi: 10.1016/S0009-2541(99)00217-X

Johansson, E., Gustafsson, L.-G., Berglund, S., Lindborg, T., Selroos, J.-O., Liljedahl, L. C., et al. (2015). Data evaluation and numerical modeling of hydrological interactions between active layer, lake and talik in a permafrost catchment, Western Greenland. *J. Hydrol.* 527, 688–703. doi: 10.1016/j.jhydrol.2015.05.026

Kimmig, S. R., Holmden, C., and Bélanger, N. (2018). Biogeochemical cycling of Mg and its isotopes in a sugar maple forest in Québec. *Geochim. Cosmochim. Acta* 230, 60–82. doi: 10.1016/j.gca.2018.03.020

Li, W.-Y., Teng, F.-Z., Xiao, Y., Gu, H.-O., Zha, X.-P., and Huang, J. (2016). Empirical calibration of the clinopyroxene-garnet magnesium isotope geothermometer and implications. *Contrib. Mineral. Petrol.* 171, 61. doi: 10.1007/s00410-016-1269-1

Li, W. Y., Teng, F. Z., Ke, S., Rudnick, R. L., Gao, S., Wu, F. Y., et al. (2010). Heterogeneous magnseium isotopic composition of the upper continental crust. *Geochim. Cosmochim. Acta* 74, 6867–6884. doi: 10.1016/j.gca.2010.08.030

Lindbäck, K., Pettersson, R., Hubbard, A. L., Doyle, S. H., van As, D., Mikkelsen, A. B., et al. (2015). Subglacial water drainage, storage, and piracy beneath the Greenland ice sheet. *Geophys. Res. Lett.* 42, 7606–7614. doi: 10.1002/2015GL065393

Liu, S., Li, Y., Liu, J., Ju, Y., Liu, J., Yang, Z., et al. (2018). Equilibrium lithium isotope fractionation in Li-bearing minerals. *Geochim. Cosmochim. Acta* 235, 360–375. doi: 10.1016/j.gca.2018.05.029

Liu, S.-A., Teng, F.-Z., He, Y., Ke, S., and Li, S. (2010). Investigation of magnesium isotope fractionation during granite differentiation: implication for Mg isotopic composition of the continental crust. *Earth Planet. Sci. Lett.* 297, 646–654. doi: 10.1016/j.epsl.2010.07.019

Liu, X.-M., Rudnick, R. L., Hier-Majumder, S., and Sirbescu, M.-L. C. (2010). Processes controlling lithium isotopic distribution in contact aureoles: a case study of the Florence County pegmatites, Wisconsin. *Geochem. Geophys. Geosys.* 11:Q08014. doi: 10.1029/2010GC003063

Marks, M. A. W., Rudnick, R. L., McCammon, C., Vennemann, T., and Markl, G. (2007). Arrested kinetic Li isotope fractionation at the margin of the Ilímaussaq complex, South Greenland: evidence for open-system processes during final cooling of peralkaline igneous rocks. *Chem. Geol.* 246, 207–230. doi: 10.1016/j.chemgeo.2007.10.001

Mazza, D. (1988). Remarks on a ternary phase in the La_2O_3-Me_2O_5-Li_2O system (Me = Nb, Ta). *Mater. Lett.* 7, 205–207. doi: 10.1016/0167-577X(88)90011-0

Meire, L., Meire, P., Struyf, E., Krawczyk, D. W., Arendt, K. E., Yde, J. C., et al. (2016). High export of dissolved silica from the Greenland Ice Sheet. *Geophys. Res. Lett.* 43, 9173–9182. doi: 10.1002/2016GL070191

Mernild, S. H., Hanna, E., McConnell, M., Adn Sigl, J. R., Beckerman, A. P., Yde, J. C., et al. (2015). Greenland precipitation trends in a long-term instrumental climate context (1890-2012): evaluation of coastal and ice core records. *Int. J. Climatol.* 35, 303–320. doi: 10.1002/joc.3986

Millot, R., Vigier, N., and Gaillardet, J. (2010). Behaviour of lithium and its isotopes during weathering in the Mackenzie Basin, Canada. *Geochim. Cosmochim. Acta* 74, 3897–3912. doi: 10.1016/j.gca.2010.04.025

Misra, S., and Froelich, P. N. (2012). Lithium isotope history of Cenozoic seawater: changes in silicate weathering and reverse weathering. *Science* 335, 818–823. doi: 10.1126/science.1214697

Neukampf, J., Ellis, B. S., Magna, T., Laurent, O., and Bachmann, O. (2019). Partitioning and isotopic fractionation of lithium in mineral phases of hot, dry rhyolites: the case of the Mesa Falls Tuff, Yellowstone. *Chem. Geol.* 506, 175–186. doi: 10.1016/j.chemgeo.2018.12.031

Nezat, C. A., Blum, J. D., and Driscoll, C. T. (2010). Patterns of Ca/Sr and $^{87}Sr/^{86}Sr$ variation before and after a whole watershed $CaSiO_3$ addition at the Hubbard Brook Experimental Forest, USA. *Geochim. Cosmochim. Acta* 74, 3129–3142. doi: 10.1016/j.gca.2010.03.013

Nutman, A. P., Hiess, J., and Friend, C. R. L. (2010). Setting of the 2560 Ma Qorqut granite complex in the Archean crustal evolution of southern West Greenland. *Am. J. Sci.* 310, 1081–1114. doi: 10.2475/09.2010.12

O'Callaghan, M. P., Powell, A. S., Titman, J. J., Chen, G. Z., and Cussen, E. J. (2008). Switching on fast lithium ion conductivity in garnets: the structure and transport properties of $Li_{3+x}Nd_3Te_{2-x}Sb_xO_{12}$. *Chem. Mater.* 20, 2360–2369. doi: 10.1021/cm703677q

Oi, T., Nomura, M., Musashi, M., Ossaka, T., Okamoto, M., and Kakihana, H. (1989). Boron isotopic compositions of some boron minerals. *Geochim. Cosmochim. Acta* 53, 3189–3195. doi: 10.1016/0016-7037(89)90099-9

Oliva, P., Dupré, B., Martin, F., and Viers, J. (2004). The role of trace minerals in chemical weathering in a high-elevation granitic watershed (Estibère, France): chemical and mineralogical evidence. *Geochim. Cosmochim. Acta* 68, 2223–2244. doi: 10.1016/j.gca.2003.10.043

Palandri, J. L., and Kharaka, Y. K. (2004). *A Compilation of Rate Parameters of Water-Mineral Interaction Kinetics for Application for Geochemical Modeling*. U.S.G.S., Open File Report 2004-1068.

Penniston-Dorland, S., Liu, X.-M., and Rudnick, R. L. (2017). Lithium isotope geochemistry. *Rev. Mineral. Geochem.* 82, 165–217. doi: 10.1515/9783110545630-007

Phan, T. T., Capo, R. C., Stewart, B. W., Macpherson, G. L., Rowan, E. L., and Hammack, R. W. (2016). Factors controlling Li concentration and isotopic composition in formation waters and host rocks of Marcellus Shale, Appalachian Basin. *Chem. Geol.* 420, 162–179. doi: 10.1016/j.chemgeo.2015.11.003

Pistiner, J. S., and Henderson, G. M. (2003). Lithium-isotope fractionation during continental weathering processes. *Earth Planet. Sci. Lett.* 214, 327–339. doi: 10.1016/S0012-821X(03)00348-0

Pogge von Strandmann, P. A. E., Dohmen, R., Marschall, H. R., Schumacher, J. C., and Elliott, T. (2015). Extreme magnesium isotope fractionation at outcrop scale records the mechanism and rate at which reaction fronts advance. *J. Petrol.* 56, 33–58. doi: 10.1093/petrology/egu070

Pogge von Strandmann, P. A. E., Elliott, T., Marschall, H. R., Coath, C., Lai, Y.-J., Jeffcoate, A. B., et al. (2011). Variations of Li and Mg isotope ratios in bulk chondrites and mantle xenoliths. *Geochim. Cosmochim. Acta* 75, 5247–5268. doi: 10.1016/j.gca.2011.06.026

Raiswell, R., Tranter, M., Benning, L. G., Siegert, M., De'ath, R., Huybrechts, P., et al. (2006). Contributions from glacially derived sediment to the global iron (oxyhydr)oxide cycle: implications for iron delivery to the oceans. *Geochim. Cosmochim. Acta* 70, 2765–2780. doi: 10.1016/j.gca.2005.12.027

Rennermalm, A. K., Smith, L. C., Chu, V. W., Forster, R. R., Box, J. E., and Hagedorn, B. (2012). Proglacial river stage, discharge, and temperature datasets from the Akuliarusiarsupp Kuua River northern tributary, Soutwest Greenland, 2008-2011. *Earth Syst. Sci. Data* 4, 1–12. doi: 10.5194/essd-4-1-2012

Rettenwander, D., Wagner, R., Langer, J., Maier, M. E., Wilkening, M., and Amthauer, G. (2016). Crystal chemistry of "$Li_7La_3Zr_2O_12$" garnet doped with Al, Ga, and Fe: a short review on local structures as revealed by NMR and Mößbauer spectroscopy studies. *Eur. J. Mineral.* 28, 619–629. doi: 10.1127/ejm/2016/0028-2543

Rickli, J., Hindshaw, R. S., Leuthold, J., Wadham, J. L., Burton, K. W., and Vance, D. (2017). Impact of glacial activity on the weathering of Hf isotopes - observations from Southwest Greenland. *Geochim. Cosmochim. Acta* 215, 295–316. doi: 10.1016/j.gca.2017.08.005

Rosner, M., Ball, L., Peucker-Ehrenbrink, B., Blusztajn, J., Bach, W., and Erzinger, J. (2007). A simplified, accurate and fast method for lithium isotope analysis of rocks and fluids, and δ^7Li values of seawater and rock reference materials. *Geostand. Geoanal. Res.* 31, 77–88. doi: 10.1111/j.1751-908X.2007.00843.x

Ryu, J. S., Jacobson, A. D., Holmden, C., Lundstrom, C., and Zhang, Z. (2011). The major ion, $\delta^{44/40}$Ca, $\delta^{44/42}$Ca, and $\delta^{26/24}$Mg geochemistry of granite weathering at pH=1 and T=25°C: power-law processes and the relative reactivity of minerals. *Geochim. Cosmochim. Acta* 75, 6004–6026. doi: 10.1016/j.gca.2011.07.025

Sauzéat, L., Rudnick, R. L., Chauvel, C., Garçon, M., and Tang, M. (2015). New perspectives on the Li isotopic composition of the upper continental crust and its weathering signature. *Earth Planet. Sci. Lett.* 428, 181–192. doi: 10.1016/j.epsl.2015.07.032

Schauble, E. A. (2004). "Applying stable isotope fractionation theory to new systems," in *Geochemistry of Non-traditional Stable Isotopes*, Vol. 55 of *Reviews in Mineralogy & Geochemistry*, eds C. M. Johnson, B. L. Beard, and F. Albarède (Washington, DC: Mineralogical Society of America), 65–111.

Schauble, E. A. (2011). First-principles calculations of equilibrium magnesium isotope fractionation in silicate, oxide, carbonate and hexaaquamagnesium(2+) crystals. *Geochim. Cosmochim. Acta* 75, 844–869. doi: 10.1016/j.gca.2010.09.044

Sharp, M., Tranter, M., Brown, G. H., and Skidmore, M. (1995). Rates of chemical denudation and CO_2 drawdown in a glacier-covered alpine catchment. *Geology* 23, 61–64. doi: 10.1130/0091-7613(1995)023<0061:ROCDAC>2.3.CO;2

Shen, B., Jacobsen, B., Lee, C.-T. A., Yin, Q.-Z., and Morton, D. M. (2009). The Mg isotopic systematics of granitoids in continental arcs and implications for the role of chemical weathering in crust formation. *Proc. Natl. Acad. Sci. U.S.A.* 106, 20652–20657. doi: 10.1073/pnas.0910663106

Stracke, A., Tipper, E. T., Klemme, S., and Bizimis, M. (2018). Mg isotope systematics during magmatic processes: Inter-mineral fractionation in mafic to ultramafic Hawaiian xenoliths. *Geochim. Cosmochim. Acta* 226, 192–205. doi: 10.1016/j.gca.2018.02.002

Stumm, W., and Morgan, J. J. (1996). *Aquatic Chemistry: Chemical Equilibria and Rates in Natural Waters, 3rd Edn*. New York, NY: Wiley.

Sullivan, P. L., Ma, L., West, N., Jin, L., Karwan, D. L., Noireaux, J., et al. (2016). CZ-tope at Suquehanna Shale Hills CZO: synthesizing multiple isotope proxies to elucidate Critical Zone processes across timescales in a temperate forested landscape. *Chem. Geol.* 445, 103–119. doi: 10.1016/j.chemgeo.2016.05.012

Teng, F.-Z. (2017). Magnesium isotope geochemistry. *Rev. Mineral. Geochem.* 82, 219–287. doi: 10.2138/rmg.2017.82.7

Teng, F.-Z., Li, W.-Y., Ke, S., Yang, W., Liu, S.-A., Sedaghatpour, F., et al. (2015). Magnesium isotopic compositions of international geological reference materials. *Geostand. Geoanal. Res.* 39, 329–339. doi: 10.1111/j.1751-908X.2014.00326.x

Teng, F.-Z., Li, W.-Y., Rudnick, R. L., and Gardner, L. R. (2010). Contrasting lithium and magnesium isotope fractionation during continental weathering. *Earth Planet. Sci. Lett.* 300, 63–71. doi: 10.1016/j.epsl.2010.09.036

Teng, F.-Z., McDonough, W. F., Rudnick, R. L., Dalpé, C., Tomascak, P. B., Chappell, B. W., et al. (2004). Lithium isotopic composition and concentration of the upper continental crust. *Geochim. Cosmochim. Acta* 68, 4167–4178. doi: 10.1016/j.gca.2004.03.031

Teng, F.-Z., McDonough, W. F., Rudnick, R. L., Walker, R. J., and Sirbescu, M.-L. C. (2006). Lithium isotopic systematics of granites and pegmatites from the Black Hills, South Dakota. *Am. Mineral.* 91, 1488–1498. doi: 10.2138/am.2006.2083

Tipper, E. T., Bickle, M. J., Galy, A., West, A. J., Pomiès, C., and Chapman, H. J. (2006). The short term climatic sensitivity of carbonate and silicate weathering fluxes: insight from seasonal variations in river chemistry. *Geochim. Cosmochim. Acta* 70, 2737–2754. doi: 10.1016/j.gca.2006.03.005

Tipper, E. T., Calmels, D., Gaillardet, J., Louvat, P., Capmas, F., and Dubacq, B. (2012a). Positive correlation between Li and Mg isotope ratios in the river waters of the Mackenzie Basin challenges the interpretation of apparent isotopic fractionation during weathering. *Earth Planet. Sci. Lett.* 333-334, 35–45. doi: 10.1016/j.epsl.2012.04.023

Tipper, E. T., Lemarchand, E., Hindshaw, R. S., Reynolds, B. C., and Bourdon, B. (2012b). Seasonal sensitivity of weathering processes: hints from magnesium isotopes in a glacial stream. *Chem. Geol.* 312–313, 80–92. doi: 10.1016/j.chemgeo.2012.04.002

Tipper, E. T., Louvat, P., Capmas, F., Galy, A., and Gaillardet, J. (2008). Accuracy of stable Mg and Ca isotope data obtained by MC-ICP-MS using the standard addition method. *Chem. Geol.* 257, 65–75. doi: 10.1016/j.chemgeo.2008.08.016

Tomascak, P. B., Magna, T., and Dohmen, R. (2016). "The surficial realm: low temperature geochemistry of lithium," in *Advances in Lithium Isotope Geochemistry*, eds P. B. Tomascak, T. Magna, and R. Dohmen (Cham: Springer), 157–189.

Torres, M. A., Moosdorf, N., Hartmann, J., Adkins, J. F., and West, A. J. (2017). Glacial weathering, sulfide oxidation, and global carbon cycle feedbacks. *Proc. Natl. Acad. Sci. U.S.A.* 114, 8716–8721. doi: 10.1073/pnas.1702953114

Tranter, M. (2003). "Geochemical weathering in glacial and proglacial environments," in *Treatise on Geochemistry*, *Vol. 5: Surface and Ground Water, Weathering and Soils*, eds H. D. Holland and K. K. Turekian (Oxford: Elsevier), 189–205.

Tranter, M., Sharp, M. J., Lamb, H. R., Brown, G. H., Hubbard, B. P., and Willis, I. C. (2002). Geochemical weathering at the bed of Haut Glacier d'Arolla, Switzerland - a new model. *Hydrol. Process.* 16, 959–993. doi: 10.1002/hyp.309

van As, D., Mikkelsen, A. B., Nielsen, M. H., Box, J. E., Liljedahl, L. C., Lindbäck, K., et al. (2017). Hypsometric amplification and routing moderation of Greenland ice sheet meltwater release. *Cryosphere* 11, 1371–1386. doi: 10.5194/tc-11-1371-2017

Van Gool, J. A. M., Connelly, J. N., Marker, M., and Mengel, F. C. (2002). The Nagssugtoqidian Orogen of West Greenland: tectonic evolution and regional correlations from a West Greenland perspective. *Can J. Earth Sci.* 39, 665–686. doi: 10.1139/e02-027

Van Tatenhove, F. G. M. (1996). Changes in morphology at the margin of the Greenland ice sheet (Leverett Glacier), in the period 1943-1992: a quantitative analysis. *Earth Surf. Process. Landforms* 21, 797–816. doi: 10.1002/(SICI)1096-9837(199609)21:9<797::AID-ESP617>3.0.CO;2-2

Vance, D., Teagle, D. A. H., and Foster, G. L. (2009). Variable Quaternary chemical weathering fluxes and imbalances in marine geochemical budgets. *Nature* 458, 493–496. doi: 10.1038/nature07828

Vigier, N., Decarreau, A., Millot, R., Carignan, J., Petit, S., and France-Lanord, C. (2008). Quantifying Li isotope fractionation during smectite formation and implications for the Li cycle. *Geochim. Cosmochim. Acta* 72, 780–792. doi: 10.1016/j.gca.2007.11.011

Walker, J. C. G., Hays, P. B., and Kasting, J. F. (1981). A negative feedback mechanism for the long term stabilization of Earth's surface temperature. *J. Geophys. Res.* 86, 9776–9782. doi: 10.1029/JC086iC10p09776

Wang, S.-J., Teng, F. Z., Li, S.-G., and Hong, J.-A. (2014). Magnesium isotope systematics of mafic rocks during continental subduction. *Geochim. Cosmochim. Acta* 143, 34–48. doi: 10.1016/j.gca.2014.03.029

Wang, S.-J., Teng, F. Z., Williams, H. M., and Li, S.-G. (2012). Magnesium isotope variations in cratonic eclogites: origins and implications. *Earth Planet. Sci. Lett.* 359-360, 219–226. doi: 10.1016/j.epsl.2012.10.016

Wedepohl, K. H. (1995). The composition of the continental crust. *Geochim. Cosmochim. Acta* 59, 1217–1232. doi: 10.1016/0016-7037(95)00038-2

Wehrmann, L. M., Formolo, M. J., Owens, J. D., Raiswell, R., Ferdelman, T. G., Riedinger, N., et al. (2014). Iron and manganese speciation and cycling in glacially influenced high-latitude fjord sediments (West Spitsbergen, Svalbard): evidence for a benthic recycling-transport mechanism. *Geochim. Cosmochim. Acta* 141, 628–655. doi: 10.1016/j.gca.2014.06.007

Wimpenny, J., Burton, K. W., James, R. H., Gannoun, A., Mokadem, F., and Gíslason, S. R. (2011). The behaviour of magnesium and its isotopes during glacial weathering in an ancient shield terrain in West Greenland. *Earth Planet. Sci. Lett.* 304, 260–269. doi: 10.1016/j.epsl.2011.02.008

Wimpenny, J., Colla, C. A., Yin, Q.-Z., Rustad, J. R., and Casey, W. H. (2014). Investigating the behaviour of Mg isotopes during the formation of clay minerals. *Geochim. Cosmochim. Acta* 128, 178–194. doi: 10.1016/j.gca.2013.12.012

Wimpenny, J., James, R. H., Burton, K. W., Gannoun, A., Mokadem, F., and Gíslason, S. R. (2010). Glacial effects on weathering processes: new insights from the elemental and lithium isotopic composition of West Greenland rivers. *Earth Planet. Sci. Lett.* 290, 427–437. doi: 10.1016/j.epsl.2009.12.042

Wunder, B., Meixner, A., Romer, R. L., Feenstra, A., Schettler, G., and Heinrich, W. (2007). Lithium isotope fractionation between Li-bearing staurolite, Li-mica and aqueous fluids: An experimental study. *Chem. Geol.* 238, 277–290. doi: 10.1016/j.chemgeo.2006.12.001

Yang, H., Konzett, J., Downs, R. T., and Frost, D. J. (2009). Crystal structure and Raman spectrum of a high-pressure Li-rich majoritic garnet, $(Li_2Mg)Si_2(SiO_4)_3$. *Am. Mineral.* 94, 630–633. doi: 10.2138/am.2009.3144

Yde, J. C., Knudsen, N. T., Hasholt, B., and Mikkelsen, A. B. (2014). Meltwater chemistry and solute export from a Greenland Ice Sheet catchment, Watson River, West Greenland. *J. Hydrol.* 519, 2165–2179. doi: 10.1016/j.jhydrol.2014.10.018

Yeghicheyan, D., Carignan, J., Valladon, M., Bouhnik Le Coz, M., Le Cornec, F., Castrec-Rouelle, M., et al. (2007). A compilation of silicon and thirty one trace elements measured in the natural river water reference material SLRS-4 (NRC-CNRC). *Geostandard. Newslett.* 25, 465–474. doi: 10.1111/j.1751-908X.2001.tb00617.x

Conflict of Interest: The authors declare that the research was conducted in the absence of any commercial or financial relationships that could be construed as a potential conflict of interest.

frontiers
in Earth Science

ORIGINAL RESEARCH
published: 30 April 2020
doi: 10.3389/feart.2020.00109

Hydrothermal and Cold Spring Water and Primary Productivity Effects on Magnesium Isotopes: Lake Myvatn, Iceland

Philip A. E. Pogge von Strandmann[1]*, Kevin W. Burton[2], Sophie Opfergelt[3], Eydís S. Eiríksdóttir[4], Melissa J. Murphy[5], Arni Einarsson[6,7] and Sigurdur R. Gislason[4]

[1] LOGIC (London Geochemistry and Isotope Centre), Institute of Earth and Planetary Sciences, University College London and Birkbeck, University of London, London, United Kingdom, [2] Department of Earth Sciences, Durham University, Durham, United Kingdom, [3] Earth and Life Institute, Université catholique de Louvain, Louvain-la-Neuve, Belgium, [4] Institute of Earth Sciences, University of Iceland, Reykjavik, Iceland, [5] Department of Earth Sciences, Oxford University, Oxford, United Kingdom, [6] Myvatn Research Station, Skútustaðahreppur, Iceland, [7] Institute of Life- and Environmental Sciences, University of Iceland, Reykjavik, Iceland

OPEN ACCESS

Edited by:
Paul Frederick Dennis,
University of East Anglia,
United Kingdom

Reviewed by:
Martin Dietzel,
Graz University of Technology, Austria
Luke Bridgestock,
University of Oxford, United Kingdom

****Correspondence:***
Philip A. E. Pogge von Strandmann
p.strandmann@ucl.ac.uk

Specialty section:
This article was submitted to Geochemistry,
a section of the journal
Frontiers in Earth Science

Received: *02 January 2020*
Accepted: *24 March 2020*
Published: *30 April 2020*

Citation:
Pogge von Strandmann PAE, Burton KW, Opfergelt S, Eiríksdóttir ES, Murphy MJ, Einarsson A and Gislason SR (2020) Hydrothermal and Cold Spring Water and Primary Productivity Effects on Magnesium Isotopes: Lake Myvatn, Iceland. Front. Earth Sci. 8:109. doi: 10.3389/feart.2020.00109

Lake Myvatn, Iceland, is one of the most biologically productive lakes in the northern hemisphere, despite seasonal ice cover. Hydrothermal and groundwater springs make up the dominant source to this lake, and we investigate their Mg isotope ratio to assess the effect of mid-ocean ridge hydrothermal springs, which are the primary modern sink of seawater magnesium. We also examine a time series in the only outflow from this lake, the Laxa River, to assess the effects of seasonal primary productivity on Mg isotopes. In the hydrothermal waters, there is a clear distinction between cold waters (largely unfractionated from primary basalt) and relatively hot waters, which exhibit over 1‰ fractionation, with consequences for the oceanic mass balance if the hydrothermal removal of Mg is not fully quantitative. The outflow Mg isotopes are similar to basalts (δ^{26}Mg = −0.2 to −0.3) during winter but reach a peak of ~0‰ in August. This fractionation corresponds to calcite precipitation during summer in Lake Myvatn, preferentially taking up light Mg isotopes and driving the residual waters isotopically heavy as observed, meaning that overall the lake is a CO_2 sink.

Keywords: weathering (IGC: D3/D5/D6), isotope geochemistry, carbonate chemistry, hydrothermal spring, groundwater (G.W.), phytoplankton

INTRODUCTION

Chemical weathering of continental silicate rocks is the primary long-term drawdown process of atmospheric CO_2 (Walker et al., 1981; Berner et al., 1983; Chamberlin, 1899). Dissolution of Ca–Mg silicates dissolves CO_2, transports it to the oceans as bicarbonate via rivers, where it, and Ca and Mg, is sequestered into marine carbonates (Berner, 2003). Continental weathering also provides many critical nutrients to the coastal oceans (e.g., Fe, P), which fertilize organic carbon growth (Gíslason et al., 2006). Finally, continental weathering and erosion processes deliver particulate clays and reactive iron to the oceans, which enhance organic carbon burial (Kennedy and Wagner, 2011; Lalonde et al., 2012; Kennedy et al., 2014; Hawley et al., 2017). In short, weathering controls the climate both on short timescales (via organic carbon growth and burial) and long timescales (via carbonate precipitation). Chemical weathering also affects the carbonate saturation state of the oceans on millennial timescales, affecting its pH and ability to store CO_2 (Archer et al., 2000).

However, there are a number of still open questions on these processes, including the ultimate controlling mechanism of silicate weathering [where both climate (via temperature and runoff) and supply of fresh primary silicates are likely important (Raymo and Ruddiman, 1992; West et al., 2005)], and the rate at which any weathering-related feedback can mitigate climate change. One reason why these questions have not been resolved is that no truly unambiguous tracers of weathering, both in the present and in the geological record, have been determined. For example, traditional radiogenic isotopes (e.g., $^{87}Sr/^{86}Sr$ or $^{188}Os/^{187}Os$) have been used to quantify palaeo-weathering (Peucker-Ehrenbrink et al., 1995; McArthur et al., 2001; Bickle et al., 2005). However, they suffer from a strong lithological control (i.e., the isotope ratio of rivers is controlled by the isotope ratio of rocks being weathered) and often cannot distinguish between weathering of silicates and carbonates (Palmer and Edmond, 1992; Oliver et al., 2003). For this reason, other isotopic tracers have been sought, often from the "non-traditional" stable metal isotopes. In this study, we not only focus on magnesium isotopes but also compare them to silicon and lithium isotopes previously measured in the same samples.

Magnesium is of interest because it is an element directly involved in the long-term carbon cycle. It is weathered from rocks on the continents and then sequestered in the oceans into carbonates (primarily dolomites and high-Mg calcites), as well as substituting for Ca in hydrothermal interactions with basalt at mid-ocean ridges. The reactions that control this process largely involve greenschist-facies metamorphism of oceanic basalts, where Mg is basically lost into high-temperature secondary minerals, such as olivine reacting to chlorite or plagioclase reacting to albite + epidote (Humphris and Thompson, 1978; Berner et al., 1983; Albarede and Michard, 1986; Elderfield and Schultz, 1996; Gaillardet et al., 1999; Holland, 2005; Tipper et al., 2006b; Higgins and Schrag, 2015). Hence, weathering is the primary source of Mg to the oceans, while the two main sinks are carbonates and hydrothermal fluids, with additional minor sinks during low-temperature clay formation (Tipper et al., 2006b).

Magnesium has three stable isotopes (^{24}Mg, ^{25}Mg, and ^{26}Mg), with isotope ratios reported as $\delta^{26}Mg$, which is the deviation of the 26/24 ratio from the standard DSM-3 (Galy et al., 2003). Simple dissolution imparts no Mg isotope fractionation (Wimpenny et al., 2010, 2014). During continental weathering, Mg isotopes in surface waters are strongly controlled by the dissolution mixing of isotopically light carbonates and heavy silicates (Tipper et al., 2006a, 2008; Brenot et al., 2008; Wombacher et al., 2011; Pogge von Strandmann et al., 2019b,c). Furthermore, there is additional isotopic fractionation during the formation of secondary minerals from silicate weathering, where these minerals tend to prefer the heavy Mg isotopes (Tipper et al., 2006a,b, 2008, 2010, 2012a; Pogge von Strandmann et al., 2008; Chapela Lara et al., 2017; Hindshaw et al., 2020). The same direction of fractionation occurs during Mg sorption onto mineral surfaces (Huang et al., 2012; Opfergelt et al., 2012, 2014; Pogge von Strandmann et al., 2012). Finally, the uptake of Mg by plants causes variable isotope fractionation (Black et al., 2006; Ra and Kitagawa, 2007; Bolou-Bi et al., 2012).

While a considerable body of literatures exists on Mg isotope behavior in rivers and occasionally groundwaters, much less is known about Mg isotope fractionation in continental hydrothermal fluids (Tipper et al., 2006b; Huang et al., 2018; Oelkers et al., 2019; Pogge von Strandmann et al., 2019c). This is potentially also important for the removal of Mg from seawater. While it has been generally considered that the hydrothermal removal of Mg is quantitative (and hence causes no isotope fractionation) (Holland, 2005; Higgins and Schrag, 2015), totally quantitative reactions are rarely observed in geochemistry and hence raises the interesting possibility of considerable isotope fractionation occurring. Equally, little is known about Mg isotope fractionation during uptake by phytoplankton, important for the budgets of all surface waters.

In this study, we present Mg isotope data from high- and low-temperature groundwaters that dominantly source Lake Myvatn, Iceland. The high-temperature, hydrothermal, waters have undergone water–rock interactions at temperatures up to ∼300°C (cooled during transport to 17–44°C), while the cold groundwaters are at temperatures of 3–7°C. These samples allow the comparison of the effect of temperature on groundwaters from the same area, and particularly the impact on Mg isotope behavior. We also report Mg isotope data from a time series from the single outflow from Lake Myvatn, the Laxa River. The lake has significant seasonal changes in primary productivity that strongly affect its water chemistry and provides an opportunity to study the effects of phytoplankton (including a large component of diatoms) on isotope fractionation.

Field Area

Lake Myvatn (65°35′ N, 17°00′ W) is a shallow eutrophic lake in the northeast of Iceland located close to the Arctic Circle (**Figure 1**). The lake's altitude is 278 m above sea level, and it has a maximum depth of ∼4.2 m, with an area of ∼37 km^2. During the summer (ice-free) season (mid-May to late-September), the entire water column is well-mixed. The primary water sources to the lake are groundwaters, with the southern basin (Sydrifloi) fed by cold springs, and the northern basin (Ytrifloi) fed by hot springs (Pogge von Strandmann et al., 2016). The heat in the hot springs stems from the Namafjall and Krafla geothermal fields (Kristmannsdottir and Armannsson, 2004). Only one river (the Laxa River) drains the lake, and the water in the lake has a residence time of about 27 days (Olafsson, 1979a).

The underlying geology of the lake is basaltic and ∼2,300 years old, formed by a major basaltic volcanic eruption. Since then, the local geology has been modified by more recent eruptions, including the Krafla Volcano's 1725–1729 and 1975–1984 eruptions (Thordarson and Hoskuldsson, 2002; Hauptfleisch and Einarsson, 2012).

Despite winter ice cover, the lake is one of the most biologically productive in the northern hemisphere. This is due to high nutrient delivery from the groundwater sources, causing very high seasonal productivity, mainly associated with diatoms, green algae, and cyanobacteria (Olafsson, 1979b; Gislason et al., 2004;

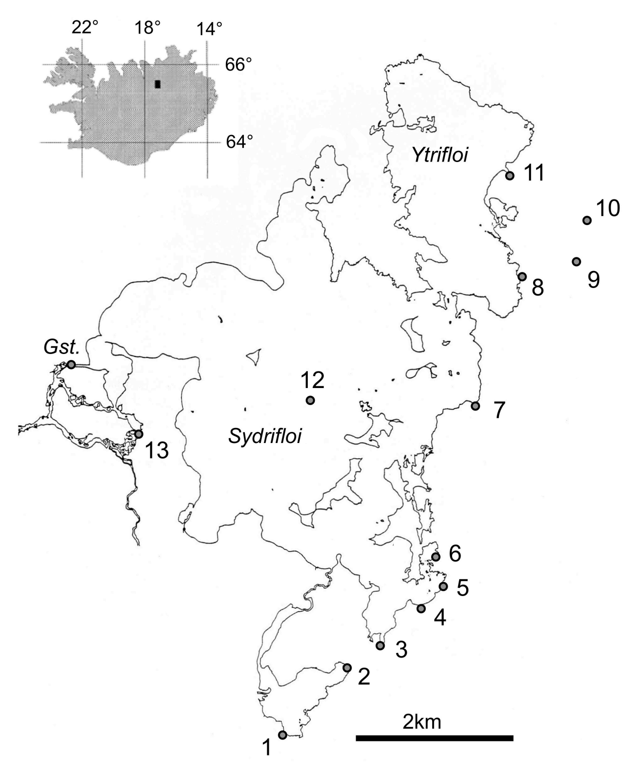

FIGURE 1 | Location map of samples within Lake Myvatn, Iceland. The sample numbers correspond to the final numbers of each sample name in **Table 1**. The monitoring for 2000–2001 was made at the outlet Geirastadaskudur (Gst.).

Thorbergsdottir and Gislason, 2004; Opfergelt et al., 2011). Biological activity in the lake also controls the concentrations of many dissolved metals. When the lake is covered by ice, sediment pore waters become enriched in nutrients relative to the lake waters by several orders of magnitude. These nutrients are then subsequently released by bioturbation, as well as sediment resuspension and diffusion, in the ice-free summer, leading to high nutrient fluxes and hence primary productivity (Gislason et al., 2004).

Samples were taken from both the "cold" and "hot" springs sourcing the lake in August 2009, and a monthly time series spanning March 2000 to March 2001 was taken from the Laxa River draining the lake following sampling protocols outlined in Opfergelt et al. (2011).

MATERIALS AND METHODS

Major and trace element concentrations were measured by Opfergelt et al. (2011) and were determined by inductively coupled plasma mass spectrometry (ICP-MS) and ion chromatography. At each site, pH and temperature were measured *in situ* (Opfergelt et al., 2011). For Mg isotope analysis, sufficient water was dried down to attain ~1 μg of Mg. This was passed through a two-step cation exchange chromatography procedure, using AG50W X-12 resin, and using 2 M HNO_3 as an eluent. Isotopic analyses were conducted on a Thermo Neptune multicollector ICP-MS at the Bristol Isotope Group, normalizing to the standard DSM-3.

This procedure has been described in detail before (Pogge von Strandmann et al., 2011), and resulting standards have been shown in multiple compilations and interlaboratory comparisons (Foster et al., 2010; Pogge von Strandmann et al., 2011; Teng et al., 2015; Shalev et al., 2018). During the analyses of this study's waters, seawater was used as a standard, with a $\delta^{26}Mg = -0.82 \pm 0.05‰$ ($n = 3$), which agrees with the long-term running average of over 10 years (Foster et al., 2010) and where $\delta^{26}Mg = (^{26}Mg/^{24}Mg_{sample}/^{26}Mg/^{24}Mg_{DSM-3} - 1) \times 1,000$.

The solution elemental concentrations were used to calculate mineral saturation states using PHREEQC and a combination of its standard thermodynamic database, plus THERMODEM and MINTEQ databases (Parkhurst and Appelo, 1999). These are reported as the logarithmic saturation index, SI, where positive numbers indicate supersaturation, and negative numbers indicate undersaturation.

RESULTS

Hydrothermal and Cold Groundwaters

All results are listed in **Table 1**, and the sample locations are shown in **Figure 1**. The groundwaters that are the primary source to Lake Myvatn are undersaturated with respect to the primary basaltic minerals of glass, olivine, pyroxene and plagioclase, as well as minerals such as calcite. Secondary minerals such as kaolinite are supersaturated, while smectites are supersaturated at relatively low pH (8–9) but undersaturated at higher pH. Secondary minerals that are known to remove Mg in seawater hydrothermal settings, such as chlorite or Mg-rich smectite (Haymon and Kastner, 1986), are also supersaturated.

Magnesium concentrations vary between 74 and 160 μmol/l, on average 50% or more lower than river waters from Iceland (Gíslason et al., 1996). The "cold" groundwaters (<7.5°C) are on average slightly less concentrated than the "hot" groundwaters (106 vs. 126 μmol/L, respectively).

Mg isotope ratios ($\delta^{26}Mg$) vary between −1.36 and −0.16‰, with the cold waters being on average significantly isotopically heavier (average, −0.40‰) compared to the hot groundwaters (−1.01‰). Overall, the Mg isotope ratios negatively covary with elemental concentrations such as Na, and overlap with, but extend to lower values than Icelandic river waters (Pogge von Strandmann et al., 2008). There is no evidence of mixing between different Mg sources (e.g., seawater via precipitation) in any of the samples (**Figure 2**).

Laxa River Outflow

The Mg concentration of the outflow time series is overall slightly higher than most of the groundwater springs, with values ranging from 130 to 170 μmol/L. There is no obvious seasonal trend, although the highest concentrations are in the summer. Mg isotope ratios, in contrast, are strongly seasonal, with $\delta^{26}Mg$ values of −0.31 to −0.24‰ in the winter (ice-covered) months,

TABLE 1 | Concentration and isotope data for the Lake Myvatn samples.

Sample	Sample month	Temperature	pH	Conductivity	Na	K	Mg	Ca	Al	Si	P	Ti	NO_3	δ^{25}Mg (%o)	2se	δ^{26}Mg (%o)	2se	Δ^{25}Mg (%o)
		°C		µ S/cm	mM	mM	mM	mM	µM	mM	µM	µM	µM					
Input springs																		
IC/MY/01.09		3.4	9.27		0.53	0.02	0.07	0.11	0.45	0.29	1.41	0.017		−0.15	0.02	−0.29	0.02	0.00
IC/MY/02.09		7	9.4	130	0.72	0.03	0.11	0.12	0.53	0.31	1.5	0.018		−0.09	0.02	−0.16	0.03	−0.01
IC/MY/03.09		6.5	9.21	141	0.67	0.03	0.15	0.15	0.5	0.3	1.6	0.019		−0.33	0.00	−0.66	0.03	0.02
IC/MY/04.09		6.2	9.23	129	0.64	0.03	0.14	0.14	0.45	0.3	1.78	0.018		−0.17	0.01	−0.29	0.02	−0.02
IC/MY/05.09		5.8	9.6	115	0.74	0.02	0.07	0.11	0.67	0.31	1.83	0.019		−0.13	0.02	−0.26	0.01	0.00
IC/MY/06.09		7	9.6	134	0.81	0.02	0.08	0.11	0.59	0.34	1.58	0.019		−0.35	0.03	−0.68	0.02	0.01
IC/MY/07.09		7.5	9.29	156	0.9	0.03	0.13	0.16	0.48	0.35	1.72	0.02		−0.23	0.02	−0.46	0.00	0.01
IC/MY/08.09		16.5	8.68	359	2.02	0.1	0.16	0.3	0.62	1.38	0.92	0.035		−0.44	0.02	−0.86	0.03	0.01
IC/MY/09.09		37.3	8.29	505	3.32	0.15	0.08	0.35	1.06	2.25	0.58	0.042		−0.48	0.03	−0.94	0.01	0.01
IC/MY/10.09		44	8.1	437	2.64	0.15	0.09	0.28	0.2	2.23	0.51	0.038		−0.68	0.01	−1.36	0.03	0.02
IC/MY/11.09		24.3	8.29	396	1.73	0.1	0.16	0.51	0.32	1.2	0.82	0.026		−0.34	0.03	−0.66	0.03	0.01
IC/MY/14.09		20	3.5	620	2.55	0.27	0.14	0.2			0.69	0.142		−0.61	0.03	−1.20	0.04	0.01
IC/MY/12.09 -	Mid-lake	10.2	9.82	157	0.77	0.03	0.11	0.15	0.39	0.15	1.07	0.018		0.00	0.04	0.00	0.02	0.00
IC/MY/13.09 -	lake outflow	10.7	10	162	0.79	0.03	0.12	0.15	0.31	0.13	0.89	0.023		0.01	0.02	0.01	0.01	0.00
Laxa River																		
00A013	March-00	1.2	8.37		1.01	0.04	0.16	0.2	0.33	0.41			2.06	−0.15	0.01	−0.31	0.02	0.01
00A023	April-00	0	9.03		0.78	0.03	0.15	0.16	0.03	0.3			0.35	−0.15	0.03	−0.25	0.01	−0.02
00A031	May-00	6	8.52		0.75	0.03	0.13	0.15	0.3	0.22			0.15	−0.12	0.02	−0.26	0.03	0.01
00A044	June-00	12.3	9.63		0.88	0.03	0.15	0.18	0.4	0.1			0.98	−0.10	0.00	−0.19	0.01	0.00
00A053	July-00	15.7	9.93		0.95	0.03	0.14	0.18	1.08	0.05			1.01	−0.05	0.03	−0.09	0.02	0.00
00A062	August-00	15.5	9.78		1.04	0.04	0.17	0.2	0.49	0.09			0.17	−0.03	0.02	−0.03	0.02	−0.01
00A071	September-00	8.3	9.35		0.94	0.04	0.15	0.18	0.26	0.1			0.17	−0.14	0.03	−0.21	0.03	−0.03
00A080	October-00	1.4	8.73		0.95	0.04	0.16	0.18	0.15	0.16			0.15	−0.15	0.02	−0.29	0.01	0.00
00A089	November-00	0.6	8.32		0.97	0.04	0.16	0.19	0.18	0.31			0.51	−0.17	0.02	−0.31	0.03	−0.01
01A006	1-January	0.9	8.34		0.97	0.04	0.16	0.19	0.47	0.41			2.75	−0.12	0.03	−0.24	0.02	0.00
01A015	1-March	0.5	8.43		0.88	0.04	0.14	0.14	0.38	0.34			0.89	−0.12	0.04	−0.26	0.01	0.01

All parameters aside from Mg isotope ratios are repeated from Opfergelt et al. (2011). The Δ^{25}Mg represent the ‰ deviation from the terrestrial fractionation line.

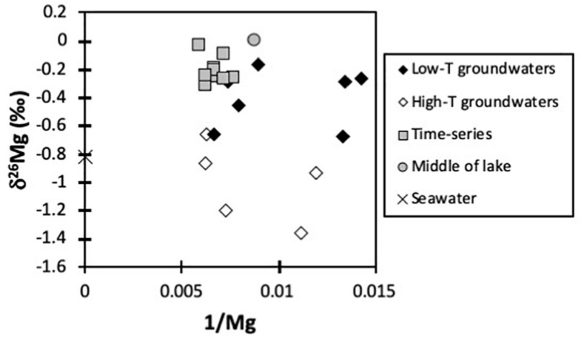

FIGURE 2 | Mixing diagram [1/Mg (in μmol/l) vs. δ^{26}Mg] for the groundwaters, outflow time series, and seawater (representing Icelandic precipitation). No mixing trends are visible.

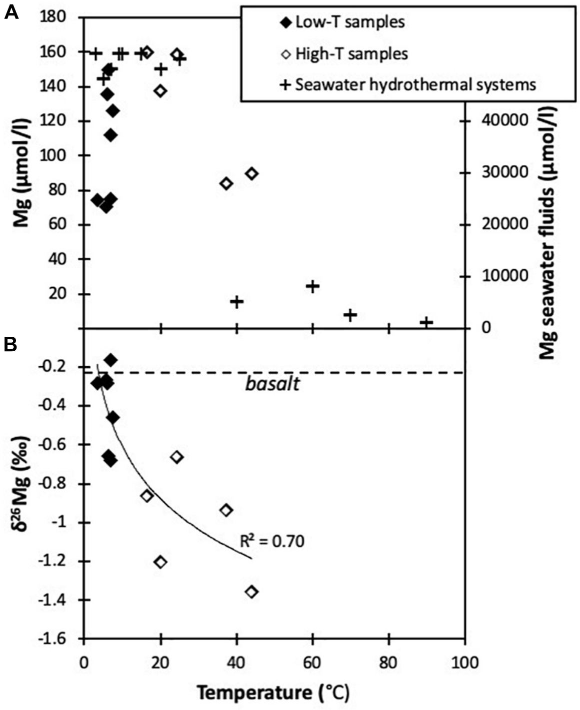

FIGURE 3 | (A) The effect of temperature on Mg concentrations during hydrothermal removal. At low temperatures, there is no effect, but as temperatures exceed 30°C, Mg concentrations both in Myvatn and seawater samples (Mottl and Wheat, 1994) rapidly decrease (note different scale for seawater samples). **(B)** This effect causes significant Mg isotope fractionation in the Myvatn hydrothermal springs. The trend line is logarithmic to correspond to stable isotope fractionation theory.

increasing to a maximum of −0.03‰ in August, within the range of Icelandic river waters (Pogge von Strandmann et al., 2008). This yearly peak is similar to that observed for Al concentrations and inversely to Si concentrations, but not other nutrients like NO_3, which exhibits two minima (Opfergelt et al., 2011).

Sample MY12 was collected from the middle of the Lake at the end of August 2009, and its δ^{26}Mg (0.00‰) is within analytical uncertainty of the outflow sample collected in August 2000 (−0.03‰), suggesting that the broad time series patterns observed in 2000–2001 are repeatable yearly cycles.

DISCUSSION

Hydrothermal and Cold Groundwaters

The primary modern sink of Mg from seawater is exchange of Mg for Ca during high-temperature basalt–water interactions (Holland, 2005). At the same time, the low-temperature alteration of the oceanic crust is likely to be at the very least a minor sink of Mg from seawater (Tipper et al., 2006b; Huang et al., 2018). The Myvatn groundwaters provide the opportunity to examine Mg isotope fractionation at various temperatures of basalt–water interaction.

Mg concentrations in the low-temperature springs (<7.5‘C) are quite variable, ranging from 70 to 150 μmol/L. However, the higher temperature springs show a negative covariation between [Mg] and temperature, such that the warmest samples have low [Mg] (**Figure 3A**). This is a broadly similar behavior to Mg concentrations during seawater–basalt interactions at mid-ocean ridges (Albarede and Michard, 1986; Mottl and Wheat, 1994; Elderfield and Schultz, 1996). There, [Mg] drops from concentrations of > 90% of that of seawater to < 10% of seawater once temperatures are > 40°C. By 90°C, Mg concentrations are < 2% of that of seawater (Mottl and Wheat, 1994).

While overall concentrations are significantly lower in the Myvatn springs, because the original solution is not seawater, the overall relationship is similar and suggests that these results may be able to inform on Mg isotope fractionation occurring during Mg removal from seawater. It is therefore significant that the Mg isotope ratios of these springs show a clear relationship with temperature (**Figure 3B**). The coldest groundwater (∼3°C) has a δ^{26}Mg value that is indistinguishable from primary basalt [−0.29 vs. −0.23‰, respectively (Pogge von Strandmann et al., 2008, 2011, 2012; Opfergelt et al., 2014)]. At slightly higher temperatures (>3, but < 7.5°C), there is more fractionation (δ^{26}Mg = −0.68 to −0.16‰), while at higher temperatures, Mg isotope ratios in the solution continue to decrease, reaching a value of -1.36‰ at 44°C. There are two general processes that could be causing greater Mg isotope fractionation at higher temperatures: (1) standard temperature-dependent stable isotope fractionation, which scales according to 1,000 × ln(α) as a function of $10^6/T^2$ (where T is temperature in K, and $\alpha_{rock/soln}$ is the isotopic fractionation factor between solution and solid, which, for geological processes, approximates the Δ^7Li between two phases) (Faure, 1986); (2) removal of Mg into high-temperature secondary minerals, such as chlorite or smectite, which is the process by which most of the present-day Mg is removed from seawater (Humphris and Thompson, 1978).

Figure 4 shows that there is a covariation between the Mg isotope fractionation and temperature (shown as $1/T^2$), such that at higher temperature, the solution δ^{26}Mg is more fractionated from the basaltic starting composition. Such a relationship is, in effect, opposite from what would be expected from stable isotope

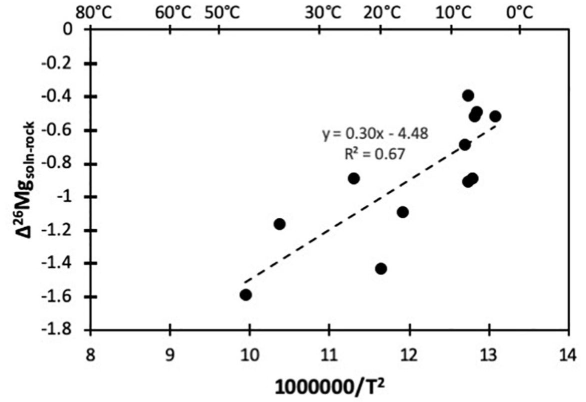

FIGURE 4 | Mg isotope fractionation factors from primary basalt as a function of temperature.

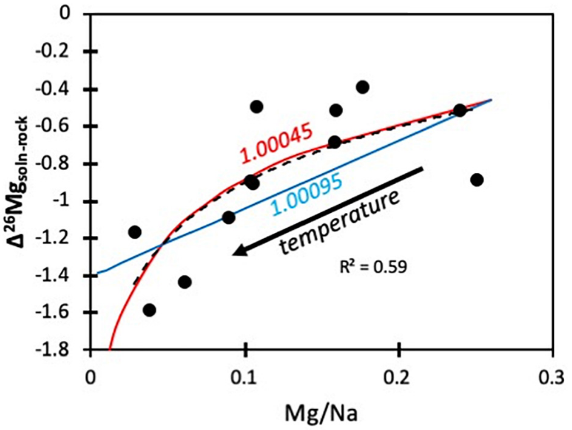

FIGURE 5 | Mg isotope fractionation in the hydrothermal springs as a function of Mg/Na ratios. The black dotted line represents a best-fit line to the data, while the red line represents the Rayleigh fractionation trend fitted to the best-fit line. The blue line is the best-fit equilibrium fractionation line. The italicized numbers represent the required α values.

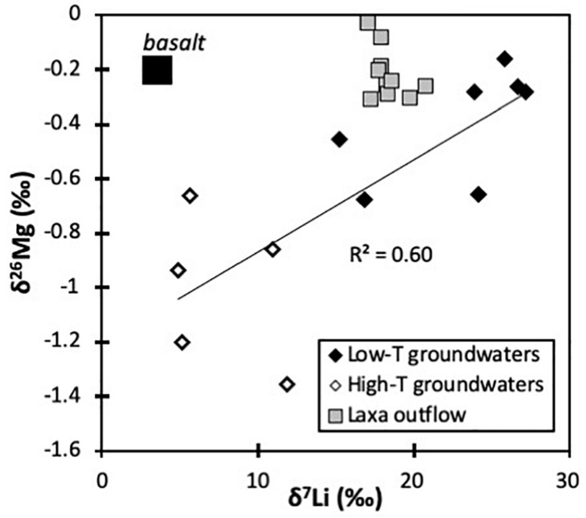

FIGURE 6 | Mg isotope ratios as a function of Li isotope ratios (Pogge von Strandmann et al., 2016). Fractionation-controlling mechanisms are clearly different in these two systems (see text for details).

fractionation theory, where more fractionation occurs at lower temperature (Urey, 1947). It therefore seems likely that, while there is a temperature effect occurring, it is not dominantly due to simple stable isotope fractionation effects, suggesting that high-temperature secondary mineral formation may be playing a role.

In the case of basalt–seawater hydrothermal reactions, Mg is removed by high-temperature secondary mineral formation [such as chlorite (Berner et al., 1983; Albarede and Michard, 1986; Elderfield and Schultz, 1996; Gaillardet et al., 1999; Holland, 2005; Tipper et al., 2006b; Higgins and Schrag, 2015), which is supersaturated in these groundwaters]. The same effect can be observed by the negative covariation between Δ^{26}Mg and the Mg/Na ratio (**Figure 5**). As temperature increases, more Mg is removed, removing Mg preferentially over Na [which is the most soluble major cation in basalt weathering (Gíslason et al., 1996)], and causing greater Mg isotope fractionation. The best-fit Rayleigh fractionation relationship requires an $\alpha_{rock-solution}$ (isotopic fractionation factor) value of 1.00045 (while for equilibrium fractionation, this would be 1.00095, although given the potential of Mg depletion during hydrothermal reactions, a Rayleigh relationship would be expected to be more accurate). The Rayleigh fractionation is given by:

$$\delta_f - \delta_i = 10^3(f^{\alpha-1} - 1)$$

where δ_i is the isotope ratio (in delta notation) of the initial material, δ_f is that of the product, and f is the fraction of material remaining. Model estimates for the high-temperature hydrothermal removal of Mg have α values of 1.0000 (i.e., no isotopic fractionation) and values of 1.0007 for low-temperature clays (Higgins and Schrag, 2015). Experimental interactions between saponite (Mg-rich smectite) and seawater at 250 and 290°C report fractionation factors of 1.000345–1.000422 (Voigt et al., 2020), similar to our fractionation values.

The effect of hydrothermal fractionation on Mg isotopes can also be observed with a comparison to lithium isotopes. For Li, the low-temperature groundwaters are highly isotopically fractionated from the original basalt (**Figure 6**), while the high-temperature waters are relatively unfractionated. In effect, this represents standard stable isotope fractionation behavior, plus the effect that, in hot waters, the secondary minerals that fractionate Li isotopes are more soluble and hence precipitate less (Pogge von Strandmann et al., 2017). The positive covariation between δ^7Li and δ^{26}Mg in these waters (**Figure 6**), where clay formation should cause a negative covariation because clays tends to preferentially take up light Li but heavy Mg isotopes, shows that temperature-dependent stable isotope fractionation is not the controlling process for Mg isotopes.

Such a relationship could have interesting effects on the oceanic Mg isotope mass balance if the removal of Mg through hydrothermal interactions is not fully quantitative. Although

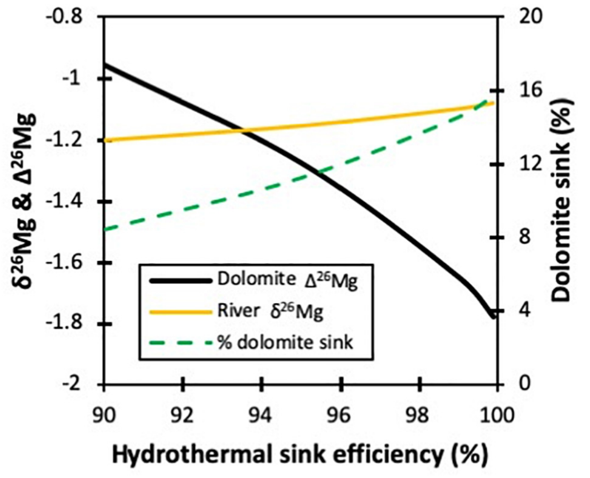

FIGURE 7 | Models on a steady-state modern seawater Mg budget, assuming that the hydrothermal sink is not fully efficient, and causes isotope fractionation as observed in our samples. See text for details.

it is debated whether the modern oceans are in concentration or isotopic equilibrium for Mg (Holland, 2005; Tipper et al., 2006b; Pogge von Strandmann et al., 2014; Higgins and Schrag, 2015; Gothmann et al., 2017; Voigt et al., 2020), if we assume for simplicity's sake that they are, the mass balance can be inverted to determine the effect of isotope fractionation caused by a not fully quantitative Mg removal associated with the Rayleigh fractionation observed in our Myvatn samples. We use the original basic steady-state oceanic Mg mass balance of Tipper et al. (2006b):

$$\delta_{SW} = f_{riv}\delta_{riv} - [f_{dol}\Delta_{dol} + f_{hyd}\Delta_{hyd} + f_{hydret}\Delta_{hydret}]$$

where f is the fraction the source or sink flux for rivers, dolomite, hydrothermal, and the hypothetical "hydrothermal return," which designates the efficiency of the hydrothermal sink, make up of the total source or sink. δ is the δ^{26}Mg of the source or of seawater (SW), and Δ is the isotopic fractionation imposed by the sinks. This is then solved for three separate individual parameters: (i) the dolomite Δ^{26}Mg [set to −1.7‰ when not varied (Pogge von Strandmann et al., 2014)], (ii) the riverine δ^{26}Mg [set to −1.09‰ when not varied (Tipper et al., 2006b)], and (iii) the amount of the total sink comprised by dolomite [set to 15% when not varied (Tipper et al., 2006b)]. For example, as summarized in **Figure 7**, to maintain a steady-state seawater δ^{26}Mg of −0.82‰ (Foster et al., 2010), if the hydrothermal sink efficiency for Mg is 90% (with a fractionation of −1.27‰, as determined from the Myvatn Rayleigh relationship), then dolomite must cause a fractionation of −0.96‰. In contrast, if that sink efficiency is 99.9%, then the dolomite fractionation must be −1.78‰.

Equally, if the dolomite fractionation were constant, then the amount of Mg that dolomite removes from seawater would have to decrease with increasing hydrothermal removal efficiency. Finally, if both the dolomite sink and Mg isotope fractionation were constant, then the global riverine δ^{26}Mg would have to change to maintain a constant seawater δ^{26}Mg, as shown in **Figure 7**. In other words, different parameters of the global ocean Mg mass balance can be significantly affected by the efficiency of Mg removal by the hydrothermal sink if, as shown here, there is an isotopic fractionation associated with that sink.

Laxa River Outflow

Previous work on these outflow samples show that two phytoplankton blooms occurred during the year, the first during May–June and the second during August–September, representing the spring and autumn diatom blooms (Opfergelt et al., 2011). During these periods, NO_3 concentrations are at a minimum, as nutrients are being scavenged for plankton growth. In general, the groundwater is thought to act as a constant source of dissolved nutrients, split between cold springs (~80% of input) and hot springs (~20%). Thus, the phytoplankton blooms are controlled by the buildup of nutrients during the ice-covered season, and the spring bloom then occurs immediately after ice breakup. A second bloom then occurs in the autumn, corresponding to the second decline in dissolved nitrate (**Table 1**).

Silicon isotopes are strongly affected by these blooms: diatoms preferentially take up the light Si isotope, driving the lake water isotopically heavy. This results in Si isotopes showing a double peak during these periods. In contrast, Si concentrations only show a single minimum, with values declining throughout spring and increasing again after the July minimum (**Figures 8**, **9**) (Opfergelt et al., 2011).

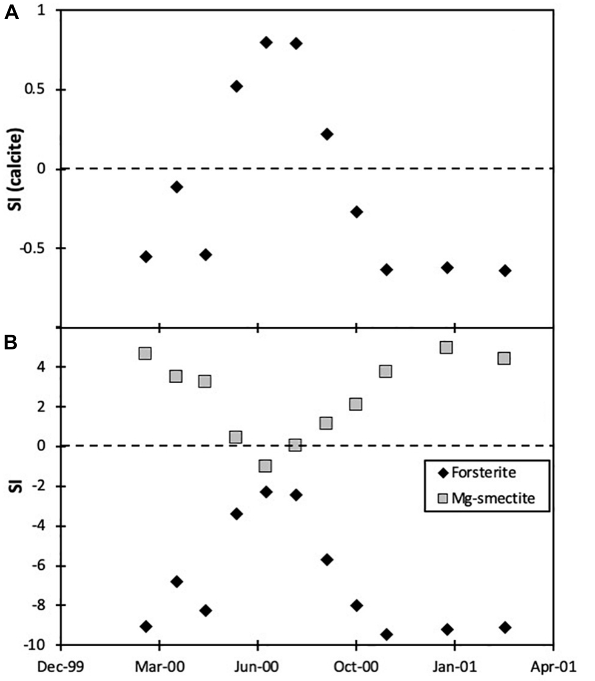

FIGURE 8 | Calcite **(A)**, forsterite, and smectite **(B)** mineral saturation indices for the Laxa River outflow time series.

In contrast, lithium is an element largely unaffected by any biology, including phytoplankton. Li concentrations are unaffected by any of the phenomenon that affect other elements in these samples (Pogge von Strandmann et al., 2016). Equally, Li isotope ratios also exhibit broadly constant values throughout the year, showing that δ^7Li is unaffected by plankton growth (**Figure 9**). Li isotopes are normally strongly affected by secondary mineral formation (Hindshaw et al., 2019; Pogge von Strandmann et al., 2019a). PHREEQC calculations show that the saturation state of several minerals changes dramatically during the year. For example, olivine is strongly undersaturated during the winter but approaches saturation in summer (**Figure 8**). Equally, secondary minerals such as smectite are supersaturated during the winter but become undersaturated in the summer. It is, however, unclear how much this change represents actual changes in mineral saturation and how much is element utilization by plankton (misinterpreted by PHREEQC as changes in saturation). The invariant Li isotopes suggest that silicate secondary mineral formation does not change much during the year, implying that plankton, rather than mineral precipitation, are primarily changing elemental concentrations during the course of the year.

Mg isotopes do not exhibit a double peak like Si isotopes or NO_3 concentrations (**Figure 9**). Instead, they more closely follow trends like pH, which also only show a single maximum (Opfergelt et al., 2011). This implies that Mg isotopes are not being fractionated by the phytoplankton (of which diatoms make up approximately two-thirds), which is also suggested by the relatively unchanging Mg concentrations, which are clearly not limiting plankton growth. This presents a contrast to coccolith growth experiments, where the phytoplankton preferentially took up light Mg isotopes (Ra and Kitagawa, 2007). On the other hand, it has been suggested that plants have little overall effect on riverine Mg isotope ratios (Tipper et al., 2012b), although this effect does appear to depend on location and stream size (Pogge von Strandmann et al., 2019b). This may present a difference between laboratory growth experiments and natural samples, and of course, the diatoms that make up a large proportion of the Myvatn phytoplankton may also not fractionate Mg isotopes.

Equally, it does not seem that Mg isotopes are being controlled by the precipitation of silicate secondary minerals. If the PHREEQC saturation calculations are correct, maximum precipitation of minerals like Mg smectite should occur in the winter months (**Figure 8**). However, smectites, and most other secondary silicates, preferentially take up heavy Mg isotopes, driving residual waters isotopically light (Tipper et al., 2006a, 2008; Opfergelt et al., 2012; Pogge von Strandmann et al., 2012; Chapela Lara et al., 2017; Hindshaw et al., 2020). Thus, if precipitation of these minerals were controlling the Mg isotopes, it would be expected that, during winter, Mg isotope ratios would be lower than that of the initial basalt (~-0.25‰). Instead, during the winter, the outflow Mg isotope ratios are within analytical uncertainty of basalt, implying only dissolution with little secondary mineral formation.

However, a secondary mineral that is suggested by PHREEQC to be undersaturated during the winter and supersaturated during the summer is calcite. From June to September, calcite precipitates in Lake Myvatn, not only suggested by our saturation calculations but also confirmed by precipitation boxes placed on the bottom of the lake (Thorbergsdottir and Gislason, 2004). Calcite preferentially takes up light Mg isotopes, driving residual waters isotopically heavy (Immenhauser et al., 2010; Wombacher et al., 2011; Mavromatis et al., 2012; Saulnier et al., 2012; Saenger and Wang, 2014). The calcite saturation state corresponds to Mg isotopes in Lake Myvatn, where values are only distinguishable from primary basalt from June to September, when they become isotopically heavier. A calcitic control on Mg isotope ratios is also suggested by a direct positive covariation between the calcite SI and δ^{26}Mg ($r^2 = 0.79$; **Figure 10**).

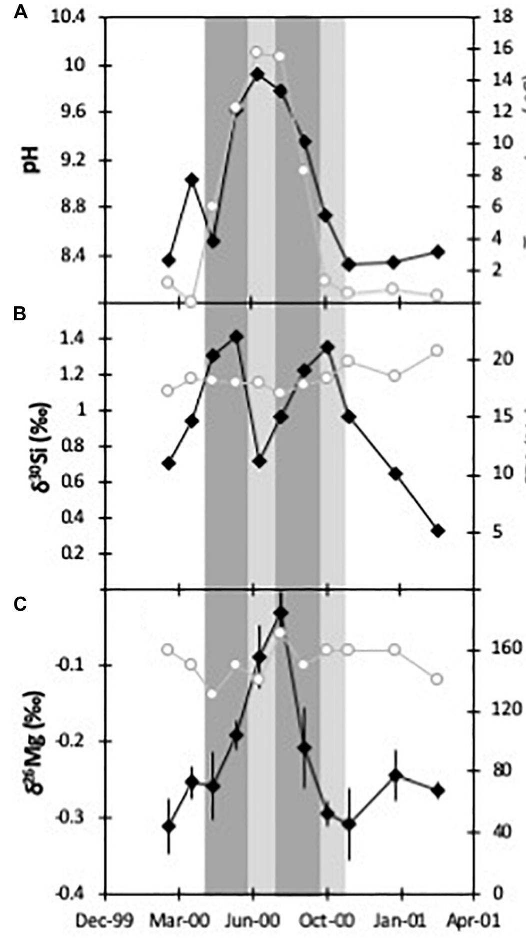

FIGURE 9 | Parameters for the Laxa River outflow time series: **(A)** pH and temperature; **(B)** Si and Li isotopes (Opfergelt et al., 2011; Pogge von Strandmann et al., 2016); **(C)** Mg isotopes and Mg concentrations. The error bars represent the 2sd analytical uncertainty. The dark gray bars represent the spring and autumn diatom blooms, while the light gray bars represent the ice-free months.

Calcite precipitation has previously been observed driving riverine Mg isotope ratios heavy in Iceland during highly supersaturated outflow from the 2010 Eyjafjallajökull eruption (Pogge von Strandmann et al., 2019c). In this case, calcite SI reached values of > 1.5, travertine precipitation was observed, and δ^{26}Mg changed by over 2.5‰. Here at Myvatn, calcite never

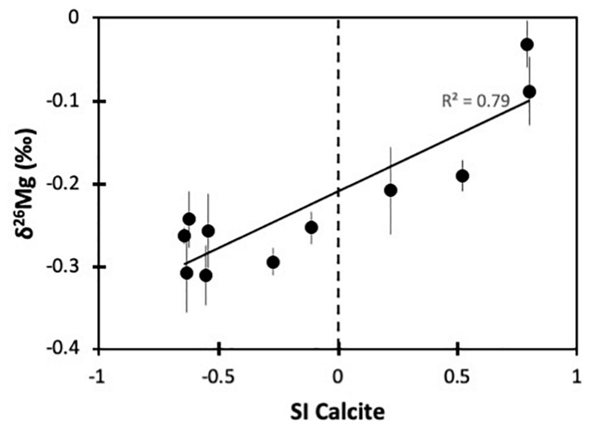

FIGURE 10 | Mg isotope ratios in the Laxa River outflow time series as a function of the saturation index of calcite.

becomes quite as supersaturated (maximum SI = 0.8), and δ^{26}Mg changes considerably less. This may also be exacerbated by the much larger water reservoir in Lake Myvatn and the Laxa River, compared to the smaller streams samples from Eyjafjallajökull.

Given that the groundwater influx rate into Lake Myvatn is fairly constant at 33 m^3/s, it follows that the outflow rate through the Laxa River is broadly the same rate (Olafsson, 1979a; Opfergelt et al., 2011). Assuming that Mg isotopes are solely being fractionated by calcite formation, with a known fractionation factor of $\alpha = 0.9965$ (Mavromatis et al., 2013; Saenger and Wang, 2014; Pogge von Strandmann et al., 2019c), up to 8% of dissolved Mg is lost into calcite (Pogge von Strandmann et al., 2019c). Following the calculations detailed in Pogge von Strandmann et al. (2019c), using the Laxa outflow rate and the volume of Lake Myvatn ($\sim 9.25 \times 10^7$ m^3), the calcite precipitation rate reaches a maximum of ~53 t/month (~6 mmol/month/m^3) in August. Over the course of a year, this results in the precipitation of ~240 t/year calcite. However, during the winter months, calcite is undersaturated, and much of this calcite may redissolve, as also predicted elsewhere (Thorbergsdottir and Gislason, 2004). Overall, this calcite precipitation is an order of magnitude less than the Si sequestration by diatom growth of ~7,500 t/year (Opfergelt et al., 2011), showing that the phytoplankton (including diatoms) in Myvatn can have a significantly larger effect on the concentration of many elements compared to calcite precipitation. In comparison, the stream draining the Eyjafjallajökull eruption exhibited a Mg isotope-based calcite precipitation rate of 3,200 t/year (Pogge von Strandmann et al., 2019c).

The precipitation of that amount of calcite would sequester ~105 t/year of atmospheric CO_2, in lake-stored carbonate. Eventual dissolution of that calcite would release alkalinity, which the Laxa River would transport to the oceans, where it would form marine carbonate, again sequestering CO_2 on the timescale of the completion of the carbonate weathering reaction, which is on the order of a few 1000 years (Archer et al., 2000). Thus, even if the carbonate that forms within Lake Myvatn is redissolved, it still acts as a medium-term CO_2 sink, meaning that, overall, the lake is a location of carbon sequestration even when not considering any potential burial of organic carbon.

CONCLUSION

This study analyzed Mg isotope ratios in hydrothermal and groundwaters of different temperatures that form the primary input into Lake Myvatn, Iceland. There is a clear trend between their δ^{26}Mg and temperature, such that δ^{26}Mg values decrease with increasing temperature. Hence, as Mg is removed, Mg isotopes become increasingly fractionated, with a fractionation factor of $\alpha \sim 1.00045$. Hydrothermal solutions are the main sink of Mg from modern seawater. While they are generally considered to be a quantitative sink (i.e., causing no isotope fractionation), if they are not fully efficient, our data suggest that they will cause significant fractionation, with consequences for the ocean mass balance.

This study also examined Mg isotopes from a time series of the Laxa River, the only outflow from Lake Myvatn. This lake is one of the most productive in the northern hemisphere and has a strong seasonal growth rate dependence that affects nutrients like NO_3 and Si. Mg isotopes do not exhibit the double peak typical of the two seasonal growth cycles but do exhibit a single peak, reaching maximum values in August. This behavior appears to correspond to the saturation behavior of calcite, which preferentially takes up light Mg isotopes driving residual water isotopically heavy. Hence, calcite is precipitated in the lake during summer and then likely dissolved again during winter when calcite is undersaturated, following which it will contribute alkalinity to the oceans. Myvatn is thus a CO_2 sink even without considering the formation and burial of its organic carbon.

DATA AVAILABILITY STATEMENT

All datasets generated for this study are included in the article/supplementary material.

AUTHOR CONTRIBUTIONS

PP analyzed the samples, interpreted the data, and wrote the manuscript. KB, SO, AE, EE, and SG provided samples and local knowledge. MM assisted with analyses. All co-authors assisted with interpretation.

FUNDING

PP and the analyses were funded by NERC grant NE/I020571/2, and PP and MM are also supported by ERC Consolidator grant 682760 CONTROLPASTCO2.

ACKNOWLEDGMENTS

We thank the two reviewers LB and MD for their comments.

REFERENCES

Albarede, F., and Michard, A. (1986). Transfer of continental Mg, S, O and U to the Mantle through Hydrothermal alteration of the Oceanic-Crust. *Chem. Geol.* 57, 1–15. doi: 10.1016/0009-2541(86)90090-2

Archer, D., Winguth, A., Lea, D. W., and Mahowald, N. (2000). What causes the glacial/interglacial atmospheric pCO2 cycles? *Rev. Geophys.* 38, 159–189.

Berner, R. A. (2003). The long-term carbon cycle, fossil fuels and atmospheric composition. *Nature* 426, 323–326. doi: 10.1038/nature02131

Berner, R. A., Lasaga, A. C., and Garrels, R. M. (1983). The Carbonate-Silicate Geochemical Cycle and Its Effect on Atmospheric Carbon-Dioxide over the Past 100 Million Years. *Am. J. Sci.* 283, 641–683. doi: 10.2475/ajs.283.7.641

Bickle, M. J., Chapman, H. J., Bunbury, J., Harris, N. B. W., Fairchild, I. J., Ahmad, T., et al. (2005). Relative contributions of silicate and carbonate rocks to riverine Sr fluxes in the headwaters of the Ganges. *Geochim. Cosmochim. Acta* 69, 2221–2240. doi: 10.1016/j.gca.2004.11.019

Black, J. R., Yin, Q. Z., and Casey, W. H. (2006). An experimental study of magnesium-isotope fractionation in chlorophyll-a photosynthesis. *Geochim. Cosmochim. Acta* 70, 4072–4079. doi: 10.1016/j.gca.2006.06.010

Bolou-Bi, E. B., Vigier, N., Poszwa, A., Boudot, J.-P., and Dambrine, E. (2012). Effects of biogeochemical processes on magnesium isotope variations in a forested catchment in the Vosges Mountains (France). *Geochim. Cosmochim. Acta* 87, 341–355. doi: 10.1016/j.gca.2012.04.005

Brenot, A., Cloquet, C., Vigier, N., Carignan, J., and France-Lanord, C. (2008). Magnesium isotope systematics of the lithologically varied Moselle river basin. France. *Geochim. Cosmochim. Acta* 72, 5070–5089. doi: 10.1016/j.gca.2008.07.027

Chamberlin, T. C. (1899). An attempt to frame a working hypothesis of the cause of glacial periods on an atmospheric basis. *J. Geol.* 7, 545–584. doi: 10.1086/608449

Chapela Lara, M., Buss, H. L., Pogge von Strandmann, P. A. E., Schuessler, J. A., and Moore, O. W. (2017). The influence of critical zone processes on the Mg isotope budget in a tropical, highly weathered andesitic catchment. *Geochim. Cosmochim. Acta* 202, 77–100. doi: 10.1016/j.gca.2016.12.032

Elderfield, H., and Schultz, A. (1996). Mid-ocean ridge hydrothermal fluxes and the chemical composition of the ocean. *Ann. Rev. Earth Planet. Sci.* 24, 191–224. doi: 10.1146/annurev.earth.24.1.191

Faure, G. (1986). *Principles of Isotope Geology*. Hoboken, NJ: Wiley.

Foster, G. L., Pogge von Strandmann, P. A. E., and Rae, J. W. B. (2010). The boron and magnesium isotopic composition of seawater. *Geochem. Geophys. Geosyst.* 11:Q08015. doi: 10.1029/2010GC003201

Gaillardet, J., Dupre, B., Louvat, P., and Allegre, C. J. (1999). Global silicate weathering and CO2 consumption rates deduced from the chemistry of large rivers. *Chem. Geol.* 159, 3–30. doi: 10.1016/s0009-2541(99)00031-5

Galy, A., Yoffe, O., Janney, P. E., Williams, R. W., Cloquet, C., Aldard, O., et al. (2003). Magnesium isotope heterogeneity of the isotopic standard SRM980 and new reference materials for magnesium-isotope-ratio measurements. *J. Anal. Atomic Spectr.* 18, 1352–1356.

Gíslason, S. R., Arnorsson, S., and Armannsson, H. (1996). Chemical weathering of basalt in southwest Iceland: effects of runoff, age of rocks and vegetative/glacial cover. *Am. J. Sci.* 296, 837–907. doi: 10.2475/ajs.296.8.837

Gislason, S. R., Eiriksdottir, E. S., and Olafsson, J. (2004). Chemical composition of interstitial water and diffusive fluxes within the diatomaceous sediment in Lake Myvatn. Iceland. *Aqua. Ecol.* 38, 163–175. doi: 10.1023/b:aeco.0000032063.15765.e4

Gíslason, S. R., Oelkers, E., and Snorrason, A. (2006). Role of river-suspended material in the global carbon cycle. *Geology* 34, 49–52.

Gothmann, A. M., Stolarski, J., Adkins, J. F., and Higgins, J. A. (2017). A Cenozoic record of seawater Mg isotopes in well-preserved fossil corals. *Geology* 45, 1039–1042. doi: 10.1130/g39418.1

Hauptfleisch, U., and Einarsson, A. (2012). Age of the Younger Laxá Lava and Lake Myvatn, northern Iceland, determined by AMS radiocarbon dating. *Radiocarbon* 54, 155–164. doi: 10.2458/azu_js_rc.v54i2.15970

Hawley, S. M., Pogge von Strandmann, P. A. E., Burton, K. W., Williams, H. M., and Gislason, S. R. (2017). Continental weathering and terrestrial (oxyhydr)oxide export: comparing glacial and non-glacial catchments in Iceland. *Chem. Geol.* 462, 55–66. doi: 10.1016/j.chemgeo.2017.04.026

Haymon, R. M., and Kastner, M. (1986). The formation of high temperature clay minerals from basalt alteration during hydrothermal discharge on the East Pacific Rise axis at 21°N. *Geochim. Cosmochim. Acta* 50, 1933–1939. doi: 10.1016/0016-7037(86)90249-8

Higgins, J. A., and Schrag, D. P. (2015). The Mg isotopic composition of Cenozoic seawater – evidence for a link between Mg-clays, seawater Mg/Ca, and climate. *Earth Planet. Sci. Lett.* 416, 73–81. doi: 10.1016/j.epsl.2015.01.003

Hindshaw, R. S., et al. (2019). Experimental constraints on Li isotope fractionation during clay formation. *Geochim. Cosmochim. Acta* 250, 219–237. doi: 10.1016/j.gca.2019.02.015

Hindshaw, R. S., Tosca, R., Tosca, N. J., and Tipper, E. T. (2020). Experimental constraints on Mg isotope fractionation during clay formation: implications for the global biogeochemical cycle of Mg. *Earth Planet. Sci. Lett.* 531:115980. doi: 10.1016/j.epsl.2019.115980

Holland, H. D. (2005). Sea level, sediments and the composition of seawater. *Am. J. Sci.* 305, 220–239. doi: 10.2475/ajs.305.3.220

Huang, K. J., Teng, F. Z., Wei, G. J., Ma, J. L., and Bao, Z. Y. (2012). Adsorption- and desorption-controlled magnesium isotope fractionation during extreme weathering of basalt in Hainan Island. China. *Earth Planet. Sci. Lett.* 35, 73–83. doi: 10.1016/j.epsl.2012.10.007

Huang, K.-J., Tosca, R., Gout, T. L., Farnan, L., Tosca, N. J., and Tipper, E. T. (2018). Magnesium isotopic composition of altered oceanic crust and the global Mg cycle. *Geochim. Cosmochim. Acta* 238, 357–373. doi: 10.1016/j.gca.2018.07.011

Humphris, S. E., and Thompson, G. (1978). Hydrothermal alteration of oceanic basalts by Seawater. *Geochim. Cosmochim. Acta* 42, 107–125. doi: 10.1016/0016-7037(78)90221-1

Immenhauser, A., Buhl, D., Richter, D., Niedermay, A., Riechelmann, D., Dietzel, M., et al. (2010). Magnesium-isotope fractionation during low-Mg calcite precipitation in a limestone cave - Field study and experiments. *Geochim. Cosmochim. Acta* 74, 4346–4364. doi: 10.1016/j.gca.2010.05.006

Kennedy, M. J., Löhr, S. C., Fraser, S. A., and Baruch, E. T. (2014). Direct evidence for organic carbon preservation as clay-organic nanocomposites in a Devonian black shale; from deposition to diagenesis. *Earth Planet. Sci. Lett.* 388, 59–70. doi: 10.1016/j.epsl.2013.11.044

Kennedy, M. J., and Wagner, T. (2011). Clay mineral continental amplifier for marine carbon sequestration in a greenhouse ocean. *Proc. Natl. Acad. Sci. U.S.A.* 108, 9776–9781. doi: 10.1073/pnas.1018670108

Kristmannsdottir, H. K., and Armannsson, H. (2004). Groundwater in the Lake Myvatn area, North Iceland: chemistry, origin and interaction. *Aqua. Ecol.* 38, 115–128. doi: 10.1111/jeb.12902

Lalonde, K., Mucci, A., Ouellet, A., and Gelinas, Y. (2012). Preservation of organic matter in sediments promoted by iron. *Nature* 483, 198–200. doi: 10.1038/nature10855

Mavromatis, V., Gautier, Q., Bosc, O., and Schott, J. (2013). Kinetics of Mg partition and Mg stable isotope fractionation during its incorporation in calcite. *Geochim. Cosmochim. Acta* 114, 188–203. doi: 10.1016/j.gca.2013.03.024

Mavromatis, V., Pearce, C. R., Shirokova, L. S., Bundeleva, I. A., Pokrovsky, O. S., Benezeth, P., et al. (2012). Magnesium isotope fractionation during hydrous magnesium carbonate precipitation with and without cyanobacteria. *Geochim. Cosmochim. Acta* 76, 161–174. doi: 10.1016/j.gca.2011.10.019

McArthur, J. M., Howarth, R. J., and Bailey, T. R. (2001). Strontium isotope stratigraphy: LOWESS version 3: best fit to the marine Sr-isotope curve for 0-509 Ma and accompanying look-up table for deriving numerical age. *J. Geol.* 109, 155–170. doi: 10.1086/319243

Mottl, M. J., and Wheat, C. G. (1994). Hydrothermal circulation through mid-ocean ridge flanks: fluxes of heat and magnesium. *Geochim. Cosmochim. Acta* 58, 2225–2237. doi: 10.1016/0016-7037(94)90007-8

Oelkers, E. H., Butcher, R., Strandmann, P. E. A. P., Schuessler, J. A., Blankenburg, F. V., Snæbjörnsdóttir, S. O., et al. (2019). Using stable Mg isotope signatures to assess the fate of magnesium during the in situ mineralisation of CO2 and H2S at the CarbFix site in SW-Iceland. *Geochim. Cosmochim. Acta* 245, 542–555. doi: 10.1016/j.gca.2018.11.011

Olafsson, J. (1979a). Physical characteristics of Lake Myvatn and River Laxá. *Oikos* 32, 38–66.

Olafsson, J. (1979b). The chemistry of Lake Myvatn and River Laxa. *Oikos* 32, 82–112.

Oliver, L., Harris, N., Bickle, M. J., Chapman, H. J., Dise, N., and Horstwood, M. S. A. (2003). Silicate weathering rates decoupled from the 87Sr/86Sr ratio of the dissolved load during Himalayan erosion. *Chem. Geol.* 201, 119–139. doi: 10.1016/s0009-2541(03)00236-5

Opfergelt, S., Burton, K. W., George, R. B., West, A. J., Guicharnaud, R., Sigfusson, B., et al. (2014). Magnesium retention on the soil exchange complex controlling Mg isotope variations in soils, soil solutions and vegetation in volcanic soils, Iceland. *Geochim. Cosmochim. Acta* 125, 110–130. doi: 10.1016/j.gca.2013.09.036

Opfergelt, S., Eiriksdottir, E., Burton, K. W., Einarsson, A., Siebert, C., Gislason, S., et al. (2011). Quantifying the impact of freshwater diatom productivity on silicon isotopes and silicon fluxes: Lake Myvatn, Iceland. *Earth Planet. Sci. Lett.* 305, 73–82. doi: 10.1016/j.epsl.2011.02.043

Opfergelt, S., Georg, R. B., Delvaux, B., Cabidoche, Y.-M., Burton, K. W., Halliday, A. N., et al. (2012). Mechanisms of magnesium isotope fractionation in volcanic soil weathering sequences. Guadeloupe. *Earth Planet. Sci. Lett.* 341, 176–185. doi: 10.1016/j.epsl.2012.06.010

Palmer, M. R., and Edmond, J. M. (1992). Controls over the strontium isotope composition of river water. *Geochim. Cosmochim. Acta* 56, 2099–2111. doi: 10.1016/0016-7037(92)90332-d

Parkhurst, D. L., and Appelo, C. A. J. (1999). *User's guide to PHREEQC (version 2) - a Computer Program For Speciation, Batch-Reaction, One-Dimensional Transport, And Inverse Geochemical Calculations*. Reston: USGS.

Peucker-Ehrenbrink, B., Ravizza, G., and Hofmann, A. W. (1995). The Marine Os-187/Os-186 Record of the Past 80-Million Years. *Earth Planet. Sci. Lett.* 130, 155–167. doi: 10.1016/0012-821x(95)00003-u

Pogge von Strandmann, P. A. E., Burton, K. W., James, R. H., van Calsteren, P., and Gislason, S. R. (2008). The influence of weathering processes on riverine magnesium isotopes in a basaltic terrain. *Earth Planet. Sci. Lett.* 276, 187–197. doi: 10.1016/j.epsl.2008.09.020

Pogge von Strandmann, P. A. E., Burton, K. W., Opfergelt, S., Eiríksdóttir, E. S., Murphy, M. J., and Gislason, S. R. (2016). The effect of hydrothermal spring weathering processes and primary productivity on lithium isotopes: Lake Myvatn. Iceland. *Chem. Geol.* 445, 4–13. doi: 10.1016/j.chemgeo.2016.02.026

Pogge von Strandmann, P. A. E., Elliott, T., Marschall, H., Coath, C., Lai, Y. J., Jeffcoate, A. B., et al. (2011). Variations of Li and Mg isotope ratios in bulk chondrites and mantle xenoliths. *Geochim. Cosmochim. Acta* 75, 5247–5268. doi: 10.1016/j.gca.2011.06.026

Pogge von Strandmann, P. A. E., Forshaw, J., and Schmidt, D. N. (2014). Modern and Cenozoic records of seawater magnesium from foraminiferal Mg isotopes. *Biogeosciences* 11, 5155–5168. doi: 10.5194/bg-11-5155-2014

Pogge von Strandmann, P. A. E., Fraseret, W. T., Hammond, S. J., Tarbuck, G., Wood, I. G., Oelkers, E. H., et al. (2019a). Experimental determination of Li isotope behaviour during basalt weathering. *Chem. Geol.* 517, 34–43. doi: 10.1016/j.chemgeo.2019.04.020

Pogge von Strandmann, P. A. E., Hendry, K. R., Hatton, J. E., and Robinson, L. F. (2019b). The Response of Magnesium, Silicon, and Calcium Isotopes to rapidly uplifting and weathering terrains: South Island, New Zealand. *Front. Earth Sci.* 7:240. doi: 10.3389/feart.2019.00240

Pogge von Strandmann, P. A. E., Olsson, J., Luu, T.-H., Gislason, S. R., and Burton, K. W. (2019c). Using Mg isotopes to estimate natural calcite compositions and precipitation rates during the 2010 Eyjafjallajökull eruption. *Front. Earth Sci.* 7:6. doi: 10.3389/feart.2019.00006

Pogge von Strandmann, P. A. E., Opfergelt, S., Lai, Y. J., Sigfusson, B., Gislason, S., Burton, K. W., et al. (2012). Lithium, magnesium and silicon isotope behaviour accompanying weathering in a basaltic soil and pore water profile in Iceland. *Earth Planet. Sci. Lett.* 33, 11–23. doi: 10.1016/j.epsl.2012.05.035

Pogge von Strandmann, P. A. E., Vaks, A., Bar-Matthews, M., Ayalon, A., Jacob, E., and Henderson, G. E. (2017). Lithium isotopes in speleothems: temperature-controlled variation in silicate weathering during glacial cycles. *Earth Planet. Sci. Lett.* 469, 64–74. doi: 10.1016/j.epsl.2017.04.014

Ra, K., and Kitagawa, H. (2007). Magnesium isotope analysis of different chlorophyll forma in marine phytoplankton using multi-collector ICP-MS. *J. Anal. Atomic Spectr.* 22, 817–821.

Raymo, M. E., and Ruddiman, W. F. (1992). Tectonic forcing of late cenozoic climate. *Nature* 359, 117–122. doi: 10.1038/359117a0

Saenger, C., and Wang, Z. (2014). Magnesium isotope fractionation in biogenic and abiogenic carbonates: implications for paleoenvironmental proxies. *Quat. Sci. Rev.* 90, 1–21. doi: 10.1016/j.quascirev.2014.01.014

Saulnier, S., Rollion-Bard, C., Vigier, N., and Chaussidon, M. (2012). Mg isotope fractionation during calcite precipitation: an experimental study. *Geochim. Cosmochim. Acta* 91, 75–91. doi: 10.1080/10256016.2018.1430692

Shalev, N., Farkas, J., Fietzke, J., Novák, M., Schuessler, J. A., von Strandmann, P. A. E. P., et al. (2018). Mg Isotope inter-laboratory comparison of reference materials from earth-surface low-temperature environments. *Geostand. Geoanal. Res.* 42, 205–221. doi: 10.1111/ggr.12208

Teng, F. Z., Yin, Q.-Z., Ullmann, C. V., Chakrabarti, R., von Strandmann, P. A. E. P., Yang, W., et al. (2015). Interlaboratory comparison of magnesium isotopic compositions of 12 felsic to ultramafic igneous rock standards analyzed by MC-ICPMS. *Geochem. Geophys. Geosyst.* 16, 3197–3209. doi: 10.1002/2015gc005939

Thorbergsdottir, I. M., and Gislason, S. R. (2004). Internal loading of nutrients and certain metals in the shallow eutrophic Lake Mývatn. Iceland. *Aqua. Ecol.* 38, 191–207.

Thordarson, T., and Hoskuldsson, A. (2002). *Classic Geology in Europe 3*. Iceland: Terra Publishing.

Tipper, E. T., Calmels, D., Gaillardet, J., Louvat, P., Capmas, F., and Dubacq, B. (2012a). Positive correlation between Li and Mg isotope ratios in the river waters of the Mackenzie Basin challenges the interpretation of apparent isotopic fractionation during weathering. *Earth Planet. Sci. Lett.* 333, 35–45. doi: 10.1016/j.epsl.2012.04.023

Tipper, E. T., Lemarchand, E., Hindshaw, R. S., Reynolds, B. C., and Bourdon, B. (2012b). Seasonal sensitivity of weathering processes: hints from magnesium isotopes in a glacial stream. *Chem. Geol.* 31, 80–92. doi: 10.1016/j.chemgeo.2012.04.002

Tipper, E. T., Gaillardet, J., Louvat, P., Capmas, F., and White, A. F. (2010). Mg isotope constraints on soil pore-fluid chemistry: evidence from Santa Cruz. California. *Geochim. Cosmochim. Acta* 74, 3883–3896. doi: 10.1016/j.gca.2010.04.021

Tipper, E. T., Galy, A., and Bickle, M. (2008). Calcium and magnesium isotope systematics in rivers draining the Himalaya-Tibetan-Plateau region: Lithological or fractionation control? *Geochim. Cosmochim. Acta* 72, 1057–1075. doi: 10.1016/j.gca.2007.11.029

Tipper, E. T., Galy, A., and Bickle, M. J. (2006a). Riverine evidence for a fractionated reservoir of Ca and Mg on the continents: implications for the oceanic Ca cycle. *Earth Planet. Sci. Lett.* 247, 267–279. doi: 10.1016/j.epsl.2006.04.033

Tipper, E. T., Galy, A., Gailardet, J., Elderfield, H., and Carder, E. A. (2006b). The magnesium isotope budget of the modern ocean: constraints from riverine magnesium isotope ratios. *Earth Planet. Sci. Lett.* 250, 241–253. doi: 10.1016/j.epsl.2006.07.037

Urey, H. C. (1947). The thermodynamic porperties of isotopic substances. *J. Chem. Soc.* 562–581. doi: 10.1039/JR9470000562

Voigt, M., Pearce, C. R., Fries, D. M., Baldermann, A., and Oelkers, E. H. (2020). Magnesium isotope fractionation during hydrothermal seawater-basalt interaction. *Geochim. Cosmochim. Acta* 272, 21–35. doi: 10.1016/j.gca.2019.12.026

Walker, J. C. G., Hays, P. B., and Kasting, J. F. (1981). A negative feedback mechanism for the long-term stabilization of earths surface-temperature. *J. Geophys. Res. Oceans Atmosph.* 86, 9776–9782.

West, A. J., Galy, A., and Bickle, M. (2005). Tectonic and climatic controls on silicate weathering. *Earth Planet. Sci. Lett.* 235, 211–228. doi: 10.1016/j.epsl.2005.03.020

Wimpenny, J., Colla, C. A., Yin, Q. Z., Rustad, J. R., and Casey, W. H. (2014). Investigating the behaviour of Mg isotopes during the formation of clay minerals. *Geochim. Cosmochim. Acta* 128, 178–194. doi: 10.1016/j.gca.2013.12.012

Wimpenny, J., Gíslason, S. R., James, R. H., Gannoun, A., Pogge von Strandmann, P. A. E., and Burton, K. W. (2010). The behaviour of Li and Mg isotopes during primary phase dissolution and secondary mineral formation in basalt. *Geochim. Cosmochim. Acta* 74, 5259–5279. doi: 10.1016/j.gca.2010.06.028

Wombacher, F., Eisenhauer, A., Böhm, F., Gussone, N., Regenberg, M., Dullo, C.-C., et al. (2011). Magnesium stable isotope fractionation in marine biogenic calcite and aragonite. *Geochim. Cosmochim. Acta* 75, 5797–5818. doi: 10.1016/j.gca.2011.07.017

Conflict of Interest: The authors declare that the research was conducted in the absence of any commercial or financial relationships that could be construed as a potential conflict of interest.

frontiers
in Earth Science

ORIGINAL RESEARCH
published: 21 May 2020
doi: 10.3389/feart.2020.00152

Experimental Evidence That Permafrost Thaw History and Mineral Composition Shape Abiotic Carbon Cycling in Thermokarst-Affected Stream Networks

Scott Zolkos*† **and Suzanne E. Tank**

Department of Biological Sciences, University of Alberta, Edmonton, AB, Canada

Edited by:
Katharine Rosemary Hendry,
University of Bristol, United Kingdom

Reviewed by:
Aga Nowak,
The University Centre in Svalbard, Norway
Francois L. L. Muller,
National Sun Yat-sen University, Taiwan

***Correspondence:**
Scott Zolkos
sgzolkos@gmail.com

†Present address:
Scott Zolkos,
Woods Hole Research Center, Falmouth, MA, United States

Specialty section:
This article was submitted to Geochemistry,
a section of the journal Frontiers in Earth Science

Received: *22 February 2020*
Accepted: *22 April 2020*
Published: *21 May 2020*

Citation:
Zolkos S and Tank SE (2020) Experimental Evidence That Permafrost Thaw History and Mineral Composition Shape Abiotic Carbon Cycling in Thermokarst-Affected Stream Networks.
Front. Earth Sci. 8:152.
doi: 10.3389/feart.2020.00152

Mounting evidence suggests that biogeochemical processing of permafrost substrate will amplify dissolved inorganic carbon (DIC $= \Sigma[CO_2,HCO_3^-,CO_3^{2-}]$) production within Arctic freshwaters. The effects of permafrost thaw on DIC may be particularly strong where terrain subsidence following thaw (thermokarst) releases large amounts of sediment into fluvial networks. The mineral composition and chemical weathering of these sediments has critical yet untested implications for the degree to which streams represent a source of CO_2 to the atmosphere vs. a source of bicarbonate to downstream environments. Here, we experimentally determine the effects of mineral weathering on fluvial CO_2 by incubating sediments collected from three retrogressive thaw slump features on the Peel Plateau (NWT, Canada). Prehistoric warming and contemporary thermokarst have exposed sediments on the Peel Plateau to varying degrees of thaw and chemical weathering, allowing us to test the role of permafrost and substrate mineral composition on CO_2:HCO_3^- balance. We found that recently-thawed sediments (within years to decades) and previously un-thawed tills from deeper permafrost generated substantial amounts of solutes and DIC. These solutes and the mineralogy of sediments suggested that carbonate weathering coupled with sulfide oxidation was a net source of abiotic CO_2. Yet, on average, more than 30% of this CO_2 was converted to bicarbonate via carbonate buffering reactions. In contrast, the mineralogy and geochemical trends associated with sediments from the modern and paleo-active layer, which were exposed to thaw over longer timescales than deeper permafrost sediments, more strongly reflected silicate weathering. In treatments with sediment from the modern and paleo-active layer, minor carbonate and sulfide weathering resulted in some DIC and net CO_2 production. This CO_2 was not measurably diminished by carbonate buffering. Together, these trends suggest that prior exposure to thaw and weathering on the Peel Plateau reduced carbonate and sulfide in upper soil layers. We conclude that thermokarst unearthing deeper tills on the Peel Plateau will amplify regional inorganic carbon cycling for decades to centuries. However, CO_2 consumption via carbonate buffering may partly counterbalance CO_2 production and release to the atmosphere. Regional variability in the mineral composition of permafrost, thaw history, and thermokarst intensity are among the primary controls on mineral weathering within permafrost carbon-climate feedbacks.

Keywords: carbonate, sulfide, carbon dioxide, thermokarst, retrogressive thaw slump

INTRODUCTION

Rapid climate warming and intensifying hydrologic cycles at northern latitudes (Serreze and Barry, 2011) are activating immense stores of organic carbon from perennially frozen permafrost soils into modern biogeochemical cycles (Biskaborn et al., 2019; Vonk et al., 2019). The biotic and abiotic processing of this relatively reactive carbon pool stands to amplify climate warming in the coming centuries by releasing large amounts of carbon dioxide (CO_2) from terrestrial and aquatic environments into Earth's atmosphere (Schuur et al., 2015; Turetsky et al., 2020). Along the terrestrial–freshwater continuum, carbonate equilibrium reactions drive the speciation of dissolved inorganic carbon ($DIC = \Sigma[CO_2, HCO_3^-, CO_3^{2-}]$) and therefore influence the susceptibility of carbon exchange with the atmosphere as CO_2 vs. export to downstream environments as carbonate alkalinity (HCO_3^-, CO_3^{2-}) (Stumm and Morgan, 1996). Changes to DIC cycling in northern permafrost-affected landscapes thus have potentially critical implications for carbon cycling and feedbacks to long-term climate, particularly where large amounts of permafrost substrate are mobilized directly into fluvial networks (Vonk et al., 2019).

Increasing fluxes of ions and carbonate alkalinity in major Arctic rivers in recent decades reflect enhanced DIC cycling coupled to a thickening of the seasonally-thawed active layer into more mineral-rich soil layers and accelerating physical erosion which exposes minerals to chemical weathering (Tank et al., 2016; Toohey et al., 2016; Drake et al., 2018b; Zolkos et al., 2018). Over geological timescales, the chemical weathering of these minerals may regulate climate by moderating atmospheric CO_2 (Berner, 1999; Maher and Chamberlain, 2014; Torres et al., 2014), while perturbation of these cycles can change contemporary carbon cycles (Gislason et al., 2009; Beaulieu et al., 2012). Carbonate and silicate weathering by carbonic acid [H_2CO_3*, including dissolved $CO_{2(g)}$] transforms atmospheric $CO_{2(g)}$ and biotic CO_2 produced by plant root respiration and microbial oxidation of soil organic matter into bicarbonate (HCO_3^-; Equations 1–3) (Berner, 1999), rendering it less susceptible to exchange with the atmosphere:

$$H_2O + CO_{2(g)} \rightleftharpoons H_2CO_3* \rightleftharpoons H^+ + HCO_3^- \rightleftharpoons 2H^+ + CO_3^{2-} \quad (1)$$

$$H_2CO_3* + (Ca,Mg)CO_3 \rightarrow (Ca^{2+}, Mg^{2+}) + 2HCO_3^- \quad (2)$$

$$2H_2CO_3* + 3H_2O + (Ca,Mg)Al_2Si_2O_8 \rightarrow (Ca^{2+}, Mg^{2+}) + 2HCO_3^- + 2Al_2Si_2O_5(OH)_4 \quad (3)$$

In contrast, sulfide oxidation (Equation 4) generates sulfuric acid (H_2SO_4) that either liberates mineral C into solution as H_2CO_3* (Equation 5) or HCO_3^- (Equation 6) via carbonate weathering, or generates no dissolved C via silicate weathering (Equation 7) (Lerman et al., 2007):

$$FeS_2 + 15/4O_2 + 7/2H_2O \rightarrow Fe(OH_3) + 2H_2SO_4 (4)$$

$$2H_2SO_4 + 2(Ca,Mg)CO_3 \rightarrow 2(Ca^{2+}, Mg^{2+}) + 2SO_4^{2-} + 2H_2CO_3* \quad (5)$$

$$H_2SO_4 + 2(Ca,Mg)CO_3 \rightarrow 2(Ca^{2+}, Mg^{2+}) + SO_4^{2-} + 2HCO_3^- \quad (6)$$

$$H_2SO_4 + H_2O + (Ca,Mg)Al_2Si_2O_8 \rightarrow (Ca^{2+}, Mg^{2+}) + SO_4^{2-} + Al_2Si_2O_5(OH)_4 \quad (7)$$

When sediments are more limited in carbonates than in sulfides, H_2SO_4 from sulfide oxidation can lower pH and increase the CO_2 proportion of DIC (Equation 1), facilitating CO_2 release to the atmosphere (Stumm and Morgan, 1996). Half of the HCO_3^- transferred from streams and rivers into the marine carbon cycle returns to the atmosphere as CO_2 over geological timescales (Calmels et al., 2007). Thus, the balance between H_2CO_3 and H_2SO_4 weathering controls the degree to which mineral weathering is carbon neutral (Equation 2) vs. a carbon sink (Equation 3) or source (Equations 5, 6) (Calmels et al., 2007; Tank et al., 2012; Hindshaw et al., 2016) and acts as a positive or negative feedback to long-term climate warming (Berner, 1999; Gislason et al., 2009; Torres et al., 2014, 2017; Pogge von Strandmann et al., 2017). Constraining the sources of mineral weathering and the balance between CO_2 and HCO_3^- in northern fluvial networks can help to understand DIC cycling and the abiotic component of permafrost carbon-climate feedbacks.

Local and regional variation in lithology, physical erosion, and temperature are primary controls on the sources and magnitude of mineral weathering (Gaillardet et al., 1999; Li et al., 2017). For instance, riverine DIC can be relatively high in catchments with carbonate lithologies (Blum et al., 1998; Tank et al., 2012) as carbonates weather more readily than silicates (Stumm and Morgan, 1996). River chemistry reveals that physical erosion enhances solute production by exposing previously un-weathered material (Riebe et al., 2001; West et al., 2005; Calmels et al., 2007) and by increasing the potential reactivity of sediments (Anderson, 2007). DIC cycling in terrains with glacial activity can be rapid. For instance, H_2CO_3* weathering of sediments during fluvial transport in pro-glacial streams can consume dissolved CO_2 to below atmospheric levels (St. Pierre et al., 2019). While much of Canada is no longer glaciated, terrain subsidence following permafrost thaw (thermokarst) across vast swaths of northwestern Canada is enabling large quantities of glaciogenic sediments that were emplaced by the former Laurentide Ice Sheet to be mobilized into fluvial networks (Kokelj et al., 2017a). In these ice- and sediment-rich glacial margin landscapes like the Peel Plateau (NWT, Canada), retrogressive thaw slump (RTS) thermokarst activity can amplify DIC cycling and increase HCO_3^- in downstream environments (Zolkos et al., 2018). While H_2SO_4 carbonate weathering in thermokarst-affected streams on the Peel Plateau is thought to be a net source of CO_2 to the atmosphere over contemporary and longer timescales (Zolkos et al., 2018, 2019), the degree to which mineral weathering by H_2CO_3 consumes CO_2 in streams on the Peel Plateau remains untested. The balance between CO_2 and HCO_3^- in thermokarst-affected streams has important implications for the Arctic inorganic carbon cycle, as hillslope thermokarst features like RTSs may affect 900,000 km^2 (5%) of the northern permafrost region (Olefeldt et al., 2016). Further, the chemistries of streams on the Peel Plateau reflect weathering from sediment sources with varying degrees of prior exposure to thaw and thus mineral composition (Lacelle et al., 2019). Determining the influence of permafrost mineral composition and weathering sources on the balance between CO_2 and HCO_3^- in streams can thus help to understand thermokarst effects on DIC cycling and potential feedbacks to long-term climate.

Here, we refine understanding of mineral weathering contributions to inorganic carbon cycling on the Peel Plateau (NWT, Canada) (Zolkos et al., 2018), where accelerating thermokarst activity is mobilizing large volumes of mineral-rich glacial tills with varying degrees of prior thaw into fluvial networks (Kokelj et al., 2013; Segal et al., 2016a; van der Sluijs et al., 2018). We build on previous research that investigated the effects of RTSs on solutes, sediments, and organic carbon in fluvial networks (Kokelj et al., 2013; Malone et al., 2013; Littlefair et al., 2017), and Holocene environmental change on the composition of permafrost soil organic carbon and solution chemistry (Lacelle et al., 2019). To do this, we characterized the mineral composition of RTS sediments that commonly enter streams on the Peel Plateau and experimentally weathered these sediments to determine how thermokarst and thaw history affect DIC concentration and speciation (Segal et al., 2016a; Lacelle et al., 2019). Our results indicate that fluvial inorganic carbon cycling on the Peel Plateau is amplified by more intense thermokarst, which thaws deeper sediments containing a greater proportion of carbonate and sulfide. We conclude that thermokarst on the Peel Plateau and in similar Arctic environments may intensify inorganic carbon cycling in fluvial networks for centuries.

MATERIALS AND METHODS

Study Area and Retrogressive Thaw Slump Sites

The Peel Plateau is characterized by permafrost tills up to 50 m in thickness underlain by sandstone and siltstone bedrock (Norris, 1985; Kokelj et al., 2017b). These tills are mainly comprised of carbonates, sulfides, silicates, and gypsum (Malone et al., 2013; Zolkos et al., 2018) likely derived from regional carbonate and shale bedrock (Norris, 1985; Stott, 1991) that was integrated into the Laurentide Ice Sheet (LIS) during its westward expansion. The last glacial maximum in the Peel Plateau region at around 18,500 cal yr BP (Lacelle et al., 2013) was followed by retreat of the LIS and early Holocene warming at 12,000–8,500 cal yr BP (Kokelj et al., 2017b). This warming promoted thaw of the ground surface, mineral weathering, and the accumulation of organic matter in the upper few meters of soil (Burn, 1997; Lacelle, 2004; Malone et al., 2013). A cooling climate 7,000–5,500 cal yr BP supported permafrost aggradation and the preservation of this solute- and organic-rich Holocene layer above the deeper, ice-rich Pleistocene sediments that have been isolated from thaw and exposure (Lacelle et al., 2013; Kokelj et al., 2017b). The shallow Holocene and the deeper Pleistocene permafrost layers are geochemically distinct and distinguished stratigraphically by an undulating thaw unconformity typically encountered 1.5–3 m below the surface (Malone et al., 2013) (**Figure 1A**).

The modern-day Peel Plateau is within the continuous permafrost zone and is comprised of ice-rich hummocky moraine, glaciofluvial, glaciolacustrine, and colluvial deposits (Duk-Rodkin and Hughes, 1992). Incised valleys and sloping terrain host hundreds of RTSs (**Figure 1**) (Kokelj et al., 2013; Lacelle et al., 2015; Segal et al., 2016a). The upslope growth of RTS features is sustained by the ablation of a vertical permafrost headwall of exposed ground ice and the downslope evacuation of a thawed slurry of slumped materials via fluidized flows which are enhanced by rainfall (Kokelj et al., 2015) (**Figure 1A**). Meltwater from the thawing headwall and its interaction with thawing substrate produce sediment- and solute-rich runoff often conveyed through rill channels in the scar zone (henceforth "runoff"), and into streams. The thawed materials that flow from thawing slopes are deposited as debris tongues that can grow over time to reach >1 km in length and tens of meters in thickness (van der Sluijs et al., 2018). These features are reshaped by the addition of debris from thawing slopes and erosion by the adjacent streams (Kokelj et al., 2015) (**Figure 1B**). Sediments unearthed by RTSs can be broadly categorized into five sources of material with varying degrees of prior exposure to thaw and weathering: (i) the seasonally-thawed *active layer*; (ii) the relatively organic- and solute-rich paleo-active layer contained in *Holocene-aged permafrost*; (iii) the un-thawed *Pleistocene-aged permafrost* sediments derived from glacial tills; and the composite of these three components, that are either recently mobilized and are undergoing active transport as fluvial suspended sediment in *runoff* (iv) or deposited in recent years to decades within the *debris tongue* (v) (**Figure 1**). Active layer and Holocene permafrost sediments in RTSs on the Peel Plateau have been exposed to thaw for decades to centuries, whereas Pleistocene permafrost sediments were frozen upon their deposition and have remained sequestered within permafrost for millennia.

The three focal RTSs in this study are situated within the ~1,100 km^2 Stony Creek watershed, west of Fort McPherson, NWT (**Figure 1**, **Table 1**). The RTS FM2 is among the largest active RTS features on the Peel Plateau (Lacelle et al., 2015) and has persisted for at least 70 years (Kokelj et al., 2015; van der Sluijs et al., 2018). The RTS HC is moderately-sized and estimates from the field suggest it is likely at least several decades old. The RTS HD scar zone was <1 ha at the time of sampling and visual

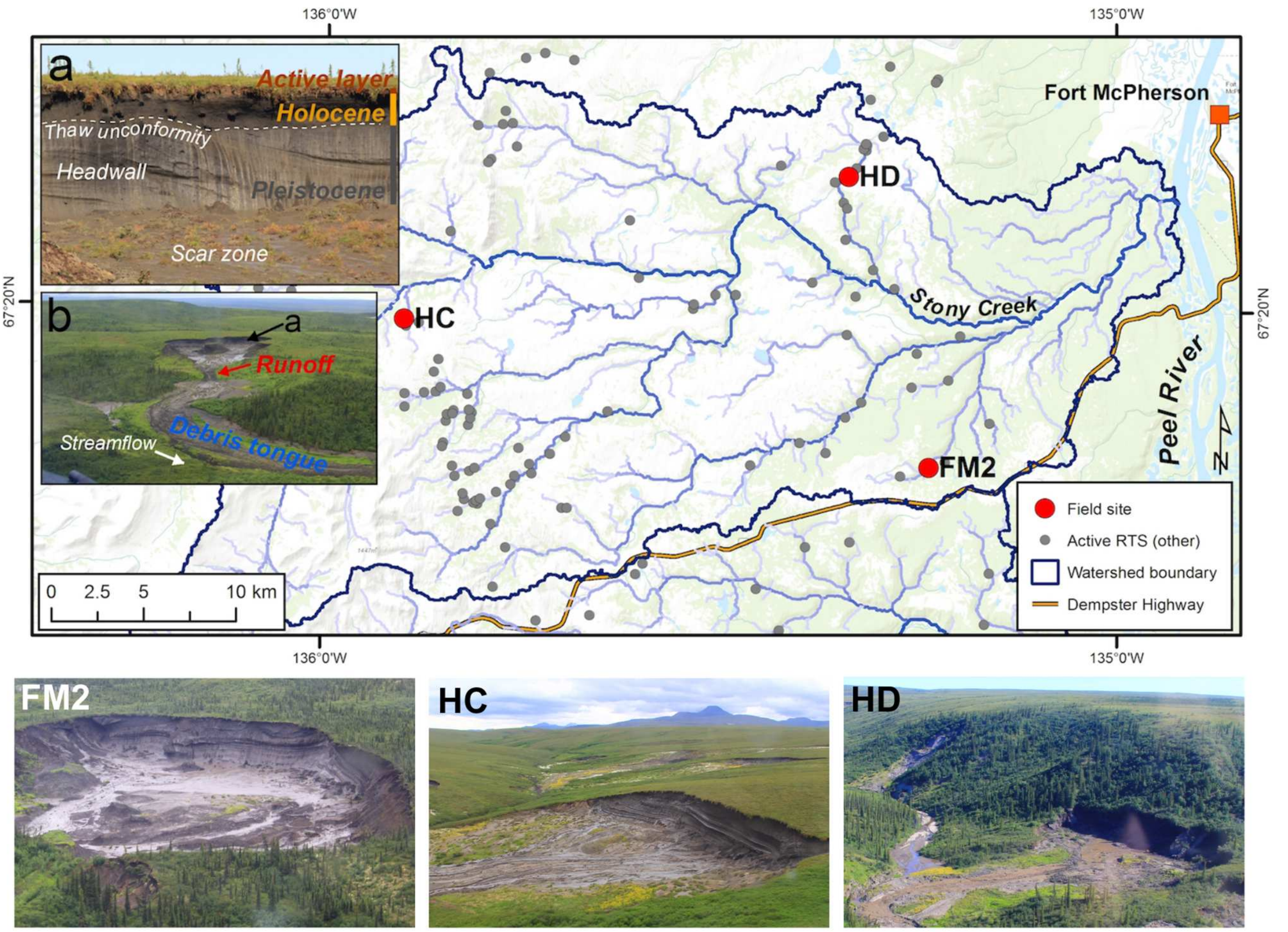

FIGURE 1 | Map of retrogressive thaw slump (RTS) study sites ($n = 3$) on the Peel Plateau (NWT, Canada) from which sediments for the experiment were collected. Sediments were collected from RTS FM2, HC, and HD (see photos below and locations on map). Photos were taken in 2014 (FM2) and 2017 (HC, HD). The photo of FM2 captures its southern lobe only. Insets (a) and (b) depict sampling locations of the five sediment sources (i.e., treatments) detailed in the text. Note location of inset (a) shown in (b). Inset photos depict sediment sources common to all RTS that were sampled for the experiment (RTS in inset photos from this region but not study). Basemap from Esri ArcGIS Online; "Active RTS" points on map from Segal et al. (2016b).

observations of Landsat 5 satellite imagery suggest that it formed circa 1998–2000.

Field sampling

During summer 2017, we collected active layer and permafrost sediments from the vertical headwall exposure, in addition to runoff and debris tongue sediments at RTS features FM2, HC, and HD (**Figure 1**, **Table 1**). These three RTS features were selected to capture potential variability in sediment geochemistry associated with varying compositions of glaciogenic materials (Duk-Rodkin and Hughes, 1992). To characterize RTS morphology, we measured headwall height at the time of sampling using a Uineye HK1200 laser range finder (±30 cm/0.35° accuracy) (Zolkos and Tank, 2019). Holocene and Pleistocene permafrost samples were collected in each RTS feature using a mallet and stainless-steel chisel. Permafrost layers were differentiated in the field based on cryostratigraphy (Lacelle et al., 2013) and later in the laboratory using stable isotopes of water ($\delta^{18}O$), to ensure isotopic values reflected previously published values for Holocene ($\delta^{18}O = -17$ to 25‰) and Pleistocene ($\delta^{18}O = -26$ to -32‰) ground-ice (Michel, 2011; Fritz et al., 2012; Lacelle et al., 2013). Active layer and debris tongue samples were collected using a stainless-steel trowel. Active layer material was composited from two roughly equal plugs of material from the A and B horizons (below the organic layer and above permafrost table). Debris tongue samples comprised of thawed, colluviated materials were collected near the adjacent stream, distant from the active headwall, reflecting sediments that have been thawed for years to decades. For active layer, permafrost, and debris tongue samples, the outer 5–10 cm of material was removed and discarded prior to sampling. Samples were stored in 5 L Whirlpak bags. Runoff was collected in pre-cleaned, triple-sample-rinsed 2 L HDPE bottles and stored chilled (4°C). Permafrost was thawed, and thawed permafrost and runoff were allowed to settle in the laboratory for 24 h at 4°C. Prior to drying sediments at

TABLE 1 | Characteristics of RTS features in this study.

RTS	Lat (DD)	Lon (DD)	$\delta^{18}O$ Holocene	$\delta^{18}O$ Pleistocene	Height (m, max)	Debris tongue length (~m)*	Scar zone (~ha)*
FM2	67.257	−135.236	−20.3	−28.3	24.2	1,600	27
HC	67.328	−135.900	−21.6	−29.2	18.3	180	2.5
HD	67.400	−135.334	−21.8	−30.3	13.6	150	0.6

*All headwall height measurements were made during July 2017. Stable water isotope ($\delta^{18}O$) values are reported in ‰ Vienna Standard Mean Ocean Water. *Estimated from satellite imagery and/or field photos; excludes area of debris tongue.*

20°C, supernatant was removed to limit the precipitation of secondary minerals.

Sediment Mineralogy and Geochemistry

Prior to mineral analysis by X-ray diffraction (XRD), dried sediments were gently disaggregated with a mallet, sieved to $<250\,\mu$m, and visible organic matter was removed. Samples were not pretreated prior to analysis and XRD spectra were visually inspected to confirm minimal interference from organic matter (Mandile and Hutton, 1995). Sieved sediments were then finely ground with a ceramic mortar and pestle, and mineralogy was analyzed at the University of Alberta by XRD (Rigaku Ultimate IV), using Cobalt radiation at 0.6 s/step and 0.02° steps (detection limit = 3%). The geochemical composition of sediments was analyzed by inductively coupled plasma mass spectrometer (Perkin Elmer Elan 6000 Quadrupole ICP-MS) at the University of Alberta Canadian Center for Isotope Microanalysis, following Cooper et al. (2008). The coefficient of variation for Al^{3+}, Fe^{2+}, K^{+}, Mg^{2+}, Ca^{2+}, Na^{+}, and Sr^{2+} is <6%. Subsamples (0.2 ± 0.02 g) of the sieved sediments were dissolved via sequential digestions using $HF + HNO_3^-$ and then $HCl + HNO_3^-$. Sediments were mixed with five mL of each acid (trace metal-grade), heated to 130°C, and digested overnight until dry. Finally, 10 mL 8N HNO_3^- were added, heated to 130°C, and a 1 mL aliquot was mixed with 0.1 mL HNO_3^-, 0.1 mL of internal standards (In, Bi, and Sc), and 8.8 mL of MilliQ deionized water.

Mineral Weathering Experiment

To determine how varying degrees of prior thaw and biogeochemical alteration of glaciogenic materials can influence DIC cycling on the Peel Plateau, we incubated active layer, Holocene, Pleistocene, runoff, and debris tongue sediments under controlled conditions. Following collection and sieving (see above), unground sediments were sterilized in precombusted aluminum trays at 200°C for 24 h in a forced-draft oven (Wolf and Skipper, 1994) to isolate the abiotic controls on DIC speciation from CO_2 production by microbial oxidation of organic matter. In our experiment this likely inhibited microbial sulfide oxidation (Singer and Stumm, 1970), which is a primary biotic mechanism of carbonate and silicate weathering in glaciated environments (Montross et al., 2013; Tranter and Wadham, 2014; Hindshaw et al., 2016), thus constraining possible sulfide oxidation to abiotic pathways involving Fe^{3+} (Rimstidt and Vaughan, 2003) and dissolved O_2 (Calmels et al., 2007). Sterilization was tested by mixing sterile MilliQ water (0.2 μm-filtered, ultraviolet light-treated) with the sterilized sediment, and extracting and incubating the supernatant on nutrient-rich agar plates (37°C, 7 d; Zuberer, 1994). Sterilization was confirmed by no observable growth compared to identical sediments that had not been sterilized. To evaluate the relative importance of sulfide oxidation and gypsum dissolution to SO_4^{2-} production, we assumed that 1 mol O_2 could yield 0.53 mol H_2SO_4 via sulfide oxidation (Equation 4) and we calculated the concentration of dissolved O_2 in the bottles under equilibrium conditions (10°C) to be 348 μM. This approach allowed us to estimate that SO_4^{2-} concentrations up to 184 μM could originate from sulfide oxidation via the dissolved O_2 pathway (Equations 5, 6). We interpreted higher SO_4^{2-} concentrations and the absence of sulfides from XRD detection as indicators of relatively greater SO_4^{2-} production from gypsum dissolution.

Sterilized sediments were incubated at total suspended solid concentrations (1,800 mg L^{-1}) and water temperatures (10°C) representative of stream reaches immediately downstream of RTS features during the 2015 sampling season (Zolkos et al., 2018). We inoculated 200 mL of MilliQ water with 3.6 g of sterilized sediment in acid-washed, precombusted (5 h, 500°C) 250 mL glass bottles and sealed them with two silicone-teflon septa (Skidmore et al., 2004). For each sediment source, 12 identical bottles were prepared and replicate bottles were terminated at 0.17, 1, 6, 24, 72, and 168 h. Two control bottles containing only MilliQ water were also terminated at 168 h. We enabled weathering to proceed under closed system conditions by flushing headspace in bottles with N_2 gas, enabling dissolved CO_2 and O_2 to contribute to carbonate weathering and sulfide oxidation. For RTS HD runoff, we had only enough sediment to run replicate bottles that were terminated at 168 h and we had no replicates for the other time points. To induce sediment suspension, all bottles were incubated on a rotary shaker set to 250 rpm during the course of the experiment, following Skidmore et al. (2004).

Chemical Analyses

At each time point, bottles were removed and water was filtered (0.45-μm, polyethersulfone, ThermoScientific) for DIC, pH, and conductivity measurements. Water was also equilibrated with nitrogen gas to extract dissolved gas for measurements of CO_2 concentration and stable carbon isotope analysis of CO_2 ($\delta^{13}C_{CO_2}$) (see below). Filtrate for DIC was stored without headspace in precombusted 12 mL exetainers, sealed with butyl septa, and refrigerated until analysis within 2 weeks (Apollo SciTech DIC analyzer). DIC standard curves were built from certified reference material (Scripps Institution of Oceanography) and, when required for low-DIC samples, from 100 or 600 μM solutions prepared from a 1,000 ppm Na_2CO_3-$NaHCO_3$ DIC standard (ACCUSPEC). pH and conductivity were analyzed within 2 h of filtering. pH was analyzed with a Mettler Toledo FiveEasy benchtop meter calibrated daily using a two-point calibration curve (7.01 and 10.01 pH, NIST). The mean pH of replicate samples was calculated by first converting pH to H^+. Conductivity was analyzed with a Thermo Orion 115 A+ meter calibrated daily using 1,413 μS cm^{-1} solution. Dissolved CO_2 was extracted by equilibrating 20 mL of sample with 40 mL of nitrogen gas in an air-tight polypropylene syringe (Hesslein et al., 1991) and measured immediately by infrared gas analyzer (IRGA; PP Systems EGM-4). IRGA drift was checked daily with 60 mL of 1,010 ppm CO_2 standard (Scotty Gases). CO_2 concentration (μM) and the partial pressure of CO_2 (pCO_2) were calculated using Henry's constants corrected for water temperature (Weiss, 1974). For instances when DIC concentration could not be measured by the Apollo, DIC concentration was calculated using pH and pCO_2 as inputs to CO_2sys (v.2.3; Pierrot et al., 2006).

At the final time point of each experiment, water was also filtered (0.45-μm, cellulose acetate, Sartorius) to determine the concentrations of cations and anions. Cations were preserved with trace metal-grade HNO_3 and all ions were refrigerated until analysis at the University of Alberta Biogeochemical Analytical Services Laboratory (BASL, ISO/EIC 17025) following standard procedures. Equilibrated headspace gas samples for $\delta^{13}C_{CO_2}$ were stored over-pressurized in bottles that were sealed with baked (12 h, 60°C) butyl stoppers and pre-evacuated. $\delta^{13}C_{CO_2}$ was analyzed within 2 months by a Picarro isotope analyzer (G2201-*I*; < 0.2‰ precision) equipped with an injection module for discrete samples (SSIM). The Picarro analyzer was checked for drift against commercial and in-house $\delta^{13}C_{CO_2}$ standards during each run.

$\delta^{18}O$ of permafrost ice was analyzed by cavity ringdown spectroscopy (Picarro L2130-i) at the University of Alberta BASL. Calibration curves for water isotopes were built from U.S. Geological Survey secondary standards (USGS45 and USGS46) and in-house tap water, and calibrated by an International Atomic Energy Agency standard as a quality control.

Data Analysis

We report treatment replicates as mean ± standard deviation for DIC, CO_2, and conductivity and mean ± range for pH. We used the proportions of solute equivalent concentrations in a Piper diagram (Piper, 1944) to characterize potential mineral weathering reactions (see also Lehn et al., 2017). Calculations were made using the concentrations of cations and anions in the experiment bottles at 168 h, first correcting for the solute concentrations measured in the MilliQ control bottles (**Table A1** and **Supplementary Material**). For the Piper diagram, we calculated HCO_3^- as $\Sigma[HCO_3^-, CO_2]$, to correct for HCO_3^- hydrolysis to CO_2. The concentrations of dissolved CO_2 measured at each time point were corrected for dissolved atmospheric CO_2 in the control bottles (15–26 μM). To test for multivariate similarity (i.e., geochemical likeness) between treatments, we first performed a hierarchical cluster analysis using the R software package *pvclust* (Suzuki and Shimodaira, 2015), which employs the R base function *hclust* to generate a bootstrapped ($n = 1{,}000$ iterations), Euclidean distance-based estimate of a stable configuration of measurement clusters. Variables were selected for the *pvclust* to yield insight about DIC concentration and speciation (HCO_3^-, CO_2) and CO_2 source ($\delta^{13}C_{CO_2}$); to help differentiate between silicate and carbonate weathering (Al^{3+}); and to evaluate contributions from sulfide oxidation and gypsum dissolution (SO_4^{2-}). We then evaluated the associations between these geochemical variables and the sample clusters defined by *pvclust* using the *metaMDS* function in the R software package *vegan* (Oksanen et al., 2013). *metaMDS* augments traditional non-metric multidimensional scaling (NMDS) by running multiple MDS iterations to find a stable solution, whereby proximity of measurements indicates similarity and vectors reveal how variables correlate with measurements. All statistics were performed in R software v.3.4.4 (R Core Team, 2018), with significance interpreted at $\alpha = 0.05$.

RESULTS

Sediment Mineral and Geochemical Composition

Permafrost sediments, RTS runoff, and debris tongue deposits contained carbonates (calcite, dolomite, and rarely siderite), pyrite, gypsum, quartz, and various Na-, Mg-, and K-aluminosilicates (**Table 2**; note the XRD detection limit of 3%). Albite, clinochlore, muscovite, and quartz were detected in all sediment sources. The XRD detected carbonates, pyrite, and gypsum in at least half of the sediment sources and in at least one source at each RTS. Carbonates, sulfides, and gypsum were generally present (>3%) in Pleistocene permafrost sediments and absent from active layer sediments (below detection), whereas the presence of these minerals in Holocene, runoff, and debris tongue sediments varied (**Table 2**). The presence of sulfide and/or carbonate varied among sediment sources, and there were no sediments where carbonate was detected by XRD and sulfide was not.

The geochemical composition of sediments was characterized by—in decreasing order of concentration—Al^{3+}, Fe^{2+}, K^+, Mg^{2+}, Ca^{2+}, Na^+, and Sr^{2+} (**Table 3**). Because concentrations of Ca^{2+} relative to Na^+ and Sr^{2+} are typically higher for carbonates than silicates (Keller et al., 2007), we used molar ratios to discern the relative proportion of carbonates (high Ca/Na and Ca/Sr) vs. silicates in sediments. Ca/Sr and Ca/Na were typically higher in sediments where carbonates were detected by XRD (**Table 2**, **Figure 2**). Some sediments with sulfides but not carbonates also had relatively high Ca/Na and Ca/Sr (e.g., FM2 Holocene and Pleistocene, HD debris tongue), perhaps reflecting the presence of carbonates below the XRD detection limit.

Weathering Experiment: Trends in Conductivity, DIC, CO_2, and pH

For all RTSs and sediment sources, conductivity increased most strongly during the first 10 min of the incubation, and increased marginally thereafter, indicating that the

TABLE 2 | Minerals detected by X-ray diffraction (x) in non-sterilized sediments.

RTS	Source	Cluster	Gypsum $CaSO_4 \cdot 2H_2O$	Pyrite FeS_2	Calcite $CaCO_3$	Dolomite $CaMg(CO_3)_2$	Albite $Na(AlSi_3O_8)$	Orthoclase/sanidine $K(AlSi_3O_8)$	Clinochlore $Mg_5Al(AlSiO_{10})(OH)_8$	Muscovite $KAl_2(AlSi_3O_{10})(OH)_2$	Quartz SiO_2	Other
FM2	AL	3							X	x	x	
FM2	HO	3		X					X	x	x	
FM2	PL	2	x	X			x	x	X	x	x	
FM2	RU	1	x	X	x	x	x	x	X	x	x	
FM2	DT	1	x	X	x	x	x	x	x	x	x	
HC	AL	3							x	x	x	
HC	HO	1	x	X		x	x	x	x	x	x	
HC	PL	1		X	x	x	x	x	x	x	x	
HC	RU	1		X		x	x	x	x	x	x	*
HC	DT	1	x	x		x	x	x	x	x	x	
HD	AL	3							x	x	x	
HD	HO	3							x	x	x	
HD	PL	1	x	x	x	x	x		x	x	x	
HD	RU	2							x	x	x	†
HD	DT	2	x	x			x	x	x	x	x	

*AL, active layer; HO, Holocene; PL, Pleistocene; RU, runoff; DT, debris tongue. Other minerals: *Siderite: $FeCO_3$; †Lepidolite: $KLi_2Al(Si_4O_{10})(F,OH)_2$.*

TABLE 3 | Geochemical composition of sediments, measured by ICP-MS. Concentrations are reported in μmol g^{-1} of dry sediment.

Site	Source	Cluster	Al^{3+}	Fe^{2+}	K^{+}	Mg^{2+}	Ca^{2+}	Na^{+}	Sr^{2+}
FM2	AL	3	1,665	650	435	319	159	218	1.15
FM2	HO*	3	1,454	635	376	291	234	194	1.21
FM2	PL*	2	2,458	684	665	480	153	152	1.60
FM2	RU**	1	1,584	627	420	395	271	246	1.31
FM2	DT**	1	1,601	629	467	388	256	208	1.34
HC	AL	3	1,811	599	454	302	53	206	1.08
HC	HO**	1	1,722	594	495	396	240	207	1.26
HC	PL**	1	1,324	526	341	284	188	201	1.17
HC	RU**	1	1,560	556	430	359	175	237	1.32
HC	DT**	1	1,586	593	441	371	169	246	1.24
HD	AL	3	1,625	600	494	302	31	198	1.15
HD	HO	3	2,010	605	511	336	49	196	1.37
HD	PL**	1	1,986	646	519	402	202	195	1.38
HD	RU	2	2,330	752	651	479	113	181	1.51
HD	DT*	2	1,799	649	506	380	142	208	1.36

*Minerals detected by XRD: **Sulfides and carbonates, *sulfides.*

majority of the most reactive component of the mineral pool weathered by 168 h (**Figures 3A–C**). At 168 h, conductivity in treatments with Pleistocene permafrost, runoff, and debris tongue sediments (mean = 264 μS cm^{-1}) was significantly higher than in treatments with active layer and Holocene permafrost sediments [mean = 138 μS cm^{-1}, excluding HC Holocene [552 μS cm^{-1}]] (t-test: $t_{18} = 3.26$, $p < 0.001$). Solutes at 168 h broadly reflected sulfide oxidation and sulfate salt (e.g., gypsum) dissolution (SSD) and relatively greater contributions from silicate and carbonate weathering by H_2SO_4 than H_2CO_3 (**Figure 4**). Across RTSs and sediment sources, SO_4^{2-} concentrations at 168 h were often greater than would be expected from sulfide oxidation alone (section Mineral Weathering Experiment) (**Table 4**), suggesting that gypsum dissolution was a primary source of SO_4^{2-} in our experiment.

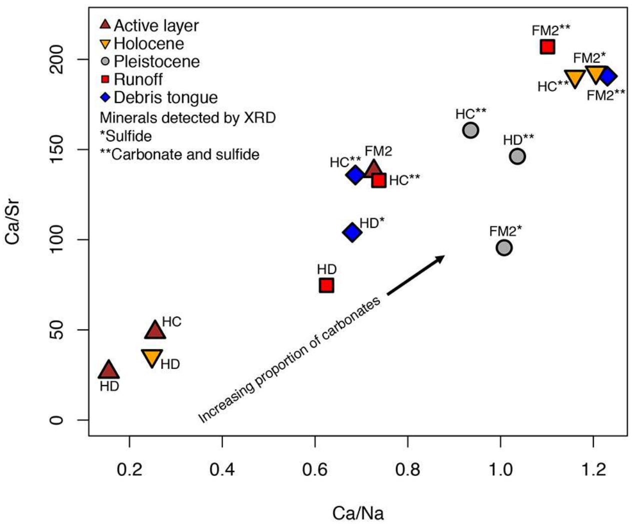

FIGURE 2 | The relationship between Ca/Sr (μmol g^{-1}/μmol g^{-1}) and Ca/Na (μmol g^{-1}/μmol g^{-1}) of sediments used in the mineral weathering experiment.

For all treatments, DIC concentrations increased rapidly during the first 6 h and more gradually after 24–48 h. Treatments containing sediments with carbonates and sulfides detected by XRD generated more DIC (mean = 728 μM after 168 h) than those in which only sulfides were detected (mean = 345 μM), or neither carbonates nor sulfides were detected (mean = 121 μM) (**Figures 3D–F**, **Table 4**). Accordingly, treatments with active layer and Holocene sediments generally had the lowest DIC at 168 h (mean = 111 and 342 μM, respectively), whereas DIC in treatments with Pleistocene, runoff, and debris tongue sediments had higher concentrations (581, 556, and 654 μM, respectively) (**Table 4**).

For all treatments, CO_2 increased rapidly within 6 h (**Figures 3G–I**) and, in treatments containing sediments with both carbonates and sulfides detected by XRD, decreased by 16–39 μM thereafter. The decrease in CO_2 was equivalent to 19–51% (mean = 33%) of the maximum CO_2 reached during the experiment for these treatments. At 168 h, CO_2 in these treatments was lower (mean = 75 μM) than in other treatments. In contrast, CO_2 in treatments containing sediments with sulfides but not carbonates detected by XRD generally reached the highest concentrations of CO_2 by 168 h (mean = 212 μM). Most of the treatments with active layer and Holocene sediments, which did not have carbonates or sulfides detected by XRD, had variable but relatively moderate CO_2 (mean = 95 μM).

pH increased in all treatments except for those with FM2 active layer sediments, which decreased from 7.04 to 6.69 pH units after 24 h. By 168 h, pH was highest where carbonates and sulfides were detected by XRD (mean = 7.23 pH units), lower when sulfides but not carbonates were detected (mean = 6.62), and the lowest in treatments where neither carbonates nor sulfides were detected (mean = 4.70) (**Figures 3J–L**).

Statistical Clusters of Treatments Based on Geochemistry

The cluster analysis revealed that treatments grouped into three geochemical clusters which broadly reflected gradients of prior thaw and exposure to weathering, and also the intensity of sulfide oxidation relative to carbonate weathering (**Figure A1**). Clusters one and two mostly included samples with more limited prior thaw compared to cluster three, which contained most of the active layer and Holocene permafrost sediments (**Figure 5**). Cluster one included sediments characterized by carbonate weathering that buffered H_2SO_4 acidity from sulfide oxidation more effectively than the sediments in cluster two. Cluster three included sediments which had relatively limited effects on DIC upon weathering. These statistical clusters help to describe the influence of prior exposure to thaw and the balance between carbonate weathering and sulfide oxidation on the evolution of DIC and CO_2 during the experiment.

Cluster 1—High DIC and pH, Low Al^{3+}

Treatments containing sediments with both carbonates and sulfides detected by XRD (**Table 2**) had consistently high DIC (mean = 728 μM), elevated pH (mean = 7.22 pH units), and low dissolved Al^{3+} (mean = 0.1 μM) (**Figure 3**, **Table 4**). In this cluster, mineral weathering resulted in rapid CO_2 production early in the experiment followed by a decrease after ∼24 h. Yet, CO_2 was always higher than in the control bottles. $\delta^{13}C_{CO_2}$ at 168 h varied between treatments, but was generally intermediate (−8.3 to −13.2‰, *n* = 7) relative to samples in the other clusters (**Table 4**). Treatments in this cluster include Pleistocene permafrost sediments or recently thawed/colluviated material (i.e., runoff or debris tongue sediments), but not sediments from the active layer or Holocene permafrost.

Cluster 2—High SO_4^{2-} and CO_2, ^{13}C-Enriched CO_2

Bottles with FM2 Pleistocene, HD runoff, and HD debris tongue sediments had the highest CO_2 concentrations (**Table 4**), with no measurable decrease in CO_2 during the 168 h incubation. Generally, these treatments had ^{13}C-enriched CO_2 (−4.7 to −7.8‰), high concentrations of SO_4^{2-} (mean = 1,307 μM), and had sulfides and gypsum detected by XRD (except for HD runoff), but not carbonates. DIC concentrations were intermediate between clusters one and three (mean = 279 μM).

Cluster 3—Low DIC and SO_4^{2-}, High Dissolved Al^{3+}, and ^{13}C-Depleted CO_2

Bottles with active layer and Holocene sediments (except HC Holocene) had high concentrations of dissolved Al^{3+} (mean = 20.3 μM), consistently lower conductivity, moderate to low DIC (mean = 160 μM), low SO_4^{2-} (mean = 202 μM), and ^{13}C-depleted CO_2 (−16.3 to −20.3‰, *n* = 5) at 168 h (**Figure 3**, **Table 4**). There were no Pleistocene permafrost, runoff, or debris tongue sediments in this cluster.

DISCUSSION

Our findings reveal several interacting controls from thermokarst on fluvial inorganic carbon cycling on the Peel Plateau. In

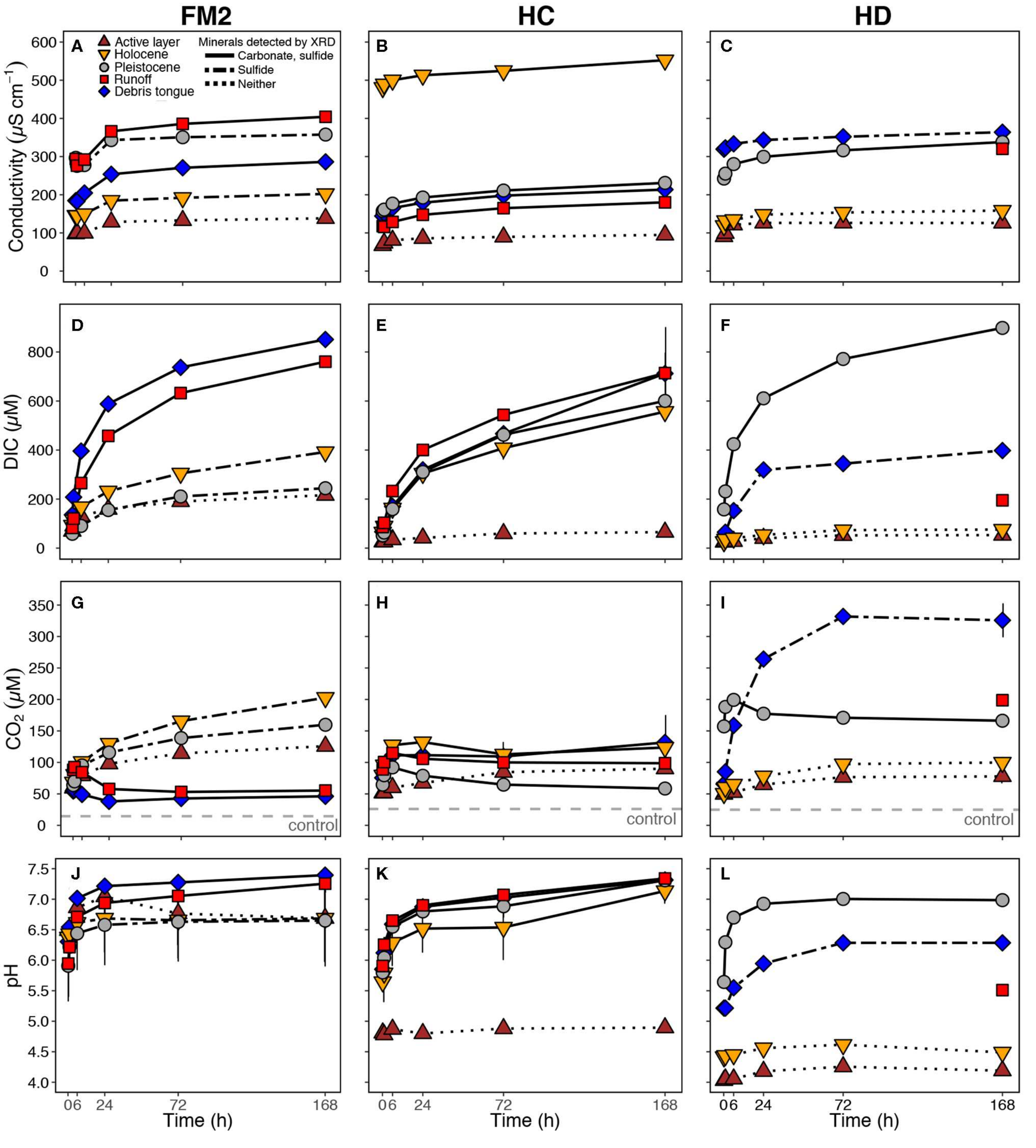

FIGURE 3 | Weathering experiment trends in **(A-C)** conductivity, **(D-F)** dissolved inorganic carbon (DIC), **(G-I)** dissolved CO2, and **(J-L)** pH by RTS and sediment source. Error bars represent ± standard deviation for conductivity, DIC, and CO_2, and range for pH (bars do not appear where smaller than symbol). See **Figure 1** for locations and **Table 1** for site characteristics. **(G–I)** Dashed lines represent CO_2 concentration in control bottles.

the modern and paleo (Holocene) active layer, we find that prior thaw and exposure of sediments to chemical weathering depleted carbonates, sulfides, and gypsum in these upper soil layers (Lacelle et al., 2019). In contrast, Pleistocene permafrost and recently thawed and colluviated sediments within the RTS runoff and debris tongue contain more of these readily

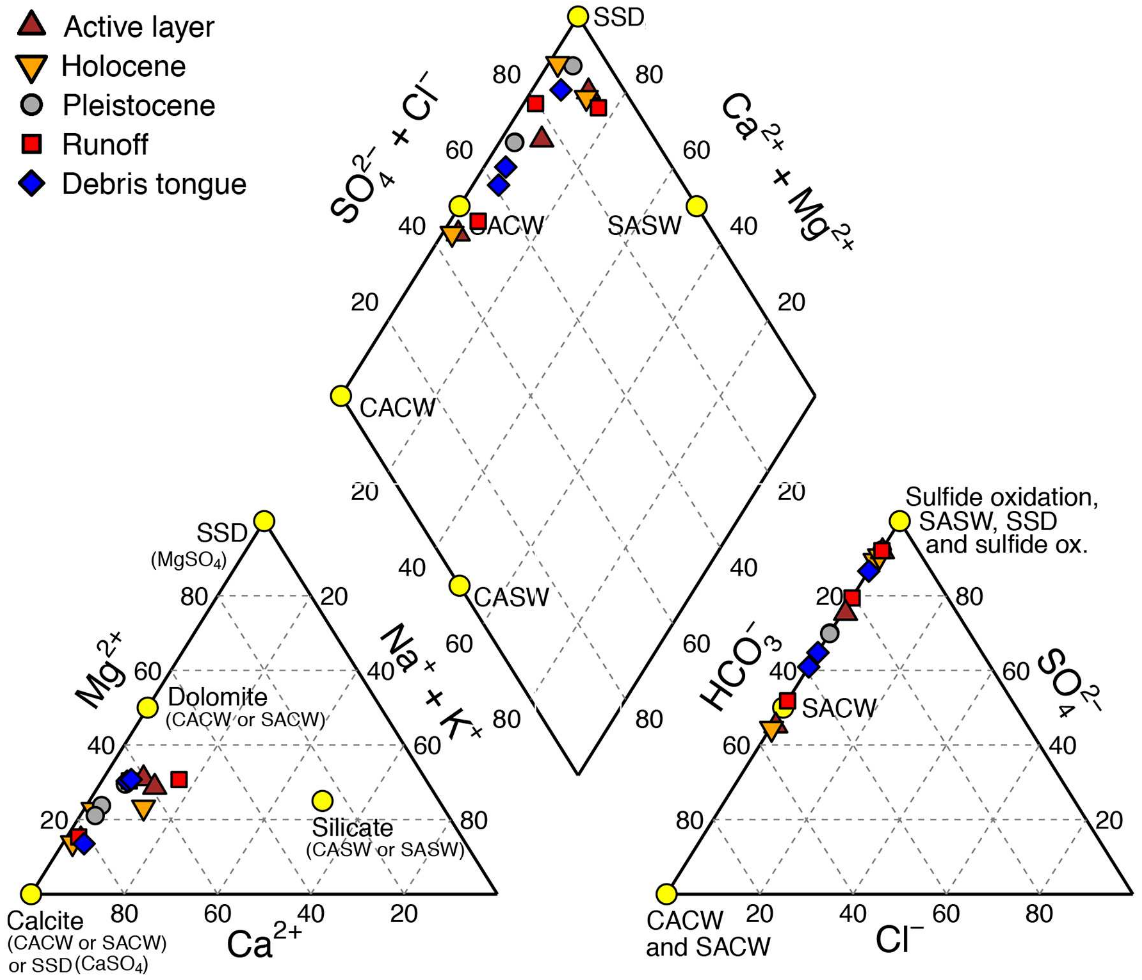

FIGURE 4 | Piper diagram showing the chemical composition of MilliQ water treated with five different retrogressive thaw slump sediments (see legend) exposed to varying degrees of prior thaw. The composition of each point reflects the relative concentrations (in meq L^{-1}) of major cations (left), anions (right), and both together (center) as a percent. See details in main text for calculation of end-members: CACW, H_2CO_3 carbonate weathering; SACW, H_2SO_4 carbonate weathering; CASW, H_2CO_3 silicate weathering; SASW, H_2SO_4 silicate weathering; SSD, sulfate salt (gypsum) dissolution.

weatherable sediments. Thus, thermokarst which unearths Pleistocene permafrost sediments at depth is more likely to intensify DIC cycling and abiotic CO_2 production by facilitating H_2SO_4 carbonate weathering, often in the presence of sulfides (Zolkos et al., 2018). Broadly, these trends show that renewed deglaciation on the Peel Plateau is accompanied by associated mineral weathering and biogeochemical dynamics documented in actively glacierized regions of the circumpolar north (Hindshaw et al., 2016; St. Pierre et al., 2019; Urra et al., 2019). These findings help to contextualize the effects of permafrost thaw on mineral weathering and inorganic carbon cycling on the Peel Plateau (**Figure 6**) and potentially in ice-rich, glaciated terrains elsewhere in northwestern Canada, Alaska, and Eurasia (Segal et al., 2016a; Kokelj et al., 2017a; Rudy et al., 2017).

Implications of Thaw History and Prior Sediment Exposure to Mineral Weathering for Inorganic Carbon Cycling

The lower conductivity observed in most treatments with active layer and Holocene sediments (except HC Holocene; **Table 2**, **Figure 5**) suggests that prior thaw of the upper layers of permafrost on the Peel Plateau promoted chemical weathering of readily-weathered minerals within the upper few meters of soil (Malone et al., 2013; Lacelle et al., 2019). Except for HC Holocene, active layer, and Holocene sediments did not have carbonate detected by XRD and also often had lower Ca/Sr and Ca/Na ratios. The relatively high DIC production associated with HC Holocene sediments may reflect the local presence of colluviated substrate from former debris flows that was integrated into permafrost during its upward aggradation

TABLE 4 | Measurements of water chemistry from the mineral weathering experiment at 168 h.

Site	Source	Cluster	pH	Cond (μS cm^{-1})	DIC (μM)	Ca^{2+} (μM)	Mg^{2+} (μM)	Na^{+} (μM)	K^{+} (μM)	SO$_4^{2-}$ (μM)	Cl^{-} (μM)	Al^{3+} (μM)	δ^{13}C$_{CO_2}$ (‰ VPDB)
FM2	AL	3	6.69	138.2	215.9	642.2	114.4	13.9	38.6	90.3	3.4	7.9	−16.3
FM2	HO*	3	6.68	202.2	392.1	1009.8	165.0	10.9	37.1	157.5	2.3	8.7	−16.3
FM2	PL*	2	6.65	357.7	244.4	1093.6	496.2	79.6	103.6	1476.0	2.3	0.1	−7.8
FM2	RU**	1	7.25	404.2	760.4	1649.5	308.6	52.2	49.1	1471.1	2.5	0.2	−12.2
FM2	DT**	1	7.39	286.2	851.0	1152.0	190.5	61.3	67.8	783.4	1.4	0.3	−13.2
HC	AL	3	4.89	94.8	65.3	177.2	90.9	23.5	27.1	102.6	2.0	25.6	−20.2
HC	HO**	1	7.13	552.5	556.6	1974.6	594.1	30.4	72.1	2349.8	0.3	0.1	−8.3
HC	PL**	1	7.31	231.0	600.4	738.8	240.7	31.3	34.0	702.0	0.0	0.1	−9.6
HC	RU**	1	7.34	180.1	713.9	510.8	243.2	51.3	43.2	384.3	0.6	0.1	−11.1
HC	DT**	1	7.31	213.5	712.2	607.6	286.8	55.2	48.1	555.4	0.3	0.1	−12.5
HD	AL	3	4.19	126.1	53.1	169.4	82.3	34.4	35.3	313.6	2.5	10.0	−20.3
HD	HO	3	4.49	158.5	75.8	283.7	102.9	75.3	35.0	381.1	2.8	49.5	−19.1
HD	PL**	1	6.98	337.9	898.1	1212.4	337.4	36.1	67.0	1041.6	1.4	0.1	−9.9
HD	RU	2	5.51	320.4	195.0	725.1	421.3	349.7	99.0	1153.0	3.4	16.1	−6.9
HD	DT*	2	6.28	363.9	398.0	1047.7	509.8	126.6	76.0	1291.3	1.7	2.9	−4.7
Cluster means (standard error, range for pH)													
		1	7.2 (0.2)	315 (49)	728 (47)	1,121 (207)	314 (50)	45 (5)	54 (5)	1,041 (256)	0.9 (0.3)	0.1 (0)	−11.0 (0.7)
		2	5.9 (0.6)	347 (14)	279 (61)	955 (116)	476 (28)	185 (83)	93 (9)	1,307 (94)	2.4 (0.5)	6.4 (4.9)	−6.5 (0.9)
		3	4.7 (1.2)	144 (18)	160 (65)	456 (163)	111 (15)	32 (12)	35 (2)	209 (59)	2.6 (0.2)	20.3 (8)	−18.4 (0.9)
Source means (standard deviation, range for pH)													
	AL		4.6 (1.2)	120 (22)	111 (91)	330 (271)	96 (17)	24 (10)	34 (6)	169 (125)	2.6 (0.7)	14.5 (9.6)	−18.9 (2.3)
	HO		5.0 (1.3)	304 (216)	342 (244)	1,089 (848)	287 (268)	39 (33)	48 (21)	963 (1,206)	1.8 (1.3)	19.4 (26.4)	−14.6 (5.6)
	PL		6.9 (0.3)	309 (68)	581 (327)	1,015 (246)	358 (129)	49 (27)	68 (35)	1,073 (388)	1.2 (1.1)	0.1 (0)	−9.1 (1.1)
	RU		6.0 (0.9)	302 (113)	556 (314)	962 (605)	324 (90)	151 (172)	64 (31)	1,003 (559)	2.2 (1.4)	5.5 (9.2)	−10.1 (2.8)
	DT		6.7 (0.6)	288 (75)	654 (232)	936 (289)	329 (164)	81 (40)	64 (14)	877 (377)	1.1 (0.7)	1.1 (1.6)	−10.1 (4.7)

*AL, active layer; HO, Holocene; PL, Pleistocene; RU, runoff; DT, debris tongue. See text for details. Minerals detected by XRD: **Sulfides and carbonates, *sulfides.*

(Lacelle et al., 2019). The greater solute production associated with debris tongue sediments (**Figure 3**) indicates relatively limited weathering prior to burial within debris tongues, where some protection from wetting within the interior may reduce weathering prior to sample collection. Where RTSs on the Peel Plateau expose the Holocene active layer, the effects on fluvial inorganic carbon cycling will likely be greater if the substrate contains paleo debris flow material (Lacelle et al., 2019). The more modest DIC generation associated with active layer and Holocene sediments that did not contain debris tongue material suggests that carbonates were present, but in amounts typically minor enough to not be detected by XRD (here, <3%). This is consistent with observations of modern and paleo-active layer soils in Alaska (USA) and the central Yukon Territory (Canada), where top-down thaw promoted chemical weathering and a reduction of carbonates relative to silicates in upper soil layers (Burn et al., 1986; Keller et al., 2010). These findings broadly demonstrate that prior thaw and local and regional heterogeneity in soil composition are among the primary abiotic controls on fluvial inorganic carbon cycling on the Peel Plateau and likely in permafrost terrains across the circumpolar north.

Thermokarst Sediment Mineral Composition As a Driver of DIC Speciation in Streams

The grouping of treatments into distinct geochemical clusters indicates that thaw history enables a differentiation in mineralogy that provides an overarching control on the abiotic component of inorganic carbon cycling in thermokarst-affected streams on the Peel Plateau. Sediments in cluster one, which contained the most carbonates and sulfides (both >3%) and had more limited prior exposure to thaw, yielded the highest DIC concentrations and showed a trend of decreasing CO_2 after ~24 h (**Figure 3**). The decrease in CO_2, high DIC, and elevated pH (mean = 7.2) associated with sediments in cluster one (**Figure 5**) suggests that H_2CO_3 carbonate weathering converted some of the initially-produced CO_2 to HCO_3^-. The decrease in $\delta^{13}C_{CO_2}$ values expected from this pH buffering (fractionation ca. −11‰) (Clark and Fritz, 1997) and the intermediate $\delta^{13}C_{CO_2}$ values for cluster one (−8 to −13‰) indicate weathering of carbonate sediments that were isotopically similar to regional bedrock (δ^{13}C carbonate = −0.7 to −5.6‰) (Hitchon and Krouse, 1972) that may be present within tills on the Peel Plateau. Together, these trends for the cluster one treatments suggests that, when carbonates are sufficiently abundant, carbonate weathering by H_2CO_3 (Equation 2) and pH buffering (Equation 1) can fix some CO_2 as HCO_3^- (Brantley et al., 2014) and thereby partially offset the high rates of CO_2 production and efflux within RTSs on the Peel Plateau (Zolkos et al., 2019). Although we did not observe it in our treatments, sediments with abundant carbonate and limited or no sulfides would have even stronger CO_2 consumption (Striegl et al., 2007; St. Pierre et al., 2019). In contrast, the striking CO_2 production in treatments with a greater proportion of sulfide (cluster two) suggests that carbonate weathering was insufficient to noticeably temper dissolved CO_2 concentrations. Rather, more intense sulfide oxidation than carbonate weathering likely sustained a relatively low pH (mean = 5.9, **Table 2**) and enabled more complete dissolution of trace carbonates, resulting in $\delta^{13}C_{CO_2}$ (−6.5‰) reflective of an abiotic CO_2 source. In cluster three, the relatively more ^{13}C-depleted $\delta^{13}C_{CO_2}$ values (−16 to −20‰) may partly reflect the abiotic breakdown of organic matter from the modern and paleo Holocene active layer soils in a relatively acidic environment (Bao et al., 2019). For all clusters, concentrations of SO_4^{2-} were typically greater than would be expected from sulfide oxidation alone (section Mineral Weathering Experiment), indicating that gypsum dissolution generated a large proportion of the SO_4^{2-} that we observed in our experiment. This suggests that even a small proportion of SO_4^{2-} derived from sulfide oxidation can have critical implications for DIC cycling.

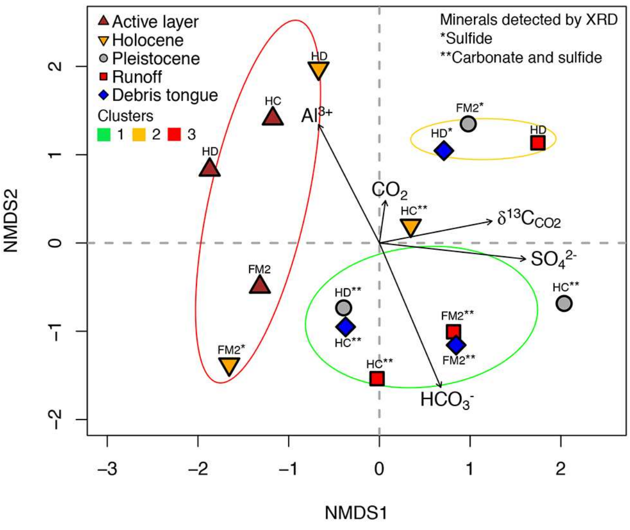

FIGURE 5 | *metaMDS* results showing similarities between measurements (proximate = more similar) and correlations between measurements and original observations (black text). Note RTS IDs included above measurements. Ellipses constrain statistical clusters in **Figure A1** (see section Results in main text).

These findings build on recent work showing that RTSs exposing Pleistocene permafrost sediments can amplify inorganic carbon cycling (Zolkos et al., 2018) by revealing that the chemical weathering of these sediments on the Peel Plateau is most likely to be a net source of abiotic CO_2. This abiotic CO_2 flux from Peel Plateau thermokarst streams to the atmosphere—which occurs at high rates, but over a small area—is likely minor relative to CO_2 release from biotic processes occurring within recently thawed permafrost substrate (Littlefair and Tank, 2018; Zolkos et al., 2019) and from thickening of the active layer (Striegl et al., 2005). As thermokarst intensifies on the Peel Plateau, RTSs may increase fluvial export of HCO_3^- into marine environments, where climatic effects would unfold over geological timescales as carbonate precipitation reactions release CO_2 to the atmosphere (Calmels et al., 2007).

Thermokarst Intensity As a Control on Inorganic Carbon Cycling on the Peel Plateau

These findings build on previous research showing that deeper RTSs on the Peel Plateau expose more solute-rich permafrost and are therefore likely to have a stronger effect on stream chemistry than shallow thermokarst (Kokelj et al., 2013; Malone et al., 2013; Lacelle et al., 2019). Here, we show that deeper RTSs also expose a greater proportion of previously unweathered carbonate- and sulfide-bearing Pleistocene permafrost sediments, and are thus likely to enhance inorganic carbon cycling upon thaw, resulting in greater DIC production (e.g., Zolkos et al., 2018). Further, the striking DIC production in treatments with runoff and debris

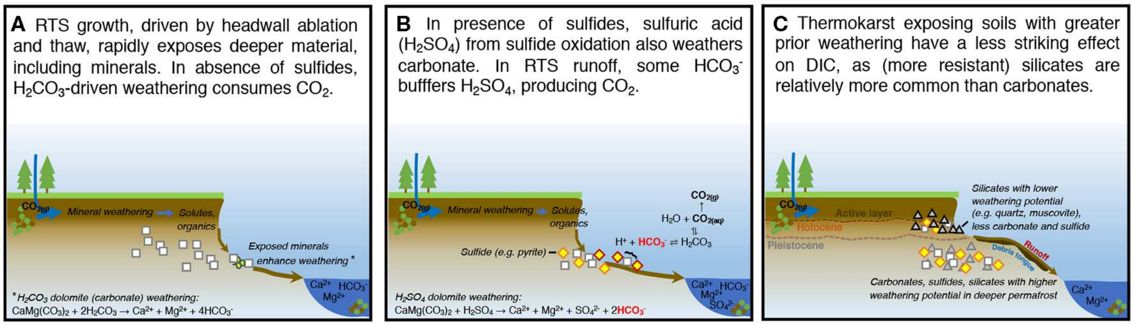

FIGURE 6 | Refined conceptual model of RTS effects on inorganic carbon cycling on the Peel Plateau **(A)** in the presence of carbonates and absence of sulfides and **(B)** in the presence of both carbonates and sulfides. **(C)** Depicts how this paper builds on previous understanding. Adapted from Zolkos et al. (2018).

tongue material reveals that these recently thawed sediments can augment fluvial inorganic carbon cycling for at least years to decades as RTSs develop. Initially, we reasoned that debris tongue sediments would have a limited effect on DIC, because this material is thawed and exposed at the surface environment prior to burial by subsequent debris flows (Kokelj et al., 2017b). Contrary to our hypothesis, RTS debris tongue sediments were associated with consistently strong DIC production, indicating greater protection from weathering and more limited depletion of carbonate and sulfide than the active layer and Holocene permafrost sediments. Mineral weathering in debris tongue environments may be enhanced as vegetation colonizes stabilized areas (Cray and Pollard, 2015) and as sediments erode into streams (van der Sluijs et al., 2018). From an inorganic carbon cycling perspective, this suggests that previously un-thawed sediments that are redistributed following thaw may be an important legacy of thermokarst on the Peel Plateau, particularly if increasing thaw and rainfall facilitate exposure and the transport of RTS sediments into stream networks (Kokelj et al., 2015; van der Sluijs et al., 2018). These interpretations align with observations of increasing downstream geochemical signals of carbonate weathering and sulfide oxidation (Zolkos et al., 2018) in conjunction with intensifying regional thermokarst in recent decades (Segal et al., 2016a). As future warming and increasing rainfall on the Peel Plateau increase RTS activity, the thawing of minerals in deeper permafrost can thus be expected to accelerate inorganic carbon cycling for decades to centuries.

Implications for the Role of Mineral Weathering Within Permafrost Carbon Feedbacks

Across the pan-Arctic, increasing riverine solute fluxes in recent decades signals a thickening of active layers, deepening flow paths, and enhanced mineral weathering in concert with climate warming and intensifying precipitation (Tank et al., 2016; Toohey et al., 2016; Drake et al., 2018a; Zolkos et al., 2018). While increasing riverine alkalinity fluxes in North America (Peel, Mackenzie; Tank et al., 2016; Zolkos et al., 2018) and Siberia (Ob', Yenisey; Drake et al., 2018a) reflect a broad scale acceleration of inorganic carbon cycling, stronger coupling between carbonate weathering and sulfide oxidation in northwestern Canada diminishes the weathering CO_2 sink compared to other Arctic regions (Beaulieu et al., 2012). From an Arctic carbon cycling perspective, regional variability in lithology, hydrology (Tank et al., 2012), and microbial processes (Hindshaw et al., 2016) influence the mineral weathering component of carbon-climate feedbacks. Recent work suggests that biotic processes drive DIC cycling in ice- and organic-rich (syngenetic) regions affected by thermokarst (Drake et al., 2018b). Working in a relatively more mineral-rich permafrost terrain, we show that intensifying thermokarst stands to amplify abiotic processes, but that the presence of sulfide oxidation is a primary control on the degree to which mineral weathering represents a CO_2 sink. Despite increasing recognition that mineral weathering is an important component of the northern carbon cycle (Calmels et al., 2007; Beaulieu et al., 2012; Tank et al., 2012, 2016), the contribution of thermokarst to these processes remains poorly constrained. This work indicates that thermokarst will have strong effects on inorganic carbon cycling where glaciated terrains coincide with carbonate lithologies (Zolkos et al., 2018; St. Pierre et al., 2019) and perhaps most strongly where sediments remain unmodified at the near surface (e.g., Rudy et al., 2017; Lewkowicz and Way, 2019; Ward Jones et al., 2019).

Thermokarst can expose large volumes of sediments to mineral weathering and fluvial transport (Kokelj et al., 2013; van der Sluijs et al., 2018), with unknown effects on CO_2 exchange between streams and the atmosphere as HCO_3^- is exported downstream. These effects are likely to be particularly strong across glacial deposits, where carbonates and sulfides are often highly reactive (Blum et al., 1998; Anderson et al., 2000; Torres et al., 2017) and even trace amounts can profoundly affect inorganic carbon cycling. Quantifying the fluvial CO_2: HCO_3^- balance across broader scales in thermokarst-affected fluvial networks will help to trace and better understand the effects of permafrost thaw on inorganic carbon cycling (Drake et al., 2018a).

CONCLUSIONS

In this study, we found evidence to suggest that thermokarst activity on the Peel Plateau will amplify inorganic carbon cycling where RTSs facilitate the exposure of deeper, previously unweathered permafrost sediments. Across the circumpolar north, future increases in inorganic carbon cycling will be strongest where thermokarst unearths carbonate-bearing tills with limited prior thaw and modification (Kokelj et al., 2017b). In these regions, the progression of—and balance between—H_2CO_3 and H_2SO_4 weathering will determine the degree to which DIC in freshwaters represents a CO_2 sink (Calmels et al., 2007; Tank et al., 2012, 2016; Drake et al., 2018a). By investigating the composition and reactivity of mineral substrate in permafrost regions elsewhere, particularly where thermokarst may expose and mobilize vast stores of minerals into fluvial networks (e.g., Olefeldt et al., 2016), future work will advance understanding of the role of mineral weathering within contemporary inorganic carbon cycling and long-term feedbacks within Earth's climate system (Schuur et al., 2015; Zolkos et al., 2018).

DATA AVAILABILITY STATEMENT

All datasets generated for this study are included in the article/**Supplementary Material**.

AUTHOR CONTRIBUTIONS

SZ and ST designed the study. SZ led data analysis and interpretation and manuscript writing. ST contributed to data interpretation and manuscript writing.

FUNDING

Natural Sciences and Engineering Research Council of Canada supported research activities (Discovery Grant #430696, Northern Research Supplement #444873), Campus Alberta

Innovates Program supported laboratory research activities, Natural Resources Canada Polar Continental Shelf Program (#61717) supported field research activities. UAlberta Northern Research Award supported field research activities. Arctic Institute of North America Grant-in-Aid supported field research activities.

ACKNOWLEDGMENTS

We thank Rosemin Nathoo, Christine Firth, Abraham Snowshoe, Keith Collins, Sarah Shakil, Erin MacDonald, Dr. Lisa Bröder, and Kirsi Keskitalo for assistance in the field, and Yomna Elshamy for assistance in the laboratory. We thank Dr. Steve Kokelj and Dr. David Olefeldt for helpful comments on a draft of the manuscript. CAIP funding awarded to Dr. David Olefeldt supported the analyses of CO_2 stable isotopes. Data are provided within the manuscript and with the online version of the manuscript.

SUPPLEMENTARY MATERIAL

The Supplementary Material for this article can be found online at: https://www.frontiersin.org/articles/10.3389/feart.2020.00152/full#supplementary-material

Supplementary Material | The Supplementary Material for this study includes geochemistry data produced from the mineral weathering experiment.

REFERENCES

Anderson, S. P. (2007). Biogeochemistry of glacial landscape systems. *Annu. Rev. Earth Planet Sci.* 35, 375–399. doi: 10.1146/annurev.earth.35.031306.140033

Anderson, S. P., Drever, J. I., Frost, C. D., and Holden, P. (2000). Chemical weathering in the foreland of a retreating glacier. *Geochim. Cosmochim. Acta* 64, 1173–1189. doi: 10.1016/S0016-7037(99)00358-0

Bao, R., McNichol, A. P., Hemingway, J. D., Lardie Gaylord, M. C., and Eglinton, T. I. (2019). Influence of different acid treatments on the radiocarbon content spectrum of sedimentary organic matter determined by RPO/accelerator mass spectrometry. *Radiocarbon* 61, 395–413. doi: 10.1017/RDC.2018.125

Beaulieu, E., Goddéris, Y., Donnadieu, Y., Labat, D., and Roelandt, C. (2012). High sensitivity of the continental-weathering carbon dioxide sink to future climate change. *Nat. Clim. Change* 2, 346–349. doi: 10.1038/nclimate1419

Berner, R. A. (1999). A new look at the long-term carbon cycle. *GSA Today* 9, 1–6.

Biskaborn, B. K., Smith, S. L., Noetzli, J., Matthes, H., Vieira, G., Streletskiy, D. A., et al. (2019). Permafrost is warming at a global scale. *Nat. Commun.* 10:264. doi: 10.1038/s41467-018-08240-4

Blum, J. D., Gazis, C. A., Jacobson, A. D., and Chamberlain, C. P. (1998). Carbonate versus silicate weathering in the Raikhot watershed within the high himalayan crystalline series. *Geology* 26, 411–414. doi: 10.1130/0091-7613(1998)026<0411:CVSWIT>2.3.CO;2

Brantley, S. L., Lebedeva, M., and Bazilevskaya, E. (2014). "Relating weathering fronts for acid neutralization and oxidation to pCO_2 and pO_2," in *Treatise on Geochemistry* (Elsevier), 327–352. Available online at: https://linkinghub.elsevier.com/retrieve/pii/B9780080959757013176 (accessed July 3, 2019).

Burn, C. R. (1997). Cryostratigraphy, paleogeography, and climate change during the early holocene warm interval, western Arctic coast, Canada. *Can. J. Earth Sci.* 34, 912–925. doi: 10.1139/e17-076

Burn, C. R., Michel, F. A., and Smith, M. W. (1986). Stratigraphic, isotopic, and mineralogical evidence for an early Holocene thaw unconformity at mayo, yukon territory. *Can. J. Earth Sci.* 23, 794–803. doi: 10.1139/e86-081

Calmels, D., Gaillardet, J., Brenot, A., and France-Lanord, C. (2007). Sustained sulfide oxidation by physical erosion processes in the mackenzie river basin: climatic perspectives. *Geology* 35, 1003–1006. doi: 10.1130/G24132A.1

Clark, I. D., and Fritz, P. (1997). *Environmental Isotopes in Hydrogeology.* Boca Raton, FL: CRC Press/Lewis Publishers.

Cooper, H. K., Duke, M. J. M., Simonetti, A., and Chen, G. (2008). Trace element and Pb isotope provenance analyses of native copper in northwestern North America: results of a recent pilot study using INAA, ICP-MS, and LA-MC-ICP-MS. *J. Archaeol. Sci.* 35, 1732–1747. doi: 10.1016/j.jas.2007.11.012

Cray, H. A., and Pollard, W. H. (2015). Vegetation recovery patterns following permafrost disturbance in a low arctic setting: case study of herschel Island, Yukon, Canada. *Arct. Antarct. Alp. Res.* 47, 99–113. doi: 10.1657/AAAR0013-076

Drake, T. W., Guillemette, F., Hemingway, J. D., Chanton, J. P., Podgorski, D. C., Zimov, N. S., et al. (2018a). The ephemeral signature of permafrost carbon in an arctic fluvial network. *J. Geophys. Res. Biogeosciences*. 123, 1–11. doi: 10.1029/2017JG004311

Drake, T. W., Tank, S. E., Zhulidov, A. V., Holmes, R. M., Gurtovaya, T., and Spencer, R. G. M. (2018b). Increasing alkalinity export from large russian arctic rivers. *Environ. Sci. Technol.* 52, 8302–8308. doi: 10.1021/acs.est.8b01051

Duk-Rodkin, A., and Hughes, O. L. (1992). Surficial geology, fort McPherson-bell river, yukon-Northwest territories. *Geol. Surv. Can*. doi: 10.4095/184002

Fritz, M., Wetterich, S., Schirrmeister, L., Meyer, H., Lantuit, H., Preusser, F., et al. (2012). Eastern beringia and beyond: late wisconsinan and holocene landscape dynamics along the Yukon Coastal Plain, Canada. *Palaeogeogr. Palaeoclimatol. Palaeoecol.* 319–320, 28–45. doi: 10.1016/j.palaeo.2011.12.015

Gaillardet, J., Dupré, B., Louvat, P., and Allegre, C. J. (1999). Global silicate weathering and CO_2 consumption rates deduced from the chemistry of large rivers. *Chem. Geol.* 159, 3–30. doi: 10.1016/S0009-2541(99)00031-5

Gislason, S. R., Oelkers, E. H., Eiriksdottir, E. S., Kardjilov, M. I., Gisladottir, G., Sigfusson, B., et al. (2009). Direct evidence of the feedback between climate and weathering. *Earth Planet. Sci. Lett.* 277, 213–222. doi: 10.1016/j.epsl.2008.10.018

Hesslein, R. H., Rudd, J. W. M., Kelly, C., Ramlal, P., and Hallard, K. A. (1991). "Carbon dioxide pressure in surface waters of Canadian lakes," in *Air-Water Mass Transfer: Selected Papers From the Second International Symposium on Gas Transfer at Water Surfaces*, eds S. C. Wilhelms and J. S. Gulliver (New York, NY: American Society of Civil Engineers), 413–431.

Hindshaw, R. S., Heaton, T. H. E., Boyd, E. S., Lindsay, M. R., and Tipper, E. T. (2016). Influence of glaciation on mechanisms of mineral weathering in two high Arctic catchments. *Chem. Geol.* 420, 37–50. doi: 10.1016/j.chemgeo.2015.11.004

Hitchon, B., and Krouse, H. R. (1972). Hydrogeochemistry of the surface waters of the mackenzie river drainage basin, Canada-III. Stable isotopes of oxygen, carbon and sulphur. *Geochim. Cosmochim. Acta* 36, 1337–1357. doi: 10.1016/0016-7037(72)90066-X

Keller, K., Blum, J. D., and Kling, G. W. (2007). Geochemistry of soils and streams on surfaces of varying ages in arctic alaska. *Arct. Antarct. Alp. Res.* 39, 84–98. doi: 10.1657/1523-0430(2007)39[84:GOSASO]2.0.CO;2

Keller, K., Blum, J. D., and Kling, G. W. (2010). Stream geochemistry as an indicator of increasing permafrost thaw depth in an arctic watershed. *Chem. Geol.* 273, 76–81. doi: 10.1016/j.chemgeo.2010.02.013

Kokelj, S. V., Lacelle, D., Lantz, T. C., Tunnicliffe, J., Malone, L., Clark, I. D., et al. (2013). Thawing of massive ground ice in mega slumps drives increases in stream sediment and solute flux across a range of watershed scales. *J. Geophys. Res. Earth Surf.* 118, 681–692. doi: 10.1002/jgrf.20063

Kokelj, S. V., Lantz, T. C., Tunnicliffe, J., Segal, R., and Lacelle, R. (2017a). Climate-driven thaw of permafrost preserved glacial landscapes, northwestern Canada. *Geology* 45, 371–374. doi: 10.1130/G38626.1

Kokelj, S. V., Tunnicliffe, J., Lacelle, D., Lantz, T. C., Chin, K. S., and Fraser, R. (2015). Increased precipitation drives mega slump development and destabilization of ice-rich permafrost terrain, northwestern Canada. *Glob. Planet. Change* 129, 56–68. doi: 10.1016/j.gloplacha.2015.02.008

Kokelj, S. V., Tunnicliffe, J. F., and Lacelle, D. (2017b). "The peel plateau of northwestern canada: an ice-rich hummocky moraine landscape in transition," in *Landscapes and Landforms of Western Canada*, ed O. Slaymaker (Cham: Springer International Publishing) 109–122. Available online at: http://link.springer.com/10.1007/978-3-319-44595-3_7 (accessed September 21, 2017).

Lacelle, D. (2004). Segregated-intrusive ice of subglacial meltwater origin in retrogressive thaw flow headwalls, Richardson Mountains, NWT, Canada. *Quat. Sci. Rev.* 23, 681–696. doi: 10.1016/j.quascirev.2003.09.005

Lacelle, D., Brooker, A., Fraser, R. H., and Kokelj, S. V. (2015). Distribution and growth of thaw slumps in the Richardson Mountains–Peel Plateau region, northwestern Canada. *Geomorphology* 235, 40–51. doi: 10.1016/j.geomorph.2015.01.024

Lacelle, D., Fontaine, M., Pellerin, A., Kokelj, S. V., and Clark, I. D. (2019). Legacy of holocene landscape changes on soil biogeochemistry: a perspective from paleo-active layers in northwestern Canada. *J. Geophys. Res. Biogeosci.* 2018:JG004916. doi: 10.1029/2018JG004916

Lacelle, D., Lauriol, B., Zazula, G., Ghaleb, B., Utting, N., and Clark, I. D. (2013). Timing of advance and basal condition of the Laurentide Ice Sheet during the last glacial maximum in the Richardson Mountains, NWT. *Quat. Res.* 80, 274–283. doi: 10.1016/j.yqres.2013.06.001

Lehn, G. O., Jacobson, A. D., Douglas, T. A., McClelland, J. W., Barker, A. J., and Khosh, M. S. (2017). Constraining seasonal active layer dynamics and chemical weathering reactions occurring in North Slope Alaskan watersheds with major ion and isotope ($\delta^{34}S_{SO4}$, $\delta^{13}C_{DIC}$, $^{87}Sr/^{86}Sr$, $\delta^{44/40}Ca$, and $\delta^{44/42}Ca$) measurements. *Geochim. Cosmochim. Acta* 217, 399–420. doi: 10.1016/j.gca.2017.07.042

Lerman, A., Wu, L., and Mackenzie, F. T. (2007). CO_2 and H_2SO_4 consumption in weathering and material transport to the ocean, and their role in the global carbon balance. *Mar. Chem.* 106, 326–350. doi: 10.1016/j.marchem.2006.04.004

Lewkowicz, A. G., and Way, R. G. (2019). Extremes of summer climate trigger thousands of thermokarst landslides in a High Arctic environment. *Nat. Commun.* 10:1329. doi: 10.1038/s41467-019-09314-7

Li, M., Peng, C., Wang, M., Xue, W., Zhang, K., Wang, K., et al. (2017). The carbon flux of global rivers: a re-evaluation of amount and spatial patterns. *Ecol. Indic.* 80, 40–51. doi: 10.1016/j.ecolind.2017.04.049

Littlefair, C. A., and Tank, S. E. (2018). Biodegradability of thermokarst carbon in a till-associated, glacial margin landscape: the case of the peel plateau, NWT, Canada. *J. Geophys. Res. Biogeosci.* 123, 3293–3307. doi: 10.1029/2018JG004461

Littlefair, C. A., Tank, S. E., and Kokelj, S. V. (2017). Retrogressive thaw slumps temper dissolved organic carbon delivery to streams of the Peel Plateau, NWT, Canada. *Biogeosciences* 14, 5487–5505. doi: 10.5194/bg-14-5487-2017

Maher, K., and Chamberlain, C. P. (2014). Hydrologic regulation of chemical weathering and the geologic carbon cycle. *Science* 343, 1502–1504. doi: 10.1126/science.1250770

Malone, L., Lacelle, D., Kokelj, S., and Clark, I. D. (2013). Impacts of hillslope thaw slumps on the geochemistry of permafrost catchments (Stony Creek watershed, NWT, Canada). *Chem. Geol.* 356, 38–49. doi: 10.1016/j.chemgeo.2013.07.010

Mandile, A. J., and Hutton, A. C. (1995). Quantitative X-ray diffraction analysis of mineral and organic phases in organic-rich rocks. *Int. J. Coal Geol.* 28, 51–69. doi: 10.1016/0166-5162(95)00004-W

Michel, F. A. (2011). Isotope characterisation of ground ice in northern Canada. *Permafr. Periglac. Process.* 22, 3–12. doi: 10.1002/ppp.721

Montross, S. N., Skidmore, M., Tranter, M., Kivimäki, A.-L., and Parkes, R. J. (2013). A microbial driver of chemical weathering in glaciated systems. *Geology* 41, 215–218. doi: 10.1130/G33572.1

Norris, D. K. (1985). *Geology of the Northern Yukon and Northwestern District of Mackenzie,* Map 1581A, scale: 1:500,000. Ottawa, ON: Geological Survey of Canada. doi: 10.4095/120537

Oksanen, J., Blanchet, F. G., Kindt, R., Legendre, P., Minchin, P. R., O'Hara, R., et al. (2013). *Package 'Vegan'. Community Ecology Package, Version 2.4-6.* Available online at: http://CRAN.R-project.org/package=vegan

Olefeldt, D., Goswami, S., Grosse, G., Hayes, D., Hugelius, G., Kuhry, P., et al. (2016). Circumpolar distribution and carbon storage of thermokarst landscapes. *Nat. Commun.* 7:13043. doi: 10.1038/ncomms13043

Pierrot, D., Lewis, E., and Wallace, D. W. R. (2006). *MS Excel Program Developed for CO_2 System Calculations*. Available online at: doi: 10.3334/CDIAC/otg. CO2SYS_XLS_CDIAC105a

Piper, A. M. (1944). A graphic procedure in the geochemical interpretation of water-analyses. *Trans. Am. Geophys. Union* 25:914. doi: 10.1029/TR025i006p00914

Pogge von Strandmann, P. A. E., Desrochers, A., Murphy, M. J., Finlay, A. J., Selby, D., and Lenton, T. M. (2017). Global climate stabilisation by chemical weathering during the Hirnantian glaciation. *Geochem. Perspect. Lett.* 3, 230–237. doi: 10.7185/geochemlet 1726

R Core Team (2018). *R: A Language and Environment for Statistical Computing*. Vienna: R Foundation for Statistical Computing. Available online at: http://www.r-project.org/

Riebe, C. S., Kirchner, J. W., Granger, D. E., and Finkel, R. C. (2001). Strong tectonic and weak climatic control of long-term chemical weathering rates. *Geology* 29, 511–514. doi: 10.1130/0091-7613(2001)029<0511:STAWCC>2.0.CO;2

Rimstidt, J. D., and Vaughan, D. J. (2003). Pyrite oxidation: a state-of-the-art assessment of the reaction mechanism. *Geochim. Cosmochim. Acta* 67, 873–880. doi: 10.1016/S0016-7037(02)01165-1

Rudy, A. C. A., Lamoureux, S. F., Kokelj, S. V., Smith, I. R., and England, J. H. (2017). Accelerating thermokarst transforms ice-cored terrain triggering a downstream cascade to the ocean. *Geophys. Res. Lett.* 44, 11080–11087. doi: 10.1002/2017GL074912

Schuur, E. A. G., McGuire, A. D., Schädel, C., Grosse, G., Harden, J. W., Hayes, D. J., et al. (2015). Climate change and the permafrost carbon feedback. *Nature* 520, 171–179. doi: 10.1038/nature14338

Segal, R. A., Lantz, T. C., and Kokelj, S. V. (2016a). Acceleration of thaw slump activity in glaciated landscapes of the Western Canadian Arctic. *Environ. Res. Lett.* 11:034025. doi: 10.1088/1748-9326/11/3/034025

Segal, R. A., Lantz, T. C., and Kokelj, S. V. (2016b). *Inventory of active retrogressive thaw slumps in the Peel Plateau, Northwest Territories, Northwest Territories Geological Survey*. NWT Open Report 2015-020. Yellowknife, NT: Northwest Territories Geological Survey, p. 7.

Serreze, M. C., and Barry, R. G. (2011). Processes and impacts of arctic amplification: a research synthesis. *Glob. Planet. Change* 77, 85–96. doi: 10.1016/j.gloplacha.2011.03.004

Singer, P. C., and Stumm, W. (1970). Acidic mine drainage: the rate-determining step. *Science* 167, 1121–1123. doi: 10.1126/science.167.3921.1121

Skidmore, M., Sharp, M., and Tranter, M. (2004). Kinetic isotopic fractionation during carbonate dissolution in laboratory experiments: Implications for detection of microbial CO_2 signatures using $\delta^{13}C$-DIC. *Geochim. Cosmochim. Acta* 68, 4309–4317. doi: 10.1016/j.gca.2003.09.024

Stott, D. F. (1991). "Geotectonic correlation chart, sheet 1, Northwest territories and yukon," in *Sedimentary Cover of the Craton in Canada*, eds D. F. Stott and J. D. Aiken (Ottawa, ON: Geological Survey of Canada).

St. Pierre, K. A., St. Louis, V. L., Schiff, S. L., Lehnherr, I., Dainard, P. G., Gardner, A. S., et al. (2019). Proglacial freshwaters are significant and previously unrecognized sinks of atmospheric CO_2. *Proc. Natl. Acad. Sci. U.S.A.* 3:17690–17695. doi: 10.1073/pnas.1904241116

Striegl, R. G., Aiken, G. R., Dornblaser, M. M., Raymond, P. A., and Wickland, K. P. (2005). A decrease in discharge-normalized DOC export by the Yukon River during summer through autumn. *Geophys. Res. Lett.* 32, 1–4. doi: 10.1029/2005GL024413

Striegl, R. G., Dornblaser, M. M., Aiken, G. R., Wickland, K. P., and Raymond, P. A. (2007). Carbon export and cycling by the Yukon, Tanana, and Porcupine rivers, Alaska, 2001-2005. *Water Resour. Res.* 43:W02411. doi: 10.1029/2006WR005201

Stumm, W., and Morgan, J. J. (1996). *Aquatic Chemistry: Chemical Equilibria and Rates in Natural Waters, 3rd Edn.* NY: John Wiley & Son, Inc.

Suzuki, R., and Shimodaira, H. (2015). *pvclust: Hierarchical Clustering with P-Values via Multiscale Bootstrap Resampling, Version 2.0-0.* Available online at: https://cran.r-project.org/web/packages/pvclust/index.html

Tank, S. E., Raymond, P. A., Striegl, R. G., McClelland, J. W., Holmes, R. M., Fiske, G. J., et al. (2012). A land-to-ocean perspective on the magnitude, source and implication of DIC flux from major Arctic rivers to the Arctic Ocean. *Glob. Biogeochem. Cycles* 26, 1–15. doi: 10.1029/2011GB 004192

Tank, S. E., Striegl, R. G., McClelland, J. W., and Kokelj, S. V. (2016). Multi-decadal increases in dissolved organic carbon and alkalinity flux from the Mackenzie drainage basin to the Arctic Ocean. *Environ. Res. Lett.* 11:054015. doi: 10.1088/1748-9326/11/5/054015

Toohey, R. C., Herman-Mercer, N. M., Schuster, P. F., Mutter, E. A., and Koch, J. C. (2016). Multidecadal increases in the Yukon River Basin of chemical fluxes as indicators of changing flowpaths, groundwater, and permafrost. *Geophys. Res. Lett.* 43, 12120–12130. doi: 10.1002/2016GL070817

Torres, M. A., Moosdorf, N., Hartmann, J., Adkins, J. F., and West, A. J. (2017). Glacial weathering, sulfide oxidation, and global carbon cycle feedbacks. *Proc. Natl. Acad. Sci. U.S.A.* 114, 8716–8721. doi: 10.1073/pnas.1702953114

Torres, M. A., West, A. J., and Li, G. (2014). Sulphide oxidation and carbonate dissolution as a source of CO_2 over geological timescales. *Nature* 507, 346–349. doi: 10.1038/nature13030

Tranter, M., and Wadham, J. L. (2014). "Geochemical weathering in glacial and proglacial environments," in *Treatise on Geochemistry* (Elsevier), 157–173. Available online at: http://linkinghub.elsevier.com/retrieve/pii/B9780080959757005052 (accessed September 21, 2017).

Turetsky, M. R., Abbott, B. W., Jones, M. C., Walter Anthony, K., Olefeldt, D., Schuur, E. A. G., et al. (2020). Carbon release through abrupt permafrost thaw. *Nat. Geosci*. 13, 138–143. doi: 10.1038/s41561-019-0526-0

Urra, A., Wadham, J., Hawkings, J. R., Telling, J., Hatton, J. E., Yde, J. C., et al. (2019). Weathering dynamics under contrasting greenland ice sheet catchments. *Front. Earth Sci.* 7:299. doi: 10.3389/feart.2019.00299

van der Sluijs, J., Kokelj, S. V., Fraser, R. H., Tunnicliffe, J., and Lacelle, D. (2018). Permafrost terrain dynamics and infrastructure impacts revealed by UAV photogrammetry and thermal imaging. *Remote Sens.* 30:1734. doi: 10.3390/rs10111734

Vonk, J. E., Tank, S. E., and Walvoord, M. A. (2019). Integrating hydrology and biogeochemistry across frozen landscapes. *Nat. Commun.* 10:5377. doi: 10.1038/s41467-019-13361-5

Ward Jones, M. K., Pollard, W. H., and Jones, B. M. (2019). Rapid initialization of retrogressive thaw slumps in the Canadian high Arctic and their response to climate and terrain factors. *Environ. Res. Lett.* 14, 1–14. doi: 10.1088/1748-9326/ab12fd

Weiss, R. F. (1974). Carbon dioxide in water and seawater: the solubility of a non-ideal gas. *Mar. Chem.* 2, 203–215. doi: 10.1016/0304-4203(74)90015-2

West, A., Galy, A., and Bickle, M. (2005). Tectonic and climatic controls on silicate weathering. *Earth Planet. Sci. Lett.* 235, 211–228. doi: 10.1016/j.epsl.2005.03.020

Wolf, D. C., and Skipper, H. D. (1994). "Soil sterilization," in *Methods of Soil Analysis: Part 2—Microbiological and Biochemical Properties*, eds R. W. Weaver, S. Angle, P. Bottomley, D. Bezdicek, S. Smith, A. Tabatabai, and A. Wollum (Madison, WI: Soil Science Society of America) 41–51.

Zolkos, S., and Tank, S. E. (2019). Permafrost geochemistry and retrogressive thaw slump morphology (Peel Plateau, Canada), v. 1.0 (2017-2017). *Nord. D.* doi: 10.5885/45573XD-28DD57D553F14BF0

Zolkos, S., Tank, S. E., and Kokelj, S. V. (2018). Mineral weathering and the permafrost carbon-climate feedback. *Geophys. Res. Lett.* 45, 9623–9632. doi: 10.1029/2018GL078748

Zolkos, S., Tank, S. E., Striegl, R. G., and Kokelj, S. V. (2019). Thermokarst effects on carbon dioxide and methane fluxes in streams on the peel plateau (NWT, Canada). *J. Geophys. Res. Biogeosci.* 2019:JG005038. doi: 10.1029/2019JG005038

Zuberer, D. A. (1994). "Recovery and enumeration of viable bacteria," in *Methods of Soil Analysis: Part 2—Microbiological and Biochemical Properties*, eds R. W. Weaver, S. Angle, P. Bottomley, D. Bezdicek, S. Smith, A. Tabatabai, and A. Wollum (Madison, WI: Soil Science Society of America) 119–144.

Conflict of Interest: The authors declare that the research was conducted in the absence of any commercial or financial relationships that could be construed as a potential conflict of interest.

APPENDIX

TABLE A1 | The chemical composition of MilliQ de-ionized water in the control bottles at 168 h.

Site	Conductivity (μS cm^{-1})	DIC (μM)	CO$_2$ (μM)	SO$_4^{2-}$ (μM)	Cl$^-$ (μM)	Ca^{2+} (μM)	Mg^{2+} (μM)	Na$^+$ (μM)	K$^+$ (μM)	Fe (μM)	Al^{3+} (μM)
FM2	1.9 ± 0.6	23.4 ± 0.2	14.5 ± 1.3	bd	bd	0.8	0.4	13.1	0.3	bd	0.1
HC	1.5 ± 0.4	26.8 ± 2.2	26.0	bd	1.1	bd	bd	bd	bd	bd	bd
HD	1.6 ± 0.6	25.1 ± 2.4	24.9 ± 1.0	bd	bd	bd	bd	bd	bd	bd	bd

Conductivity, dissolved inorganic carbon (DIC), and CO$_2$ are reported as mean of replicates ± standard deviation. bd, below detection.

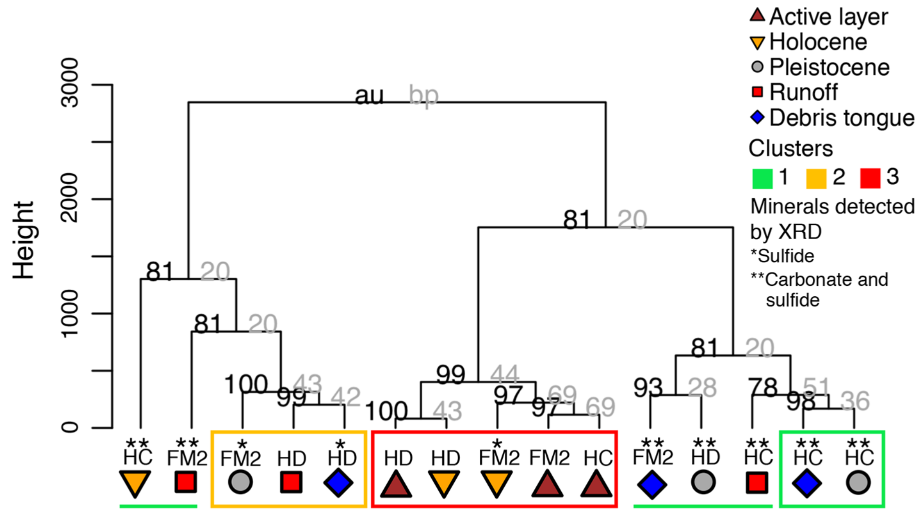

FIGURE A1 | Geochemical clusters from the *pvclust* analysis. Rectangles denote clusters where $p < 0.05$. au, approximately unbiased p-value; bp, bootstrapped probability.

frontiers
in Earth Science

ORIGINAL RESEARCH
published: 26 June 2020
doi: 10.3389/feart.2020.00229

Silicon Isotopes Reveal a Non-glacial Source of Silicon to Crescent Stream, McMurdo Dry Valleys, Antarctica

Catherine Hirst[1]*, Sophie Opfergelt[1], François Gaspard[1], Katharine R. Hendry[2], Jade E. Hatton[2], Susan Welch[3], Diane M. McKnight[4] and W. Berry Lyons[3]

[1] Earth and Life Institute, Environmental Sciences, Université catholique de Louvain, Louvain-la-Neuve, Belgium, [2] School of Earth Sciences, University of Bristol, Bristol, United Kingdom, [3] School of Earth Sciences, Byrd Polar and Climate Research Center, The Ohio State University, Columbus, OH, United States, [4] Institute of Arctic and Alpine Research, University of Colorado Boulder, Boulder, CO, United States

In high latitude environments, silicon is supplied to river waters by both glacial and non-glacial chemical weathering. The signal of these two end-members is often obscured by biological uptake and/or groundwater input in the river catchment. McMurdo Dry Valleys streams in Antarctica have no deep groundwater input, no connectivity between streams and no surface vegetation cover, and thus provide a simplified system for us to constrain the supply of dissolved silicon (DSi) to rivers from chemical weathering in a glacial environment. Here we report dissolved Si concentrations, germanium/silicon ratios (Ge/Si) and silicon isotope compositions ($\delta^{30}Si_{DSi}$) in Crescent Stream, McMurdo Dry Valleys for samples collected between December and February in the 2014–2015, 2015–2016, and 2016–2017 austral seasons. The $\delta^{30}Si_{DSi}$ compositions and DSi concentrations are higher than values reported in wet-based glacial meltwaters, and form a narrow cluster within the range of values reported for permafrost dominated Arctic Rivers. High $\delta^{30}Si_{DSi}$ compositions, ranging from +0.90‰ to +1.39‰, are attributed to (i) the precipitation of amorphous silica during freezing of waters in isolated pockets of the hyporheic zone in the winter and the release of Si from unfrozen pockets during meltwater-hyporheic zone exchange in the austral summer, and (ii) additional Si isotope fractionation via long-term Si uptake in clay minerals and seasonal Si uptake into diatoms superimposed on this winter-derived isotope signal. There is no relationship between $\delta^{30}Si_{DSi}$ compositions and DSi concentrations with seasonal and daily discharge, showing that stream waters contain DSi that is in equilibrium with the formation of secondary Si minerals in the hyporheic zone. We show that $\delta^{30}Si_{DSi}$ compositions can be used as tracers of silicate weathering in the hyporheic zone and possible tracers of freeze-thaw conditions in the hyporheic zone. This is important in the context of the ongoing warming in McMurdo Dry Valleys and the supply of more meltwaters to the hyporheic zone of McMurdo Dry Valley streams.

Keywords: silicon isotopes, hyporheic zone, permafrost, weathering, Antarctica

Edited by:
Andrew Jonathan Hodson,
The University Centre in Svalbard,
Norway

Reviewed by:
Yigal Erel,
Hebrew University of Jerusalem, Israel
Martin Guitreau,
Université Clermont Auvergne, France

****Correspondence:***
Catherine Hirst
catherine.hirst@uclouvain.be

Specialty section:
This article was submitted to
Geochemistry,
a section of the journal
Frontiers in Earth Science

Received: *09 March 2020*
Accepted: *28 May 2020*
Published: *26 June 2020*

Citation:
Hirst C, Opfergelt S, Gaspard F, Hendry KR, Hatton JE, Welch S, McKnight DM and Berry Lyons W (2020) Silicon Isotopes Reveal a Non-glacial Source of Silicon to Crescent Stream, McMurdo Dry Valleys, Antarctica. Front. Earth Sci. 8:229. doi: 10.3389/feart.2020.00229

INTRODUCTION

McMurdo Dry Valleys (MDV), the largest ice-free area of Antarctica, is covered in continuous permafrost, with low surface temperatures and low rates of precipitation. Under these polar desert conditions, groundwater and surface soil water reservoirs are absent (Conovitz et al., 1998), and first-order streams and their surrounding hyporheic zones are isolated conduits for supra-glacial meltwater transport and a loci of weathering (Lyons et al., 1998; McKnight et al., 1998, 1999, 2004).

A wealth of evidence using dissolved element concentrations and ratios (Lyons et al., 1998; Nezat et al., 2001), Sr and Li isotope analysis (Lyons et al., 2002; Witherow et al., 2010; Dowling et al., 2013) and mineralogical studies (Gooseff et al., 2002; Maurice et al., 2002) shows that Si is supplied to the streams by weathering of stream sediments with silicate mineral weathering rates an order of magnitude greater than rates in lower latitude, warmer locations (Gooseff et al., 2002). These studies demonstrate that chemical weathering of silicates occurs in MDV streams (Lyons et al., 2002), despite the cold temperatures, lack of precipitation and low abundance of complexing organic material (Burkins et al., 2001), and thereby contribute to the atmospheric CO_2 draw down over geological timescales (Berner and Berner, 1997).

Taylor Valley streams in MDV are characterized by extensive hyporheic zones, which comprise the sediment pore spaces adjacent to and underneath the stream through which stream water exchanges. This zone also is the accommodation space that must be filled before stream flow occurs. Mineral dissolution in the hyporheic zone is the commonly accepted contributor to stream geochemistry (Gooseff et al., 2002), but the model of Gooseff et al. (2002) assumes no precipitation reactions of secondary weathering products, including only the net release of solutes from weathering reactions. Secondary weathering products such as clay minerals may form, but the extent to which this occurs within streams is unknown (Lyons et al., 1998; Gooseff et al., 2002). Considering only the net release of solutes from weathering reactions, and not accounting for the formation of secondary weathering products in the near and extended hyporheic zone in MDV streams may contribute to an underestimation of actual weathering rates in this polar region and associated atmospheric CO_2 consumption.

The hyporheic zones in Antarctic streams include near-stream zones where rapid stream-water exchange occurs within hours to days, and extended hyporheic zones, where stream-water exchange occurs over weeks to months (Gooseff et al., 2003). During the austral summer months (November−February), glacial meltwaters, with low Si concentrations (Lyons et al., 2003) are transported through the near and extended hyporheic zone sediments and rapidly react with mineral surfaces (Gooseff et al., 2002) resulting in DSi concentrations that are in near equilibrium with minerals and independent of flow rates (Wlostowski et al., 2018). The questions arise: (i) is the Si released from weathering within the hyporheic zone transferred to the stream with limited formation of secondary weathering products; and (ii) are the controlling factors of the Si transfer from the hyporheic zone to the stream constant, or do they change through the summer with the changing contribution of waters from the extended hyporheic zone and near-stream hyporheic zone? To answer these questions we use dissolved silicon isotope composition ($\delta^{30}Si_{DSi}$) and the germanium/silicon ratios (Ge/Si) to pull apart primary silicate weathering processes, biotic processes and abiotic secondary weathering processes in a permafrost-dominated stream in Antarctica.

The $\delta^{30}Si_{DSi}$ composition of river waters reflect the processes occurring after silicate mineral dissolution (Opfergelt and Delmelle, 2012; Frings et al., 2016) resulting from secondary mineral formation and dissolution (Georg et al., 2006), adsorption of Si onto Al and Fe (oxy)hydroxides (Delstanche et al., 2009; Oelze et al., 2014), diatom uptake (Alleman et al., 2005; Opfergelt et al., 2011) and dissolution (Demarest et al., 2009; Egan et al., 2012; Wetzel et al., 2014) and phytolith formation (Opfergelt et al., 2008) and dissolution (Ziegler et al., 2005) in vascular plants during dissolved silicon transport in the river basin. At present, $\delta^{30}Si_{DSi}$ compositions in large Arctic rivers are used to constrain the drivers of terrestrial-ocean silicon supply in high latitude permafrost-dominated systems with an average flux-weighted Arctic River $\delta^{30}Si_{DSi}$ composition of +1.3‰ (Pokrovsky et al., 2013; Mavromatis et al., 2016; Sun et al., 2018). During winter months, $\delta^{30}Si_{DSi}$ compositions are higher than average values, attributed to aluminosilicate dissolution and secondary mineral precipitation in groundwater systems (Pokrovsky et al., 2013). During spring flood, the $\delta^{30}Si_{DSi}$ compositions are lower than or similar to silicate rock values, attributed to the dissolution of suspended matter within rivers and leaching of biomass (Pokrovsky et al., 2013; Mavromatis et al., 2016; Sun et al., 2018). During summer months, $\delta^{30}Si_{DSi}$ compositions show a wide range in values resulting from Si uptake into vascular plants and phytoplankton alongside the mixing of tributaries with different Si isotope compositions (Sun et al., 2018). In these large river basins, the role of secondary mineral precipitation and its impact on riverine $\delta^{30}Si_{DSi}$ compositions is often obscured by biological and plant uptake and/or mixing of surface and sub-surface waters in the river basin.

The simplified and well characterized MDV streams, with no vegetation and no groundwater supply to streams, provides an ideal natural laboratory to test whether the silicate mineral weathering release is affected by the formation secondary weathering products or by biological uptake of diatoms in a permafrost environment. To disentangle biogenic and non-biogenic contributions to rivers, the germanium/silicon ratio (Ge/Si) of river waters is complementary to Si isotopes (Cornelis et al., 2011). During weathering, Ge substitutes for Si during clay mineral formation resulting in soils with higher Ge/Si ratios and soil porewaters and rivers with lower Ge/Si ratios than the silicate parent material (Murnane and Stallard, 1990; Kurtz et al., 2002). During biological Si uptake by plants and diatoms, Ge is either unfractionated or fractionated with respect to Si to form biogenic amorphous silica with a Ge/Si ratio the same or lower than the starting solution (Froelich et al., 1992; Derry et al., 2005; Delvigne et al., 2009).

The $\delta^{30}Si_{DSi}$ composition and the Ge/Si ratios are determined on waters in Crescent Stream, collected during three different seasons between 2014 and 2017, and at different times of day in order to understand the effect of daily and seasonal variations in hydrology on silicate weathering in the hyporheic zone. Crescent Stream is one of the longest streams in Taylor Valley, resulting in longer water residence times in the hyporheic zone, increased chemical weathering and higher long-term solute concentrations compared to shorter streams in Taylor Valley (Wlostowski et al., 2018). Using these findings as a basis, we discuss how $\delta^{30}Si_{DSi}$ compositions could be used to monitor changes in hyporheic zone functioning in response to future increases in stream flow (Doran et al., 2008), active layer depth (Doran et al., 2008), permafrost temperature (Biskaborn et al., 2019; Obu et al., 2020), and thermokarst erosion (Levy et al., 2013) in MDV.

STUDY SITE

Samples were collected from Crescent Stream in Fryxell Basin, McMurdo Dry Valleys, Antarctica. The McMurdo Dry Valleys (77°S, 162°E) are located on the western coast of McMurdo Sound and have a polar desert environment with mean annual temperatures less than −15°C and mean annual precipitation less than 100 mm (Doran et al., 2002). Soils are developed on glacial tills that were deposited by the grounded Ross Sea Ice Sheet in the Last Glacial Maximum, 19,000 to 23,000 years ago (Hall et al., 2000) and derived from granitic, sandstone and dioritic parent lithologies (Campbell and Claridge, 1987). There is 3−7% contribution of mafic material to Taylor Valley glacial tills derived from the McMurdo Volcanic Group and Ferrar Dolerite (e.g., Cooper et al., 2007). Soils are distinguished by the amount and distribution of salts and degree of chemical weathering. Permafrost is present across the McMurdo Dry Valleys with 43% characterized as dry frozen, 55% characterized as ice-cemented and 2% characterized as massive ice bodies (Bockheim, 2002). Active layer depths range from 45 to 70 cm in coastal areas to 20−45 cm in the polar plateau (Bockheim et al., 2007). There is no vascular vegetation in McMurdo Dry Valleys (Campbell and Claridge, 1987) and soil organic carbon concentrations are <0.5 mg C g soil^{-1} (Burkins et al., 2001).

Dry-based glaciers are the main source of liquid water to McMurdo Dry Valleys. Supra-glacial meltwaters are transported via first-order streams to confined lake basins. Streams range from 1 to 11.2 km in length, are typically 5−10 m wide and incised in some places by up to 3 m (Conovitz et al., 1998). The extensive hyporheic zones of the streams are characterized by loose, unconsolidated sediments (Bockheim, 2002) and active layer depths up to 75 cm (Conovitz et al., 2006). The hyporheic zone extends several meters either side of the streambed, with a lateral cross section of ∼ 12 m^2 at maximum thaw during the austral summer months (Gooseff et al., 2003). Microbial mats are abundant in MDV streams and are mainly found in streambed areas with flowing water and along stream margins that are submerged at occasional high flows (McKnight and Tate, 1997). The mats are dominated by filamentous cyanobacteria, with varying abundances of diatoms, chlorophytes and other microorganisms (Alger, 1997).

McMurdo Dry Valley stream flow occurs for approximately 6−10 weeks per year during the austral summer between December and February and is characterized by inter-annual, seasonal and daily variations in discharge. Streams typically exhibit a low flow in December, maximum flow in January and low flow again at the start of February (McKnight et al., 1999). During cold and cloudy periods, there is intermittent stream flow and water is mainly accommodated in the hyporheic zone; whereas, warm and sunny periods drive more surface glacier melt and a larger volume of water is transported as stream flow (Conovitz et al., 1998). Daily diel flood pulses result in a 5−10 fold variation in stream flow depending on the solar aspect, insolation and air temperature (Conovitz et al., 1998).

Crescent Stream in the south Fryxell Basin, Taylor Valley (77°37′8.6″S, 163°11′4.1″E) transports meltwater from Crescent Glacier along two branches (east and west) that converge about 500 m upstream of where Crescent Stream discharges into Lake Fryxell (**Figure 1**).

MATERIALS AND METHODS

Sample Collection

Water samples were collected at gauging stage F8 (**Figure 1**), located 5.5 km downstream from Crescent Glacier (Gooseff and McKnight, 2019), during three austral seasons: 2014−2015 (2/1/2015 to 17/1/2015); 2015−2016 (11/12/2015 to 18/1/2016); and 2016−2017 (17/12/2016 to 24/1/2017) and at different times of day from 10.13 am to 11.58 pm. Water samples were collected in 1 L polyethylene bottles and filtered through 0.4 μm Nucleopore filters using an Antlia filtration unit within 4–6 h after collection. Water samples were stored at >8°C, but not frozen.

Discharge, conductivity and water temperature were measured at 15-min intervals at gauging stage F8 during the three austral seasons. Data are available on the LTER McMurdo Dry Valleys database, collecting data since 1990 (Gooseff and McKnight, 2019).

Silicon Concentrations Analysis

Dissolved Si concentrations were determined on the water samples from Crescent Stream (austral summer seasons 2014−2015, 2015−2016, and 2016−2017) using a Skalar San++ nutrient analyzer at The Ohio State University, following the protocols of Mullin and Riley (1955). The precision of the Si concentrations and check standards, calculated as the average percent difference between duplicate samples, is <2%. Blank values for DI water processed as a sample and stored in our clean bottles were always below the detection limit of the method.

Germanium Concentrations Analysis

Ge concentrations were determined on the water samples from Crescent Stream (austral seasons 2014−2015, 2015−2016, and 2016−2017) by ICP-mass spectrometry (ICP-MS, ICAPQ Thermo Fisher Scientific) using the ^{74}Ge isotope at Earth & Life Institute, UCLouvain, Belgium. Indium was used as the internal standard to correct for both instrumental (i.e., mass) drift, and sensitivity drift potentially arising from the sample matrix (Pretorius et al., 2006). The accuracy and

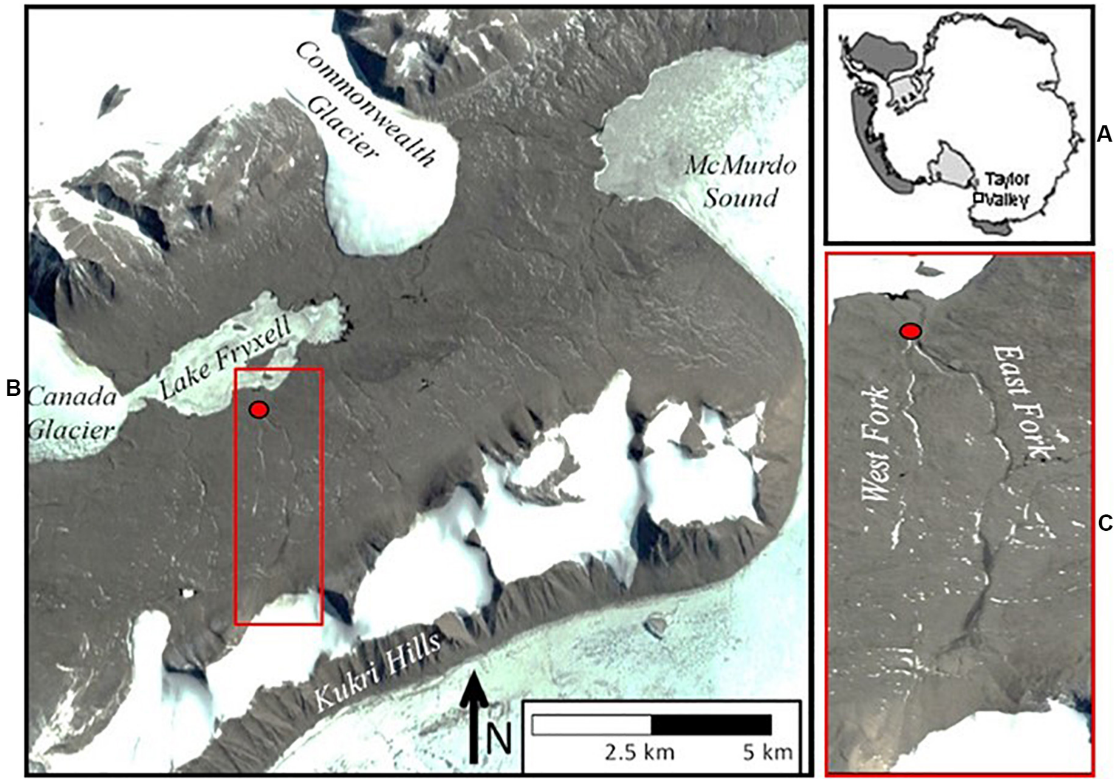

FIGURE 1 | Crescent Stream is located in Taylor Valley in the Lake Fryxell basin, McMurdo Dry Valleys **(A)**. Crescent Stream is supplied by glacial meltwaters in the Kukri Hills and drains into Lake Fryxell **(B)**. Samples were collected during the Austral summer in 2014–2017 at the F8 gauge (red circle), located 150 meters above the 1999 Lake Fryxell lake level **(C)**. Figure adapted from Gooseff et al. (2002, 2016).

long-term reproducibility of the analysis were assessed by measuring two international riverine standards, namely SLRS-5 ([Ge] = 0.083 ± 0.014 nmol.l^{-1}; $n = 3$) and SLRS-6 ([Ge] = 0.097 ± 0.0069 nmol.l^{-1}; $n = 3$) (Yeghicheyan et al., 2001). The limit of detection for Ge was 0.04 nmol.l^{-1}, and the precision on Ge/Si ratio is 10%.

Silicon Isotope Analysis

Silicon isotope compositions were determined on the water samples from Crescent Stream (austral seasons 2014−2015, 2015−2016, and 2016−2017). Si was pre-concentrated using MAGIC brucite precipitation (Brzezinski et al., 2003) with Si recoveries of 85 to 100%. Si was separated from the remaining anion-rich matrix with a two stage column chemistry procedure using an anion exchange resin (Biorad AG MP-1; Gaspard et al., 2019) followed by a cation exchange resin (Biorad AG50W-X12; Georg et al., 2006). Si recoveries were >95% and Na^+, SO_4^{2-} and Cl^- concentrations were below detection limit following the two-stage column chemistry. The combined procedural Si blank for MAGIC and column chemistry was below 0.36 $\mu\text{mol.l}^{-1}$.

$\delta^{30}Si_{DSi}$ composition was analyzed by MC-ICP-MS (Neptune Plus^{TM} High Resolution Multicollector ICP-MS, Thermo Fisher Scientific, Earth & Life Institute, UCLouvain, Belgium) in wet plasma mode in medium resolution ($\Delta m/m \sim 6000$) using a PFA nebulizer of 100 μl/min uptake rate. The instrumental mass bias was corrected using the standard-sample bracketing technique and an external Mg doping (Cardinal et al., 2003). The analyses were performed in 2% HNO_3 matrix, with a typical sensitivity of 7V for 2ppm Si and an instrumental blank <30 mV. $\delta^{30}Si_{DSi}$ compositions are expressed in relative deviations of $^{30}Si/^{28}Si$ ratio from the NBS-28 reference standard using the common δ-notation (‰) as follows: $\delta^{30}Si = [(^{30}Si/^{28}Si)_{sample}/(^{30}Si/^{28}Si)_{NBS-28}\ -1] \times 1000$. One measurement comprises 30 cycles with 4.2s integration time corrected by blank in a 2% HNO_3 matrix. Each single δ-value (n) represents one sample run and two bracketing standards. $\delta^{30}Si$-values are reported as the mean of isotopic analyses from multiple analytical sessions (**Table 1**). The $\delta^{30}Si$ and $\delta^{29}Si$ measurements fit within error onto the theorical mass dependent fractionation array (Young et al., 2002) supporting the interference-free determination of all three Si isotopes via MC-ICP-MS (**Supplementary Figure 1**). The long-term precision and accuracy of the MC-ICP-MS $\delta^{30}Si$ values was assessed from multiple measurements within each analytical session on reference materials: the values obtained for Diatomite ($\delta^{30}Si = 1.31 \pm 0.08$‰, SD, $n = 21$) and Quartz Merck ($\delta^{30}Si = -0.01 \pm 0.08$‰, SD, $n = 8$) are consistent with previously reported values for these standards [Quartz Merck: $\delta^{30}Si = -0.01 \pm 0.12$‰ (Abraham et al., 2008); Diatomite: $\delta^{30}Si = 1.26 \pm 0.10$‰ (Reynolds et al., 2007)].

TABLE 1 | Sampling date, time, field measurements (discharge, conductivity, and water temperature), dissolved silicon and dissolved germanium concentrations, Ge/Si ratios, and silicon isotope compositions (SD) for all samples in this study collected in the austral seasons: 2014−2015, 2015−2016, and 2016−2017.

Sample	Date	Time	Discharge L/sec	Conductivity μS/cm	Water temp °C	Si μmol L^{-1}	Ge pmol L^{-1}	Ge/Si μmol mol^{-1}	δ^{29}Si ‰	SD ‰	δ^{30}Si ‰	SD ‰
Crescent Stream F8 2/1/15	02-01-2015	1325	0	253	10.98	136.1			0.65	0.02	1.22	0.07
Crescent Stream F8 7/1/15	07-01-2015	1347	17	185.4	3.51	99.2	41.3	0.41	0.69	0.03	1.24	0.11
Crescent Stream F8 13/1/15	13-01-2015	1855	0	241.8	−0.73	122.9	41.3	0.33	0.68	0.05	1.33	0.08
Crescent Stream F8 17/1/15	17-01-2015	1327	0	152	5.34	117.3	41.3	0.34	0.61	0.06	1.23	0.08
Crescent Stream F8 11/12/15	11-12-2015	1209	0.38	133.6	7.29	142.7	41.3	0.28	0.60	0.05	1.13	0.08
Crescent Stream F8 14/12/15	14-12-2015	1425	50.97	206.2	5.01	89.3						
Crescent Stream F8 21/12/15	21-12-2015	1708	0.58	215.9	9.77	126.6	41.3	0.32	0.60	0.05	1.12	0.07
Crescent Stream F8 7/1/16	07-01-2016	1213	0.26	194.8	7.79	137.6						
Crescent Stream F8 12/1/16	12-01-2016	1319	0.93	208	6.43	136.4	55.1	0.39	0.48	0.03	0.90	0.05
Crescent Stream F8 16/1/16	16-01-2016	1753	9.07	139.4	7.85	112.7	41.3	0.36	0.67	0.08	1.25	0.12
Crescent Stream F8 18/1/16	18-01-2016	1753	43.71	174.1	5.81	111.2						
Crescent Stream F8 17/12/16	17-12-2016	1013	0.03	188.9	1.3	101.9	55.1	0.53	0.57	0.09	1.02	0.10
Crescent Stream F8 21/12/16	21-12-2016	1613	2.46	131.9	4.27	107.7	41.3	0.37	0.73	0.05	1.39	0.09
Crescent Stream F8 28/12/16	28-12-2016	1558	0.14		9.2	130.2			0.68	0.03	1.32	0.07
Crescent Stream F8 1/1/17	01-01-2017	2358	0.03	216.4	2.64	116.7	55.1	0.46	0.52	0.14	1.05	0.13
Crescent Stream F8 6/1/17	06-01-2017	1607	0.03	276.4	11.51	126.0						
Crescent Stream F8 11/1/17	11-01-2017	2358	3.96	101.2	3.16	116.7						
Crescent Stream F8 16/1/17	16-01-2017	2232	2.74	138.1	4.63	129.2						
Crescent Stream F8 24/1/17	24-01-2017	1600	1.86	39.6	6.09	115.5	41.3	0.35	0.69	0.06	1.31	0.08

Scanning Electron Microscopy

Sediment for SEM imaging was collected from Crescent Stream during the 2002−2003 austral summer, as described in Dowling et al. (2019). Briefly, samples were stored at room temperature after collection and were allowed to air dry. Samples were placed on carbon tape on an aluminum stub and then coated with gold/palladium with a Denton Desk V precious metal coater. Scanning electron microscopy was done with an FEI Quanta FEG 250 Field Emission SEM equipped with a Bruker EDX detector. Images were collected at 15 kV using either a secondary electron (SE) or back scattered electron detector (BSE).

RESULTS

Seasonal Variations in Field Parameters in Crescent Stream

For the austral seasons between 2014 and 2017, discharge, conductivity, and water temperature measurements ranged from 0 to 153 L/sec, 25−290 μS/cm, and −2 to +12°C, respectively (**Table 1**). These values lie within the range of long-term (1994−2014) measurements in Crescent Stream (**Figure 2A**, LTER McMurdo Dry Valleys database, Gooseff and McKnight, 2019). Discharge values were lowest during 2016−2017, when stream flow did not exceed 8.20 L/sec and highest during 2015−2016 when discharge reached 146 L/sec (**Supplementary Figure 2A**). The range of water temperature and conductivity values were similar for the three seasons (**Supplementary Figures 2B,C**). For the samples collected, discharge values ranged from 0.0 to 57 L/sec (**Table 1**) and do not correspond with the pulses of peak seasonal discharge.

Si Concentrations and Ge/Si Ratios in Crescent Stream

Si concentrations for samples collected in Crescent Stream ranged from 89 to 136 μM between 2014 and 2017 (**Figure 3** and **Table 1**). These values lie within the long-term (1994−2014) range of values measured in Crescent Stream, 83 to 163 μM (LTER McMurdo Dry Valleys database, Lyons and Welch, 2015; **Figure 2B**). DSi concentrations show no relationship with long-term stream discharge data (R^2 = 0.01) (**Supplementary Figure 3**) and no relationship with discharge data in the 2014−2017 austral summers (R^2 = 0.00).

Germanium/silicon ratios (Ge/Si) in Crescent Stream ranged from 0.28 to 0.46 μmol mol^{-1} for samples collected between 2014 and 2017 (**Figure 4** and **Table 1**), lower than the range of Ge/Si values expected in silicate rocks (Bernstein, 1985). There was no significant variation in Si concentrations and Ge/Si ratios during the three austral summers, and no significant variation between these seasons.

Silicon Isotope Compositions of Crescent Stream

Si isotope compositions (δ^{30}Si) in Crescent Stream ranged from +1.22‰ to +1.33‰ in 2014−2015, +0.90‰ to +1.25‰ in 2015−2016 and +1.02‰ to +1.39‰ in 2016−2017 (**Figure 5** and **Table 1**), higher than δ^{30}Si values in silicate rocks (Opfergelt and Delmelle, 2012). There was no significant variation in

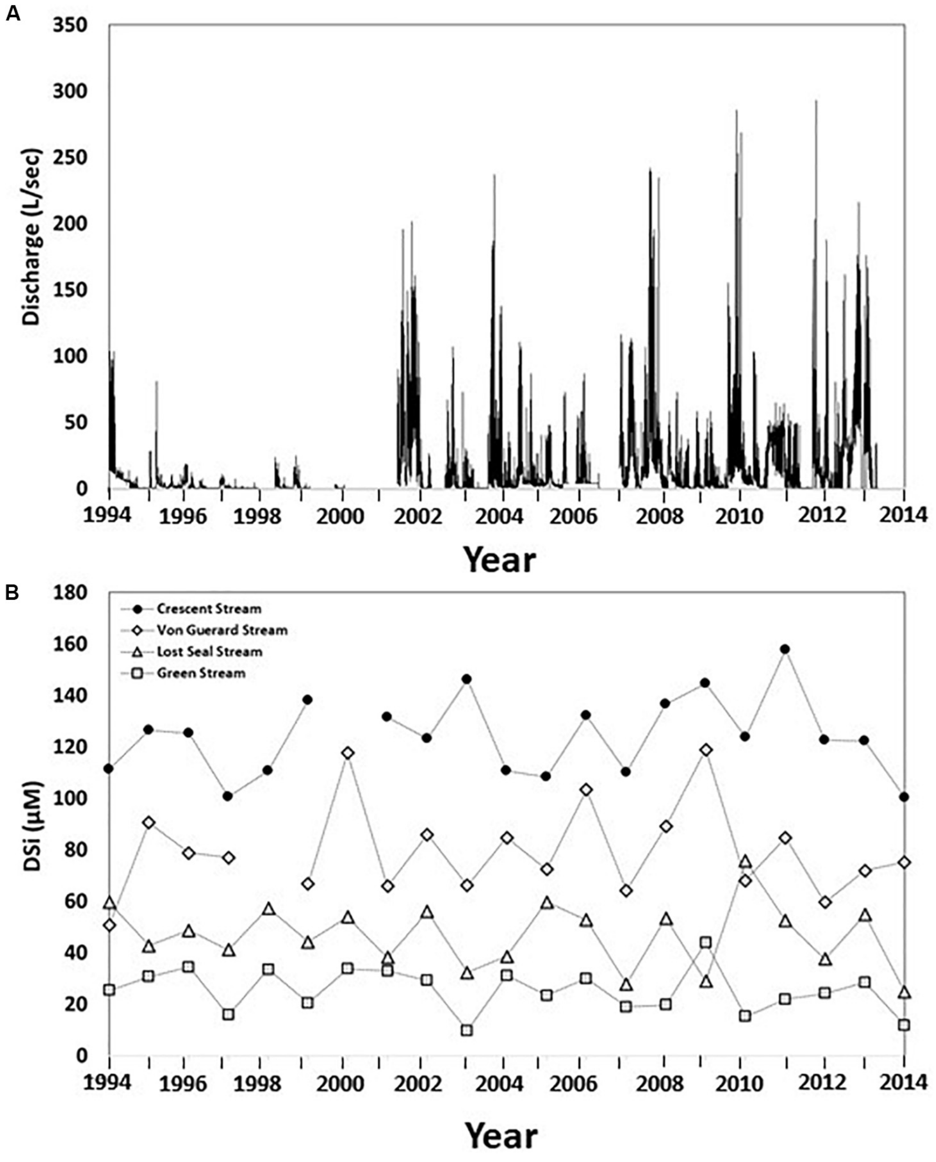

FIGURE 2 | (A) Long-term (1994–2014) discharge data at gauge F8 in Crescent Steam, from Gooseff and McKnight (2019). There are two main trends: (i) decreasing discharge during the 1990–2000, (ii) sharp increase in discharge in 2001–2002. **(B)** Long-term (1994–2014) dissolved silicon (DSi, <0.4 μm filtered water) concentrations in Crescent Stream compared with other streams in Taylor Valley, McMurdo Dry Valleys, using average concentrations for each year from Lyons and Welch (2015). Crescent Stream is one of the longest streams in Taylor Valley with elevated Si concentrations compared with other Taylor Valley streams.

δ^{30}Si compositions during the three austral summers, and no significant variation between these seasons.

Scanning Electron Microscope Images of Stream Sediment

Scanning Electron Microscope images of mineral grains from Crescent Stream sediments show that the sediment is composed of silicate-bearing minerals such as pyroxene, biotite, olivine and volcanic glass with preserved vesicles and non-silicate bearing minerals, including apatite grains and calcite grains (**Figure 6**). All minerals show evidence for chemical and physical alteration of the mineral surface including linear etching over pyroxene and apatite mineral surfaces (**Figures 6A,E**), exfoliation of biotite minerals along a crystal plane (**Figure 6B**), etch pits and rounded facets on olivine mineral surfaces (**Figure 6C**), or extensive etching over calcite mineral surfaces (**Figure 6D**).

More specifically, volcanic ash spherules are associated with chemical alteration products in Crescent Stream sediments (**Figure 7**). SEM images show that spherules about 100 to 200 μm wide may present long cracks (~120 μm; **Figure 7A**) and a surface with a "sugary" texture, indicative of an alteration crust (**Figure 7B**). This crust is composed of micron-nano sized amorphous to poorly crystalline secondary minerals.

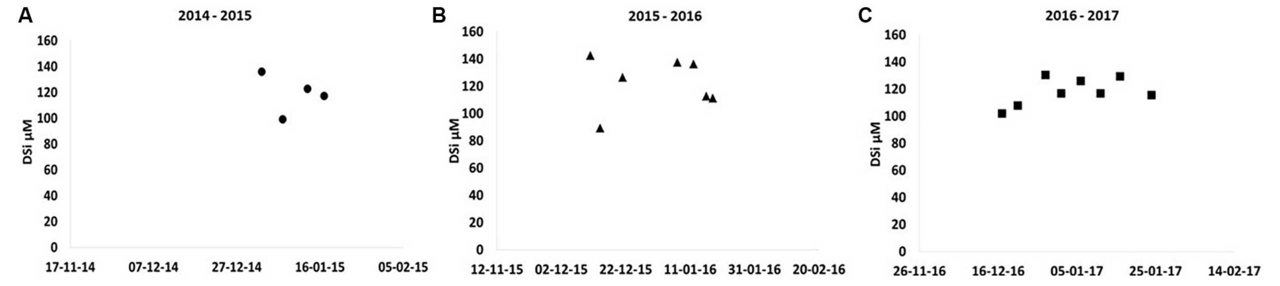

FIGURE 3 | Dissolved silicon concentrations in <0.4 µm filtered water from Crescent Stream. Samples were collected between December and February 2014–2015 **(A)**; 2015–2016 **(B)**; 2016–2017 **(C)**.

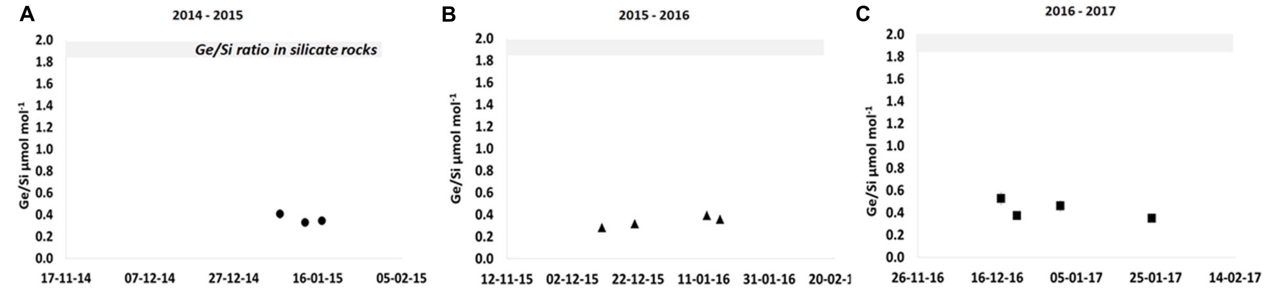

FIGURE 4 | Ge/Si ratios in <0.4 µm filtered water from Crescent Stream for samples collected between December and February 2014–2015 **(A)**; 2015–2016 **(B)**; 2016–2017 **(C)**. The gray bar represents the lower bound for Ge/Si ratios in silicate rocks (Bernstein, 1985). The precision on Ge/Si ratios (10%) is included in the marker size.

There is evidence of chemical alteration in fractured spherules, with coating patches on euhedral, ∼5 −10 µm long minerals (**Figure 7C**). A high-resolution SEM image of these patches indicates that these are hydrous or amorphous phases coating the surface of the euhedral minerals (**Figure 7D**).

DISCUSSION

Comparison Between Si Isotope Compositions in Crescent Stream, Permafrost-Dominated Rivers and Sub-Glacial Rivers

Glacial and permafrost-dominated river basins have contrasting weathering regimes (Anderson et al., 1997) resulting in contrasting dissolved silicon isotope compositions (Pokrovsky et al., 2013; Mavromatis et al., 2016; Sun et al., 2018; Hatton et al., 2019a,b). **Figure 8A** shows the Si concentrations and Si isotope composition of waters in sub-glacial meltwaters, permafrost-dominated Arctic Rivers and Crescent Stream (*this study*). Sub-glacial meltwaters have low DSi concentrations ranging from 3 to 94 µM and $\delta^{30}Si_{DSi}$ compositions ranging from −0.58‰ to +0.87‰, attributed to amorphous Si and clay mineral dissolution during sub-glacial water-mineral interaction (Hatton et al., 2019a,b). Permafrost-dominated large Arctic Rivers have higher DSi concentrations ranging from 25 to 310 µM, and $\delta^{30}Si_{DSi}$ compositions ranging from +0.39‰ to +2.72‰ (Pokrovsky et al., 2013; Mavromatis et al., 2016; Sun et al., 2018). The wide scatter of compositions in large permafrost-dominated rivers prevents the isolation of a $\delta^{30}Si_{DSi}$ signal from mineral weathering in permafrost soils.

Crescent Stream, MDV has a narrow range of DSi and $\delta^{30}Si_{DSi}$ compositions, falling in a tight cluster within the range of values reported for Arctic Rivers (**Figure 8A**) showing that non-glacial weathering processes are contributing to $\delta^{30}Si_{DSi}$ compositions in this Antarctic stream. In an attempt to connect permafrost-weathering conditions in Arctic and Antarctic streams, we compare $\delta^{30}Si_{DSi}$ compositions in Crescent Stream with the $\delta^{30}Si_{DSi}$ compositions for (i) wet-based glacial streams, (ii) Arctic rivers during winter baseflow, and (iii) Arctic rivers during the spring flood period (**Figure 8B**). Samples from the summer period (included in **Figure 8A**) are omitted because Si isotope fractionation during Si plant uptake obscures the weathering signal (Sun et al., 2018), a process that is not relevant in Antarctica. In the Arctic, $\delta^{30}Si_{DSi}$ compositions during spring flood reflect DSi derived from dissolution of minerals and vegetation in the suspended load (Pokrovsky et al., 2013; Mavromatis et al., 2016; Sun et al., 2018) and so represent the bulk $\delta^{30}Si$ composition of permafrost surface soils washed into the river during river ice-break up. In **Figure 8B**, the $\delta^{30}Si_{DSi}$ compositions and DSi concentrations fall on a line that passes through this spring flood $\delta^{30}Si_{DSi}$ composition, with the lowest $\delta^{30}Si_{DSi}$ compositions in wet-based glacial streams attributed to secondary mineral dissolution (Hatton et al., 2019a) and highest $\delta^{30}Si_{DSi}$ compositions during winter baseflow attributed

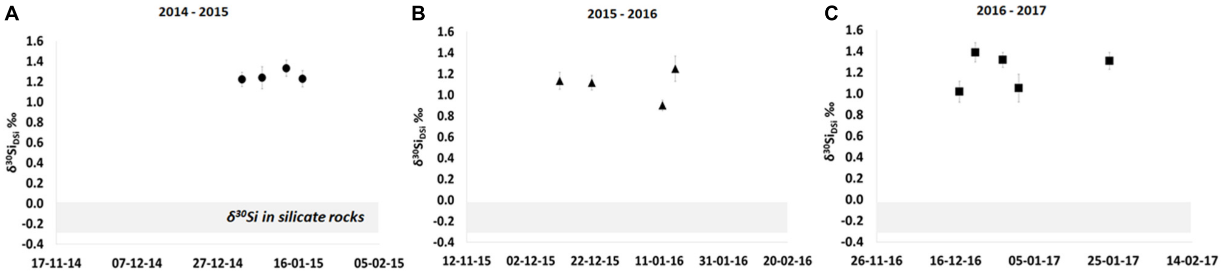

FIGURE 5 | Dissolved silicon isotope composition ($\delta^{30}Si_{DSi}$) in <0.4 μm filtered water from Crescent Stream. Samples were collected between December and February 2014–2015 **(A)**; 2015–2016 **(B)**; 2016–2017 **(C)**. The gray band shows the range of δ^{30}Si in silicate rocks (Georg et al., 2007b; Savage et al., 2010, 2011; Armytage et al., 2011). The error bars correspond to the standard deviation for silicon isotope measurements (2SD).

to secondary mineral formation in sub-permafrost groundwaters (Pokrovsky et al., 2013). The $\delta^{30}Si_{DSi}$ compositions in Crescent Stream during the austral summer also fall on this line and are similar to $\delta^{30}Si_{DSi}$ compositions for winter baseflow in Siberian rivers (Pokrovsky et al., 2013; Sun et al., 2018) suggesting that processes driving Si isotope fractionation during winter baseflow in Arctic Rivers likely also occur in Crescent Stream, Antarctica.

The Arctic River basins span a range of lithology, from basaltic (Kochehumo River, Pokrovsky et al., 2013) to terrigenous siliciclastic sediments (Lena River tributaries, Sun et al., 2018). However the distribution of DSi and $\delta^{30}Si_{DSi}$ compositions during winter baseflow does not reflect lithology specific silicate-mineral weathering signatures but rather reflects the extent of secondary mineral formation and dissolution processes occurring in sub and supra-permafrost groundwaters in these Arctic basins (Pokrovsky et al., 2013).

The main pool of DSi entering Crescent Stream is derived from silicate mineral weathering in the hyporheic zone (Nezat et al., 2001; Gooseff et al., 2002; Maurice et al., 2002). The initial supra-glacial meltwaters have Si concentrations ranging from 4 to 8 μM (Lyons et al., 1998; Nezat et al., 2001), contributing <10% of the Si transported in Crescent Stream between 2014 and 2017. This glacially derived Si in MDV originates from stratospheric aerosols, aeolian salt and dust deposition onto glacier surfaces blown from the valley floor (Lyons et al., 2003). Assuming no isotope fractionation during mineral dissolution on the glacier surface, the DSi contribution to Crescent Stream from glacial waters will have $\delta^{30}Si_{DSi}$ compositions within the array of basaltic to granitic $\delta^{30}Si_{DSi}$ compositions (Savage et al., 2011). This allows us to use Si isotopes and Ge/Si ratios as a tracer of biotic and abiotic secondary mineral formation in the hyporheic zone and stream bed to constrain the processes that trap Si in the terrestrial system after being released from mineral dissolution.

Si Cycling and Isotope Fractionation in the Hyporheic Zone of Crescent Stream

Biotic Processes

Diatom growth preferentially incorporates the lighter Si isotopes, with an isotope fractionation factor, $^{30}\varepsilon$, of−1.1‰ for Si uptake in fresh water systems (Alleman et al., 2005; Opfergelt et al., 2011). Diatoms are substantial contributors to microbial mats in most Taylor Valley streams (McKnight et al., 1998; Pugh et al., 2002; Esposito et al., 2008) with biogenic silica in modern and paleo diatoms making up 2−8% dry weight of stream sediments in meanders, pools and riffles (Heindel et al., personal communication). The microbial mats remain dormant during the winter months, are photosynthetically active within hours of the return of flow at the start of the austral summer (Howard-Williams et al., 1986) and mat biomass varies with seasonal flow patterns with loss due to scouring of the mats occurring during high flow (Stanish et al., 2011; Cullis et al., 2014) over the austral summer. In streams with lower annual discharge, which are generally longer and have higher DSi concentrations, the larger more silicified diatom taxa, such as *Hantzchia* spp. (about 100 μm in length), are more abundant; whereas *Psammothidium* spp. and other smaller taxa (about 12 μm in length) are common in streams which have higher annual flows and are usually shorter with lower DSi concentrations (Stanish et al., 2011). In general, because smaller cells have a higher surface area to volume ratio and would be better able to meet their Si requirement for growth, this suggests that DSi availability may influence the diatom community composition, but the DSi does not limit diatom growth rate. Diatom growth can therefore contribute to the uptake of a fraction of mineral-derived DSi over the austral summer months.

The diatom community composition at the study site in the lower reaches of Crescent Stream was similar in the summer of 2014 and 2016 for both the black mats that grow at the stream margin and the orange mats that grow in the main channel (**Supplementary Table 1**). The species richness of these samples ranged from 9 to 20, which is typical for microbial mats in Dry Valley streams. A distinctive aspect of the diatom community in these mats was the consistent dominance by the monoraphid diatom *Achnanthes taylorensis*, which accounted for 41% or more of the total diatom cells counted. This species ranges in length from 25 to 38 μm and is commonly present at relatively low abundance (a few percent or less) in microbial mats in streams adjacent to Crescent Streams (Spaulding et al., 2020). However, this species has been found to be more abundant in microbial mats in the nearby Spaulding Pond at the base of the Howard Glacier and in a few ponds at Cape Royds across McMurdo Sound. Furthermore, *A. taylorensis* was common in the hyporheic sediments studied in the adjacent Von Guerard

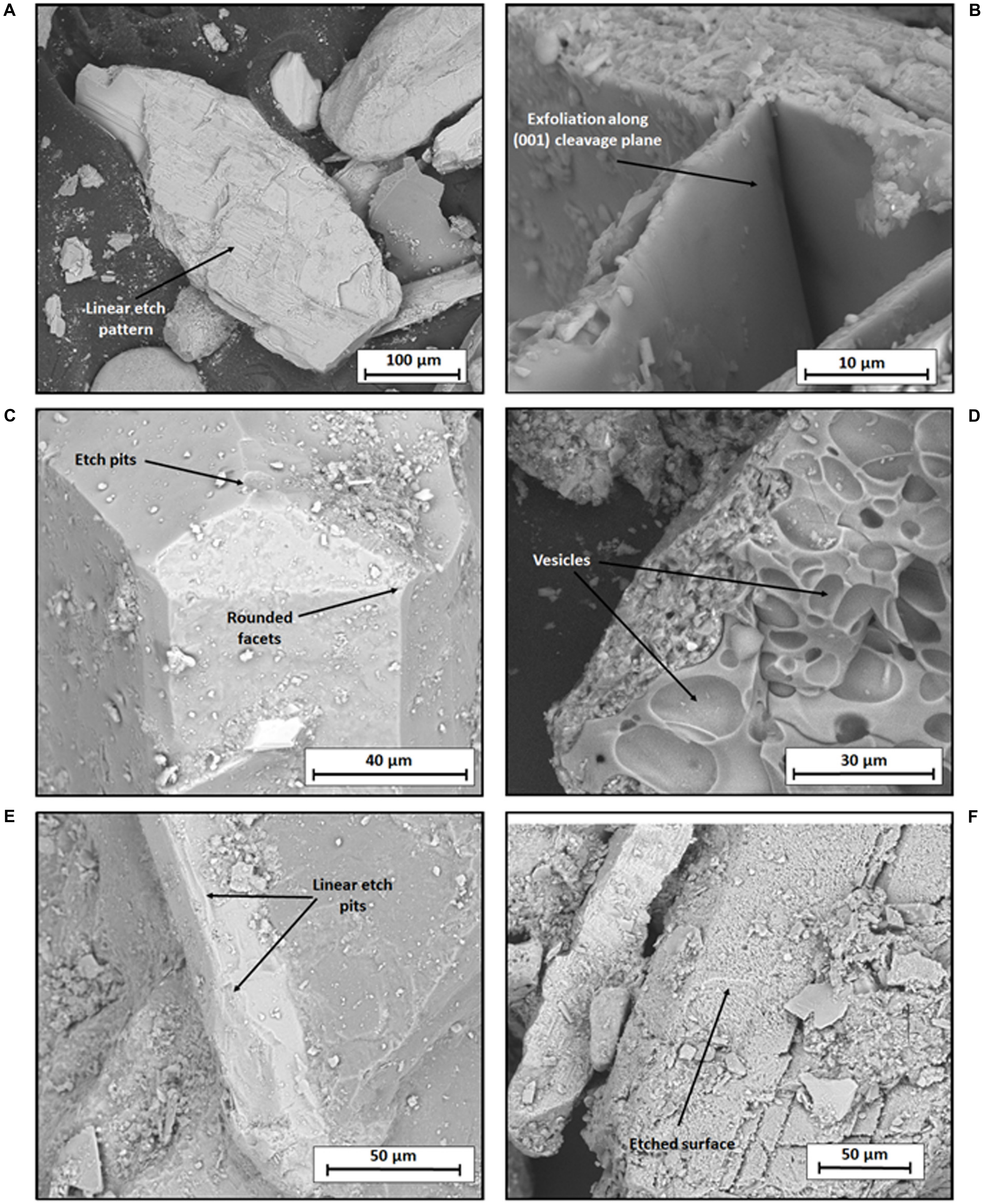

FIGURE 6 | SEM images of minerals in the hyporheic zone sediments of Crescent Stream, including silicate-bearing minerals **(A–D)** and calcium and phosphate bearing minerals **(E,F)**. **(A)** shows a large (300 µm long) euhedral pyroxene grain with physical abrasions and linear etched pattern on the surface; **(B)** shows a biotite grain with physical alteration and exfoliation along the (001) cleavage plane; **(C)** shows an olivine grain with a euhedral surface, slightly rounded facets and few small etch pits on the surfaces; **(D)** shows volcanic glass and ash with a vesicular surface and coating of fine grained amorphous-nanocrystalline on the left side of the glassy particle surface; **(E)** shows an elongate apatite grain with crystallographically controlled etch pits; **(F)** shows calcite minerals with extensively etched surfaces.

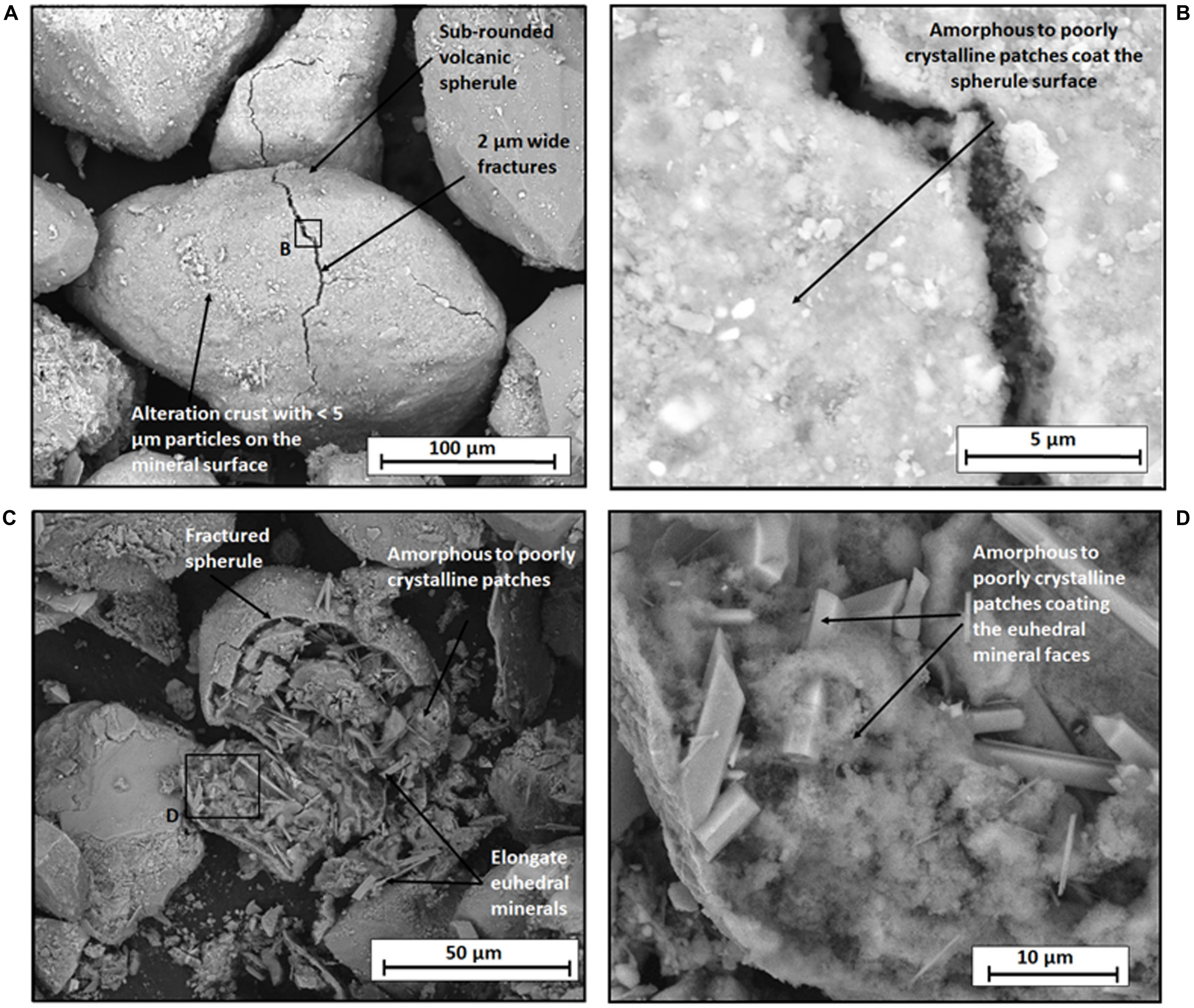

FIGURE 7 | SEM images showing the chemical alteration of volcanic ash spherules in the hyporheic zone sediments of Crescent Stream, **(A)** shows a ∼200 µm long spherule of volcanic ash with rounded edges, fractures over the grain surface and micron-nano sized alteration crust on the grain surface; **(B)** shows a high resolution backscatter electron (BSE) image of the spherule surface in panel **(A)** showing an amorphous to poorly crystalline "sugary" texture on the spherule surface; **(C)** shows a ∼70 µm long volcanic spherule that has chemically altered to form secondary mineral products. These products include euhedral elongate minerals and amorphous to poorly crystalline minerals; **(D)** shows a high resolution BSE image of the secondary mineral products in panel **(C)** showing that the poorly crystalline to amorphous material coats the surface of euhedral mineral faces.

Stream (Heindel, unpublished data). Another distinctive aspect of the diatom community is the relatively low abundance of *Hantzschia* species, which are large highly silicified taxa commonly abundant in mats in adjacent streams. There were a total of 11 species of the genus *Luticola* found in these mat samples, which is typical for these streams. It is interesting that *L. dolia* and *L. elegans* were relatively more abundant among the *Luticola* species than is typical for the diatom communities in adjacent streams. Overall, these results confirm that benthic diatoms were present in microbial mats in Crescent Stream during the sampling period and that the dominant diatom taxa is known to accumulate in hyporheic sediments in another adjacent stream. Here we discuss the extent to which DSi incorporation into diatoms contributes to the sequestration of primary mineral derived-DSi and the high $\delta^{30}\mathrm{Si}_{\mathrm{DSi}}$ compositions in Crescent Stream.

The extent to which Si isotope fractionation during DSi uptake is sufficient to impact the $\delta^{30}\mathrm{Si}_{\mathrm{DSi}}$ in the stream water depends on the Si demand from the diatom growth relative to the rate of silicate mineral dissolution in the hyporheic zone. If the rate of production from silicate mineral dissolution is greater than the rate of uptake by diatoms, the Si concentration would still increase in the downstream direction but at a lower rate. Thus, the DSi concentration would not necessarily decrease downstream if diatom uptake were influencing the $\delta^{30}\mathrm{Si}_{\mathrm{DSi}}$ composition. A synoptic study of downstream patterns of Si concentrations in Von Guerard Stream shows that Si weathering rates were similar for moderate and low flow streams

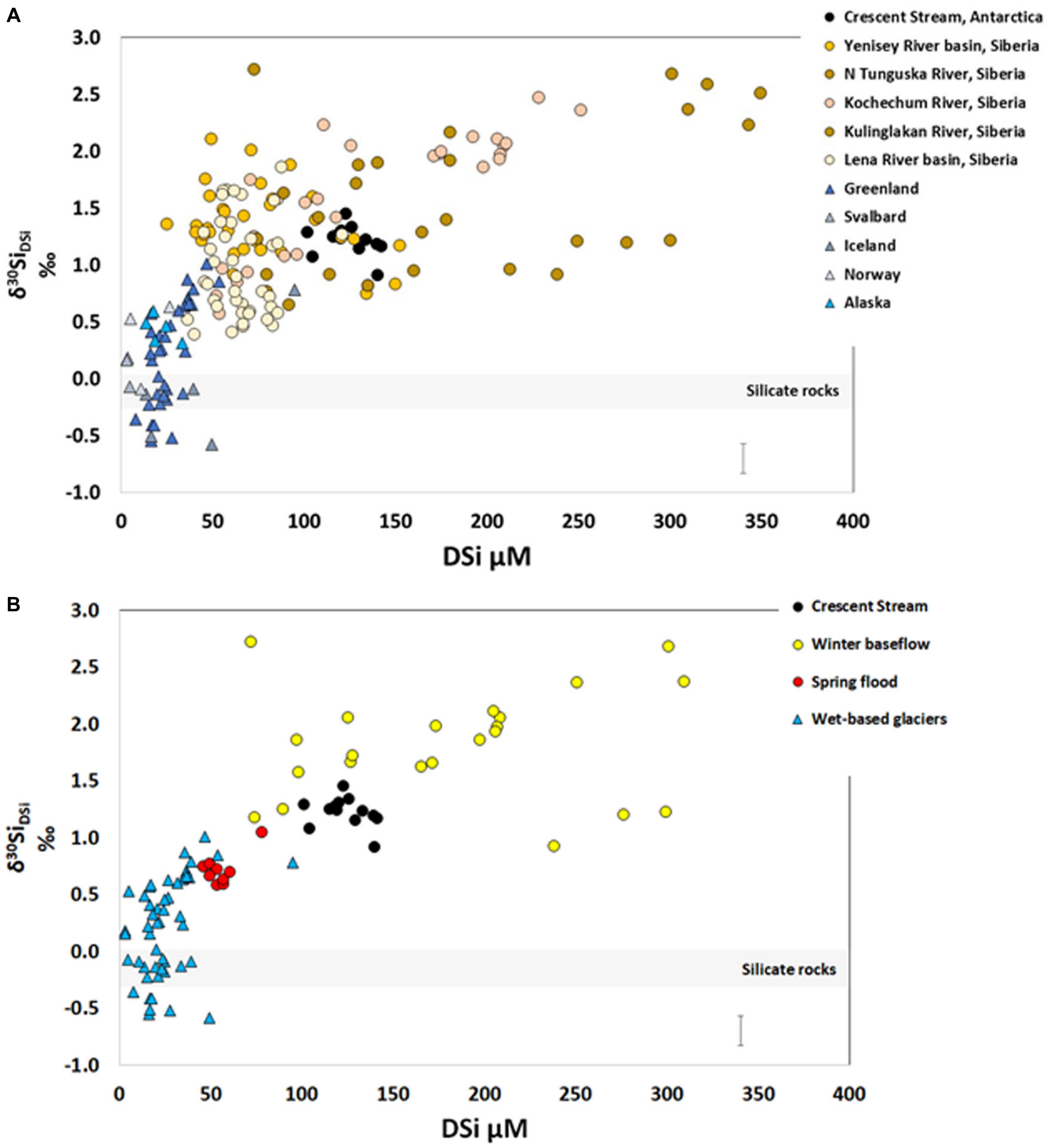

FIGURE 8 | (A) Synthesis of dissolved silicon isotope ($\delta^{30}Si_{DSi}$) compositions in glacial rivers (different blue colors), non-glacial permafrost-dominated river basins (different brown colors), and Crescent Stream for 2014–2015, 2015–2016, 2016–2017 seasons (black). Data sources: Pokrovsky et al., 2013; Mavromatis et al., 2016; Sun et al., 2018; Hatton et al., 2019b. **(B)** Comparison between $\delta^{30}Si_{DSi}$ compositions in Crescent Stream, with those in (i) permafrost-dominated rivers during winter baseflow, (ii) permafrost-dominated rivers during spring flood (Pokrovsky et al., 2013; Sun et al., 2018), and (iii) wet-based glacial rivers (Hatton et al., 2019b), showing that $\delta^{30}Si_{DSi}$ compositions in Crescent Steam during the austral summer months correspond to $\delta^{30}Si_{DSi}$ compositions in Arctic rivers during winter baseflow. The gray band shows the range of $\delta^{30}Si$ in silicate rocks (Georg et al., 2007b; Savage et al., 2010, 2011; Armytage et al., 2011). The error bar corresponds to the maximum standard deviation (2SD) for silicon isotope measurements.

(Gooseff et al., 2002) suggesting that an additional process, such as increased microbial mat growth during low to moderate stream flow (Stanish et al., 2011) sequesters a portion of the DSi in streams. This is evidence to show that diatoms incorporate a relatively significant portion of the DSi released from silicate weathering in hyporheic zone sediments in MDV stream. Diatom growth rates in the laboratory are slow and independent of temperature for four of the dominant diatoms isolated from the MDV, which could support a stable biotic Si uptake rate per area of microbial mat in the streams (Darling et al., 2017) over the duration of the austral summer, consistent with the relatively constant $\delta^{30}Si_{DSi}$ compositions (**Figure 5**).

Here we use Ge/Si ratios to understand the extent to which the DSi, released via silicate weathering, is taken up into diatoms in Crescent Stream. Diatoms generally do not discriminate between Ge and Si during growth i.e., the Ge/Si ratio of diatom opal reflects that of ambient water (Froelich et al., 1992). The exception to this occurs at low DSi concentrations where diatoms might start to discriminate against Ge, therefore raising the Ge/Si ratio in water (Sutton et al., 2010). The use of Ge/Si ratios to understand Si uptake into diatoms is difficult in Arctic river basins draining organic-rich permafrost soils because a portion of the Ge released from silicate weathering can form complexes with dissolved organic carbon (DOC) (Pokrovski and Schott, 1998). The contribution of Ge-organic complexes can be considered as limited in Crescent Stream given that the DOC concentrations in the MDV is low (<50 μM; Gooseff et al., 2002), except for an initial pulse when the streams are first wetted. Therefore, we can be confident to use the Ge/Si ratio in this Antarctic stream without being concerned about Ge-Si fractionation by organic colloids, such as in boreal rivers (Pokrovski and Schott, 1998). If only diatom uptake is mediating the net DSi concentrations and $\delta^{30}Si_{DSi}$ compositions, Ge/Si should stay the same (Froelich et al., 1992) or increase relative to the silicate rock ratio at low DSi concentrations (Sutton et al., 2010). However, Ge/Si ratios are lower than in silicate rocks (**Figure 4**; Bernstein, 1985) showing that DSi uptake into diatoms could contribute to increase $\delta^{30}Si$ compositions relative to the signature of silicate rocks but is not the only mechanism behind the heavy $\delta^{30}Si_{DSi}$ compositions in Crescent Stream.

An additional supply of DSi from diatom dissolution in hyporheic zone sediments must also be accounted for when considering the net contribution of diatoms to the silicate weathering flux. Diatom dissolution preferentially releases the lighter Si isotope, with an isotope fractionation factor, $^{30}\varepsilon$, of -0.55‰ (Demarest et al., 2009) in fresh water systems. Thus the dissolution of diatoms in the hyporheic zone would act to lower $\delta^{30}Si_{DSi}$ compositions in streams. During the austral summer months, there is a continuous input of diatoms in the particulate organic matter entering the hyporheic zone from upstream scouring events (Cullis et al., 2014). From a mass balance perspective, the present-day quantity of modern diatoms in hyporheic zone sediments can be explained by (i) the continuous supply of diatoms to sediments from microbial mats upstream and (ii) dissolution of diatoms in the hyporheic zone sediments. However, the high $\delta^{30}Si_{DSi}$ compositions in Crescent Stream indicate that diatom dissolution likely had a negligible contribution to silicate weathering rates in Crescent Stream between 2014 and 2017.

The combined evidence shows that only a fraction of DSi released from silicate mineral weathering is taken up by diatoms growing on the stream bed, resulting in a constant background supply of DSi (in equilibrium with diatoms) with higher $\delta^{30}Si_{DSi}$ compositions to Crescent Stream during austral summer months.

Abiotic Processes

Silicon incorporation in secondary weathering products

Clay minerals preferentially incorporate the lighter Si isotopes, with isotope fractionation factors varying from -1.8‰ to -2.0‰ (Opfergelt and Delmelle, 2012) driving $\delta^{30}Si_{DSi}$ compositions in soil porewaters to heavier values (Georg et al., 2007a). In MDV, hyporheic waters are oversaturated with respect to kaolinite (Gooseff et al., 2002) and some secondary products (kaolinite, illite and smectite) have been observed in the fine fraction (<2 μm) of hyporheic zone sediments (Lyons et al., 1998; Gooseff et al., 2002), with some controversy raised about their extent (Lyons et al., 1998). SEM images of sediments in Crescent Stream show micron-sized clay minerals on the surface and within broken volcanic spherules (**Figures 7A,C**), suggesting that a fraction of DSi released during primary mineral weathering is incorporated into clay minerals on altered mineral surfaces. Volcanic spherules contribute <1% of Crescent Stream sediments (Dowling et al., 2019) but are subject to extensive chemical and physical alteration (**Figure 7**) and are likely an important site for secondary clay mineral formation in Crescent Stream sediments.

Here we use Ge/Si ratios to confirm that clay mineral formation is occurring during meltwater-sediment exchange in Crescent Stream between 2014 and 2017. Ge/Si ratios in Crescent Stream range from 0.28 to 0.53 μmol mol^{-1} (**Figure 4**) which is lower than Ge/Si ratios in silicate rocks (1–3 μmol mol^{-1}, Bernstein, 1985) suggesting that a fraction of DSi released from parent materials is incorporated into clay minerals during water transport in Crescent Stream. Ge/Si ratios would also decrease if amorphous silica (ASi) dissolution occurs providing Si and not Ge to stream waters. However, it is unlikely that significant ASi dissolution occurs because this would also decrease the $\delta^{30}Si$ of DSi (Li et al., 1995).

The Ge/Si ratios in the samples collected between 2014 and 2017 were relatively similar, with no obvious trends throughout the season or over the 3 years of samples collected. There are no seasonal or daily variation in Ge/Si ratios (**Figure 4**), consistent with the evidence showing that meltwaters are in chemical equilibrium with mineral surfaces during transport in the hyporheic zone (Wlostowski et al., 2018). Under these weathering conditions, any changes in Ge and Si supply from the water-clay mineral interface during the austral summer are dependent on water transit times rather than variations in clay mineral formation showing that DSi is in equilibrium with clay minerals and supplies a constant background $\delta^{30}Si_{DSi}$ composition to Crescent Stream during the 2014–2017 austral summers.

Additional Si isotope fractionation may occur via preferential absorption of lighter Si isotopes onto Fe and Al (oxy)hydroxides (Delstanche et al., 2009; Opfergelt et al., 2009; Oelze et al., 2014). Moreover, Ge may be sequestered on Fe (oxy)hydroxides (Scribner et al., 2006) and also contribute to the low Ge/Si ratios in Crescent Stream. The quantity of Fe (oxy)hydroxides and Al oxides in stream sediments and conditions for element absorption during glacial meltwater-sediment exchange are poorly understood. However, the fine sediment fraction (<2 μm) is made up of 40–65% by weight of amorphous weathering products (Gooseff et al., 2002). This amorphous fraction only represents 0.3 wt% of the bulk sediment (Gooseff et al., 2002) but is distributed over the primary mineral surfaces in Crescent Stream sediments (Dowling et al., 2019). That fraction may contain amorphous to poorly crystalline Fe oxy-hydroxides that contribute to the high $\delta^{30}Si_{DSi}$ compositions in Crescent Stream.

Cryogenic amorphous silica precipitation

In Crescent Stream, MDV, the high $\delta^{30}Si_{DSi}$ compositions cannot be controlled by silicate mineral dissolution only and clay mineral formation likely contributes to modify the silicate rock signal. Amorphous silica precipitation is an additional important process that has to be considered in this environment, which is subjected to sub-zero temperatures for the majority of the year with mean annual temperatures between −17°C and −20°C (Doran et al., 2002).

At the freezing point of waters in soils and sediments, ice formation occurs and DSi is concentrated in the surrounding brines (Channing and Butler, 2007). If Si saturation occurs, up to 90 mol% of the starting DSi can be precipitated as amorphous silica (Dietzel, 2005) and Si is fractionated with an isotope fractionation factor, $^{30}\varepsilon$, of$-1.0‰$ (Li et al., 1995). This occurs either by a steady-state fractionation where the final solid has the same Si isotope composition as the starting fluid (assuming all DSi precipitates), $\Delta^{30}\mathrm{Si}_{\mathrm{solid-hyporheic\ zone\ solution}} = [\delta^{30}\mathrm{Si}_{\mathrm{solid}} - \delta^{30}\mathrm{Si}_{\mathrm{hyporheic\ zone\ solution}}] \approx 0‰$; or by unidirectional kinetic isotope fractionation where the final solid has a lighter isotope composition than the starting fluid, $\Delta^{30}\mathrm{Si}_{\mathrm{solid-hyporheic\ zone\ solution}} \approx < 0‰$ (Frings et al., 2016 and references therein). This is assuming no re-equilibration of Si isotopes in amorphous silica after precipitation (Fernandez et al., 2019). Unidirectional kinetic isotope fractionation occurs if (i) there is a closed system with no Si inputs or outputs; (ii) there is no change to the δ^{30}Si composition of DSi in the starting solution; (iii) dissolved Al concentrations are greater than 0.1 mM (Li et al., 1995; Oelze et al., 2015; Frings et al., 2016). Under these conditions, amorphous silica precipitation during cryogenic precipitate formation in permafrost soils can fractionate Si isotopes and drive riverine $\delta^{30}\mathrm{Si}_{\mathrm{DSi}}$ compositions to heavier values. This process has been invoked to explain the heavier Si isotope compositions in large Arctic rivers during winter months (Pokrovsky et al., 2013) and heavy Si isotope in soils porewaters in seasonally frozen Icelandic soils (Opfergelt et al., 2017).

In Crescent Stream, glacial meltwaters are transported along preferential flow paths in isolated areas of the hyporheic zone (Cozzetto et al., 2013) and water can collect in these isolated pockets at periods of high flow during the austral summer and when flow stops at the end of the austral summer (Cozzetto et al., 2006). The waters in the hyporheic zone and active layer soils freeze, likely at temperatures below 0°C because of the high concentrations of salts. During freezing and ice formation, dissolved Si accumulates in surrounding unfrozen waters and dissolved Si becomes saturated with respect to amorphous silica. Si isotope fractionation occurs by unidirectional kinetic isotope fractionation preferentially incorporating the light isotopes in amorphous silica and leaving a heavy Si isotope composition in surrounding waters. SEM images of sediments in Crescent Stream (**Figures 7B,C**) suggest the presence of an amorphous mineral phase on the surface of primary minerals. This phase may be composed of amorphous silica suggesting that amorphous silica precipitation occurs in hyporheic zone sediments in Crescent Stream. Assuming there are no freeze-thaw cycles, the heavy isotope signal remains trapped in the isolated pockets during the winter months and this preserved signal may contribute to the high $\delta^{30}\mathrm{Si}_{\mathrm{DSi}}$ compositions of Crescent Stream in the austral summer months.

The contribution of a winter-derived $\delta^{30}\mathrm{Si}_{\mathrm{DSi}}$ signal to stream water $\delta^{30}\mathrm{Si}_{\mathrm{DSi}}$ over the austral summer months depends on the rate at which these winter waters exchange with Crescent Stream waters. Evidence from δ^{18}O and δD compositions suggests that winter waters are flushed from the hyporheic zone at the start of the austral summer and not continuously supplied over the summer months (Gooseff et al., 2003). In early December, water in the extended hyporheic zone have enriched δ^{18}O and δD compositions resulting from evaporation and sublimation in the previous winter and summer. At the start of the austral summer, this enriched signal is transferred to stream waters providing evidence for early season hyporheic-stream water exchange. Gooseff et al. (2003) show that stream water δ^{18}O and δD enrichment decreased substantially between the first sampling date (Dec 7) at the beginning of flow, and the subsequent dates during the main flow period (Dec 21 and Jan 7), indicating that the relative contribution of waters from the extended hyporheic decreases in the 1st weeks of the austral summer.

Further, we can place physical constraints on how much water with a heavy $\delta^{30}\mathrm{Si}_{\mathrm{DSi}}$ can enter the stream from the hyporheic zone. The volumetric content of unfrozen water in the hyporheic zone was 10% at the end of the summer (Wlostowski et al., 2018). We can calculate a high estimate for the potential volume of the hyporheic zone for Crescent Stream as 5 km × 0.2 m × 10 m (stream length × hyporheic zone depth × width) to be 10×10^6 L. Using these estimates of unfrozen water content and hyporheic zone volume we estimate that 10^6 L of water is present in the hyporheic zone at the end of the Austral summer months. Given the rapid hyporheic exchange, we can estimate how fast that volume would be flushed out of the near and extended hyporheic zone contributing 10% of the water at a low flow rate in the stream of 10 L/sec (**Supplementary Figure 2**), corresponding to 1 L/sec. As a result, it can be estimated 10^6 L of water would take 10^6 sec or about 12 days to be flushed out at a flow rate of 1 L/sec. The 10 L/sec flow rate is a low value and flushing could happen more rapidly with higher flows. These constraints are consistent with evidence from δ^{18}O and δD compositions (Gooseff et al., 2003) and show that winter waters are flushed out of the extended hyporheic zone at the beginning of the austral summer.

Consistent with this evidence for an early season flushing of winter waters, we could therefore expect to observe an increase in DSi and $\delta^{30}\mathrm{Si}_{\mathrm{DSi}}$ compositions at the start of summer. However, this early season pulse is not observed in the samples collected at the start of the austral season (December 11th to December 28th, **Table 1**). One scenario is that early season sampling did not coincide with the release of waters stored in the hyporheic zone over the austral winter. For all seasons, sampling began 0–6 days after the onset of river discharge (**Supplementary Figure 2A**, LTER McMurdo Dry Valleys database, Gooseff and McKnight, 2019). Considering that active layer thaw coincides with glacial surface melt at the start of the austral summer (Gooseff et al., 2002), the collected samples likely coincided with the onset of hyporheic zone development and thus would capture the early release of waters stored during winter months. To improve on this effort, a high resolution (e.g., daily) sampling during early season thaw is required to detect a winter-derived $\delta^{30}\mathrm{Si}_{\mathrm{DSi}}$ signal. A second scenario is that the winter-derived DSi made up a relatively small fraction of the total DSi in Crescent Stream, and the pulse of DSi with high $\delta^{30}\mathrm{Si}_{\mathrm{DSi}}$

compositions did not affect the relatively constant stream Si isotope composition. Alternatively, to explain a constant supply of winter-derived high $\delta^{30}Si_{DSi}$ compositions to Crescent Stream, we consider the entire hyporheic zone as individual "nested storage zones with unique timescales of exchange" (Gooseff et al., 2003). In this scenario, the nested storage zones each represent pockets of frozen sediment at the start of the austral summer. During gradual thaw over several weeks between December and January (Conovitz, 2000), the pockets of unfrozen water associated with amorphous silica are incrementally unlocked and the unfrozen water is connected to the stream during sediment-stream water exchange. In this hypothesis, the high $\delta^{30}Si$ compositions are gradually added to the stream waters as the hyporheic zone is established over the summer months. Further work is required to understand the development of winter-derived $\delta^{30}Si_{DSi}$ compositions and their contribution to summer river waters in permafrost dominated-basins.

A conceptual model of these processes is presented in **Figure 9**, highlighting the processes driving Si isotope fractionation in the hyporheic zone, which are visualized as individual segments of water−mineral interactions. The $\delta^{30}Si_{DSi}$ compositions in waters collected at Gauge F8 in Crescent Stream results from the mixing of DSi from pockets of the hyporheic zone, influenced by amorphous silica formation during winter months, by diatom growth during summer months and ongoing clay mineral formation in these sediments. In this system, DSi concentrations increase as hyporheic zone pockets are connected with stream water but there is no evolution of the silicon isotope signal.

Dissolved Stream Si Isotope Composition as a Tool to Monitor Future Hyporheic Zone Functioning

Given the consistency of the DSi concentrations, Ge/Si ratios and $\delta^{30}Si_{DSi}$ compositions during three austral summers and our understanding of these Si isotopes compositions in Crescent Stream, we can assess the potential use of stream water $\delta^{30}Si_{DSi}$ compositions to trace future changes in hyporheic zone functioning in response to predicted scenarios in McMurdo Dry Valleys (Doran et al., 2008; Fountain et al., 2014).

Increased air temperatures in Antarctica (Bekryaev et al., 2010) are driving increased glacial melting with subsequent impact on stream flow with exceptionally high flow events reported in 2001−2002, 2008−2009, and 2011−2012 (Doran et al., 2008). In this study, we observe no relationship between $\delta^{30}Si_{DSi}$ values and stream flow in Crescent Stream between 2014 and 2017 suggesting that $\delta^{30}Si_{DSi}$ values will not respond to increased stream water flow in the future. However, increases in stream flow and decreases in fluid transit time in MDV streams will likely move the hyporheic zone toward a weathering limited regime (Wlostowski et al., 2018) where secondary clay

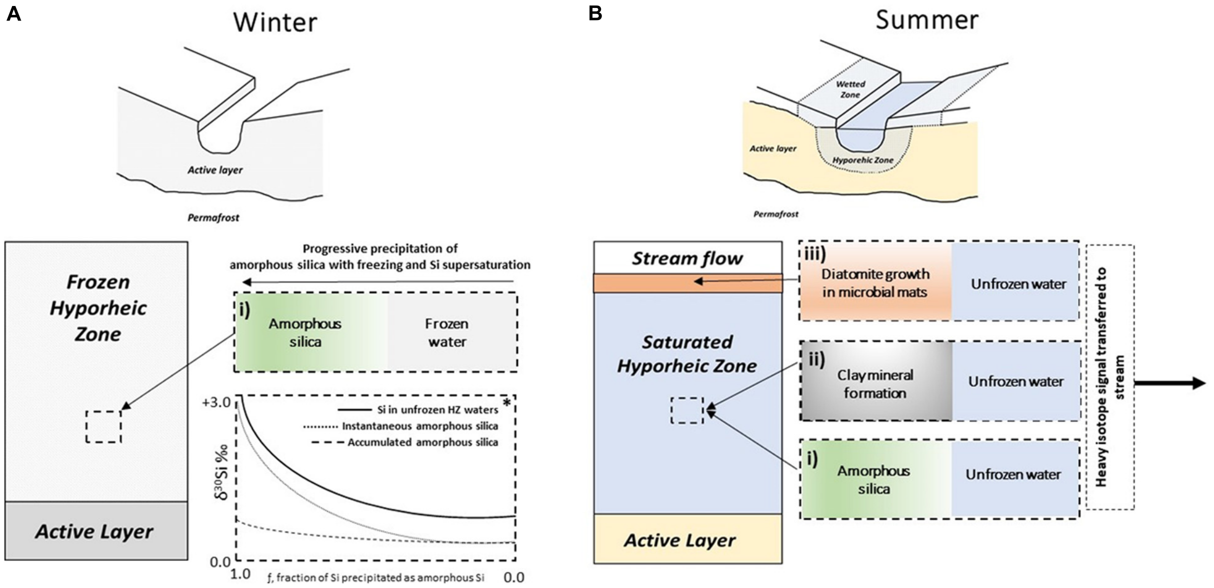

FIGURE 9 | Schematic showing the principal processes controlling dissolved Si isotope compositions in Crescent Stream during the austral winter **(A)** and summer **(B)** months. The initial pool of $Si(OH)_4$ is supplied by primary mineral dissolution (Gooseff et al., 2002) in the hyporheic zone. Si isotope fractionation occurs during subsequent secondary inorganic and biologically mediated Si phases formation. During winter **(A)** waters in isolated pockets of the hyporheic zone freeze, resulting in supersaturation of $Si(OH)_4$ and precipitation of amorphous silica (i). Under these conditions, unidirectional kinetic isotope fractionation occurs in accordance with the Rayleigh fractionation model (*) and amorphous silica preferentially incorporates the light isotopes ($^{30}\varepsilon = -1.0‰$), leaving the remaining unfrozen water with relatively high $\delta^{30}Si$ compositions. With progressive amorphous silica formation, the Si isotope composition of $Si(OH)_4$ in unfrozen water evolves to heavier values. During summer **(B)**, ice in the hyporheic zone thaws and the remaining DSi (in equilibrium with amorphous Si) presenting high $\delta^{30}Si_{DSi}$ compositions is released from the isolated pockets into Crescent Stream. In addition, diatoms are actively forming in microbial mats (ii) in the hyporheic zone during summer months, preferentially taking up light Si isotopes, providing a background contribution of higher $\delta^{30}Si_{DSi}$ compositions in Crescent Stream. These processes are superimposed onto clay mineral formation (iii), also preferentially taking up light Si isotopes.

minerals are dissolved and removed faster than they can be replaced via incongruent silicate mineral dissolution. This change in weathering regime may alter the $\delta^{30}Si_{DSi}$ composition of waters in contact with clay minerals during summer months.

Soil and water temperatures are predicted to increase in MDV (Fountain et al., 2014). Under future conditions, saline waters may not reach the low temperatures required for cryogenic precipitates to form, leaving a larger pool of silicon unfrozen during winter months and altering the isotope composition of DSi released into Crescent Stream during the summer. One scenario might be that in earlier warming stages, more regular freeze-thaw cycles would promote higher proportions of amorphous silica precipitation and therefore enhance Si isotope fractionation towards heavier values in the residual solution (Dietzel, 2005). In later stages, increased soil temperatures and induced thaw are likely to connect hyporheic zone pockets. Under these conditions, amorphous silica precipitation would no longer occur in a closed system and the heavy $\delta^{30}Si_{DSi}$ would not be preserved in the isolated pockets during the winter months.

Thermokarst erosion is also predicted to increase in MDV streams (Levy et al., 2013). In January 2012, thermokarst erosion in the west fork of Crescent Stream resulted in a brief (hours to days) increase in DSi concentrations (Gooseff et al., 2016), suggesting that more frequent thermokarst events may increase the supply of Si to streams. During these events, Si may be transported as particulate and colloidal amorphous silica and clay minerals and so contribute silicon with silicate rock to lower $\delta^{30}Si_{DSi}$ values. Increased thermokarst may also lead to increased disturbance of the stream bed and transport of diatoms in particulate organic matter (McKnight et al., 1999; Cullis et al., 2014) as has been observed during the 2001–2002, 2008–2009, and 2011–2012 high flow seasons (Kohler et al., 2015). In this study water samples were filtered at 0.4 μm. At this pore size, colloids can pass through 0.4 μm filters and contribute to the dissolved Si concentration. In the future, the silicon concentrations and Si isotope compositions of separate particulate, colloidal and truly dissolved fractions would be required to fully capture variations in the supply of silicon to MDV streams in response to these erosion events.

CONCLUSION

This study reports the first $\delta^{30}Si_{DSi}$ isotope compositions and Ge/Si ratios of dissolved Si in Crescent Stream, Antarctica during three austral seasons between 2014 and 2017. The $\delta^{30}Si_{DSi}$ isotope compositions and Si concentrations in Antarctica streams are higher than reported in northern latitude wet-based glaciers and form a narrow cluster within the values reported in permafrost-dominated Arctic rivers, evidence for a non-glacial silicate weathering in Antarctica.

The $\delta^{30}Si_{DSi}$ compositions in Crescent Stream are higher than $\delta^{30}Si$ compositions in silicate rocks showing that no direct weathering signal from primary mineral dissolution is transferred to the stream. Instead, the $\delta^{30}Si_{DSi}$ and Ge/Si data highlight that biotic and abiotic interactions occur within the hyporheic zone and influence the dissolved silicon released to the stream. Stream water-derived silicate mineral weathering rates in high latitudes are likely underestimated because a fraction of DSi is incorporated into secondary weathering products (i.e., clay minerals and amorphous silica) in the hyporheic zone. Amorphous silica precipitation within isolated pockets of hyporheic zone during winter months likely contributes to the stream $\delta^{30}Si_{DSi}$ isotope compositions showing that a winter process can affect the summer-dissolved signal.

$\delta^{30}Si_{DSi}$ values, Ge/Si ratios and Si concentrations show no seasonal or diurnal variation because glacial meltwaters are in equilibrium with these secondary Si products on the water transit timescales of hours to days. The constant $\delta^{30}Si_{DSi}$ compositions through the summer demonstrates a homogeneous functioning of the hyporheic zone, whether it is a near-stream zone or an extended zone.

The ongoing summer warming of the glacial surfaces of dry based glaciers and increased soil surface temperatures in McMurdo Dry Valleys is leading to increased glacial meltwater supply, changing hyporheic zone capacity and possible thermokarst erosion in streams. Here we show that Si isotopes are a useful tool to monitor possible shifts in the formation of secondary weathering products in the hyporheic zone of the McMurdo Dry Valley streams.

DATA AVAILABILITY STATEMENT

All datasets generated for this study are included in the article/**Supplementary Material**.

AUTHOR CONTRIBUTIONS

SO, CH, WB, and DM conceived the project. CH, FG, and SO analyzed the samples. All authors contributed to the discussion of data and manuscript writing.

FUNDING

This project received funding from the European Union's Horizon 2020 research and innovation program under grant agreement Nos. 714617 and 678371. FG and SO acknowledge funding from the National Funds for Scientific Research FNRS (Grant Nos. 26043653 and FC69480). JH and KH acknowledge funding from the Royal Society Enhancement Award (Grant RGF\EA\181036). SW, DM, and WB acknowledge the NSF grant to the MCM LTER project OPP-ANT 1115249.

ACKNOWLEDGMENTS

We would like to thank Anne Iserentant, Claudine Givron, Elodie Devos, and Hélène Dailly from the analytical platform MOCA at UCLouvain. The McMurdo Dry Valleys LTER team is acknowledged for their long-term collection of gauge data and sample collection during 2014–2017 field seasons at

Crescent Stream, MDV. We acknowledge Joshua Darling for the identification of diatom taxa in microbial mats in Crescent Stream. We also acknowledge the Subsurface Energy Materials Characterization and Analysis Laboratory (SEMCAL), School of Earth Sciences, The Ohio State University for SEM images.

SUPPLEMENTARY MATERIAL

The Supplementary Material for this article can be found online at: https://www.frontiersin.org/articles/10.3389/feart.2020.00229/full#supplementary-material

REFERENCES

Abraham, K., Opfergelt, S., Fripiat, F., Cavagna, A.-J., de Jong, J., Foley, S. F., et al. (2008). δ^{30}Si and δ^{29}Si determinations on USGS BHVO-1 and BHVO-2 reference materials with a new configuration on a Nu Plasma Multi-Collector ICP-MS. *Geostand. Geoanal. Res.* 32, 193–202. doi: 10.1111/j.1751-908x.2008.00879.x

Alger, A. S. (1997). *Ecological Processes in a Cold Desert Ecosystem: The Abundance and Species Distribution of Algal Mats in Glacial Meltwater Streams in Taylor Valley, Antarctica*. Boulder: University of Colorado.

Alleman, L. Y., Cardinal, D., Cocquyt, C., Plisnier, P. D., Descy, J. P., Kimirei, I., et al. (2005). Silicon isotopic fractionation in Lake Tanganyika and its main tributaries. *J. Great Lakes Res.* 31, 509–519. doi: 10.1016/s0380-1330(05)70280-x

Anderson, S. P., Drever, J. I., and Humphrey, N. F. (1997). Chemical weathering in glacial environments. *Geology* 25, 399–402.

Armytage, R. M. G., Georg, G. R. B., Savage, P. S., Williams, H. M., and Halliday, A. N. (2011). Silicon isotopes in meteorites and planetary core formation. *Geochim. Cosmochim. Acta* 75, 3662–3676. doi: 10.1016/j.gca.2011.03.044

Bekryaev, R. V., Polyakov, I. V., Vladimir, A., and Alexeev, V. A. (2010). Role of polar amplification in long-term surface air temperature variations and modern Arctic warming. *J. Clim.* 23, 3888–3906. doi: 10.1175/2010jcli3297.1

Berner, R. A., and Berner, E. K. (1997). "Silicate weathering and climate," in *Tectonic Uplift and Climate Change*, ed. W. F. Ruddiman (Boston, MA: Springer), 353–365. doi: 10.1007/978-1-4615-5935-1_15

Bernstein, L. R. (1985). Germanium geochemistry and mineralogy. *Geochim. Cosmochim. Acta* 49, 2409–2422. doi: 10.1016/0016-7037(85)90241-8

Biskaborn, B. K., Smith, S. L., Noetzli, J., Matthes, H., Vieira, G., Streletskiy, D. A., et al. (2019). Permafrost is warming at a global scale. *Nat. Commun.* 10:264.

Bockheim, J. G. (2002). Landform and soil development in the McMurdo Dry Valleys, Antarctica: a regional synthesis. *Arctic Antarctic Alpine Res.* 34, 308–317. doi: 10.1080/15230430.2002.12003499

Bockheim, J. G., Campbell, I. B., and McLeod, M. (2007). Permafrost distribution and active—layer depths in the McMurdo Dry Valleys, Antarctica. *Permafr. Periglac. Process.* 18, 217–227. doi: 10.1002/ppp.588

Brzezinski, M. A., Jones, J. L., Bidle, K. D., and Azam, F. (2003). The balance between silica production and silica dissolution in the sea: insights from Monterey Bay, California, applied to the global data set. *Limnol. Oceanogr.* 48, 1846–1854. doi: 10.4319/lo.2003.48.5.1846

Burkins, M. B., Virginia, R. A., and Wall, D. H. (2001). Organic carbon cycling in Taylor Valley, Antarctica: quantifying soil reservoirs and soil respiration. *Glob. Change Biol.* 7, 113–125. doi: 10.1046/j.1365-2486.2001.00393.x

Campbell, I. B., and Claridge, G. G. C. (1987). *Antarctica: Soils, Weathering Processes and Environment*, Vol. 16. Amsterdam: Elsevier.

Cardinal, D., Alleman, L. Y., De Jong, J., Ziegler, K., and André, L. (2003). Isotopic composition of silicon measured by multicollector plasma source mass spectrometry in dry plasma mode. *J. Anal. Atom. Spectr.* 18, 213–218. doi: 10.1039/b210109b

Channing, A., and Butler, I. B. (2007). Cryogenic opal-A deposition from Yellowstone hot springs. *Earth Planet. Sci. Lett.* 257, 121–131. doi: 10.1016/j.epsl.2007.02.026

Conovitz, P. A. (2000). *Active Layer Dynamics and Hyporheic Zone Storage in Three Streams in the McMurdo Dry Valleys, Antarctica*. Doctoral dissertation, Colorado State University, Fort Collins.

Conovitz, P. A., MacDonald, L. H., and McKnight, D. M. (2006). Spatial and temporal active layer dynamics along three glacial meltwater streams in the McMurdo Dry Valleys, Antarctica. *Arctic Antarctic Alpine Res.* 38, 42–53. doi: 10.1657/1523-0430(2006)038[0042:satald]2.0.co;2

Conovitz, P. A., McKnight, D. M., MacDonald, L. H., and Fountain, A. G. (1998). *Fryxell Basin, Antarctica*, Vol. 72. Washington, DC: American Geophysical Union, 93.

Cooper, A. F., Adam, L. J., Coulter, R. F., Eby, G. N., and McIntosh, W. C. (2007). Geology, geochronology and geochemistry of a basanitic volcano, White Island, Ross Sea, Antarctica. *J. Volcanol. Geother. Res.* 165, 189–216. doi: 10.1016/j.jvolgeores.2007.06.003

Cornelis, J. T., Delvaux, B., Georg, R., Lucas, Y., Ranger, J., and Opfergelt, S. (2011). Tracing the origin of dissolved silicon transferred from various soil-plant systems towards rivers: a review. *Biogeosci. Discuss.* 8, 89–112. doi: 10.5194/bg-8-89-2011

Cozzetto, K., McKnight, D. M., Nylen, T., and Fountain, A. (2006). Experimental investigations into processes controlling stream and hyporheic temperatures, Fryxell Basin, Antarctica. *Adv. Water Res.* 29, 130–153. doi: 10.1016/j.advwatres.2005.04.012

Cozzetto, K. D., Bencala, K. E., Gooseff, M. N., and McKnight, D. M. (2013). The influence of stream thermal regimes and preferential flow paths on hyporheic exchange in a glacial meltwater stream. *Water Resour. Res.* 49, 5552–5569. doi: 10.1002/wrcr.20410

Cullis, J. D., Stanish, L. F., and McKnight, D. M. (2014). Diel flow pulses drive particulate organic matter transport from microbial mats in a glacial meltwater stream in the McMurdo Dry Valleys. *Water Resour. Res.* 50, 86–97. doi: 10.1002/2013wr014061

Darling, J. P., Garland, D. D., Stanish, L. F., Esposito, R. M., Sokol, E. R., and McKnight, D. M. (2017). Thermal autecology describes the occurrence patterns of four benthic diatoms in McMurdo Dry Valley streams. *Polar Biol.* 40, 2381–2396. doi: 10.1007/s00300-017-2151-y

Delstanche, S., Opfergelt, S., Cardinal, D., Elsass, F., André, L., and Delvaux, B. (2009). Silicon isotopic fractionation during adsorption of aqueous monosilicic acid onto iron oxide. *Geochim. Cosmochim. Acta* 73, 923–934. doi: 10.1016/j.gca.2008.11.014

Delvigne, C., Opfergelt, S., Cardinal, D., Delvaux, B., and André, L. (2009). Distinct silicon and germanium pathways in the soil-plant system: Evidence from banana and horsetail. *J. Geophys. Res.* 114:G02013. doi: 10.1029/2008JG000899

Demarest, M. S., Brzezinski, M. A., and Beucher, C. P. (2009). Fractionation of silicon isotopes during biogenic silica dissolution. *Geochim. Cosmochim. Acta* 73, 5572–5583. doi: 10.1016/j.gca.2009.06.019

Derry, L. A., Kurtz, A. C., Ziegler, K., and Chadwick, O. A. (2005). Biological control of terrestrial silica cycling and export fluxes to watersheds. *Nature* 433, 728–731. doi: 10.1038/nature03299

Dietzel, M. (2005). Impact of cyclic freezing on precipitation of silica in Me–SiO2–H2O systems and geochemical implications for cryosoils and-sediments. *Chem. Geol.* 216, 79–88. doi: 10.1016/j.chemgeo.2004.11.003

Doran, P. T., McKay, C. P., Fountain, A. G., Nylen, T., McKnight, D. M., Jaros, C., et al. (2008). Hydrologic response to extreme warm and cold summers in the McMurdo Dry Valleys, East Antarctica. *Antarctic Sci.* 20, 499–509. doi: 10.1017/s0954102008001272

Doran, P. T., Priscu, J. C., Lyons, W. B., Walsh, J. E., Fountain, A. G., McKnight, D. M., et al. (2002). Antarctic climate cooling and terrestrial ecosystem response. *Nature* 415:517. doi: 10.1038/nature710

Dowling, C. B., Lyons, W. B., and Welch, K. A. (2013). Strontium isotopic signatures of streams from Taylor Valley, Antarctica, revisited: the role of carbonate mineral dissolution. *Aquat. Geochem.* 19, 231–240. doi: 10.1007/s10498-013-9189-4

Dowling, C. B., Welch, S. A., and Lyons, W. B. (2019). The geochemistry of glacial deposits in Taylor Valley, Antarctica: comparison to upper continental crustal abundances. *Appl. Geochem.* 107, 91–104. doi: 10.1016/j.apgeochem.2019.05.006

Egan, K. E., Rickaby, R. E., Leng, M. J., Hendry, K. R., Hermoso, M., Sloane, H. J., et al. (2012). Diatom silicon isotopes as a proxy for silicic acid utilisation: a

Southern Ocean core top calibration. *Geochim. Cosmochim. Acta* 96, 174–192. doi: 10.1016/j.gca.2012.08.002

Esposito, R. M. M., Spaulding, S. A., McKnight, D. M., Van de Vijver, B. A. R. T., Kopalová, K., Lubinski, D., et al. (2008). Inland diatoms from the McMurdo dry valleys and James Ross Island, Antarctica. *Botany* 86, 1378–1392. doi: 10.1139/b08-100

Fernandez, N. M., Zhang, X., and Druhan, J. L. (2019). Silicon isotopic re-equilibration during amorphous silica precipitation and implications for isotopic signatures in geochemical proxies. *Geochim. Cosmochim. Acta* 262, 104–127. doi: 10.1016/j.gca.2019.07.029

Fountain, A. G., Levy, J. S., Gooseff, M. N., and Van Horn, D. (2014). The McMurdo Dry Valleys: a landscape on the threshold of change. *Geomorphology* 225, 25–35. doi: 10.1016/j.geomorph.2014.03.044

Frings, P. J., Clymans, W., Fontorbe, G., Christina, L., and Conley, D. J. (2016). The continental Si cycle and its impact on the ocean Si isotope budget. *Chem. Geol.* 425, 12–36. doi: 10.1016/j.chemgeo.2016.01.020

Froelich, P. N., Blanc, V., Mortlock, R. A., Chillrud, S. N., Dunstan, W., Udomkit, A., et al. (1992). River fluxes of dissolved silica to the ocean were higher during glacials: Ge/Si in diatoms, rivers, and oceans. *Paleoceanography* 7, 739–767. doi: 10.1029/92pa02090

Gaspard, F., Opfergelt, S., Amerijeiras-Marino, Y., Dessert, C., Derry, L., and Delmelle, P. (2019). "Si isotopes and Ge/Si ratios as weathering proxy in streams of Guadeloupe: methodological development and first results," in *Symposium « Non-Traditional Stable Isotopes in Glacial and Non-Glacial Environments », 7th January 2019* (Louvain-la-Neuve: UCLouvain).

Georg, R. B., Halliday, A. N., Schauble, E. A., and Reynolds, B. C. (2007b). Silicon in the Earth's core. *Nature* 447, 1102–1106.

Georg, R. B., Reynolds, B. C., Frank, M., and Halliday, A. N. (2006). New sample preparation techniques for the determination of Si isotopic compositions using MC-ICP-MS. *Chem. Geol.* 235, 95–104. doi: 10.1016/j.chemgeo.2006.06.006

Georg, R. B., Reynolds, B. C., West, A. J., Burton, K. W., and Halliday, A. N. (2007a). Silicon isotope variations accompanying basalt weathering in Iceland. *Earth Planet. Sci. Lett.* 261, 476–490. doi: 10.1016/j.epsl.2007.07.004

Gooseff, M., and McKnight, D. (2019). *McMurdo Dry Valleys LTER: High Frequency Seasonal Stream Gage Measurements from Crescent Stream at F8 in Taylor Valley, Antarctica from 1990 to present. Environmental Data Initiative*. Available online at: https://doi.org/10.6073/pasta/86bce67070a2e3b37bf5ca805059feee (accessed June 1, 2020).

Gooseff, M. N., McKnight, D. M., Lyons, W. B., and Blum, A. E. (2002). Weathering reactions and hyporheic exchange controls on stream water chemistry in a glacial meltwater stream in the McMurdo Dry Valleys. *Water Resour. Res.* 38, 15–11.

Gooseff, M. N., McKnight, D. M., Runkel, R. L., and Vaughn, B. H. (2003). Determining long time−scale hyporheic zone flow paths in Antarctic streams. *Hydrol. Process.* 17, 1691–1710. doi: 10.1002/hyp.1210

Gooseff, M. N., Van Horn, D., Sudman, Z., McKnight, D. M., Welch, K. A., and Lyons, W. B. (2016). Stream biogeochemical and suspended sediment responses to permafrost degradation in stream banks in Taylor Valley, Antarctica. *Biogeosciences* 13, 1723–1732. doi: 10.5194/bg-13-1723-2016

Hall, B. L., Denton, G. H., and Hendy, C. H. (2000). Evidence from Taylor Valley for a grounded ice sheet in the Ross Sea, Antarctica. *Geografiska Annaler Ser. A Phys. Geogr.* 82, 275–303. doi: 10.1111/1468-0459.00126

Hatton, J. E., Hendry, K. R., Hawkings, J. R., Wadham, J. L., Kohler, T. J., Stibal, M., et al. (2019). Investigation of subglacial weathering under the Greenland Ice Sheet using silicon isotopes. *Geochim. Cosmochim. Acta* 247, 191–206. doi: 10.1016/j.gca.2018.12.033

Hatton, J. E., Hendry, K. R., Hawkings, J. R., Wadham, J. L., Opfergelt, S., Kohler, T. J., et al. (2019). Silicon isotopes in Arctic and sub-Arctic glacial meltwaters: the role of subglacial weathering in the silicon cycle. *Proc. R. Soc. A* 475, 20190098. doi: 10.1098/rspa.2019.0098

Howard-Williams, C., Vincent, C. L., Broady, P. A., and Vincent, W. F. (1986). Antarctic stream ecosystems: variability in environmental properties and algal community structure. *Int. Rev. Gesamten Hydrobiol. Hydrogr.* 71, 511–544. doi: 10.1002/iroh.19860710405

Kohler, T. J., Stanish, L. F., Crisp, S. W., Koch, J. C., Liptzin, D., Baeseman, J. L., et al. (2015). Life in the main channel: long-term hydrologic control of microbial mat abundance in McMurdo Dry Valley streams, Antarctica. *Ecosystems* 18, 310–327. doi: 10.1007/s10021-014-9829-6

Kurtz, A. C., Derry, L. A., and Chadwick, O. A. (2002). Germanium-silicon fractionation in the weathering environment. *Geochim. Cosmochim. Acta* 66, 1525–1537. doi: 10.1016/s0016-7037(01)00869-9

Levy, J. S., Fountain, A. G., Dickson, J. L., Head, J. W., Okal, M., Marchant, D. R., et al. (2013). Accelerated thermokarst formation in the McMurdo Dry Valleys, Antarctica. *Sci. Rep.* 3, 1–8.

Li, Y., Tiping, D., and Defang, W. (1995). Experimental study of silicon isotope dynamic fractionation and its application in geology. *Chin. J. Geochem.* 14, 212–219. doi: 10.1007/bf02842044

Lyons, W., and Welch, K. (2015). McMurdo Dry Valleys LTER: stream chemistry and ion concentrations. *Environ. Data Initiat.* doi: 10.6073/pasta/be9f781814330116f68844a8957962e4

Lyons, W. B., Nezat, C. A., Benson, L. V., Bullen, T. D., Graham, E. Y., Kidd, J., et al. (2002). Strontium isotopic signatures of the streams and lakes of Taylor Valley, Southern Victoria Land, Antarctica: chemical weathering in a polar climate. *Aquat. Geochem.* 8, 75–95.

Lyons, W. B., Welch, K. A., Fountain, A. G., Dana, G. L., Vaughn, B. H., and McKnight, D. M. (2003). Surface glaciochemistry of Taylor Valley, southern Victoria Land, Antarctica and its relationship to stream chemistry. *Hydrol. Process.* 17, 115–130. doi: 10.1002/hyp.1205

Lyons, W. B., Welch, K. A., Neumann, K., Toxey, J. K., Mcarthur, R., Williams, C., et al. (1998). Geochemical linkages among glaciers, streams and lakes within the Taylor Valley, Antarctica. *Antarctic Res. Ser.* 72, 77–92. doi: 10.1029/ar072p0077

Maurice, P. A., McKnight, D. M., Leff, L., Fulghum, J. E., and Gooseff, M. (2002). Direct observations of aluminosilicate weathering in the hyporheic zone of an Antarctic Dry Valley stream. *Geochim. Cosmochim. Acta* 66, 1335–1347. doi: 10.1016/s0016-7037(01)00890-0

Mavromatis, V., Rinder, T., Prokushkin, A. S., Pokrovsky, O. S., Korets, M. A., Chmeleff, J., et al. (2016). The effect of permafrost, vegetation, and lithology on Mg and Si isotope composition of the Yenisey River and its tributaries at the end of the spring flood. *Geochim. Cosmochim. Acta* 191, 32–46. doi: 10.1016/j.gca.2016.07.003

McKnight, D. M., Alger, A. S., Tate, C. M., Shupe, G., and Spaulding, S. (1998). "Longitudinal patterns in algal abundance and species distribution in meltwater streams in Taylor Valley, Southern Victoria Land, Antarctica," in *Ecosystem Dynamics in a Polar Desert: The McMurdo Dry Valleys, Antarctica: Antarctic Research Series*, Vol. 73, ed. J. C. Priscu (Washington, DC: American Geophysical Union), 109–128.

McKnight, D. M., Niyogi, D. K., Alger, A. S., Bomblies, A., Conovitz, P. A., and Tate, C. M. (1999). Dry Valley streams in Antarctica: ecosystems waiting for water. *BioScience* 49, 985–995.

McKnight, D. M., Runkel, R. L., Duff, J. H., Tate, C. M., and Moorhead, D. (2004). Inorganic nitrogen and phosphorous dynamics of Antarctic glacial meltwater streams as controlled by hyporheic exchange and benthic autotrophic communities. *J. N. Am. Benthol. Soc.* 23, 171–188. doi: 10.1899/0887-3593(2004)023<0171:inapdo>2.0.co;2

McKnight, D. M., and Tate, C. M. (1997). Canada stream: a glacial meltwater stream in Taylor Valley, south Victoria Land, Antarctica. *J. N. Am. Benthol. Soc.* 16, 14–17. doi: 10.2307/1468224

McKnight, D. M., Tate, C. M., Andrews, E. D., Niyogi, D. K., Cozzetto, K., Welch, K., et al. (2007). Reactivation of a cryptobiotic stream ecosystem in the McMurdo Dry Valleys, Antarctica: a long-term geomorphological experiment. *Geomorphology* 89, 186–204. doi: 10.1016/j.geomorph.2006.07.025

Mortlock, R. A., and Froelich, P. N. (1996). Determination of germanium by isotope dilution-hydride generation inductively coupled plasma mass spectrometry. *Anal. Chim. Acta* 332, 277–284. doi: 10.1016/0003-2670(96)00230-9

Mullin, J., and Riley, J. P. (1955). The colorimetric determination of silicate with special reference to sea and natural waters. *Anal. Chim. Acta* 12, 162–176. doi: 10.1016/s0003-2670(00)87825-3

Murnane, R. J., and Stallard, R. F. (1990). Germanium and silicon in rivers of the Orinoco drainage basin. *Nature* 344, 749–752. doi: 10.1038/344749a0

Nezat, C. A., Lyons, W. B., and Welch, K. A. (2001). Chemical weathering in streams of a polar desert (Taylor Valley, Antarctica). *Geol. Soc. Am. Bull.* 113, 1401–1408. doi: 10.1130/0016-7606(2001)113<1401:cwisoa>2.0.co;2

Obu, J., Westermann, S., Vieira, G., Abramov, A., Balks, M., Bartsch, A., et al. (2020). Pan-Antarctic map of near-surface permafrost temperatures at 1 km2 scale. *Cryosphere* 14, 497–519. doi: 10.5194/tc-14-497-2020

Oelze, M., Von Blanckenburg, F., Bouchez, J., Hoellen, D., and Dietzel, M. (2015). The effect of Al on Si isotope fractionation investigated by silica precipitation experiments. *Chem. Geol.* 397, 94–105. doi: 10.1016/j.chemgeo.2015.01.002

Oelze, M., von Blanckenburg, F., Hoellen, D., Dietzel, M., and Bouchez, J. (2014). Si stable isotope fractionation during adsorption and the competition between kinetic and equilibrium isotope fractionation: Implications for weathering systems. *Chem. Geol.* 380, 161–171. doi: 10.1016/j.chemgeo.2014.04.027

Opfergelt, S., Bournonville, G., Cardinal, D., André, D., Delstanche, S., and Delvaux, B. (2009). Impact of soil weathering degree on silicon isotopic fractionation during adsorption onto iron oxides in basaltic ash soils, Cameroon. *Geochim. Cosmochim. Acta* 73, 7226–7240. doi: 10.1016/j.gca.2009.09.003

Opfergelt, S., and Delmelle, P. (2012). Silicon isotopes and continental weathering processes: Assessing controls on Si transfer to the ocean. *Comptes Rend. Geosci.* 344, 723–738. doi: 10.1016/j.crte.2012.09.006

Opfergelt, S., Delvaux, B., André, L., and Cardinal, D. (2008). Plant silicon isotopic signature might reflect soil weathering degree. *Biogeochemistry* 91, 163–175. doi: 10.1007/s10533-008-9278-4

Opfergelt, S., Eiriksdottir, E. S., Burton, K. W., Einarsson, A., Siebert, C., Gislason, S. R., et al. (2011). Quantifying the impact of freshwater diatom productivity on silicon isotopes and silicon fluxes: Lake Myvatn, Iceland. *Earth Planet. Sci. Lett.* 305, 73–82. doi: 10.1016/j.epsl.2011.02.043

Opfergelt, S., Williams, H. M., Cornelis, J.-T., Guicharnaud, R. A., Georg, R. B., Siebert, C., et al. (2017). Iron and silicon isotope behaviour accompanying weathering in Icelandic soils, and the implications for iron export from peatlands. *Geochim. Cosmochim. Acta* 217, 273–291. doi: 10.1016/j.gca.2017.08.033

Pokrovski, G. S., and Schott, J. (1998). Experimental study of the complexation of silicon and germanium with aqueous organic species: implications for germanium and silicon transport and Ge/Si ratio in natural waters. *Geochim. Cosmochim. Acta* 62, 3413–3428. doi: 10.1016/s0016-7037(98)00249-x

Pokrovsky, O. S., Reynolds, B. C., Prokushkin, A. S., Schott, J., and Viers, J. (2013). Silicon isotope variations in Central Siberian rivers during basalt weathering in permafrost-dominated larch forests. *Chem. Geol.* 355, 103–116. doi: 10.1016/j.chemgeo.2013.07.016

Pretorius, W., Weis, D., Williams, G., Hanano, D., Kieffer, B., and Scoates, J. (2006). Complete trace elemental characterisation of granitoid (USGS G−2, GSP−2) reference materials by high resolution inductively coupled plasma−mass spectrometry. *Geostand. Geoanal. Res.* 30, 39–54. doi: 10.1111/j.1751-908x.2006.tb00910.x

Pugh, H. E., Welch, K. A., Lyons, W. B., Priscu, J. C., and McKnight, D. M. (2002). The biogeochemistry of Si in the McMurdo Dry Valley lakes, Antarctica. *Int. J. Astrobiol.* 1, 401–413. doi: 10.1017/s1473550403001332

Reynolds, B. C., Aggarwal, J., André, L., Baxter, D., Beucher, C., Brzezinski, M. A., et al. (2007). An inter-laboratory comparison of Si isotope reference materials. *J. Anal. AtomicSpectrometry* 22, 561–568.

Savage, P. S., Georg, R. B., Armytage, R. M. G., Williams, H. M., and Halliday, A. N. (2010). Silicon isotope homogeneity in the mantle. *Earth Planet. Sci. Lett.* 295, 139–146. doi: 10.1016/j.epsl.2010.03.035

Savage, P. S., Georg, R. B., Williams, H. M., Burton, K. W., and Halliday, A. N. (2011). Silicon isotope fractionation during magmatic differentiation. *Geochim. Cosmochim. Acta* 75, 6124–6139. doi: 10.1016/j.gca.2011.07.043

Scribner, A. M., Kurtz, A. C., and Chadwick, O. A. (2006). Germanium sequestration by soil: targeting the roles of secondary clays and Fe-oxyhydroxides. *Earth Planet. Sci. Lett.* 243, 760–770. doi: 10.1016/j.epsl.2006.01.051

Spaulding, S., Esposito, R., Lubinski, D., Horn, S., Cox, M., McKnight, D., et al. (2020). *Antarctic Freshwater Diatoms Website*. Available online at: http://huey.colorado.edu/diatoms/about/index.php (accessed June 9, 2020)

Stanish, L. F., Nemergut, D. R., and McKnight, D. M. (2011). Hydrologic processes influence diatom community composition in Dry Valley streams. *J. N. Am. Benthol. Soc.* 30, 1057–1073. doi: 10.1899/11-008.1

Sun, X., Mörth, C. M., Porcelli, D., Kutscher, L., Hirst, C., Murphy, M. J., et al. (2018). Stable silicon isotopic compositions of the Lena River and its tributaries: implications for silicon delivery to the Arctic Ocean. *Geochim. Cosmochim. Acta* 241, 120–133. doi: 10.1016/j.gca.2018.08.044

Sutton, J., Ellwood, M. J., Maher, W. A., and Croot, P. L. (2010). Oceanic distribution of inorganic germanium relative to silicon: germanium discrimination by diatoms. *Glob. Biogeochem. Cycles* 24, 1–13. doi: 10.1029/2009GB003689

Wetzel, F., De Souza, G. F., and Reynolds, B. C. (2014). What controls silicon isotope fractionation during dissolution of diatom opal? *Geochim. Cosmochim. Acta* 131, 128–137. doi: 10.1016/j.gca.2014.01.028

Witherow, R. A., Lyons, W. B., and Henderson, G. M. (2010). Lithium isotopic composition of the McMurdo Dry Valleys aquatic systems. *Chem. Geol.* 275, 139–147. doi: 10.1016/j.chemgeo.2010.04.017

Wlostowski, A. N., Gooseff, M. N., McKnight, D. M., and Lyons, W. B. (2018). Transit times and rapid chemical equilibrium explain chemostasis in glacial meltwater streams in the McMurdo Dry Valleys, Antarctica. *Geophys. Res. Lett.* 45, 13–322.

Yeghicheyan, D., Carignan, J., Valladon, M., Le Coz, M. B., Cornec, F. L., Castrec−Rouelle, M., et al. (2001). A compilation of silicon and thirty one trace elements measured in the natural river water reference material SLRS−4 (NRC−CNRC). *Geostand. Newsl.* 25, 465–474. doi: 10.1111/j.1751-908x.2001.tb00617.x

Young, E. D., Galy, A., and Nagahara, H. (2002). Kinetic and equilibrium mass-dependent isotope fractionation laws in nature and their geochemical and cosmochemical significance. *Geochim. Cosmochim. Acta* 66, 1095–1104. doi: 10.1016/s0016-7037(01)00832-8

Ziegler, K., Chadwick, O. A., Brzezinski, M. A., and Kelly, E. F. (2005). Natural variations of δ30Si ratios during progressive basalt weathering, Hawaiian Islands. *Geochim. Cosmochim. Acta* 69, 4597–4610. doi: 10.1016/j.gca.2005.05.008

Conflict of Interest: The authors declare that the research was conducted in the absence of any commercial or financial relationships that could be construed as a potential conflict of interest.

frontiers in Earth Science

ORIGINAL RESEARCH
published: 14 July 2020
doi: 10.3389/feart.2020.00286

Silicon Isotopic Composition of Dry and Wet-Based Glaciers in Antarctica

Jade E. Hatton[1]*, Katharine R. Hendry[1], Catherine Hirst[2], Sophie Opfergelt[2], Susann Henkel[3], Adrián Silva-Busso[4], Susan A. Welch[5,6], Jemma L. Wadham[7], W. Berry Lyons[5,6], Elizabeth Bagshaw[8], Michael Staubwasser[9] and Diane M. McKnight[10]

[1] School of Earth Sciences, Faculty of Science, University of Bristol, Bristol, United Kingdom, [2] Earth and Life Institute, Université catholique de Louvain, Louvain-la-Neuve, Belgium, [3] Alfred Wegener Institute, Helmholtz Centre for Polar and Marine Research, Bremerhaven, Germany, [4] Facultad de Cs. Exactas y Naturales, Universidad de Buenos Aires, Buenos Aires, Argentina, [5] Byrd Polar and Climate Research Center, College of Arts and Sciences, The Ohio State University, Columbus, OH, United States, [6] School of Earth Sciences, The Ohio State University, Columbus, OH, United States, [7] School of Geographical Sciences, Faculty of Science, University of Bristol, Bristol, United Kingdom, [8] School of Earth and Ocean Sciences, College of Physical Sciences and Engineering, Cardiff University, Cardiff, United Kingdom, [9] University of Cologne, Cologne, Germany, [10] Institute of Arctic and Alpine Research, University of Colorado Boulder, Boulder, CO, United States

Glaciers and ice sheets export significant amounts of silicon (Si) to downstream ecosystems, impacting local and potentially global biogeochemical cycles. Recent studies have shown Si in Arctic glacial meltwaters to have an isotopically distinct signature when compared to non-glacial rivers. This is likely linked to subglacial weathering processes and mechanochemical reactions. However, there are currently no silicon isotope (δ^{30}Si) data available from meltwater streams in Antarctica, limiting the current inferences on global glacial silicon isotopic composition and its drivers. To address this gap, we present dissolved silicon (DSi), $\delta^{30}\mathrm{Si}_{\mathrm{DSi}}$, and major ion data from meltwater streams draining a polythermal glacier in the region of the West Antarctic Peninsula (WAP; King George Island) and a cold-based glacier in East Antarctica [Commonwealth Stream, McMurdo Dry Valleys (MDV)]. These data, alongside other global datasets, improve our understanding of how contrasting glacier thermal regime can impact upon Si cycling and therefore the $\delta^{30}\mathrm{Si}_{\mathrm{DSi}}$ composition. We find a similar $\delta^{30}\mathrm{Si}_{\mathrm{DSi}}$ composition between the two sites, with the streams on King George Island varying between -0.23 and +1.23‰ and the Commonwealth stream varying from -0.40 to +1.14‰. However, meltwater streams in King George Island have higher DSi concentrations, and the two glacial systems exhibit opposite DSi – $\delta^{30}\mathrm{Si}_{\mathrm{DSi}}$ trends. These contrasts likely result from differences in weathering processes, specifically the role of subglacial processes (King George Island) and, supraglacial processes followed by in-stream weathering in hyporheic zones (Commonwealth Stream). These findings are important when considering likely changes in nutrient fluxes from Antarctic glaciers under climatic warming scenarios and consequent shifts in glacial thermal regimes.

Keywords: silicon isotope geochemistry, Antarctica, stream weathering, subglacial weathering, silicon cycle

OPEN ACCESS

Edited by:
Ramanathan Alagappan,
Jawaharlal Nehru University, India

Reviewed by:
Andrew Jonathan Hodson,
The University Centre in Svalbard, Norway
Jon Telling,
Newcastle University, United Kingdom

***Correspondence:**
Jade E. Hatton
j.e.hatton@bristol.ac.uk

Specialty section:
This article was submitted to Geochemistry, a section of the journal Frontiers in Earth Science

Received: *13 March 2020*
Accepted: *19 June 2020*
Published: *14 July 2020*

Citation:
Hatton JE, Hendry KR, Hirst C, Opfergelt S, Henkel S, Silva-Busso A, Welch SA, Wadham JL, Lyons WB, Bagshaw E, Staubwasser M and McKnight DM (2020) Silicon Isotopic Composition of Dry and Wet-Based Glaciers in Antarctica. Front. Earth Sci. 8:286. doi: 10.3389/feart.2020.00286

INTRODUCTION

There is growing evidence that links nutrient fluxes to the ocean with the export of glacial meltwater and icebergs, especially from the Greenland Ice Sheet (Hood et al., 2009; Gerringa et al., 2012; Hawkings et al., 2014, 2015, 2017; Lawson et al., 2014; Hendry et al., 2019). However, predictions of how nutrient fluxes may change under climatic warming scenarios are poorly constrained, due to the complexity of these systems, and the lack of data available from large glaciers (Hopwood et al., 2018). The vast majority of data currently available are only from the Arctic or sub-Arctic. Recent studies of the West Antarctic Peninsula (WAP) have shown that glacial meltwater may provide iron to coastal waters (Annett et al., 2015; Lyons et al., 2015; Hodson et al., 2017; Henkel et al., 2018; Höfer et al., 2019). Furthermore, upwelling marine waters can be modified due to benthic fluxes of iron and silica in shallow marine shelf sediments, which are in turn affected by the inputs of particles from glacial sources both in the Arctic and Antarctic (Henley et al., 2018; Sherrell et al., 2018; Hendry et al., 2019), highlighting a potentially significant role of glacial nutrients derived from particle dissolution.

The WAP has experienced some of the most rapid warming of the Southern Hemisphere and ice shelves have undergone retreat over the past 50 years (Turner et al., 2005). Under climatic warming scenarios, ice free areas on Antarctica could expand by 25% by 2100 (Lee et al., 2017), highlighting the future potential for further glacial retreat. This clearly has implications for the delivery of glacially derived nutrients to downstream ecosystems and may impact wider biogeochemical cycles. But in order to improve our predictions, we need to gain a better understanding of the underlying biogeochemical processes, including subglacial and periglacial weathering processes.

Stable silicon isotope data have been used previously to improve understanding of weathering processes in glacial and permafrost covered environments (Georg et al., 2007; Opfergelt et al., 2013; Hatton et al., 2019a). Previous studies have found that glacial rivers export isotopically distinct silicon compared to non-glacial rivers (Hatton et al., 2019b). It is hypothesized that the subglacial weathering processes, fueled by high physical erosion, drive the export of isotopically light glacial silicon due to large amounts of fine grained material enriched in ^{28}Si, high mineral surface areas and elevated rock to water ratios. This has implications for understanding of the global silicon cycle over glacial to interglacial timescales when considering oceanic diatom utilization of silicon (Hawkings et al., 2018). However, the current silicon isotope dataset for glacial rivers is limited to Arctic and sub-Arctic regions, and it remains unclear whether this understanding is transferrable to Antarctica. Using silicon concentration data from subglacial Lake Whillans, the potential flux of DSi from the Antarctic ice sheet via melt and icebergs is equivalent to the Greenland Ice Sheet (Hawkings et al., 2017), highlighting the potential importance of better constraining Antarctic silicon sources, especially as glacial retreat occurs.

To address the role of Antarctic glaciers in silicon cycling, we investigate the dissolved silicon isotope composition ($\delta^{30}Si_{DSi}$) of riverine waters fed by two contrasting glacial environments; Fourcade Glacier, a polythermal glacier on King George Island, and Commonwealth Glacier, a cold-based glacier in McMurdo Dry Valleys (MDV). Analysis of streams fed by glaciers with contrasting thermal regimes and stream properties allows us to consider the impact differing conditions may have upon Si export and how we may use the $\delta^{30}Si_{DSi}$ composition of proglacial streams to infer different weathering processes within different glacial environments. This will allow a greater understanding of global glacial silicon cycling.

Currently, studies of $\delta^{30}Si_{DSi}$ composition from glacial environments do not include any cold-based systems. We can use the $\delta^{30}Si_{DSi}$ composition of Commonwealth Stream, MDV, East Antarctica to assess the current state of these environments and how these systems behave differently to warm-based glaciers, so we can begin to determine a global glacial Si cycle, its drivers, and potential changes in the future. The MDV are home to a collection of largely cold-based glaciers, providing the ideal glacial thermal regime endmember in conceptual models of silicon cycling in cold regions. Commonwealth Stream is fed mainly by the supraglacial melt from Commonwealth Glacier. A cold-based glacier is defined by the basal ice being below the temperature of the basal melting point (Waller, 2001). Such low temperatures result in a lack in active subglacial biogeochemical weathering, which is the process that has been suggested to drive the distinct silicon isotope signature of warm-based glaciers (Hatton et al., 2019b). Despite this, there is evidence that cold-based glaciers can erode, transport, and deposit sediments (Cuffey et al., 2000; Hambrey and Fitzsimons, 2010). Although streams in the MDV are not impacted by subglacial chemical weathering, they are influenced by weathering processes within cryoconite holes via supraglacial melt (Fortner et al., 2005; Bagshaw et al., 2013; Fountain, 2014). In addition, most streams have extensive hyporheic zones, where chemical weathering and dissolution occurs (Gooseff et al., 2002; Welch et al., 2010; Olund et al., 2018). Previous studies have found these streams to be a potential source of Fe and P to coastal phytoplankton communities (Lyons et al., 2015; Olund et al., 2018). Despite the cold and dry conditions in the Dry Valleys, analysis of stream hyporheic zones has shown primary silicate weathering rates to be comparable to temperate environments (Gooseff et al., 2002). This concurs with other studies challenging the assumption that high latitude systems have lower weathering rates (Huh et al., 1998; Wadham et al., 2010; Urra et al., 2019).

We contrast the study of silicon isotope geochemistry in the MDV with analysis of silicon isotopes in streams influenced by the polythermal Fourcade Glacier on Potter Peninsula on King George Island (Falk et al., 2018). King George Island (also known as Isla 25 de Mayo) is the largest of the South Shetland Archipelago and 92% of the island is ice-covered (Leal et al., 2008). The more frequent occurrence of positive Southern Annual Mode phases is responsible for warmer air temperatures at the Southern Shetland Islands, increasing surface melt and glacier retreat (Jerosch et al., 2018). Therefore, the study of $\delta^{30}Si_{DSi}$ composition from glacial streams on King George Island captures the *status quo* of a rapidly changing environment, by sampling streams in contrasting hydrogeological basins (fed by glacial melt or not), building a basis for the assessment of changes related to deglaciation. It was estimated that 44%

of the coastline on King George Island was ice-free in 2008 (Rückamp et al., 2011), a figure likely to have increased over the past decade. This glacial retreat has impacted the downstream fjord ecosystem, with contrasting effects on marine biota by decreased light penetration due to increased suspended matter discharge and increased nutrient availability (Schloss et al., 1999, 2014; Ardelan et al., 2010; Monien et al., 2017; Jerosch et al., 2018). The impact the retreat may have on the silicon cycle has not been studied, but such knowledge could enable us to decipher how other glaciers may behave in the future under climatic warming scenarios where glacial retreat is increasing.

MATERIALS AND METHODS

Sampling Locations

Commonwealth Stream is located in the MDV, and the bedrock is made up from the Beacon Supergroup sandstone, Ferrar Dolerite, crystalline basement igneous and metamorphic rocks, and the McMurdo Volcanics (Hall and Denton, 2000). Supraglacial meltwater from Commonwealth Glacier feeds into Commonwealth stream, which flows for 4–10 weeks of the year. The stream is 4.2 km long, has an average gradient of 0.044 m/m, and discharges directly into the McMurdo Sound (Wlostowski et al., 2016). The stream channel is bounded by permafrost and there is also a hyporheic zone present, which expands to up to 60 cm depth throughout the summer (McKnight et al., 1999; Olund et al., 2018). The daily and seasonal discharge varies greatly due to solar incidence, temperature, and precipitation (McKnight et al., 1999; Olund et al., 2018), as highlighted in **Supplementary Figure S1**. Commonwealth Stream has been gauged for 24 years by the MCM-LTER program, with flow data collected every 15 min using Campbell CR10 data loggers (McKnight et al., 1999; Wlostowski et al., 2016). Water samples from Commonwealth Stream were collected in the austral summers between 2014 and 2017 (**Supplementary Table S1**). Most of the samples were collected at the discharge gauging station, approximately 0.7 km from the glacier terminus (**Figure 1**, sampling location 1, hereafter referred to as Gauging Station). A partial diurnal set of samples was also collected on 1 January 2016 close to the river mouth, approximately 3.4 km downstream from the Gauging Station and 100 m from where the stream discharges into the McMurdo Sound (as described in Olund et al., 2018, **Figure 1**, sampling location 2, subsequently referred to as the Mouth Station).

King George Island is the largest island of the mostly ice capped South Shetland Islands, located 130 km from the north-western tip of the Antarctic peninsula (Jerosch et al., 2018). Streams were sampled on Potter Peninsula, which is on the southern-most tip of King George Island. Water samples were collected from a range of streams on Potter Peninsula in February 2012 and January–March 2013 (**Figure 1** and **Supplementary Table S1**). Each sample was collected from a different stream, with estimated stream locations on marked on **Figure 1** (see photos in Henkel et al., 2018). The transient nature of the streams on Potter Peninsula means we cannot accurately mark all the stream paths, especially as samples were collected over two melt seasons. In the summer, streams on Potter Peninsula are fed by a combination of precipitation, glacial melt, groundwaters, and permafrost thaw. It was not within the scope of this study to quantify the different water sources to each stream, but the Peninsula can be separated into hydrogeological basins (**Figure 1**, further details in provided in the **Supplementary Material** and **Supplementary Figure S2**), which we used to consider whether or not the streams are fed by glacial meltwater (Silva-Busso, 2009). Glacial meltwater originates from Fourcade Glacier, a polythermal glacier, which drains from the Warzawa Ice Field, which then feeds into Potter Cove and Bransfield Strait. Fourcade Glacier was classified as marine terminating (into Potter Cover), until 2016, but rapid retreat (mean rate of 20 m a^{-1} between 1956 and 2008, Rückamp et al., 2011), has led to it being land-based (Jerosch et al., 2018). We sampled streams in the three basins; Potter South, Potter North, and Fourcade Basin (**Figure 1**), which are fed, at least in part by Fourcade Glacier. The drainage network in Potter North and Potter South are composed of ephemeral, short, shallow, and unstable channels that develop a sub-dendritic design on top of modern glacial deposits of homogenous lithology. Melt processes can explain about 98–99% of the water supply to streams in the basins on the glaciated parts of the catchment, based upon a proposed hydrological discharge model (Falk et al., 2018). There are no existing systematic studies of Fourcade Basin to date; however, some geohydrological observations can be made to characterize the basin. Fourcade Glacier is the main contribution of water to the basin, but large lakes have a storage effect before the water discharges into the Brandsfield Strait.

We also sampled streams in Matías Basin, where water is sourced from rainfall and permafrost, but no glacial meltwaters feed the streams (Ermolin and Silva-Busso, 2008). The basin is interpreted as a hummocky moraine related to Warszawa glacial retreat. It is an area of the discontinuous permafrost, with closed talik formation in the surface drainage area and open talik below Lake Matías. The groundwater is considered as an active and integrated supra-permafrost aquifer system throughout the southern summer (September to May inclusive), which flows toward Potter Cove (Silva-Busso, 2009).

The dynamic nature of the streams on the Potter Peninsula meant it was not possible to quantify discharge of the sampled streams. However, annual discharge into Potter Cove from Fourcade Glacier is estimated as 25 ± 6 hm^3 $year^{-1}$ (Falk et al., 2018), leading to an estimate of annual specific discharge of 1.1 ± 0.26 m $year^{-1}$. This is lower than the specific discharge of Greenlandic Glaciers previously studied for $\delta^{30}Si_{DSi}$ composition (Leverett Glacier and Kiattuut Sermiat Glacier, Hatton et al., 2019a), but Leverett Glacier has the most similar specific discharge (1.8–3.7 m $year^{-1}$, Hawkings et al., 2016), thus was chosen as the site to compare results from this study. The streams on Potter Peninsula overlay modern glacial deposits which have high lithological homogeneity (Falk et al., 2018). The bedrock of Potter Peninsula mainly consists of the King George Island Supergroup, which is made up of lavas and volcanoclastic rocks of basaltic and andesitic characteristics (Birkenmajer, 1980; Kraus, 2005; Ye et al., 2018).

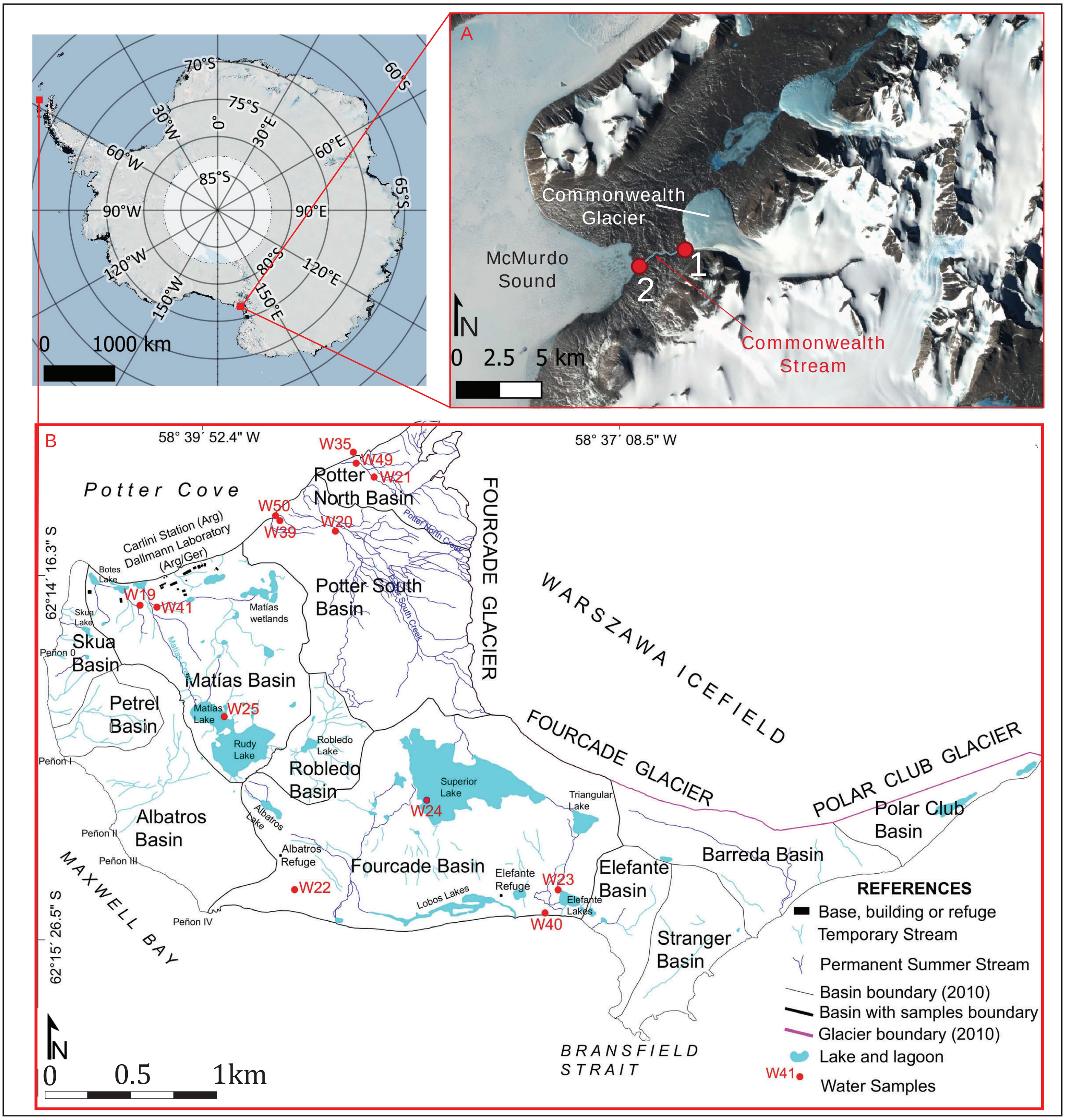

FIGURE 1 | Sampling location map. Sample locations shown in red, with labeling corresponding to sample points described in Section "Materials and Methods." **(A)** Two sampling locations (red circles) on Commonwealth Stream (drawn in blue). 1 shows the location of the majority of samples and the discharge gauge station (Commonwealth Gauge) and 2 shows the location of the partial diurnal samples collected at the stream mouth (Commonwealth Mouth). Figure created using Quantarctica and QGIS, produced by the Norwegian Polar Institute (Matsuoka et al., 2018). **(B)** Sampling location of streams on Potter Peninsula, King George Island (red circles), with the estimated drainage network and the hydrogeological basins. Due to the transient nature of the streams and it is very likely that not all the streams present in the basins are marked. Base map by Lusky et al. (2001), which was geohydrologically corrected over successive field campaigns.

It was not within the scope of this study to examine streams from more than one area of King George Island; however, major ion analysis of streams on Potter Peninsula shows similar geochemical compositions to rivers previously studied on King George Island (Ye et al., 2018). Meltwater streams on Fildes Peninsula have Si concentrations of 34 ± 20 μM (Ye et al., 2018), which compares well with the Si concentrations reported in this study [29.2 (11.1–58.0) μM], suggesting we can apply the $\delta^{30}Si_{DSi}$ composition of Potter Peninsula to other glacially fed streams on King George Island.

Sampling Protocol and Analysis

Water samples from Commonwealth Stream were filtered through 0.4 μm Whatman Nuclepore polycarbonate membrane filters within 24 h of collection (Olund et al., 2018). Samples were kept refrigerated and in the dark until analysis. Samples from King George Island were sequentially filtered through 5 and 0.45 μm Millipore Durapore PFDF filters which were pre-cleaned with 3% Elma Clean 70 (an alkaline detergent), deionized water, aqua regia (distilled HCl and HNO_3), and ultra-pure water. The filtration was performed on the day of sampling. The filtrate was acidified with double distilled HCl to ~pH 2 and sample bottles were kept in the dark until processing and analysis. All sample bottles were cleaned with 3% Elma 70 (7 days), deionized water (three rinses), 3 M HNO_3 (p.a.) (21 days), deionized water (1 day), 0.4 M HCl distilled. (7 days), 0.01 M HCl double distilled (7 days), and MilliQ (1 day) before use.

Dissolved silicon (DSi) was measured spectrophotometrically using flow injection analysis (FIA) on a LaChat 8500 series (QuikChem Method 31-114-27-1-D) at the University of Bristol and using a Skalar San^{++} Automated Wet Chemistry Analyzer at The Ohio State University, as detailed previously by Hawkings et al. (2017) and Olund et al. (2018).

Major ions for Commonwealth Stream samples were determined using a Dionex 120 at the Crary Laboratory at McMurdo Station, as detailed by Welch et al. (2010). Major ions for King George Island were determined by ion chromatography, using a Thermo Scientific^{TM} Dionex^{TM} capillary ICS-5000 fitted with anion and cation columns at the University of Bristol (Hawkings et al., 2015). We used the divalent/monovalent ion ratio (D:M) as an indication of carbonate and silicate weathering, with elevated proportions of monovalent ions linked to enhanced silicate mineral weathering (Wadham et al., 2010).

As both sampling locations at Commonwealth Stream are within close proximity to the ocean, atmospheric inputs were corrected for using a normalization to chloride (Stallard and Edmond, 1981; Grosbois et al., 2000). The riverine portion of the major ions for samples from Commonwealth Stream was calculated by Eq. 1:

$$X_{[Riv]} = X_{[Measured]} - (Cl_{[Measured]} \times (X/Cl)_{[Mar]}) \qquad (1)$$

where $X_{[Measured]}$ and $Cl_{[Measured]}$ are the original molar concentrations of the element of interest and Cl, respectively, and (X/Cl)[Mar] is the molar ratio of the element of interest to Cl in seawater, according to Millero et al. (2008). Samples collected from Potter Peninsula were acidified on collection with HCl, so a correction based on Cl was not possible. Therefore, we applied the average atmospheric input correction that was previously used for samples from Fildes Peninsula, King George Island (Ye et al., 2018). When applying the atmospheric input correction, the D:M ratio for Commonwealth Stream samples were impacted more strongly than those from Potter Peninsula and some samples resulted in negative Na^+ values (**Supplementary Table S2**). This overcorrection likely arose from the assumption that all Cl^- in the samples derived from atmospheric input. Crompton et al. (2015) described elevated Cl^- in subglacial waters, which could be associated with Na dissolution and/or precipitation into secondary weathering products during basal freeze-on, and higher Cl^- concentrations of the supraglacial waters reaching the bed, due to preferential retention of Cl^- in the snow and ice pack. However, we chose to maintain this correction to ensure our dataset is comparable with other studies in close proximity.

Silicon isotope analysis was completed at the Bristol Isotope Laboratories (University of Bristol) using Thermo Scientific Neptune Plus High Resolution MC-ICP-MS. Detailed methods have been published previously (Hawkings et al., 2018; Hatton et al., 2019a) but, briefly, a standard-sample bracketing procedure was employed, with Mg-doping to correct for instrumental mass bias (Cardinal et al., 2003). Samples were also doped with 100 μL 0.1 M sulfuric acid (Romil-UpA) to ensure matrix match between sample and standard and reduce the mass bias effects of anion loading (Hughes et al., 2011). Most samples were measured in triplicate, with typical reproducibility of ±0.07‰ (0.01–0.15‰, 2SD). Long-term reproducibility of $\delta^{30}Si$ of reference standards LMG and Diatomite were -3.44 ± 0.07 (2SD, n = 138) and +1.22 ± 0.07 (2SD, n = 99) respectively. A comparison of $\delta^{30}Si$ and $\delta^{29}Si$ showed a mass-dependent fractionation line with gradient 0.5130 (**Supplementary Figure S3**, Reynolds et al., 2007).

Some samples from Potter Peninsula were collected in duplicate with one sample being additionally filtered using Vivaflow 200 cross flow cassettes which were pre-cleaned with EDTA and ultrapure water. Ultra-filtration was performed to determine potential differences between the methodologically defined dissolved fraction that may still contain colloids and nanoparticles and the truly dissolved fraction, as highlighted in Patagonian glacial rivers (Pryer et al., Submitted). $\delta^{30}Si_{DSi}$ composition analysis was completed on both sets of water samples to assess potential effects of colloidal phases on the $\delta^{30}Si_{DSi}$ composition in the 0.45 μm filtered samples. **Supplementary Table S3** shows that $\delta^{30}Si_{DSi}$ compositions of 0.45 μm and ultra-filtered samples are similar. It was therefore decided to use the 0.45 μm samples throughout this study for consistency.

Stream bed sediments from Commonwealth Stream were analyzed using scanning electron microscopy (SEM), to evaluate mineral alteration. Samples were collected close to the Gauging Station, stored at room temperature, and allowed to air dry. Prior to analysis, samples were placed on carbon tape on an aluminum stub and then coated with gold/palladium with a Denton Desk V precious metal coater. SEM was completed with a FEI Quanta FEG 250 Field Emission SEM equipped with a Bruker EDX detector. Most images were collected at 15 kV using backscattered electron detector (BSE), with grayscale images providing some compositional information.

RESULTS

Both Commonwealth Stream and the streams of the Potter Peninsula have a similar average and range of $\delta^{30}Si_{DSi}$

TABLE 1 | Summary of geochemical data for Commonwealth Stream and Potter Peninsula (this study) and Leverett Glacier Greenland (Hatton et al., 2019a) for comparison to a well-categorized polythermal glacial system.

	Commonwealth Stream*		**Potter Peninsula***		**Leverett Glacier, Greenland[1]**		**Commonwealth Glacier Cryoconite Holes[2]***	
	Average (*n* = 18)	**Range**	**Average (*n* = 12)**	**Range**	**Average (*n* = 129)****	**Range**	**Average (*n* = 24)****	**Range**
DSi (μmol)	23.1	8.7–89.7	31.7	15.5–58.0	26.4	9.2–56.9	–	–
δ^{30}Si (‰)	0.42	−0.40 to 1.14	0.56	−0.23 to 1.23	0.07 (*n* = 17)	−0.55 to 0.87	–	–
Na^+ (μeq)	346.9	2.87–1504	379.4	47.3–1037	53.1	19.6–88.1	33.3 (*n* = 13)	9.37–104.0
K^+ (μeq)	29.2	9.57–83.8	7.59	0.90–22.25	28.4	9.7–59.3	40.6	10.7–60.7
Ca^{2+} (μeq)	167.6	95.6–357.5	267.5	52.3–779.0	154	52.2–528	336.6	52.3–646.4
Mg^{2+} (μeq)	34.0	8.28–65.5	70.16	10.8–194.8	38.5	11.1–158	81.6	9.40–169.8
D:M (μeq)	3.04	0.14–12.4	1.21	0.40–2.98	2.3	0.98–5.2	5.25 (*n* = 13)	1.76–9.12
SO_4^{2-} (μeq)	60.5	31.8–110.4	148.6	16.8–348.3	83.9	20.4–355	204.5	12.9–594.2

*Average values for Commonwealth Stream and Potter Peninsula are not discharge-weighted due to lack of discharge data. Major ion data from Commonwealth Stream and Potter Peninsula reported here have been corrected for atmospheric deposition. [1] Data from Leverett Glacier, Greenland from 2015 melt season (Hatton et al., 2019a). [2] Data from McMurdo Dry Valleys LTER (Fountain, 2014). *Major ion data corrected for atmospheric deposition. **Unless stated otherwise in table.*

composition, +0.42‰ (-0.40 to +1.14‰) and +0.54‰ (-0.23 to +1.23‰) respectively (**Table 1** and **Figure 2**). These values are isotopically light in comparison with recent global data compilations of non-glacial rivers [+1.37‰ (-0.14 to +4.66‰), Frings et al., 2016; Hatton et al., 2019b], and they correspond well to the average $\delta^{30}\mathrm{Si}_{\mathrm{DSi}}$ composition of glacial rivers [+0.16‰ (-0.58 to +1.01‰), Hatton et al., 2019b]. However, when considering each location in more detail, we see differences in the $\delta^{30}\mathrm{Si}_{\mathrm{DSi}}$ composition dependent on the predominance of specific weathering processes.

There is a significant difference between the $\delta^{30}\mathrm{Si}_{\mathrm{DSi}}$ composition measured at the Gauging Station and Mouth Station in Commonwealth Stream, with the lightest $\delta^{30}\mathrm{Si}_{\mathrm{DSi}}$ composition at the Mouth Station. When separating the gauge and mouth samples, we see a much narrower $\delta^{30}\mathrm{Si}_{\mathrm{DSi}}$ composition range at both locations. The average gauge $\delta^{30}\mathrm{Si}_{\mathrm{DSi}}$ composition was +0.67‰ (+0.27 to +1.14‰) for the 3-year study period, and the average mouth $\delta^{30}\mathrm{Si}_{\mathrm{DSi}}$ composition was -0.08‰ (-0.40 to +0.38‰), for the 1 day of sample collection in January 2016. Sampling location is also an important factor on Potter Peninsula: samples collected from streams with no glacial influence in Matías Basin have consistently higher $\delta^{30}\mathrm{Si}_{\mathrm{DSi}}$ compositions (+0.8 to +1.23‰) than streams in Potter South, Potter North, and Fourcade Basin (-0.23 to +0.72‰), which are mainly influenced by glacial meltwaters.

The relationship between $\delta^{30}\mathrm{Si}_{\mathrm{DSi}}$ composition and DSi is contrasting between the Commonwealth Stream and Potter Peninsula (**Figure 2**), with higher DSi concentrations resulting in lower $\delta^{30}\mathrm{Si}_{\mathrm{DSi}}$ values in Commonwealth Stream ($R^2 = 0.665$, p-value < 0.0001) but higher $\delta^{30}\mathrm{Si}_{\mathrm{DSi}}$ composition in Potter Peninsula ($R^2 = 0.545$, p-value < 0.001). **Figure 2** shows Potter Peninsula and Leverett Glacier, Greenland have similar relationships between $\delta^{30}\mathrm{Si}_{\mathrm{DSi}}$ composition, DSi, and D:M ratio. In contrast, Commonwealth Stream follows the typical relationship between $\delta^{30}\mathrm{Si}_{\mathrm{DSi}}$ composition and DSi in non-glacial rivers (Frings et al., 2016). We have chosen to use Leverett Glacier to consider how Potter Peninsula streams behave when compared to Arctic glaciers because Leverett Glacier is one of the most well-studied Arctic glaciers. The $\delta^{30}\mathrm{Si}_{\mathrm{DSi}}$ record from Leverett Glacier is also the most complete time-series, spanning almost the entire 2015 melt season, which was considered a relatively "typical" melt season in terms of discharge in recent years, with annual specific discharge in the same order of magnitude as Fourcade Glacier (see section "Materials and Methods"). While $\delta^{30}\mathrm{Si}_{\mathrm{DSi}}$ data exist from other glacial rivers in Arctic and sub-Arctic regions (see Hatton et al., 2019b for a complete dataset to date), these are mainly spot samples, without wider context. The data from Leverett Glacier provide the most comprehensive study of $\delta^{30}\mathrm{Si}_{\mathrm{DSi}}$ composition thus far, considering changes in dissolved and amorphous δ^{30}Si over a melt season within the context of wider hydrogeochemical parameters, due to the large numbers of studies that have focused upon Leverett Glacier over several years. The relationships between $\delta^{30}\mathrm{Si}_{\mathrm{DSi}}$ and DSi or D:M compiled in Hatton et al. (2019b) are not statistically significant, but this is likely a reflection of the complexities in comparing a snapshot of numerous glacial systems with differing subglacial geologies, hydrological drainage developments, and/or water residence times. Thus we compare our data with Leverett Glacier in an attempt to ensure the comparisons are straightforward and inferences about the systems can be made.

Figure 2 also shows that there are systematically lower D:M ratios with lower $\delta^{30}\mathrm{Si}_{\mathrm{DSi}}$ composition in both systems, although relationships are not statistically significant, likely due to complexity of the environments. This concurs with the data from Arctic and sub-Arctic glaciers (Hatton et al., 2019b). There is also a narrower range (at lower values) of D:M ratios at Potter Peninsula, which may be expected as the bedrock is made up basaltic volcanic rocks, compared to a more heterogenous bedrock lithology in the MDV. However, this is unlikely to impact our interpretations of $\delta^{30}\mathrm{Si}_{\mathrm{DSi}}$ composition. This is because

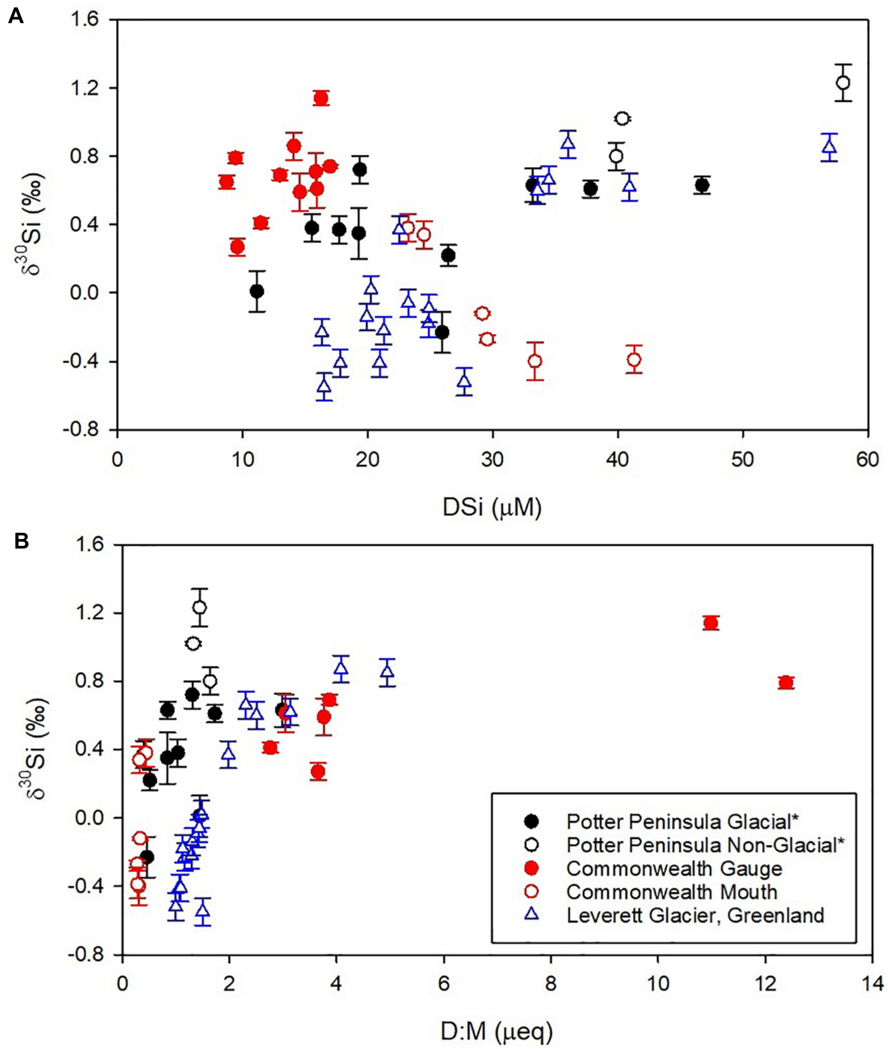

FIGURE 2 | Silicon isotope (δ^{30}Si) composition of Potter Peninsula, King George Island (black), Commonwealth Stream (red), Antarctica and Leverett Glacier, Greenland (blue). **(A)** δ^{30}Si composition versus dissolved silicon (DSi) concentration and **(B)** δ^{30}Si composition versus divalent/monovalent ratio (D:M) as a proxy for carbonate to silicate weathering. D:M ratios are calculated from major ion data corrected for atmospheric deposition for Potter Peninsula and Commonwealth Stream (demoted by *). Major ions from Leverett Glacier have not been corrected for atmospheric deposition, in line with standard practice of published data from Leverett Glacier. Error bars for Potter Peninsula and Commonwealth Stream are calculated from the 2SD of the external error of triplicated measurements, with an average of 0.07‰. Error bars for Leverett Glacier are 2SD external error of replicated standards (0.08‰, Hatton et al., 2019a).

bedrock has little impact on riverine $\delta^{30}\mathrm{Si}_{\mathrm{DSi}}$ composition, due to the relatively homogeneous $\delta^{30}\mathrm{Si}_{\mathrm{DSi}}$ composition of bulk bedrock and the upper continental crust (Bulk Silicate Earth = -0.29 ± 0.08‰) compared to the large fractionation induced by weathering and biological processes (Savage et al., 2010; Frings et al., 2016).

DISCUSSION

The similarity in the range of $\delta^{30}\mathrm{Si}_{\mathrm{DSi}}$ composition for both Potter Cove and Commonwealth Streams is surprising given the differences in glacier thermal regime and retreat history. However, a closer analysis of other geochemical parameters suggests these streams drain catchments in which there are contrasting geochemical weathering processes, which in turn influence the $\delta^{30}\mathrm{Si}_{\mathrm{DSi}}$ composition in each catchment. This is highlighted by the opposing relationships between DSi and $\delta^{30}\mathrm{Si}_{\mathrm{DSi}}$ composition in the two catchments. The negative relationship between DSi and $\delta^{30}\mathrm{Si}_{\mathrm{DSi}}$ composition in Commonwealth Stream is consistent with that found in the majority of global rivers and reflects the removal of Si from solution into secondary weathering products or biogenic silica (Sutton et al., 2018). In comparison, DSi and $\delta^{30}\mathrm{Si}_{\mathrm{DSi}}$ composition in Potter Peninsula follow a positive relationship, which is also reported in Greenlandic glacial rivers, and likely reflects an addition of Si from dissolution processes (Hatton et al., 2019a). This suggests that the absence of an active subglacial environment in the Dry Valley's stream is a primary influence upon its chemical composition and renders the $\delta^{30}Si_{DSi}$ composition more similar to other non-glacial rivers. We can also use the D:M ratio of each catchment to infer differing processes between the two catchments, with changes in $\delta^{30}Si_{DSi}$ composition and the D:M ratio at Potter Peninsula driven by subglacial weathering, compared to in-stream weathering reactions in Commonwealth Stream in absence of subglacial weathering. In the following sections, we explore the key differences in ion ratios and $\delta^{30}Si_{DSi}$ composition in MDVs and Potter Peninsula.

In-Stream Weathering Impacts $\delta^{30}Si_{DSi}$ Composition in McMurdo Dry Valleys

Previous studies have found that the chemistry of streams in MDV is dominated by in-stream weathering processes, involving the dissolution of minerals from the stream bed and the hyporheic zone (Gooseff et al., 2002; McKnight et al., 2004; Welch et al., 2010). Interestingly, the major ion composition of stream waters at the Gauging Station was very similar to that of cryoconite holes on Commonwealth Glacier, although the Mouth Station samples differed significantly (**Figure 3**). Cryoconite holes are small, water filled holes (covered with an ice lid in MDV), which are created by the solar heating of aeolian debris on the surface of the glacier (Bagshaw et al., 2013; Fortner and Lyons, 2018). There is evidence that supraglacial melt impacts upon the streams and lakes downstream, particularly during high flow conditions (Lyons et al., 2003; Fortner et al., 2005; Bagshaw et al., 2007, 2013). Fortner et al. (2005) estimated that >80% of the discharge into Lake Hoare is of supraglacial origin from Canada Glacier, and Fountain et al. (2004) estimated that cryoconite holes contribute approximately 15% of the total water flux, highlighting the potential importance of the supraglacial melt system on stream chemistry. The interaction between meltwater and sediment in the cryoconite is the primary opportunity for solute acquisition before the water enters the ephemeral stream system. The similarity in major ion composition between cryoconite holes and stream water at the Gauging Station supports the assertion that the network of cryoconite holes is a critical geochemical component in the cold-based glacier system.

The $\delta^{30}Si_{DSi}$ composition at the Gauging Station is higher than other glacial rivers, indicating that the lack of high physical erosion rates and mechanochemical reactions beneath cold-based glaciers results in a riverine $\delta^{30}Si_{DSi}$ composition most similar to non-glacial rivers. The $\delta^{30}Si_{DSi}$ composition may also be impacted by diatom-containing microbial mats, which have been observed upstream of the Gauging Station in Commonwealth Stream. Diatoms utilize and potentially drawdown DSi, which would result in isotopic fractionation and residual waters downstream to be isotopically heavier. There is evidence of a relationship between high discharge events and particulate organic matter (Cullis et al., 2014), but there is a suggestion that the microbial mats are generally resilient under normal flow events. Thus, we would not expect large amounts of biogenic Si dissolution to occur from these

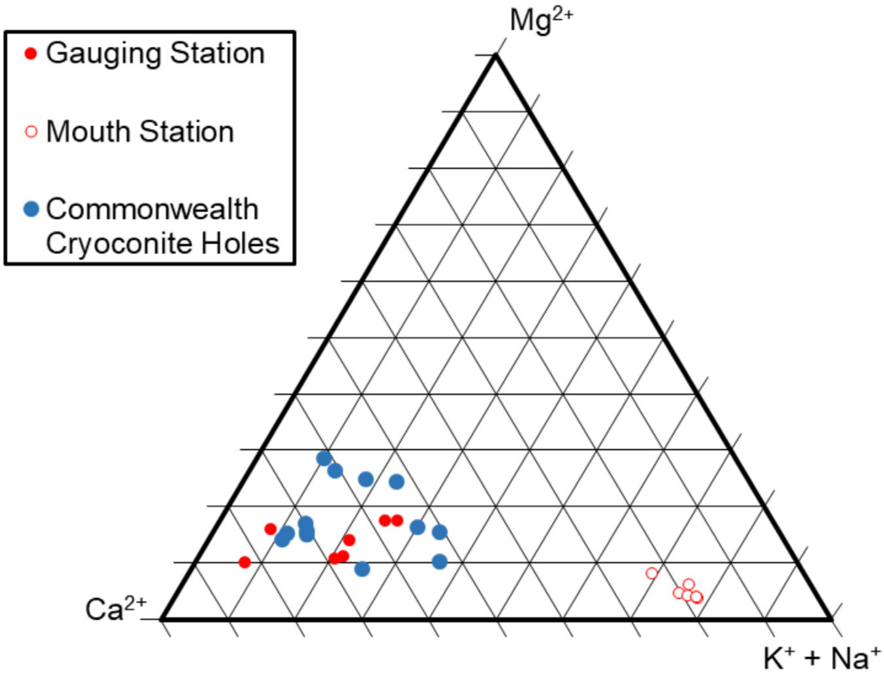

FIGURE 3 | Ternary diagram comparing major ion composition of Commonwealth Stream and Commonwealth Cryoconite holes. All major ion data have been corrected for atmospheric deposition. Commonwealth Stream have been separated by gauge (closed red circles) and mouth (open red circles) samples. Data from Cryoconite holes on Commonwealth Glacier are from McMurdo Dry Valleys LTER (Fountain, 2014).

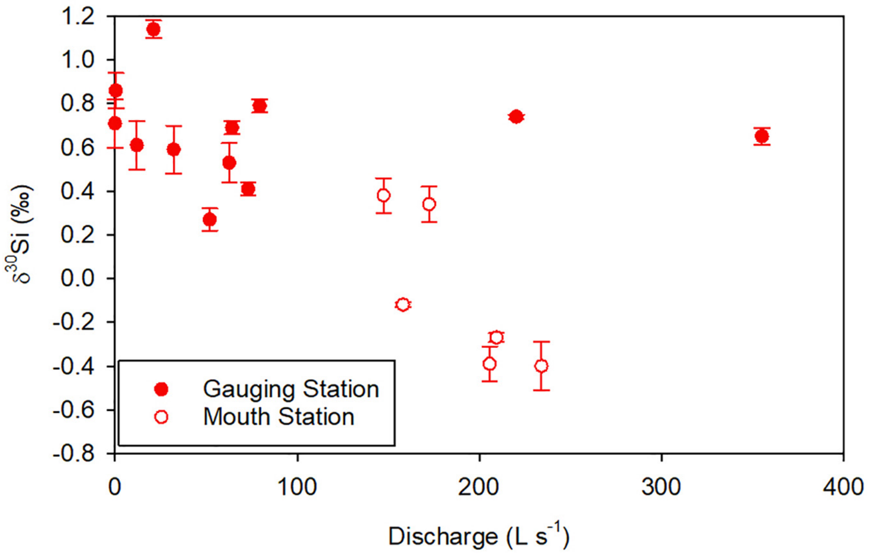

FIGURE 4 | Impact of sampling location on silicon isotopic (δ^{30}Si) composition in Commonwealth Stream. Samples collected further downstream at the mouth (open circles) have lower δ^{30}Si composition at the same discharge as those collected upstream at the gauging station (closed circles). Error bars are calculated from the 2SD of the external error of triplicated measurements, with an average of 0.07‰.

microbial mats except potentially at very high flow events (above 100 L s^{-1}). However, even at these high flow events at the Gauging Station, we see no impact upon $\delta^{30}Si_{DSi}$ composition (**Figure 4**), suggesting minimal fractionation inducing processes, such as precipitation or re-dissolution associated with changes in flow conditions. This is consistent with previous work in MDV that indicates that concentration-discharge relationships are chemostatic (Wlostowski et al., 2018), as high chemical weathering rates (e.g., Gooseff et al., 2002) result in short equilibrium timescales (Wlostowski et al., 2018).

In comparison, the $\delta^{30}Si_{DSi}$ composition at the Mouth Station is isotopically light, and the significant deviation from the cryoconite major ion proportions at this location demonstrates that in-stream weathering adds additional solute as the water progresses further through the Dry Valley hydrological system. However, it must be noted that we only have samples from the Mouth Station from one day in the 2016 melt season, at relatively high flow conditions and following a large discharge event. The flow conditions within the streams have a major impact on the geochemistry further downstream, since they control the interaction with the hyporheic zone (Gooseff et al., 2002). Hyporheic zones are the sediment and pore space adjacent to the streams, where water exchange occurs, and are zones of chemical weathering and sources of inorganic solutes (Gooseff et al., 2002). Interactions between the hyporheic zone and the stream increase downstream under all flow conditions, particularly in longer streams and interactions also increase as the season progresses as the temperature warms and the active layer depth increases. Under high flow conditions, the extent of the hyporheic may be further expanded due to the warmer conditions associated with high flow, resulting in further deepening of active layer. The similarity between stream major ion composition at the Mouth Station and hyporheic zone composition supports that the stream waters are influenced by the hyporheic zone during our sampling at the Mouth Station.

We hypothesize that the high flow and interactions with the hyporheic zone may also have influenced the $\delta^{30}Si_{DSi}$ composition at the Mouth Station, via enhanced silicate dissolution. For example, there is a relationship between discharge and δ^{30}Si composition at the Mouth Station. The stream was sampled over a 4-h period while discharge was increasing (**Supplementary Figure S1**) and higher discharge resulted in lower δ^{30}Si composition (**Figure 3**). The discharge during the 2015/16 flow season was generally much higher than preceding and subsequent flow seasons, with a peak flow 2 weeks prior to sample collection at the Mouth Station of 900 L s^{-1} (**Supplementary Figure S1**), which is nine times greater than the threshold for a "flood event" (Cullis et al., 2014). We would expect the active layer to have thawed more by the time we sampled at the Mouth Station, as the active layer thaws more later in the season (Conovitz et al., 2006) and this large flood event will have promoted greater active layer thaw due to the associated higher temperatures. We therefore predict geomorphic disturbances of the stream bed may have occurred, which could have altered flow paths and may have resulted in water exchange in areas of the hyporheic zone that have been undergoing weathering for longer in relative isolation. The creation of new flow paths could therefore promote the dissolution of weathering products, which would result in isotopically lighter $\delta^{30}Si_{DSi}$ composition of the stream waters. There is also evidence of increased suspended particulate matter (SPM) in the MDV streams in recent years, with fine sediments coming from the stream banks (Gooseff et al., 2016; Leslie et al., 2017) and expansion of the wetted perimeter during high flow may have led to the dissolution of channel-margin salt crusts (Wlostowski et al., 2018). While the streams are usually very clear and lack suspended sediments (Gooseff et al., 2016), it may have been that during this high flow event a higher proportion of fine sediment was entrained into the stream. Previous studies of Commonwealth Stream have shown an increase in dissolved Si concentrations downstream (Olund et al., 2018), indicating a dissolution of primary minerals and SEM images of stream sediments provide evidence of primary mineral alteration (**Supplementary Figure S4**). This is consistent with the $\delta^{30}Si_{DSi}$ composition data, since primary mineral dissolution will result in lower $\delta^{30}Si_{DSi}$ composition and this dissolution would be promoted in an undersaturated system. Hyporheic waters have been shown to be undersaturated with respect to albite, chlorite, illite, K-feldspar, quartz, and SiO_2 (Gooseff et al., 2002), which further supports the notion that silicate dissolution continues to add solute to river waters downstream. SEM images (**Supplementary Figure S4**) also indicate the presence of secondary weathering products, potentially smectite or zeolite, which would be expected, considering findings from suspended sediments from other streams in MDV. Sediments from both Huey and Green Creeks have considerable amorphous weathering products, with a higher proportion of clay materials compared to primary minerals (Gooseff et al., 2002). Dissolution of these secondary weathering products would also result in an influx of isotopically light silicon, which could have lowered the $\delta^{30}Si$ composition of the stream.

The difference in $\delta^{30}Si_{DSi}$ composition between the Gauging Station and the Mouth Station, and the consistent $\delta^{30}Si_{DSi}$ composition at the Gauging Station despite changes in discharge suggests that downstream transport impacts stream chemistry and $\delta^{30}Si_{DSi}$ composition, likely due to mineral dissolution. However, we must also consider that the high flow conditions during sampling at the Mouth Station may have an impact, which may not wholly reflect the downstream conditions and $\delta^{30}Si_{DSi}$ composition exported into the McMurdo Sound under present climatic conditions. It would be advisable to consider the average $\delta^{30}Si_{DSi}$ composition from the Gauging Station as more likely to be representative of streams within the MDV, as most streams are relatively short resulting in less interactions with the hyporheic zones and thus less mineral dissolution, which is consistent with findings from Hirst et al. (Submitted to this Special Issue). The heavier $\delta^{30}Si_{DSi}$ compositions of Crescent Stream indicate that the precipitation of secondary weathering products, rather than mineral dissolution is driving the stream $\delta^{30}Si_{DSi}$ composition, with additional influence of different stream bed and hyporheic zone weathering conditions. These could include variations in (i) the starting primary mineral compositions, (ii) extent of secondary mineral formation, (iii) hyporheic zone width and thus area over which weathering can occur, (iv) stream flow and thus stream erosive capacity, and (v) extent of diatom uptake and dissolution in stream microbial mats. The discrepancy between Si concentrations and isotopic compositions between the Mouth and Gauging stations are related to downstream weathering processes and/or high flow conditions. The data from the Mouth Station may represent a high-flow endmember which could be useful when considering future changes to the MDV. In combination, these observations highlight the potential for different hyporheic zone processes to mediate the $\delta^{30}Si_{DSi}$ composition in MDV streams. These findings contribute to our understanding of Si weathering fluxes in MDV streams and provide a baseline for predicting future Si weathering fluxes in response to future climate change. There is evidence that the MDV is responding to climatic warming, with annual discharge between 2001 and 2016 being higher than the 8 years measured prior (Olund et al., 2018, MCM-LTER record[1]). Increasing temperatures are predicted to increase glacial melt and potentially increase the prevalence of "warm years" that experience higher than average temperatures and associated melt (Fountain et al., 2016). This may also lead to deepening of active layers, and increases of hyporheic zones and melt of buried ice (Fountain et al., 2014). These changes are likely to impact rock–water interaction times, weathering regimes and biogeochemical reactions within the streams (Olund et al., 2018), and $\delta^{30}Si_{DSi}$ data from the Mouth Station of Commonwealth Stream suggest that this could lead to stream waters with isotopically lighter $\delta^{30}Si_{DSi}$ composition.

Glacial Meltwaters of Potter Peninsula Impact Stream $\delta^{30}Si_{DSi}$ Composition

In contrast to MDV, which may see warming and associated changes in the future but are currently extremely cold, dry environments, the Fourcade Glacier on King George Island, has undergone rapid and significant retreat over the past decades. We have noted that the overall $\delta^{30}Si_{DSi}$ composition of Commonwealth Stream and Potter Peninsula is relatively similar; however, the DSi concentrations and major ion chemistry highlight differences in weathering processes. The geochemical relationships in surficial meltwater streams of Potter Peninsula reflect those of rivers draining glaciers with active subglacial environments, thus indicating that the difference in thermal regime between Commonwealth Glacier and Fourcade Glacier impacts upon silicon cycling.

It is important to note that streams on Potter Peninsula are fed from a mixture of sources; glacial melt, permafrost thaw, precipitation, and snow melt. It was not within the scope of this study to estimate the proportion of glacially derived waters into these streams due to complex and heterogenous nature of the mixed stream inputs (Silva-Busso et al., 2004), so we use hydrological basins defined by Silva-Busso (2009) to consider the likelihood of streams being impacted by glacial meltwater (**Supplementary Figure S2**).

Streams sampled in Matías Basin are considered as the non-glacial endmember, as this basin has no input from Fourcade glacial melt, as evidenced by the strong correlation between precipitation and discharge. Instead, streams in Matías Basin are likely dominated by precipitation, snowmelt, and seasonal permafrost melt, with the rapid development of the permafrost active layer in the summer. Below 60 m.a.s.l, permafrost on Potter Peninsula is discontinuous and there is evidence of approximately 30 m of thawed talik in the sediments of Matías Basin, covering basaltic bedrock. Streams

---

[1] http://mcmlter.org

in Matías Basin have consistently higher $\delta^{30}Si_{DSi}$ composition than all other streams on the Peninsula, consistent with previous observations of streams impacted by permafrost, where amorphous Si precipitation and clay formation result in fractionation (Pokrovsky et al., 2013; Sun et al., 2018; Hirst et al., 2020).

Streams in Potter North, Potter South, and Fourcade Basins have inputs from glacial meltwater; therefore, we group these streams together as "glacial" for discussion purposes (see **Supplementary Material** for further information). Glacial melt is routed via the subglacial environment, and then drains directly into surficial streams or enters streams via groundwater flow. However, we recognize that the proportion of glacial meltwater varies between streams and over time due to climatic factors and we are unable to quantify that in this study. Field observations indicate that subglacial meltwater contributes to the streams within Potter South, Potter North, and Fourcade Basin (Silva-Busso, 2009; Monien et al., 2017). Previously studied rivers draining warm or polythermal glaciers exhibit a positive relationship between $\delta^{30}Si_{DSi}$ composition and DSi concentration (Opfergelt et al., 2013; Sutton et al., 2018; Hatton et al., 2019a), which is opposite to the general trend seen in non-glacial rivers (Frings et al., 2016; Sutton et al., 2018). This positive relationship has been attributed to subglacial weathering processes and changes in discharge over the melt season. Subglacial weathering and changes in discharge are likely what is driving the $\delta^{30}Si_{DSi}$ composition of Potter Peninsula glacial streams. However, without discharge data from Potter Peninsula, we have to infer similar processes are occurring, based upon the similar relationship between DSi and $\delta^{30}Si_{DSi}$ as at Leverett Glacier. It has been hypothesized that the high physical erosion rates in the subglacial environment result in freshly ground mineral surfaces which are enriched in isotopically light Si (Ziegler et al., 2005; Hatton et al., 2019b). During times of high discharge, the melt waters access amorphous silica (ASi) surface layers, leading to re-dissolution and driving an increase in DSi concentration and a lower $\delta^{30}Si_{DSi}$ composition. However, the proportion of ASi that needs to undergo dissolution is minimal, thus the absolute DSi concentration decreases, due to the dilution effect of overall higher discharge (Hatton et al., 2019a).

The similar patterns between $\delta^{30}Si_{DSi}$ and DSi and major ion composition seen in Potter Peninsula glacial streams compared to Leverett Glacier suggest that the subglacial weathering processes under Fourcade Glacier may be comparable to those in under Arctic and sub-Arctic polythermal glaciers. Monien et al. (2017) describe higher SPM concentrations in streams in Potter South (2011 average of 283 ± 99 mg L^{-1}) compared to Matías Basin (consistently < 38 mg L^{-1}). This suggests that the glacially linked erosion processes could result in weathering product dissolution and therefore influence the $\delta^{30}Si_{DSi}$ composition of these streams. However, it is important to consider that the high SPM in the streams of Potter South (and other glacial basins) are likely resulting from the proglacial environment in addition to the active subglacial system. For example, sites that are more recently ice free (such as those in Potter South) have higher proportions of freshly ground material (Monien et al., 2017). While measurements of proglacial till at Leverett Glacier, Greenland, showed very low ASi concentrations (Hatton et al., 2019a), the relatively recent retreat of Fourcade Glacier could mean that these sediments have not undergone as much weathering in the proglacial environment and the dissolution processes that occur when the streams flow in summer are similar to subglacial dissolution of ASi.

When considering the drivers of $\delta^{30}Si_{DSi}$ composition in the glacial streams on Potter Peninsula, we must also acknowledge that the streams in this study were not sampled immediately at the glacier terminus and thus other water sources may contribute to the streams. Therefore, the variation in meltwater proportion to the streams on Potter Peninsula may help to explain the range of $\delta^{30}Si_{DSi}$ values for streams, with higher proportions of glacial meltwater and/or less influence from permafrost thaw resulting in lower $\delta^{30}Si_{DSi}$ composition. Lentic systems also exist with the basins, which host active phytoplankton communities. This may help to explain why, although isotopically light, the $\delta^{30}Si_{DSi}$ composition of the stream waters from Fourcade Glacier is not as light as at Leverett Glacier, where no phytoplankton activity is present and the proglacial river measured is almost entirely sourced from the subglacial environment.

Interestingly, the lightest $\delta^{30}Si_{DSi}$ value measured on Potter Peninsula (-0.23‰) was from a stream within the Fourcade Basin, downstream of a lake. The presence of microbial mats in the lakes of Potter Peninsula (Vinocur and Pizarro, 2000) may result in biological uptake of Si and isotopic fractionation, leading to higher $\delta^{30}Si_{DSi}$ composition in outflow streams. However, it may be that a large proportion of the stream is fed by groundwater flow, originating subglacially. This could help to explain the isotopically light DSi via re-dissolution of mineral weathering products, similar to the processes hypothesized in subglacial environments with elevated rock–water interaction times (Hatton et al., 2019a), especially considering the present of fluvial-glacial sediments in the region. However, we are unable to quantify this with the present dataset, and would recommend an integrated study of these streams in the future, quantifying both water sources and flow paths to better understand the drivers of stream geochemistry in the region.

The Si fluxes from King George Island may not be as significant as Si export from Arctic glaciers for the downstream ecosystem, as surrounding coastal waters are already elevated in DSi. For example, subsurface seawater of adjacent seas of King George Island has an average Si concentration of 60 μM (Ye et al., 2018). However, this environment does provide an interesting study location, with streams potentially impacted by contrasting weathering regimes depending on the influence of glacial meltwaters. The glacial streams provide further understanding of silicon cycling below polythermal glaciers and allow glacial $\delta^{30}Si_{DSi}$ composition to be informed by glaciers beyond the Arctic and sub-Arctic. That the $\delta^{30}Si_{DSi}$ composition of streams fed by Fourcade Glacier is within the range of other well-established glacial rivers may indicate that isotopically light $\delta^{30}Si_{DSi}$ composition of (polythermal) glacial meltwaters is a bi-polar phenomenon and will assist in informing global Si models.

However, the complexity of the streams within Potter Peninsula also highlights the importance of understanding the hydrogeochemistry of these environments when considering potential nutrient fluxes into the marine environment. For example, the potential differences in the streams not fed by glacial meltwaters in Matías Basin, which are a greater distance from the glacier front may present an interesting consideration of the importance of characterizing these rapidly changing environments, so that we can better estimate the likely changes to the glacial Si cycle in the future. As Fourcade Glacier retreats further, more areas of the Peninsula will be exposed resulting in higher proportions of recently eroded sediments to be transported. However, streams closer to the coast may be increasingly dominated by permafrost-weathering processes as meltwater streams have less of an impact further from the retreating glacier front. It is therefore likely that the $\delta^{30}Si_{DSi}$ composition of these streams will be impacted in the future under climatic warming and improving of our understanding of the drivers of Si cycling in these environments is key to being able to better predict these changes.

CONCLUSION

Silicon export and corresponding $\delta^{30}Si_{DSi}$ composition from glacially environments has recently been of interest due to its usefulness in understanding subglacial weathering processes and potential implications for downstream ecosystems. We have presented the first $\delta^{30}Si_{DSi}$ composition data for Antarctic streams, helping to extend the data availability of $\delta^{30}Si_{DSi}$ composition in glaciated areas. We have shown that the $\delta^{30}Si_{DSi}$ composition of streams from two contrasting environments on the Antarctic continent is very similar, yet both systems are driven by differing processes. In-stream weathering processes dominate the geochemistry of Commonwealth Stream in MDV, as highlighted by previous studies of the area, and there is a negative relationship between DSi and $\delta^{30}Si$ composition, resembling non-glacial rivers. These in-stream processes include the dissolution of primary minerals, resulting in lower $\delta^{30}Si_{DSi}$ composition at the stream mouth compared to further upstream toward to glacier. In comparison, glacially fed streams on Potter Peninsula behave very similarly to previously studied Arctic and sub-Arctic glacial rivers, and there is a positive relationship between DSi and $\delta^{30}Si$ composition. It is therefore likely that dissolution of weathering products from subglacial or recently exposed sediments impact the $\delta^{30}Si_{DSi}$ composition of glacial streams on Potter Peninsula. We expect that these weathering processes, dominated by high physical erosion rates, are ubiquitous to wet-based glaciers and we should expect low $\delta^{30}Si_{DSi}$ composition from the glacial rivers compared to non-glacial rivers.

The MDV and WAP are expected to undergo major changes due to climatic warming, which could impact on weathering processes, sediment loads, and export to the downstream ecosystems. Therefore, understanding the processes occurring at present is fundamental to being able to predict what changes may occur and inform future predictions.

DATA AVAILABILITY STATEMENT

The datasets generated for this study are available from https://doi.pangaea.de/10.1594/PANGAEA.914103.

AUTHOR CONTRIBUTIONS

KH and JH conceived the project. SH, SW, MS, WL, AS-B, and DM conducted fieldwork, sample collection, and hydrological monitoring. JH and SW completed laboratory analysis. All authors contributed to the data discussion and writing of the manuscript.

FUNDING

JH and KH were funded by the European Research Council starting grant ICY-LAB (agreement number 678371) and Royal Society Enhancement Award (RGF\EA\181036). Field campaigns to King George Island were funded via the German Research Foundation (DFG grant numbers STA 936/5-1 and KA 2769/3-1). CH and SO were funded by the European Research Council starting grant WeThaw (agreement number 714617) and National Funds for Scientific Research FNRS (Grant Nos. 26043653 and FC69480). WL and SW were funded by NSF grant to the MCM LTER project, OPP-ANT 1115249.

ACKNOWLEDGMENTS

The authors thank Jochen Scheld (University of Cologne), Jan Hartmann (MARUM), the staff of the Argentinian research station Carlini, and the adjoint Dallmann laboratory of AWI for field support on King George Island. The authors also thank the McMurdo Dry Valleys LTER team, particularly the Stream Team for assistance and use of the flow data. The authors are also grateful for laboratory support from Dr. Christopher D. Coath (Bristol Isotope Group) for isotopic data and Subsurface Energy Materials Characterization and Analysis Laboratory (SEMCAL), School of Earth Sciences, The Ohio State University for SEM images. The authors also thank the editor, Ramanathan Alagappan, and reviewers for their time and thorough reviews to improve the manuscript.

SUPPLEMENTARY MATERIAL

The Supplementary Material for this article can be found online at: https://www.frontiersin.org/articles/10.3389/feart.2020.00286/full#supplementary-material

REFERENCES

Annett, A. L., Skiba, M., Henley, S. F., Venables, H. J., Meredith, M. P., Statham, P. J., et al. (2015). Comparative roles of upwelling and glacial iron sources in Ryder Bay, coastal western Antarctic Peninsula. *Mar. Chem.* 176, 21–33. doi: 10.1016/j.marchem.2015.06.017

Ardelan, M. V., Holm-Hansen, O., Hewes, C. D., Reiss, C. S., Silva, N. S., Dulaiova, H., et al. (2010). Natural iron enrichment around the Antarctic Peninsula in the Southern Ocean. *Biogeosciences* 7, 11–25. doi: 10.5194/bg-7-11-2010

Bagshaw, E. A., Tranter, M., Fountain, A. G., Welch, K., Basagic, H. J., and Lyons, W. B. (2013). Do cryoconite holes have the potential to be significant sources of C, N, and P to downstream depauperate ecosystems of Taylor valley, Antarctica? *Arctic Antarctic Alpine Res.* 45, 440–454. doi: 10.1657/1938-4246-45.4.440

Bagshaw, E. A., Tranter, M., Fountain, A. G., Welch, K. A., Basagic, H., and Lyons, W. B. (2007). Biogeochemical evolution of cryoconite holes on Canada Glacier, Taylor Valley, Antarctica. *J. Geophys. Res.* 112:442.

Birkenmajer, K. (1980). Geology of admiralty bay, King George Island (South Shetland Islands) - an outline. *Pol. Polar Res.* 1, 29–54.

Cardinal, D., Alleman, L. Y., De Jong, J., Ziegler, K., and Andre, L. (2003). Isotopic composition of silicon measured by multicollector plasma source mass spectrometry in dry plasma mode. *J. Analyt. Atom. Spectrom.* 18, 213–218. doi: 10.1039/b210109b

Conovitz, P. A., Macdonald, L. H., and Mcknight, D. M. (2006). Spatial and temporal active layer dynamics along three glacial meltwater streams in the McMurdo Dry Valleys, Antarctica. *Arctic Antarctic Alpine Res.* 38, 42–53. doi: 10.1657/1523-0430(2006)038[0042:satald]2.0.co;2

Crompton, J. W., Flower, G. E., Kirste, D., Hagedorn, B., and And Sharp, M. J. (2015). Clay mineral precipitation and low silica in glacier meltwaters explored through reaction-path modelling. *J. Glaciol.* 61, 1061–1078. doi: 10.3189/2015jog15j051

Cuffey, K. M., Conway, H., Gades, A. M., Hallet, B., Lorrain, R., Severinghaus, J. P., et al. (2000). Entrainment at cold glacier beds. *Geology* 28, 351–354. doi: 10.1130/0091-7613(2000)028<0351:eacgb>2.3.co;2

Cullis, J. D. S., Stanish, L. F., and Mcknight, D. M. (2014). Diel flow pulses drive particulate organic matter transport from microbial mats in a glacial meltwater stream in the McMurdo Dry Valleys. *Science* 50, 86–97. doi: 10.1002/2013wr014061

Ermolin, E., and Silva-Busso, A. (2008). "Interaction between permafrost and groundwater on the potter Peninsula, King george Island, (Isla 25 de Mayo), Antarctica," in *The Antarctic Ecosystem Of Potter Cove, King-George Island (Isla 25 de MAYO). Synopsis of Research Performed 1999-2006 at the Dallmann Laboratory and Jubany Station Alfred Wegener Institute*, eds C. Wiencke, G. A. Ferreyra, D. Abele, and S. Marenssi, (Villa Lynch: Instituto Antartico Argentino).

Falk, U., López, D. A., and Silva-Busso, A. (2018). Multi-year analysis of distributed glacier mass balance modelling and equilibrium line altitude on King George Island, Antarctic Peninsula. *Cryosphere* 12, 1211–1232. doi: 10.5194/tc-12-1211-2018

Fortner, S. K., and Lyons, W. B. (2018). Dissolved trace and minor elements in cryoconite holes and supraglacial streams, Canada glacier, Antarctica. *Front. Earth Sci.* 6:31. doi: 10.3389/feart.2018.00031

Fortner, S. K., Tranter, M., Fountain, A., Lyons, W. B., and Welch, K. A. J. A. G. (2005). The geochemistry of supraglacial streams of canada glacier, Taylor Valley (Antarctica), and their evolution into Proglacial waters. *Cryosphere* 11, 391–412. doi: 10.1007/s10498-004-7373-2

Fountain, A. G. (2014). McMurdo Dry Valleys Lter: geochemistry data of cryoconite holes collected from Canada, commonwealth, howard, hughes and Taylor glaciers in Nov 2001 and Jan 2002. *Environ. Data Initiat.* doi: 10.6073/pasta/ba862a096fbc7fca4063c44ad3af3c0f

Fountain, A. G., Levy, J. S., Gooseff, M. N., and Van Horn, D. (2014). The McMurdo Dry Valleys: a landscape on the threshold of change. *Geomorphology* 225, 25–35. doi: 10.1016/j.geomorph.2014.03.044

Fountain, A. G., Saba, G., Adams, B., Doran, P., Fraser, W., Gooseff, M., et al. (2016). The impact of a large-scale climate event on antarctic ecosystem processes. *Bioscience* 66, 848–863. doi: 10.1093/biosci/biw110

Fountain, A. G., Tranter, M., Nylen, T. H., Lewis, K. J., and Mueller, D. R. (2004). Evolution of cryoconite holes and their contribution to meltwater runoff from glaciers in the McMurdo Dry Valleys, Antarctica. *J. Glaciol.* 50, 35–45. doi: 10.3189/172756504781830312

Frings, P. J., Clymans, W., Fontorbe, G., De La Rocha, C., and Conley, D. J. (2016). The continental Si cycle and its impact on the ocean Si isotope budget. *Chem. Geol.* 425, 12–36. doi: 10.1016/j.chemgeo.2016.01.020

Georg, R. B., Reynolds, B. C., West, A. J., Burton, K. W., and Halliday, A. N. (2007). Silicon isotope variations accompanying basalt weathering in Iceland. *Earth Planet. Sci. Lett.* 261, 476–490. doi: 10.1016/j.epsl.2007.07.004

Gerringa, L. J. A., Alderkamp, A. C., Laan, P., Thuroczy, C. E., De Baar, H. J. W., Mills, M. M., et al. (2012). Iron from melting glaciers fuels the phytoplankton blooms in Amundsen Sea (Southern Ocean): iron biogeochemistry. *Deep Sea Res. Part Top. Stud. Oceanogr.* 71–76, 16–31. doi: 10.1016/j.dsr2.2012.03.007

Gooseff, M. N., Mcknight, D. M., Lyons, W. B., and Blum, A. E. (2002). Weathering reactions and hyporheic exchange controls on stream water chemistry in a glacial meltwater stream in the McMurdo Dry Valleys. *Chem. Geol.* 38, 15–17.

Gooseff, M. N., Van Horn, D., Sudman, Z., Mcknight, D. M., Welch, K. A., and Lyons, W. B. (2016). Stream biogeochemical and suspended sediment responses to permafrost degradation in stream banks in Taylor Valley, Antarctica. *Biogeosciences* 13, 1723–1732. doi: 10.5194/bg-13-1723-2016

Grosbois, C., Négrel, P., Fouillac, C., and Grimaud, D. (2000). Dissolved load of the loire river: chemical and isotopic characterization. *Chem. Geol.* 170, 179–201. doi: 10.1016/s0009-2541(99)00247-8

Hall, B. L., and Denton, G. H. (2000). Radiocarbon chronology of ross sea drift, eastern taylor valley, antarctica: evidence for a grounded ice sheet in the ross sea at the last glacial maximum. *Geograf. Ann.* 82, 305–336. doi: 10.1111/j.0435-3676.2000.00127.x

Hambrey, M. J., and Fitzsimons, S. J. (2010). Development of sediment-landform associations at cold glacier margins, Dry Valleys, Antarctica. *Sedimentology* 57, 857–882. doi: 10.1111/j.1365-3091.2009.01123.x

Hatton, J. E., Hendry, K. R., Hawkings, J. R., Wadham, J. L., Kohler, T. J., Stibal, M., et al. (2019a). Investigation of subglacial weathering under the Greenland Ice Sheet using silicon isotopes. *Geochim. Cosmochim. Acta* 247, 191–206. doi: 10.1016/j.gca.2018.12.033

Hatton, J. E., Hendry, K. R., Hawkings, J. R., Wadham, J. L., Opfergelt, S., Kohler, T. J., et al. (2019b). Silicon isotopes in arctic and sub-arctic glacial meltwaters: the role of subglacial weathering in the silicon cycle. *R. Soc. Proc. A* 475:98.

Hawkings, J., Wadham, J., Tranter, M., Telling, J., Bagshaw, E., Beaton, A., et al. (2016). The Greenland Ice Sheet as a hot spot of phosphorus weathering and export in the Arctic. *Glob. Biogeochem. Cycles* 30, 191–210. doi: 10.1002/2015gb005237

Hawkings, J. R., Hatton, J. E., Hendry, K. R., De Souza, G. F., Wadham, J. L., Ivanovic, R., et al. (2018). The silicon cycle impacted by past ice sheets. *Nat. Commun.* 9:3210.

Hawkings, J. R., Wadham, J. L., Benning, L. G., Hendry, K. R., Tranter, M., Tedstone, A., et al. (2017). Ice sheets as a missing source of silica to the polar oceans. *Nat. Commun.* 8:14198.

Hawkings, J. R., Wadham, J. L., Tranter, M., Lawson, E., Sole, A., Cowton, T., et al. (2015). The effect of warming climate on nutrient and solute export from the Greenland Ice Sheet. *Geochem. Perspect. Lett.* 1, 94–104. doi: 10.7185/geochemlet.1510

Hawkings, J. R., Wadham, J. L., Tranter, M., Raiswell, R., Benning, L. G., Statham, P. J., et al. (2014). Ice sheets as a significant source of highly reactive nanoparticulate iron to the oceans. *Nat. Commun.* 5:3929.

Hendry, K. R., Huvenne, V. A. I., Robinson, L. F., Annett, A., Badger, M., Jacobel, A. W., et al. (2019). The biogeochemical impact of glacial meltwater from Southwest Greenland. *Prog. Oceanogr.* 176:102126. doi: 10.1016/j.pocean.2019.102126

Henkel, S., Kasten, S., Hartmann, J. F., Silva-Busso, A., and Staubwasser, M. (2018). Iron cycling and stable Fe isotope fractionation in Antarctic shelf sediments, King George Island. *Geochim. Cosmochim. Acta* 237, 320–338. doi: 10.1016/j.gca.2018.06.042

Henley, S. F., Jones, E. M., Venables, H. J., Meredith, M. P., Firing, Y. L., Dittrich, R., et al. (2018). Macronutrient and carbon supply, uptake and cycling across the Antarctic Peninsula shelf during summer. *J. Oceanogr.* 376:20170168. doi: 10.1098/rsta.2017.0168

Hirst, C., Opfergelt, S., Gaspard, F., Hendry, K. R., Hatton, J. E., Welch, S., et al. (2020). Silicon isotopes reveal a non-glacial source of silicon to Crescent Stream, McMurdo Dry Valleys, Antarctica. *Front. Earth Sci*. 8:299. doi: 10.3389/feart.2020.00229

Hodson, A., Nowak, A., Sabacka, M., Jungblut, A., Navarro, F., Pearce, D., et al. (2017). Climatically sensitive transfer of iron to maritime Antarctic ecosystems by surface runoff. *Nat. Commun.* 8:14499.

Höfer, J., Giesecke, R., Hopwood, M. J., Carrera, V., Alarcón, E., and González, H. E. (2019). The role of water column stability and wind mixing in the production/export dynamics of two bays in the Western Antarctic Peninsula. *Prog. Oceanogr.* 174, 105–116. doi: 10.1016/j.pocean.2019.01.005

Hood, E., Fellman, J., Spencer, R. G. M., Hernes, P. J., Edwards, R., D'amore, D., et al. (2009). Glaciers as a source of ancient and labile organic matter to the marine environment. *Nature* 462, 1044–U100.

Hopwood, M. J., Carroll, D., Browning, T. J., Meire, L., Mortensen, J., Krisch, S., et al. (2018). Non-linear response of summertime marine productivity to increased meltwater discharge around Greenland. *Nature* 9:3256.

Hughes, H. J., Delvigne, C., Korntheuer, M., De Jong, J., André, L., and Cardinal, D. (2011). Controlling the mass bias introduced by anionic and organic matrices in silicon isotopic measurements by Mc-Icp-Ms. *J. Analyt. Atom. Spectrom.* 26:1892. doi: 10.1039/c1ja10110b

Huh, Y., Chan, L.-H., Zhang, L., and Edmond, J. M. (1998). Lithium and its isotopes in major world rivers: implications for weathering and the oceanic budget. *Geochim. Cosmochim. Acta* 62, 2039–2051. doi: 10.1016/s0016-7037(98)00126-4

Jerosch, K., Pehlke, H., Monien, P., Scharf, F., Weber, L., Kuhn, G., et al. (2018). Benthic meltwater fjord habitats formed by rapid glacier recession on King George Island, Antarctica. *Philos. Trans. R. Soc. A* 376:20170178. doi: 10.1098/rsta.2017.0178

Kraus, S. (2005). *Magmatic Dyke Systems Of The South Shetland Islands Volcanic Arc (West Antarctica): Reflections Of The Geodynamic History*. Ph.D. Munich University Library, Munich.

Lawson, E. C., Wadham, J. L., Tranter, M., Stibal, M., Lis, G. P., Butler, C. E. H., et al. (2014). Greenland ice sheet exports labile organic carbon to the Arctic oceans. *Biogeosciences* 11, 4015–4028. doi: 10.5194/bg-11-4015-2014

Leal, M. A., Joppert, M., Licínio, M. V., Evangelista, H., Maldonado, J., Dalia, K. C., et al. (2008). Atmospheric impacts due to anthropogenic activities in remote areas: the case study of admiralty bay/king george island/Antarctic peninsula. *Water Air Soil Pollut.* 188, 67–80. doi: 10.1007/s11270-007-9525-7

Lee, J. R., Raymond, B., Bracegirdle, T. J., Chadès, I., Fuller, R. A., Shaw, J. D., et al. (2017). Climate change drives expansion of Antarctic ice-free habitat. *Nature* 547, 49–54. doi: 10.1038/nature22996

Leslie, D. L., Welch, K. A., and Lyons, W. B. (2017). A temporal stable isotopic (δ18O, δD, d-excess) comparison in glacier meltwater streams, Taylor Valley, Antarctica. *Cell* 31, 3069–3083. doi: 10.1002/hyp.11245

Lusky, J., Vallverdú, E., Gómez, I., Del Valle, R., and Felske, H. (2001). *Map of Potter Peninsula. King George (25 de Mayo) Island, South Shetland Islands, Antarctica*. Münich: Instituto Antártico Argentino-Institut für Allgemeine und Angewandte.

Lyons, W. B., Dailey, K. R., Welch, K. A., Deuerling, K. M., Welch, S. A., and Mcknight, D. M. (2015). Antarctic streams as a potential source of iron for the Southern Ocean. *Geology* 43, 1003–1006. doi: 10.1130/g36989.1

Lyons, W. B., Welch, K. A., Fountain, A. G., Dana, G. L., Vaughn, B. H., and Mcknight, D. M. (2003). Surface glaciochemistry of Taylor Valley, southern Victoria Land, Antarctica and its relationship to stream chemistry. *Hydrol. Process.* 17, 115–130. doi: 10.1002/hyp.1205

Matsuoka, K., Skoglund, A., and Roth, G. (2018). *Quantarctica*. Tromsø, NO: Norwegain Polar Institute.

McKnight, D., Runkel, R., Tate, C., Duff, J., and Moorhead, D. (2004). Inorganic N and P dynamics of Antarctic glacial meltwater streams as controlled by hyporheic exchange and benthic autotrophic communities. *J. North Am. Benthol. Soc.* 23, 171–188. doi: 10.1899/0887-3593(2004)023<0171:inapdo>2.0.co;2

McKnight, D. M., Niyogi, D. K., Alger, A. S., Bomblies, A., Conovitz, P. A., and Tate, C. M. (1999). Dry valley streams in antarctica: ecosystems waiting for water. *Bioscience* 49, 985–995.

Millero, F. J., Feistel, R., Wright, D. G., and Mcdougall, T. J. (2008). The composition of standard seawater and the definition of the Reference-composition salinity scale. *Deep Sea Res. Part I Oceanogr. Res. Pap.* 55, 50–72. doi: 10.1016/j.dsr.2007.10.001

Monien, D., Monien, P., Brünjes, R., Widmer, T., Kappenberg, A., Silva Busso, A. A., et al. (2017). Meltwater as a source of potentially bioavailable iron to Antarctica waters. *Antarct. Sci.* 29, 277–291. doi: 10.1017/s095410201600064x

Olund, S., Lyons, W. B., Welch, S. A., and Welch, K. A. (2018). Fe and nutrients in coastal antarctic streams: implications for primary production in the ross Sea. *JGR Sci.* 123, 3507–3522. doi: 10.1029/2017jg004352

Opfergelt, S., Burton, K. W., Pogge Von Strandmann, P. A. E., Gislason, S. R., and Halliday, A. N. (2013). Riverine silicon isotope variations in glaciated basaltic terrains: implications for the Si delivery to the ocean over glacial-interglacial intervals. *Earth Planet. Sci. Lett.* 369–370, 211–219. doi: 10.1016/j.epsl.2013.03.025

Pokrovsky, O. S., Reynolds, B. C., Prokushkin, A. S., Schott, J., and Viers, J. (2013). Silicon isotope variations in Central Siberian rivers during basalt weathering in permafrost-dominated larch forests. *Chem. Geol.* 355, 103–116. doi: 10.1016/j.chemgeo.2013.07.016

Reynolds, B. C., Aggarwal, J., Andre, L., Baxter, D., Beucher, C., Brzezinski, M. A., et al. (2007). An inter-laboratory comparison of Si isotope reference materials. *J. Analyt.cal Atomic Spectrom.* 22, 561–568. doi: 10.1039/b616755a

Rückamp, M., Braun, M., Suckro, S., and Blindow, N. (2011). Observed glacial changes on the King George Island ice cap, Antarctica, in the last decade. *Glob. Planet. Chang.* 79, 99–109. doi: 10.1016/j.gloplacha.2011.06.009

Savage, P. S., Georg, R. B., Armytage, R. M. G., Williams, H. M., and Halliday, A. N. (2010). Silicon isotope homogeneity in the mantle. *Earth Planet. Sci. Lett.* 295, 139–146. doi: 10.1016/j.epsl.2010.03.035

Schloss, I. R., Ferreyra, G. A., Mercuri, G., and Kowalke, J. (1999). Particle flux in an Antarctic shallow coastal environment: a sediment trap study. *Sci. Mar.* 63, 99–111. doi: 10.3989/scimar.1999.63s199

Schloss, I. R., Wasilowska, A., Dumont, D., Almandoz, G. O., Hernando, M. P., Michaud-Tremblay, C.-A., et al. (2014). On the phytoplankton bloom in coastal waters of southern King George Island (Antarctica) in January 2010: an exceptional feature? *Limnol. Oceanogr.* 59, 195–210. doi: 10.4319/lo.2014.59.1.0195

Sherrell, R. M., Annett, A. L., Fitzsimmons, J. N., Roccanova, V. J., and Meredith, M. P. (2018). A "shallow bathtub ring" of local sedimentary iron input maintains the palmer deep biological hotspot on the West Antarctic Peninsula shelf. *Sci. Mar.* 376:20170171. doi: 10.1098/rsta.2017.0171

Silva-Busso, A. (2009). "Aguas superficiales Y subterràneas en el área Norte da la PenÍnsula Antaràrtica," in *El agua en el Norte de la Península Antártica. INA, DNA-IAA, Fundación de Historia Natural Félix de Azara Cap. 4* ed. A. Silva-Busso. Buenos Aires. 47–82.

Silva-Busso, A., Fresina, M., and Vodopivez, C. (2004). *Congress Xxxiii Aih - Ahsud Groundwater Flow Understanding. Hidrodinámica e Hidroquímica Subterránea En La Cuenca Del Arroyo Matías, Península Potter, Islas Shetland Antártic*. Zacatecas: Asociación Geológica Española.

Stallard, R. F., and Edmond, J. M. (1981). Geochemistry of the amazon: 1. precipitation chemistry and the marine contribution to the dissolved load at the time of peak discharge. *J. Geophys. Res. Oceans* 86, 9844–9858.

Sun, X., Mörth, C.-M., Porcelli, D., Kutscher, L., Hirst, C., Murphy, M. J., et al. (2018). Stable silicon isotopic compositions of the Lena River and its tributaries: implications for silicon delivery to the Arctic Ocean. *Geochim. Cosmochim. Acta* 241, 120–133. doi: 10.1016/j.gca.2018.08.044

Sutton, J. N., André, L., Cardinal, D., Conley, D. J., De Souza, G. F., Dean, J., et al. (2018). A review of the stable isotope bio-geochemistry of the global silicon cycle and its associated trace elements. *Front. Earth Sci.* 5:112. doi: 10.3389/feart.2017.00112

Turner, J., Colwell, S. R., Marshall, G. J., Lachlan-Cope, T. A., Carleton, A. M., Jones, P. D., et al. (2005). Antarctic climate change during the last 50 years. *Intern. J. Climatol.* 25, 279–294. doi: 10.1002/joc.1130

Urra, A., Wadham, J., Hawkings, J., Telling, J., Hatton, J., Hasholt, B., et al. (2019). Weathering dynamics under contrasting greenland ice sheet catchments. *Front. Earth Sci.* 7:299. doi: 10.3389/feart.2019.00299

Vinocur, A., and Pizarro, H. (2000). Microbial mats of twenty-six lakes from potter Peninsula, King George Island, Antarctica. *Hydrobiologia* 437, 171–185.

Wadham, J. L., Tranter, M., Skidmore, M., Hodson, A. J., Priscu, J., Lyons, W. B., et al. (2010). Biogeochemical weathering under ice: size matters. *Glob. Biogeochem. Cycles* 24:3688.

Waller, R. I. (2001). The influence of basal processes on the dynamic behaviour of cold-based glaciers. *Q. Intern.* 86, 117–128. doi: 10.1016/s1040-6182(01)00054-4

Welch, K. A., Lyons, W. B., Whisner, C., Gardner, C. B., Gooseff, M. N., Mcknight, D. M., et al. (2010). Spatial variations in the geochemistry of glacial meltwater streams in the Taylor Valley, Antarctica. *Antarct. Sci.* 22, 662–672. doi: 10.1017/s0954102010000702

Wlostowski, A. N., Gooseff, M. N., Mcknight, D. M., Jaros, C., and Lyons, W. B. (2016). Patterns of hydrologic connectivity in the McMurdo Dry Valleys, Antarctica: a synthesis of 20years of hydrologic data. *Hydrol. Proc.* 30, 2958–2975. doi: 10.1002/hyp.10818

Wlostowski, A. N., Gooseff, M. N., Mcknight, D. M., and Lyons, W. B. (2018). Transit times and rapid chemical equilibrium explain chemostasis in glacial meltwater streams in the McMurdo Dry Valleys, Antarctica. *Hydrol. Proc.* 13:322.

Ye, L., Zhang, R., Sun, Q., Jin, J., and Zhang, J. (2018). Hydrochemistry of the meltwater streams on Fildes Peninsula, King George Island, Antarctica. *J. Sci. Limnol.* 36, 2181–2193. doi: 10.1007/s00343-019-7193-2

Ziegler, K., Chadwick, O. A., Brzezinski, M. A., and Kelly, E. F. (2005). Natural variations of δ30Si ratios during progressive basalt weathering, Hawaiian Islands. *Geochim. Cosmochim. Acta* 69, 4597–4610. doi: 10.1016/j.gca.2005.05.008

Conflict of Interest: The authors declare that the research was conducted in the absence of any commercial or financial relationships that could be construed as a potential conflict of interest.

frontiers
in Earth Science

ORIGINAL RESEARCH
published: 27 August 2020
doi: 10.3389/feart.2020.00341

Stable Isotopes of Nitrate, Sulfate, and Carbonate in Soils From the Transantarctic Mountains, Antarctica: A Record of Atmospheric Deposition and Chemical Weathering

Melisa A. Diaz[1,2]*, Jianghanyang Li[3], Greg Michalski[3,4], Thomas H. Darrah[1,5], Byron J. Adams[6], Diana H. Wall[7], Ian D. Hogg[8,9], Noah Fierer[10], Susan A. Welch[1,2], Christopher B. Gardner[1,2] and W. Berry Lyons[1,2]

[1] School of Earth Sciences, The Ohio State University, Columbus, OH, United States, [2] Byrd Polar and Climate Research Center, The Ohio State University, Columbus, OH, United States, [3] Department of Earth, Atmospheric, and Planetary Sciences, Purdue University, West Lafayette, IN, United States, [4] Department of Chemistry, Purdue University, West Lafayette, IN, United States, [5] Global Water Institute, The Ohio State University, Columbus, OH, United States, [6] Department of Biology, Evolutionary Ecology Laboratories and Monte L. Bean Museum, Brigham Young University, Provo, UT, United States, [7] Department of Biology and School of Global Environmental Sustainability, Colorado State University, Fort Collins, CO, United States, [8] Canadian High Arctic Research Station, Polar Knowledge Canada, Cambridge Bay, NU, Canada, [9] School of Science, University of Waikato, Hamilton, New Zealand, [10] Department of Ecology and Evolutionary Biology and Cooperative Institute for Research in Environmental Science, University of Colorado Boulder, Boulder, CO, United States

Edited by:
*Melissa Jean Murphy,
University College London,
United Kingdom*

Reviewed by:
*Ruth Hindshaw,
University of Cambridge,
United Kingdom
Peter Michael Wynn,
Lancaster University, United Kingdom*

***Correspondence:**
*Melisa A. Diaz
diaz.237@osu.edu*

Specialty section:
*This article was submitted to
Geochemistry,
a section of the journal
Frontiers in Earth Science*

Received: *12 March 2020*
Accepted: *21 July 2020*
Published: *27 August 2020*

Citation:
*Diaz MA, Li J, Michalski G,
Darrah TH, Adams BJ, Wall DH,
Hogg ID, Fierer N, Welch SA,
Gardner CB and Lyons WB (2020)
Stable Isotopes of Nitrate, Sulfate,
and Carbonate in Soils From
the Transantarctic Mountains,
Antarctica: A Record of Atmospheric
Deposition and Chemical Weathering.
Front. Earth Sci. 8:341.
doi: 10.3389/feart.2020.00341*

Soils in ice-free areas in Antarctica are recognized for their high salt concentrations and persistent arid conditions. While previous studies have investigated the distribution of salts and potential sources in the McMurdo Dry Valleys, logistical constraints have limited our investigation and understanding of salt dynamics within the Transantarctic Mountains. We focused on the Shackleton Glacier (85° S, 176° W), a major outlet glacier of the East Antarctic Ice Sheet located in the Central Transantarctic Mountains (CTAM), and collected surface soil samples from 10 ice-free areas. Concentrations of water-soluble nitrate (NO_3^-) and sulfate (SO_4^{2-}) ranged from <0.2 to ~ 150 μmol g^{-1} and <0.02 to ~ 450 μmol g^{-1}, respectively. In general, salt concentrations increased with distance inland and with elevation. However, concentrations also increased with distance from current glacial ice position. To understand the source and formation of these salts, we measured the stable isotopes of dissolved water-soluble NO_3^- and SO_4^{2-}, and soil carbonate ($HCO_3 + CO_3$). δ^{15}N-NO_3 values ranged from -47.8 to 20.4‰ and, while all Δ^{17}O-NO_3 values are positive, they ranged from 15.7 to 45.9‰. δ^{34}S-SO_4 and δ^{18}O-SO_4 values ranged from 12.5 and 17.9‰ and -14.5 to -7.1‰, respectively. Total inorganic carbon isotopes in bulk soil samples ranged from 0.2 to 8.5‰ for δ^{13}C and -38.8 to -9.6‰ for δ^{18}O. A simple mixing model indicates that NO_3^- is primarily derived from the troposphere (0–70%) and stratosphere (30–100%). SO_4^{2-} is primarily derived from secondary atmospheric sulfate (SAS) by the oxidation of reduced sulfur gases and compounds in the atmosphere by H_2O_2, carbonyl sulfide (COS), and ozone. Calcite and perhaps nahcolite ($NaHCO_3$) are formed through both slow and rapid freezing and/or the evaporation/sublimation of HCO_3 + CO_3-rich fluids. Our results indicate that the origins of salts from ice-free areas within the CTAM represent a complex interplay of atmospheric deposition, chemical weathering, and post-depositional processes related to glacial history and persistent arid conditions. These findings have important implications for the use of these salts in deciphering past climate and atmospheric conditions, biological habitat suitability, glacial history, and can possibly aid in our future collective understanding of salt dynamics on Mars.

Keywords: Antarctica, geochemistry, salts, stable isotopes, nitrate, sulfate, carbonate

INTRODUCTION

Ice-free areas within the Transantarctic Mountains (TAM) have been of scientific interest throughout the 20th and 21st centuries due in part to their unique polar desert soil environments. They are characterized by average annual temperatures below freezing, low amounts of precipitation, and low biomass. Throughout the mid to late Cenozoic, much of the currently exposed areas along the TAM were re-worked by the advance and retreat of the East Antarctic Ice sheet (EAIS), but some soils are believed to have remained primarily ice-free for possibly millions of years (Mayewski and Goldthwait, 1985; Anderson et al., 2002). As a result of persistent arid conditions since at least the Miocene, salts have accumulated in some Antarctic soils (Marchant and Denton, 1996).

Early geochemical work in the McMurdo Dry Valleys (MDV) (77° S, 162° E), the largest ice-free area in Antarctica, showed that the soil environments in Antarctica are among the most saline systems on Earth (Jones and Faure, 1967; Keys and Williams, 1981). The binary salts, which are primarily nitrate-, sulfate-, chloride-, and carbonate- bearing, have been used for determining relative chronology, and have important implications for habitat suitability and hence soil biodiversity (Claridge and Campbell, 1977; Keys and Williams, 1981; Magalhães et al., 2012; Bockheim and McLeod, 2013; Sun et al., 2015; Lyons et al., 2016). Antarctic ice-free environments are often utilized as Martian analogs, and salt formation processes in Antarctica may aid in our understanding of salt sources and the current and past availability of water on Mars (Wynn-Williams and Edwards, 2000; Vaniman et al., 2004; Bishop et al., 2015).

By interpreting the relationship between the types of salts in the soils, the pH, and the distribution of calcite crusts, Claridge and Campbell (1977) and Keys and Williams (1981) proposed that the majority of MDV salts were derived from marine sources, however, *in situ* chemical weathering and deposition of oxidized atmospheric compounds are also important. While Cl^- salts are generally derived from marine aerosols, and HCO_3^- salts from lacustrine deposits and chemical weathering, the origins of NO_3^- and SO_4^{2-} salts are more complex (Claridge and Campbell, 1977; Nezat et al., 2001; Bisson et al., 2015). Additionally, when liquid water is present, the dissolution of salts and ion exchange in soils can alter the original salt geochemistry (Toner and Sletten, 2013; Toner et al., 2013).

The measurement of stable isotopes of NO_3^-, and SO_4^{2-} has greatly improved our understanding of the sources and transport of these salts in Antarctica. Potential sources of NO_3^- include deposition from polar stratospheric clouds, tropospheric oxidation of HNO_3 emitted from ice, nitrification and denitrification of nitrogen species by organisms, and oxidation of oceanic organic matter (Savarino et al., 2007; Frey et al., 2009; Campbell et al., 2013; Erbland et al., 2015), while potential sources of SO_4^{2-} include pyrite weathering, marine biogenic sulfate, sea-salt sulfate, and S from volcanic eruptions (Legrand and Delmas, 1984; Patris et al., 2000; Rech et al., 2003; Shaheen et al., 2013). Additional work has used ^{17}O isotopes to attribute NO_3^- and SO_4^{2-} salt abundances to the deposition of atmospheric oxidized compounds, particularly in old, high elevation, and hyper-arid environments in Antarctic ice-free areas (Bao et al., 2000; Michalski et al., 2005; Bao and Marchant, 2006).

The majority of isotopic measurements of NO_3^- and SO_4^{2-} in Antarctic terrestrial systems have been made on soils from the MDV (e.g., Nakai et al., 1975; Bao et al., 2000; Michalski et al., 2005; Bao and Marchant, 2006; Jackson et al., 2016). Few studies have investigated the geochemistry, distribution, and source of salts from the Central Transantarctic Mountains (CTAM), which are believed to contain some of the most saline soils on Earth (Sun et al., 2015; Lyons et al., 2016). We measured the concentrations and isotopic composition of NO_3^-, SO_4^{2-}, and HCO_3 + CO_3 in samples collected from the Shackleton Glacier region, located in the CTAM, to identify potential salt sources. We show that salt composition varies throughout the region, likely related to differences in the availability of water, and atmospheric deposition is the primary source of both NO_3^- and SO_4^-, while carbonate minerals are formed from the freezing and evaporation/sublimation of water. These data provide insights into the processes that lead to salt formation and accumulation in CTAM soils.

MATERIALS AND METHODS

Study Site

During the 2017–2018 austral summer, a multi-disciplinary field camp was established at the Shackleton Glacier (∼84.5°S), a major outlet glacier of the EAIS in the CTAM. The Shackleton Glacier flows between several exposed peaks of the Queen Maud Mountains, which are the basis of this study (**Figure 1**). Though climate data for the region are sparse, winter temperatures are well below freezing and summer months

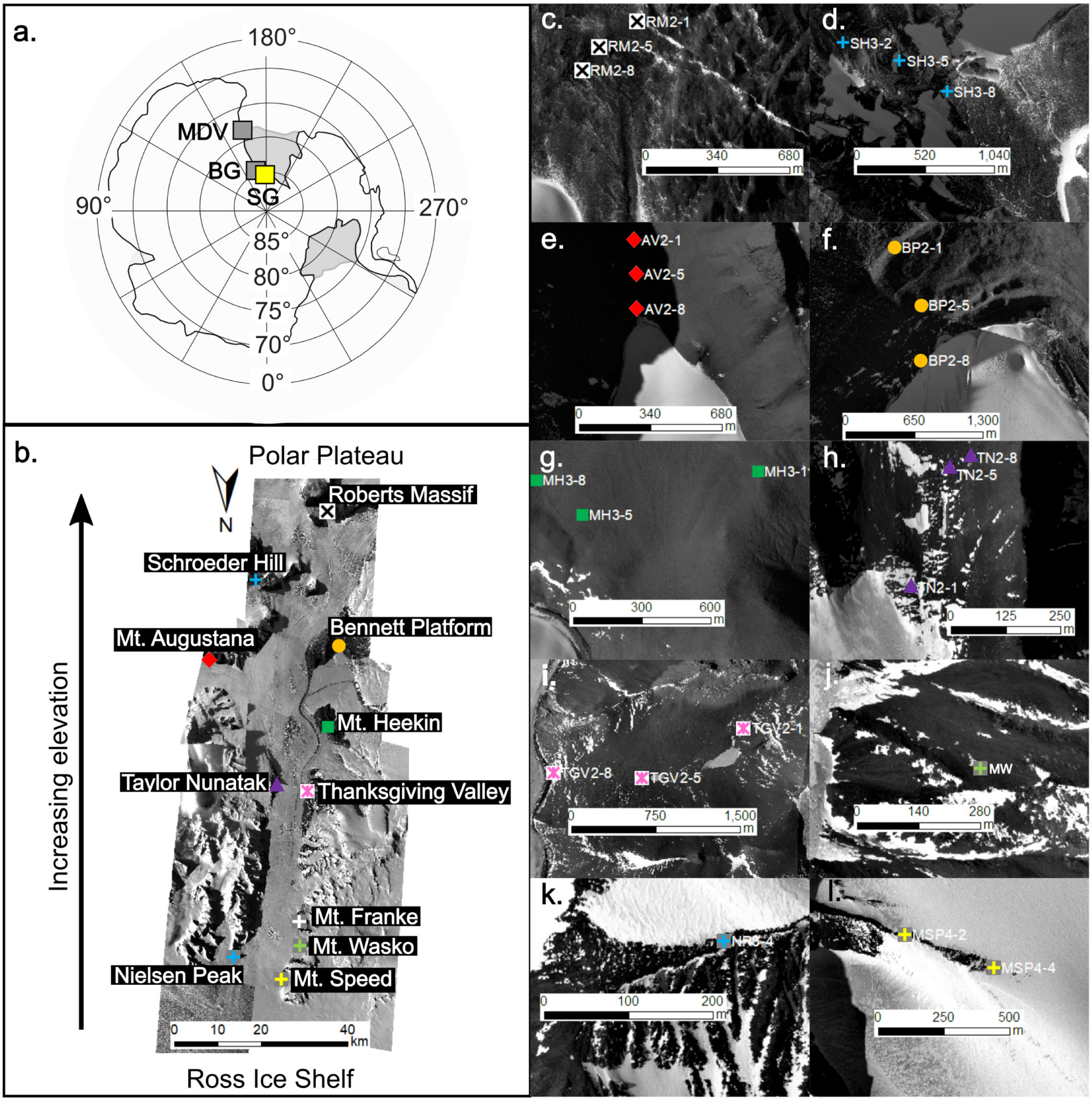

FIGURE 1 | Map of Antarctica highlighting the Shackleton Glacier (SG; yellow box) in relation to the McMurdo Dry Valleys (MDV) and Beardmore Glacier (BG) (gray boxes) **(a)**. The Shackleton Glacier is the focus of this study and flows from the Polar Plateau to the Ross Ice Shelf **(b)**. Soil samples were collected from 11 features along the glacier: Roberts Massif **(c)**, Schroeder Hill **(d)**, Mt. Augustana **(e)**, Bennett Platform **(f)**, Mt. Heekin **(g)**, Taylor Nunatak **(h)**, Thanksgiving Valley **(i)**, Mt. Wasko **(j)**, Nilsen Peak **(k)**, Mt. Speed **(l)**, and Mt. Franke (not shown). The symbols represent sampling locations, though no accurate GPS coordinate could be recorded from Mt. Wasko. Images of the Shackleton Glacier were acquired from the Polar Geospatial Center (PGC).

are closer to 0°C (LaPrade, 1984). Elevations of the ice-free areas range from ~150 m.a.s.l. toward the Ross Ice Shelf to >3,500 m.a.s.l. further inland. The soils in this study were collected between ~300 m.a.s.l. and 2,100 m.a.s.l. (**Table 1**). The geologic basement consists of gneiss, schist, slate, and quartzite formed from sedimentary and igneous strata which were intruded by granitoid batholiths in the Ross Orogeny. Devonian to Triassic rocks of the Beacon Supergroup overlie the basement, which have been cut by dolerite/basaltic sills (Elliot and Fanning, 2008). Near the Ross Ice Shelf, the exposed surfaces are primarily comprised of metamorphic and igneous rocks, while the Beacon Supergroup and Ferrar Dolerite are more abundant toward the Polar Plateau along with sediments from the Sirius Group. These rocks serve as primary sources of weathering products for salt formation (e.g., carbonates and cations).

TABLE 1 | Sample geographic information and concentrations of water-soluble ions in soil leaches determined by ion chromatography and nutrient analysis in μmol g^{-1}.

Sample name	Location	Latitude	Longitude	Elevation	Distance from coast	Distance from glacier	Cl^-	NO_3^-	SO_4^{2-}	Na^+	Mg^{2+}	K^+	Ca^{2+}
				m	km	m	μmol g^{-1}	μmol g^{-1}	μmol g^{-1}	μmol g^{-1}	μmol g^{-1}	μmol g^{-1}	μmol g^{-1}
AV2-1	Mt. Augustana	−85.1706	−174.1338	1410	72	388	4.53	18.5	78.1	18.9	11.3	0.53	52.2
AV2-5	Mt. Augustana	−85.1691	−174.1372	1388	72	226	9.86	23.3	46.6	20.6	20.1	1.06	52.1
AV2-8	Mt. Augustana	−85.1676	−174.1393	1378	72	61	0.50	1.01	0.55	2.15	0.26	0.09	0.24
BP2-1	Bennett Platform	−85.2121	−177.3576	1410	82	1007	5.26	4.13	16.2	17.4	3.44	0.13	8.77
BP2-5	Bennett Platform	−85.2072	−177.3887	1294	82	396	0.19	10.6	42.5	24.0	8.76	0.31	37.1
BP2-8	Bennett Platform	−85.2024	−177.3907	1222	82	27	0.51	0.22	0.67	10.5	b.d.l.	0.09	0.10
MF2-1	Mt. Franke	−84.6236	−176.7353	480	9	1098	0.13	b.d.l.	b.d.l.	0.23	0.08	0.07	0.10
MF2-4	Mt. Franke	−84.6237	−176.7252	424	9	450	0.29	b.d.l.	b.d.l.	0.06	0.04	0.05	0.04
MH3-1	Mt. Heekin	−85.0332	−177.3292	1200	63	533	25.1	27.4	142.0	22.7	8.84	1.47	71.5
MH3-5	Mt. Heekin	−85.0311	−177.2489	1080	63	300	30.7	21.8	59.4	37.8	14.0	0.60	48.1
MH3-8	Mt. Heekin	−85.0324	−177.2265	1045	63	502	0.81	0.36	0.26	1.71	0.17	0.12	0.38
MSP4-2	Mt. Speed	−84.4657	−177.1357	n.d.	0	11	0.20	0.17	0.02	0.48	0.08	0.18	2.48
MSP4-4	Mt. Speed	−84.4647	−177.1685	308	0	4	0.20	0.18	0.004	0.04	0.03	0.08	0.80
MW 4-3	Mt. Wasko	n.d.	n.d.	350	∼10	∼1	0.16	0.17	0.002	0.13	0.06	0.07	0.17
NP3-4	Nilsen Peak	−84.5344	−175.4166	673	0	146	0.35	0.32	b.d.l.	0.31	0.10	0.13	0.44
RM2-1	Roberts Massif	−85.4879	−177.1844	1776	120	882	3.93	23.0	415.5	0.41	0.03	b.d.l.	0.16
RM2-5	Roberts Massif	−85.4868	−177.1639	1754	120	706	0.10	5.66	35.6	35.6	3.29	0.52	13.8
RM2-8	Roberts Massif	−85.4857	−177.1549	1747	120	564	0.13	23.41	138.7	91.2	7.19	1.53	29.7
SH3-2	Schroeder Hill	−85.3597	−175.0693	2137	94	900	0.23	149.5	218.7	166.9	128.7	1.43	66.7
SH3-5	Schroeder Hill	−85.3588	−175.1198	2092	94	1214	0.39	147.5	443.6	737.6	237.9	6.85	70.6
SH3-8	Schroeder Hill	−85.3569	−175.1621	2057	94	1381	0.85	93.0	126.2	85.0	39.2	3.18	67.0
TGV2-1	Thanksgiving Valley	−84.919	−177.0603	1107	45	1758	1.20	0.85	0.81	3.43	0.13	0.07	0.13
TGV2-5	Thanksgiving Valley	−84.9145	−176.9688	1082	45	311	49.0	15.9	34.9	21.7	20.8	0.93	30.8
TGV2-8	Thanksgiving Valley	−84.9145	−176.8860	912	45	1701	0.16	0.15	b.d.l.	0.63	0.02	0.03	0.02
TN2-1	Taylor Nunatak	−84.9238	−176.0988	1030	45	40	5.59	1.77	0.66	7.86	0.36	0.14	0.74
TN2-5	Taylor Nunatak	−84.9264	−176.1060	1056	45	298	113.2	54.1	13.5	65.9	19.3	0.94	33.9
TN2-8	Taylor Nunatak	−84.9266	−176.1108	1070	45	350	4.74	1.40	10.3	6.84	1.72	0.31	8.04

Values are corrected for a 1:5 soil to water leach ratio. Samples that were below the analytical detection limit are listed as b.d.l.

Sample Collection

The top 5 cm of soil was collected from 11 locations along the Shackleton Glacier (total of 27 samples) using a clean plastic scoop, stored in Whirlpak bags, and shipped at −20°C to The Ohio State University (**Figure 1**). We attempted to collect three samples in transects perpendicular to the Shackleton Glacier or local tributary/alpine glaciers at each of the 11 locations. One sample was collected near the glacier, one near our estimate of the glacier's trim line during the Last Glacial Maximum (LGM), and the third further inland to represent long-term exposure. The soil ages are not known, but samples from the southern portion of the region, such as Roberts Massif, are likely at least 4 Myr due to the presence of Sirius Group sediments (Hambrey et al., 2003). The sample locations represent the variable ambient summer temperatures, elevations, rock types and landscape features characteristic of the Shackleton Glacier region, and include soils from low elevation sites near the Ross Ice Shelf to high elevation sites near the Polar Plateau.

GPS coordinates and elevation were recorded in the field and used to estimate the aerial distance to the Ross Ice Shelf ("distance to coast") and the distance to the nearest glacier (**Table 1**). In the latter measurement, the term "glacier" was used to represent any glacier, including the Shackleton Glacier, tributary glaciers, alpine glaciers, etc. While this distance does not account for topography, it can be used as an estimate of potential modern and past hydrologic influence and impact on salt formation and mobility.

Water-Soluble Leaches

The soil samples were leached at a 1:5 soil to water ratio for 24 h, following procedures previously described (Nkem et al., 2006; Diaz et al., 2018). The leachate was filtered through 0.4 μm Nucleopore membrane filters using a polyether sulfone (PES) filter funnel that was thoroughly cleaned with deionized (DI) water between samples. The leachate was stored in the dark at +4°C until sample analysis. Filter blanks were collected and analyzed to account for any possible contamination from the filtration and storage process.

Major Ions

Concentrations of water-soluble Cl^- and SO_4^{2-} were measured using a Dionex ICS-2100 ion chromatograph and an AS-DV automated sampler, as originally described by Welch et al. (2010).

Water-soluble cations (K^+, Na^+, Ca^{2+}, Mg^{2+}) were measured on a PerkinElmer Optima 8300 Inductively Coupled Plasma-Optical Emission Spectrometer (ICP-OES) at The Ohio State University Trace Element Research Laboratory (TERL). Nitrate (NO_3^- + NO_2^-) concentrations were measured on a Skalar San++ Automated Wet Chemistry Analyzer with an SA 1050 Random Access Auto-sampler. The precision of replicated check standards and samples was better than 10% for all anions, cations and nutrients. Accuracy was better than 5% for all analytes, as determined by the NIST1643e external reference standard and the 2015 USGS interlaboratory calibration standard (M-216).

Nitrogen and Oxygen Isotope Analysis of Nitrate

Aliquots of the sample leachates were analyzed for $\Delta^{17}O$ and $\delta^{15}N$ of nitrate at Purdue University following procedures described by Michalski et al. (2005). Dissolved nitrate solutions were first injected into air-tight vials and the headspace was flushed with Ar. The nitrate in the solutions were reduced to N_2O using $TiCl_3$ (Altabet et al., 2019), then the isotopic composition of N_2O was analyzed on a Finnigan-Mat 251 isotope ratio mass spectrometer (IRMS). Mass independent fractionation of oxygen isotopes, calculated by $\Delta^{17}O = \delta^{17}O - 0.52^* \delta^{18}O$ ($\Delta^{17}O \pm 1.0‰$), are reported in units of per mille (‰) with respect to Vienna Standard Mean Ocean Water (VSMOW) and nitrogen isotopes ($\delta^{15}N \pm 0.3‰$) are reported with respect to N_2. Nitrate concentrations were high enough for isotopic analysis on 21 of 27 samples attempted. Though the relationship between $\delta^{18}O$ and $\delta^{17}O$ was used in the $\Delta^{17}O$ calculation, the absolute values of these isotopes could not be determined.

Sulfur and Oxygen Isotope Analysis of Sulfate

The same samples that were analyzed for $\Delta^{17}O$ and $\delta^{15}N$ of nitrate were analyzed for $\delta^{18}O$ and $\delta^{34}S$ of sulfate at the University of Tennessee Knoxville. The leachates were acidified with HCl to pH ~2 to remove any dissolved carbonate/bicarbonate ions. Sulfate was then precipitated as $BaSO_4$, after the addition of $BaCl_2$ (~10% wt./vol). The precipitate was rinsed several times with DI water and dried at 80°C. The $\delta^{34}S$ and $\delta^{18}O$ values of $BaSO_4$ were determined using a Costech Elemental Analyzer and a Thermo Finnigan TC/EA, respectively, coupled to a Thermo Finnigan Delta Plus XL mass spectrometer at the Stable Isotope Laboratory at University of Tennessee (e.g., Szynkiewicz et al., 2020). Isotopic values are reported in units of ‰ with respect to Vienna Canyon Diablo Troilite (VCDT) for $\delta^{34}S$ and VSMOW for $\delta^{18}O$ with analytical precision < 0.4‰ based on replicate measurements. Sulfur sequential extractions for $\delta^{34}S$ of sedimentary sulfur were performed on seven dried, bulk soils from seven locations following methods from Szynkiewicz et al. (2009). The samples were ground and treated with 30 ml of 6 N HCl to measure acid-soluble SO_4^{2-}. Then the samples were treated with 20 mL of 12 N HCl and 20 mL of 1 M $CrCl_2 \cdot 6H_2O$ under N_2 to dissolve disulfide to measure Cr-reducible sulfide.

Of the 27 initially prepared for $\delta^{34}S$ and ^{18}O analysis, eight samples had sulfate concentrations too low for sufficient precipitation of $BaSO_4$. Therefore, in these samples, $\delta^{34}S$ was analyzed using a Nu Instruments multi-collector inductively coupled plasma mass spectrometer (MC-ICP-MS) at the US Geological Survey High Resolution ICP-MS laboratory, Denver with analytical precision < 0.3‰ (Pribil et al., 2015).

Carbon and Oxygen Isotope Analysis of Carbonate

Between 5 and 10 g of bulk soil from five locations (Roberts Massif, Bennett Platform, Mt. Heekin, Taylor Nunatak, and Nilsen Peak) were dried and ground to fine powder using a ceramic mortar and pestle for carbonate isotope analysis at the Stable Isotope Laboratory at Southern Methodist University. Total inorganic carbon (TIC) was measured by adding phosphoric acid kept at 90°C to the sample, liberating the carbonate as CO_2. The ^{13}C and ^{18}O composition of the CO_2 was measured using a dual-inlet Finnigan MAT 252 mass spectrometer. $\delta^{13}C$ and $\delta^{18}O$ are reported in units of ‰ with respect to Peedee belemnite (PDB) with an overall analytical precision of ±0.2‰ or better.

Scanning Electron Microscopy

One sample from Schroeder Hill (SH3-2) was analyzed using a FEI Quanta FEG 250 Field Emission scanning electron microscope (SEM) equipped with a backscattered electron detector for imaging and a Bruker energy dispersive x-ray (EDX) detector for spot chemical analysis. The sample was allowed to air dry and was then affixed to an aluminum stub with carbon tape. The stub was coated using Au-Pd with a Denton Desk V precious metal coater before analysis by SEM.

RESULTS

Major Ion Concentrations

The concentrations of all measured water-soluble ions are variable across the sampling locations and span up to six orders of magnitude for SO_4^{2-} (**Table 1**). In general, the most abundant anion is SO_4^{2-}, however Cl^- is the more dominant species in samples closest to the Ross Ice Shelf, such as those at Mt. Speed and Mt. Wasko (**Table 1** and **Figure 2**). NO_3^- concentrations vary with distance from the coast, but also within individual sample locations (**Table 1**). For example, concentrations at Mt. Augustana vary from ~1 to 23 μmol g^{-1}. The most abundant cation is Ca^{2+} for nearly all soils, except for the Schroeder Hill samples, where Na^+ is the most abundant and concentrations approach 700 μmol g^{-1}. Additionally, the two Schroeder Hill samples furthest from the glacier have the lowest Ca: Mg molar ratios (0.52–0.30), indicating an enrichment of Mg^{2+} compared to Ca^{2+}, while most other samples are dominated by Ca^{2+}. Concentrations of K^+ range from <0.03 μmol g^{-1} at Thanksgiving Valley to 6.85 μmol g^{-1} at Schroeder Hill (**Table 1**).

Trends in Salt Distributions

Molar ratios of NO_3^-/Cl^-, SO_4^{2-}/Cl^-, and NO_3^-/SO_4^{2-} with distance from the Ross Ice Shelf are compared for

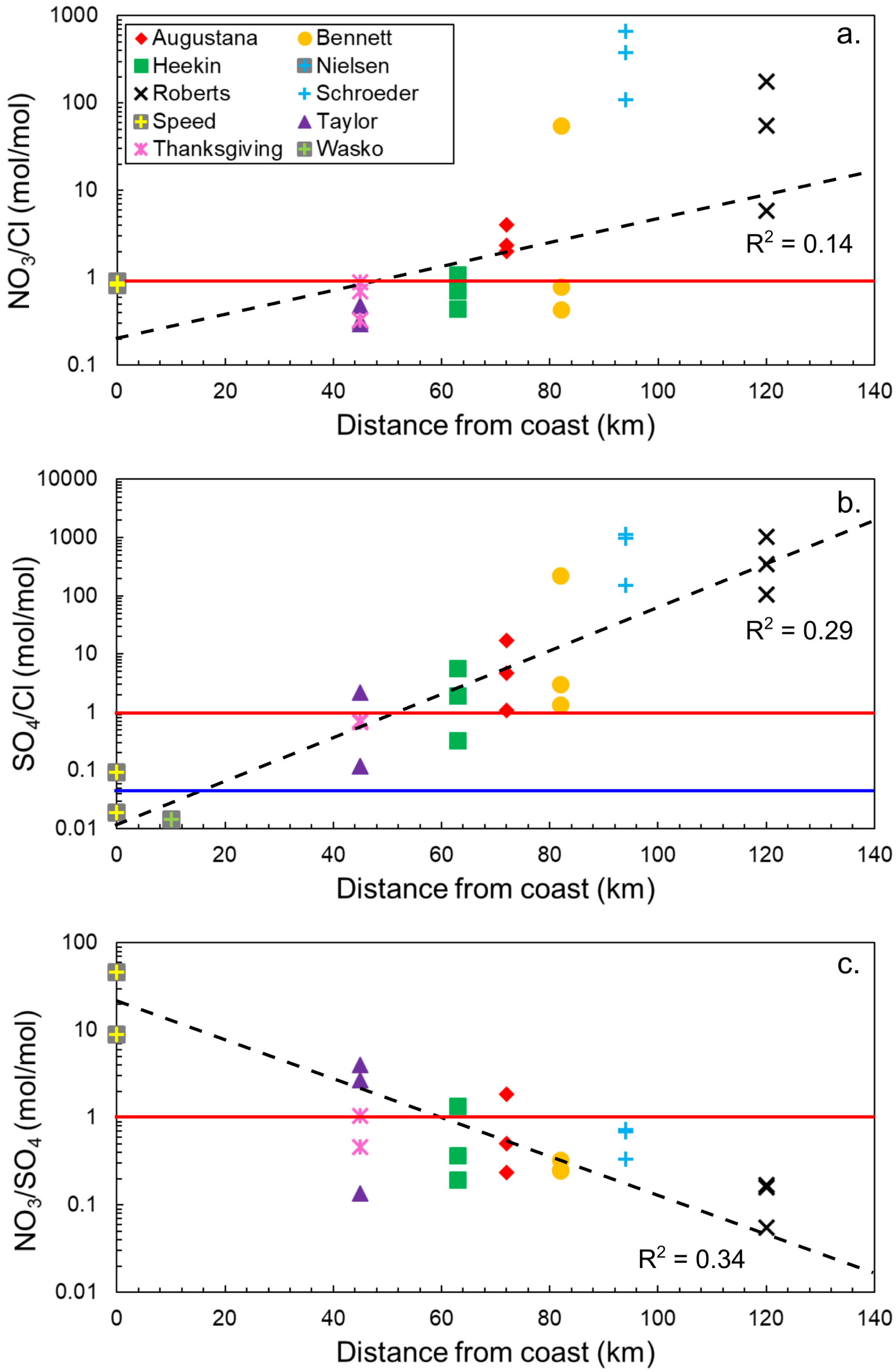

FIGURE 2 | Molar ratios of major anion species typically associated with salts in high latitude, polar desert soils [**(a)** NO_3^-/Cl^-, **(b)** SO_4^{2-}/Cl^-, and **(c)** NO_3^-/SO_4^{2-}] compared to distance from the coast of the Ross Ice Shelf. The black dotted lines represent general trends in the data, while the red solid line represents equal molar proportions of the anions and the blue line represents the SO_4:Cl molar ratio in seawater.

the different locations in **Figure 2**. Between the coast and approximately halfway up the Shackleton Glacier, NO_3^- and Cl^- are in approximately equal proportions, but nitrate-bearing salts become more dominant closer to the Polar Plateau (**Figure 2a**). The trend for sulfate-bearing salts is similar. Near the coast, chloride is about two orders of magnitude higher in concentration than sulfate. However, SO_4^{2-} becomes the dominant species for most locations beyond 50 km inland, and concentrations increase to nearly four orders of magnitude higher than Cl^- (**Figure 2b**). The molar ratio of NO_3^-/SO_4^{2-} with distance from the coast exhibits an inverse trend compared to the species normalized to Cl^- (**Figure 2c**), where the ratio is highest near the coast. As observed with the SO_4^{2-}/Cl^- ratio, approximately 50 km inland, sulfate becomes dominant. The relative enrichment of SO_4^{2-} increases further away from the coast and closer to the Polar Plateau. In general, both nitrate and sulfate have a positive relationship with distance from the Ross Ice Shelf. These results show that, contrary to trends observed in the MDV and the Beardmore Glacier region (83°4′ S, 171°0′ E) where NO_3^- was the dominant salt for inland and high elevation locations, sulfate is instead the most abundant in the Shackleton Glacier region (Keys and Williams, 1981; Lyons et al., 2016).

δ^{15}N and Δ^{17}O of Nitrate

Values of δ^{15}N and Δ^{17}O are widely variable within and between the different locations. δ^{15}N values range from −47.8 to 20.4‰ and while all Δ^{17}O values are positive, they range from 15.7 to 45.9‰ (**Table 2**). The highest Δ^{17}O and δ^{15}N values were at Mt. Augustana and Thanksgiving Valley, respectively. The isotopic composition of NO_3^- does not appear directly related to elevation and distance from the coast, though there is a slight ($R^2 = 0.20$, p-value = 0.05) positive relationship between δ^{15}N and distance from the glacier (**Figures 3a–c**).

TABLE 2 | δ^{15}N and Δ^{17}O of NO_3^- and δ^{34}S and δ^{18}O of SO_4^{2-}.

Sample	Δ^{17}O	δ^{15}N	δ^{34}S	δ^{18}O
	VSMOW	Air	VCDT	VSMOW
AV2-1	25.9	−18.9	14.3	−9.7
AV2-5	28.0	−17.6	14.3	−9.3
AV2-8	45.9	−9.8	14.7	−7.7
BP2-1	26.9	−8.9	13.7	−9.4
BP2-5	31.9	−4.2	14.9	*n.d.*
BP2-8	28.5	−8.9	13.9	−8.3
MF2-1	*b.d.l.*	*b.d.l.*	15.5	*n.d.*
MF2-4	*b.d.l.*	*b.d.l.*	13.2	*n.d.*
MH3-1	36.0	8.8	14.2	−7.9
MH3-5	15.7	−1.2	14.1	−6.8
MH3-8	*b.d.l.*	*b.d.l.*	14.0	−12.3
MSP4-2	24.9	−47.8	12.5	*n.d.*
MSP4-4	*b.d.l.*	*b.d.l.*	13.5	*n.d.*
MW4-3	*b.d.l.*	*b.d.l.*	15.8	*n.d.*
NP3-4	*b.d.l.*	−35.1	15.0	−7.1
RM2-1	30.8	−6.1	13.4	−10.1
RM2-5	19.0	−8.3	13.8	−9.4
RM2-8	40.8	−5.0	14.1	−10.4
SH3-2	11.2	−3.7	13.0	−14.5
SH3-5	22.4	−12.0	13.1	−11.7
SH3-8	31.9	−6.4	13.7	−10.1
TGV2-1	19.9	20.4	12.9	−14.5
TGV2-5	*n.d.*	0.9	15.7	−9.2
TGV2-8	40.4	3.5	14.5	*n.d.*
TN2-1	18.1	9.7	15.3	−7.2
TN2-5	*b.d.l.*	*b.d.l.*	14.7	−8.2
TN2-8	19.0	−4.9	15.0	−8.5

Samples that were below the analytical detection limit are listed as b.d.l. Samples with low SO_4^{2-} concentrations were only analyzed for δ^{34}S and not δ^{18}O (represented as n.d.).

δ^{34}S and δ^{18}O of Sulfate

Despite a wide range of SO_4^{2-} concentrations, δ^{34}S values are well constrained between 12.5 and 15.8‰, even for the low SO_4^{2-} concentration samples that were analyzed by MC-ICP-MS (**Table 2**). δ^{18}O values are slightly more variable, though all values are negative and range from −14.5 to −6.8‰. The highest δ^{34}S value is from Mt. Heekin and the most negative δ^{18}O value is from Schroeder Hill. Values of δ^{34}S do not vary significantly with geography, however δ^{18}O exhibits negative trends with elevation and distance from the glacier (**Figures 3d–f**).

Inorganic δ^{13}C and δ^{18}O of Carbonate

Although dissolved inorganic carbon species were not directly measured for the soil extracts in this work, carbonate and bicarbonate minerals have been identified throughout the MDV, and therefore, these minerals are assumed to also be present in CTAM soils (Bisson et al., 2015; Lyons et al., 2020). The amount of carbonate in the nine bulk soil samples analyzed ranges from 0.07% at Roberts Massif near the Polar Plateau to 2.5% at Taylor Nunatak further North (**Table 3**). δ^{13}C values are positive for all samples, ranging from 0.2 to 8.5‰, with the exception of Bennett Platform, which has a value of −13.0‰. All δ^{18}O values are negative and range from −38.8 to −9.6‰. One sample from Taylor Nunatak (TN1-6), noted in **Table 3**, yielded NO gas which froze out of the system and interfered with the δ^{18}O analysis.

DISCUSSION

These Shackleton Glacier region data represent the highest southern latitude δ^{15}N and Δ^{17}O of NO_3^-, δ^{34}S and δ^{18}O of SO_4^{2-}, and δ^{13}C and δ^{18}O of $HCO_3 + CO_3$ measurements made on soils and soil leaches. We evaluate water-soluble ion concentrations and compare the isotopic compositions to potential source reservoirs to understand the types of salts, sources of salts, and possible post-deposition alteration in remote, hyper-arid Antarctic terrestrial environments.

Water-Soluble Salt Compositions

Molar ratios of water-soluble ions and SEM images suggest that a variety of salts exist within the soils of the Shackleton Glacier region. Salt dissolution diagrams indicate that the major nitrate salt is $Na(K)NO_3$, though some samples, such as those from the high elevation and distant locations of Roberts Massif and Schroeder Hill, have $Na^+ + K^+$ concentrations that are higher than the 1:1 dissolution line (**Figure 4a**). These samples likely have some $Na^+(K^+)$ associated with HCO_3 (forming nahcolite, trona, thermonatrite and/or sodium bicarbonate), as observed in MDV and Beardmore Glacier region (Bisson et al., 2015; Sun et al., 2015), or possibly bloedite $[Na_2Mg(SO_4)_2{\cdot}4H_2O]$ in

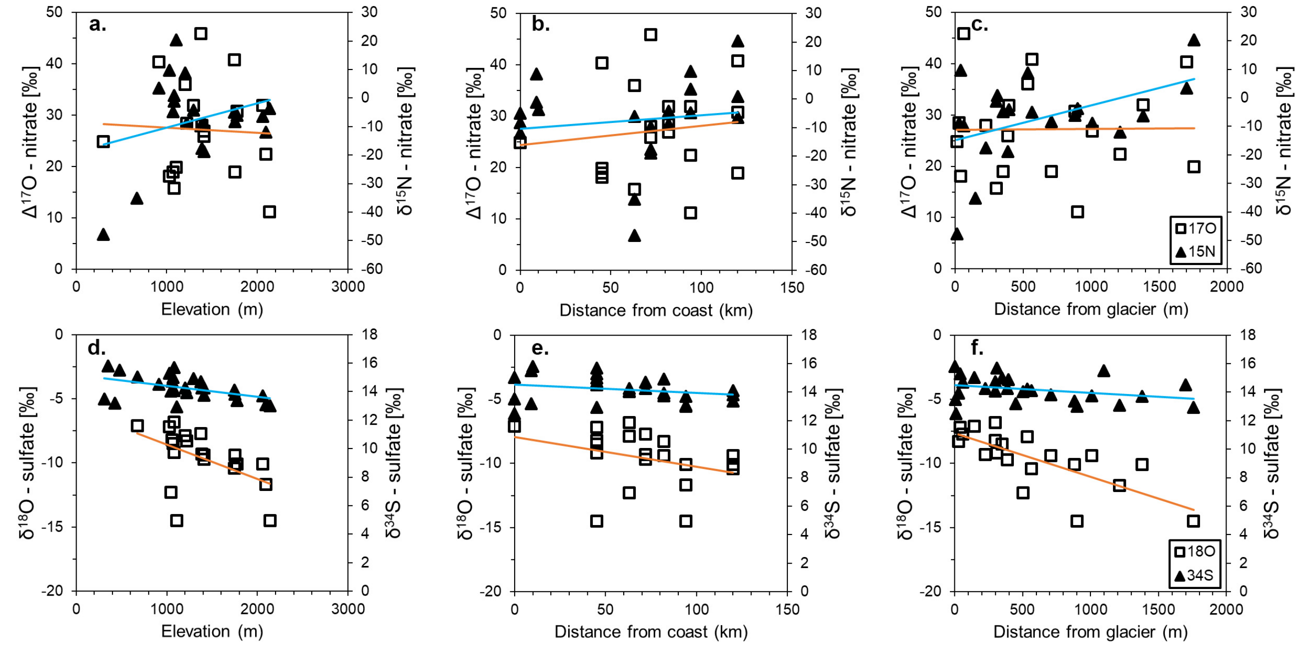

FIGURE 3 | Stable isotope values of $\delta^{15}N$ and $\Delta^{17}O$ in nitrate **(a–c)** and $\delta^{34}S$ and $\delta^{18}O$ in sulfate **(d–f)** with elevation, distance from the coast of the Ross Ice Shelf, and distance from the nearest glacier. Blue lines are trend lines for $\delta^{15}N$ and $\delta^{34}S$, while orange lines are trend lines for $\Delta^{17}O$ and $\delta^{18}O$.

addition to Na(K)-NO_3, which is observed in the SEM images of Schroeder Hill (**Figure 5**).

There appear to be a range of possible sulfate salts across the region and within individual samples. Anhydrite and/or gypsum ($CaSO_4$ or $CaSO_4 \cdot 2H_2O$) have been previously identified in MDV soils (Keys and Williams, 1981; Bisson et al., 2015) and some of the Shackleton samples plot on the salt dissolution line, consistent with the dissolution of Ca-SO_4 salts. Mirabilite ($Na_2SO_4{\cdot}10H_2O$) and thenardite (Na_2SO_4), however, have also been identified in soils and aeolian material in the MDV (Keys and Williams, 1981; Bisson et al., 2015; Diaz et al., 2018) and high Na^+ and SO_4^{2-} concentrations which are outside the stoichiometric lines for gypsum/anhydrite are likely due to the dissolution of these salts (**Figures 5c,d**). The Schroeder Hill SEM images and EDX spot analysis show that SO_4^{2-} from this location is likely from the dissolution of gypsum or anhydrite, epsomite ($MgSO_4 \cdot 7H_2O$), thenardite or mirabilite, and/or glauberite [$Na_2Ca(SO_4)_2$]. Mg-SO_4 salts are also suggested to be abundant in Martian soils and may reflect the water content potential of the soils (Clark and Van Hart, 1981; Vaniman et al., 2004). We also identify an unusually abundant Na–Mg–SO_4 salt, possibly bloedite ($Na_2Mg(SO_4)_2 \cdot 4H_2O$), which, along with the other salts observed at Schroeder Hill, was previously described at Roberts Massif (Claridge and Campbell, 1968) (**Figure 5**). We did not observe any HCO_3 and CO_3 salts in the Schroeder Hill SEM images. The variability in the salt concentrations and compositions is likely due to the heterogeneous lithology of the Shackleton Glacier region, and differences in salt solubilities. While sulfate salts, such as gypsum do not readily solubilize even with multiple wetting events, nitrate salts, such as soda niter ($NaNO_3$), are highly soluble and only form in hyper-arid soils (Toner et al., 2013). The presence of $NaNO_3$ and Na_2SO_4 salts in the high elevation and inland samples indicates that these soils likely have had prolonged arid conditions.

TABLE 3 | $\delta^{13}C$ and $\delta^{18}O$ of total inorganic carbon (TIC).

Sample	Carb.%	$\delta^{13}C$	$\delta^{18}O$	$\delta^{18}O$
		PDB	PDB	VSMOW
BP1-4	0.24	−13.03	−39.82	−10.19
BP2-8	0.35	0.24	−20.53	9.70
MH3-10	0.38	7.13	−35.64	−5.87
NP4-6	0.11	1.40	−21.11	9.10
RM1-1	0.04	8.45	−9.55	21.01
RM3-7	0.07	4.17	−15.02	15.37
TN1-6	1.6	5.58	0.94*	31.83*
TN1-9	1.6	1.34	−15.80	14.57
TN3-5	2.5	4.21	−14.13	16.29
TN3-3	0.84	3.08	−13.93	16.51

TN1-6 produced NO gas which interfered with the isotopic analysis for* $\delta^{18}O$*. The sample is not included in **Figure 8.*

Stratospheric and Photochemical Processes as Sources of NO_3^-

The $\delta^{15}N$ and $\Delta^{17}O$ composition of NO_3^- in our samples suggests that NO_3^- is derived primarily from the atmosphere, with a component derived from photolysis in snowpack or another post-deposition alteration process. Atmospheric NO_3^-

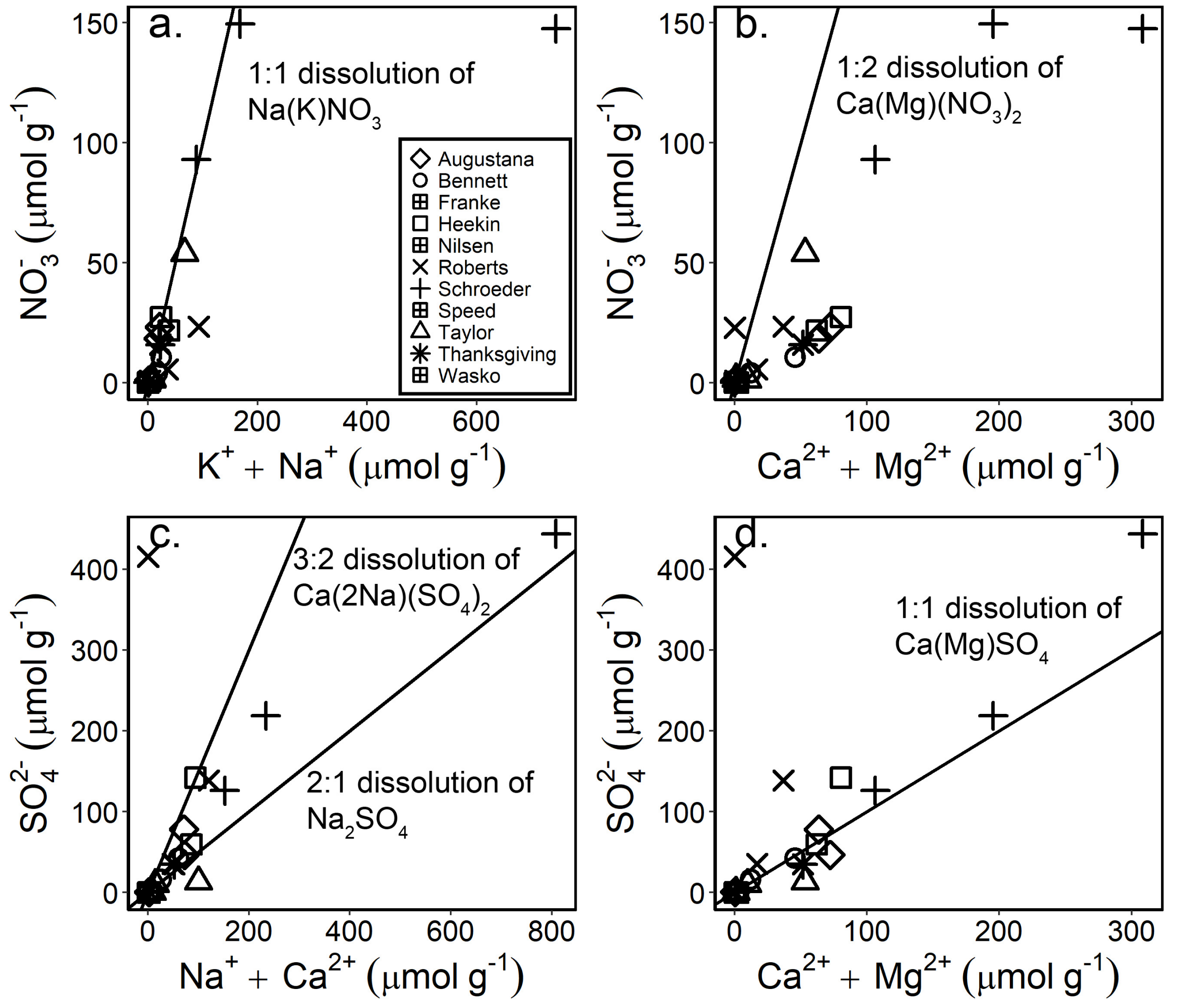

FIGURE 4 | Salt dissolution diagrams for the major NO_3^- **(a,b)** and SO_4^{2-} **(c,d)** salts typically observed in high latitude polar desert soils. The solid black lines are dissolution lines, suggesting that samples which fall on the lines likely have salts derived from the ions represented on the *x* and *y* axes.

has a distinct isotopic signature, with a $\delta^{15}N$ value of 0‰ if derived from N_2, or ∼ −6 to 7‰, if derived from multiple N species, and $\Delta^{17}O$ values > 15‰ (Moore, 1977; Michalski et al., 2003). However, upon deposition to the surface, $\delta^{15}N$ values of NO_3^- can be altered by photolysis (the breakdown of molecules due to intense and prolonged UV radiation) and volatilization in the absence of biologic activity, which could cause $\delta^{15}N$ to either increase or decrease depending on HNO_3 equilibrium between the aqueous solution and vapor (Walters and Michalski, 2015). The range of our $\delta^{15}N$ values suggests that the NO_3^- is not simply from oxidized N_2.

All of the Shackleton Glacier region samples have $\Delta^{17}O$ values > 15‰, indicating an atmospheric source (**Figure 6**). Positive $\Delta^{17}O$ values are an indicator of NO_3^- derived from ozone and ozone-derived oxygen in the atmosphere, which has a high non-mass dependent ^{17}O enrichment. The ^{17}O signal is preserved in NO_3^- and is believed to only be altered by denitrification (Reich and Bao, 2018). However, because biological denitrification is thought to be a minor process in Antarctic soils (Cary et al., 2010), the $\Delta^{17}O$ compositions are likely minimally altered.

Isotopic variations of N and O in NO_3^- have been previously measured in exposed sediments from the MDV and the Beardmore Glacier region to elucidate the source of NO_3^- to these systems. We compared the Shackleton Glacier region samples to these data, and while our isotopic values are not as well constrained, they generally plot near the MDV and Beardmore samples (**Figure 6**). These variations are also independent of NO_3^- concentration (**Figure 6b**). In the MDV, $\delta^{15}N$ values ranged from −9.5 to −26.2‰ and $\Delta^{17}O$ ranged from 28.9 to 32.7‰ (Michalski et al., 2005; Jackson et al., 2015, 2016). Further south, isotopic compositions of NO_3^- along the Beardmore Glacier ranged from 1.8 to 8.8‰ and 28.4 to 33.5‰ for $\delta^{15}N$ and $\Delta^{17}O$, respectively (Lyons et al., 2016). Between the two locations, $\Delta^{17}O$ values are identical, but $\delta^{15}N$ values are not similar. The $\delta^{15}N$ and $\Delta^{17}O$ range for the Beardmore overlaps

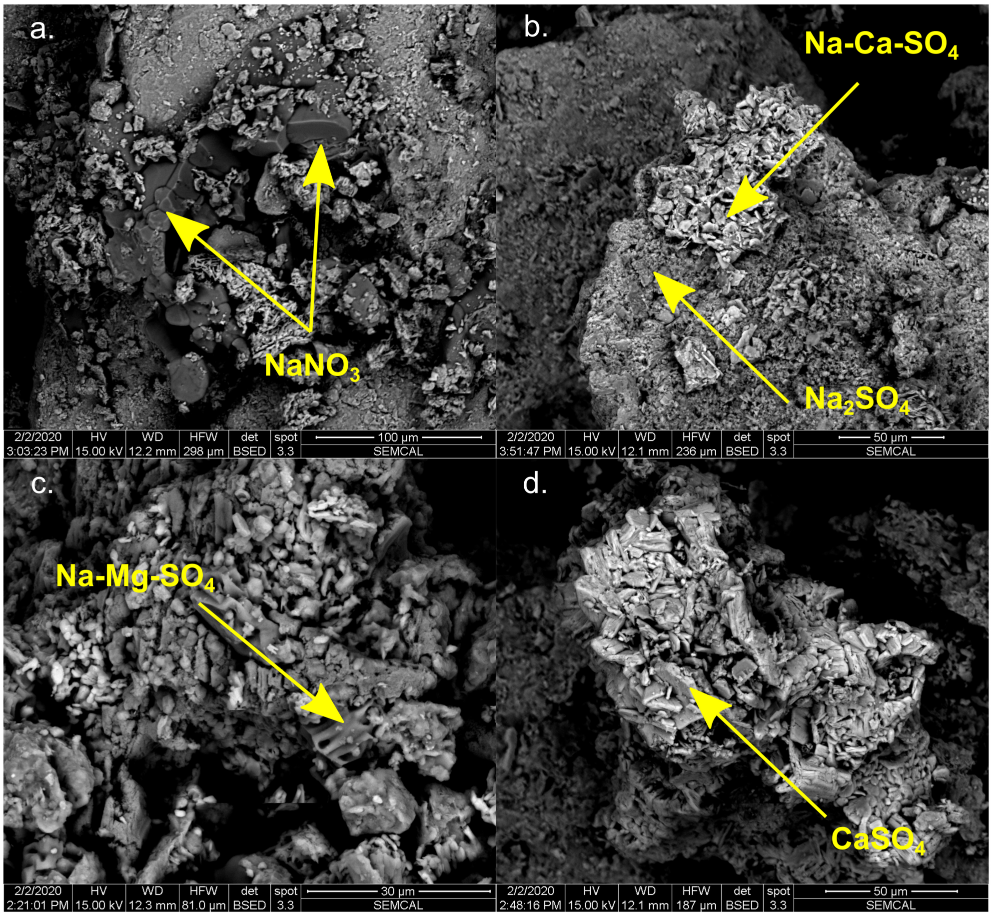

FIGURE 5 | Scanning electron microscopy (SEM) backscatter emission (BSE) images of salt encrustations from Schroeder Hill. The salts include soda nitre (NaNO$_3$) **(a)**, and a variety of sodium, magnesium, and calcium sulfate salts **(b–d)**. The chemical composition of the salts was determined by energy dispersive x-ray spectroscopy (EDX).

with measured values of atmospheric NO$_3$$^-$ (Moore, 1977; Michalski et al., 2003) (**Figure 6**), and Lyons et al. (2016) suggested that approximately 50% of the NO$_3$$^-$ was produced in the troposphere and 50% in the stratosphere based on the high Δ^{17}O values. In other words, the NO$_3$$^-$ in Beardmore Glacier region soils, as in the Shackleton Glacier region, is entirely atmospheric in origin and has preserved the atmosphere isotopic signature.

Post-depositional Alteration and Snowpack Emission of NO$_3$$^-$ in Antarctica

Though the Shackleton Glacier samples are likely initially derived from the atmosphere, the δ^{15}N values differ from the δ^{15}N range of atmospheric NO$_3$$^-$ (**Figure 4**). While not measured in this study, our data suggest that post-depositional alteration of NO$_3$$^-$ likely occurs in CTAM soils, potentially due to photolysis or local oxidation of N species (either modern or ancient). Previous studies have used both direct measurements and theoretical models to argue that the isotopic composition of NO$_3$$^-$ at the Antarctic surface can be affected by post-depositional fractionation processes, particularly re-emission of NO$_x$ (NO + NO$_2$) from snowpack due to photolysis and evaporation of HNO$_3$ (Savarino et al., 2007; Frey et al., 2009; Morin et al., 2009). Photolysis has been previously documented in glacial environments in both Greenland and Antarctica where snow accumulation rates are low (Honrath et al., 1999; Jones et al., 2001), and in photochemical experiments using snow and NO$_3$$^-$ which show direct production of NO$_x$ when exposed to sunlight (Honrath et al., 2000). Savarino et al. (2007) estimated the emission flux of NO$_y$ [NO + NO$_2$ + HNO$_3$ + HONO + 2 x (N$_2$O$_5$), etc.] from oxidized NO$_x$ species to be ΔN = 1.2 × 10^7 kg yr^{-1}, which is similar to the flux from polar stratospheric clouds at ΔN = 6.3 × 10^7 kg yr^{-1} (Muscari et al., 2003). In other words, photolysis and NO$_x$ emission is an important source of NO$_3$$^-$ to the Antarctic N cycle.

Spatial and temporal variations in the δ^{15}N composition of Antarctic snow are similar to the variability in the Shackleton Glacier soils, reflecting both stratospheric and tropospheric production of NO$_3$$^-$. Savarino et al. (2007) found that the composition of NO$_3$$^-$ in coastal Antarctic snowpack was dependent on the season, where winter was dominated by deposition of NO$_3$$^-$ from polar stratospheric clouds (δ^{15}N ≈ 19‰) and the summer and late-spring composition was influenced by snow reemissions of NO$_x$ and HNO$_3$ from further

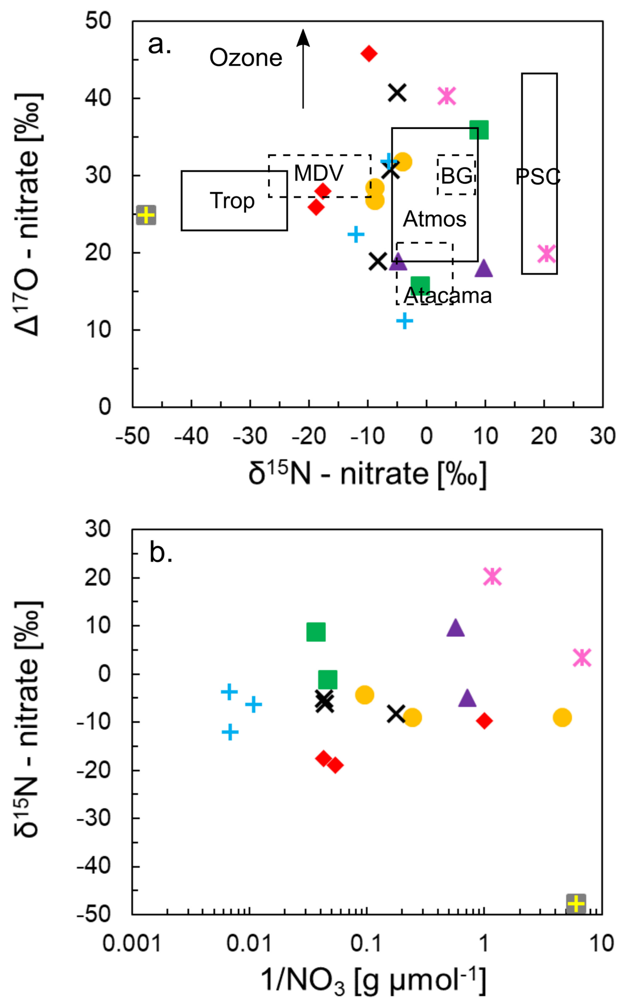

FIGURE 6 | Isotopic composition of NO_3^- for Shackleton Glacier soils **(a)** and the variation of $\delta^{15}N$ with inverse nitrate concentrations **(b)**. The shapes and colors representing the different sampling locations correlate with the key in **Figure 2**. The solid black boxes represent the isotopic composition of NO_3^- from the mixed atmosphere, stratosphere [polar stratospheric clouds (PSC)], and troposphere (re-emission from snowpack) (Moore, 1977; Michalski et al., 2003; Savarino et al., 2007). The dashed boxes represent the Beardmore Glacier region (BG), McMurdo Dry Valleys (MDV), and Atacama Desert for comparison (Michalski et al., 2004, 2005; Jackson et al., 2015, 2016; Lyons et al., 2016). The black arrow indicates a potential NO_3^- formation pathway with higher $\Delta^{17}O$ values from ozone.

inland ($\delta^{15}N \approx -34$‰). Frey et al. (2009) measured the spatial distribution of NO_3^- concentrations and $\delta^{15}N$ and $\Delta^{17}O$ values of NO_3^- between the Antarctic coast and the interior. They found that $\delta^{15}N$ values were highly positive in the interior, with values > 200‰, and highly negative on the coast, with values as low as −15‰. Frey et al. (2009) and Erbland et al. (2013) show that the $\delta^{15}N$-NO_3^- of snowpack in the interior of the continent is positive and argue that subsequent photolysis and evaporation cause gaseous loss of that NO_3^- as NO_x. This process results in enriched $\delta^{15}N$ in the remaining snow, and a lighter $\delta^{15}N$ of NO_x released to the atmosphere, which is later re-deposited elsewhere on the continent, including soils, as HNO_3^-.

It should be noted that no studies have directly investigated or measured post-depositional fractionation of $\delta^{15}N$ and $\Delta^{17}O$ in NO_3^- in Antarctic soils. Jackson et al. (2016) argued that the isotopic signature of NO_3^- in MDV soils is preserved and more resistant to post-depositional alteration, likely due to acid neutralization by soil carbonate minerals and limited light penetration into soils. These authors assumed that NO_3^- which was deposited directly on soil surfaces from the atmosphere was not influenced by volatilization, photolysis, or water exchange. Instead, they suggested that the soil $\delta^{15}N$ values of NO_3^- were affected by post-depositional alteration when overlain by ephemeral snow and near glaciers due to photolysis in the snowpack, as supported by decreasing $\delta^{15}N$ values further from the glacier. We do not observe a trend of decreasing $\delta^{15}N$ values further from snow and ice in our samples. However, considering the range of $\delta^{15}N$ values and positive $\Delta^{17}O$ values along the Shackleton Glacier, we hypothesize that our samples contain a mixture of NO_3^- produced in the stratosphere (sedimentation from polar stratospheric clouds, oxidation of NO_x by ozone) and the troposphere (oxidation of HNO_3 by ozone, snowpack remission, and long range transport of gases and aerosols), both of which could be affected by evaporation and photolysis upon deposition on soils.

Estimating the Atmospheric Contribution of NO_3^- to Shackleton Glacier Region Soils

Production, transport and alteration of NO_3^- in soils requires further investigation to effectively determine the relative fraction of NO_3^- derived from both stratospheric and tropospheric sources. However, we estimate the fluxes from the two reservoirs following conceptual and theoretical models from Savarino et al. (2007), Frey et al. (2009), and Erbland et al. (2015). Our data suggest that for inland locations in Antarctica, NO_3^- is deposited from the stratosphere onto the surface of the EAIS and soils of the TAM, and initially maintains a stratospheric signal (typically $\delta^{15}N$ near 0‰ and $\delta^{17}O$ > 15‰). Intense UV radiation induces photolysis and mobilization of HNO_3 plus other reduced N species, especially in snow, which are later re-oxidized by tropospheric ozone and re-introduced to the surface through wet and dry deposition. This mechanism is further supported by results from Jackson et al. (2016), who found that $\delta^{15}N$ values in soils from the MDV were similar to values from aerosols near Dumont d'Urville in the coastal Antarctic (Savarino et al., 2007).

$$\delta^{15}N_{soil} = f \cdot \delta^{15}N_{strat} + f \cdot \delta^{15}N_{trop(emit)} \pm f \cdot \delta^{15}N_{post-dep} \quad (1)$$

$$f_{strat} + f_{trop(emit)} = 1 \quad (2)$$

A simple mixing model using Equations 1 and 2 can be solved to determine the relative fractions of the different atmospheric sources to the Shackleton soils. In Equation 1, the $\delta^{15}N$ composition of NO_3^- is derived from the fractions (f) of $\delta^{15}N$ from the stratosphere (*strat*), photolytic emission from snowpack to the troposphere [*trop(emit)*], and post-depositional processes (*post-dep*). Post-depositional alteration of NO_3^- is still poorly

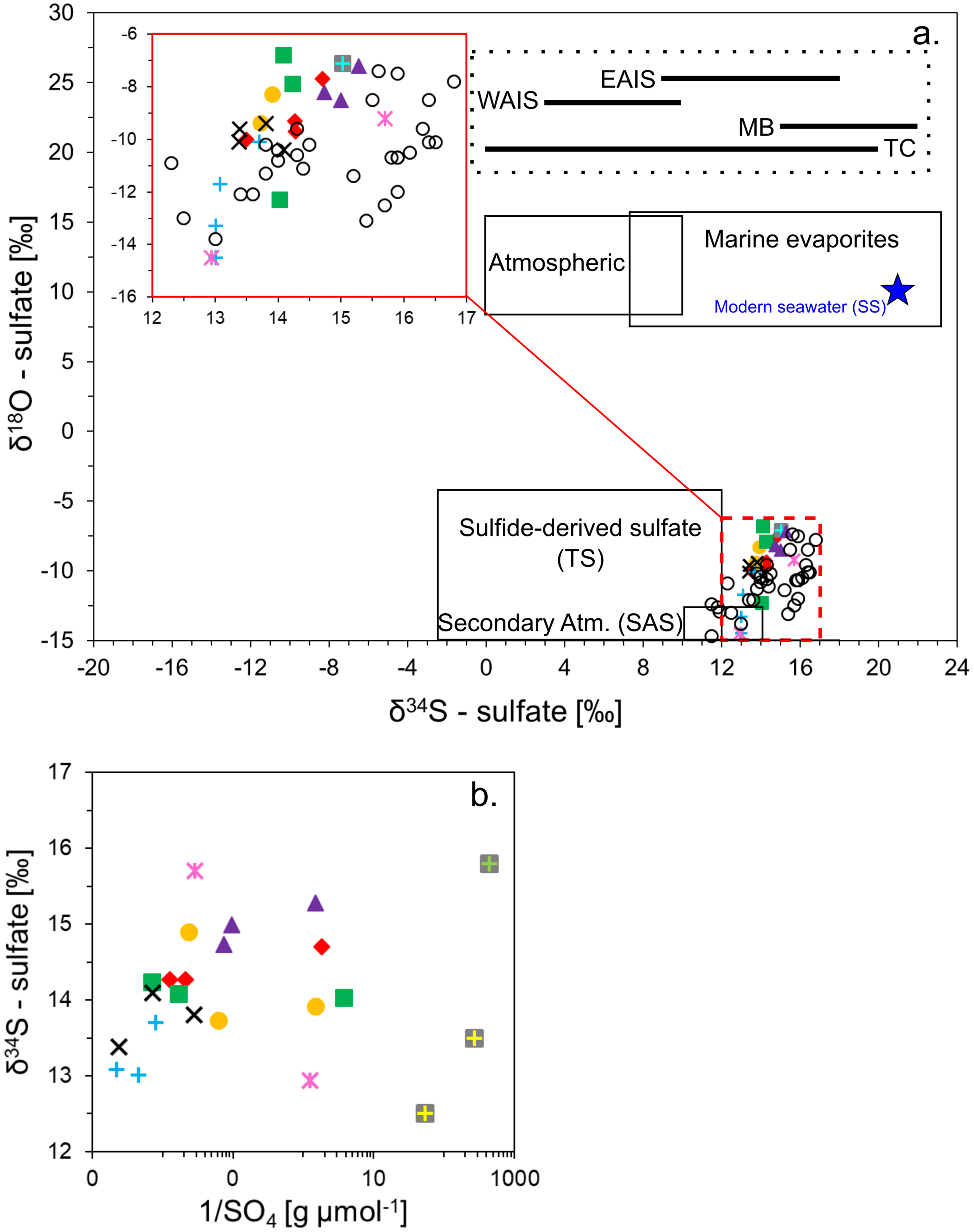

FIGURE 7 | Isotopic composition of SO_4^{2-} **(a)** and the variation of $\delta^{34}S$ with inverse sulfate concentrations **(b)**. The shapes and colors representing the different sampling locations correlate with the key in **Figure 2**. The clear circles represent MB11 samples (Asgard Tills) from the McMurdo Dry Valleys (Bao and Marchant, 2006). The solid red box shows the distribution of the samples at a higher resolution. The solid and dotted black boxes represent potential SO_4^{2-} sources and the blue star is the SO_4^{2-} isotopic composition of modern seawater (Holser and Kaplan, 1966; Faure and Felder, 1981; Calhoun and Chadson, 1991; Legrand et al., 1991; Alexander et al., 2003; Pruett et al., 2004; Jonsell et al., 2005; Bao and Marchant, 2006; Baroni et al., 2008; Tostevin et al., 2014).

understood in soils, but over prolonged periods of exposure, we anticipate that the modern influence on isotopic composition would be minimal. Therefore, we simplify the Equation 1 and assume that stratospheric deposition and emission to the troposphere (followed by redeposition) are the primary sources of NO_3^- in Equation 2. We use end-member values of $\delta^{15}N \approx 19‰$ for deposition from polar stratospheric clouds to represent the stratospheric deposition and $\delta^{15}N \approx -34‰$ for NO_3^- species liberated by photolysis to represent tropospheric deposition (Savarino et al., 2007). Solving these equations, we estimate between 30 and 100% of NO_3^- is from the stratosphere and up to 70% is from the troposphere, with the exception of one sample from Nilsen Peak which appears entirely derived from the troposphere (**Table 4**). Slightly negative fraction values for Nilsen Peak and Thanksgiving Valley are likely due to minor variations in the source isotopic compositions. However, Mt. Speed has an anomalously low $\delta^{15}N$ value of −47.8‰, which cannot be explained by our simple model.

Primary and Secondary Atmospheric, and Chemical Weathering Derived SO_4^-

Sulfide Weathering as a Source of SO_4^{2-}

The $\delta^{34}S$ and $\delta^{18}O$ isotopic values of SO_4^{2-} indicate that sulfide weathering is likely a minor source of SO_4^{2-} to the Shackleton Glacier region compared to other sources, such as atmospheric deposition. Though the $\delta^{18}O$ values are similar between the sulfide end-member and the Shackleton soil leaches, the Shackleton $\delta^{34}S$ values are greater (**Figure 7**). This is probably due to the low abundance of sulfide minerals in the local lithology since the $\delta^{34}S$ signature is preserved during sulfide weathering (Balci et al., 2007).

In sedimentary rocks, sulfide is almost exclusively found as the mineral pyrite (FeS_2). Pyrite has been observed and characterized in the metasandstone of both Bowers Terrane (Molar Formation and Pyrite Pass) and Robertson Bay Terrane near the MDV. Further South, till found on Mt. Sirius in the Beardmore Glacier region contained detrital pyrite, which is likely the major source of pyrite for the TAM (Hagen et al., 1990). Tills of the Sirius Group can be found throughout much of the TAM at high and low elevations, but along the Shackleton Glacier the till was most abundant at Roberts Massif and Bennett Platform, with smaller outcrops observed at Schroeder Hill (Hambrey et al., 2003). Pyrite-bearing tills have been identified in these regions, but their distributions and isotopic compositions are variable (Holser and Kaplan, 1966; Balci et al., 2007; Pisapia et al., 2007; Bao, 2015).

The SO_4^{2-} isotopic composition of the Shackleton soils is not reflective of a predominately pyrite source. Sulfur sequential extractions were performed on seven samples representing the range of elevations, local lithology, and glacial histories found along the Shackleton Glacier to investigate pyrite weathering as a potential source of S. Percentages of acid-soluble sulfate and Cr-reducible sulfide (i.e., pyrite) were generally low for nearly all samples with less than 0.5 and 0.003% (∼150 to 1 μmol-S g^{-1}), respectively (**Table 5**). Concentrations of acid-soluble sulfate were of sufficient mass for $\delta^{34}S$ analysis only for the high elevation and further inland locations of Roberts Massif, Mt. Augustana and Schroeder Hill. Interestingly, the acid-soluble $\delta^{34}S$ values are only 0.2–0.3‰ higher than the water-soluble $\delta^{34}S$ values, which is within our analytical error. We suggest that this extractable phase may be primarily from gypsum/anhydrite dissolution in acid and therefore is of a common source with the water-soluble SO_4^{2-} since the acid extraction solubilizes both the water and acid soluble constituents. For the Cr-reducible phase, S concentrations were sufficient for $\delta^{34}S$ analysis for two samples, Mt. Heekin and Nilsen Peak. These $\delta^{34}S$ values are more negative than both the

TABLE 4 | Two-component mixing model to determine relative contributions of different sources of NO_3^-.

Sample	f(strat)	f(trop(emit))
AV2-1	0.29	0.71
AV2-5	0.31	0.69
AV2-8	0.46	0.54
BP2-1	0.47	0.53
BP2-5	0.56	0.44
BP2-8	0.47	0.53
MH3-1	0.81	0.19
MH3-5	0.62	0.38
MSP4-2	−0.26*	1.26
NP3-4	−0.02*	1.02
RM2-1	0.53	0.47
RM2-5	0.49	0.51
RM2-8	0.55	0.45
SH3-2	0.57	0.43
SH3-5	0.42	0.58
SH3-8	0.52	0.48
TGV2-1	1.03	−0.03*
TGV2-5	0.66	0.34
TGV2-8	0.71	0.29
TN2-1	0.83	0.17
TN2-8	0.55	0.45

End-member values of $\delta^{15}N$ from stratospheric clouds (strat) (19‰) and tropospheric remission [trop(emit)] (−34‰) were originally reported by Savarino et al. (2007). Negative values are indicated (*), which identify samples where the model parameters were insufficient.

TABLE 5 | Sulfur sequential extractions on bulk sediment and $\delta^{34}S$ values associated with each fraction.

	wt. S% Acid-soluble SO_4	wt. S% Cr-reducible sulfide	$\delta^{34}S$ Acid-soluble SO_4	$\delta^{34}S$ Cr-reducible sulfide
			VCDT	VCDT
TGV2-1	0.004	<0.001	b.d.l.	b.d.l.
TN2-1	<0.001	<0.001	b.d.l.	b.d.l.
MH3-5	0.001	0.00t3	b.d.l.	−2.3
AV2-1	0.268	<0.001	14.6	b.d.l.
NP3-4	0.001	0.002	b.d.l.	12.1
RM2-8	0.432	<0.001	14.3	b.d.l.
SH3-2	0.87	<0.001	13.3	b.d.l.

Samples that were below the analytical detection limit are listed as b.d.l.

water-soluble and acid-soluble values at −2.3 and 12.1‰. As a comparison, Sirius Group tills had $\delta^{34}S$ values ranging from −1.4 to +3.1‰, representing an isotopic composition similar to elemental sulfur (S^0), though it is well-known that sedimentary sulfides are isotopically variable (Hagen et al., 1990).

Our data show that some Shackleton Glacier region soils contain sulfide (likely as pyrite), however, sulfide weathering is unlikely to be a major source of $SO_4{}^{2-}$. The concentrations of water-soluble $SO_4{}^{2-}$ in our samples are as high as 450 μmol g^{-1}, while most samples had sulfide concentrations too low for analysis (<0.001% or 0.3 μmol-S g^{-1}). Though Mt. Heekin had quantifiable sulfide, the concentration was only 0.003% (∼1 μmol-S g^{-1}), compared to 0.19% (∼50 μmol-S g^{-1}) for water-soluble S. Unless the sulfide reservoirs were at least 100x greater in the past and experienced complete oxidation, the majority of our $SO_4{}^{2-}$ was derived from another source, likely the atmosphere as we proposed previously. Additionally, the distinct trends between $SO_4{}^{2-}$ concentrations and isotopic composition with elevation, distance from the coast, and distance from the nearest glacier suggest that similar processes are controlling $SO_4{}^{2-}$ formation throughout the region. Finally, the $\delta^{34}S$ values of the Cr-reducible sulfide from Mt. Heekin and Nilsen Peak are too negative to explain the isotopic composition of the water-soluble $SO_4{}^{2-}$. All the available information suggest that chemical weathering of pyrite may occur in some Shackleton Glacier region soils, but it is a minor process and is overwhelmed by an atmospheric source.

Atmospheric Sulfate as the Primary Source of $SO_4{}^{2-}$

We used end-member values of $\delta^{34}S$ and $\delta^{18}O$ for non-sea salt secondary atmospheric sulfate (SAS) ($\delta^{34}S$ = 12.0‰, $\delta^{18}O$ = −16.0‰), sea salt sulfate (SS) ($\delta^{34}S$ = 22‰, $\delta^{18}O$ = 10‰), and terrestrial sulfate from sulfides (TS) ($\delta^{34}S$ = 5‰, $\delta^{34}S$ = −20‰) reported by Bao and Marchant (2006) to estimate the contributions of each source to the Shackleton Glacier region soils. We solved a three-component mixing model (Equations 3–5) for the fractions of SAS, SS, and TS comprising the observed $SO_4{}^{2-}$ isotopic composition. With the exception of one sample from Mt. Heekin, the $SO_4{}^{2-}$ in our samples appears predominately derived from an SAS source, followed by SS, and lastly TS (**Table 6**). In particular, the higher elevation and furthest inland locations, such as Schroeder Hill and Roberts Massif, have the highest contributions from SAS (>70%). These results are similar to those from high and inland locations in the MDV (Bao and Marchant, 2006). Though the isotopic composition of most samples can be explained by a combination of the three end members, our simple model was not sufficient for two Thanksgiving Valley samples and three additional samples from Mt. Heekin, Taylor Nunatak, and Schroeder Hill, probably due to unaccounted variability in the values for the SAS and TS end-members. As stated in section "Sulfide Weathering as a Source of $SO_4{}^{2-}$," the sulfide isotopic composition in terrestrial systems is highly variable, but the least constrained end-member is likely SAS.

$$\delta^{34}S_{soil} = f \cdot \delta^{34}S_{SAS} + f \cdot \delta^{34}S_{SS} \pm f \cdot \delta^{34}S_{TS} \tag{3}$$

$$\delta^{18}O_{soil} = f \cdot \delta^{18}O_{SAS} + f \cdot \delta^{18}O_{SS} \pm f \cdot \delta^{18}O_{TS} \tag{4}$$

$$f_{SAS} + f_{SS} + f_{TS} = 1 \tag{5}$$

SAS can have a large range of $\delta^{34}S$, $\delta^{18}O$, and $\Delta^{17}O$ values due to differences in the initial source of S and the chemical composition of the oxidizing compounds. Sulfur gases in the atmosphere (SO_2) are derived from volcanic emissions, DMS oxidation from the ocean, and anthropogenic emissions. The latter is thought to comprise the least important source for Antarctica. SO_2 can be oxidized by both ozone and H_2O_2 to form SAS in the troposphere and stratosphere, where the oxygenic isotopic transfer is one oxygen (0.25) and two oxygen (0.5) of the total four oxygen atoms in $SO_4{}^{2-}$ for ozone and H_2O_2, respectively, which produces a positive $\Delta^{17}O$ anomaly in $SO_4{}^{2-}$ and a wide range of $\delta^{18}O$ values (Savarino et al., 2000; Uemura et al., 2010; Bao, 2015). Additionally, SAS can be produced in the stratosphere by photolysis of carbonyl sulfide (COS), the most abundant sulfur gas in the atmosphere, and by SO_2 oxidation by OH radicals, which also produce positive $\Delta^{17}O$ anomalies (Kunasek et al., 2010; Brühl et al., 2012). Though we could not determine the $\Delta^{17}O$ composition of the Shackleton Glacier region $SO_4{}^{2-}$, we suspect $\Delta^{17}O$ would be positive and similar to the MDV and Beardmore Glacier region (Bao et al., 2000; Bao and Marchant, 2006; Sun et al., 2015). Future measurements

TABLE 6 | Three-component mixing model to determine relative contributions of different sources of $SO_4{}^{2-}$.

Sample	f(SAS)	f(SS)	f(TS)
AV2-1	0.73	0.25	0.03
AV2-5	0.68	0.27	0.06
AV2-8	0.58	0.33	0.09
BP2-1	0.58	0.28	0.15
BP2-8	0.48	0.33	0.19
MH3-1	0.50	0.34	0.16
MH3-5	0.34	0.39	0.27
MH3-8	0.99	0.13	−0.11*
NP3-4	0.58	0.35	0.07
RM2-1	0.58	0.25	0.16
RM2-5	0.59	0.27	0.13
RM2-8	0.77	0.22	0.01
SH3-2	1.03	0.05	−0.08*
SH3-5	0.71	0.18	0.10
SH3-8	0.65	0.24	0.10
TGV2-1	1.02	0.05	−0.07*
TGV2-5	0.97	0.23	−0.20*
TN2-1	0.64	0.34	0.02
TN2-5	0.64	0.31	0.05
TN2-8	0.73	0.29	−0.02*

End-member values of $\delta^{34}S$ and $\delta^{18}O$ for non-sea salt secondary atmospheric sulfate (SAS) (12.0 and −16.0‰), sea salt sulfate (SS) (22 and 10‰), and terrestrial sulfate from sulfides (TS) (5 and −20‰) were originally reported by Bao and Marchant (2006). Negative values are indicated (*), which identify samples where the model parameters were insufficient.

of $\Delta^{17}O$ in SO_4^{2-} would provide additional evidence for SAS accumulation in CTAM soils.

Accumulation of Secondary Atmospheric Sulfate (SAS) and Wetting History

The relatively small variability in $\delta^{34}S$ values indicates that the SO_4^{2-} in the Shackleton Glacier region is derived from a common, large-scale source, such as the atmosphere. Additionally, when compared to the concentrations of SO_4^{2-} in the water leaches, $\delta^{34}S$ does not vary systematically indicating that the variability is not due to differences in source, but instead from varying accumulation periods (**Figure 7b**).

Though exposure ages have yet to be determined for these areas in the Shackleton Glacier region, modeling studies have shown that the height of the Shackleton Glacier was probably higher than current levels during the LGM (MacKintosh et al., 2011; Golledge et al., 2013), and likely inundated much of the currently ice-free areas near the Ross Ice Shelf. While these surfaces were inundated, some soils closer to the Polar Plateau may have been ice-free and would have accumulated salts from the atmospheric deposition of SAS. When the EAIS retreated in the late Pleistocene/early Holocene, the recently exposed soils could begin accumulating salts again. The small variations in $\delta^{34}S$ values likely reflect isotopic changes of SAS through time due to changes in volcanic activity and DMS and/or MSA production, and changes in the concentrations of ozone, OH, COS, and H_2O_2 in the atmosphere, as reflected in the wide-range of values for Antarctic background sources in **Figure 7a** (Legrand et al., 1991; Bao, 2015). The variability in $\delta^{18}O$ values is possibly due to the removal of ^{18}O during atmospheric transport, changes in temperature, changes in the ocean isotopic composition during glacial and interglacial periods, and/or differences in the relative abundance of oxidizing atmospheric compounds. However, without the ability to decipher the difference between contemporary and paleo SO_4^{2-} deposits, these mechanisms remain speculative.

Cryogenic Carbonate Mineral Formation and Isotope Equilibrium

Pedogenic carbonates in Antarctic soils are thought to be formed by authigenesis in the presence of liquid water. It is assumed that Ca^{2+} ions for carbonate formation are derived from the weathering of Ca-rich aluminosilicate minerals, the dissolution of primary calcite within the soils, and/or calcium associated with aeolian dust (Lyons et al., 2020). In solution, carbonate minerals are precipitated during dissolved $Ca\text{-}HCO_3/CO_3$ saturation when the ion activity product is greater than the solubility product. In polar region soils, this typically occurs during evaporation/sublimation or cryoconcentration due to freezing of soil solutions or films (Courty et al., 1994; Vogt and Corte, 1996; Burgener et al., 2018).

The isotopic composition of $HCO_3 + CO_3$ in the Shackleton Glacier region bulk soil samples suggests that the carbonate is originally formed by cryogenic processes, such as rapid freezing and evaporation/sublimation, with possible kinetic isotope effects (KIE) (**Figure 8**). Previous studies have shown that the formation of authigenic calcite deposits is controlled by dissolved CO_2 concentrations and carbonate alkalinity of $Ca\text{-}HCO_3$ solutions (Nezat et al., 2001; Neumann et al., 2004; Lacelle et al., 2006; Lacelle, 2007; Burgener et al., 2018). The $\delta^{13}C$ and $\delta^{18}O$ isotopic composition of carbonate minerals is dependent on the isotopic composition and temperature of the formation fluid when in equilibrium with both the fluid and atmosphere (Lacelle, 2007). Further, the $\delta^{18}O$ isotopic composition of the fluid is influenced by evaporation/sublimation, which depletes the fluid of the lighter oxygen isotope, and freezing, which incorporates the heavier isotope in ice (Jouzel and Souchez, 1982). However, during rapid dehydration, freezing, and carbonate dissolution, KIE can result in temperature-independent fractionation and isotopically variable carbonate species (Clark and Lauriol, 1992; Skidmore et al., 2004; Burgener et al., 2018).

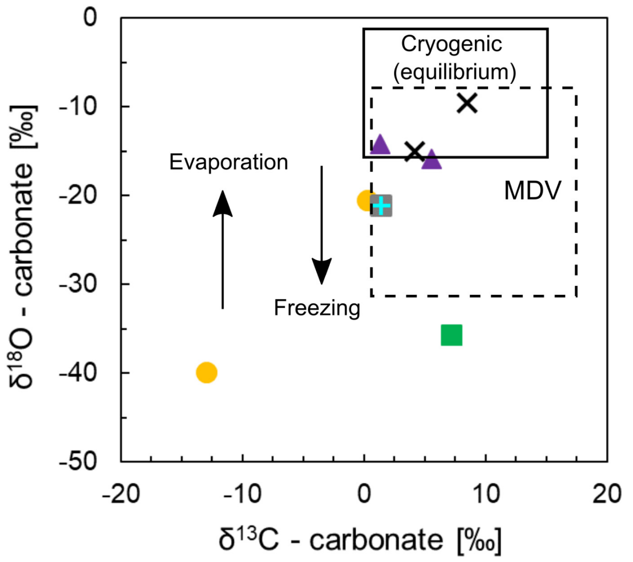

FIGURE 8 | Isotopic composition of total inorganic carbon ($HCO_3 + CO_3$) for Shackleton Glacier soils. $\delta^{13}C$ and $\delta^{18}O$ are reported in terms of VPDB. The shapes and colors representing the different sampling locations correlate with the key in **Figure 2**. The solid black box represents the composition of cryogenic carbonates formed in equilibrium with the source fluid and atmosphere (slow process). The arrows represent the direction of $\delta^{18}O$ fractionation with rapid freezing and evaporation/sublimation, and the dashed box represents samples from the McMurdo Dry Valleys (MDV) for comparison (Nakai et al., 1975; Lacelle et al., 2006; Lacelle, 2007; Burgener et al., 2018; Lyons et al., 2020).

Previous studies have measured the isotopic composition of soil carbonate minerals from the MDV and have elucidated the formation mechanisms for cryogenic carbonates (see Lacelle, 2007). In summary, isotopic values of soil carbonate in Taylor and Victoria Valleys in the MDV ranged from 6.73 to 11.02‰ for $\delta^{13}C$ and −8.13 to −20.34‰ for $\delta^{18}O$ (VPDB) (Burgener et al., 2018; Lyons et al., 2020). Nakai et al. (1975) measured $\delta^{13}C$ and $\delta^{18}O$ of carbonate coatings on rocks in the Lake Vanda Basin, MDV, and their $\delta^{13}C$ values ranged from 1.5 to 17.6‰ while their $\delta^{18}O$ ranged from −9.2 to −31.2‰ (VPDB). Lacelle (2007) argued that the Lake Vanda basin carbonates were cryogenic in origin, forming from bicarbonate dehydration and subsequent CO_2 degassing in isotopic disequilibrium. Disequilibrium during rapid evaporation/sublimation or freezing results in more positive $\delta^{13}C$ and $\delta^{18}O$ values relative to equilibrium carbonate formation (Clark and Lauriol, 1992; Lacelle et al., 2007). Using a clumped isotope method, Burgener et al. (2018) arrived at similar conclusions regarding disequilibrium during carbonate formation. The authors suggested that negative Δ_{47} (notation from clumped isotopes of mass 47) with positive $\delta^{18}O$ anomalies, and positive $\delta^{13}C$ values with respect to equilibrium were consistent with cryogenic calcite formation and KIE from CO_2 degassing during bicarbonate dehydration. Additionally, $\delta^{13}C$ values from Taylor Valley carbonates, which were sampled as mineral coatings on rocks, were near 7.4‰ indicating an atmospheric origin of CO_2 (Lyons et al., 2020), and were similar to the values reported by Burgener et al. (2018).

The Shackleton samples are generally within the range of $\delta^{13}C$ for cryogenic carbonate in equilibrium with the atmosphere (**Figure 8**) (Lacelle et al., 2006; Lacelle, 2007). Since we collected surface samples (up to 5 cm at depth), the carbonates were formed under conditions allowing for rapid exchange of CO_2. However, some samples have lower $\delta^{18}O$ values, possibly due to KIE, and rapid freezing and evaporation/sublimation. As stated previously, the formation of carbonate minerals in soils from rapid evaporation/sublimation of glacial meltwater results in a relatively heavier $\delta^{18}O$ signature compared to the ice isotopic composition (Lacelle et al., 2006; Lyons et al., 2020). While the isotopic composition of ice in the Shackleton Glacier region is unknown, due to its distance inland, we expect $\delta^{18}O$ values ∼ -45‰ (Mayewski et al., 1990; Gooseff et al., 2006). Evaporation/sublimation carbonate formation from this water may explain the relatively more positive $\delta^{18}O$ values in the Shackleton soils compared to glacial ice. Most of our data can be explained by these mechanisms, but one sample from Bennett Platform and a second from Mt. Heekin have highly negative $\delta^{18}O$ values, and the Bennett Platform sample is the only sample we measured with a negative $\delta^{13}C$ value (**Figure 8**). These outliers demonstrate the need for more geochemical data from CTAM ice-free areas to definitively elucidate carbonate formation and kinetics in ice-free Antarctic environments.

CONCLUSION

Ice-free areas from the Shackleton Glacier region, Antarctica represent polar desert environments that have been modified throughout the Cenozoic, which is reflected in the variable salt geochemistry. Along a transect moving inland and up in elevation along the Shackleton Glacier toward the Polar Plateau, water-soluble salt concentrations increased, and the dominant salt species also changed. Near the Ross Ice Shelf, Cl^- was the dominant salt, while $NO_3{}^-$ and $SO_4{}^{2-}$ were more abundant further inland. High $NO_3{}^-$ and $SO_4{}^{2-}$ concentrations are likely associated with soda niter ($NaNO_3$), anhydrite or gypsum ($CaSO_4$ or $CaSO_4 \cdot 2H_2O$), epsomite ($MgSO_4 \cdot 7H_2O$), thenardite or mirabilite (Na_2SO_4 or $Na_2SO_4 \cdot 10H_2O$) and glauberite ($Na_2Ca(SO_4)_2$). We also identified abundant Na–Mg–SO_4 salts at Schroeder Hill, potentially bloedite.

The $\delta^{15}N$ and $\Delta^{17}O$ isotopic composition of $NO_3{}^-$ indicated that $NO_3{}^-$ is primarily derived from the atmosphere, with varying contributions from the troposphere (0–70%) and stratosphere (30–100%). Neither $\delta^{15}N$ nor $\Delta^{17}O$ exhibited trends with elevation, distance from the coast of the Ross Ice Shelf, or distance from the glacier. We argue that post-depositional alteration of $NO_3{}^-$, potentially due to photolysis or volatilization, likely occurs in CTAM soils and possibly explains the variability in the $NO_3{}^-$ isotopic composition. However, the occurrence and degree of soil photolysis of $NO_3{}^-$ is unknown and requires further investigation.

Results from a three-component mixing model suggested that $SO_4{}^{2-}$ in Shackleton Glacier region soils was predominately deposited as secondary atmospheric sulfate (SAS) and derived from the oxidation of SO_2, H_2S, and/or dimethyl sulfide by H_2O_2, COS, and ozone in the atmosphere. While there is evidence to suggest that some $SO_4{}^{2-}$ was produced by the weathering of pyrite and other sulfide minerals, the atmospheric source was likely much more important, especially in soils which have been exposed for prolonged periods at higher elevations and near the Polar Plateau.

While $SO_4{}^{2-}$ and $NO_3{}^-$ were primarily derived from atmospheric deposition, carbonate minerals were formed at the surface as cryogenic carbonate. Based on the $\delta^{13}C$ and $\delta^{18}O$ values of soil total inorganic carbon (TIC), we conclude that both equilibrium and disequilibrium occur through slow and rapid evaporation/sublimation or freezing of fluids. Disequilibrium between the fluid and the precipitated carbonate resulted in the negative $\delta^{18}O$ values observed due to bicarbonate dehydration.

Our analysis and interpretation of the isotopic composition of $NO_3{}^-$, $SO_4{}^{2-}$, and HCO_3 + CO_3 show that atmospheric deposition and chemical weathering at the soil surface are important for salt formation in Antarctica. While $NO_3{}^-$ and $SO_4{}^{2-}$ are both oxyanions and thought to maintain their isotopic composition post-formation, post-depositional processes, such as volatilization and photolysis, may alter both N and O in $NO_3{}^-$, while $SO_4{}^{2-}$ appears less affected by these processes. As a result, the isotopic composition of $NO_3{}^-$ can potentially be used to constrain $NO_3{}^-$ recycling in soils, $SO_4{}^{2-}$ can be used as an indicator of past atmospheric oxidation processes, and carbonate can be used to understand current and past availability of water. We suggest that similar processes likely occur(ed) for other hyper-arid environments in the CTAM and Mars.

DATA AVAILABILITY STATEMENT

All datasets generated for this study are included in the article/**Supplementary Material**.

AUTHOR CONTRIBUTIONS

BA, DW, IH, NF, and WL designed and funded the project. BA, DW, IH, NF, and MD conducted the fieldwork. JL, GM, and MD analyzed the samples for N and O isotope ratios in nitrate. MD prepared the samples for S and O isotopic analysis in sulfate. TD and MD analyzed the samples for C and O isotope ratios in carbonate. SW, CG, and MD analyzed the samples for water-soluble ions. MD wrote the manuscript with contributions and edits from all authors. All authors contributed to the article and approved the submitted version.

FUNDING

This work was funded by NSF OPP grants (1341631, 1341618, 1341629, and 1341736) awarded to WL, DW, NF, and BA, the NSF GRFP fellowship (60041697) awarded to MD, the International Association of Geochemistry (IAGC) Student Research Grant awarded to MD, and the Geological Society of America (GSA) Student Research Grant awarded to MD.

ACKNOWLEDGMENTS

Many thanks to the United States Antarctic Program (USAP), the Antarctic Science Contractors (ASC), the Petroleum Helicopters Inc. (PHI), and Dr. Marci Shaver-Adams for logistical and field support. We especially thank Dr. Anna Szynkiewicz at The University of Tennessee, Knoxville for her generous time, resources, and assistance with the sulfate isotope analysis. Additionally, we gratefully acknowledge Daniel Gilbert for help with initial laboratory analyses at The Ohio State University, the Stable Isotope Lab directed by Dr. Robert Gregory and John Robbins at Southern Methodist University for assistance in the carbonate analysis, and the Subsurface Energy Materials Characterization & Analysis Laboratory (SEMCAL) and Dr. David Cole at The Ohio State University for the usage of the SEM. Geospatial support for this work provided by the Polar Geospatial Center under NSF-OPP awards 1043681 and 1559691. We appreciate the thoughtful comments and suggests from two reviewers, which have improved this manuscript.

SUPPLEMENTARY MATERIAL

The Supplementary Material for this article can be found online at: https://www.frontiersin.org/articles/10.3389/feart.2020.00341/full#supplementary-material

REFERENCES

Alexander, B., Thiemens, M. H., Farquhar, J., Kaufman, A. J., Savarino, J., and Delmas, R. J. (2003). East Antarctic ice core sulfur isotope measurements over a complete glacial-interglacial cycle. *J. Geophys. Res. Atmos.* 108:4786. doi: 10.1029/2003jd003513

Altabet, M. A., Wassenaar, L. I., Douence, C., and Roy, R. (2019). A Ti(III) reduction method for one-step conversion of seawater and freshwater nitrate into N 2 O for stable isotopic analysis of 15 N/ 14 N, 18 O/ 16 O and 17 O/ 16 O. *Rapid Commun. Mass Spectrom.* 33, 1227–1239. doi: 10.1002/rcm.8454

Anderson, J. B., Shipp, S. S., Lowe, A. L., Wellner, J. S., and Mosola, A. B. (2002). The Antarctic ice sheet during the last glacial maximum and its subsequent retreat history: a review. *Quat. Sci. Rev.* 21, 49–70. doi: 10.1016/S0277-3791(01)00083-X

Balci, N., Shanks, W. C., Mayer, B., and Mandernack, K. W. (2007). Oxygen and sulfur isotope systematics of sulfate produced by bacterial and abiotic oxidation of pyrite. *Geochim. Cosmochim. Acta* 71, 3796–3811. doi: 10.1016/j.gca.2007.04.017

Bao, H. (2015). Sulfate: a time capsule for Earth's O. *Chem. Geol.* 395, 108–118. doi: 10.1016/j.chemgeo.2014.11.025

Bao, H., Campbell, D. A., Bockheim, J. G., and Thiemens, M. H. (2000). Origins of sulphate in Antarctic dry-valley soils as deduced from anomalous 17O compositions. *Nature* 407, 499–502. doi: 10.1038/35035054

Bao, H., and Marchant, D. R. (2006). Quantifying sulfate components and their variations in soils of the McMurdo Dry valleys. Antarctica. *J. Geophys. Res.* 111:D16301. doi: 10.1029/2005JD006669

Baroni, M., Savarino, J., Cole-dai, J., Rai, V. K., and Thiemens, M. H. (2008). Anomalous sulfur isotope compositions of volcanic sulfate over the last millennium in Antarctic ice cores. *J. Geophys. Res.* 113, 1–12. doi: 10.1029/2008JD010185

Bishop, J. L., Englert, P. A. J., Patel, S., Tirsch, D., Roy, A. J., Koeberl, C., et al. (2015). Mineralogical analyses of surface sediments in the Antarctic dry valleys: coordinated analyses of raman spectra, reflectance spectra and elemental abundances. *Philos. Trans. R. Soc.* 372:20140198. doi: 10.1098/rsta.2014.0198

Bisson, K. M., Welch, K. A., Welch, S. A., Sheets, J. M., Lyons, W. B., and Levy, A. (2015). Patterns and processes of salt efflorescences in the McMurdo region, Arctic, Antarct. *Alp. Res.* 47, 407–425. doi: 10.1657/AAAR0014-024

Bockheim, J. G., and McLeod, M. (2013). Glacial geomorphology of the Victoria valley system, ross sea region, Antarctica. *Geomorphology* 193, 14–24. doi: 10.1016/j.geomorph.2013.03.020

Brühl, C., Lelieveld, J., Crutzen, P. J., and Tost, H. (2012). The role of carbonyl sulphide as a source of stratospheric sulphate aerosol and its impact on climate. *Atmos. Chem. Phys.* 12, 1239–1253. doi: 10.5194/acp-12-1239-2012

Burgener, L. K., Huntington, K. W., Sletten, R., Watkins, J. M., Quade, J., and Hallet, B. (2018). Clumped isotope constraints on equilibrium carbonate formation and kinetic isotope effects in freezing soils. *Geochim. Cosmochim. Acta* 235, 402–430. doi: 10.1016/j.gca.2018.06.006

Calhoun, J. A., and Chadson, R. J. (1991). Sulfur isotope measurements of submicrometer sulfate aerosol particles over the Pacific Ocean. *Geophys. Res. Lett.* 18, 1877–1880. doi: 10.1029/91gl02304

Campbell, I. B., Claridge, G. G. C., Campbell, D. I., and Balks, M. R. (2013). "The Soil Environment of the Mcmurdo Dry valleys, Antarctica," in *Ecosystem dynamics in a polar desert; the McMurdo Dry Valleys, Antarctica*, ed. J. C. Priscu (Cham: Springer), 297–322. doi: 10.1029/ar072p0297

Cary, S. C., McDonald, I. R., Barrett, J. E., and Cowan, D. A. (2010). On the rocks: the microbiology of Antarctic dry valley soils. *Nat. Rev. Microbiol.* 8, 129–138. doi: 10.1038/nrmicro2281

Claridge, G. G. C., and Campbell, I. B. (1968). Soils of the shackleton glacier region, queen maud range, Antarctica, New Zealand. *J. Sci.* 11, 171–218.

Claridge, G. G. C., and Campbell, I. B. (1977). Salts in Antarctic soils, their distribution and relationship to soil processes. *Soil Sci.* 123, 377–384. doi: 10.1097/00010694-197706000-00006

Clark, B. C., and Van Hart, D. C. (1981). The salts of Mars. *Icarus* 45, 370–378. doi: 10.1016/0019-1035(81)90041-90045

Clark, I. D., and Lauriol, B. (1992). Kinetic enrichment of stable isotopes in cryogenic calcites. *Chem. Geol.* 102, 217–228. doi: 10.1016/0009-2541(92)90157-Z

Courty, M. A., Marlin, C., Dever, L., Tremblay, P., and Vachier, P. (1994). The properties, genesis and environmental significance of calcitic pendents from the High Arctic (Spitsbergen). *Geoderma* 61, 71–102. doi: 10.1016/0016-7061(94)90012-90014

Diaz, M. A., Adams, B. J., Welch, K. A., Welch, S. A., Opiyo, S. O., Khan, A. L., et al. (2018). Aeolian material transport and its role in landscape connectivity in the McMurdo Dry Valleys, Antarctica. *J. Geophys. Res. Earth Surf.* 123, 3323–3337. doi: 10.1029/2017JF004589

Elliot, D. H., and Fanning, C. M. (2008). Detrital zircons from upper permian and lower triassic victoria group sandstones, Shackleton Glacier region, Antarctica:

evidence for multiple sources along the Gondwana plate margin. *Gondwana Res.* 13, 259–274. doi: 10.1016/j.gr.2007.05.003

Erbland, J., Savarino, J., Morin, S., France, J. L., Frey, M. M., and King, M. D. (2015). Air-snow transfer of nitrate on the East Antarctic Plateau-Part 2: an isotopic model for the interpretation of deep ice-core records. *Atmos. Chem. Phys* 15, 12079–12113. doi: 10.5194/acp-15-12079-12015

Erbland, J., Vicars, W. C., Savarino, J., Morin, S., Frey, M. M., Frosini, D., et al. (2013). Air-snow transfer of nitrate on the East Antarctic Plateau – Part 1: isotopic evidence for a photolytically driven dynamic equilibrium in summer. *Atmos. Chem. Phys.* 13, 6403–6419. doi: 10.5194/acp-13-6403-2013

Faure, G., and Felder, R. P. (1981). Isotopic composition of stronium and sulfur in secondary gypsum crystals, Brown Hills, Transantarctic Mountains. *J. Geochemical Explor.* 14, 265–270. doi: 10.1038/201599b0

Frey, M. M., Savarino, J., Morin, S., Erbland, J., and Martins, J. M. F. (2009). Photolysis imprint in the nitrate stable isotope signal in snow and atmosphere of East Antarctica and implications for reactive nitrogen cycling. *Atmos. Chem. Phys. Atmos. Chem. Phys.* 9, 8681–8696. doi: 10.5194/acp-9-8681-2009

Golledge, N. R., Levy, R. H., McKay, R. M., Fogwill, C. J., White, D. A., Graham, A. G. C., et al. (2013). Glaciology and geological signature of the Last glacial maximum Antarctic ice sheet. *Quat. Sci. Rev.* 78, 225–247. doi: 10.1016/j.quascirev.2013.08.011

Gooseff, M. N., Berry Lyons, W., McKnight, D. M., Vaughn, B. H., Fountain, A. G., and Dowling, C. (2006). A stable isotopic investigation of a polar desert hydrologic system, McMurdo Dry Valleys, Antarctica, Arctic, Antarct. *Alp. Res.* 38, 60–71. doi: 10.1657/1523-0430(2006)038[0060:asiioa]2.0.co;2

Hagen, E. H., Koeberl, C., and Faure, G. (1990). "extraterrestrial spherules in glacial sediment, beardmore glacier area, transantarctic mountains," in *Contributions to Antarctic Research I, Antarctic Research Series*, ed. D. H. Elliot (Washington, DC: American Geophysical Union), 19–24. doi: 10.1029/ar050p0019

Hambrey, M. J., Webb, P. N., Harwood, D. M., and Krissek, L. A. (2003). Neogene glacial record from the Sirius group of the shackleton glacier region, central Transantarctic Mountains, Antarctica. *GSA Bull.* 115, 994–1015. doi: 10.1130/B25183.1

Holser, W. T., and Kaplan, I. R. (1966). Isotope geochemistry of sedimentary sulfates. *Chem. Geol.* 1, 93–135. doi: 10.1016/0009-2541(66)90011-8

Honrath, R. E., Guo, S., Peterson, M. C., Dziobak, M. P., Dibb, J. E., and Arsenault, M. A. (2000). Photochemical production of gas phase NOx from ice crystal NO3. *J. Geophys. Res. Atmos.* 105, 24183–24190. doi: 10.1029/2000JD900361

Honrath, R. E., Peterson, M. C., Guo, S., Dibb, J. E., Shepson, P. B., and Campbell, B. (1999). Evidence of NOx production within or upon ice particles in the Greenland snowpack. *Geophys. Res. Lett.* 26, 695–698. doi: 10.1029/1999gl900077

Jackson, A., Davila, A. F., Böhlke, J. K., Sturchio, N. C., Sevanthi, R., Estrada, N., et al. (2016). Deposition, accumulation, and alteration of Cl-, NO3-, ClO4- and ClO3- salts in a hyper-arid polar environment: mass balance and isotopic constraints. *Geochim. Cosmochim. Acta* 182, 197–215. doi: 10.1016/j.gca.2016.03.012

Jackson, W. A., Böhlke, J. K., Andraski, B. J., Fahlquist, L., Bexfield, L., Eckardt, F. D., et al. (2015). Global patterns and environmental controls of perchlorate and nitrate co-occurrence in arid and semi-arid environments. *Geochim. Cosmochim. Acta* 164, 502–522. doi: 10.1016/J.GCA.2015.05.016

Jones, A. E., Weller, R., Anderson, P. S., Jacobi, H. W., Wolff, E. W., Schrems, O., et al. (2001). Measurements of NOx emissions from the Antarctic snowpack. *Geophys. Res. Lett.* 28, 1499–1502. doi: 10.1029/2000GL011956

Jones, L. M., and Faure, G. (1967). Origin of the salts in Lake Vanda, Wright Valley, Southern Victoria Land, Antarctica. *Earth Planet. Sci. Lett.* 3, 101–106. doi: 10.1016/0012-821x(67)90019-90012

Jonsell, U., Hansson, M. E., Mörth, C.-M., and Torssander, P. (2005). Sulfur isotopic signals in two shallow ice cores from Dronning Maud Land, Antarctica. *Tellus B Chem. Phys. Meteorol.* 57, 341–350. doi: 10.3402/tellusb.v57i4.16558

Jouzel, J., and Souchez, R. A. (1982). Melting- refreezing at the glacier sole and the isotopic composition of the ice. *J. Glaciol.* 28:98.

Keys, J. R., and Williams, K. (1981). Origin of crystalline, cold desert salts in the McMurdo region, Antarctica. *Geochim. Cosmochim. Acta* 45, 2299–2309. doi: 10.1016/0016-7037(81)90084-90083

Kunasek, S. A., Alexander, B., Steig, E. J., Sofen, E. D., Jackson, T. L., Thiemens, M. H., et al. (2010). Sulfate sources and oxidation chemistry over the past 230 years from sulfur and oxygen isotopes of sulfate in a West Antarctic ice core. *J. Geophys. Res.* 115:D18313. doi: 10.1029/2010JD013846

Lacelle, D. (2007). Environmental setting, (micro) morphologies and stable C-O isotope composition of cold climate carbonate precipitates — a review and evaluation of their potential as paleoclimatic proxies. *Quat. Sci. Rev.* 26, 1670–1689. doi: 10.1016/j.quascirev.2007.03.011

Lacelle, D., Lauriol, B., and Clark, I. D. (2006). Effect of chemical composition of water on the oxygen-18 and carbon-13 signature preserved in cryogenic carbonates, Arctic Canada: implications in paleoclimatic studies. *Chem. Geol.* 234, 1–16. doi: 10.1016/j.chemgeo.2006.04.001

Lacelle, D., Lauriol, B., and Clark, I. D. (2007). Origin, age, and palaeoenvironmental significance of carbonate precipitates from a granitic environment, Akshayuk Pass, southern Baffin Island, Canada. *Can. J. Earth Sci.* 44, 61–79. doi: 10.1139/E06-088

LaPrade, K. E. (1984). Climate, geomorphology, and glaciology of the Shackleton Glacier area, Queen Maud Mountains, Transantarctic Mountains, Antarctica. *Antarct. Res. Ser.* 36, 163–196. doi: 10.1029/ar036p0163

Legrand, M., Feniet-Saigne, C., and Saltzmant, E. S. (1991). Ice-core record of oceanic emissions of dimethylsulphide during the last climate cycle. *Nature* 350, 144–146. doi: 10.1038/350144a0

Legrand, M. R., and Delmas, R. J. (1984). The ionic balance of Antarctic snow: a 10-year detailed record. *Atmos. Environ.* 18, 1867–1874. doi: 10.1016/0004-6981(84)90363-90369

Lyons, W. B., Deuerling, K., Welch, K. A., Welch, S. A., Michalski, G., Walters, W. W., et al. (2016). The soil geochemistry in the beardmore glacier region, antarctica: implications for terrestrial ecosystem history. *Sci. Rep.* 6:26189. doi: 10.1038/srep26189

Lyons, W. B., Foley, K. K., Carey, A. E., Diaz, M. A., Bowen, G. J., and Cerling, T. (2020). The isotopic geochemistry of CaCO3 encrustations in Taylor Valley, Antarctica: implications for their origin. *Acta Geogr. Slov.* 60, 105–119.

MacKintosh, A., Golledge, N., Domack, E., Dunbar, R., Leventer, A., White, D., et al. (2011). Retreat of the East Antarctic ice sheet during the last glacial termination. *Nat. Geosci.* 4, 195–202. doi: 10.1038/ngeo1061

Magalhães, C., Stevens, M. I., Cary, S. C., Ball, B. A., Storey, B. C., Wall, D. H., et al. (2012). At limits of life: multidisciplinary insights reveal environmental constraints on biotic diversity in continental Antarctica, edited by F. de Bello. *PLoS One* 7:e44578. doi: 10.1371/journal.pone.0044578

Marchant, D. R., and Denton, G. H. (1996). Miocene and pliocene paleoclimate of the Dry Valleys region, Southern Victoria land: a geomorphological approach. *Mar. Micropaleontol. Micropaleontol.* 27:253. doi: 10.1016/0377-8398(95)00065-68

Mayewski, P. A., and Goldthwait, R. P. (1985). Glacial events in the Transantarctic mountains: a record of the East Antarctic ice sheet. *Antarct. Res. Ser.* 36, 275–324. doi: 10.1029/ar036p0275

Mayewski, P. A., Twickler, M. S., Lyons, W. B., Spencer, M. J., Meese, D. A., Gow, A. J., et al. (1990). The dominion range ice core, Queen Maud Mountains, Antarctica - general site and core characteristics with implications. *J. Glaciol.* 36, 11–16. doi: 10.1017/S0022143000005499

Michalski, G., Bockheim, J. G., Kendall, C., and Thiemens, M. (2005). Isotopic composition of Antarctic Dry Valley nitrate: implications for NOy sources and cycling in Antarctica. *Geophys. Res. Lett.* 32, 1–4. doi: 10.1029/2004GL022121

Michalski, G., Böhlke, J. K., and Thiemens, M. (2004). Long term atmospheric deposition as the source of nitrate and other salts in the Atacama Desert, Chile: new evidence from mass-independent oxygen isotopic compositions. *Geochim. Cosmochim. Acta* 68, 4023–4038. doi: 10.1016/j.gca.2004.04.009

Michalski, G., Scott, Z., Kabiling, M., and Thiemens, M. H. (2003). First measurements and modeling of Δ17O in atmospheric nitrate. *Geophys. Res. Lett.* 30:1870. doi: 10.1029/2003GL017015

Moore, H. (1977). The isotopic composition of ammonia, nitrogen dioxide and nitrate in the atmosphere. *Atmos. Environ.* 11, 1239–1243. doi: 10.1016/0004-6981(77)90102-90100

Morin, S., Savarino, J., Frey, M. M., Domine, F., Jacobi, H. W., Kaleschke, L., et al. (2009). Comprehensive isotopic composition of atmospheric nitrate in the Atlantic Ocean boundary layer from 65°S to 79°N. *J. Geophys. Res. Atmos.* 114, 1–19. doi: 10.1029/2008JD010696

Muscari, G., de Zafra, R. L., and Smyshlyaev, S. (2003). Evolution of the NOy-N2O correlation in the Antarctic stratosphere during 1993 and 1995. *J. Geophys. Res. D Atmos.* 108:2871. doi: 10.1029/2002jd002871

Nakai, N., Wada, H., Kiyosu, Y., and Takimoto, M. (1975). Stable isotope of water and studies on the origin and geological history salts in the Lake Vanda area, Antarctica. *Geochem. J.* 9, 7–24. doi: 10.2343/geochemj.9.7

Neumann, K., Lyons, W. B., Priscu, J. C., Desmarais, D. J., and Welch, K. A. (2004). The carbon isotopic composition of dissolved inorganic carbon in perennially ice-covered Antarctic lakes: searching for a biogenic signature. *Ann. Glaciol.* 39, 1–7. doi: 10.3189/172756404781814465

Nezat, C. A., Lyons, W. B., and Welch, K. A. (2001). Chemical weathering in streams of a polar desert (Taylor Valley, Antarctica). *Geol. Soc. Am. Bull.* 113, 1401–1408. doi: 10.1130/0016-7606(2001)113<1401:cwisoa>2.0.co;2

Nkem, J. N., Virginia, A. R. A., Barrett, A. J. E., Wall, D. H., and Li, A. G. (2006). Salt tolerance and survival thresholds for two species of Antarctic soil nematodes. *Polar Biol.* 29, 643–651. doi: 10.1007/s00300-005-0101-106

Patris, N., Delmas, R. J., and Jouzel, J. (2000). Isotopic signatures of sulfur in shallow Antarctic ice cores. *J. Geophys. Res.* 105, 7071–7078. doi: 10.1029/1999JD900974

Pisapia, C., Chaussidon, M., Mustin, C., and Humbert, B. (2007). O and S isotopic composition of dissolved and attached oxidation products of pyrite by *Acidithiobacillus ferrooxidans*: comparison with abiotic oxidations. *Geochim. Cosmochim. Acta* 71, 2474–2490. doi: 10.1016/j.gca.2007.02.021

Pribil, M. J., Ridley, W. I., and Emsbo, P. (2015). Sulfate and sulfide sulfur isotopes (δ34S and δ33S) measured by solution and laser ablation MC-ICP-MS: an enhanced approach using external correction. *Chem. Geol.* 412, 99–106. doi: 10.1016/j.chemgeo.2015.07.014

Pruett, L. E., Kreutz, K. J., Wadleigh, M., Mayewski, P. A., and Kurbatov, A. (2004). Sulfur isotopic measurements from a West Antarctic Ice core: implications for sulfate source and transport. *Ann. Glaciol.* 39, 161–168. doi: 10.3189/172756404781814339

Rech, J. A., Quade, J., and Hart, W. S. (2003). Isotopic evidence for the source of Ca and S in soil gypsum, anhydrite and calcite in the Atacama Desert, Chile. *Geochim. Cosmochim. Acta* 67, 575–586. doi: 10.1016/S0016-7037(02)01175-1174

Reich, M., and Bao, H. (2018). Nitrate deposits of the Atacama Desert: a marker of long-term hyperaridity. *Elements* 14, 251–256. doi: 10.2138/gselements.14.4.251

Savarino, J., Kaiser, J., Morin, S., Sigman, D. M., and Thiemens, M. H. (2007). Nitrogen and oxygen isotopic constraints on the origin of atmospheric nitrate in coastal Antarctica. *Atmos. Chem. Phys.* 7, 1925–1945. doi: 10.5194/acp-7-1925-2007

Savarino, J., Lee, C. C. W., and Thiemens, M. H. (2000). Laboratory oxygen isotopic study of sulfur (IV) oxidation: origin of the mass-independent oxygen isotopic anomaly in atmospheric sulfates and sulfate mineral deposits on Earth. *J. Geophys. Res.* 105, 29079–29088. doi: 10.1029/2000jd900456

Shaheen, R., Abauanza, M., Jackson, T. L., Mccabe, J., Savarino, J., and Thiemens, M. H. (2013). Tales of volcanoes and El-Niño southern oscillations with the oxygen isotope anomaly of sulfate aerosol. *Proc. Natl. Acad. Sci. U.S.A.* 110, 17662–17667. doi: 10.1073/pnas.1213149110

Skidmore, M., Sharp, M., and Tranter, M. (2004). Kinetic isotopic fractionation during carbonate dissolution in laboratory experiments: implications for detection of microbial CO_2 signatures using δ13C-DIC. *Geochim. Cosmochim. Acta* 68, 4309–4317. doi: 10.1016/j.gca.2003.09.024

Sun, T., Socki, R. A., Bish, D. L., Harvey, R. P., Bao, H., Niles, P. B., et al. (2015). Lost cold Antarctic deserts inferred from unusual sulfate formation and isotope signatures. *Nat. Commun.* 6:7579. doi: 10.1038/ncomms8579

Szynkiewicz, A., Moore, C. H., Glamoclija, M., and Pratt, L. M. (2009). Sulfur isotope signatures in gypsiferous sediments of the Estancia and Tularosa Basins as indicators of sulfate sources, hydrological processes, and microbial activity. *Geochim. Cosmochim. Acta* 73, 6162–6186. doi: 10.1016/j.gca.2009.07.009

Szynkiewicz, A., Olichwer, T., and Tarka, R. (2020). Delineation of groundwater provenance in Arctic environment using isotopic compositions of water and sulphate. *J. Hydrol.* 580:124232. doi: 10.1016/j.jhydrol.2019.124232

Toner, J. D., and Sletten, R. S. (2013). The formation of Ca-Cl-rich groundwaters in the Dry Valleys of Antarctica: field measurements and modeling of reactive transport. *Geochim. Cosmochim. Acta* 110, 84–105. doi: 10.1016/j.gca.2013.02.013

Toner, J. D., Sletten, R. S., and Prentice, M. L. (2013). Soluble salt accumulations in Taylor Valley, Antarctica: implications for paleolakes and Ross Sea Ice Sheet dynamics. *J. Geophys. Res. Earth Surf.* 118, 198–215. doi: 10.1029/2012JF002467

Tostevin, R., Turchyn, A. V., Farquhar, J., Johnston, D. T., Eldridge, D. L., Bishop, J. K. B., et al. (2014). Multiple sulfur isotope constraints on the modern sulfur cycle. *Earth Planet. Sci. Lett.* 396, 14–21. doi: 10.1016/J.EPSL.2014.03.057

Uemura, R., Barkan, E., Abe, O., and Luz, B. (2010). Triple isotope composition of oxygen in atmospheric water vapor. *Geophys. Res. Lett.* 37, 1–5. doi: 10.1029/2009GL041960

Vaniman, D. T., Bish, D. L., Chipera, S. J., Fialips, C. I., Carey, J. W., and Feldman, W. G. (2004). Magnesium sulphate salts and the history of water on Mars. *Nature* 431, 663–665. doi: 10.1038/nature02973

Vogt, T., and Corte, A. E. (1996). Secondary precipitates in pleistocene and present cryogenic environments (Mendoza Precordillera, Argentina, Transbaikalia, Siberia, and Seymour Island, Antarctica). *Sedimentology* 43, 53–64. doi: 10.1111/j.1365-3091.1996.tb01459.x

Walters, W. W., and Michalski, G. (2015). Theoretical calculation of nitrogen isotope equilibrium exchange fractionation factors for various NOy molecules. *Geochim. Cosmochim. Acta* 164, 284–297. doi: 10.1016/j.gca.2015.05.029

Welch, K. A., Lyons, W. B., Whisner, C., Gardner, C. B., Gooseff, M. N., Mcknight, D. M., et al. (2010). Spatial variations in the geochemistry of glacial meltwater streams in the Taylor Valley, Antarctica. *Antarct. Sci.* 22, 662–672. doi: 10.1017/S0954102010000702

Wynn-Williams, D., and Edwards, H. G. (2000). Antarctic ecosystems as models for extraterrestrial surface habitats. *Planet. Space Sci.* 48, 1065–1075. doi: 10.1016/S0032-0633(00)00080-85

Conflict of Interest: The authors declare that the research was conducted in the absence of any commercial or financial relationships that could be construed as a potential conflict of interest.

frontiers in Earth Science

ORIGINAL RESEARCH
published: 02 September 2020
doi: 10.3389/feart.2020.00342

Biogeochemical Processes in the Active Layer and Permafrost of a High Arctic Fjord Valley

Eleanor L. Jones[1,2], Andrew J. Hodson[2,3], Steven F. Thornton[4], Kelly R. Redeker[5], Jade Rogers[1], Peter M. Wynn[6], Timothy J. Dixon[7], Simon H. Bottrell[7] and H. Brendan O'Neill[8]*

[1] Department of Geography, The University of Sheffield, Sheffield, United Kingdom, [2] Department of Arctic Geology, The University Centre in Svalbard, Longyearbyen, Norway, [3] Department of Environmental Sciences, Western Norway University of Applied Sciences, Sogndal, Norway, [4] Department of Civil and Structural Engineering, The University of Sheffield, Sheffield, United Kingdom, [5] Department of Biology, University of York, York, United Kingdom, [6] Lancaster Environment Centre, Lancaster University, Lancaster, United Kingdom, [7] School of Earth and Environment, University of Leeds, Leeds, United Kingdom, [8] Geological Survey of Canada, Natural Resources Canada, Ottawa, ON, Canada

OPEN ACCESS

Edited by:
Melissa Jean Murphy,
University College London,
United Kingdom

Reviewed by:
Christian Schröder,
University of Stirling, United Kingdom
Ziming Yang,
Oakland University, United States

****Correspondence:***
Steven F. Thornton
s.f.thornton@sheffield.ac.uk

Specialty section:
This article was submitted to
Geochemistry,
a section of the journal
Frontiers in Earth Science

Received: *06 April 2020*
Accepted: *21 July 2020*
Published: *02 September 2020*

Citation:
Jones EL, Hodson AJ, Thornton SF, Redeker KR, Rogers J, Wynn PM, Dixon TJ, Bottrell SH and O'Neill HB (2020) Biogeochemical Processes in the Active Layer and Permafrost of a High Arctic Fjord Valley. Front. Earth Sci. 8:342. doi: 10.3389/feart.2020.00342

Warming of ground is causing microbial decomposition of previously frozen sedimentary organic carbon in Arctic permafrost. However, the heterogeneity of the permafrost landscape and its hydrological processes result in different biogeochemical processes across relatively small scales, with implications for predicting the timing and magnitude of permafrost carbon emissions. The biogeochemical processes of iron- and sulfate-reduction produce carbon dioxide and suppress methanogenesis. Hence, in this study, the biogeochemical processes occurring in the active layer and permafrost of a high Arctic fjord valley in Svalbard are identified from the geochemical and stable isotope analysis of aqueous and particulate fractions in sediment cores collected from ice-wedge polygons with contrasting water content. In the drier polygons, only a small concentration of organic carbon (<5.40 dry weight%) has accumulated. Sediment cores from these drier polygons have aqueous and solid phase chemistries that imply sulfide oxidation coupled to carbonate and silicate dissolution, leading to high concentrations of aqueous iron and sulfate in the pore water profiles. These results are corroborated by $\delta^{34}S$ and $\delta^{18}O$ values of sulfate in active layer pore waters, which indicate the oxidative weathering of sedimentary pyrite utilising either oxygen or ferric iron as oxidising agents. Conversely, in the sediments of the consistently water-saturated polygons, which contain a high content of organic carbon (up to 45 dry weight%), the formation of pyrite and siderite occurred via the reduction of iron and sulfate. $\delta^{34}S$ and $\delta^{18}O$ values of sulfate in active layer pore waters from these water-saturated polygons display a strong positive correlation ($R^2 = 0.98$), supporting the importance of sulfate reduction in removing sulfate from the pore water. The significant contrast in the dominant biogeochemical processes between the water-saturated and drier polygons indicates that small-scale hydrological variability between polygons induces large differences in the concentration of organic carbon and in the cycling of iron and sulfur, with ramifications for the decomposition pathway of organic carbon in permafrost environments.

Keywords: permafrost, biogeochemistry, iron-sulfur, carbon, Svalbard

INTRODUCTION

Permafrost regions account for 24% of the land area of the Northern Hemisphere and store immense quantities (1330 to 1580 Pg) of organic carbon (Tarnocai et al., 2009; Hugelius et al., 2014). Permafrost ecosystems are currently a net sink of carbon, due to the drawdown of carbon dioxide exceeding emissions of methane and carbon dioxide (Schaefer et al., 2011; Kirschke et al., 2013; Parmentier et al., 2013). As rapid climate change occurs in the high Arctic, rising permafrost temperatures and progressively deeper active layers are exposing previously frozen soil organic carbon to microbial decomposition (Romanovsky et al., 2010; Koven et al., 2011; Schuur et al., 2015). This releases carbon dioxide and methane to the atmosphere and is predicted to cause permafrost ecosystems to become a net carbon source by the mid-2020s (Lee et al., 2012; Elberling et al., 2013; Schuur et al., 2015).

To predict the impact of permafrost thaw on biogeochemical cycling, it is necessary to understand the spatial heterogeneity of biogeochemical processes in Arctic soils. The distribution of stored organic carbon varies across the permafrost landscape, and with depth (Kuhry et al., 2010). Organic carbon accumulation and storage in permafrost is maximised in regions where waterlogged conditions dominate, as under these conditions, net primary production exceeds decomposition (Kolka et al., 2015). Hydrology exerts a powerful influence on the type of gaseous products released from decomposing permafrost organic carbon. For example, drained soil allows previously frozen organic carbon to decompose rapidly under oxic conditions, producing carbon dioxide (Liljedahl et al., 2012; Elberling et al., 2013), whereas water saturation limits the oxygen supply and enhances anaerobic respiration and methane production (Turetsky et al., 2008; Lipson et al., 2012; Olefeldt et al., 2013). However, under anaerobic conditions, alternative electron acceptors such as nitrate, manganese, iron and sulfate may be used preferentially in the microbial respiration of organic carbon, and inhibit the production of methane (Kristjansson and Schönheit, 1983; Dise and Verry, 2001). The use of alternative electron acceptors increases carbon dioxide production relative to methane, and hence the coupling between hydrology and the availability of alternative electron acceptors plays a crucial role in determining the magnitude of permafrost carbon emissions.

Hodson et al. (2016) conducted hydrological monitoring that demonstrated how lowland runoff draining the reactive, fine-grained sediments of Svalbard's Central Tertiary Basin (i.e., Adventdalen, the site of the present study) acquires reactive iron from pyrite oxidation. Pyrite oxidation exerted a major control upon the composition of this runoff, as evidenced by the presence of high sulfate and cation concentrations (Hodson et al., 2016). This process has also been documented in several nearby catchments (Fardalen, Bolterdalen and Longyeardalen; Yde et al., 2008; Rutter et al., 2011; Hindshaw et al., 2016). Therefore, sediments and water in Adventdalen and the surrounding area have an abundance of alternative electron acceptors, such as ferric iron and sulfate, for the microbial oxidation of organic carbon. The abundance of ferric iron and sulfate in the waters draining through Adventdalen is important in the context of greenhouse gas emissions because Fe(III)- and sulfate-reduction are thermodynamically favourable, and therefore competitive, relative to methanogenesis. The availability of Fe(III) has been reported to decrease methanogenesis in the permafrost landscape of Barrow, Alaska (Lipson et al., 2012; Miller et al., 2015) and the availability of sulfate can decrease methane production in wetlands (e.g., Pester et al., 2012). Hodson et al. (2016) used the decrease in concentrations of sulfate and *Fe (i.e., dissolved and colloidal iron that passed through a 0.45 μm filter) at low flow to infer removal by sulfate reduction and precipitation of pyrite (FeS_2), iron monosulfide (FeS) and possibly elemental sulfur in ground waters draining through an alluvial sediment fan in Endalen (a tributary to Adventdalen). However, the processes removing *Fe and sulfate from these waters were hypothesised to be limited by a lack of organic matter (e.g., Raiswell and Canfield, 2012). A scarcity of organic matter has also been observed to limit the removal of *Fe and sulfate from pore water in fjord sediment cores in Svalbard (Wehrmann et al., 2014). From these findings, it is clearly necessary to understand if the accumulation of organic carbon in such environments results in enhanced removal of iron and sulfate from solution.

The objective of this study is to determine how the vertical and lateral heterogeneity of organic carbon accumulation in a high Arctic fjord valley influences the biogeochemical processes in the active layer and shallow permafrost sediments and pore water. This study presents and discusses geochemical analyses of pore water and sediment sampled from cores collected from the active layer and shallow permafrost of ice-wedge polygonal terrain in a high Arctic fjord valley.

MATERIALS AND METHODS

Field Site Description

Adventdalen (78°19′N, 15°93′E) is a 12 km × 4 km valley, oriented NW-SE, in central Svalbard. The van Mijenfjord and Adventdalen Groups, which contain sedimentary rocks (sandstones, shales, and carbonates), comprise the lithology of the Adventdalen catchment. The sandstones and shales contain iron-bearing mineral phases, such as pyrite, siderite and glauconite (Dallmann et al., 1999; Riber, 2009; Svinth, 2013). There is also a small amount of iron in biotite and chlorite (chamosite; Hodson et al., 2016).

Glacial retreat and postglacial isostatic rebound influence landscape evolution (Milne and Shennan, 2007). Consequently, permafrost aggradation in many high Arctic fjord valleys has involved the freezing of reactive, fine-grained sediment originally deposited on the fjord floor via glacio-marine sedimentation and delta progradation throughout deglaciation (Haldorsen et al., 2010; Gilbert et al., 2018). During the Last Glacial Maximum, Adventdalen was filled with an erosive ice stream; this caused permafrost to thaw (Humlum et al., 2003; Humlum, 2005; Landvik et al., 2005). After retreat of the ice sheet, the glacial isostatic rebound of Svalbard meant that relative sea level fell, and a Gilbert-type delta prograded into Adventfjorden (Lønne and Nemec, 2004). In Adventdalen, the deeper permafrost is epigenetic, as it formed after the progradation of the delta (Gilbert et al., 2018). The shallower syngenetic permafrost in the aeolian terraces of Adventdalen aggraded concurrently with aeolian sedimentation (Gilbert et al., 2018). Although permafrost only aggraded since deglaciation, it is continuous in Svalbard, where it reaches a thickness of 80−100 m near the coast (Brown et al., 1997; Humlum, 2005). The seasonally thawed layer, or "active layer," can be 0.4−6 m thick in Svalbard (Christiansen, 2005). In Adventdalen, the active layer thickness is around 1 m (Christiansen et al., 2010). This study focuses on the zone 0−2 m depth, which involves sampling the active layer and shallow permafrost.

The climate of Svalbard is polar tundra (Kottek et al., 2006) and in Longyearbyen between 1981 and 2010, the mean annual air temperature (MAAT) was −4.6°C (Førland et al., 2011). Between 1989 and 2011, MAAT increased by 1.25°C per decade (Førland et al., 2011) and in 2018, the MAAT was −1.8°C (eklima.met.no). The mean annual ground temperature (MAGT) ranges from −5.6°C to −3.2°C in the Adventdalen area (Christiansen et al., 2010) and the rising air temperatures have caused a recent increase in permafrost temperatures (Isaksen et al., 2019). The vegetation cover in the valley varies between 1.3 g m^{-2} and 27.2 g m^{-2} (moss) and 2.8 g m^{-2} and 9.6 g m^{-2} (vascular plants), with the amount of moss dependent on the soil moisture (Sjögersten et al., 2006).

The study sites (**Figures 1A–C**) were selected with the aim of sampling the heterogeneity of permafrost environments in the fjord valley. **Table 1** lists the sample locations with details of the sampling methods. The sites are covered with Late Holocene loess (aeolian) deposits overlying alluvial and deltaic deposits (Cable et al., 2017; Gilbert et al., 2018). The aeolian deposits and alluvial fans dominate the syngenetic permafrost aggradation, whilst the permafrost beneath constitutes the epigenetic permafrost aggradation (following downward freezing; Gilbert et al., 2018; Toft-Hornum et al., In Review). The study sites are situated in areas of low-centred ice-wedge polygons, which are common in Adventdalen (Sørbel and Tolgensbakk, 2002). Ice Wedge North (**Figure 1B**) is a water-saturated wetland, mainly fed by springs, whereas Ice Wedge South (**Figure 1C**) is mainly precipitation-fed and only sporadically inundated by local snowmelt and rainfall.

Coring and Core Subdivision

Coring was undertaken before the onset of thaw, when air temperatures were below 0°C. Sediment cores of the frozen active layer and shallow permafrost were extracted in segments (5 cm diameter; between 5 and 50 cm length) to a depth of 2 m using motorised hand drilling equipment (a Stihl BT 130 drilling engine with a cylindrical drill head and rods). The core segments were extruded into sterile Whirl Pak®bags, which were sealed and frozen during transport to the University of Sheffield, where they were stored at −18°C. Cores were subdivided by sawing into 2 cm depth slices while frozen. The freshly cut surfaces were scraped with a scalpel, and the outer 2 cm removed with a hollow brass tube (3 cm diameter), to prevent contamination. The sawblade, scalpel and brass tube were cleaned with 70% isopropanol between slices.

Pore Water Extractions

A pore water extraction method was adapted from Spence et al. (2005). Vials containing samples were transferred to a Coy Vinyl Anaerobic chamber with a N_2 atmosphere (0 ppm oxygen). Each vial was weighed to determine the sample mass. Nitrogen-sparged de-ionised water (Milli-Q) was added to fill each vial. The vials were reweighed to determine the mass and volume of water added. A 3 mL volume of water was subsequently removed from the top of the vial to create a headspace. The vials were crimp-capped, inverted and stored for 5 days at 4°C whilst submerged in water (to prevent gas diffusion across the septa). This storage time enabled the de-ionised water to equilibrate with the sediment pore water (e.g., Spence et al., 2005). 7 days after first saturation of the sample, the vials were centrifuged at 7750 rpm for 5 minutes and transferred back to the anaerobic chamber. The equilibrated supernatant was filtered (0.22 μm nylon syringe filter) for chemical analysis and the sediment remaining in the vials was weighed after drying at 105°C for 24 h (Kokelj and Burn, 2003; Ernakovich et al., 2017). The vials were then reweighed to determine the initial moisture content of the samples.

Major ions (Ca^{2+}, Mg^{2+}, Na^{+}, K^{+}, Cl^{-}, NO_3^{-}, and SO_4^{2-}) were determined by ion chromatography (Dionex ion chromatograph, DX 90; limit of detection or "LOD" = 0.02 mg L^{-1} for the lowest, undiluted analysis; precision <5% for the mid-range standards). Trace metals (Fe, Mn) were determined on a 5 mL sample acidified with 50 μL reagent grade HNO_3 (Fisher Scientific Trace Metal Grade), using Inductively Coupled Plasma Mass Spectrometry or ICPMS (PerkinElmer Elan DRC II, MA, United States). The precision errors for repeat analyses of mid-range standards were <5%, and the detection limits were 1.0 μg L^{-1}. Analyte concentrations were corrected for blank analyses and corrected for the dilution during the pore water extraction.

Solid Phase Analyses

Carbon and nitrogen elemental abundance were determined by drying sediment samples at 105°C, acidifying in 6 M HCl, rinsing, drying, homogenising, weighing between 25 and 50 mg of each sample into a tin capsule and analysing on an Elementar vario EL cube (Animal and Plant Sciences Department, University of Sheffield). Elemental concentrations were checked with acetanilide standards (C_8H_9NO; Merck; $n = 28$, % $C = 70.96 \pm 0.67$, % $N = 10.34 \pm 0.10$), with 2 blanks and 2 acetanilide standards run every 15 samples.

Acid-volatile sulfur (AVS) and chromium-reducible sulfur (CRS) were determined at the University of Leeds. A two-step distillation method was applied to freeze-dried and milled sediment samples, first using 6 M HCl and then boiling 3 M $CrCl_2$ solution (Canfield et al., 1986; Fossing and Barker Jørgensen, 1989). In each extraction, H_2S was precipitated as Ag_2S, filtered, dried, and sulfide was determined gravimetrically. The stoichiometry of the phase was used to convert the mass to weight percent (FeS for AVS; FeS_2 for CRS).

Different operationally defined iron mineral phases were targeted with a four-step sequential extraction procedure applied to 100 mg freeze-dried and milled sediment samples. To extract amorphous and nanoparticulate iron (oxyhydr)oxide phases

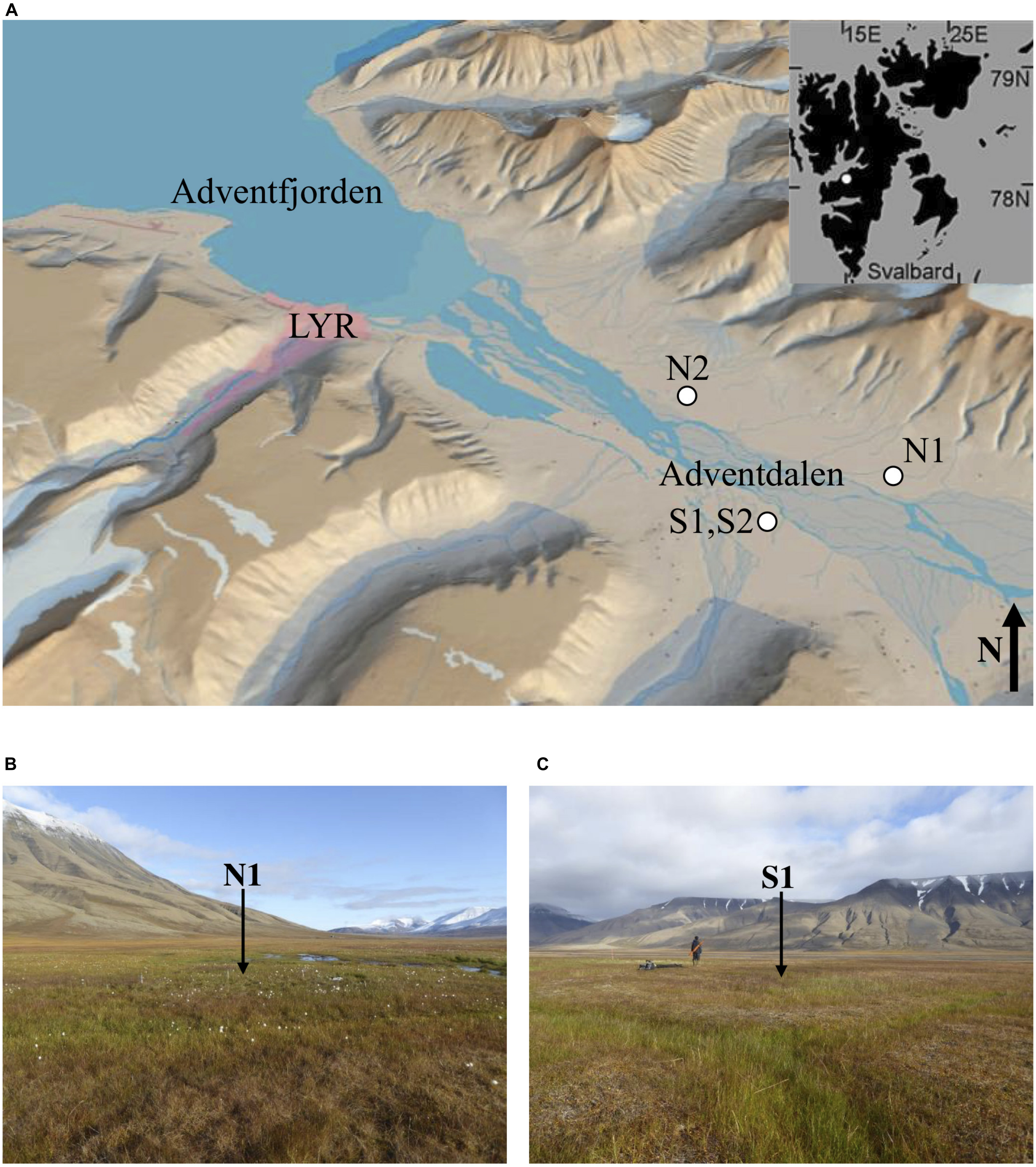

FIGURE 1 | (A) The Svalbard archipelago (inset) and Adventdalen, with a white circle indicating each site where ice-wedge polygons were sampled (courtesey of the Norwegian Polar Institute), **(B)** overlooking polygon N1, facing east, and **(C)** overlooking polygon S1, facing north. Photo credit: E. L. Jones.

($Fe_{ascorbate}$), each sample was shaken for 24 h with 10 mL ascorbate solution (50 g L^{-1} sodium citrate, 50 g L^{-1} sodium bicarbonate and 10 g L^{-1} of ascorbic acid; buffered at pH 7.5; Raiswell et al., 2008). To target iron bound in carbonates ($Fe_{acetate}$), the residual sample was shaken for 48 h at 50°C with 10 mL sodium acetate solution (1 M sodium acetate solution buffered with acetic acid to pH 4.5; Poulton and Canfield, 2005). To target crystalline iron (oxyhydr)oxides ($Fe_{dithionite}$), the residual sample was then shaken for 2 h with 10 mL dithionite solution (50 g L^{-1} sodium dithionate buffered to pH 4.8 with

TABLE 1 | Sampling locations, in UTM zone 33X.

Site Name	Site Code	Latitude (UTM)	Longitude (UTM)	Sample Type	Sampling Date	Shipping Date
Ice Wedge South	S1	8679400	521010	1 core 8 water samples	15.06.15 26.08.17 & 27.08.17	28.09.15 29.09.17
	S2a	8679343	521042	1 core	12.02.17	19.06.17
	S2b	8679343	521042	1 core	14.02.17	19.06.17
Ice Wedge North	N1	8680446	522541	1 core	02.05.16	10.05.16
	N2	8681819	519780	1 core	15.04.14	29.04.14
	N1w	8680446	522541	9 water samples	31.08.17 & 01.09.17	29.09.17

The sample types are cores of the active layer and shallow permafrost and waters from the active layer extracted via Macro Rhizon samplers. All samples were extracted from the polygon centre.

acetic acid and sodium citrate; Poulton and Canfield, 2005). Lastly, for magnetite ($Fe_{oxalate}$), the residual sample was shaken with 10 mL ammonium oxalate solution (0.2 M ammonium oxalate/0.17 mL oxalic acid buffered with ammonium hydroxide to pH 3.2) for 6 h (Poulton and Canfield, 2005). These extractions were performed at room temperature (except for $Fe_{acetate}$ at 50°C). After centrifugation (4000 rpm for 4 min at 21°C), the supernatant from each extraction was stored at 4°C until analysis by atomic absorption spectroscopy (AAS). Recent research has shown that mineralogical associations based on sequential chemical extractions need to be treated with caution (Oonk et al., 2017; Slotznick et al., 2020; Hepburn et al., 2020). For instance, the efficacy of the $Fe_{acetate}$ stage in extracting iron bound in carbonates ranges from 3 to 85% (Oonk et al., 2017; Hepburn et al., 2020). The solubility of the targeted minerals depends upon their grain size, crystallinity and mineralogical association (Slotznick et al., 2020). Therefore, this study draws only tentative links between the extraction steps and the specific minerals represented by each step.

In situ Pore Water Sampling and Analyses

In late summer 2017, pore waters from the S1 polygon at Ice Wedge South and the N1 polygon at Ice Wedge North were sampled *in situ* using MacroRhizon soil moisture samplers (Van Walt Ltd.). Water samples for the analysis of $\delta^{18}O\text{-}SO_4$ and $\delta^{34}S\text{-}SO_4$ were collected to fill 50 mL centrifuge tubes and were stored at 4°C until processing and analysis at Lancaster Environment Centre, Lancaster University, United Kingdom. Water samples for the analysis of $\delta^{18}O\text{-}H_2O$ were collected to fill Eppendorf tubes and were stored at 4°C until analysis at the University of East Anglia (UEA). Water samples for the analysis of $\delta^{18}O\text{-}SO_4$ and $\delta^{34}S\text{-}SO_4$ were loaded onto ion exchange resins (Supelite^{TM} DAX-8 for removal of dissolved organic matter; Dowex 50 W-X8 for removal of cations; and Dowex AG2 X8 for removal of anions). Anions were eluted from the Dowex® AG2 X8 using aliquots of 1 M ultrapure HCl to a total volume of 1.5 mL. A 0.2 mL volume of 1 M $BaCl_2$ was added to the eluted sample, and the samples were left for 48 h at 4°C to allow $BaSO_4$ to precipitate. Each sample was rinsed three times with Milli-Q de-ionised water using centrifugation and re-suspension to remove any interfering products (e.g., chlorides). The samples were dried at 40°C.

The dry samples were weighed into tin or silver capsules for analysis of $\delta^{34}S\text{-}SO_4$ and $\delta^{18}O\text{-}SO_4$, respectively. Isotopic analysis was undertaken by Elemental Analyser (Elementar Pyrocube) linked to a continuous flow isotope ratio mass spectrometer (Isoprime 100 with dual inlet capability for injection of monitoring gases), following methods in Wynn et al. (2015). Combustion of $BaSO_4$ within tin capsules yielded SO_2 for determination of $\delta^{34}S$. Analytical conditions demanded the use of vanadium pentoxide as an oxidizing agent and a combustion temperature of 1120°C. Pyrolysis of $BaSO_4$ at 1450°C within silver capsules and in the presence of carbon black, yielded CO for the determination of $\delta^{18}O$. $\delta^{34}S$ values were corrected against Vienna Cañon Diablo Troilite (VCDT) using within run analyses of international standards NBS-127 and SO5. $\delta^{18}O$ values were corrected to Vienna Standard Mean Ocean Water (VSMOW) using within-run analyses of NBS-127 and SO6. Internal standard MLSG (a subglacial meltwater precipitate of $BaSO_4$) was used to monitor drift and precision within each run as well as external precision between analytical sequences. Within-run standard replication (1SD) was better than $\pm$ 0.3‰ for both sulfur and oxygen isotope values.

Water samples for the analysis of $\delta^{18}O\text{-}H_2O$ were analysed at the University of East Anglia (UEA) with a Picarro 1102i analyser, by direct injection of 2.6 μL of water. Samples were measured together with two United States Geological Survey (USGS) standards: USGS 64444 and USGS 67400 and a UEA Norwich Tap Water (NTW) internal laboratory standard. Using the calibration line defined by the USGS standards, the true isotopic composition of the samples was calculated, relative to VSMOW.

Precipitation Correction

Pre-melt snowpack chemistry data from Svalbard were compiled (Hodgkins et al., 1997; Wynn et al., 2006; Tye and Heaton, 2007; Yde et al., 2008) to calculate the mean X/Cl ratios (where X is a major anion or cation). The following ratios in the snowpack were established: Na/Cl = 0.82; K/Cl = 0.02; Mg/Cl = 0.10; Ca/Cl = 0.08; SO_4/Cl = 0.11. By assuming that chloride behaves conservatively and originates only from precipitation (*pd*), these ratios were used to calculate the fraction of each anion or cation in pore water

(pw) derived from precipitation (fX_{pd}; Equation 1):

$$fX_{pd} = \left(\frac{X}{Cl}\right)_{snow} \cdot \left(\frac{Cl}{X}\right)_{pw} \quad (1)$$

The residual (fX_{npd}) represents the fraction of each anion or cation in pore water derived from weathering (Equation 2):

$$fX_{npd} = 1 - fX_{pd} \quad (2)$$

The $\delta^{34}S\text{-}SO_4$ values were corrected for snow inputs, following Equation (3) (from Hindshaw et al., 2016) and using the mean snowpack $\delta^{34}S\text{-}SO_4$ value of 17.5‰ from the compilation of pre-melt snowpack chemistry from Svalbard.

$$\delta^{34}S_{npd} = \frac{\left(\delta^{34}S_{pw} - f \cdot \delta^{34}S_{snow}\right)}{\left(1 - f\right)} \quad (3)$$

Where f is the fraction of sulfate derived from snowmelt. The $\delta^{18}O\text{-}SO_4$ values were corrected in the same way as in Equation (3), using the mean snowpack $\delta^{18}O\text{-}SO_4$ value of 9.28‰ from the compilation of pre-melt snowpack chemistry from Svalbard.

Bedrock Sulfide δ^{34}S Sampling and Analyses

Bedrock samples (sandstones, siltstones, shales) from each geological formation in the Adventdalen Group and the Carolinefjellet Formation were obtained from cores 13/2013 (33X E522859 N8685197, Dirigenten), BH9/05 (Urdkollbreen, 33X E528365 N8647669) and outcrops in Adventdalen. Rock samples were cut into small blocks using a lapidary trim saw (Lortone, United States) and weathered surfaces removed using a grinding surface (Saphir 330, ATM, Germany). Rocks were washed with de-ionised water in an ultrasonic bath before being dried in an oven at 50°C. Dried rocks were pulverised in a steel pestle and mortar into small chips which were further crushed to a fine powder in an agate disc mill (Tema, United Kingdom). Crushing equipment was washed with water, dried with compressed air and cleaned with ethanol between samples to prevent contamination. Chromium-reducible sulfur (CRS) was extracted from ground rock using the method previously described (Section "Solid Phase Analyses"). The resultant Ag_2S precipitates were weighed into tin capsules for δ^{34}S analysis via combustion in an Elementar Pyrocube elemental analyser coupled to an Isoprime continuous flow mass spectrometer at the University of Leeds. Samples were combusted at 1150°C to SO_2 in the presence of pure oxygen (N5.0) into a stream of helium (CP grade). The SO_2 produced flowed through tungstic oxide packed into the combustion column to ensure quantitative conversion. Excess oxygen was removed by reaction with hot copper wires at 850°C and water was removed in a Sicapent trap. Duplicate aliquots of silver sulfide were prepared because of a small sulfur isotope memory effect incurred during SO_2 processing in the pyrocube. δ^{34}S values were corrected to the VCDT scale using international standard IAEA S-3 (−32.06‰) and an inter-lab chalcopyrite standard CP-1 (−4.56‰). Reproducibility of a within-run check standard ($BaSO_4$) was ± 0.24‰ (1 SD).

Data Analyses

Data analyses were performed in Microsoft Excel and R Core Team (2017) and graphics were prepared with Excel or the ggplot2 R package. Prior to testing correlations between variables, Shapiro Wilk's method was used to test whether data were normally distributed. Many variables were not normally distributed and their inter-relationships were non-linear. Therefore, monotonous relationships between the variables were tested using Spearman correlation, which is appropriate for non-normally distributed data and is particularly robust for dealing with skewed distributions and outliers (du Prel et al., 2010).

RESULTS

Figure 2 shows that the Ice Wedge North cores had a significantly higher gravimetric water content (g water g^{-1} dry sediment) than the Ice Wedge South cores according to Welch's t-test (**Table 2**). The mean gravimetric water content in the N1 core was 2.79 g g^{-1} (maximum was 9.14 g g^{-1}) and was highest both at the surface and below 90 cm depth, whereas N2 had a mean gravimetric water content of 6.05 g g^{-1}, with no clear patterns with depth. In S1, however, the mean water content was 0.57 g g^{-1}, with peaks near the surface, and at 105, 141 and 169 cm, and the maximum water content was 1.32 g g^{-1}. The mean gravimetric water content of S2a and S2b was similar (0.58 and 0.45 g g^{-1}, respectively). Both these cores had an increased water content near the surface.

The concentration of chloride was higher in the cores from Ice Wedge South, compared to those from Ice Wedge North (**Figures 2F–J**). The concentration of chloride peaked close to the base of the active layer in cores from both sites (**Figures 2F–J**). There was also a peak in chloride concentration near the ground surface at N1 (**Figure 2F**). There was an accumulation of chloride in the underlying permafrost of cores N2, S2a and S2b (**Figures 2G–J**).

The sedimentary organic carbon content for the two sites also differed significantly according to Welch's t-test (**Table 2**). **Figure 2** and **Table 2** show that Ice Wedge North had a higher organic carbon content than Ice Wedge South. The surface of N1 had a high organic carbon content (29.7 wt.%). In the permafrost, the organic carbon content was high, but variable (low at 30−70 cm depths, peaking at 100−140 cm depth). S1, however, had a more uniform and lower organic carbon content (mean of 2.38 wt.%), but with a peak near the surface (5.40 wt.%) and at 61 cm depth (4.65 wt.%).

The concentrations of $Fe_{(aq)}$ and sulfate in pore waters differed significantly between the two sites, according to Welch's t-test (**Table 2**). **Figures 3A,B** show that the $Fe_{(aq)}$ in N1 and N2 was <3.0 mmol L^{-1}. In N1, peaks in aqueous iron occurred at 31, 67, 93, and 155 cm depth. In N2, the peaks were broader and at depths of 15−73 cm, 109−139 cm, and 197 cm. **Figures 3F,G** show that while N2 had a sulfate concentration <1.3 mmol L^{-1}, N1 had up to 4.7 mmol L^{-1} in the peak at the active layer base. N1 had a clear pattern in sulfate, increasing from the surface

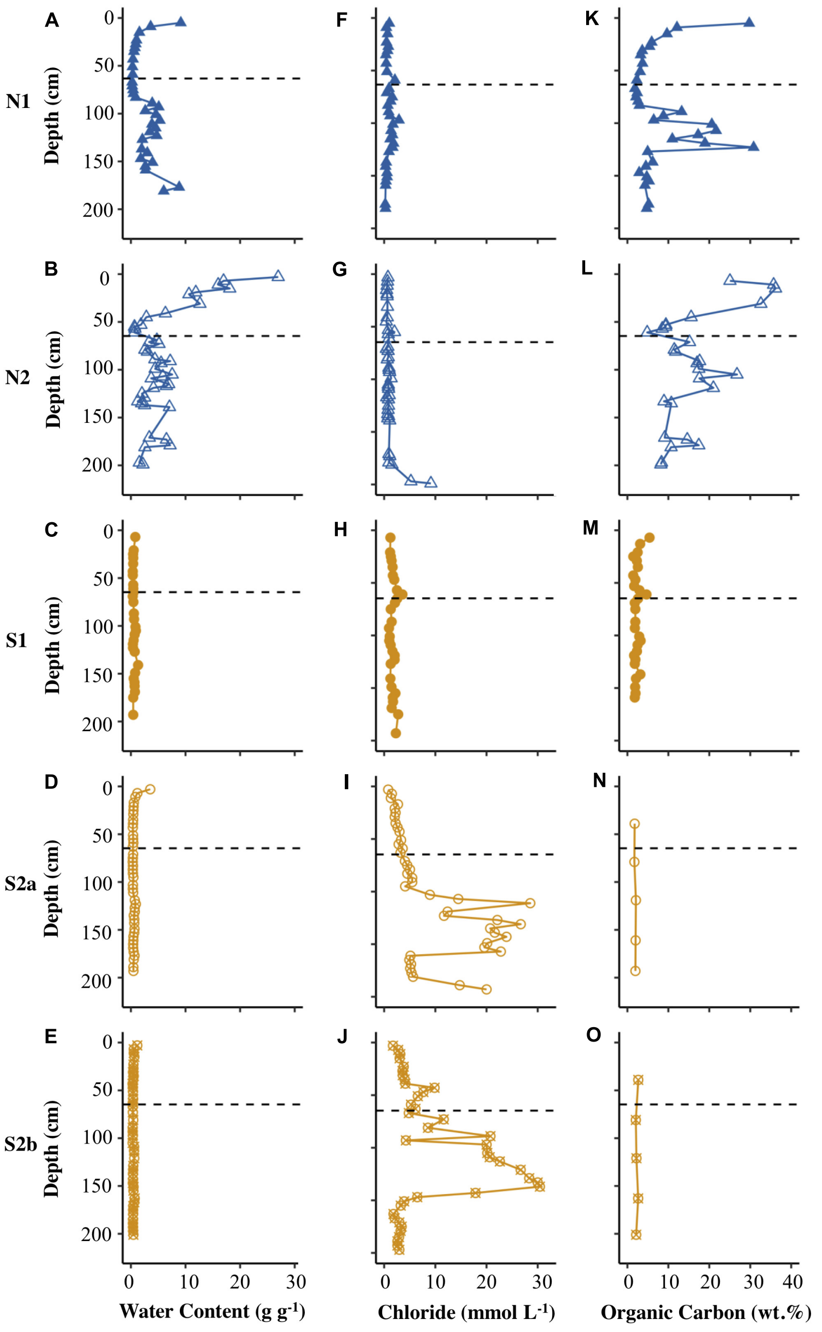

FIGURE 2 | Depth profiles of water content **(A–E)**, chloride concentration **(F–J),** and concentration of organic carbon **(K–O)** for N1, N2, S1, S2a, and S2b. The horizontal dashed line on each plot represents the base of the active layer in 2017.

toward the base of the active layer, and then decreasing into the permafrost (with a small peak ~150 cm).

Figures 3C–E show that the concentration of $Fe_{(aq)}$ was low (<1.5 mmol L^{-1}) in the active layer of all the Ice Wedge South cores. $Fe_{(aq)}$ in S1 peaked at 75 cm and 123 cm depth. The $Fe_{(aq)}$ concentration in the permafrost of S2a and S2b had less distinct peaks, but increased with depth, reaching over 7.5 mmol L^{-1}. **Figures 3H–J** show that sulfate followed similar depth trends to $Fe_{(aq)}$ for all three Ice Wedge South cores, reaching >20 mmol L^{-1} in core S2b. The sulfate concentration in the active layer was higher than the $Fe_{(aq)}$ concentration.

Figures 4A–F show that N1 had only low concentrations of calcium and magnesium in pore water (<6 mmol L^{-1}), with the highest values of both cations in the uppermost core sample. N2 had similarly low concentrations of calcium and magnesium (**Figures 4B,G**). S1 displayed distinct peaks in all

TABLE 2 | Results of Welch's *t*-tests comparing organic carbon, gravimetric water content, $\text{Fe}_{(\text{aq})}$, sulfate, $\text{CH}_{4(\text{aq})}$, CRS, $\text{Fe}_{\text{ascorbate}}$, $\text{Fe}_{\text{dithionite}}$, $\text{Fe}_{\text{acetate}}$, and $\text{Fe}_{\text{oxalate}}$ for Ice Wedge South and Ice Wedge North.

Variable	***t***	***df***	***p*-value**	**Ice Wedge South**			**Ice Wedge North**			**Units of mean**
				Mean	***SD***	***n***	**Mean**	***SD***	***n***	
Organic carbon	−7.9	61	***	2.30	0.86	30	12.5	9.94	60	Dry wt.%
Gravimetric water content	−7.4	73	***	0.53	0.34	113	4.6	4.68	73	g g^{-1}
$\text{Fe}_{(\text{aq})}$	8.7	128	***	2.92	2.76	113	0.6	0.60	73	mmol L^{-1}
Sulfate	14.6	126	***	7.49	4.81	113	0.7	0.97	73	mmol L^{-1}
$\text{CH}_{4(\text{aq})}$	−10.3	70	***	1.24	2.13	113	98.0	79.0	71	$\mu\text{mol L}^{-1}$
CRS	−3.1	6	*	0.01	0.01	9	0.1	0.04	7	Dry wt.%
$\text{Fe}_{\text{ascorbate}}$	−4.1	12	**	0.47	0.14	10	1.0	0.36	10	Dry wt.%
$\text{Fe}_{\text{dithionite}}$	7.5	18	***	0.44	0.09	10	0.1	0.10	10	Dry wt.%
$\text{Fe}_{\text{acetate}}$	−3.5	10	**	0.50	0.11	10	1.0	0.43	10	Dry wt.%
$\text{Fe}_{\text{oxalate}}$	5.1	17	***	0.76	0.17	10	0.3	0.21	10	Dry wt.%

t is the t statistic, df is the degrees of freedom, p is the significance level, SD is the standard deviation of the mean and n is the number of samples. Asterisks indicate level of significance: $p < 0.05$ (*), $p < 0.01$ (**), and $p < 0.001$ (***).

cations at the base of the active layer and >1 m depth in the permafrost (**Figures 4**, **5C,H**). S2a and S2b show the greatest range in concentrations of calcium and magnesium (reaching ∼15 mmol L^{-1}), with higher concentrations in the permafrost (**Figures 4D,E,I,J**). The concentration of potassium was generally <2.5 mmol L^{-1} in N2, S1, S2a and S2b (**Figure 5**), but reached >20 mmol L^{-1} in N2. The sodium concentration was <10 mmol L^{-1} in all the cores (**Figures 5F–J**).

The concentration of solid phase iron species was variable in the N1 core, with concentrations: $\text{Fe}_{\text{ascorbate}} < 1.6$ wt.%, $\text{Fe}_{\text{dithionite}} < 0.35$ wt.%. $\text{Fe}_{\text{acetate}}$ was the dominant extracted iron phase at N1, reaching a maximum of 1.57 wt.% (**Table 3** and **Supplementary Figures S1A,C,E**). $\text{Fe}_{\text{oxalate}}$ at N1 was < 0.71 wt.% (**Supplementary Figure S1G**). N1 had the highest CRS at 15 cm depth and at 115 cm depth (**Supplementary Figure S1K**), which tracked the organic carbon content. AVS was detected at 15 cm in N1, and also in all three samples measured between 114 and 156 cm (**Supplementary Figure S1I**). Compared with the porewater $\text{Fe}_{(\text{aq})}$ and sulfate profiles, the concentration of solid phase iron species was constant with depth in S1 (**Supplementary Figures S1B,D,F,H,J,L**). $\text{Fe}_{\text{ascorbate}}$ was <0.8 wt.%, $\text{Fe}_{\text{dithionite}}$ was <0.6 wt.%, $\text{Fe}_{\text{acetate}}$ was <0.8 wt.%, $\text{Fe}_{\text{oxalate}}$ was <1 wt.%, CRS was <0.05 wt.%, and no AVS was detected in this core (**Table 3**). Overall, N1 had less $\text{Fe}_{\text{dithionite}}$ and $\text{Fe}_{\text{oxalate}}$ than S1. N1 contained an order of magnitude more CRS than S1 (**Table 3**).

Table 4 summarises the $\delta^{34}\text{S-SO}_4$ results obtained from samples of water within the active layer. Overall, water from Ice Wedge North water was more enriched in ^{34}S than water from Ice Wedge South. The Ice Wedge North $\delta^{34}\text{S-SO}_4$ was increasingly depleted in ^{34}S with increasing depth. At Ice Wedge South, the water $\delta^{34}\text{S-SO}_4$ was most enriched in ^{34}S at 30 cm depth, whereas the $\delta^{34}\text{S-SO}_4$ was more depleted in ^{34}S at depths of 9 cm and 60 cm.

DISCUSSION

Since emergence from the sea during the Holocene epoch, permafrost aggradation and ongoing organic carbon accumulation have most likely caused significant changes in the biogeochemical processes and mineral precipitation reactions within this high Arctic floodplain. The two sites described above help understand these changes because their contrasting hydrological regimes result in marked differences in the accumulation and decomposition of permafrost organic carbon, in spite of their proximity within the same valley. Below, we describe how the quantity of organic carbon regulates the consumption of alternative electron acceptors used for microbial oxidation of organic carbon, thus causing a switch in the water-saturated areas of the floodplain to iron- and sulfate-reduction, with net iron and carbon storage via increased CRS and $\text{Fe}_{\text{acetate}}$ precipitation. In contrast, the drier areas store far less organic carbon and instead remain dominated by the biogeochemical signatures of pyrite oxidation. These processes seem most likely during the earlier stages of floodplain development, when they play a dominant role in the weathering of fresh mineral surfaces, as expressed by the composition of glacial meltwaters in the nearby Endalen, Bolterdalen and Longyeardalen catchments (Yde et al., 2008; Rutter et al., 2011; Hodson et al., 2016, respectively). In the following discussion, we therefore explore first of all the dominant weathering processes that are linked to pyrite oxidation, before examining the other processes associated with sulfur and iron biogeochemistry that better explain the later stages of biogeochemical evolution, once more organic carbon has become available.

Dominant Weathering Reactions

The pore water profiles in **Figures 2–5** represent the following attributes of both the active layer and the underlying permafrost: (1) the *in situ* distribution of extractable or adsorbed solutes, reactive mineral phases, and gases, and (2) the products of additional rock-water-microorganism interactions following thaw. Across both sites, except for N1 where potassium dominated, calcium and magnesium were the dominant cations (**Figures 4**, **5**), indicating that carbonate dissolution prevails over silicate dissolution, despite a low carbonate content in

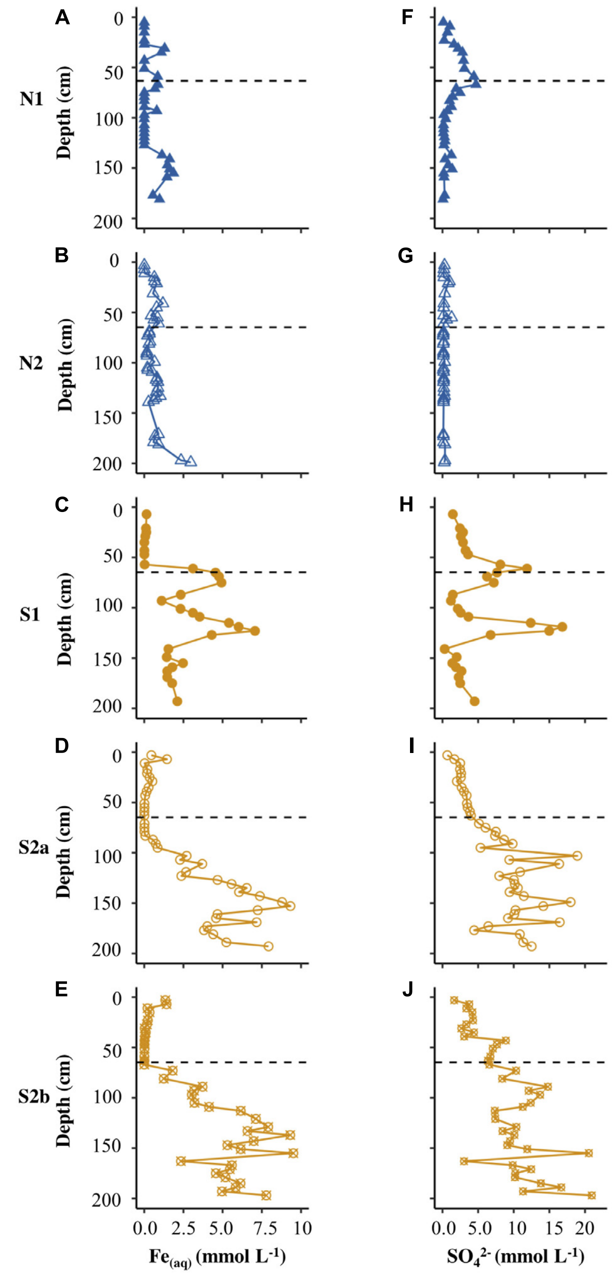

FIGURE 3 | Depth profiles of $Fe_{(aq)}$ **(A–E)** and SO_4^{2-} **(F–J)** for N1, N2, S1, S2a, and S2b. The horizontal dashed line on each plot represents the base of the active layer in 2017.

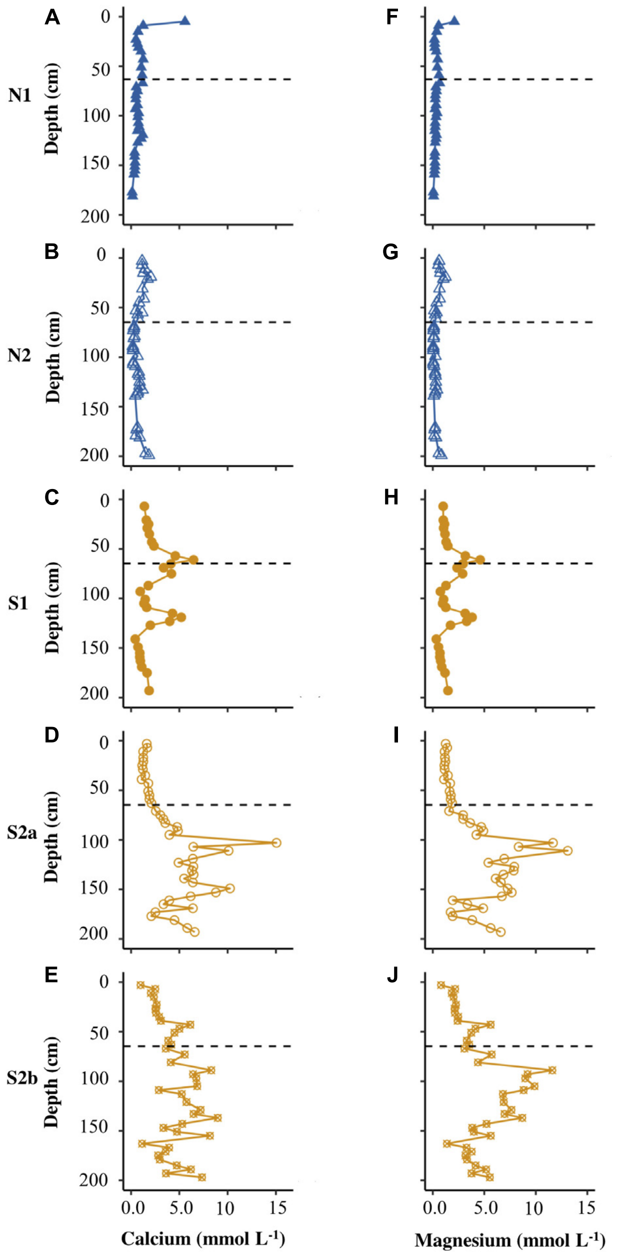

FIGURE 4 | Depth profiles of calcium **(A–E)** and magnesium **(F–J)** for N1, N2, S1, S2a, and S2b. The horizontal dashed line on each plot represents the base of the active layer in 2017.

the sediments (< 0.8 dry wt.% at Ice Wedge South) and low volumetric carbonate contents (~0.3 to 1.8%, but up to 10.7%) in rocks from the Todalen and Endalen endmembers (Svinth, 2013). This contrasts with a study in a nearby unglaciated catchment (Fardalen) that found a relatively high proportion of silicate weathering, suggested to be the result of a combination of relatively rapid leaching of carbonate phases from the active layer and low rates of physical weathering in the sediments, failing to expose fresh carbonates to weathering (Hindshaw et al., 2016). However, carbonate weathering has previously been shown to control the water chemistry of both glacial and non-glacial watersheds, even where the bedrock is predominantly silicate, with only trace amounts of carbonate (Blum et al., 1998; Horton et al., 1999). This strongly suggests that although the low carbonate content coupled with the potential for active layer leaching might limit the importance of carbonate weathering in Adventdalen to some degree, the reactivity of the carbonate phases (compared to silicates) compensated for these factors.

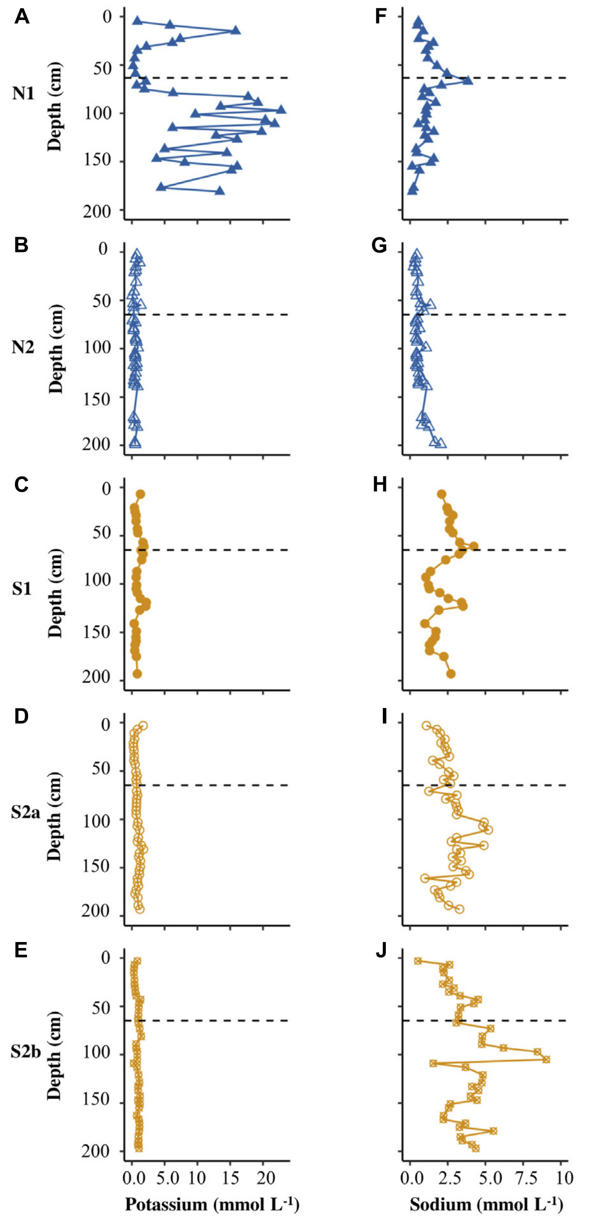

FIGURE 5 | Depth profiles of potassium **(A–E)** and sodium **(F–J)** for N1, N2, S1, S2a, and S2b. The horizontal dashed line on each plot represents the base of the active layer in 2017.

The weathering processes responsible for the acquisition of Ca^{2+} and Mg^{2+} in the sediment pore water are most likely to be represented by the following reactions (after Tranter et al., 2002; Yde et al., 2008; Hindshaw et al., 2016):

(1) Carbonate dissolution with carbonic acid (where x is equal to 1 or 0):

$$Ca_{1-x}Mg_xCO_3 + CO_2 + H_2O \rightarrow (1-x)Ca^{2+} + xMg^{2+} + 2HCO_3^- \tag{4}$$

(2) Sulfide oxidation coupled to carbonate weathering (where x is equal to 1 or 0):

$$4FeS_2 + 16Ca_{1-x}(Mg_x)CO_3 + 15O_2 + 14H_2O \rightarrow 4Fe(OH)_3 + 16(1-x)Ca^{2+} + 16xMg^{2+} + 16HCO_3^- + 8SO_4^{2-} \tag{5}$$

The covariance between ions is used here to identify the dominant weathering processes in the entire active layer and permafrost. Evidence for dolomite weathering as a source of both Ca^{2+} and Mg^{2+} was therefore provided by the strong positive correlation between these ions at Ice Wedge South ($p < 0.0001$, $\rho = 0.95$) and a regression slope close to unity (0.89). When corrected for precipitation inputs (rain and snow) of both cations, the slope remained unchanged (**Figure 6**), but the intercept decreased significantly toward zero (0.24 mmol L^{-1}). Therefore dolomite represents a credible, common source for both ions.

Although $(Ca + Mg)_{npd}$ was strongly correlated with $SO_4^{2-}{}_{npd}$ ($p < 0.0001$, $\rho = 0.81$), the regression slope was 0.73, which suggests that some of the sulfate was associated with other processes. Given the presence of silicates in the catchment, sulfide oxidation coupled to silicate dissolution may play a role in making up the deficit. Since silicates in the catchment are mainly present as Na- and K-feldspars, they may be represented by the formulae: $NaAlSi_3O_8$ and $KAlSi_3O_8$ in the following reactions (Tranter et al., 2002; Hindshaw et al., 2016):

(1) Silicate dissolution with carbonic acid (where x is equal to 1 or 0):

$$2Na_{(1-x)}K_xAlSi_3O_8\,(s) + 2CO_2\,(aq) + 11H_2O\,(l) \rightleftharpoons 2(1-x)Na^+\,(aq) + 2xK^+ + 2HCO_3^-\,(aq) + Al_2Si_2O_5(OH)_4\,(s) + 4H_4SiO_4 \tag{6}$$

(2) Sulfide oxidation coupled to silicate dissolution (where x is equal to 1 or 0):

$$16Na_{1-x}K_xAlSi_3O_8\,(s) + 4FeS_2\,(aq) + 15O_2\,(aq) + 86H_2O\,(l) \rightleftharpoons 16(1-x)Na^+\,(aq) + 16xK^+ + 8SO_4^{2-}\,(aq) + 4Al_4Si_4O_{10}\,(OH)_8\,(s) + 4Fe\,(OH)_3\,(s) + 32H_4SiO_4(aq) \tag{7}$$

When silicate and carbonate dissolution are both driven by sulfide oxidation, the total base cation ($Ca^{2+} + Mg^{2+} + Na^+ + K^+$) ratio to SO_4^{2-} tends toward unity when precipitation inputs are insignificant (Fairchild et al., 1994; Tranter et al., 2002; Wadham et al., 2010). However, this characteristic signature can be overprinted or masked by gypsum dissolution, ion exchange reactions or mineral precipitation reactions that remove base cations from solution. Of these, gypsum may be ignored, because it is absent from the bedrock (Svinth, 2013). Prior to

TABLE 3 | Summary statistics calculated for the length of each core for the solid phase data of the cores S1 and N1 from Ice Wedge South and Ice Wedge North, including AVS, CRS, $Fe_{ascorbate}$, $Fe_{dithionite}$, $Fe_{acetate}$, $Fe_{oxalate}$, and organic carbon.

			Ice Wedge North		Ice Wedge South		
	Unit		**N1**	**N2**	**S1**	**S2a**	**S2b**
AVS	dry wt.%	mean	0.02	na	0	na	na
		(*min-max*)	(*0.00–0.05*)	na	(*0–0*)	na	na
		n	*7*	na	*9*	na	na
CRS	dry wt.%	mean	0.12	na	0.02	na	na
		(*min-max*)	(*0.02–0.27*)	na	(*0.00–0.05*)	na	na
		n	*7*	na	*9*	na	na
$Fe_{ascorbate}$	dry wt.%	mean	0.97	na	0.44	na	na
		(*min-max*)	(*0.32–1.64*)	na	(*0.30–0.77*)	na	na
		n	*10*	na	*12*	na	na
$Fe_{dithionite}$	dry wt.%	mean	0.13	na	0.44	na	na
		(*min-max*)	(*0.05–0.32*)	na	(*0.24–0.52*)	na	na
		n	*10*	na	*12*	na	na
$Fe_{acetate}$	dry wt.%	mean	1.00	na	0.53	na	na
		(*min-max*)	(*0.38–1.57*)	na	(*0.39–0.73*)	na	na
		n	*10*	na	*12*	na	na
$Fe_{oxalate}$	dry wt.%	mean	1.58	na	4.11	na	na
		(*min-max*)	(*0.55–3.43*)	na	(*2.48–5.78*)	na	na
		n	*10*	na	*12*	na	na
Organic Carbon	dry wt.%	mean	8.55	16.7	2.41	1.9	2.34
		(*min-max*)	(*1.84–30.8*)	(*4.83–45.6*)	(*1.44–5.41*)	(*1.71–2.08*)	(*2.06–2.66*)
		n	*33*	*29*	*28*	*5*	*5*

TABLE 4 | $\delta^{34}S-SO_4$ in water from the active layer in polygons S1 and N2.

Site	**Depth (cm)**	$\delta^{34}S-SO_4$			
		Mean	***min***	***max***	***n***
S1	9	−6.90	*−6.95*	*−6.85*	*2*
S1	30	−2.23	*−3.74*	*−0.13*	*3*
S1	60	−6.78	*−8.37*	*−5.70*	*3*
N1	9	15.1	*3.33*	*25.3*	*3*
N1	30	5.19	*−0.98*	*11.4*	*2*
N1	60	−2.83	*−4.03*	*−2.16*	*3*

correction for precipitation inputs, the total base cation ratio to sulfate at Ice Wedge South was 0.98 (r^2 = 0.68). The standard correction for precipitation inputs resulted in a lower regression slope of 0.76 (r^2 = 0.70; **Figure 7A**). Of the base cations, sodium was particularly affected by the above masking effects, with non-precipitation inputs appearing negative, similar to that which may be inferred from pore water data for Adventdalen sediment cores presented by Cable et al. (2017). This is indicative of ion exchange reactions or mineral precipitation (e.g., albite) and hence precludes the use of the non-precipitation ion ratios to estimate the importance of sulfide oxidation coupled to silicate dissolution.

Since the concentration of SO_4^{2-} derived from pyrite oxidation was high and developed within a sometimes-anoxic environment, alternative processes of pyrite oxidation to those shown by Equations 5 and 7 require identification. For instance, under acidic conditions, the $Fe(OH)_3$ produced via Equations 5 and 7 dissociates to form Fe^{3+}, the reduction of which could result in a significant contribution of ferrous iron to the total cations in solution (Raiswell and Canfield, 2012; Hodson et al., 2016; Raiswell et al., 2018).

$$14Fe^{3+} + FeS_2 + 8H_2O \rightarrow 15Fe^{2+} + 2SO_4^{2-} + 16H^+ \quad (8)$$

However, the reduction of iron (oxyhydr)oxide need not be achieved in combination with sulfide oxidation (Equation 9).

$$4Fe(OH)_3 + CH_2O + 8H^+ \rightarrow 4Fe^{2+} + 11H_2O + CO_2 \quad (9)$$

In contrast to Ice Wedge South, **Figure 7B** shows that the Ice Wedge North pore waters generally do not plot on the 1:1 line, and so there is no relationship between sulfate and total cations for these. Despite this, some samples from this site have a sulfate to chloride ratio greater than the snowpack sulfate to chloride ratio. This indicates that sulfide oxidation has enhanced the sulfate concentrations. The absence of a 1:1 relationship between total cations and sulfate at this site therefore strongly suggests that the sulfate produced by sulfide oxidation is removed in part by sulfate reduction during respiration of organic matter (Equation 10; Wadham et al., 2004).

$$SO_4^{2-} + 2CH_2O \rightleftharpoons H_2S + 2HCO_3^- \quad (10)$$

The major ion ratios show that sulfide oxidation coupled to carbonate dissolution can contribute substantial quantities of

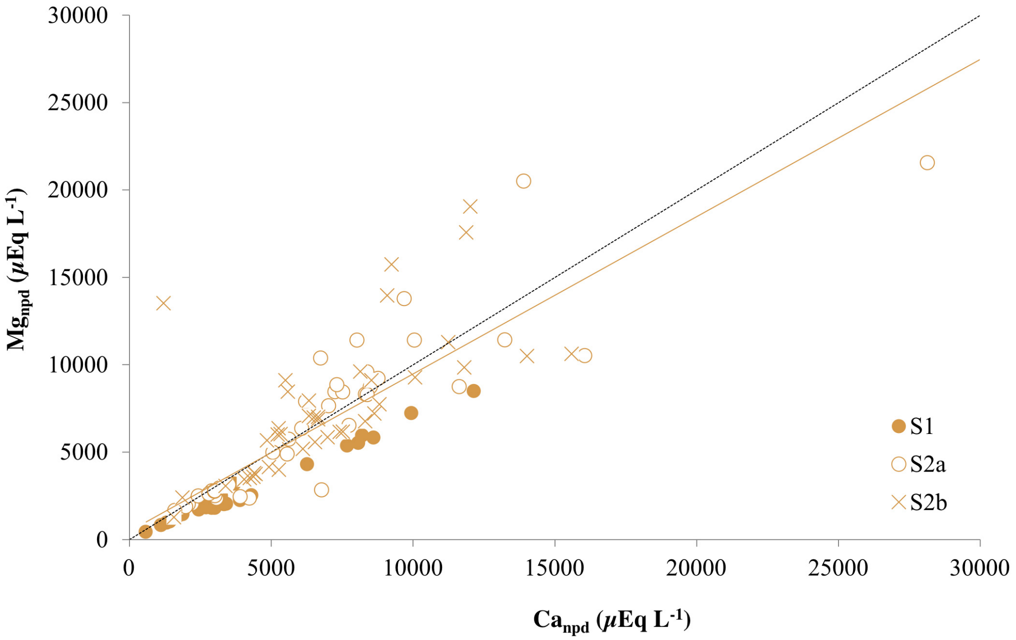

FIGURE 6 | Non-precipitation-derived magnesium (Mg_{npd}) and non-precipitation-derived calcium (Ca_{npd}) in the three cores from Ice Wedge South. The dashed black line corresponds to a 1:1 relationship between Ca_{npd} and Mg_{npd} that represents dolomite dissolution. The solid orange line is a regression for all points from the three cores from Ice Wedge South (R^2 = 0.69).

sulfate to the sediment pore water at Ice Wedge South. The weathering mechanisms here are analogous to those reported in glacial catchments of the area, which is intuitive when the source of the sediments is considered (i.e., the aeolian deposition of glaciofluvial sediments dessicated during early winter). The sulfuric acid produced by sulphide oxidation may further act as a weathering agent in this system, akin to in glacial catchments, potentially producing carbon dioxide during weathering of carbonates (e.g., Torres et al., 2017). In contrast, processes removing sulfate from the sediment pore water at Ice Wedge North preclude the use of major ion ratios to determine the significance of sulfide oxidation. In spite of this, sulphide oxidation is still very likely to occur because the provenance of the sediments is the same as that at Ice Wedge South.

Sources and Sinks of Sulfate

Sulfur and oxygen isotopic values of sulfate in waters provide compelling evidence for the identification of the sources and sinks of sulfate (e.g., Wynn et al., 2006, 2015; Turchyn et al., 2013; Hindshaw et al., 2016). Pre-melt snowpacks in Svalbard at Midtre Lovenbreen (Wynn et al., 2006) and near Ny Ålesund (Tye and Heaton, 2007) suggest a δ^{34}S range of +17 to +18‰ and a δ^{18}O range of +8.6 to +9.7‰ for the precipitation-derived sulfate contribution to the active layer pore water (i.e., $SO_4^{2-}{}_{pd}$). A study of dissolved organosulfur compounds in a raised peat bog showed that atmospheric sulfur in surface water sulfate is also taken up by plants (plant δ^{34}S was 0.1‰ and 4.2‰) and released when they decay, producing humic organosulfur with δ^{34}S values reflecting the precipitation-derived origin of the sulfate (Bottrell et al., 2010). Other sources of sulfate to the pore water include the oxidative weathering of pyrite (OWP), as in Equations 5, 7, and 8. The mass-weighted mean sulfide δ^{34}S values in the geological formations of the study region vary widely, from −40.6‰ in the Grumantbyen Formation to 1.78‰ in the Aspelintoppen Formation (**Table 5**). In the geological formations measured closest to the sites, the range in mass weighted mean sulfide δ^{34}S values is narrower, from −13.8‰ in the Carolinefjellet Formation to −2.01‰ in the Firkanten Formation. These nearby δ^{34}S values are therefore used to discriminate the rock-derived sulfate from the snowpack-derived sulfate.

TABLE 5 | The mean quantity of sulfide (wt.%) in bedrock, the numerical mean sulfide δ^{34}S (‰) in bedrock and the mass-weighted mean sulfide δ^{34}S (‰) in bedrock.

Formation	n	Mean S	Numerical mean δ^{34}S	Mass weighted mean δ^{34}S
		wt.%	‰	‰
Aspelintoppen	4	0.09	0.44	1.78
Battfjellet	3	0.06	1.56	1.49
Frysjaodden (Gilsonryggen)	4	0.15	−4.98	1.34
Grumantbyen	3	0.10	−32.35	−40.60
Basilika	4	1.71	8.45	2.04
Firkanten (Endalen)	3	0.24	−6.22	−7.88
Firkanten (Todalen)	3	3.55	−0.76	−2.01
Carolinefjellet	3	0.15	−13.27	−13.79

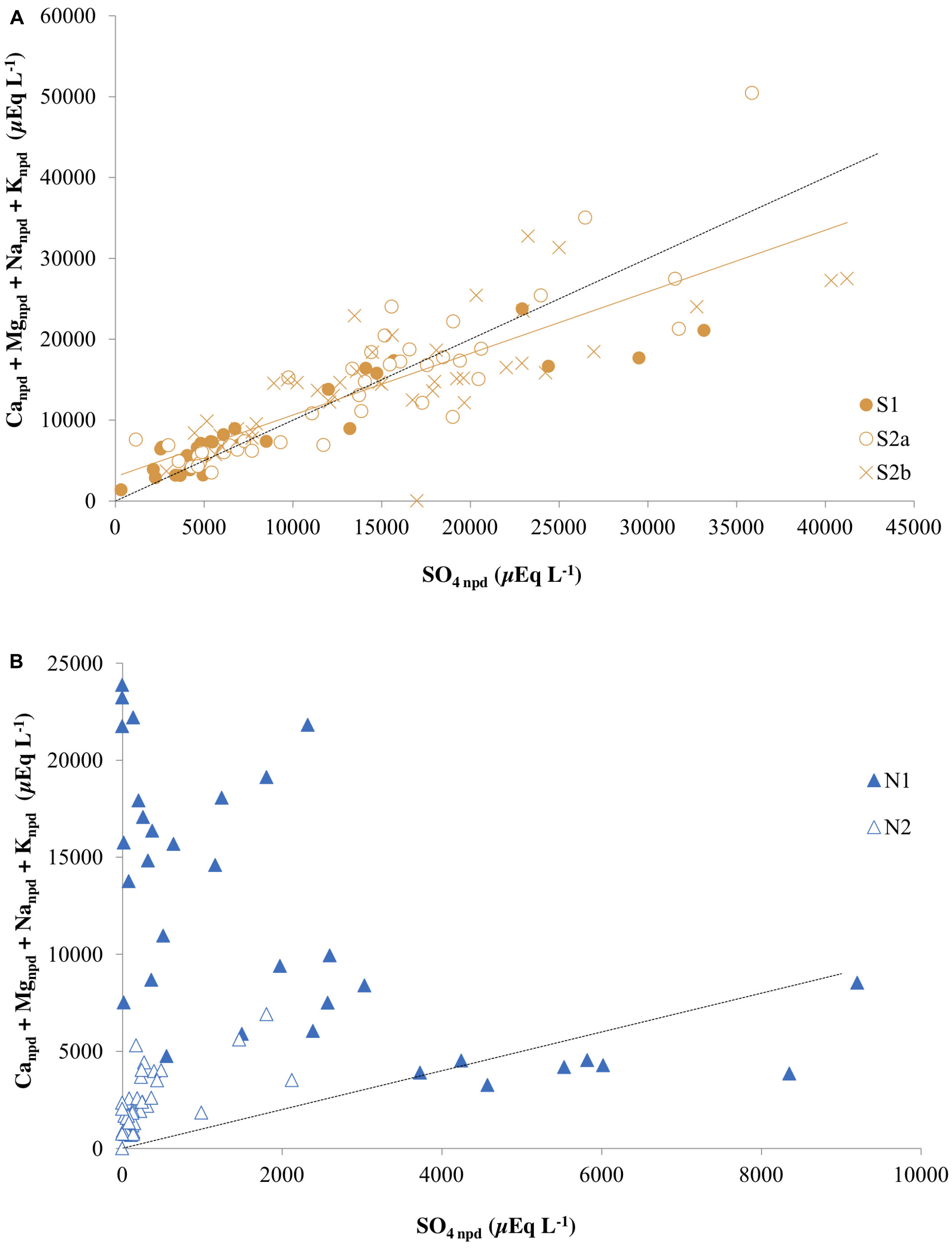

FIGURE 7 | Total non-precipitation-derived base cations and non-precipitation-derived sulfate in **(A)** the three cores from Ice Wedge South and **(B)** the two cores from Ice Wedge North. The dashed black line corresponds to a 1:1 relationship between $SO_{4\ npd}$ and (Ca_{npd} + Mg_{npd} + Na_{npd} + K_{npd}) that represents sulfide oxidation coupled to silicate dissolution. The solid orange line is a regression for all points from the three cores from Ice Wedge South (R^2 = 0.70).

The $\delta^{18}O$ of sulfate depends on the oxidation pathway; the oxygen atoms in the sulfate can originate either from atmospheric oxygen (+23.5‰) or from the surrounding water (−11‰ to −14‰ at our sites). In sulfate produced by OWP via Fe^{3+} (Equation 8), the oxygen atoms are derived solely from the surrounding water molecules. Experiments have demonstrated that there is no isotopic discrimination during the incorporation of oxygen atoms from water molecules into sulfate (Lloyd, 1968). In contrast, the incorporation of oxygen atoms from O_2 molecules into sulfate molecules during OWP via O_2 causes an isotopic fractionation of −8.7‰. Consequently, sulfate produced by OWP via O_2 is depleted in ^{18}O by −8.7‰ compared with

TABLE 6 | Oxygen isotopes of weathering-derived sulfate ($\delta^{18}O\text{-}SO_4^{2-}{}_{npd}$) and water ($\delta^{18}O\text{-}H_2O$) compared to the threshold for anoxic oxidation of pyrite ($\delta^{18}O_{THRESH}$).

Site	Depth	$\delta^{18}O\text{-}SO_4^{2-}{}_{npd}$	$\delta^{18}O\text{-}H_2O$	$\delta^{18}O_{THRESH}$	OWP
	cm	‰	‰	‰	
S	9	−5.36	−11.4	−4.78	anoxic
S	9	−3.36	−11.3	−4.75	oxic
S	30	3.47	−12.3	−5.45	oxic
S	30	3.48	−12.3	−5.45	oxic
S	30	2.54	−12.4	−5.57	oxic
S	30	3.95	−12.1	−5.30	oxic
S	60	1.39	−12.0	−5.24	oxic
S	60	3.83	−13.1	−6.05	oxic
S	60	5.66	−12.4	−5.57	oxic
N	9	9.16	−13.0	−6.00	oxic
N	9	5.65	−13.0	−6.01	oxic
N	9	1.40	−13.0	−5.96	oxic
N	30	5.06	−13.7	−6.56	oxic
N	30	6.12	−13.5	−6.34	oxic
N	60	5.33	−14.1	−6.79	oxic
N	60	5.39	−14.1	−6.79	oxic
N	60	4.32	−13.8	−6.59	oxic
N	60	4.32	−13.5	−6.38	oxic

atmospheric O_2, which is strongly enriched in ^{18}O at +23.7‰ (Bottrell and Tranter, 2002). However, during OWP via O_2, there can be isotopic exchange between water and oxygen atoms in sulfoxy anions of intermediate valency, obscuring the isotopic signal of atmospheric oxygen (Balci et al., 2007). Hence, even in OWP via O_2, three out of four oxygen atoms in the sulfate molecule could show an isotopic signal from water (Bottrell and Tranter, 2002).

To elucidate whether the sulfate in the samples from Adventdalen could derive from OWP only via O_2, the approach of Bottrell and Tranter (2002) was applied to the $\delta^{18}O$ values of sulfate from the pore waters in the active layer. This conservative approach assumed that only the final oxygen atom incorporated into sulfate will still carry an isotopic signature indicative of its source (water or atmospheric oxygen). Only if there is less than 25% of the oxygen in a sulfate molecule derived from O_2 can it be certain that part of the sulfate was produced anoxically, by OWP via Fe^{3+}. Equation 11 uses the measured $\delta^{18}O\text{-}H_2O$ water isotopic compositions (**Table 6**) to calculate a threshold sulfate $\delta^{18}O$ ($\delta^{18}O_{THRESH}$) for the formation of sulfate with one oxygen atom from O_2 and three from water (Bottrell and Tranter, 2002).

$$\delta^{18}O_{THRESH} = (23.7 - 8.7) \times 0.25 + 0.75 \times \delta^{18}O_{THRESH} \tag{11}$$

Comparing $\delta^{18}O\text{-}SO_4^{2-}$ and $\delta^{18}O_{THRESH}\text{-}SO_4^{2-}$ data, only one sample from the Adventdalen active layer pore water falls below the threshold for OWP via Fe^{3+} (**Table 6**), indicating that $SO_4^{2-}{}_{npd}$ in this sample originates from OWP via Fe^{3+}. In the rest of the samples, $SO_4^{2-}{}_{npd}$ could have originated from OWP via Fe^{3+}, but the isotopic data do not require that and it is probable that $SO_4^{2-}{}_{npd}$ in the remaining samples instead originated from OWP via O_2. This is a surprising result, as these samples are from between 9 and 60 cm below the ground surface and it was anticipated that oxygen penetration would decrease with profile depth. However, it is possible that radial oxygen loss from the roots of wetland plants may have provided an oxygen source to this deeper pore water (e.g., Johnston et al., 2014). In addition, ice-wedge cracking and shallower cracking restricted to the active layer (O'Neill and Christiansen, 2018) provide a route for ingress of oxygenated rain and meltwater.

Figure 8 shows how plotting sulfate $\delta^{18}O$ and $\delta^{34}S$ in sulfur and oxygen isotopic space can provide a unique solution to elucidating the sulfate sources. The stoichiometric stage of pyrite oxidation results in sulfur isotopic fractionation between pyrite and sulfate ($\varepsilon_{SO4-pyrite}$) of −1.3‰ to −0.6‰ (Balci et al., 2007; Pisapia et al., 2007; Brunner et al., 2008). The mass-weighted mean sulfide $\delta^{34}S$ of the nearby Firkanten and Carolinefjellet Formations, combined with the sulfur isotopic fractionation during the stoichiometric stage of sulfide oxidation, indicates that any pore water sample with a $\delta^{34}S\text{-}SO_4^{2-}{}_{npd}$ value between −15.1‰ and −2.6‰ is likely to have derived all of its sulfur from the stoichiometric oxidation of pyrite. **Figure 8** shows that half of the pore water samples from Adventdalen contain $SO_4^{2-}{}_{npd}$ within this $\delta^{34}S\text{-}SO_4^{2-}{}_{npd}$ range, indicating that the stoichiometric oxidation of pyrite is an important process contributing sulfate to active layer pore water in Adventdalen. This corroborates the evidence from the $\delta^{18}O\text{-}SO_4^{2-}$ results presented earlier.

Although all samples except for the most ^{34}S-enriched sample have a $\delta^{34}S$ range between that of the bedrock and snowpack $\delta^{34}S$ values (**Figure 8**), the origin of sulfate in these samples in ^{34}S and ^{18}O cannot be explained purely as a mixing of sulfate derived from these two sources. There are two lines of evidence for this. Firstly, if mixing between (relatively ^{34}S-enriched) precipitation-derived sulfate and (relatively ^{34}S-depleted) weathering-derived sulfate were solely responsible for the $\delta^{34}S$ values of pore water sulfate in the active layer, a negative linear correlation between the concentration and $\delta^{34}S$ values of sulfate would result. There is no such negative linear correlation in the pore water samples from Adventdalen ($R^2 < 0.2$). Secondly, a negative correlation between $\delta^{34}S\text{-}SO_4^{2-}$ and the sulfate-to-chloride molar ratio (SO_4^{2-}/Cl^-) would result from mixing between weathering-derived sulfate (high SO_4^{2-}/Cl^-, relatively ^{34}S-depleted) and precipitation-derived sulfate (low SO_4^{2-}/Cl^-, relatively ^{34}S-enriched). In fact, there is a positive correlation between $\delta^{34}S\text{-}SO_4^{2-}$ and SO_4^{2-}/Cl^- ($R^2 = 0.49$). Neither line of evidence supports mixing between snowmelt and pyrite oxidation as the sole reason for the $\delta^{34}S\text{-}SO_4^{2-}$ values observed in the pore water samples from Adventdalen. Hence, these statistical tests indicate that sulfate removal from the pore water by sulfate-reducing bacteria (SRB) may be a factor in enriching the remaining sulfate in these samples. SRB preferentially reduce the lighter isotopes of sulfur and oxygen, leading to isotopic enrichment of the residual sulfate. It is common for the product H_2S to be incorporated into iron sulfides or organic matter

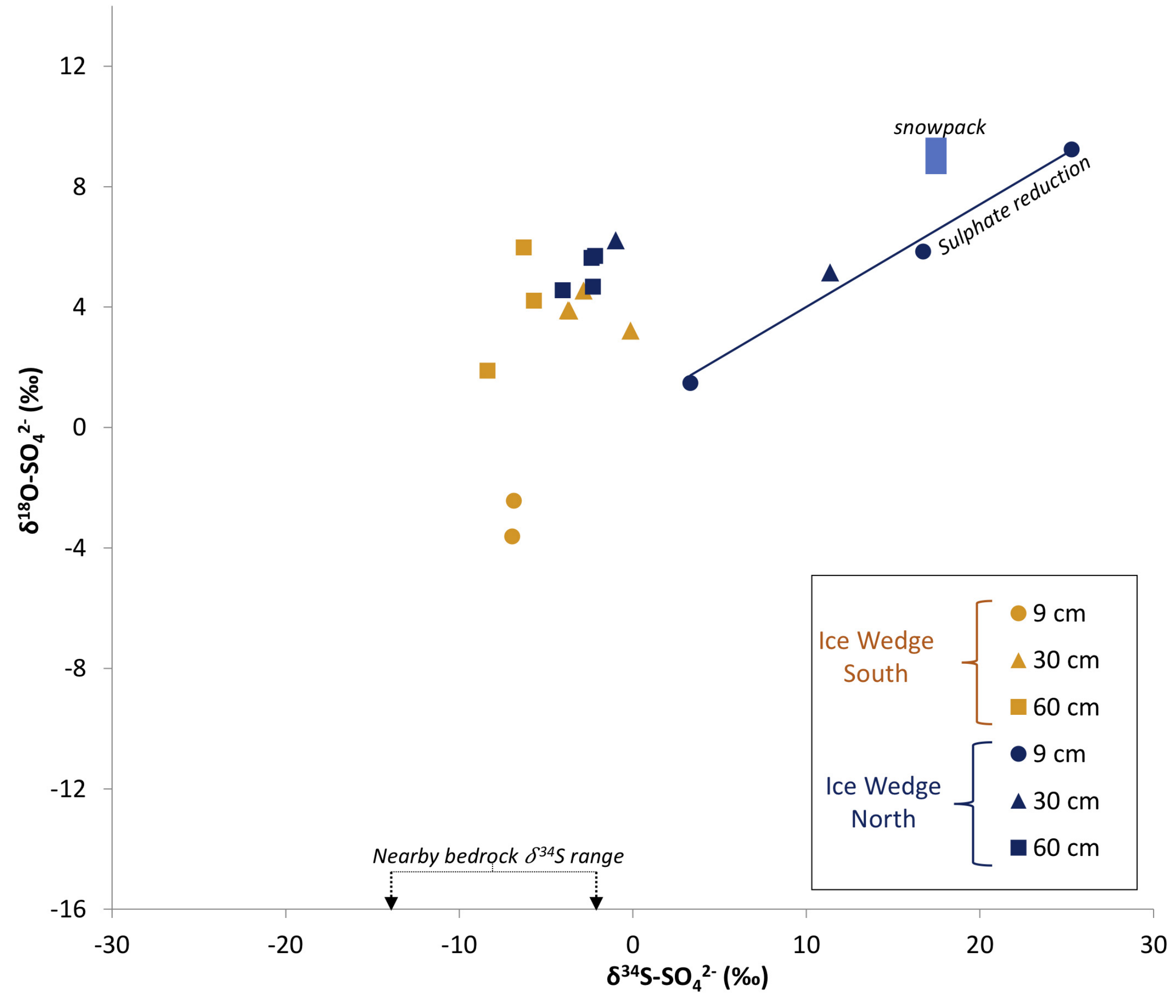

FIGURE 8 | Water samples from the active layer of Ice Wedge South and Ice Wedge North in δ^{18}O-SO_4 and δ^{34}S-SO_4 isotope space. The blue box represents the isotopic range of pre-melt snowpacks in Svalbard at Midtre Lovenbreen (Wynn et al., 2006) and near Ny Ålesund (Tye and Heaton, 2007). The solid blue line is a regression line illustrating reduction of sulphate by SRB (R^2 = 0.98). The nearby bedrock range is of the mass-weighted mean sulfide δ^{34}S in the Firkanten and Carolinefjellet Formations.

(Brown, 1985, 1986; Blodau et al., 2007). This causes both δ^{34}S and δ^{18}O values in the remaining sulfate to increase, producing a positive correlation between them (Mandernack et al., 2003). Since there is a positive correlation ($R^2 = 0.98$) between δ^{34}S and δ^{18}O in four samples from Ice Wedge North, and δ^{34}S in one sample exceeds the snowpack δ^{34}S, it seems highly likely that SRB are active in the pore water of the active layer at Ice Wedge North.

Iron and Sulfur Mineral Precipitation

The δ^{34}S and δ^{18}O values of pore water sulfate in the active layer are indicative of sulfate reduction at Ice Wedge North. The sulfate concentration was relatively low at Ice Wedge North (< 4.7 mmol l^{-1}; **Figures 3F,G**), supporting the isotopic evidence for sulfate reduction. To produce a distinctive δ^{18}O-δ^{34}S signature of sulfate reduction, the reduced sulfur must be sequestered in the solid phase (iron sulfide or carbon-bonded sulfur). The reactions of iron with hydrogen sulfide can be expressed with the following simplified equation scheme, where Equation 12 represents hydrogen sulfide reacting with iron oxides to form iron monosulfide (AVS) and sulfur, and Equation 13 represents the formation of the more stable pyrite (CRS) from the metastable iron monosulfide and sulfur (Raiswell and Canfield, 2012):

$$2FeOOH + 3H_2S \rightarrow 2FeS + S^0 + 4H_2O \tag{12}$$

$$FeS + S^0 \rightarrow FeS_2 \tag{13}$$

The AVS formed in Equation 12 consists mainly of the iron sulfide minerals mackinawite, greigite and amorphous FeS. These phases are usually only stable for short periods before their re-oxidation or further reduction to pyrite (Chesworth, 2008). **Table 3** and **Supplementary Figure S1I** show that the AVS concentrations in the Ice Wedge North sediments were low, but detectable, in just over half the samples, reaching a maximum of 0.05 dry weight percent (equivalent to 6.02 μmoles g^{-1}

dry sediment; 115 cm depth). The low concentrations of AVS indicate that AVS is not a significant long-term store of the products of iron and sulfate reduction. The CRS includes pyrite, which is the most thermodynamically stable iron sulfide (Berner, 1967). Concentrations of CRS are higher than AVS, reaching 0.27 dry weight percent (equivalent to 22.4 μmoles g^{-1} dry sediment; 115 cm depth) at Ice Wedge North (**Table 3** and **Supplementary Figure S1K**).

The Ice Wedge North sediments contain abundant iron in $Fe_{ascorbate}$, $Fe_{dithionite}$, $Fe_{oxalate}$, $Fe_{acetate}$ and CRS. Ferrous iron in the porewaters is probably derived from the dissimilatory reduction of iron (oxyhydr)oxides (Equation 9), as well as the oxidation of allogenic and authigenic pyrite (Equation 8). In addition to reacting with hydrogen sulfide to form AVS or CRS, the dissolved ferrous iron reacts with bicarbonate ions to form $Fe_{acetate}$ (iron bound in carbonates). Siderite ($FeCO_3$) is an iron carbonate, and tends to occur in reducing, CO_2-rich, hydromorphic environments, such as peatlands (Chesworth, 2008). **Table 3** shows that $Fe_{acetate}$ reaches >1.5 dry weight% in the sediments at Ice Wedge North, indicating that it is a more significant sink of ferrous iron than CRS. As the precipitation of $Fe_{acetate}$ dominates over the precipitation of CRS, it is possible that an additional sink for the hydrogen sulfide is carbon-bonded sulfur (CBS), which has previously been shown to be an important sink for reduced sulfur in peat soils (Spratt and Morgan, 1990; Blodau et al., 2007). Although CBS was not measured in these cores, a strong positive correlation between organic carbon content and CRS ($\rho = 0.9$; $p < 0.001$) and also $Fe_{acetate}$ ($\rho = 0.67$; $p < 0.01$) indicates that where the organic carbon content is high, sulfate reduction, CRS precipitation and $Fe_{acetate}$ precipitation occur. Given the high concentration of sedimentary organic carbon, it seems likely that CBS exists and is forming at this location.

In contrast to Ice Wedge North, the $\delta^{34}S$ and $\delta^{18}O$ values of sulfate in pore water from the drier active layer of S1 indicate primarily OWP via O_2, and some OWP via Fe^{3+}. Evidence for a mostly oxidised active layer at S1 is in the mostly low $Fe_{(aq)}$ concentration in the pore water from the active layer and the low water table (summer 2017). CRS and AVS concentrations at this site are low, corroborating the isotopic evidence that sulfate reduction is negligible at this site. In addition, the concentration of iron bound in carbonate ($Fe_{acetate}$) is lower than at Ice Wedge North. Finally, **Figures 3C,H** show that aqueous iron and sulfate co-vary at this site, which is indicative of pyrite oxidation (e.g., Hodson et al., 2016).

The quantity of sedimentary organic carbon exerts a strong control on biogeochemical processes and mineral precipitation across both sites. Firstly, the organic carbon content is strongly positively correlated with CRS ($\rho = 0.90$; $p < 0.001$), $Fe_{acetate}$ ($\rho = 0.67$; $p < 0.01$), and $Fe_{ascorbate}$ ($\rho = 0.75$; $p < 0.001$). In addition, the sedimentary organic carbon content is negatively correlated with pore water sulfate ($\rho = -0.68$; $p < 0.001$) and aqueous iron ($\rho = -0.61$; $p < 0.001$). This further supports the mechanisms discussed above, whereby in organic carbon-poor sediment, the oxidation of pyrite produces aqueous iron and sulfate that are not reduced to form authigenic CRS (primarily pyrite) and $Fe_{acetate}$ (primarily siderite). In contrast, in organic carbon-rich sediment, the dissolved iron and sulfate are reduced, forming $Fe_{acetate}$ and CRS. Finally, sedimentary organic carbon content appears to influence the formation of $Fe_{dithionite}$ (primarily crystalline iron (oxyhydr)oxides) and $Fe_{oxalate}$ (primarily magnetite). Organic carbon content was negatively correlated with $Fe_{dithionite}$ ($\rho = -0.85$; $p < 0.001$) and $Fe_{oxalate}$ ($\rho = -0.89$; $p < 0.001$). A plausible explanation is a combination of cycling redox conditions and dissolved oxygen levels at Ice Wedge South, which increase the crystallinity of ferrihydrite, coupled with an inhibition of the change from $Fe_{ascorbate}$ (primarily poorly crystalline ferrihydrite) to $Fe_{dithionite}$ (primarily crystalline goethite) by organic compounds at Ice Wedge North (e.g., Schwertmann and Murad, 1988; Thompson et al., 2006; Amstaetter et al., 2012; Herndon et al., 2017). These significant relationships demonstrate that the quantity of sedimentary organic carbon exerts a landscape-scale control on the active layer and permafrost biogeochemistry.

Variations in Pore Water Geochemistry Due to Physical Processes

The distribution of chemical species described above is partly governed by a set of complex physical processes, including hydrological inputs to the active layer (precipitation, advection and ground ice melt; Throckmorton et al., 2016), hydrological outputs from the active layer (evaporation, freezing and advection) and the diffusion of ions from regions of high concentration to regions of low concentration. Each of these physical processes can influence the distribution of chemical constituents in the active layer and their signatures commonly overlap or mask one another. For instance, both evaporation of water and ion freeze-out from the active layer concentrate the pore water chemistry and enrich the $\delta^{18}O$ and δD of the remaining water (Throckmorton et al., 2016). However, these physical processes are secondary to the ion ratio interpretations discussed earlier.

The sediments in this study were dominantly fine-grained, with the median grain size in the cores at Ice Wedge South ranging from 34 to 60 μm. In fine-grained sediments, migration of unfrozen water (and solutes) occurs along temperature-induced pressure gradients toward colder ground (Kokelj and Burn, 2003, 2005), and forms segregated ice lenses behind the freezing front. During active layer freezeback, the migration is upward toward the freezing front descending from the surface, and downward toward the permafrost table during upward freezing from the permafrost table (Cheng, 1983). This results in the formation of ice lenses and the concentration of solutes close to the ground surface, in the transient layer and at the top of permafrost, whereas the middle of the active layer becomes desiccated (Mackay, 1983). During thawing of the active layer in summer, unfrozen water and solute migration occurs downward into frozen ground below the advancing thaw front (Cheng, 1983). As the thaw front reaches its maximum depth, moisture and solutes can migrate into the top of permafrost. The downward migration into the top of permafrost in summer is greater than the upward migration out in winter when the temperature and pressure gradients are reversed, because

TABLE 7 | Results from Welch's *t*-test, which was used to test whether the concentration of chloride was significantly different for permafrost (PF) versus active layer (AL) in each core.

Core	Variable	*t*	*df*	*p*	AL			PF			Units for mean
					Mean	*SD*	*n*	Mean	*SD*	*n*	
S1	chloride	0.59	11.42	n.s.	1.84	0.77	9	1.67	0.52	20	mmol L^{-1}
S2a	chloride	6.44	28.01	***	2.39	0.81	14	12.60	8.31	28	mmol L^{-1}
S2b	chloride	3.52	31.62	**	4.66	2.20	14	11.81	10.29	28	mmol L^{-1}
N1	chloride	1.22	22.15	n.s.	0.75	0.52	10	1.01	0.67	23	mmol L^{-1}
N2	chloride	1.62	31.10	n.s.	0.76	0.40	13	1.35	1.78	27	mmol L^{-1}

t is the t statistic, df is the degrees of freedom, p is the significance level, SD is the standard deviation of the mean and n is the number of samples. Asterisks indicate level of significance: $p < 0.05$ (*); $p < 0.01$ (**); and $p < 0.001$ (***); n.s., not significant.

the unfrozen water content and hydraulic conductivity are greatly reduced at lower temperature (Cheng, 1983). Consequently, there is a net annual downward migration that enriches the top of permafrost with segregated ice and solutes following repeated freeze-thaw cycles (Cheng, 1983; Kokelj and Burn, 2003, 2005).

There are multiple lines of evidence that indicate that these mechanisms contribute to redistributing solutes at the study sites. Segregated ice lenses were observed at the base of the active layer in cores from Ice Wedge South, and the top of permafrost was enriched with segregated ice at Ice Wedge North, indicated by the elevated water contents (**Figures 2A,B**). Assuming that chloride behaves conservatively, without participating in dissolution or precipitation reactions, its concentration profile in each core can be used to establish the net effect of moisture distribution by repeated freeze-thaw in the sediments (Jessen et al., 2014). The peak in the concentration of chloride close to the base of the active layer in cores from both sites coincides with the presence of ice lenses and is likely to have been caused by unfrozen water and solute migration during upward freezing of the active layer (**Figures 2F,G,H,J**). The peak in chloride concentration, coincident with an increase in water content near the ground surface at N1, may be indicative of upward moisture migration during active layer freezing.

The upper permafrost at Ice Wedge South formed syngenetically as the permafrost table rose in conjunction with sediment deposition (Gilbert et al., 2018), which means that the present-day permafrost is comprised of material formerly in the active layer. The accumulation of chloride in the permafrost is thus probably due to a combination of moisture migration into the top of permafrost at the end of summer (Cheng, 1983) and incorporation into permafrost of solutes from the base of the active layer during permafrost aggradation (**Figures 2H–J**). Cores S2a and S2b have significantly more concentrated chloride in the permafrost compared with the active layer (**Table 7**), and the chloride concentration in the active layer is greater than in the other cores. The formation of efflorescent salts on the ground surface at Ice Wedge South (Mora et al., 2015) further highlights the role of solute migration along potential gradients at the site.

The higher concentration of chloride in the cores from Ice Wedge South, compared to those from Ice Wedge North, could be the result of diffusion of chloride from the underlying deltaic sediments. Nearby cores display an increase in chloride concentration from a mean of ∼1 mmol L^{-1} in the loess sediments to a mean of ∼68 mmol L^{-1} in the underlying deltaic sediments (Cable et al., 2017). Diffusion upward from these marine sediments may enhance the pore water chloride concentration at shallower depths in some locations, although the reasons for the location-specific diffusion are not clear. Additionally, it is likely that the topography of the sites has changed over time with the development of depositional landforms and ice-wedge polygons (Gilbert et al., 2018; O'Neill and Christiansen, 2018). Changes in topography are likely to have influenced patterns of water movement through the active layer, while variations in active layer thickness changed the amount of ground subject to advection over time. The data do not enable enhanced chloride concentration due to upward diffusion to be distinguished from enhanced chloride concentration due to low advection rates. However, greater rates of advection most likely occur at Ice Wedge North due to the spring-fed hydrologic regime and high water content.

In summary, unfrozen water and solute migration along potential gradients contribute to water content and solute variations with depth observed in the cores. The complex depositional and periglacial history at the sites makes further interpretation of chloride concentration patterns difficult. Ice Wedge South cores display evidence of chloride diffusion from underlying sediments and/or variations in rates of advection as the aeolian terrace aggraded. Despite the complexity introduced by these physical processes, the use of covariance between ions has enabled the dominant biogeochemical processes in Adventdalen to be elucidated.

CONCLUSION

This study highlights the importance of landscape evolution and demonstrates that permafrost aggradation and organic carbon accumulation have caused significant changes in the biogeochemical processes and mineral precipitation reactions within this high Arctic floodplain. The contrasting hydrological regimes of the study sites result in marked differences in the accumulation and decomposition of permafrost organic carbon. The drier areas of the floodplain store little organic carbon and are representative of the earlier stages of floodplain development. These areas are dominated by the biogeochemical signatures of pyrite oxidation and the weathering of fresh mineral surfaces, similar to glacial meltwaters in nearby catchments. In contrast, the water-saturated areas of the floodplain represent the later stages of floodplain development, where the accumulation of organic carbon causes a switch to iron- and sulfate-reduction, with net iron and carbon storage via increased CRS (FeS_2) and $Fe_{acetate}$ (siderite) precipitation. In addition, contrasting chloride concentrations demonstrate the geochemical contrast between sediments of marine and aeolian origin. As air temperatures continue to rise in the high Arctic and as thaw progresses deeper into the permafrost, there are likely to be major changes in the iron, sulfur and carbon cycling in this valley, depending on how permafrost thaw impacts the geomorphology and hydrology of the ice-wedge polygonal terrain.

DATA AVAILABILITY STATEMENT

Jones (2019). Permafrost and active layer biogeochemical data from Adventdalen (2015–2017) (Version 1.0) in the UK Polar Data Centre, Natural Environment Research Council, UK Research & Innovation (https://doi.org/10.5285/4c90d954-3db2-4084-9fe9-e050c839a6fe).

AUTHOR CONTRIBUTIONS

EJ wrote the manuscript. EJ, AH, and HO’N collected the cores of permafrost and water from the active layer. EJ and JR processed and analysed the cores of permafrost. TD analysed the rock cores. ST and PW facilitated the laboratory analyses of permafrost cores and active layer waters. All authors interpreted data and contributed feedback on this manuscript.

FUNDING

The authors acknowledge the Joint Programming Initiative (JPI-Climate Topic 2: Russian Arctic and Boreal Systems) Award No. 71126, a NERC studentship NE/L002450/1 to EJ, a Research Council of Norway grant (NRC no. 294764), and NRCan contribution number 20200053. Open Access Support was received from the University of Sheffield.

ACKNOWLEDGMENTS

We thank the two reviewers for their constructive reviews and Sharon Smith for a helpful internal review. Gwilym Jones, Gunnar Mallon, Graham Gilbert, Ebbe Bak, Dotan Rotem, Yishai Weinstein, Sarah St Germain, Simon Norum, and Knut Lindland Tveit are thanked for their field assistance, and Alan Smalley, Rob Ashurst, Joe Hufton, Andy Fairburn, Dave Hughes, Roscoe Blevins, Anthony Turner, Gerd-Irene Signeres, Andy Hobson, and Alina Marca are thanked for their assistance with the laboratory analyses. The content of this manuscript appears online in EJ’s Ph.D. thesis (Jones, 2019).

SUPPLEMENTARY MATERIAL

The Supplementary Material for this article can be found online at: https://www.frontiersin.org/articles/10.3389/feart.2020.00342/full#supplementary-material

REFERENCES

Amstaetter, K., Borch, T., and Kappler, A. (2012). Influence of humic acid imposed changes of ferrihydrite aggregation on microbial Fe(III) reduction. *Geochim. Cosmochim. Acta* 85, 326–341. doi: 10.1016/J.GCA.2012.02.003

Balci, N., Shanks, W. C., Mayer, B., and Mandernack, K. W. (2007). Oxygen and sulfur isotope systematics of sulfate produced by bacterial and abiotic oxidation of pyrite. *Geochim. Cosmochim. Acta* 71, 3796–3811. doi: 10.1016/j.gca.2007.04.017

Berner, R. A. (1967). Thermodynamic stability of sedimentary iron sulfides. *Am. J. Sci.* 265, 773–785. doi: 10.2475/ajs.265.9.773

Blodau, C., Mayer, B., Peiffer, S., and Moore, T. R. (2007). Support for an anaerobic sulfur cycle in two *Canadian peatland* soils. *J. Geophys. Res. Biogeosci.* 112:G02004. doi: 10.1029/2006JG000364

Blum, J. D., Gazis, C. A., Jacobson, A. D., and Chamberlain, C. P. (1998). Carbonate versus silicate weathering in the Raikhot watershed within the High Himalayan crystalline series. *Geology* 26:411.

Bottrell, S. H., Hatfield, D., Bartlett, R., Spence, M. J., Bartle, K. D., and Mortimer, R. J. G. (2010). Concentrations, sulfur isotopic compositions and origin of organosulfur compounds in pore waters of a highly polluted raised peatland. *Organ. Geochem.* 41, 55–62. doi: 10.1016/j.orggeochem.2009.07.005

Bottrell, S. H., and Tranter, M. (2002). Sulphide oxidation under partially anoxic conditions at the bed of the Haut Glacier d’Arolla, Switzerland. *Hydrol. Process.* 16, 2363–2368. doi: 10.1002/hyp.1012

Brown, J., Ferrians, O. J. Jr., Heginbottom, J. A., and Melnikov, E. S. (1997). *Circum-Arctic Map of Permafrost and Ground-Ice Conditions. U.S. Geological Survey Map CP-45*. Washington, DC: U.S. Department of the Interior.

Brown, K. A. (1985). Sulfur distribution and metabolism in waterlogged peat. *Soil Biol. Biogeochem.* 17, 39–45. doi: 10.1016/0038-0717(85)90088-4

Brown, K. A. (1986). Formation of organic sulfur in anaerobic peats. *Soil Biol. Biogeochem.* 18, 131–140. doi: 10.1016/0038-0717(86)90017-9

Brunner, B., Yu, J.-Y., Mielke, R. E., MacAskill, J. A., Madzunkov, S., McGenity, T. J., et al. (2008). Different isotope and chemical patterns of pyrite oxidation related to lag and exponential growth phases of *Acidithiobacillus ferrooxidans* reveal a microbial growth strategy. *Earth Planet. Sci. Lett.* 270, 63–72. doi: 10.1016/j.epsl.2008.03.019

Cable, S., Elberling, B., and Kroon, A. (2017). Holocene permafrost history and cryostratigraphy in the High-Arctic Adventdalen Valley, central Svalbard. *Boreas* 47, 423–442. doi: 10.1111/bor.12286

Canfield, D. E., Raiswell, R., Westrich, J. T., Reaves, C. M., and Berner, R. A. (1986). The use of chromium reduction in the analysis of reduced inorganic sulfur in sediments and shales. *Chem. Geol.* 54, 149–155. doi: 10.1016/0009-2541(86)90078-1

Cheng, G. (1983). The mechanism of repeated-segregation for the formation of thick layered ground ice. *Cold Reg. Sci. Technol.* 8, 57–66. doi: 10.1016/0165-232X(83)90017-4

Chesworth, W. (ed.) (2008). *Encyclopedia of Soil Science*. Dordrecht: Springer.

Christiansen, H. H. (2005). Thermal regime of ice-wedge cracking in Adventdalen, Svalbard. *Permafrost Periglac. Process.* 16, 87–98. doi: 10.1002/ppp.523

Christiansen, H. H., Etzelmüller, B., Isaksen, K., Juliussen, H., Farbrot, H., Humlum, O., et al. (2010). The thermal state of permafrost in the nordic area during the international polar year 2007-2009. *Permafrost Periglac. Process.* 21, 156–181. doi: 10.1002/ppp.687

Dallmann, W. K., Midbø, P. S., Nøttvedt, A., and Steel, R. J. (1999). *Lithostratigraphic Lexicon Of Svalbard: Review And Recommendations For*

Nomenclature Use: Upper Palaeozoic to Quaternary Bedrock. Tromsø, NO: Norsk Polarinstitutt.

Dise, N. B., and Verry, E. S. (2001). Suppression of peatland methane emission by cumulative sulfate deposition in simulated acid rain. *Biogeochemistry* 53, 143–160.

du Prel, J.-B., Röhrig, B., Hommel, G., and Blettner, M. (2010). Choosing statistical tests: part 12 of a series on evaluation of scientific publications. *Deutsch. Arzteblatt Intern.* 107, 343–348. doi: 10.3238/arztebl.2010.0343

Elberling, B., Michelsen, A., Schädel, C., Schuur, E. A. G., Christiansen, H. H., Berg, L., et al. (2013). Long-term CO_2 production following permafrost thaw. *Nat. Clim. Chang.* 3, 890–894. doi: 10.1038/nclimate1955

Ernakovich, J. G., Lynch, L. M., Brewer, P. E., Calderon, F. J., and Wallenstein, M. D. (2017). Redox and temperature-sensitive changes in microbial communities and soil chemistry dictate greenhouse gas loss from thawed permafrost. *Biogeochemistry* 134, 183–200. doi: 10.1007/s10533-017-0354-5

Fairchild, I. J., Bradby, L., Sharp, M., and Tison, J. –L. (1994). Hydrochemistry of carbonate terrains in alpine glacial settings. *Earth Surf. Process. Landf.* 9, 33–54. doi: 10.1002/esp.3290190104

Førland, E. J., Benestad, R., Hanssen-Bauer, I., Haugen, J. E., and Skaugen, T. E. (2011). Temperature and precipitation development at Svalbard 1900-2100. *Adv. Meteorol.* 2011, 1–14. doi: 10.1155/2011/893790

Fossing, H., and Barker Jørgensen, B. (1989). Measurement of bacterial sulfate reduction in sediments: evaluation of a single-step chromium reduction method. *Biogeochemistry* 8, 205–222. doi: 10.1007/BF00002889

Gilbert, G. L., O'Neill, H. B., Nemec, W., Thiel, C., Christiansen, H. H., and Buylaert, J.-P. (2018). Late Quaternary sedimentation and permafrost development in a Svalbard fjord-valley, Norwegian High Arctic. *Sedimentology* 65, 2531–2558. doi: 10.1111/sed.12476

Haldorsen, S., Heim, M., Dale, B., Landvik, J. Y., van der Ploeg, M., Leijnse, A., et al. (2010). Sensitivity to long-term climate change of subpermafrost groundwater systems in Svalbard. *Q. Res.* 73, 393–402. doi: 10.1016/j.yqres.2009.11.002

Hepburn, L. E., Butler, I. B., Boyce, A., and Schröder, C. (2020). The use of operationally-defined sequential Fe extraction methods for mineralogical applications: a cautionary tale from Mössbauer spectroscopy. *Chem. Geol.* 543:e0119584. doi: 10.1016/j.chemgeo.2020.119584

Herndon, E., AlBashaireh, A., Singer, D., Roy Chowdhury, T., Gu, B., and Graham, D. (2017). Influence of iron redox cycling on organo-mineral associations in Arctic tundra soil. *Geochim. Cosmochim. Acta* 207, 210–231. doi: 10.1016/j.gca.2017.02.034

Hindshaw, R. S., Heaton, T. H. E., Boyd, E. S., Lindsay, M. R., and Tipper, E. T. (2016). Influence of glaciation on mechanisms of mineral weathering in two high Arctic catchments. *Chem. Geol.* 420, 37–50. doi: 10.1016/j.chemgeo.2015.11.004

Hodgkins, R., Tranter, M., and Dowdeswell, J. A. (1997). Solute provenance, transport and denudation in a high Arctic glacierized catchment. *Hydrol. Process.* 11, 1813–1832.

Hodson, A., Nowak, A., and Christiansen, H. (2016). Glacial and periglacial floodplain sediments regulate hydrologic transfer of reactive iron to a high arctic fjord. *Hydrol. Process.* 30, 1219–1229. doi: 10.1002/hyp.10701

Horton, T. W., Chamberlain, C. P., Fantle, M., and Blum, J. D. (1999). Chemical weathering and lithologic controls of water chemistry in a high-elevation river system: Clark's Fork of the Yellowstone river, Wyoming and Montana. *Water Resour. Res.* 35, 1643–1655. doi: 10.1029/1998WR900103

Hugelius, G., Strauss, J., Zubrzycki, S., Harden, J. W., Schuur, E. A. G., Ping, C.-L., et al. (2014). Estimated stocks of circumpolar permafrost carbon with quantified uncertainty ranges and identified data gaps. *Biogeosciences* 11, 6573–6593. doi: 10.5194/bg-11-6573-2014

Humlum, O. (2005). Holocene permafrost aggradation in Svalbard. *Geol. Soc. Lond. Spec. Public.* 242, 119–129. doi: 10.1144/GSL.SP.2005.242.01.11

Humlum, O., Instanes, A., and Sollid, J. L. (2003). Permafrost in Svalbard: a review of research history, climatic background and engineering challenges. *Polar Res.* 22, 191–215. doi: 10.1111/j.1751-8369.2003.tb00107.x

Isaksen, K., Christiansen, H. H., and Westermann, S. (2019). Climate in Svalbard 2100-a knowledge base for climate adaptation, Report Chapter 7.1. *Norwegian Cent. Clim. Serv. Rep. Num.* 2019, 113–118.

Jessen, S., Holmslykke, H. D., Rasmussen, K., Richardt, N., and Holm, P. E. (2014). Hydrology and pore water chemistry in a permafrost weland, Ilulissat, Greenland. *Water Resourc. Res.* 50, 1–15. doi: 10.1002/2013WR014376

Johnston, S. G., Burton, E. D., Aaso, T., and Tuckerman, G. (2014). Sulfur, iron and carbon cycling following hydrological restoration of acidic freshwater wetlands. *Chem. Geol.* 371, 9–26. doi: 10.1016/j.chemgeo.2014.02.001

Jones, E. L. (2019). *The Biogeochemistry of the Active Layer and Shallow Permafrost in a High Arctic Fjord Valley, Svalbard*. Ph. D. thesis, University of Sheffield, Sheffield.

Kirschke, S., Bousquet, P., Ciais, P., Saunois, M., Canadell, J. G., Dlugokencky, E. J., et al. (2013). Three decades of global methane sources and sinks. *Nat. Geosci.* 6, 813–823. doi: 10.1038/ngeo1955

Kokelj, S. V., and Burn, C. R. (2003). Ground ice and soluble cations in near-surface permafrost, Inuvik, Northwest Territories, Canada. *Permafrost Periglac. Process.* 14, 275–289. doi: 10.1002/ppp.458

Kokelj, S. V., and Burn, C. R. (2005). Geochemistry of the active layer and near-surface permafrost, Mackenzie delta region, Northwest Territories, Canada. *Can. J. Earth Sci.* 42, 37–48. doi: 10.1139/e04-089

Kolka, R., Bridgham, S., and Ping, C.-L. (2015). "Soils of peatlands: histosols and gelisols," in *Wetlands Soils: Genesis, Hydrology, Landscapes And Classification*, eds M. J. Vepraskas and C. L. Craft (Boca Raton, FL: Lewis Publishing), 277–310. doi: 10.1201/b18996-13

Kottek, M., Grieser, J., Beck, C., Rudolf, B., and Rubel, F. (2006). World map of the Köppen-geiger climate classification updated. *Meteorol. Zeitschrift* 15, 259–263. doi: 10.1127/0941-2948/2006/0130

Koven, C. D., Ringeval, B., Friedlingstein, P., Ciais, P., Cadule, P., Khvorostyanov, D., et al. (2011). Permafrost carbon-climate feedbacks accelerate global warming. *Proc. Natl. Acad. Sci. U.S.A.* 108, 14769–14774. doi: 10.1073/pnas.1103910108

Kristjansson, J. K., and Schönheit, P. (1983). Why do sulfate-reducing bacteria outcompete methanogenic bacteria for substrates? *Oecologia* 60, 264–266. doi: 10.1007/BF00379530

Kuhry, P., Dorrepaal, E., Hugelius, G., Schuur, E. A. G., and Tarnocai, C. (2010). Potential remobilization of belowground permafrost carbon under future global warming. *Permafrost Periglac. Process.* 21, 208–214. doi: 10.1002/ppp.684

Landvik, J. Y., Ingólfsson, Ó, Mienert, J., Lehman, S. J., Solheim, A., Elverhøi, A., et al. (2005). Rethinking Late Weichselian ice-sheet dynamics in coastal NW Svalbard. *Boreas* 34, 7–24. doi: 10.1080/03009480510012809

Lee, H., Schuur, E. A. G., Inglett, K. S., Lavoie, M., and Chanton, J. P. (2012). The rate of permafrost carbon release under aerobic and anaerobic conditions and its potential effects on climate. *Glob. Chang. Biol.* 18, 515–527. doi: 10.1111/j.1365-2486.2011.02519.x

Liljedahl, A., Hinzman, L. D., and Schulla, J. (2012). "Ice-wedge polygon type controls low-gradient watershed-scale hydrology," in *Proceedings of the Tenth International Conference on Permafrost*, Zurich.

Lipson, D. A., Zona, D., Raab, T. K., Bozzolo, F., Mauritz, M., and Oechel, W. C. (2012). Water-table height and microtopography control biogeochemical cycling in an Arctic coastal tundra ecosystem. *Biogeosciences* 9, 577–591. doi: 10.5194/bg-9-577-2012

Lloyd, R. M. (1968). Oxygen isotope behaviour in the Sulfate-Water System. *J. Geophys. Res.* 73, 6099–6110. doi: 10.1029/jb073i018p06099

Lønne, I., and Nemec, W. (2004). High-arctic fan delta recording deglaciation and environment disequilibrium. *Sedimentology* 51, 553–589. doi: 10.1111/j.1365-3091.2004.00636.x

Mackay, J. R. (1983). Downward water movement into frozen ground, western arctic coast, Canada. *Can. J. Earth Sci.* 20, 120–134. doi: 10.1139/e83-012

Mandernack, K. W., Krouse, H. R., and Skei, J. M. (2003). A stable sulfur and oxygen isotopic investigation of sulfur cycling in an anoxic marine basin, Framvaren Fjord, Norway. *Chem. Geol.* 195, 181–200. doi: 10.1016/S0009-2541(02)00394-7

Miller, K. E., Lai, C. T., Friedman, E. S., Angenent, L. T., and Lipson, D. A. (2015). Methane suppression by iron and humic acids in soils of the Arctic Coastal Plain. *Soil Biol. Biochem.* 83, 176–183. doi: 10.1016/j.soilbio.2015.01.022

Milne, G., and Shennan, I. (2007). "Sea Level Studies | Isostasy," in *Encyclopedia of Quaternary Science*, eds S. A. Elias and C. J. Mock (Amsterdam: Elsevier), 3043–3051. doi: 10.1016/b0-44-452747-8/00142-3

Mora, C., Vieira, G., Pina, P., Lousada, M., and Christiansen, H. H. (2015). Land cover classification using high-resolution aerial photography in Adventdalen, Svalbard. *Swedish Soc. Anthropol. Geogr.* 97, 473–488. doi: 10.1111/geoa.12088

Olefeldt, D., Turetsky, M. R., Crill, P. M., and Mcguire, A. D. (2013). Environmental and physical controls on northern terrestrial methane emissions across permafrost zones. *Glob. Chang. Biol.* 19, 589–603. doi: 10.1111/gcb.12071

O'Neill, H. B., and Christiansen, H. H. (2018). Detection of ice wedge cracking in permafrost using miniature accelerometers. *J. Geophys. Res. Earth Surf.* 123, 642–657. doi: 10.1002/2017JF004343

Oonk, P. B. H., Tsikos, H., Mason, P. R. D., Henkel, S., Staubwasser, M., Fryer, L., et al. (2017). Fraction-specific controls on the trace element distribution in iron formations: implications for trace metal isotope proxies. *Chem. Geol.* 474, 17–32. doi: 10.1016/j.chemgeo.2017.10.018

Parmentier, F.-J. W., Christensen, T. R., Sørensen, L. L., Rysgaard, S., McGuire, A. D., Miller, P. A., et al. (2013). The impact of lower sea-ice extent on Arctic greenhouse-gas exchange. *Nat. Clim. Chang.* 3, 195–202. doi: 10.1038/nclimate1784

Pester, M., Knorr, K.-H., Friedrich, M. W., Wagner, M., and Loy, A. (2012). Sulfate-reducing microorganisms in wetlands – fameless actors in carbon cycling and climate change. *Front. Microbiol.* 3:72. doi: 10.3389/fmicb.2012.00072

Pisapia, C., Chaussidon, M., Mustin, C., and Humbert, B. (2007). O and S isotopic composition of dissolved and attached oxidation products of pyrite by *Acidithiobacillus ferrooxidans*: comparison with abiotic oxidations. *Geochim. Cosmochim. Acta* 71, 2474–2490. doi: 10.1016/J.GCA.2007.02.021

Poulton, S. W., and Canfield, D. E. (2005). Development of a sequential extraction procedure for iron: implications for iron partitioning in continentally derived particulates. *Chem. Geol.* 214, 209–221. doi: 10.1016/J.CHEMGEO.2004.09.003

R Core Team (2017). *A Language And Environment For Statistical Computing*. Vienna: R Foundation for Statistical Computing.

Raiswell, R., Benning, L. G., Tranter, M., and Tulaczyk, S. (2008). Bioavailable iron in the Southern Ocean: the significance of the iceberg conveyor belt. *Geochem. Transact.* 9, 1–9. doi: 10.1186/1467-4866-9-7

Raiswell, R., and Canfield, D. E. (2012). The iron biogeochemical cycle past and present. *Geochem. Perspect.* 1:220. doi: 10.7185/geochempersp.1.1

Raiswell, R., Hawkings, J., Elsenousy, A., Death, R., Tranter, M., and Wadham, J. (2018). Iron in glacial systems: speciation, reactivity, freezing behaviour, and alteration during transport. *Front. Earth Sci.* 6:222. doi: 10.3389/feart.2018.00222

Riber, L. (2009). *Paleogene Depositional Conditions And Climatic Changes Of The Frysjaodden Formation In Central Spitsbergen (Sedimentology And Mineralogy)*. MSc thesis, University of Oslo, Oslo.

Romanovsky, V. E., Drozdov, D. S., Oberman, N. G., Malkova, G. V., Kholodov, A. L., Marchenko, S. S., et al. (2010). Thermal state of permafrost in Russia. *Permafrost Periglac. Process.* 21, 136–155. doi: 10.1002/ppp.689

Rutter, N., Hodson, A., Irvine-Fynn, T., and Solås, M. K. (2011). Hydrology and hydrochemistry of a deglaciating high-Arctic catchment, Svalbard. *J. Hydrol.* 410, 39–50. doi: 10.1016/J.JHYDROL.2011.09.001

Schaefer, K., Zhang, T., Bruhwiler, L., and Barrett, A. P. (2011). Amount and timing of permafrost carbon release in response to climate warming. *Tellus Ser. B Chem. Phys. Meteorol.* 63, 165–180. doi: 10.1111/j.1600-0889.2011.00527.x

Schuur, E. A. G., McGuire, A. D., Schädel, C., Grosse, G., Harden, J. W., Hayes, D. J., et al. (2015). Climate change and the permafrost carbon feedback. *Nature* 520, 171–179. doi: 10.1038/nature14338

Schwertmann, U., and Murad, E. (1988). The nature of an iron oxide—organic iron association in a peaty environment. *Clay Miner.* 23, 291–299. doi: 10.1180/claymin.1988.023.3.06

Sjögersten, S., Van Der Wal, R., and Woodin, S. J. (2006). Small-scale hydrological variation determines landscape CO_2 fluxes in the high Arctic. *Biogeochemistry* 80, 205–216. doi: 10.1007/s10533-006-9018-6

Slotznick, S. P., Sperling, E. A., Tosca, N. J., Miller, A. J., Clayton, K. E., van Helmond, N. A. G. M., et al. (2020). Unraveling the mineralogical complexity of sediment iron speciation using sequential extractions. *Geochem. Geophys. Geosyst.* 21:8666. doi: 10.1029/2019GC008666

Sørbel, L., and Tolgensbakk, J. (2002). Ice-wedge polygons and solifluction in the Adventdalen area, Spitsbergen, Svalbard. *Norsk Geografisk Tidsskrift Norwegian J. Geogr.* 56, 62–66. doi: 10.1080/002919502760056369

Spence, M. J., Thornton, S. F., Bottrell, S. H., and Spence, K. H. (2005). Determination of interstitial water chemistry and porosity in consolidated aquifer materials by diffusion equilibrium-exchange. *Environ. Sci. Technol.* 39, 1158–1166. doi: 10.1021/es049401v

Spratt, H. G., and Morgan, M. D. (1990). Sulfur cycling in a cedar-dominated, freshwater wetland. *Limnol. Oceanogr.* 35, 1586–1593. doi: 10.4319/lo.1990.35.7.1586

Svinth, A. A. G. (2013). *A Sedimentological and Petrographical Investigation of the Todalen Member and the Boundary Beds of the Endalen Member.: Within the Firkanten Formation (Paleocene) in the Central Basin of Spitsbergen, Svalbard*. Masters thesis, Norwegian University, Trondheim, NO.

Tarnocai, C., Canadell, J. G., Schuur, E. A. G., Kuhry, P., Mazhitova, G., and Zimov, S. (2009). Soil organic carbon pools in the northern circumpolar permafrost region. *Glob. Biogeochem. Cycles* 23:3327.

Thompson, A., Chadwick, O. A., Rancourt, D. G., and Chorover, J. (2006). Iron-oxide crystallinity increases during soil redox oscillations. *Geochim. Cosmochim. Acta* 70, 1710–1727. doi: 10.1016/J.GCA.2005.12.005

Throckmorton, H. M., Newman, B. D., Heikoop, J. M., Perkins, G. B., Feng, X., Graham, D. E., et al. (2016). Active layer hydrology in an arctic tundra ecosystem: quantifying water sources and cycling using water stable isotopes. *Hydrol. Process.* 30, 4972–4986. doi: 10.1002/hyp.10883

Torres, M. A., Moosdorf, N., Hartmann, J., Adkins, J. F., and West, J. (2017). Glacial weathering, sulfide oxidation, and global carbon cycle feedbacks. *Proc. Natl. Acad. Sci. U.S.A.* 33, 8716–8721. doi: 10.1073/pnas.1702953114

Tranter, M., Sharp, M. J., Lamb, H. R., Brown, G. H., Hubbard, B. P., and Willis, I. C. (2002). Geochemical weathering at the bed of Haut Glacier d'Arolla, Switzerland—a new model. *Hydrol. Process.* 16, 959–993. doi: 10.1002/hyp.309

Turchyn, A. V., Tipper, E. T., Galy, A., Lo, J. K., and Bickle, M. J. (2013). Isotope evidence for secondary sulfide precipitation along the Marsyandi River, Nepal, Himalayas. *Earth Planet. Sci. Lett.* 374, 36–46. doi: 10.1016/j.epsl.2013.04.033

Turetsky, M. R., Treat, C. C., Waldrop, M. P., Waddington, J. M., Harden, J. W., and McGuire, A. D. (2008). Short-term response of methane fluxes and methanogen activity to water table and soil warming manipulations in an Alaskan peatland. *J. Geophys. Res.* 113:G00A10. doi: 10.1029/2007JG000496

Tye, A. M., and Heaton, T. H. E. (2007). Chemical and isotopic characteristics of weathering and nitrogen release in non-glacial drainage waters on Arctic tundra. *Geochim. Cosmochim. Acta* 71, 4188–4205. doi: 10.1016/j.gca.2007.06.040

Wadham, J. L., Bottrell, S., Tranter, M., and Raiswell, R. (2004). Stable isotope evidence for microbial sulphate reduction at the bed of a polythermal high Arctic glacier. *Earth Planet. Sci. Lett.* 219, 341–355. doi: 10.1016/S0012-821X(03)00683-6

Wadham, J. L., Tranter, M., Skidmore, M., Hodson, A. J., Priscu, J., Lyons, W. B., et al. (2010). Biogeochemical weathering under ice: size matters. *Glob. Biogeochem. Cycles* 24:3688. doi: 10.1029/2009GB003688

Wehrmann, L. M., Formolo, M. J., Owens, J. D., Raiswell, R., Ferdelman, T. G., Riedinger, N., et al. (2014). Iron and manganese speciation and cycling in glacially influenced high-latitude fjord sediments (West Spitsbergen, Svalbard): evidence for a benthic recycling-transport mechanism. *Geochim. Cosmochim. Acta* 141, 628–655. doi: 10.1016/j.gca.2014.06.007

Wynn, P. M., Hodson, A., and Heaton, T. (2006). Chemical and isotopic switching within the subglacial environment of a High Arctic glacier. *Biogeochemistry* 78, 173–193. doi: 10.1007/s10533-005-3832-0

Wynn, P. M., Morrell, D. J., Tuffen, H., Barker, P., Tweed, F. S., and Burns, R. (2015). Seasonal release of anoxic geothermal meltwater from the Katla volcanic system at Sólheimajökull, Iceland. *Chem. Geol.* 396, 228–238. doi: 10.1016/J.CHEMGEO.2014.12.026

Yde, J. C., Riger-Kusk, M., Christiansen, H. H., Knudsen, N. T., and Humlum, O. (2008). Hydrochemical characteristics of bulk meltwater from an entire ablation season, Longyearbreen, Svalbard. *J. Glaciol.* 54, 259–272. doi: 10.3189/002214308784886234

Conflict of Interest: The authors declare that the research was conducted in the absence of any commercial or financial relationships that could be construed as a potential conflict of interest.

frontiers in Earth Science

ORIGINAL RESEARCH
published: 30 November 2020
doi: 10.3389/feart.2020.00368

The Effects of Glacial Cover on Riverine Silicon Isotope Compositions in Chilean Patagonia

Helena V. Pryer[1,2]*, *Jade E. Hatton*[2], *Jemma L. Wadham*[1], *Jon R. Hawkings*[3,4], *Laura F. Robinson*[2], *Anne M. Kellerman*[3], *Matthew G. Marshall*[1], *Alejandra Urra*[1,5], *Anna Covey*[1], *Giovanni Daneri*[6,7], *Vreni Häussermann*[8] and *Katharine R. Hendry*[2]

[1] Department of Geographical Sciences, Bristol Glaciology Centre, University of Bristol, Bristol, United Kingdom, [2] Department of Earth Sciences, University of Bristol, Bristol, United Kingdom, [3] Department of Earth, Ocean and Atmospheric Sciences, Florida State University, Tallahassee, FL, United States, [4] German Research Centre for Geosciences GFZ, Potsdam, Germany, [5] Centro de Estudios Científicos, Valdivia, Chile, [6] Centro de Investigación en Ecosistemas de la Patagonia, Coyhaique, Chile, [7] COPAS Sur-Austral, Universidad de Concepción, Concepción, Chile, [8] Huinay Scientific Field Station, Pontificia Universidad Católica de Valparaíso, Valparaíso, Chile

OPEN ACCESS

Edited by:
Zhilei Sun,
Qingdao Institute of Marine Geology (QIMG), China

Reviewed by:
Aiguo Dong,
China University of Geosciences, China
Luke Bridgestock,
University of Oxford, United Kingdom

***Correspondence:**
Helena V. Pryer
helena.pryer@bristol.ac.uk

Specialty section:
This article was submitted to Geochemistry, a section of the journal Frontiers in Earth Science

Received: *10 May 2020*
Accepted: *07 August 2020*
Published: *30 November 2020*

Citation:
Pryer HV, Hatton JE, Wadham JL, Hawkings JR, Robinson LF, Kellerman AM, Marshall MG, Urra A, Covey A, Daneri G, Häussermann V and Hendry KR (2020) The Effects of Glacial Cover on Riverine Silicon Isotope Compositions in Chilean Patagonia. Front. Earth Sci. 8:368. doi: 10.3389/feart.2020.00368

Proglacial rivers have been shown to have distinctive silicon (Si) isotope compositions, providing new insights into the mechanisms controlling Si cycling in the subglacial environment and suggesting terrestrial Si isotope exports may have varied between glacial and interglacial periods. However, Si isotope data are currently limited to a small number of glacial systems in the northern hemisphere, and it is unclear how compositions might vary across a spectrum of glacial influence. Using Chilean Patagonia as a unique natural laboratory, we present Si isotope compositions of 0.45 μm filtered (fSi), 0.02 μm filtered (DSi), and reactive amorphous (ASi) fractions from 40 river catchments with variable glacial cover and explore the key controls on Si cycling. The 0.45 μm filtered glacier-fed river samples displayed isotopically light compositions and a positive linear correlation with upstream glacial cover. This relationship was controlled by the inclusion of an isotopically light colloidal-nanoparticulate (0.02–0.45 μm) silicate phase that was only present in glacier-fed rivers and dominated Si budgets in these catchments. This phase was predominately composed of feldspars and its lability in seawater is uncertain, representing a significant unknown in resolving glacial Si isotope exports from this region. When the colloidal-nanoparticulates were removed from solution by ultra-filtration, the resultant DSi isotope compositions of glacier-fed catchments were not isotopically distinct from some non-glacial rivers and exhibited no clear relationship with glacial cover. The colloidal-nanoparticulate concentration of other weathering-sensitive elements (Li, Mg, Ba, Sr) also showed a linear relationship with glacial cover, suggesting that their isotopic compositions could be affected in a similar manner. These findings highlight the benefit of size-fractionated sampling and the need for more research to understand the lability of colloidal-nanoparticulate species, especially in glacier-fed rivers. Finally, we explore the controls on river ASi isotope compositions and show how including these reactive particulate phases is critical to quantifying terrestrial Si isotope budgets, both in Patagonia and other global regions.

Keywords: silicon isotopes, Patagonia, glaciers, amorphous silicon, colloidal silicon, dissolved silicon, rivers

1. INTRODUCTION

The silicon (Si) cycle is intricately linked to the carbon cycle, with climatic controls on silicate weathering regulating the drawdown of atmospheric CO_2 on geological timescales (Urey, 1952; Berner et al., 1983; Berner and Caldeira, 1997). Additionally, Si is an essential nutrient for many photosynthetic organisms including diatoms, which account for up to 70% of primary productivity in the ocean, form the base of food-chains and maintain the efficiency of the biological carbon pump (Nelson et al., 1995; Treguer and De La Rocha, 2013). Rivers deliver roughly 80% of the terrestrial Si flux to the oceans, acting as the critical link between continental and marine sub-cycles and affecting the rate of siliceous primary productivity in the ocean (Tréguer et al., 1995; Treguer and De La Rocha, 2013). As such, understanding the controls on riverine Si exports is critical for our understanding of climate feedback mechanisms, both during the past and with future change. Si isotope compositions are increasingly used to understand the Si cycle (Frings et al., 2016; Sutton et al., 2018) and as a valuable palaeo-oceanographic proxy (De La Rocha et al., 1998; Hendry and Robinson, 2012; Hendry and Brzezinski, 2014). However, there are still gaps in our knowledge, particularly relating to how changing glacial cover could impact the Si cycle and global Si isotope budgets (Hawkings et al., 2018; Sutton et al., 2018).

Until recently, glaciers and ice sheets were not considered to be active components of the Si cycle. The dissolved Si (DSi) concentrations of glacier-fed rivers tend to be much lower than non-glacial rivers, which is generally interpreted to reflect suppressed chemical weathering of silicate minerals in near-freezing subglacial environments (Tranter et al., 2002; Anderson, 2007). However, research from the Greenland Ice Sheet has shown that glacial meltwaters also contain high concentrations of a labile amorphous Si phase (ASi) bound to riverine suspended sediments (Hawkings et al., 2017; Hatton et al., 2019a). Concentrations of ASi from Leverett Glacier were roughly 40 times higher than the DSi phase, suggesting that glacial meltwaters could represent a significant missing component of terrestrial Si exports to the ocean (Hawkings et al., 2017). These ASi phases have been shown to readily dissolve in seawater to form bioavailable DSi, which could fuel siliceous primary productivity in downstream ecosystems (Frings, 2017; Hawkings et al., 2017). Similar ASi components have also been reported from other proglacial rivers in the Arctic and sub-Arctic (Hatton et al., 2019b), although the controls on concentrations and glacial ASi formation mechanisms are still the subject of active debate (Blackburn et al., 2019; Hatton et al., 2019b).

Biogeochemical reactions involving Si can cause subtle but measurable shifts away from the natural abundance ratios of the three stable isotopes of Si (^{28}Si, ^{29}Si, and ^{30}Si; Ding et al., 2005). Variations in these ratios function as a tracer for processes operating within the Si cycle. Riverine Si isotope compositions integrate basin-wide signals and reflect a dynamic balance between upstream catchment characteristics, silicate weathering processes, variable primary productivity by diatoms and other siliceous organisms, and inputs from Si-rich plant phytoliths (Frings et al., 2016; Sutton et al., 2018). During the formation of secondary weathering products (e.g., clays) and biogenic Si, solid phase material preferentially incorporates the lighter ^{28}Si isotope, leaving the residual river water enriched in the heavier ^{30}Si isotope relative to the parent rock (Ziegler et al., 2005; Georg et al., 2006; Frings et al., 2016). Conversely, incongruent dissolution of solid Si phases leads to the preferential release of the lighter isotope back into the river water (Cardinal et al., 2010). Si isotope compositions have been measured for many of the world's largest rivers, where signals have been used to infer the rates and congruency of silicate weathering (Georg et al., 2006; Cardinal et al., 2010; Opfergelt and Delmelle, 2012; Opfergelt et al., 2013), the degree of biological uptake (Hughes et al., 2011; Panizzo et al., 2017; Sun et al., 2018), anthropogenic impacts on the Si cycle (Hughes et al., 2012; Cockerton et al., 2013; Delvaux et al., 2013), and the terrestrial Si isotope composition exported to the ocean (Opfergelt et al., 2013; Frings et al., 2016; Hawkings et al., 2018; Sun et al., 2018).

Glacial processes also appear to affect the Si isotope composition of downstream river waters. Proglacial rivers in Iceland and Greenland have been shown to have distinct, isotopically light DSi compared to non-glacial river systems (Georg et al., 2007; Opfergelt et al., 2013; Hawkings et al., 2018; Hatton et al., 2019a). Such light DSi isotope compositions are interpreted to reflect extensive dissolution of ASi and other secondary weathering products in undersaturated, high pH meltwaters at the base of glaciers (Hawkings et al., 2018; Hatton et al., 2019a). These findings have brought into question the long-held assumption that terrestrial Si isotope exports to the ocean have remained stable over glacial-interglacial cycles, with implications for interpreting Si isotope paleoclimate proxies (Opfergelt et al., 2013; Hawkings et al., 2018). However, compiled Si isotope data from proglacial rivers across the Arctic and sub-Arctic show complex variability in Si isotope compositions exported from different glacial systems (Hatton et al., 2019b). At present, glacial Si isotope data are limited to glacier-fed rivers in high-latitude environments of the northern hemisphere, and it is unknown how compositions could vary in other regions and across a spectrum of glacial cover.

Furthermore, the Si isotope composition of ASi phases is generally overlooked when quantifying riverine Si isotope budgets. Estimates of riverine Si isotope compositions are usually based on 0.45 or 0.22 μm filtered Si and do not include reactive ASi associated with the suspended particulate material (SPM; > 0.45 μm) load. Since ASi phases are estimated to account for between ∼23 and 58% of reactive riverine Si exports (Conley, 1997; Dürr et al., 2011; Frings et al., 2014), excluding these phases likely represents an incomplete picture of the labile flux of Si isotopes and could hinder our understanding of the terrestrial Si cycle. In proglacial river systems, ASi phases have been shown to have isotopically light Si compositions, although the controls and potential variability are not fully understood (Hatton et al., 2019b). In particular, measurements of the isotopic composition of riverine ASi are currently only available for a handful of high-latitude glacier-fed rivers (Hawkings et al., 2018; Hatton et al., 2019a,b) and have never been reported from non-glacial river systems.

Chilean Patagonia is a unique and under-studied natural laboratory to investigate Si cycling processes for several reasons. First, this region has a wide spectrum of glacial cover, with rivers spanning completely deglaciated land, catchments with small mountain top glaciers and rivers draining from the large glacial systems of the Northern and Southern Patagonian Ice Fields. Second, it is a near-pristine environment with very low population density and minimal agriculture. As such, Si cycling processes are not overprinted or affected by anthropogenic signals, and we can observe the natural controls on riverine isotopic compositions. Finally, Patagonia is rapidly deglaciating and experiencing dramatic landscape change, with evidence that the Patagonian Ice Fields shrank by roughly 30 km^2 per year between 1986 and 2011 (Davies and Glasser, 2012) and 1,226 new glacial lakes formed between 1986 and 2016 (Wilson et al., 2018). Therefore, our data acts as a valuable baseline to understand future change to Si cycling processes across this region.

Here, we present data from 40 rivers in Chilean Patagonia and explore the key controls on the isotopic composition of dissolved (<0.02 μm), colloidal-nanoparticulate (0.02–0.45 μm) and amorphous (>0.45 μm) Si phases. We discuss the relative lability of each component and highlight how size-fractionated analyses are needed to understand the controls on riverine isotope signals. We also explore the dissolved and colloidal-nanoparticulate concentrations of several additional weathering-sensitive elements (Li, Sr, Ba, Mg) to infer if similar controls are likely to influence their size-partitioning and isotopic compositions. Finally, by combining the relative proportions, isotopic composition and potential lability of each Si phase, we test the hypothesis that glacier-fed rivers in Patagonia have distinct Si isotope compositions compared to non-glacial rivers.

2. METHODS AND MATERIALS

2.1. Sampling Campaign

River water samples were collected from 40 rivers located between 42 and 48° S in Chilean Patagonia during the austral summer in January 2017 (**Figure 1**). The pH, electrical

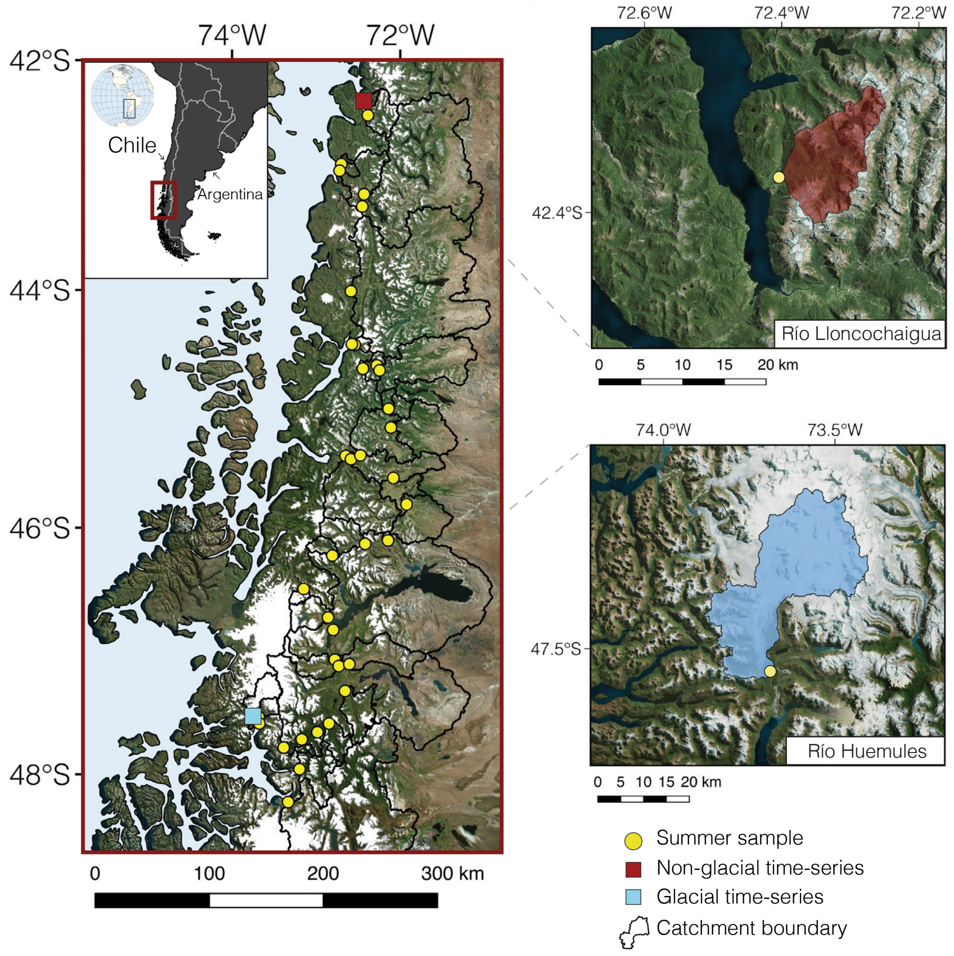

FIGURE 1 | Map showing river sampling locations in Patagonia. Yellow dots show river sampling locations collected in January 2017. The red square and top inset show the location and catchment area of the non-glacial time-series location (PTR01-R4, Río Lloncochaigua) and the blue square and bottom inset show the location and catchment area of the proglacial time-series location (PFC01-SA, Río Huemules-Steffen Glacier). Upstream catchment areas are outlined in black and were modeled using Q-GIS and Whitebox GAT (Lindsay, 2016).

conductivity and water temperature were measured using handheld sensors. Water samples were collected from fast-flowing sections of the river and upstream of settlements. Aliquots for major ions, DSi and Si isotope analysis were filtered immediately through 0.45 μm pore-size Whatman GD/XP polypropylene (PP) syringe filters and stored in acid-cleaned high-density polyethene (HDPE) bottles. Trace metal samples were collected by sequentially filtering river water through 0.45 μm Whatman GD/XP (PP) and 0.02 μm Whatman Anotop 25 syringe filters. These pore sizes were chosen to investigate differences between operationally defined filterable (<0.45 μm), colloidal-nanoparticulate (0.02–0.45 μm) and truly dissolved (<0.02 μm) concentrations, following protocols defined by Shiller (2003) and used in multiple glacial river studies (Schroth et al., 2011; Hawkings et al., 2014; Raiswell et al., 2018). Samples for Si isotope analysis were subsequently refiltered through 0.02 μm Whatman Anotop 25 syringe filters to investigate differences between dissolved and colloidal-nanoparticulate Si isotope signatures. SPM samples for determination of ASi concentrations and isotopic composition were collected by filtering 1–5 L of river water through pre-weighed 47 mm diameter Millipore 0.45 μm polyethersulfone (PES) membrane filters using an acid-washed Nalgene filter tower. The exact volume of water that passed through the membrane was recorded to calculate SPM concentrations, and the filter papers were stored in the dark at 4°C until analysis. The Si, iron (Fe), and SPM concentration data from these samples are also reported in Pryer et al. (2020).

To constrain temporal and seasonal variability in riverine Si isotope composition, a glacial and non-glacial end-member catchment were sampled repeatedly over multiple periods of 2 weeks to 5 months from January 2017 until November 2018, covering both the austral summer and winter at each location. The glacial site was the Río Huemules, draining from Steffen Glacier at the southern edge of the Northern Patagonian Icefield (NPI). The non-glacial site was the Río Lloncochaigua, located on the eastern edge of the Comau Fjord (**Figure 1**).

2.2. Geospatial Analysis

Geospatial analysis of this region was conducted using a combination of Q-GIS and Whitebox-GAT (Lindsay, 2016). Upstream catchment areas were calculated using the NASA Shuttle Radar Topography Mission (SRTM) 3 arc-second digital elevation model (DEM). The glacial cover was calculated as a percentage of each catchment area using the Randolph Glaciers Inventory (RGI Consortium, 2017) and is used as a proxy to understand the influence of variable glaciation across this region. We define glacier-fed systems as all catchments with >20% glacial cover, where the main tributary is a proglacial river. The significance of differences between catchments grouped by glacial cover was analyzed using unpaired, two-tail *t*-tests assuming unequal variance. Catchment lithology and lake area were calculated using datasets from Hartmann and Moosdorf (2012) and Messager et al. (2016), respectively.

2.3. Silicon and Major Ion Concentration Analysis

Truly dissolved Si concentrations (DSi, as silicic acid) were measured colorimetrically using a LaChat 8500 Series 2 flow injection analyser (FIA) (QuikChem Method 31-114-27-1-D) using an external calibration curve that spanned the range of sample concentrations, gravimetrically diluted from a 1,000 ppm Si ISO 17034-certified stock standard (TraceCERT®). Mean accuracy for DSi measurements was 2.6% and mean precision was ±1.2%. Colloidal-nanoparticulate Si (0.02–0.45 μm; CNSi) concentrations were calculated as the difference between 0.02 and 0.45 μm filtered concentrations measured by multi-collector inductively coupled plasma mass spectrometry (MC-ICP-MS), with errors of ±5.0%. Concentrations of ASi associated with SPM were measured using the 0.1 M Na_2CO_3 extraction method adapted from DeMaster (1981). Aliquots of the extraction solutions were analyzed using the same method as for DSi to obtain ASi concentrations in μM, with propagated errors of ±7.5%. Major cation and anion concentrations were measured using a Thermo Scientific^{TM} Dionex^{TM} capillary ICS-5000 ion chromatograph. Mean accuracy was 0.2 ± 2.5% and precision for all ions was better than ±2.5%. Bicarbonate (HCO_3^-) concentrations were estimated using the mass charge deficit (Tranter et al., 2002; Hawkings et al., 2015), with a propagated error of ±3.3%. Major ion concentrations were seasalt-corrected, using values from Millero et al. (2008). Total dissolved solid (TDS) concentrations were calculated as the sum of all major ions and DSi, with a propagated error of ±6.0%.

2.4. Trace Metal Concentration Analysis

Dissolved (<0.02 μm) and filterable (<0.45 μm) trace metal concentrations were analyzed using a Thermo Scientific X-SERIES 2 quadrupole ICP-MS with a collision-reaction cell at the National Oceanography Centre, Southampton. Berylium, indium and rhenium were used as internal standards to correct for drift and matrix effects, and external calibration solutions ($n = 7$) matched the concentration range observed in samples. For trace metals presented in this study, precision and accuracy were always within ± 10% of a multi-element standard, prepared from a gravimetrically weighed mix of NIST-traceable SPEX CertiPrep standards. Colloidal-nanoparticulate (0.02–0.45 μm) concentrations were calculated as the difference between 0.45 μm filterable and dissolved size-fractions (Shiller, 2003).

2.5. Silicon Isotope Analysis

Si isotope analyses were carried out at the University of Bristol Isotope Group clean laboratories and mass spectrometer facility. River water samples filtered through 0.02 μm filters were measured for DSi isotope analyses ($\delta^{30}Si_{DSi}$) and samples filtered through 0.45 μm filters were measured for filterable Si compositions ($\delta^{30}Si_{fSi}$). Sample volumes ranged from 0.9 to 20 mL, to target 7.2 μg of Si. Aliquots of filtered river water with Si concentrations <150 μM were pre-concentrated by evaporating to ~2 mL volume at 90°C in acid-cleaned Teflon vials, whereas other samples were added directly to the column. To measure the ASi isotopic composition ($\delta^{30}Si_{ASi}$), 10–30 mg of dry SPM was weighed into Teflon vials, before adding 1 mL of 0.2 M NaOH for every 0.1 mg of ASi, using concentrations previously measured using the DeMaster (1981) method described in section 2.3. Samples were refluxed at 100°C for an hour to extract the reactive ASi phase, neutralized with trace-metal grade 8M HNO_3, diluted with Milli-Q and passed through 0.22 μm pore-size PES syringe filters to remove sediment particles from the solution. This extraction method compares well with the more established Na_2CO_3 method, extracting equal or slightly lower concentrations of ASi and giving assurance that more refractory phases of Si were not incorporated into solution (Hawkings et al., 2018). Isotopic analysis of ASi could only be measured for a subset of samples ($n = 11$), as insufficient particulate material was collected from rivers with low SPM loads.

All samples were added to pre-cleaned BioRad exchange resin columns (AG50W-X12 200-400 mesh) using a method adapted from Georg et al. (2006) and eluted with Milli-Q to give a solution with a concentration of 2 ppm Si. A 1 mL aliquot of each sample was taken for each analysis, doped with 100 μL of 10 ppm magnesium (Mg) standard to correct for mass bias (Cardinal et al., 2003; Hendry and Robinson, 2012) and 100 μL of 0.1 M sulphuric acid to balance matrix differences between samples and standards (Hughes et al., 2011). Si and Mg isotope ratios were measured on a Thermo Scientific Neptune Plus^{TM} MC-ICP-MS using a standard-sample bracketing protocol. International reference standard NBS-28 (RM8546) was used as the bracketing standard, and all isotope results were calculated using δ^{30}Si notation (Equation 1), as the deviation of the ^{30}Si/^{28}Si ratio of each sample from NBS-28 in parts per mille (‰).

$$\delta^{30}\mathrm{Si} = \left[\frac{\left(^{30}\mathrm{Si}/^{28}\mathrm{Si}\right)_{\mathrm{sample}} - \left(^{30}\mathrm{Si}/^{28}\mathrm{Si}\right)_{\mathrm{NBS28}}}{\left(^{30}\mathrm{Si}/^{28}\mathrm{Si}\right)_{\mathrm{NBS28}}}\right] \times 1000 \qquad (1)$$

Instrument blanks of 0.1 M distilled HCl were always <1% of the intensity of the ^{28}Si signal of samples, and procedural blanks were always below the limit of detection. Long-term reproducibility was quantified by repeat measurement of two reference standards; LMG08 and Diatomite. The mean measured δ^{30}Si value for LMG08 was −3.45‰ ($n = 70$, $\sigma = 0.04$; δ^{29}Si = −1.76‰) and the mean δ^{30}Si value for Diatomite was +1.23‰ ($n = 25$, $\sigma = 0.04$; δ^{29}Si = +0.66‰). The values of these standards are within error of published values that have been calibrated between multiple labs (Reynolds et al., 2007; Hendry et al., 2011). A three-isotope plot of all standards and samples measured during this study fit along a straight line with a gradient of 0.517 ± 0.04 ($r^2 = 1.0$, $p < 0.01$, $n = 526$; **Supplementary Figure 1**), showing mass-dependant fractionation (Reynolds et al., 2007). All samples were measured at least in duplicate and a conservative error of ± 0.08‰ was assigned to all δ^{30}Si values, equalling ± 2σ variability of δ^{30}Si values from repeat measurements of internal standards and replicate samples.

The isotopic composition of the colloidal-nanoparticulate Si phase ($\delta^{30}\mathrm{Si}_{\mathrm{CNSi}}$, 0.02–0.45 μm) was calculated using a mass balance approach to account for the relative proportions and isotopic composition of 0.02 and 0.45 μm filtered Si fractions. Total riverine Si isotope budgets were calculated using a mass balance accounting for the relative proportions and isotope ratios of the DSi and ASi components ($\delta^{30}\mathrm{Si}_{\mathrm{DSi+ASi}}$), and the DSi and fSi components ($\delta^{30}\mathrm{Si}_{\mathrm{fSi+ASi}}$). The mean measured $\delta^{30}\mathrm{Si}_{\mathrm{ASi}}$ was used as an estimate for river systems where no data were available. Using the mean value had little impact on the total budget compared to analytical uncertainty, since most rivers where $\delta^{30}\mathrm{Si}_{\mathrm{ASi}}$ was not measured had very low SPM loads.

3. RESULTS

3.1. Riverine Silicon Concentrations

Dissolved Si (DSi) concentrations ranged from 15.5 to 259.6 μM (mean = 89.3 ± 64.2 μM (1σ), $n = 40$) and showed an inverse logarithmic relationship with glacial cover ($r^2 = 0.58$; **Figure 2A**). Glacier-fed rivers (i.e., >20% glacial cover) had relatively low and invariant DSi concentrations ranging from 15.5 to 43.8 μM (mean = 32.0 ± 8.6 μM, $n = 8$). The concentrations of 0.45 μm filterable Si (fSi) ranged from 27.7 to 259.6 μM (mean = 101.0 ± 58.1 μM, $n = 29$) and were within analytical error of DSi concentrations for most rivers. However, for all glacier-fed river systems, fSi concentrations were significantly higher than the DSi component, with concentrations ranging from 53.5 to 114.3 μM (mean = 78.1 ± 24.5 μM, $t_9 = 5.02$, $p < 0.01$). These differences between DSi and fSi concentrations in glacier-fed river systems show the presence of a colloidal-nanoparticulate Si phase (0.02–0.45 μm; CNSi). Where detected, CNSi concentrations ranged from 15.2 to 98.9 μM (mean = 42.7 ± 25.5 μM, $n = 11$; **Figure 2B**). All catchments with >20% glacial cover had a significant CNSi and concentrations showed a positive linear relationship with increasing glacial cover ($r^2 = 0.85$, $p < 0.01$, $n = 8$). CNSi was only detected in three rivers with <20% glacial cover, which were all large catchments (>15,000 km^2) that had significant inputs from the Northern or Southern Patagonian Ice Fields. No CNSi was found in any other river systems, with DSi and fSi concentrations within analytical error. Amorphous Si (ASi) phases, associated with the SPM, were found in all rivers where particulate samples were available for extraction. ASi concentrations varied from 0.3 to 56.8 μM (mean = 7.2 ± 9.7 μM, $n = 36$; **Figure 2B**).

3.2. Filterable and Dissolved Silicon Isotope Compositions

The silicon isotope composition of fSi ($\delta^{30}\mathrm{Si}_{\mathrm{fSi}}$) ranged from −0.36 to +1.25‰ (mean = +0.42 ± 0.36‰, $n = 40$; **Figure 2C**). Where glacial cover exceeded 20% of the total catchment area, there was a strong linear correlation between glacial cover and $\delta^{30}\mathrm{Si}_{\mathrm{fSi}}$ values, whereby the isotopic composition of the river water became increasingly enriched in the light ^{28}Si isotope with increasing glacial cover ($r^2 = 0.93$, $p < 0.01$). All glacier-fed river samples in this region had isotopically light $\delta^{30}\mathrm{Si}_{\mathrm{fSi}}$ values compared to catchments with <20% glacial cover, with compositions varying from −0.36 to +0.14‰ (mean = −0.07 ± 0.16‰, $n = 8$; **Table 1**). Rivers with less or no glacial cover had a wide range of $\delta^{30}\mathrm{Si}_{\mathrm{fSi}}$ values, varying from +0.14 to +1.25‰ (mean = +0.54 ± 0.28‰, $n = 32$). No significant differences in $\delta^{30}\mathrm{Si}_{\mathrm{fSi}}$ compositions were observed

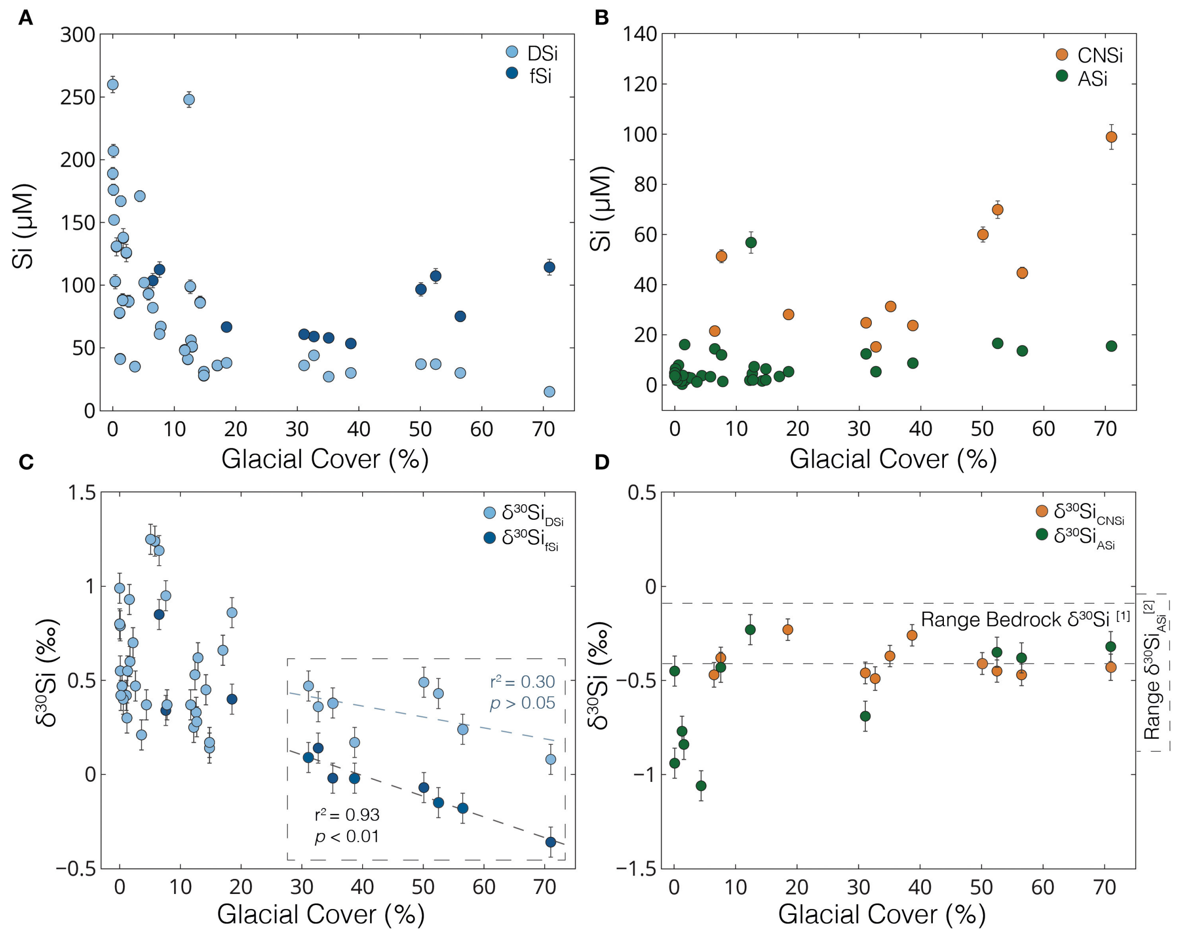

FIGURE 2 | Riverine silicon concentration and silicon isotope data. **(A)** Dissolved Si (DSi; light blue) and <0.45 μm filterable Si (fSi; dark blue) concentrations (μM) vs. glacial cover (%); **(B)** Colloidal-nanoparticulate Si (CNSi; orange) and amorphous Si (ASi; green) concentrations (μM) vs. glacial cover (%); **(C)** Si isotope values of 0.45 μm filtered river water ($\delta^{30}Si_{fSi}$; dark blue) and 0.02 μm filtered river water ($\delta^{30}Si_{DSi}$; light blue) (‰) vs. glacial cover (%); **(D)** Colloidal-nanoparticulate (0.02–0.45 μm) Si isotope values ($\delta^{30}Si_{CNSi}$; orange) and amorphous silicon isotope values ($\delta^{30}Si_{ASi}$; green) (‰) vs. glacial cover (%). Dotted lines show the range of bedrock $\delta^{30}Si$ values [1] (Savage et al., 2013) (mean = −0.25 ± 0.16‰) and the previous range of $\delta^{30}Si_{ASi}$ [2] (Hatton et al., 2019b) measured in proglacial rivers (range = −0.05 to −0.86‰). Error bars for DSi, fSi, CNSi, and ASi concentrations show ±2.5, 5.5, 5.0, and 7.5%, respectively. Error bars for $\delta^{30}Si$ show ±0.08‰.

TABLE 1 | Mean and range of $\delta^{30}Si$ (‰) values categorized by glacial cover.

	$\delta^{30}Si_{fSi}$ (‰)			$\delta^{30}Si_{DSi}$ (‰)			$\delta^{30}Si_{CNSi}$ (‰)			$\delta^{30}Si_{ASi}$ (‰)		
Glacial cover	**Mean**	**Range**	***n***	**Mean**	**Range**	***n***	**Mean**	**Range**	***n***	**Mean**	**Range**	***n***
>20%	−0.07	−0.36 to +0.14	8	+0.33	+0.08 to +0.49	8	−0.40	−0.49 to −0.23	8	−0.43	−0.69 to −0.32	4
5–20%	+0.52	+0.14 to +1.25	16	+0.60	+0.14 to +1.25	16	−0.36	−0.47 to −0.23	3	−0.33	−0.43 to −0.23	2
<5%	+0.56	+0.21 to +0.99	16	+0.56	+0.21 to +0.99	16	n.a.	n.a.	0	−0.81	−1.06 to −0.45	5

The glacial cover categories are: >20% glacial cover, which were all proglacial rivers, where the main tributary was fed by a glacier; 5–20% glacial cover, where there were some inputs of glacial meltwaters by tributary rivers; <5% glacial cover, where glacial meltwater inputs were negligible. $\delta^{30}Si_{fSi}$ *compositions are from the 0.45 μm filtered aliquot,* $\delta^{30}Si_{DSi}$ *are from the 0.02 μm filtered aliquot,* $\delta^{30}Si_{CNSi}$ *are the colloidal-nanoparticulate Si phases (0.02–0.45 μm) and the* $\delta^{30}Si_{ASi}$ *are the isotopic compositions of the amorphous Si phases associated with SPM. The n values represent the number of measurements in each category.*

between catchments with 5–20% or <5% glacial cover ($t_{26} = 0.5$, $p > 0.5$; **Table 1**).

For all rivers where CNSi was detected, the $\delta^{30}Si_{DSi}$ values were significantly higher than respective $\delta^{30}Si_{fSi}$ values with offsets ($\Delta^{30}Si_{DSi-fSi}$) ranging from +0.19 to +0.61‰ (mean = +0.42 ± 0.13‰, $n = 11$; **Figure 2C**). Glacier-fed river $\delta^{30}Si_{DSi}$ values ranged from +0.08 to +0.49‰ (mean = +0.33 ± 0.15‰, $n = 8$) and showed no significant relationship with glacial cover ($r^2 = 0.30$, $p > 0.05$). For all rivers where no CNSi was detected, $\delta^{30}Si_{fSi}$ and $\delta^{30}Si_{DSi}$ values were within

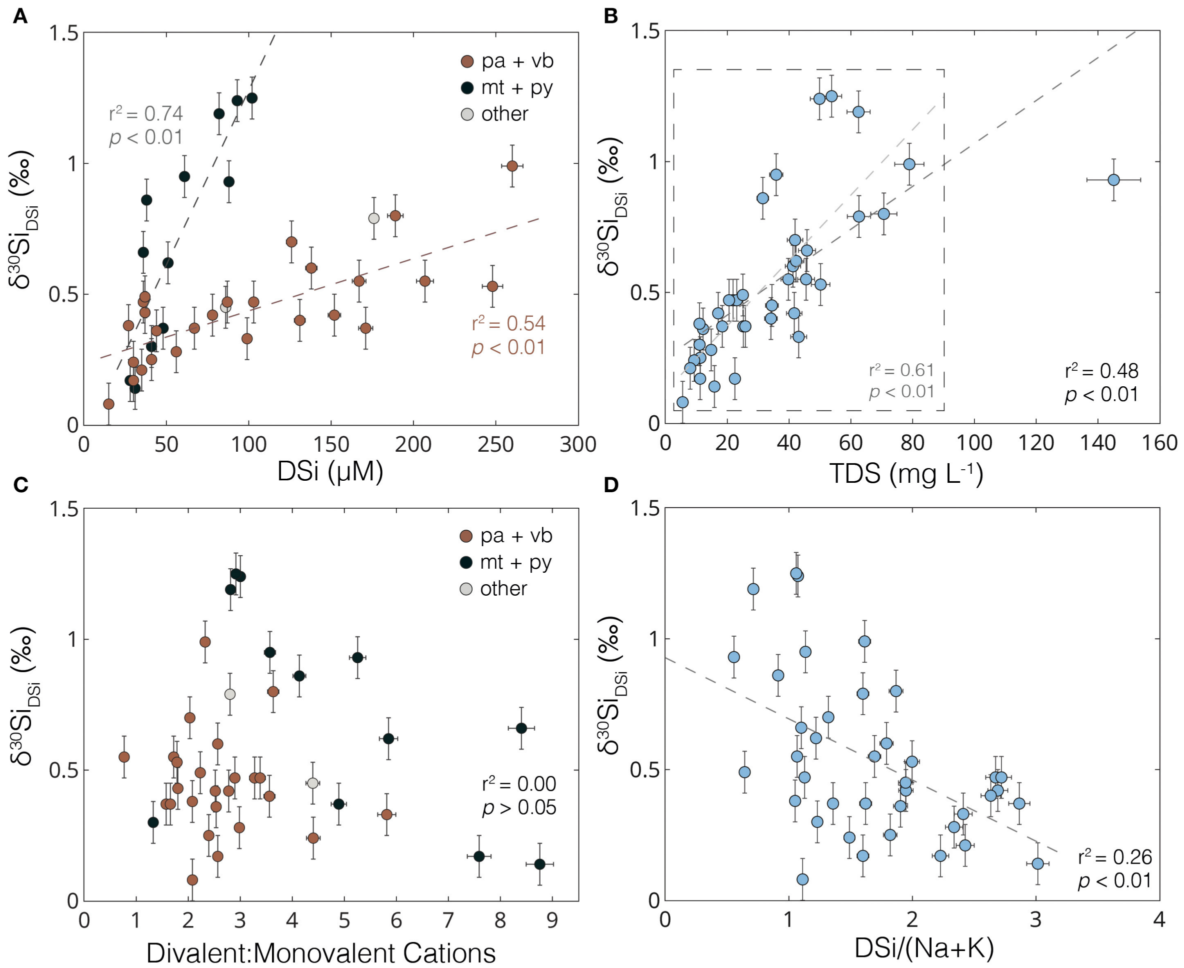

FIGURE 3 | Relationships between $\delta^{30}Si_{DSi}$ and other chemical species. **(A)** $\delta^{30}Si_{DSi}$ (‰) vs. DSi concentrations (μM) colored relative to the dominant lithology as categorized by Hartmann and Moosdorf (2012)—pa, acid plutonic; vb, basic volcanic; mt, metamorphic; py, pyroclastic (**Supplementary Table 1**); **(B)** $\delta^{30}Si_{DSi}$ (‰) vs. total dissolved solid concentrations (mg L^{-1}) calculated as the sum of all major ions and DSi; **(C)** $\delta^{30}Si_{DSi}$ (‰) vs. divalent:monovalent cations (μM) colored relative to the dominant lithology; **(D)** $\delta^{30}Si_{DSi}$ (‰) vs. DSi normalized to sodium (Na) and potassium (K) ion concentrations (μM). Error bars for $\delta^{30}Si_{DSi}$ show ±0.08‰. Error bars for DSi and TDS show ± 2.5 and 6.0%, respectively. Error bars for divalent:monovalent and DSi/Na+K ratios show ± 3.0%.

analytical uncertainty. The $\delta^{30}Si_{DSi}$ values showed a positive linear relationship with DSi concentrations when rivers were categorized by the dominant lithology in the upstream catchment area ($r^2 = 0.54$–0.74, $p < 0.01$, $n = 40$; **Figure 3A**), which is either composed of Patagonian batholith granite and basic volcanic rocks or metamorphosed sediments and pyroclastic rocks within the Magallanes foreland basin (Weaver et al., 1990; Hartmann and Moosdorf, 2012). The $\delta^{30}Si_{DSi}$ values also showed a positive linear relationship with total dissolved solid concentrations (mg L^{-1}) ($r^2 = 0.48$, $p < 0.01$, $n = 39$; **Figure 3B**). No correlation was observed between $\delta^{30}Si_{DSi}$ and divalent:monovalent major cation ratios ($r^2 = 0.00$, $p > 0.05$, $n = 39$; **Figure 3C**) and a weak negative correlation was observed with DSi concentrations normalized to sodium (Na^+) and potassium (K^+) ($r^2 = 0.26$, $p < 0.01$, $n = 37$; **Figure 3D**). Correlations between $\delta^{30}Si_{DSi}$ values and other chemical parameters and catchment properties are shown in **Supplementary Figure 2**. Principle component analysis (PCA) of geochemical and environmental parameters are shown in **Supplementary Figure 3**, with the two largest components explaining 58.2% of the data variance.

The isotopic composition of the colloidal-nanoparticulate phase ($\delta^{30}Si_{CNSi}$) ranged from −0.49 to −0.23‰ (mean = −0.40 ± 0.09‰, $n = 11$; **Figure 2D**). Relative proportions of the CNSi phase, reported as a percentage of 0.45 μm filterable Si (CNSi/fSi (%)), showed a positive linear correlation with glacial cover for catchments with >20% glacial cover ($r^2 = 0.82$, $p < 0.01$, $n = 8$; **Figure 4A**). The relative CNSi concentrations also showed a strong linear correlation with the $\delta^{30}Si_{fSi}$ values ($r^2 = 0.91$, $p < 0.01$, $n = 8$; **Figure 4B**). For the three catchments with <20% glacial cover where CNSi phases were detected, CNSi varied from 21 to 46% of the fSi concentration but did not fit along the linear regression with glacial cover or $\delta^{30}Si_{fSi}$ values defined by catchments with >20% glacial cover.

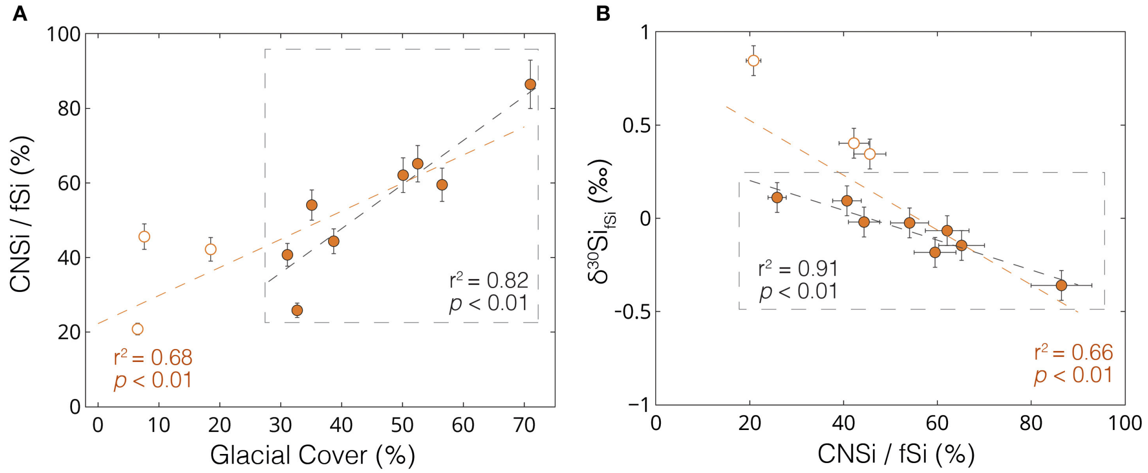

FIGURE 4 | Colloidal-nanoparticulate size silicon in all glacier-fed rivers in Patagonia. **(A)** Concentrations of colloidal-nanoparticulate Si (CNSi) as a percentage of the total filterable Si (fSi; DSi + CNSi) vs. glacial cover (%) for all rivers where CNSi phases were detected; **(B)** CNSi/fSi (%) plotted against respective $\delta^{30}\mathrm{Si}_{\mathrm{fSi}}$ (‰). Filled orange dots and regression analyses are for all catchments with >20% glacial cover. Unfilled orange dots are from three catchments with <20% glacial cover where CNSi phases were present. These catchments all receive glacial meltwater inputs from tributary rivers draining from the Patagonian Icefields, but where glacial cover values are disproportionately low due to very large catchment areas. Error bars for $\delta^{30}\mathrm{Si}$ (‰) values show ± 0.08‰ and errors for CNSi proportions show propagated errors of ± 7.5%.

3.3. Amorphous Silicon Isotope Composition

The isotopic composition of the ASi phases ($\delta^{30}\mathrm{Si}_{\mathrm{ASi}}$) ranged from −1.06 to −0.23‰ (mean = −0.59 ± 0.28‰, $n = 11$; **Figure 2D**), with values overlapping or significantly lower than the range reported for the upper continental crust (mean = −0.25 ± 0.16‰; Savage et al., 2013). Rivers with significant glacial meltwater inputs or that drained from volcanoes had substantially higher $\delta^{30}\mathrm{Si}_{\mathrm{ASi}}$ values compared to other river systems with mean values of −0.41 ± 0.14‰ ($n = 7$) and −0.90 ± 0.13‰ ($n = 4$), respectively ($t_7 = 5.88$, $p < 0.01$).

3.4. Size-Partitioning of Other Elements

The relative proportions of colloidal-nanoparticulate and dissolved phases were also investigated for other weathering-sensitive elements, including lithium (Li), magnesium (Mg), strontium (Sr), and barium (Ba). Similar to Si, all of these elements showed a significant positive relationship, with higher relative proportions of the colloidal-nanoparticulate phases with increasing glacial cover ($r^2 = 0.78$–0.86, $p < 0.01$, $n = 26$; **Figures 5A–D**). In the rivers with the highest glacial cover, over 70% of 0.45 μm filterable Li (fLi), 55% of filterable Mg (fMg), 35% of filterable Sr (fSr), and 80% of filterable Ba (fBa) was in the colloidal-nanoparticulate size-fraction.

3.5. Seasonal Variability

The DSi concentrations of the glacial time-series river (Río Huemules; PFC01-SA) ranged from 13.2 to 18.6 μM (mean = 15.5 ± 1.3 μM, $n = 60$) in summer and 16.2 to 19.1 μM (mean = 17.0 ± 0.7 μM, $n = 16$) in winter (**Figure 6C**). The $\delta^{30}\mathrm{Si}$ values of the river water were also invariant (**Figure 6D**), with $\delta^{30}\mathrm{Si}_{\mathrm{fSi}}$ values varying from −0.42 to −0.28‰ (mean = −0.35 ± 0.05‰, $n = 9$) in summer and −0.32 to −0.20‰ (mean = −0.27 ± 0.06‰, $n = 3$) in winter. The $\delta^{30}\mathrm{Si}_{\mathrm{DSi}}$ values were always significantly higher than $\delta^{30}\mathrm{Si}_{\mathrm{fSi}}$, but were also invariant with time (+0.08 to +0.10‰, $n = 3$). The measurements of $\delta^{30}\mathrm{Si}_{\mathrm{ASi}}$ values of the Río Huemules were also stable across the sampling period, with values ranging from −0.28 to −0.36‰ (mean = −0.32 ± 0.04‰, $n = 4$).

The time-series data collected from the non-glacial river (Río Lloncochaigua; PTR01-R4) showed more variability of DSi concentrations than the glacial site, with values ranging from 21.5 to 58.3 μM (mean = 41.6 ± 9.2 μM, $n = 78$; **Figure 6A**), although with no obvious seasonal trends between summer and winter. Despite variable DSi concentrations, the $\delta^{30}\mathrm{Si}$ values of the river water were always within analytical error, with $\delta^{30}\mathrm{Si}_{\mathrm{fSi}}$ values ranging from +0.32 to +0.45‰ (mean = +0.37 ± 0.04‰, $n = 6$; **Figure 6B**). No differences were observed between $\delta^{30}\mathrm{Si}_{\mathrm{fSi}}$ and $\delta^{30}\mathrm{Si}_{\mathrm{DSi}}$ of the Río Lloncochaigua, with all values within analytical error.

3.6. Silicon Isotope Budgets in Patagonian Rivers

The $\delta^{30}\mathrm{Si}_{\mathrm{DSi+ASi}}$ values of rivers sampled in Patagonia ranged from −0.12 to +1.17‰ (mean = +0.43 ± 0.29‰, $n = 36$; **Figure 7A**). For glacier-fed rivers, $\delta^{30}\mathrm{Si}_{\mathrm{DSi+ASi}}$ ranged from −0.12 to +0.26‰ (mean = +0.09 ± 0.14‰, $n = 6$) and were lower than mean $\delta^{30}\mathrm{Si}_{\mathrm{DSi+ASi}}$ of non-glacial rivers (mean = +0.50 ± 0.26‰, $t_{13} = 5.43$, $p < 0.01$). When the CNSi was also included in riverine Si isotope budget, ($\delta^{30}\mathrm{Si}_{\mathrm{fSi+ASi}}$), values shifted to significantly lighter values compared to $\delta^{30}\mathrm{Si}_{\mathrm{DSi+ASi}}$ for all rivers where CNSi was detected (**Figure 7A**). The $\delta^{30}\mathrm{Si}_{\mathrm{fSi+ASi}}$ values ranged from −0.35 to +1.17 (mean = +0.36 ± 0.32‰, $n = 36$). The offset between $\delta^{30}\mathrm{Si}_{\mathrm{DSi}}$ and $\delta^{30}\mathrm{Si}_{\mathrm{DSi+ASi}}$

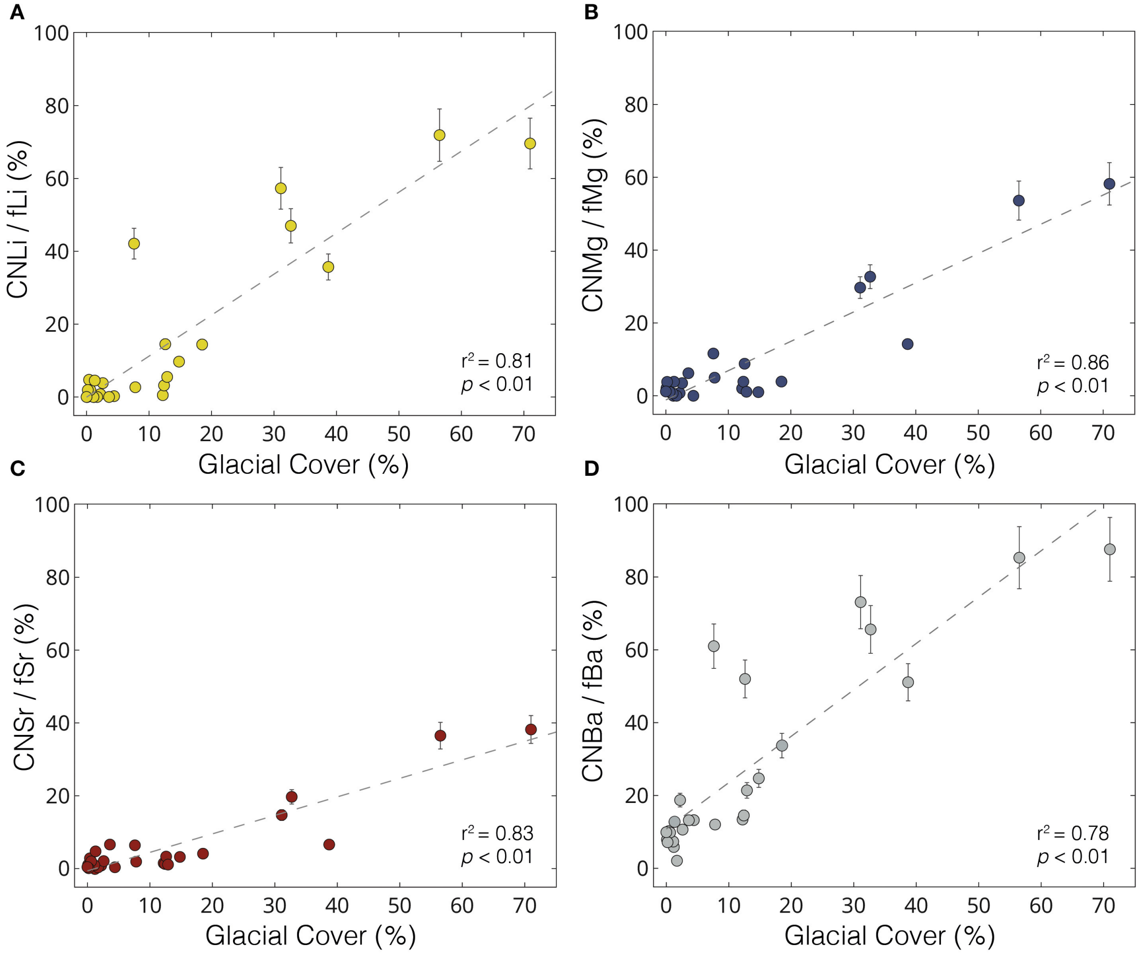

FIGURE 5 | Colloidal-nanoparticulate element concentrations in Patagonian rivers. **(A)** Concentrations of colloidal-nanoparticulate Li (CNLi) plotted as a percentage of 0.45 μm filterable Li (fLi) vs. glacial cover (%); **(B)** Concentrations of colloidal-nanoparticulate Mg (CNMg) plotted as a percentage of total filterable Mg (fMg) vs. glacial cover (%); **(C)** Concentrations of colloidal-nanoparticulate Sr (CNSr) plotted as a percentage of filterable Sr (fSr) vs. glacial cover (%); **(D)** Concentrations of colloidal-nanoparticulate Ba (CNBa) plotted as a percentage of filterable Ba (fBa) vs. glacial cover (%). Error bars for all elements show ±10%.

($\Delta^{30}\text{Si}_{\text{DSi}-(\text{DSi}+\text{ASi})}$) ranged from +0.01 to +0.30‰ and showed a positive linear relationship with the proportions of ASi ($r^2 = 0.64$, $p < 0.01$; **Figure 7B**). For all rivers where ASi concentrations accounted for >10% of the Si budget ($n = 14$), $\delta^{30}\text{Si}_{\text{DSi}+\text{ASi}}$ values were outside analytical error of $\delta^{30}\text{Si}_{\text{DSi}}$ values (**Figure 7B**).

4. DISCUSSION

4.1. Colloidal-Nanoparticulate Phases Control Filterable Silicon Isotope Compositions in Glacier-Fed Rivers

A key observation in our dataset was that glacier-fed rivers in Patagonia had low 0.45 μm filtered Si isotope compositions ($\delta^{30}\text{Si}_{\text{fSi}}$), with values that varied as a linear function of upstream glacial cover (**Figure 2C**). Similar light Si isotope compositions have been reported from proglacial rivers in Greenland, where signals were interpreted to reflect leaching of mineral surfaces and dissolution of secondary weathering products such as clays and ASi in undersaturated subglacial meltwaters (Hawkings et al., 2018; Hatton et al., 2019a). However, in Patagonia we found significant differences in the Si concentrations and isotopic compositions of the 0.45 and 0.02 μm samples from glacier-fed rivers, which highlighted the presence of an isotopically light colloidal-nanoparticulate silicate phase (CNSi). This phase was present in all rivers with >20% glacial cover, and relative proportions increased linearly with increasing glacial cover (**Figure 4A**). As the CNSi dominated the 0.45 μm Si budget in many glacial rivers, this phase effectively controlled the $\delta^{30}\text{Si}_{\text{fSi}}$ and shifted values to isotopically light compositions (**Figure 4B**). As such, the low $\delta^{30}\text{Si}_{\text{fSi}}$ observed in glacial rivers in Patagonia reflect variable amounts of CNSi, rather than the release of isotopically light DSi due to subglacial secondary weathering product dissolution as inferred in Greenland (Hawkings et al., 2018; Hatton et al., 2019a).

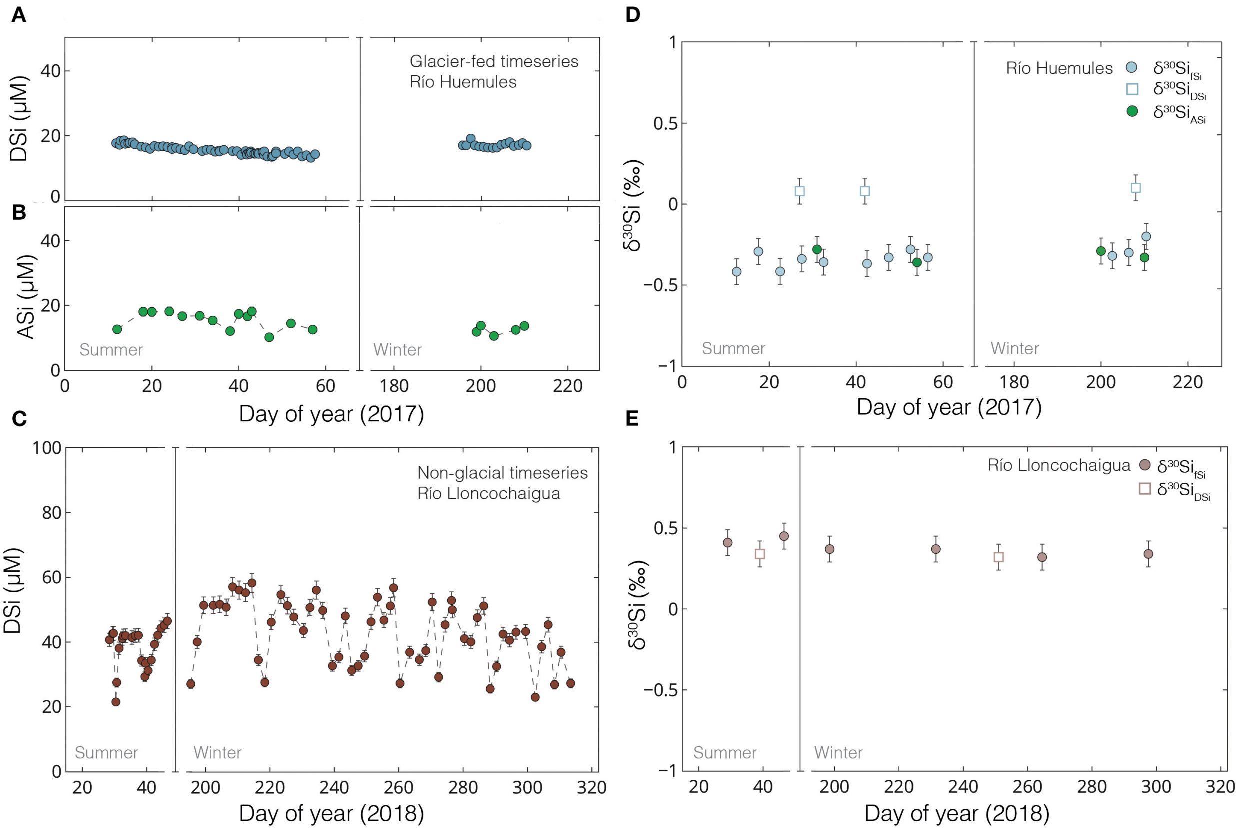

FIGURE 6 | Temporal and seasonal variability of DSi and δ^{30}Si. **(A)** DSi concentrations vs. decimal day of the year for river samples collected from the Río Huemules draining Steffen Glacier (PFC01-SA; 70% glacial cover) in 2017; **(B)** ASi concentrations vs. decimal day of the year for river samples collected from the Río Huemules draining Steffen Glacier (PFC01-SA) in 2017; **(C)** $\delta^{30}\mathrm{Si}_{\mathrm{fSi}}$ and $\delta^{30}\mathrm{Si}_{\mathrm{DSi}}$ values and $\delta^{30}\mathrm{Si}_{\mathrm{ASi}}$ values for Río Huemules vs. decimal day of the year; **(D)** DSi concentrations vs. decimal day of the year for river samples collected from the Río Lloncochaigua (PTR01-R4; 1% glacial cover) in 2018; **(E)** $\delta^{30}\mathrm{Si}_{\mathrm{fSi}}$ and $\delta^{30}\mathrm{Si}_{\mathrm{DSi}}$ values from Río Lloncochaigua vs. decimal day of the year. The locations of these samples are shown in **Figure 1** and **Supplementary Figure 1**.

CNSi was also detected in three rivers with <20% glacial cover (**Figure 4A**). These rivers all had very large catchment areas (>15,000 km^2) and significant glacial meltwater inputs from tributaries draining from the Patagonian Ice Fields, implying that glacial cover was not a good proxy for meltwater inputs in these systems. The Si isotope composition of these rivers also fell above the linear regression between $\delta^{30}\mathrm{Si}_{\mathrm{fSi}}$ and the proportions of CNSi defined by glacier-fed rivers with <20% glacial cover (**Figure 4B**). The higher $\delta^{30}\mathrm{Si}_{\mathrm{fSi}}$ values of these three rivers were likely caused by the presence of large non-glacial lakes in their upstream catchment area, as lake waters typically have higher δ^{30}Si values due to enhanced uptake of the light ^{28}Si isotope by diatoms, which leaves the water enriched in ^{30}Si (De La Rocha et al., 1997; Opfergelt et al., 2011). The fact that no CNSi was detected in any other river systems sampled across the region gives inference that these phases were formed as a glacial weathering product (Pryer et al., 2020).

The relatively narrow range of isotope values of the CNSi ($\delta^{30}\mathrm{Si}_{\mathrm{CNSi}}$; −0.49 to −0.23‰; **Figure 2D**) suggests that compositions were similar across the sampling region, despite differences in glacial size and catchment properties. The majority of $\delta^{30}\mathrm{Si}_{\mathrm{CNSi}}$ values were within error of δ^{30}Si values reported for the upper continental crust (mean = −0.25 ± 0.16‰; Savage et al., 2013), indicating that the CNSi phase is a lithogenic weathering product. The range of values for $\delta^{30}\mathrm{Si}_{\mathrm{CNSi}}$ were most similar to the isotopic values reported for low temperature smectites (−0.52 to −0.16‰; Georg et al., 2009) and ASi from Greenland (−0.44 to −0.21‰; Hawkings et al., 2018; Hatton et al., 2019a). However, previous investigation of these CNSi phases indicated that they were predominately composed of alkali feldspars, without a significant ASi component, and were formed by glacial comminution of silicate bedrock (Pryer et al., 2020). The $\delta^{30}\mathrm{Si}_{\mathrm{CNSi}}$ values we observed in this region were significantly lower than the isotopic compositions reported for unweathered feldspar (mean = −0.15 ± 0.04‰ (2σ); Georg et al., 2009), likely due to variability in feldspar composition, the fine-grained particle size, the incorporation of minor amounts of other mineral phases, and/or the possibility of isotopically light Si adsorbed to the iron-oxyhydroxide phases present in this size-fraction (Delstanche et al., 2009; Opfergelt et al., 2009; Pryer et al., 2020).

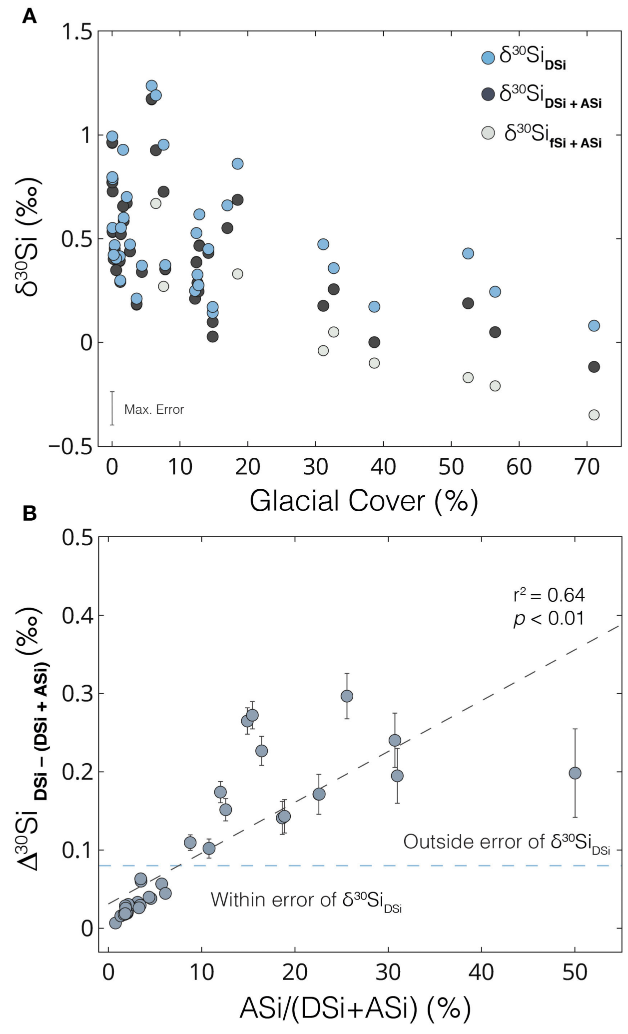

FIGURE 7 | Silicon isotope budgets in Patagonian Rivers. **(A)** Estimates of the Si isotope budgets of different Si components in Patagonian rivers relative to glacial cover. Blue dots show just the 0.02 μm filtered Si (i.e., DSi). Black dots show the Si isotope value of DSi + ASi components ($\delta^{30}Si_{DSi+ASi}$), assuming that all ASi phases will dissolve in downstream ecosystems. Gray dots show the Si isotope value of fSi + ASi components ($\delta^{30}Si_{fSi+ASi}$), assuming that all CNSi and ASi phases will dissolve in downstream ecosystems. Error bars for δ^{30}Si show a maximum error of ±0.08‰; **(B)** Isotopic offset between $\delta^{30}Si_{DSi}$ and $\delta^{30}Si_{DSi+ASi}$ components [$\Delta^{30}Si_{fSi-(DSi+ASi)}$] relative to the ASi concentrations as a proportion of ASi + DSi concentrations (%). The blue dashed line shows values above which $\delta^{30}Si_{DSi+ASi}$ values are outside analytical uncertainty of $\delta^{30}Si_{DSi}$. Error bars for $\delta^{30}Si_{DSi-(DSi+ASi)}$ show propagated uncertainties from 0.00 to 0.06‰.

The potential lability of CNSi phases is currently unknown and represents a significant uncertainty in resolving bioavailable Si fluxes and Si isotope exports from glacier-fed rivers in Chilean Patagonia (Pryer et al., 2020). Traditionally feldspars and other aluminosilicate minerals are not considered to be reactive in seawater, and potential contributions to oceanic elemental cycles and isotope budgets are therefore overlooked. Assuming that the CNSi feldspars are unreactive in seawater, their inclusion could lead to significant misinterpretation of glacial river isotope compositions if $\delta^{30}Si_{fSi}$ values are interpreted to represent truly dissolved signatures. However, recent research has suggested that dissolution of feldspars in seawater may be more significant than previously appreciated, with dissolution rates an order of magnitude higher than in freshwater (Gruber et al., 2019). Indeed, dissolution of the CNSi from glacier-fed rivers in Patagonia may be even more pronounced given the sub-micron particle size, associated large surface area and the potential for distal transport away from the coast. Furthermore, rock-crushing experiments have demonstrated how submicron size feldspar particles are formed due to physical grinding and that these phases are highly unstable in solution and rapidly dissolve to form DSi (Holdren and Berner, 1979). As such, we speculate that CNSi phases could potentially contribute to the labile Si concentrations and isotope compositions exported from glacial rivers, with implications for resolving marine elemental budgets and understanding how variable glaciation could impact the Si cycle. However, more research about the solubility, transformations and fate of these phases is needed to fully resolve their potential impact on downstream ecosystems.

4.2. Implications of Riverine Colloidal-Nanoparticulate Phases

At present, it is unclear whether CNSi phases are ubiquitous in proglacial rivers in other glaciated regions, or how environmental or geochemical processes control their formation and abundance. Samples for DSi analysis are typically filtered through either 0.45 or 0.22 μm filter membranes and concentrations are commonly measured using colorimetric techniques, which only measure truly dissolved Si in the form of silicic acid. As such, CNSi phases can go undetected unless using samples that have been size-fractionated (e.g., 0.45 and 0.02 μm filtered; Shiller, 2003) and measured by mass spectrometry techniques that ionize all Si present in the solution (e.g., ICP-MS). CNSi was only detected in Patagonian rivers because both colorimetric and ICP methods were used, giving Si concentrations that differed by almost an order of magnitude (Pryer et al., 2020). These large differences between methods were not reported from proglacial rivers in Greenland (Hawkings et al., 2018; Hatton et al., 2019a), indicating that CNSi phases were negligible or absent in these river systems. We speculate that the presence of CNSi phases could be affected by a combination of factors including variable filtering techniques, transport through proglacial lakes, the surrounding geology or riverine pH conditions, which could influence the concentrations of fine-grained species in the filtrate (Horowitz et al., 1992, 1996), the grain-size distribution of eroded bedrock (Crompton and Flowers, 2016) or the solubility of finely-ground feldspars (Yuan et al., 2019). High concentrations of CNSi have been reported in glacier-fed rivers in Alaska (mean = 61.1 ± 67.6 μM; Schroth et al., 2011), showing that these phases are present in other glaciated regions. We emphasize that CNSi may have been overlooked in other glacier-fed rivers and should be considered when interpreting Si isotope compositions.

The size-partitioning of several other weathering-sensitive elements including Li, Sr, Mg, and Ba (**Figures 5A–D**) indicate that these size-fractionated trends may not be unique to Si isotopes. All of these elements had a significant colloidal-nanoparticulate component in glacier-fed rivers, and relative proportions varied as a linear function of glacial cover, suggesting associations with the CNSi or similar glaciogenic controls. For all of these elements, primary mineral phases and secondary weathering products are generally isotopically different from the composition of dissolved species (Peucker-Ehrenbrink et al., 2010; Wimpenny et al., 2010, 2011; Pogge von Strandmann et al., 2019; Gou et al., 2020). As such, it is likely that isotopic trends would show similar offsets between 0.45 μm filtered and dissolved (0.02 μm) compositions as observed for Si. This could potentially obscure the true controls on riverine isotope values and affect terrestrial isotope budgets. These results highlight that size-fractionated filtering is needed to quantify colloidal-nanoparticulate concentrations and isotopic compositions, especially in glacier-fed river systems where these phases may dominate.

Furthermore, there are currently no standardized sampling protocols for analysing "dissolved" stable isotopic composition in rivers, with 0.45 μm or 0.2/0.22 μm pore-sizes and a wide variety of filter membrane types commonly used. We postulate that filtering protocols may dramatically affect filterable concentrations and isotopic composition when a significant colloidal-nanoparticulate fraction is present. These filtering artifacts have been shown to affect the concentration of colloidal-nanoparticulate species by up to an order of magnitude in non-glacial rivers (Horowitz et al., 1992), but the implications for glacier-fed riverine concentrations or for isotope signatures have not been tested before. Quantifying these filtering artifacts and the size-partitioning of different chemical species in glacier-fed rivers may provide valuable insight and help to disentangle the controls on riverine isotope signatures.

4.3. Controls on the Isotopic Composition of Dissolved Silicon in Patagonian Rivers

The dissolved Si isotope composition ($\delta^{30}Si_{DSi}$) of all rivers with a CNSi component shifted to significantly heavier values compared to corresponding $\delta^{30}Si_{fSi}$. These offsets were well outside analytical error, reinforcing the importance of accounting for contributions from colloidal-nanoparticulate species. Glacier-fed river $\delta^{30}Si_{DSi}$ values were still lower than the mean for non-glacial rivers in this region, likely due to suppressed diatom primary productivity, limited secondary mineral formation and enhanced dissolution of isotopically light ASi phases in turbid, low temperature and undersaturated glacial meltwaters (Hawkings et al., 2018; Hatton et al., 2019b). However, the mean $\delta^{30}Si_{DSi}$ composition from glacier-fed rivers in Patagonia (+0.33 ± 0.15‰) was higher than the mean for glacial rivers in Iceland (+0.17 ± 0.18‰, $n = 9$; Opfergelt et al., 2013), and much higher than mean values from Leverett Glacier in Greenland (−0.25 ± 0.12‰, $n = 16$; Hawkings et al., 2018) or Qeqertarsuaq (Disko Island) (−0.01 ± 0.29‰, $n = 4$; Hatton et al., 2019b). These differences in $\delta^{30}Si_{DSi}$ are potentially due to the sampling of Patagonian rivers downstream of glacial outlets and after transport through large proglacial lakes, with variable non-glacial inputs, secondary weathering processes, and/or because samples from other regions were not ultra-filtered through 0.02 μm and could potentially contain CNSi phases. Recent research has found that riverine $\delta^{30}Si_{DSi}$ values can also be highly variable within glacial regions, with $\delta^{30}Si_{DSi}$ values in Icelandic proglacial rivers ranging from −0.58 to +0.78‰ (Hatton et al., 2019b). The controls on the variability of glacial meltwater $\delta^{30}Si_{DSi}$ signatures are not fully understood at present, with values likely to be influenced by the geology, catchment size, hydrology, and water residence times in subglacial environments, as well as physical and chemical weathering conditions controlling the dissolution and precipitation of primary and secondary weathering products (Hawkings et al., 2018; Hatton et al., 2019a,b).

Non-glacial river samples showed a wide range of $\delta^{30}Si_{DSi}$ values, reflecting the heterogeneity of Si cycling processes across the region. The $\delta^{30}Si_{fSi}$ and $\delta^{30}Si_{DSi}$ values were always within error as there was no detectable CNSi present in rivers without glacial meltwater inputs. The highest $\delta^{30}Si_{DSi}$ values (+0.95 to +1.25‰) were from non-glacial rivers fed by large lake systems, likely due to enhanced diatom productivity (De La Rocha et al., 1997; Opfergelt et al., 2011). However, the lake-related high $\delta^{30}Si_{DSi}$ values were similar to the global mean riverine $\delta^{30}Si_{DSi}$ of +1.25‰ (Frings et al., 2016) and significantly lower than other large lake values such as Lake Baikal in Russia (mean = +2.30 ± 0.38‰; Panizzo et al., 2017). As lakes in Patagonia are generally oligotrophic and primary production is limited by inputs of nitrogen and phosphorus (Baigún et al., 2006), unrestricted diatom growth and further ^{30}Si enrichment of DSi may be curtailed by nutrient availability in this region. The lightest non-glacial $\delta^{30}Si_{DSi}$ values were found in tea-colored, organic-rich rivers, which drained from catchments with wetlands and peat-bogs. All rivers of this type had a very narrow range of $\delta^{30}Si_{DSi}$ values from +0.14 to +0.21‰ and relatively low DSi concentrations of 31 to 40 μM. Such low $\delta^{30}Si_{DSi}$ and low DSi concentrations are similar to findings from "blackwater" tributaries of the Congo and Amazon rivers and are interpreted to reflect enhanced dissolution of isotopically light clays by organic acids (Cardinal et al., 2010; Hughes et al., 2013).

The relationships observed between $\delta^{30}Si_{DSi}$ and other geochemical variables highlight how chemical weathering plays a key role in driving riverine Si isotope compositions. The positive linear correlations between $\delta^{30}Si_{DSi}$ and concentrations of DSi (**Figure 3A**), total dissolved solids (TDS) (**Figure 3B**) and other ions such as bicarbonate (**Supplementary Figure 2**) indicate that progressive chemical weathering of the bedrock creates high $\delta^{30}Si_{DSi}$ values, similar to trends reported from other global regions such as the Congo (Cardinal et al., 2010), the Himalaya (Fontorbe et al., 2013), and Iceland (Opfergelt et al., 2013). The weak negative correlation observed between $\delta^{30}Si_{DSi}$ values and DSi/Na+K ratios (**Figure 3D**) demonstrates how the removal of DSi relative to Na and K causes preferential loss of the ^{28}Si isotope, indicating that secondary clay and biogenic Si formation may explain some of the variability in riverine Si isotope compositions (Cardinal et al., 2010; Cockerton et al., 2013; Sun et al., 2018). No relationship was observed between $\delta^{30}Si_{DSi}$ and indicators of silicate and carbonate weathering such as divalent:monovalent cation ratios (Tranter et al., 2002; Wadham et al., 2010; **Figure 3C**) or end-member mixing plots (Gaillardet et al., 2014; **Supplementary Figure 4**), which have been inferred to influence temporal trends in Si isotope compositions in single catchment systems (Hatton et al., 2019a). The lack of significant trends is likely due to the diverse environmental controls on Si cycling and weathering in Patagonia, combined with mixed catchment lithologies complicating signals.

4.4. Isotopic Composition of Amorphous Silicon Phases

Amorphous silicon (ASi) phases associated with suspended particulate material (SPM) have been shown to readily dissolve in seawater and represent an important component of reactive riverine Si exports (Conley, 1997; Treguer and De La Rocha, 2013; Frings et al., 2014; Hawkings et al., 2017). However, measurements of ASi isotope compositions are currently limited to high-latitude proglacial rivers (Hawkings et al., 2018; Hatton et al., 2019a,b), potentially representing a significant gap in resolving terrestrial Si isotope budgets. ASi was present in all rivers where particulate samples were available for extraction, with concentrations that varied primarily as a function of the SPM load (Pryer et al., 2020) and equalled 1–100% of the respective DSi concentration (**Figure 2B**). All $\delta^{30}Si_{ASi}$ values from Patagonian rivers were far lower than corresponding riverine $\delta^{30}Si_{DSi}$ showing that the lighter ^{28}Si isotope is preferentially incorporated into ASi phases (**Figure 2D**) with mean $\Delta^{30}Si_{ASi-DSi}$ values of -1.06 ± 0.42‰. These offsets are similar but more variable than empirically derived values for abiogenic ASi formation in freshwater (-0.98 ± 0.12‰; Zheng et al., 2019), likely due to the presence of biogenic ASi phases such as diatoms, which can have a variable $\Delta^{30}Si_{ASi-DSi}$ of -1 to -2‰ (Frings et al., 2016). Coupled to this, the dissolution of ASi phases can impart $\Delta^{30}Si_{ASi-DSi}$ of $+0.25$ to -2.5‰, depending on the initial isotopic composition of the ASi phase and the congruency of weathering (Frings et al., 2016). The range of ASi isotopic compositions in Patagonian rivers therefore likely reflects a dynamic balance between the composition of ASi material from biogenic and abiogenic sources, combined with variable dissolution of these phases controlled by factors such as temperature, pH and the saturation state of the river water (Ziegler et al., 2005; Stamm et al., 2019; Zheng et al., 2019).

The $\delta^{30}Si_{ASi}$ compositions in some non-glacial rivers in Patagonia were lower than the range of values reported for proglacial rivers (-0.86 to -0.05‰; **Figure 2D**; Hatton et al., 2019b). Such low $\delta^{30}Si_{ASi}$ values from non-glacial river systems are likely due to the presence of phytoliths, diatoms and other biogenic ASi phases, which have large fractionation factors and are consequently highly enriched in ^{28}Si (Opfergelt et al., 2008; Frings et al., 2016; Sutton et al., 2018). The $\delta^{30}Si_{ASi}$ values from glacier and volcano-fed rivers were notably higher than $\delta^{30}Si_{ASi}$ compositions in other river systems, likely due to the reduction or absence of biogenic ASi phases in turbid, light-limited waters (**Figure 2D**). Additionally, dissolution of ASi phases in subglacial environments and glacier-fed rivers, where rates of physical erosion are high and DSi concentrations are low, may cause preferential loss of ^{28}Si from the ASi (Hawkings et al., 2018; Hatton et al., 2019a), and drive residual ASi phases to heavier isotopic compositions. The $\delta^{30}Si_{ASi}$ values observed for glacier-fed rivers in Patagonia are similar to data from two glacial systems in Greenland (-0.21 ± 0.06‰ and -0.47 ± 0.06‰; Hawkings et al., 2018; Hatton et al., 2019a), suggesting broad similarities in the formation mechanisms and composition of glacial ASi between regions.

4.5. Seasonal Variability in Riverine Si Isotope Compositions

For the two catchments where time-series and seasonal data were collected, both $\delta^{30}Si_{fSi}$ and $\delta^{30}Si_{DSi}$ values showed no significant variability (**Figure 6**). For the glacier-fed site (Río Huemules, 70% glacial cover), the consistent DSi concentrations, $\delta^{30}Si_{fSi}$ and $\delta^{30}Si_{DSi}$ compositions were likely due to the presence of a large proglacial lake homogenizing and modulating temporal variability (**Figures 6A–C**). This lack of variability was also observed in the ASi concentrations and $\delta^{30}Si_{ASi}$ values, suggesting no seasonal change in ASi composition. We also observed no large discharge events, such as glacial lake outburst floods, or obvious seasonal shifts in the hydrological regime of the glacier (i.e., channelized vs. distributed drainage pathways), which are the primary drivers of variability in $\delta^{30}Si_{DSi}$ values in proglacial rivers in Greenland (Hawkings et al., 2018; Hatton et al., 2019a). As all glacier-fed rivers sampled in Patagonia drain through large proglacial lakes, we speculate that other glacial catchments will also show negligible temporal variability and our Si isotope compositions are likely to be broadly representative of mean annual values from these catchments.

At the non-glacial time-series site (Río Lloncochaigua, 1.2% glacial cover), consistent riverine Si isotopic compositions were observed, despite variability in DSi concentrations (**Figures 6D,E**). This lack of isotopic variability indicates that Si sources and biogeochemical cycling within this river catchment were stable across the sampling period. However, other non-glacial rivers in Patagonia may show greater temporal variability in $\delta^{30}Si_{DSi}$ values, especially in catchments with non-glacial lakes that likely experience seasonal shifts in siliceous productivity (Alleman et al., 2005; Hughes et al., 2011; Opfergelt et al., 2011). Seasonal variability in $\delta^{30}Si_{DSi}$ on the order of $\pm$ 1‰ has been reported from other global river systems, driven by factors such as snow-melt influencing groundwater flow, shifts in weathering intensity, variable inputs and dissolution of phytoliths from plants, and changes in water temperature that can affect the precipitation or solubility of secondary weathering products (Ding et al., 2004; Pokrovsky et al., 2013; Sun et al., 2018). As such, investigating seasonal controls on riverine Si cycling should be accounted for in future sampling campaigns to fully resolve the Si isotope composition of freshwater flowing into the coastal region of Chilean Patagonia.

4.6. Importance of Including ASi Phases in Labile Riverine δ^{30}Si Export Budgets

We calculated a mass balance accounting for the relative proportions and isotopic compositions of the DSi and ASi components in Patagonian rivers to investigate whether including ASi is important for resolving the "labile" Si isotope composition ($\delta^{30}Si_{DSi+ASi}$) of rivers in this region. The potential contributions from CNSi were excluded in the following discussion, as their solubility and fate in seawater are currently uncertain (Pryer et al., 2020). All rivers with >20% glacial cover had significantly lower $\delta^{30}Si_{DSi+ASi}$ compared to $\delta^{30}Si_{DSi}$, with differences that ranged from −0.10 to −0.30‰ (mean = −0.20 ± 0.07‰; **Figure 7A**). These values were well outside analytical error and show how including ASi components can significantly change estimates of the riverine Si isotope flux to downstream fjords. However, it is not only glacial rivers where the labile Si isotope composition was affected by including ASi. Other rivers with high SPM loads, such as those draining from active volcanoes (e.g., Río Ibanez) or with unconsolidated sediments (e.g., Río Chacabuco), also exhibited large offsets between $\delta^{30}Si_{DSi+ASi}$ and $\delta^{30}Si_{DSi}$ values, with differences ranging from −0.27 to −0.14‰. Conversely, including the ASi phase did not influence the labile Si isotope budget for non-glacial rivers with low SPM concentrations, where $\delta^{30}Si_{DSi+ASi}$ and $\delta^{30}Si_{DSi}$ compositions were within analytical uncertainty. Overall, we find that in all river systems where the ASi phases exceed 10% of the labile Si budget (i.e., DSi + ASi), the $\delta^{30}Si_{DSi+ASi}$ values were significantly different to $\delta^{30}Si_{DSi}$ compositions (**Figure 7B**). Although there is variability around this trend caused by independent factors that can influence the relative proportions and isotopic compositions of ASi and DSi, this relationship provides a useful indication of river systems where ASi phases are likely to significantly affect estimates of Si isotope exports.

We extend our analysis to investigate whether including ASi phases could change the Si isotope exports from other global watersheds. An example is the Lena River, which has one of the world's largest catchment areas and provides ~20% of the freshwater flux to the Arctic Ocean (Walker, 1998; Holmes et al., 2012). Previous research explored the $\delta^{30}Si_{DSi}$ values of the Lena river to quantify the Si isotope composition exported to the Arctic Ocean but did not discuss contributions from reactive ASi phases (Sun et al., 2018). Assuming that ASi concentrations are similar to rivers in Patagonia (mean = 1.12 wt. %; Pryer et al., 2020) and scaling by the mean SPM concentrations of the Lena River (40.5 mg L^{-1}; Fedorova et al., 2015), we approximate that ASi could deliver an additional ~16 μM of reactive Si from this catchment to downstream ecosystems. These assumptions are likely broadly valid due to the relatively narrow range of ASi (wt. %) values reported from global rivers (Frings et al., 2014; Hatton et al., 2019b; Pryer et al., 2020) and the strong linear relationship between SPM and ASi (μM) concentrations (Frings et al., 2014; Pryer et al., 2020). As such, ASi phases in the Lena River could represent ~20% of the total labile Si flux from this catchment, relative to mean annual DSi values of 69.7 μM (Sun et al., 2018). Using the mean $\delta^{30}Si_{ASi}$ of −0.59‰ from this study, we calculate that including ASi in the Si isotope budget for the Lena river could shift δ^{30}Si values by −0.27‰, from $\delta^{30}Si_{DSi}$ values of +0.86‰ (Sun et al., 2018) to $\delta^{30}Si_{DSi+ASi}$ of +0.59‰. We speculate that including ASi components will significantly change the terrestrial Si isotope flux to the ocean from many other rivers and should be considered in future work.

4.7. Do Glacier-Fed Rivers in Patagonia Have Distinct Si Isotope Compositions?

A key hypothesis of this research was that glacier-fed rivers in Patagonia have distinct Si isotope compositions compared to non-glacial rivers. This has been shown to be true in other regions such as Iceland (Georg et al., 2007; Opfergelt et al., 2013) and Greenland (Hawkings et al., 2018), and suggests that glacial meltwater inputs could influence the oceanic Si isotope inventory over glacial—interglacial periods, with implications for understanding Si isotope paleoclimate records (Hawkings et al., 2018). Initially, the $\delta^{30}Si_{fSi}$ data showed that glacier-fed rivers in Patagonia were isotopically light compared to non-glacial rivers and compositions varied as a linear function of upstream glacial cover (**Figure 2C**). However, more detailed analyses showed that this trend was mainly controlled by variable proportions of an isotopically light CNSi phase, which shifted $\delta^{30}Si_{fSi}$ to lower values. Once the CNSi were removed by ultra-filtration, the $\delta^{30}Si_{DSi}$ values of glacier-fed rivers were still very low (mean = +0.33‰; **Figure 2C**) relative to the global riverine mean (+1.25‰; Frings et al., 2016), and were statistically different to the mean composition of rivers with <20% glacial cover (+0.54‰, $t_{24} = 3.3$, $p < 0.01$). However, the $\delta^{30}Si_{DSi}$ values of glacier-fed rivers were no longer isotopically distinct from some non-glacial rivers in Patagonia and were often isotopically heavier than organic-rich rivers (mean = +0.17‰).

When ASi phases were included to give $\delta^{30}Si_{DSi+ASi}$ as estimates of the labile Si isotope budget, glacier-fed rivers still did not have significantly lower isotope compositions than some non-glacial river systems (**Figure 7A**). Although all glacier-fed rivers in this region had low $\delta^{30}Si_{DSi+ASi}$ (range = −0.12 to +0.26‰), there was overlap with rivers with <20% glacial cover (range = +0.03 to +1.17‰). These results demonstrate that low δ^{30}Si values are not necessarily indicative of glacial meltwater inputs into the Patagonian fjords. Ultimately, the reactivity of CNSi is a key uncertainty in quantifying riverine Si isotope exports from glacier-fed rivers in Patagonia. If the CNSi dissolves in seawater, the reactive Si isotope composition of all rivers with >50% glacial cover would be isotopically distinct compared to non-glacial river systems in this region. Additional research is therefore needed to understand the lability and fate of CNSi within downstream fjords to fully resolve reactive Si isotope exports from glacial rivers in Patagonia. Overall, these data show that glacier-fed rivers have light Si isotope compositions, similar to findings from other glaciated regions. However, glacial river signatures were not isotopically distinct from some non-glacial river systems, highlighting the complex controls on riverine Si isotope exports in Chilean Patagonia.

5. CONCLUSIONS

This study provides new insights into how variable glacial cover can affect Si cycling processes and riverine Si isotope compositions using a latitudinal transect of rivers in Chilean Patagonia. A negative linear trend between glacial cover and $\delta^{30}\mathrm{Si}_{\mathrm{fSi}}$ in glacier-fed rivers initially indicated that glacial meltwaters could have a distinctive, light Si isotope composition and that the relationship could represent broadly proportional mixing with non-glacial water. However, significant differences between 0.45 and 0.02 µm filtered Si concentrations and Si isotopic compositions of all glacier-fed rivers indicated that an isotopically light colloidal-nanoparticulate Si phase was present and often dominated Si budgets. This CNSi was primarily composed of feldspars and its lability in seawater is currently uncertain, representing a significant gap in resolving glacial Si exports from this region. Similar linear relationships between glacial cover and the colloidal-nanoparticulate concentrations of other weathering sensitive elements, such as Li, Sr, Mg, and Ba, highlight that this issue is not unique to Si and that the isotopic compositions of these elements could also show size-dependent trends in glacial rivers. Once the CNSi phases were removed by ultra-filtration, glacier-fed rivers still had light Si isotope compositions relative to the non-glacial mean, but did not show a significant trend with glacial cover and were no longer isotopically distinct from non-glacial rivers with the lowest $\delta^{30}\mathrm{Si}_{\mathrm{DSi}}$ values. The variability observed in $\delta^{30}\mathrm{Si}_{\mathrm{DSi}}$ compositions reflects the diverse landscape and biogeochemical weathering pathways, with productivity in lakes, interactions with organic-rich waters and chemical weathering intensity exerting important controls. These data give new insights into the factors influencing riverine Si cycling and isotope compositions, providing a baseline to understand future change in Chilean Patagonia.

ASi isotope data from a range of non-glacial and glacial rivers showed that ASi phases were isotopically lighter than DSi and provided preliminary evidence that riverine turbidity affects ASi isotope compositions. Currently, the contribution of ASi phases to Si fluxes and corresponding Si isotope compositions are not routinely measured, and interpretations of riverine Si exports are based on DSi alone. Since ASi was found in all rivers sampled in Patagonia and can equal the flux of DSi, excluding this reactive component potentially gives an incomplete picture, with implications for quantifying terrestrial Si exports, understanding Si cycling and interpreting Si-based paleoclimate records. We postulate that including ASi phases is critical for resolving riverine Si export and isotope budgets both in Chilean Patagonia and other global rivers. Future research on glacial isotope compositions should account for the size-partitioning and potential reactivity of different phases to fully disentangle how terrestrial exports may have varied in the past and are likely to change in our warming world.

DATA AVAILABILITY STATEMENT

The raw data supporting the conclusions of this article will be made available by the authors, without undue reservation. All data used in this study are freely available to download (https://zenodo.org/record/4114629#.X5AjjC2ZMkg).

AUTHOR CONTRIBUTIONS

The PISCES project was devised by JW, LR, and KH. Data analysis was conducted by HP, with assistance from JHat and JHaw. HP, JHaw, JW, LR, AK, MM, AU, AC, GD, and VH were involved with fieldwork in Patagonia. The manuscript was written by HP, with comments provided by all coauthors. All authors contributed to the article and approved the submitted version.

FUNDING

This work was funded as part of the NERC-CONICYT project PISCES (NE/P003133/1—PII20150106). HP was supported by the NERC GW4+ DTP and the Natural Environment Research Council (NE/L002434/1). KH and JHat were funded by the European Research Council ERC-ICY-LAB (#678371) and Royal Society grant (RGF-EA-181036). JW was supported by a Royal Society Wolfson Merit Award. JHaw was supported by a European Commission Horizon 2020 Marie Skłodowska-Curie Actions fellowship ICICLES (#793962). This is publication #182 of Huinay Scientific Field Station.

ACKNOWLEDGMENTS

We thank the editor, Zhilei Sun, and two reviewers for their time and constructive comments, which helped to improve this manuscript. We also thank everyone who assisted with fieldwork in Patagonia and sample analysis in LOWTEX and the Bristol Isotope Research labs.

SUPPLEMENTARY MATERIAL

The Supplementary Material for this article can be found online at: https://www.frontiersin.org/articles/10.3389/feart.2020.00368/full#supplementary-material

REFERENCES

Alleman, L. Y., Cardinal, D., Cocquyt, C., Plisnier, P.-D., Descy, J.-P., Kimirei, I., et al. (2005). Silicon isotopic fractionation in Lake Tanganyika and its main tributaries. *J. Great Lakes Res.* 31, 509–519. doi: 10.1016/S0380-1330(05)70280-X

Anderson, S. P. (2007). Biogeochemistry of glacial landscape systems. *Annu. Rev. Earth Planet. Sci.* 35, 375–399. doi: 10.1146/annurev.earth.35.031306.140033

Baigún, C., Mugni, H., and Bonetto, C. (2006). Nutrient concentrations and trophic state of small Patagonian Andean lakes. *J. Freshw. Ecol.* 21, 449–456. doi: 10.1080/02705060.2006.9665022

Berner, R. A., and Caldeira, K. (1997). The need for mass balance and feedback in the geochemical carbon cycle. *Geology* 25, 955–956. doi: 10.1130/0091-7613(1997)025<0955:TNFMBA>2.3.CO;2

Berner, R. A., Lasaga, A. C., and Garrels, R. M. (1983). The carbonate-silicate geochemical cycle and its effect on atmospheric carbon-dioxide over the past 100 million years. *Am. J. Sci*. 283, 641–683. doi: 10.2475/ajs.283.7.641

Blackburn, T., Siman-Tov, S., Coble, M. A., Stock, G. M., Brodsky, E. E., and Hallet, B. (2019). Composition and formation age of amorphous silica coating glacially polished surfaces. *Geology* 47, 347–350. doi: 10.1130/G45737.1

Cardinal, D., Alleman, L. Y., de Jong, J., Ziegler, K., and Andre, L. (2003). Isotopic composition of silicon measured by multicollector plasma source mass spectrometry in dry plasma mode. *J. Anal. Atom. Spectrom*. 18, 213–218. doi: 10.1039/b210109b

Cardinal, D., Gaillardet, J., Hughes, H. J., Opfergelt, S., and Andre, L. (2010). Contrasting silicon isotope signatures in rivers from the Congo Basin and the specific behaviour of organic-rich waters. *Geophys. Res. Lett*. 37, 1–6. doi: 10.1029/2010GL043413

Cockerton, H., Street-Perrott, F., Leng, M., Barker, P., Horstwood, M., and Pashley, V. (2013). Stable-isotope (H, O, and Si) evidence for seasonal variations in hydrology and Si cycling from modern waters in the Nile Basin: implications for interpreting the Quaternary record. *Quater. Sci. Rev*. 66, 4–21. doi: 10.1016/j.quascirev.2012.12.005

Conley, D. J. (1997). Riverine contribution of biogenic silica to the oceanic silica budget. *Limnol. Oceanogr*. 42, 774–777. doi: 10.4319/lo.1997.42.4.0774

Crompton, J. W., and Flowers, G. E. (2016). Correlations of suspended sediment size with bedrock lithology and glacier dynamics. *Ann. Glaciol*. 57, 142–150. doi: 10.1017/aog.2016.6

Davies, B. J., and Glasser, N. F. (2012). Accelerating shrinkage of Patagonian glaciers from the Little Ice Age (similar to AD 1870) to 2011. *J. Glaciol*. 58, 1063–1084. doi: 10.3189/2012JoG12J026

De La Rocha, C. L., Brzezinski, M. A., and DeNiro, M. J. (1997). Fractionation of silicon isotopes by marine diatoms during biogenic silica formation. *Geochim. Cosmochim. Acta* 61, 5051–5056. doi: 10.1016/S0016-7037(97)00300-1

De La Rocha, C. L., Brzezinski, M. A., DeNiro, M. J., and Shemesh, A. (1998). Silicon-isotope composition of diatoms as an indicator of past oceanic change. *Nature* 395, 680–683. doi: 10.1038/27174

Delstanche, S., Opfergelt, S., Cardinal, D., Elsass, F., André, L., and Delvaux, B. (2009). Silicon isotopic fractionation during adsorption of aqueous monosilicic acid onto iron oxide. *Geochim. Cosmochim. Acta* 73, 923–934. doi: 10.1016/j.gca.2008.11.014

Delvaux, C., Cardinal, D., Carbonnel, V., Chou, L., Hughes, H., and André, L. (2013). Controls on riverine δ^{30}Si signatures in a temperate watershed under high anthropogenic pressure (Scheldt–Belgium). *J. Mar. Syst*. 128, 40–51. doi: 10.1016/j.jmarsys.2013.01.004

DeMaster, D. J. (1981). The supply and accumulation of silica in the marine environment. *Geochim. Cosmochim. Acta* 45, 1715–1732. doi: 10.1016/0016-7037(81)90006-5

Ding, T., Wan, D., Bai, R., Zhang, Z., Shen, Y., and Meng, R. (2005). Silicon isotope abundance ratios and atomic weights of NBS-28 and other reference materials. *Geochim. Cosmochim. Acta* 69, 5487–5494. doi: 10.1016/j.gca.2005.06.015

Ding, T., Wan, D., Wang, C., and Zhang, F. (2004). Silicon isotope compositions of dissolved silicon and suspended matter in the Yangtze River, China. *Geochim. Cosmochim. Acta* 68, 205–216. doi: 10.1016/S0016-7037(03)00264-3

Dürr, H., M, M., Hartmann, J., Laruelle, G., and Roubeix, V. (2011). Global spatial distribution of natural river silica inputs to the coastal zone. *Biogeosciences* 8, 597–620. doi: 10.5194/bg-8-597-2011

Fedorova, I., Chetverova, A., Bolshiyanov, D., Makarov, A., Boike, J., Heim, B., et al. (2015). Lena Delta hydrology and geochemistry: long-term hydrological data and recent field observations. *Biogeosciences* 12, 345–363. doi: 10.5194/bg-12-345-2015

Fontorbe, G., De La Rocha, C. L., Chapman, H. J., and Bickle, M. J. (2013). The silicon isotopic composition of the Ganges and its tributaries. *Earth Planet. Sci. Lett*. 381, 21–30. doi: 10.1016/j.epsl.2013.08.026

Frings, P. J. (2017). Revisiting the dissolution of biogenic Si in marine sediments: a key term in the ocean Si budget. *Acta Geochim*. 36, 429–432. doi: 10.1007/s11631-017-0183-1

Frings, P. J., Clymans, W., and Conley, D. (2014). Amorphous silica transport in the Ganges basin: implications for Si delivery to the oceans. *Proc. Earth Planet. Sci*. 10, 271–274. doi: 10.1016/j.proeps.2014.08.059

Frings, P. J., Clymans, W., Fontorbe, G., De La Rocha, C. L., and Conley, D. J. (2016). The continental Si cycle and its impact on the ocean Si isotope budget. *Chem. Geol*. 425, 12–36. doi: 10.1016/j.chemgeo.2016.01.020

Gaillardet, J., Viers, J., and Dupré, B. (2014). Trace elements in river waters, in *Treatise on Geochemistry, 2nd Edn*, eds H. D. Holland and K. K. Turekian (Oxford: Elsevier), 195–235. doi: 10.1016/B978-0-08-095975-7.00507-6

Georg, R. B., Reynolds, B. C., Frank, M., and Halliday, A. N. (2006). New sample preparation techniques for the determination of Si isotopic compositions using MC-ICPMS. *Chem. Geol*. 235, 95–104. doi: 10.1016/j.chemgeo.2006.06.006

Georg, R. B., Reynolds, B. C., West, A. J., Burton, K. W., and Halliday, A. N. (2007). Silicon isotope variations accompanying basalt weathering in Iceland. *Earth Planet. Sci. Lett*. 261, 476–490. doi: 10.1016/j.epsl.2007.07.004

Georg, R. B., Zhu, C., Reynolds, B. C., and Halliday, A. N. (2009). Stable silicon isotopes of groundwater, feldspars, and clay coatings in the Navajo Sandstone aquifer, Black Mesa, Arizona, USA. *Geochim. Cosmochim. Acta* 73, 2229–2241. doi: 10.1016/j.gca.2009.02.005

Gou, L.-F., Jin, Z., Galy, A., Gong, Y.-Z., Nan, X.-Y., Jin, C., et al. (2020). Seasonal riverine barium isotopic variation in the middle Yellow River: sources and fractionation. *Earth Planet. Sci. Lett*. 531, 1–12. doi: 10.1016/j.epsl.2019.115990

Gruber, C., Harlavan, Y., Pousty, D., Winkler, D., and Ganor, J. (2019). Enhanced chemical weathering of albite under seawater conditions and its potential effect on the Sr ocean budget. *Geochim. Cosmochim. Acta* 261, 20–34. doi: 10.1016/j.gca.2019.06.049

Hartmann, J., and Moosdorf, N. (2012). The new global lithological map database GLiM: a representation of rock properties at the Earth surface. *Geochem. Geophys. Geosyst*. 13:119. doi: 10.1029/2012GC004370

Hatton, J. E., Hendry, K. R., Hawkings, J. R., Wadham, J. L., Kohler, T. J., Stibal, M., et al. (2019a). Investigation of subglacial weathering under the Greenland Ice Sheet using silicon isotopes. *Geochim. Cosmochim. Acta* 247, 191–206. doi: 10.1016/j.gca.2018.12.033

Hatton, J. E., Hendry, K. R., Hawkings, J. R., Wadham, J. L., Opfergelt, S., Kohler, T. J., et al. (2019b). Silicon isotopes in Arctic and sub-Arctic glacial meltwaters: the role of subglacial weathering in the silicon cycle. *Proc. R. Soc. A* 475:2228. doi: 10.1098/rspa.2019.0098

Hawkings, J. R., Hatton, J., Hendry, K., Souza, G., Wadham, J., Ivanovic, R., et al. (2018). The silicon cycle impacted by past ice sheets. *Nat. Commun*. 9:3210. doi: 10.1038/s41467-018-05689-1

Hawkings, J. R., Wadham, J., Tranter, M., O'Donnell, E., Sole, A., Cowton, T., et al. (2015). The effect of warming climate on nutrient and solute export from the Greenland Ice Sheet. *Geochem. Perspect. Lett*. 1, 94–104. doi: 10.7185/geochemlet.1510

Hawkings, J. R., Wadham, J. L., Benning, L. G., Hendry, K. R., Tranter, M., Tedstone, A., et al. (2017). Ice sheets as a missing source of silica to the polar oceans. *Nat. Commun*. 8:14198. doi: 10.1038/ncomms14198

Hawkings, J. R., Wadham, J. L., Tranter, M., Raiswell, R., Benning, L. G., Statham, P. J., et al. (2014). Ice sheets as a significant source of highly reactive nanoparticulate iron to the oceans. *Nat. Commun*. 5:3929. doi: 10.1038/ncomms4929

Hendry, K. R., and Brzezinski, M. A. (2014). Using silicon isotopes to understand the role of the Southern Ocean in modern and ancient biogeochemistry and climate. *Quatern. Sci. Rev*. 89, 13–26. doi: 10.1016/j.quascirev.2014.01.019

Hendry, K. R., Leng, M. J., Robinson, L. F., Sloane, H. J., Blusztjan, J., Rickaby, R. E. M., et al. (2011). Silicon isotopes in Antarctic sponges: an interlaboratory comparison. *Antarct. Sci*. 23, 34–42. doi: 10.1017/S0954102010000593

Hendry, K. R., and Robinson, L. F. (2012). The relationship between silicon isotope fractionation in sponges and silicic acid concentration: modern and core-top studies of biogenic opal. *Geochim. Cosmochim. Acta* 81, 1–12. doi: 10.1016/j.gca.2011.12.010

Holdren, G. R., and Berner, R. A. (1979). Mechanism of feldspar weathering-I. experimental studies. *Geochim. Cosmochim. Acta* 43, 1161–1171. doi: 10.1016/0016-7037(79)90109-1

Holmes, R., McClelland, J., Peterson, B., Tank, S., Bulygina, E., Eglinton, T., et al. (2012). Seasonal and annual fluxes of nutrients and organic matter from large rivers to the arctic ocean and surrounding seas. *Estuar. Coasts* 35, 369–382. doi: 10.1007/s12237-011-9386-6

Horowitz, A. J., Elrick, K. A., and Colberg, M. R. (1992). The effect of membrane filtration artifacts on dissolved trace element concentrations. *Water Res*. 26, 753–763. doi: 10.1016/0043-1354(92)90006-P

Horowitz, A. J., Lum, K. R., Garbarino, J. R., Hall, G. E. M., Lemieux, C., and Demas, C. R. (1996). Problems associated with using filtration to define dissolved trace element concentrations in natural water samples. *Environ. Sci. Technol*. 30, 954–963. doi: 10.1021/es950407h

Hughes, H., Bouillon, S., André, L., and Cardinal, D. (2012). The effects of weathering variability and anthropogenic pressures upon silicon cycling in an intertropical watershed (Tana River, Kenya). *Chem. Geol*. 308, 18–25. doi: 10.1016/j.chemgeo.2012.03.016

Hughes, H. J., Sondag, F., Cocquyt, C., Laraque, A., Pandi, A., André, L., et al. (2011). Effect of seasonal biogenic silica variations on dissolved silicon fluxes and isotopic signatures in the Congo River. *Limnol. Oceanogr*. 56, 551–561. doi: 10.4319/lo.2011.56.2.0551

Hughes, H. J., Sondag, F., Santos, R. V., Andre, L., and Cardinal, D. (2013). The riverine silicon isotope composition of the Amazon Basin. *Geochim. Cosmochim. Acta* 121, 637–651. doi: 10.1016/j.gca.2013.07.040

Lindsay, J. B. (2016). Whitebox GAT: A case study in geomorphometric analysis. *Comput. Geosci*. 95, 75–84. doi: 10.1016/j.cageo.2016.07.003

Messager, M. L., Lehner, B., Grill, G., Nedeva, I., and Schmitt, O. (2016). Estimating the volume and age of water stored in global lakes using a geo-statistical approach. *Nat. Commun*. 7:13603. doi: 10.1038/ncomms13603

Millero, F. J., Feistel, R., Wright, D. G., and McDougall, T. J. (2008). The composition of standard seawater and the definition of the reference-composition salinity scale. *Deep Sea Res. Part I* 55, 50–72. doi: 10.1016/j.dsr.2007.10.001

Nelson, D. M., Tréguer, P., Brzezinski, M. A., Leynaert, A., and Quéguiner, B. (1995). Production and dissolution of biogenic silica in the ocean: revised global estimates, comparison with regional data and relationship to biogenic sedimentation. *Glob. Biogeochem. Cycles* 9, 359–372. doi: 10.1029/95GB01070

Opfergelt, S., Burton, K. W., Pogge von Strandmann, P. A. E., Gislason, S. R., and Halliday, A. N. (2013). Riverine silicon isotope variations in glaciated basaltic terrains: implications for the Si delivery to the ocean over glacial–interglacial intervals. *Earth Planet. Sci. Lett*. 369, 211–219. doi: 10.1016/j.epsl.2013.03.025

Opfergelt, S., de Bournonville, G., Cardinal, D., André, L., Delstanche, S., and Delvaux, B. (2009). Impact of soil weathering degree on silicon isotopic fractionation during adsorption onto iron oxides in basaltic ash soils, Cameroon. *Geochim. Cosmochim. Acta* 73, 7226–7240. doi: 10.1016/j.gca.2009.09.003

Opfergelt, S., and Delmelle, P. (2012). Silicon isotopes and continental weathering processes: assessing controls on Si transfer to the ocean. *Comptes Rendus Geosci*. 344, 723–738. doi: 10.1016/j.crte.2012.09.006

Opfergelt, S., Delvaux, B., André, L., and Cardinal, D. (2008). Plant silicon isotopic signature might reflect soil weathering degree. *Biogeochemistry* 91, 163–175. doi: 10.1007/s10533-008-9278-4

Opfergelt, S., Eiriksdottir, E. S., Burton, K. W., Einarsson, A., Siebert, C., Gislason, S. R., et al. (2011). Quantifying the impact of freshwater diatom productivity on silicon isotopes and silicon fluxes: Lake Myvatn, Iceland. *Earth Planet. Sci. Lett*. 305, 73–82. doi: 10.1016/j.epsl.2011.02.043

Panizzo, V. N., Swann, G. E. A., Mackay, A. W., Vologina, E., Alleman, L., André, L., et al. (2017). Constraining modern-day silicon cycling in Lake Baikal. *Glob. Biogeochem. Cycles* 31, 556–574. doi: 10.1002/2016GB005518

Peucker-Ehrenbrink, B., Miller, M. W., Arsouze, T., and Jeandel, C. (2010). Continental bedrock and riverine fluxes of strontium and neodymium isotopes to the oceans. *Geochem. Geophys. Geosyst*. 11, 1–22. doi: 10.1029/2009GC002869

Pogge von Strandmann, P. A. E., Hendry, K. R., Hatton, J. E., and Robinson, L. F. (2019). The response of magnesium, silicon, and calcium isotopes to rapidly uplifting and weathering terrains: South Island, New Zealand. *Front. Earth Sci*. 7:240. doi: 10.3389/feart.2019.00240

Pokrovsky, O. S., Reynolds, B. C., Prokushkin, A. S., Schott, J., and Viers, J. (2013). Silicon isotope variations in Central Siberian rivers during basalt weathering in permafrost-dominated larch forests. *Chem. Geol*. 355, 103–116. doi: 10.1016/j.chemgeo.2013.07.016

Pryer, H. V., Hawkings, J. R., Wadham, J. L., Robinson, L. F., Hendry, K. R., Hatton, J. E., et al. (2020). The influence of glacial cover on riverine silicon and iron export in Chilean Patagonia. *Glob. Biogeochem. Cycles*. 34:e2020GB006611. doi: 10.1029/2020GB006611

Raiswell, R., Hawkings, J., Eisenousy, A., Death, R., Tranter, M., and Wadham, J. (2018). Iron in glacial systems: speciation, reactivity, freezing behavior, and alteration during transport. *Front. Earth Sci*. 6:222. doi: 10.3389/feart.2018.00222

Reynolds, B. C., Aggarwal, J., André, L., Baxter, D., Beucher, C., Brzezinski, M. A., et al. (2007). An inter-laboratory comparison of Si isotope reference materials. *J. Anal. Atom. Spectrom*. 22, 561–568. doi: 10.1039/B616755A

RGI Consortium (2017). *Randolph Glacier Inventory-A Dataset of Global Glacier Outlines: Version 6.0*. Technical Report, Global Land Ice Measurements from Space, Colorado, USA, 3, 1–11.

Savage, P., Georg, B., Williams, H., and Halliday, A. (2013). The silicon isotope composition of the upper continental crust. *Geochim. Cosmochim. Acta* 109, 384–399. doi: 10.1016/j.gca.2013.02.004

Schroth, A., Crusius, J., Chever, F., Bostick, B. C., and Rouxel, O. J. (2011). Glacial influence on the geochemistry of riverine iron fluxes to the Gulf of Alaska and effects of deglaciation. *Geophys. Res. Lett*. 38, 1–6. doi: 10.1029/2011GL048367

Shiller, A. M. (2003). Syringe filtration methods for examining dissolved and colloidal trace element distributions in remote field locations. *Environ. Sci. Technol*. 37, 3953–3957. doi: 10.1021/es0341182

Stamm, F., Zambardi, T., Chmeleff, J., Schott, J., Blanckenburg, F., and Oelkers, E. (2019). The Experimental determination of equilibrium Si isotope fractionation factors among $H_4SiO_4^{\circ}$, $H_3SiO_4^{-}$ and amorphous Silica ($SiO_2{\cdot}0.32\ H_2O$) at 25 and 75°C using the three-isotope method. *Geochim. Cosmochim. Acta* 255, 49–68. doi: 10.1016/j.gca.2019.03.035

Sun, X., Mörth, C.-M., Porcelli, D., Kutscher, L., Hirst, C., Murphy, M. J., et al. (2018). Stable silicon isotopic compositions of the Lena River and its tributaries: Implications for silicon delivery to the Arctic Ocean. *Geochim. Cosmochim. Acta* 241, 120–133. doi: 10.1016/j.gca.2018.08.044

Sutton, J. N., André, L., Cardinal, D., Conley, D. J., de Souza, G. F., Dean, J., et al. (2018). A review of the stable isotope bio-geochemistry of the global silicon cycle and its associated trace elements. *Front. Earth Sci*. 5:112. doi: 10.3389/feart.2017.00112

Tranter, M., Sharp, M. J., Lamb, H. R., Brown, G. H., Hubbard, B. P., and Willis, I. C. (2002). Geochemical weathering at the bed of Haut Glacier d'Arolla, Switzerland - a new model. *Hydrol. Process*. 16, 959–993. doi: 10.1002/hyp.309

Tréguer, P., Nelson, D. M., Van Bennekom, A. J., DeMaster, D. J., Leynaert, A., and Quéguiner, B. (1995). The silica balance in the world ocean: a reestimate. *Science* 268, 375–379. doi: 10.1126/science.268.5209.375

Treguer, P. J., and De La Rocha, C. L. (2013). The world ocean silica cycle. *Annu. Rev. Mar. Sci*. 5, 477–501. doi: 10.1146/annurev-marine-121211-172346

Urey, H. C. (1952). On the early chemical history of the earth and the origin of life. *Proc. Natl. Acad. Sci. U.S.A*. 38, 351–363. doi: 10.1073/pnas.38.4.351

Wadham, J. L., Tranter, M., Skidmore, M., Hodson, A. J., Priscu, J., Lyons, W. B., et al. (2010). Biogeochemical weathering under ice: size matters. *Glob. Biogeochem. Cycles* 24, 1–11. doi: 10.1029/2009GB003688

Walker, H. J. (1998). Arctic deltas. *J. Coast. Res*. 14, 719–738.

Weaver, S. G., Bruce, R., Nelson, E. P., Brueckner, H. K., and Le-Huray, A. P. (1990). The Patagonian batholith at 48° S latitude, Chile; Geochemical and isotopic variations. *Spec. Pap. Geol. Soc. Am*. 241, 33–50. doi: 10.1130/SPE241-p33

Wilson, R., Glasser, N. F., Reynolds, J. M., Harrison, S., Anacona, P. I., Schaefer, M., et al. (2018). Glacial lakes of the Central and Patagonian Andes. *Glob. Planet. Change* 162, 275–291. doi: 10.1016/j.gloplacha.2018.01.004

Wimpenny, J., Burton, K. W., James, R. H., Gannoun, A., Mokadem, F., and Gíslason, S. R. (2011). The behaviour of magnesium and its isotopes during glacial weathering in an ancient shield terrain in West Greenland. *Earth Planet. Sci. Lett*. 304, 260–269. doi: 10.1016/j.epsl.2011.02.008

Wimpenny, J., Gíslason, S. R., James, R. H., Gannoun, A., Strandmann, P. A. P. V., and Burton, K. W. (2010). The behaviour of Li and Mg isotopes during primary phase dissolution and secondary mineral formation in basalt. *Geochim. Cosmochim. Acta* 74, 5259–5279. doi: 10.1016/j.gca.2010.06.028

Yuan, G., Cao, Y., Schulz, H.-M., Hao, F., Gluyas, J., Liu, K., et al. (2019). A review of feldspar alteration and its geological significance in sedimentary basins: from shallow aquifers to deep hydrocarbon reservoirs. *Earth-Sci. Rev*. 191, 114–140. doi: 10.1016/j.earscirev.2019.02.004

Zheng, X.-Y., Beard, B. L., and Johnson, C. M. (2019). Constraining silicon isotope exchange kinetics and fractionation between aqueous and amorphous Si at room temperature. *Geochim. Cosmochim. Acta* 253, 267–289. doi: 10.1016/j.gca.2019.03.031

Ziegler, K., Chadwick, O. A., Brzezinski, M. A., and Kelly, E. F. (2005). Natural variations of δ^{30}Si ratios during progressive basalt weathering, Hawaiian Islands. *Geochim. Cosmochim. Acta* 69, 4597–4610. doi: 10.1016/j.gca.2005.05.008

Conflict of Interest: The authors declare that the research was conducted in the absence of any commercial or financial relationships that could be construed as a potential conflict of interest.

frontiers
in Earth Science

ORIGINAL RESEARCH
published: 15 March 2021
doi: 10.3389/feart.2021.551900

Ge/Si and Ge Isotope Fractionation During Glacial and Non-glacial Weathering: Field and Experimental Data From West Greenland

J. Jotautas Baronas[1,2]*, *Douglas E. Hammond*[1], *Mia M. Bennett*[3,4], *Olivier Rouxel*[5], *Lincoln H. Pitcher*[3†] *and Laurence C. Smith*[3†]

[1]Department of Earth Sciences, University of Southern California, Los Angeles, CA, United States, [2]Department of Earth Sciences, University of Cambridge, Cambridge, United Kingdom, [3]Department of Geography, University of California Los Angeles, Los Angeles, CA, United States, [4]Department of Geography, The University of Hong Kong, Hong Kong, China, [5]IFREMER, Centre De Brest, Unité Géosciences Marines, Plouzané, France

Glacial environments offer the opportunity to study the incipient stages of chemical weathering due to the high availability of finely ground sediments, low water temperatures, and typically short rock-water interaction times. In this study we focused on the geochemical behavior of germanium (Ge) in west Greenland, both during subglacial weathering by investigating glacier-fed streams, as well as during a batch reactor experiment by allowing water-sediment interaction for up to 2 years in the laboratory. Sampled in late August 2014, glacial stream Ge and Si concentrations were low, ranging between 12–55 pmol/L and 7–33 μmol/L, respectively (Ge/Si = 0.9–2.2 μmol/mol, similar to parent rock). As reported previously, the dissolved stable Ge isotope ratio (δ^{74}Ge) of the Watson River was 0.86 ± 0.24‰, the lowest among global rivers and streams measured to date. This value was only slightly heavier than the suspended load (0.48 ± 0.23‰), which is likely representative of the bulk parent rock composition. Despite limited Ge/Si and δ^{74}Ge fractionation, both Ge and Si appear depleted relative to Na during subglacial weathering, which we interpret as the relatively congruent uptake of both phases by amorphous silica (aSi). Continued sediment-water interaction over 470–785 days in the lab produced a large increase in dissolved Si concentrations (up to 130–230 μmol/L), a much smaller increase in dissolved Ge (up to ~70 pmol/L), resulting in a Ge/Si decrease (to 0.4–0.5 μmol/mol) and a significant increase in δ^{74}Ge (to 1.9–2.2‰). We argue that during the experiment, both Si and Ge are released by the dissolution of previously subglacially formed aSi, and Ge is then incorporated into secondary phases (likely adsorbed to Fe oxyhydroxides), with an associated $\Delta^{74}\mathrm{Ge}_{\mathrm{secondary-dissolved}}$ fractionation factor of −2.15 ± 0.46‰. In summary, we directly demonstrate Ge isotope fractionation during the dissolution-precipitation weathering reactions of natural sediments in the absence of biological Ge and Si uptake, and highlight the significant differences in Ge behavior during subglacial and non-glacial weathering.

Keywords: glacial weathering, germanium, isotope fractionation, Amorphous silica, experimental dissolution

Edited by:
Katharine Rosemary Hendry,
University of Bristol, United Kingdom

Reviewed by:
Jade Hatton,
University of Bristol, United Kingdom
Jon Hawkings,
Florida State University, United States

***Correspondence:**
J. Jotautas Baronas
jotautas.baronas@gmail.com

†Present address:
Lincoln H. Pitcher,
Cooperative Institute for Research in Environmental Sciences (CIRES),
University of Colorado–Boulder, Boulder, CO, United States
Laurence C. Smith,
Brown University, Providence, RI, United States

Specialty section:
This article was submitted to Geochemistry,
a section of the journal Frontiers in Earth Science

Received: *14 April 2020*
Accepted: *15 January 2021*
Published: *15 March 2021*

Citation:
Baronas J J, Hammond DE, Bennett MM, Rouxel O, Pitcher LH and Smith LC (2021) Ge/Si and Ge Isotope Fractionation During Glacial and Non-glacial Weathering: Field and Experimental Data From West Greenland.
Front. Earth Sci. 9:551900.
doi: 10.3389/feart.2021.551900

1 INTRODUCTION

Glacial rivers typically have low solute concentrations, reflecting the limited degree of mineral dissolution due to low temperatures and relatively short water-rock interaction times in the subglacial environment (e.g., Anderson, 2007; Bartholomew et al., 2011; Tranter and Wadham, 2014; Chu et al., 2016). The preferential dissolution of highly reactive trace minerals such as pyrite has been observed during subglacial weathering, especially in alpine glaciers (Anderson et al., 1997; Brown, 2002; Graly et al., 2014; Andrews et al., 2018). When coupled with carbonate dissolution, it results in the net release of CO_2 to the atmosphere, with important implications for the climate-weathering feedback over glacial cycles (Torres et al., 2017). Subglacial weathering also mobilizes a wide range of macro- and micro-nutrients (Yde et al., 2014; Aciego et al., 2015; Hawkings et al., 2016; Dubnick et al., 2017; Hawkings et al., 2020). A number of studies have found that (nano)particulates dominate the export of potentially (co-)limiting nutrients such as iron (Fe), phosphorus (P), and silica (Si) from glacial systems (Raiswell et al., 2006; Hawkings et al., 2015; Hawkings et al., 2017). If labile and bioavailable, this material may serve as an important source of nutrients for the subglacial and marine offshore ecosystems (Yde et al., 2010; Gerringa et al., 2012; Lawson et al., 2014; Meire et al., 2016; Vick-Majors et al., 2020).

The uniqueness of subglacial weathering is also reflected in the signatures of silicate weathering intensity proxies such as germanium to silicon (Ge/Si) or Si isotope (δ^{30}Si) ratios, which in non-glacial settings are strongly fractionated by secondary weathering phases, as well as biological uptake by plants (e.g., Froelich et al., 1992; Derry et al., 2005; Cornelis et al., 2011; Frings et al., 2016; Baronas et al., 2018; Baronas et al., 2020). Germanium is a trace element primarily present in part-per-million concentrations in silicate rocks. Its low-temperature chemical behavior is similar but not identical to that of Si, making it a useful tracer of the global Si cycle (e.g., Froelich et al., 1985; Cornelis et al., 2011; Baronas et al., 2016; Rouxel and Luais, 2017). Globally, dissolved riverine Ge/Si ratios have been observed to vary from 0.1 to 3 μmol/mol, often significantly lower than silicate rock ratios of 1–3 μmol/mol, which are the primary source of Ge and Si to solution (Froelich et al., 1985; Mortlock and Froelich, 1987; Murnane and Stallard, 1990; Froelich et al., 1992; Rouxel and Luais, 2017; Baronas et al., 2018). In contrast, secondary weathering phases (such as Fe oxides and aluminosilicates like kaolinite) exhibit Ge/Si ratios commonly above 5 μmol/mol, reflecting the preferential incorporation of Ge (Mortlock and Froelich, 1987; Murnane and Stallard, 1990; Kurtz et al., 2002; Lugolobi et al., 2010; Baronas et al., 2020).

In glaciated catchments, however, both dissolved Ge/Si and δ^{30}Si have been shown to generally be less fractionated relative to the silicate parent rock composition (e.g., Mortlock and Froelich, 1987; Chillrud et al., 1994; Anders et al., 2003; Georg et al., 2007; Opfergelt et al., 2013; Hawkings et al., 2018; Hatton et al., 2019b), indicating either the limited formation of secondary phases overall, or the formation of different secondary phases that have little effect on these signatures, during subglacial weathering. Given the contrast between glacial and non-glacial signatures, extensive changes in glaciation over geological history could have therefore impacted the seawater composition of these proxies, which need to be accounted for in the interpretation of marine paleorecords (Froelich et al., 1992; Opfergelt et al., 2013; Frings et al., 2016; Jochum et al., 2017; Hawkings et al., 2018). While seawater δ^{30}Si is strongly controlled by diatom productivity dynamics which mask the continental signal, biological Ge/Si fractionation is limited (e.g., De La Rocha et al., 1998; Sutton et al., 2010, 2018). Seawater Ge/Si paleorecords show consistent increases during deglaciations (Shemesh et al., 1989; Mortlock et al., 1991; Jochum et al., 2017) which are thus thought to primarily reflect a change in either the continental inputs or the authigenic outputs, or both (Froelich et al., 1992; Hammond et al., 2004; Baronas et al., 2016, Baronas et al., 2017).

Recently, it has been shown that dissolved Ge isotope ratios in rivers (δ^{74}Ge = 1.7–5.5‰) also primarily reflect fractionation via secondary weathering phases and that this fractionation is much less pronounced in the single glaciated catchment analyzed to date, the Watson River in west Greenland [0.86 ± 0.24‰; Baronas et al. (2018)]. Coupled with the remarkably homogeneous Ge isotope composition among different silicate rocks [δ^{74}Ge = 0.4–0.8‰; Rouxel and Luais (2017)], this proxy can yield important new insights into chemical weathering of silicates and Si cycling in different Earth surface environments. The global seawater Ge budget is primarily controlled by the balance between continental weathering and hydrothermal inputs and biogenic silica (chiefly diatom) and authigenic clay outputs (Baronas et al., 2017, Baronas et al., 2019).

Studying the chemical and isotopic composition of glacial discharge offers an opportunity to better understand the incipient stages of silicate weathering in a subglacial environment where secondary aluminosilicate clay precipitation is limited and where vegetation is absent. This is especially informative for solutes whose elemental and isotopic ratios can be fractionated by plant uptake in vegetated catchments, such as Si and Ge. For these same reasons, glacial river sediments also present an ideal substrate to experimentally quantify how weathering proxy signatures are fractionated with increasing water-rock interaction times.

In this study, we analyzed the major solute concentrations and Ge/Si signatures of a number of streams and rivers in a well-studied area of west Greenland. In addition, we performed lab weathering experiments, allowing water-rock interaction for up to 2 years in unfiltered river samples and observing the evolution of dissolved Ge/Si and δ^{74}Ge signatures. The data provide direct evidence for the distinct weathering reactions controlling these proxy signatures during subglacial and non-glacial weathering and allow us to directly measure δ^{74}Ge fractionation during Ge uptake into secondary weathering phases.

2 METHODS

2.1 Study Site and Sample Collection

The study site is located in southwest Greenland, in the proglacial area between the Isunnguata Sermia, Russell, and Leverett glaciers to the east and the settlement of Kangerlussuaq in the west

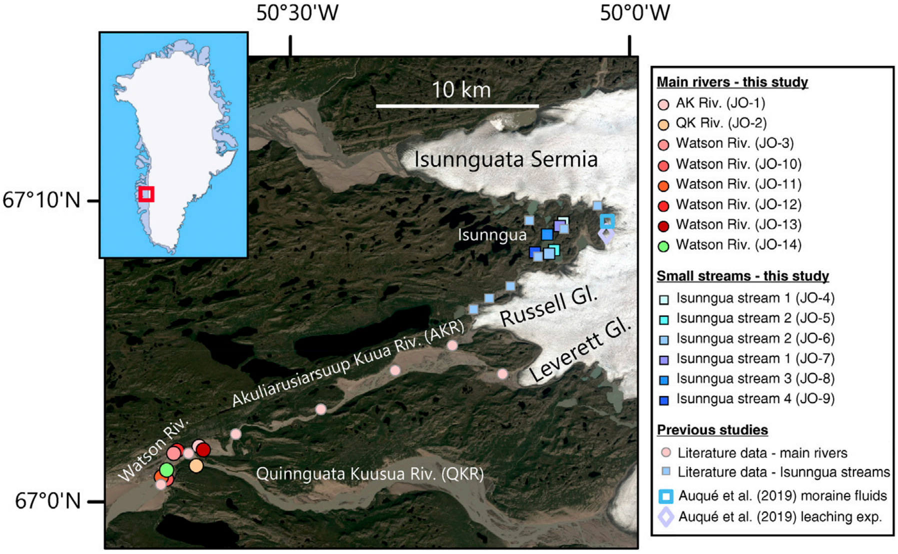

FIGURE 1 | Satellite image (Landsat 8) showing the river sample locations in west Greenland, collected as part of this study, as well as the locations of samples from previous studies whose data is compiled here for comparison. Inset shows the study region location within Greenland.

(**Figure 1**), a region which has been the focus of many previous geochemical studies on chemical weathering and non-traditional stable isotope dynamics (e.g., Wimpenny et al., 2010, Wimpenny et al., 2011; Graly et al., 2014; Hindshaw et al., 2014; Yde et al., 2014; Graly et al., 2016; Rickli et al., 2017; Stevenson et al., 2017; Andrews and Jacobson, 2018; Hatton et al., 2019a; Auqué et al., 2019; Hindshaw et al., 2019). The local geology has been described in detail previously (e.g., Van Gool et al., 2002; Engström and Klint, 2014) and a good summary was recently provided by Hindshaw et al. (2019), and references therein. Briefly, the bedrock underneath the Leverett and Russel glaciers is composed of two distinct Archean orthogneiss units with different degrees of metamorphic alteration, intruded by a mafic dyke swarm.

The area lies just above the Arctic Circle (66°30′ N) with average winter and summer air temperatures of −18.0 and 9.3°C, respectively (for 1961–1990), and low annual precipitation of ~120 mm (Smeets et al., 2018). The hydrology of glacial catchments is complex, with a seasonal evolution from an inefficient distributed drainage during early melt season, toward increasing channelization draining previously isolated pockets of meltwater during mid-melt season, to an efficient channelized system with rapid flushing of meltwater and supraglacial lake evacuation events in the late season (Bartholomew et al., 2011; Cowton et al., 2013; Lindbäck et al., 2015; Smith et al., 2015; Chu et al., 2016; Davison et al., 2019). In terms of total water flux, more than 98% is thought to occur as efficient drainage with short transit times (on the order of hours to days) in the Leverett Glacier catchment (Linhoff et al., 2017) and this is likely to be similar for the whole Watson River catchment.

For this study, a number of water samples were collected between August 19–27, 2014 (**Table 1**) during the late melt season. One set of samples was collected from small marginal glacial streams draining the southern edge of the Isunnguata Sermia glacier and ultimately flowing past the Russell Glacier to join with the Akuliarusiarsuup Kuua (AK) River fed by the Rusell and Leverett Glaciers. Further downstream, the Qinnguata Kuussua (QK) River draining the Ørkendalen and Isorlersuup Glaciers joins AK to form the Watson River. Another set of samples was collected from AK, QK, and Watson rivers in the vicinity of Kangerlussuaq settlement (**Figure 1**).

The samples were collected into HDPE plastic bottles, pre-cleaned using 10% HNO_3 and deionized water. For a number of samples, an aliquot was filtered in the field using 0.45 μm polyethersulfone (PES) syringe filters (Millipore). An additional 5 L sample (JO-14) was collected on the last day of the expedition. This sample, along with the remaining unfiltered aliquots of other samples (volume ranging from 100 to 500 ml), was shipped the next day to the University of Southern California (USC). The large 5 L sample (JO-14) was then allowed to settle for a few hours and filtered (in total ~48 h after collection) through 0.45 μm PES membrane, using a peristaltic pump. The suspended sediment was collected by centrifuging the settled slurry and combining it with the sediment collected on the filter membrane, recovering all of the initial suspended particulate material (SPM) present in the sample. The dissolved Ge and Si concentrations and stable isotope ratios of this sample, as well as the Ge concentration and isotope composition of the suspended sediment, were previously published by Baronas et al. (2018). The Si concentration of the Watson suspended sediment is taken as the average value of previously published data in order to calculate its Ge/Si ratio (**Table 1**).

2.2 River Sediment Weathering Experiment

To assess how dissolved stream chemistry evolves over longer water-sediment interaction timescales, unfiltered river and

TABLE 1 | Details and solute composition of field-filtered west Greenland stream samples.

River	Sample ID	Date	Hour	Lat. (°)	Long. (°)	Na (µmol/L)	K (µmol/L)	Ca (µmol/L)	Mg (µmol/L)	Ge (pmol/L)	Si (µmol/L)	Ge/Si (µmol/mol)	δ^{74}Ge (‰)
Akuliarusiarsuup kuua (AK)	JO-1 field	2014–08–19	14:04	67.021	–50.645	–	–	–	–	–	–	–	–
Qinnguata kuussua (QK)	JO-2 field	2014–08–19	14:50	67.014	–50.643	–	–	–	–	–	–	–	–
Watson	JO-3 field	2014–08–19	17:19	67.020	–50.669	–	–	–	–	–	–	–	–
Isunngua stream 1	JO-4 field	2014–08–20	13:37	67.147	–50.107	–	–	–	–	–	–	–	–
Isunngua stream 2	JO-5 field	2014–08–20	14:36	67.135	–50.117	3.9	4.6	13.4	5.7	16	7.3	2.17	–
Isunngua stream 2	JO-6 field	2014–08–22	15:42	67.135	–50.117	7.3	12.8	27.4	12.8	23	18.2	1.29	–
Isunngua stream 1	JO-7 field	2014–08–22	16:27	67.147	–50.107	5.1	4.8	13.1	5.4	12	6.6	1.85	–
Isunngua stream 3	JO-8 field	2014–08–22	17:08	67.143	–50.123	6.1	6.8	17.2	7.9	14	16.0	0.89	–
Isunngua stream 4	JO-9 field	2014–08–22	18:30	67.133	–50.136	3.7	4.8	14.9	6.5	14	9.5	1.50	–
Watson	JO-10 field	2014–08–23	17:24	67.005	-50.689	23.3	18.6	26.7	8.6	24	16.4	1.46	–
Watson	JO-11 field	2014–08–24	10:06	67.005	–50.689	28.2	21.3	30.0	10.4	46	24.3	1.88	–
Watson	JO-12 field	2014–08–24	14:15	67.020	–50.669	35.8	23.0	34.2	10.5	39	23.6	1.63	–
Akuliarusiarsuup kuua (AK)	JO-13 field	2014–08–24	14:45	67.021	–50.645	36.0	22.8	34.5	10.8	39	24.1	1.62	–
Watson	JO-14 field	2014–08–27	09:01	67.010	–50.682	51.5[a]	33.1[a]	68.5	17.3[a]	55.1[a]	33.3[a]	1.66[a]	0.86 ± 0.24[a]
										(ppm)	(SiO_2 wt%)[b]		
Watson suspended load	JO-14 SPM	2014–08–27	09:01	67.010	–50.682	–	–	–	–	1.1 ± 0.2[a]	68 ± 7	1.3 ± 0.3	0.48 ± 0.23[a]

[a] *Previously published in Baronas et al. (2018).*

[b] *Average of Watson, Akuliarusiarsuup Kuua, and Qinnguata Kuussua river sediments (Wimpenny et al., 2010; Hindshaw et al., 2014).*

stream sample aliquots were allowed to continue reacting in the laboratory for up to 470 or 785 days. The unfiltered samples were left in the original sample bottles and placed on a shaker table inside a temperature-controlled incubator. The experimental setup was not designed to simulate subglacial weathering conditions because it was done in an oxygenated environment and the rock/water ratio in rivers is considerably lower than in the subglacial environment. Instead, the goal of the experiment was to determine how solution composition evolves with the continued dissolution of phases present in the riverine sediment (and the potential precipitation of any secondary phases). Therefore, in order to increase reaction rates, the temperature was set to 25°C. The samples were continually agitated to keep the sediment suspended, and left in the dark. No magnetic stir bars were used, eliminating the possibility of physical grinding during the experiment. Periodically, 4–10 ml aliquots were sub-sampled from each bottle and filtered using 0.2 µm PES syringe filters (Millipore). At the end of the experiment, two ~500 ml samples were filtered for Ge isotope analyses. For several of the samples, suspended sediment concentrations were determined by weighing the dry sediment retained on the filters.

2.3 Major and Trace Element Analyses

Both field and experimental water samples were acidified with trace grade HNO_3 several weeks prior to chemical analyses. Major cation concentrations were measured using Agilent 4100 MP-AES at USC and Agilent 5100 ICP-AES at the University of Cambridge. Si concentration measurements were done using molybdate blue colorimetry (Mullin and Riley, 1955) at USC. Ge concentrations were measured using isotope dilution-hydride generation-ICP-MS on a Thermo Element 2 at USC, following the method developed by Mortlock and Froelich (1996), as modified by Baronas et al. (2016). Trace metal concentrations were measured using ICP-MS (Thermo Element 2) and ICP-AES. Measurement accuracy was determined through repeated analyses of standard reference materials SLRS-6, ION-915, and TMDA-51.4, which agreed within 10% of certified values for all elements, and with a precision of 5% for major elements, 5% for Ge and Si, 10% for Mn, and 20% or 0.2 µmol/L, whichever was higher, for Fe and Al. The propagated uncertainty of measured Ge/Si ratios is around 7%.

2.4 Thermodynamic Calculations

The saturation indices of common mineral and amorphous phases were calculated using the PHREEQC 3.6.2 software (Parkhurst and Appelo, 2013) for a number of sample solutions throughout the course of the weathering experiment. Because pH was not measured in the experimental solutions, we did three sets of calculations by assuming pH = 7, 8, and 9, respectively, bracketing the range of pH values measured in the Leverett Glacier outflow and Watson River previously (Wimpenny et al., 2010; Hatton et al., 2019a). Although Cl^- and HCO_3^- concentrations were not measured in this study, Cl^- concentrations were previously shown to be very low in west Greenland rivers in the late melt season, typically 1–5 µmol/L for AK, QK, and Watson, and frequently below detectable levels

(< 1 μmol/L) for the more dilute Isunngua streams (Wimpenny et al., 2010; Hindshaw et al., 2014; Andrews et al., 2018; Hatton et al., 2019a). We therefore assigned Cl^- = 3 and 0.5 μmol/L for the main rivers and Isunngua streams during PHREEQC simulations, respectively. The concentrations of HCO_3^- were then calculated as the difference between the measured cation concentrations and the sum of sulfate and chloride concentrations (in charge equivalents) and ranged 35–210 μmol/L. The temperature was assigned to 25°C, matching the temperature set during the experiment.

2.5 Ge Isotope Analyses

Ge isotope composition was measured using hydride generation-multi-collector-ICP-MS (Thermo Neptune) at Ifremer, as previously described in detail by Baronas et al. (2018); Baronas et al. (2019). The sample preparation and analytical procedure is briefly summarized below. The dissolved and suspended sediment Ge isotope composition of the "JO-14" sample was previously published by Baronas et al. (2018).

Ge Co-precipitation

The samples "JO-14 Field" (filtered two days after collection), "JO-2 Final", and "JO-3A Final" (filtered after reacting for 470 days in the lab) containing 19, 1.5, and 1.9 ng of Ge, respectively, were processed as follows. The filtered and acidified aliquots were spiked with a Ge isotope double spike [$^{73}Ge/^{70}Ge \approx 1$, previously calibrated and used by Escoube et al. (2012); Escoube et al. (2015); Guillermic et al. (2017); Baronas et al. (2018)] in a spike/sample Ge mass ratio of 1–2 and a purified $FeCl_3$ solution to obtain a Fe concentration of ~0.2 mmol/L. The samples were well mixed and allowed to equilibrate for at least 16 h. Next, $Fe(OH)_3$ flock was precipitated by bubbling pure NH_3 gas through the sample until the solution reached a pH of 8–10. The flock was collected by settling and centrifugation, redissolved in 2 ml concentrated Teflon-distilled HNO_3 and diluted to 10 ml with doubly deionized water (DDIW). The samples were then dried down, redissolved in 1 ml concentrated Optima-grade HF and diluted to 30 ml with ultrapure H_2O to obtain a final 1 M HF solution that was then purified through anion exchange columns as described below. The full procedural blank was determined by processing several "samples" of spiked ultrapure H_2O and was on average ~0.1 ng Ge. Ge recovery for the three Fe-coprecipitated samples ranged between 92 and 98%, as determined later during δ^{74}Ge analysis.

Anion-Exchange Chromatographic Separation

A procedure adapted from Rouxel et al. (2006) was used. All reagents used were either in-house Teflon-distilled or Optima-grade. A 10 ml column was loaded with 1.8 ml (wet volume) of BioRad AG1-X8 resin, washed with 10 ml of 3M HNO_3, 0.28M HNO_3, and DDIW in sequence, and conditioned with 5 ml 1M HF. Samples in 1M HF solution as prepared above were centrifuged to separate insoluble fluorides. The presence or amount of insoluble fluorides at this stage did not appear to affect the final Ge recovery. After centrifugation, 10–29 ml of solution was carefully added to columns. The remaining matrix was eluted with 5 ml of 1M HF followed by 3 ml of DDIW, leaving fluorinated Ge retained on the column. Ge was then eluted with 10 ml 0.28M HNO_3. If needed, the solution was dried down and redissolved in a smaller volume of 0.28M HNO_3 to obtain the 2–10 ppb Ge concentration required for isotope measurements.

HG-MC-ICP-MS

Ge isotope analyses were performed on a Thermo Neptune multi-collector ICP-MS at IFREMER using a method adapted from Rouxel et al. (2006) and Escoube et al. (2015). Sample solutions of 2–10 ppb natural Ge in 0.28M HNO_3 were introduced into an online hydride generation system (CETAC HGX-200) at a rate of 150 μl/min where they were mixed with 0.25M $NaBH_4$ solution (in 1.5M NaOH) introduced at an equal rate. The dissolved $Ge(OH)_4$ species was reduced to gaseous GeH_4 and transported into the ICP-MS torch using Ar carrier gas. The Neptune MC-ICP-MS was operated in low mass resolution mode, measuring ^{70}Ge, ^{72}Ge, ^{73}Ge, and ^{74}Ge in L2, C, H1 and H2 cups, respectively. In addition, L4, L3, L1, and H4 cups were also monitored for ^{68}Zn (possible interference as ^{70}Zn), ^{69}Ga, ^{71}Ga (possible interferences at m/z 70), and ^{77}Se (possible interference as ^{74}Se), respectively. No interferences were detected in any of the runs. The samples were bracketed using a NIST-3120a standard solution that had a total Ge concentration generally within ~20% of the bracketed sample, and was double-spiked to have a spike/sample ratio within ~20% of the bracketed sample. Each sample or standard run consisted of 6 measurement blocks each lasting 2 min (30 cycles of 4 s), and in most cases 4–5 blocks displaying the most stable signal were retained. Therefore, each measurement represents 8–10 min of counting statistics at signal intensities ranging from 0.4 to 6 Vat ^{74}Ge (depending on Ge concentration in sample solution, instrument tuning, and the age of $NaBH_4$ solution). The δ^{74}Ge values are calculated for each block using the double-spike data reduction routine of Siebert et al. (2001) and are reported in ‰ as ^{74}Ge/^{70}Ge sample ratio normalized to the average ^{74}Ge/^{70}Ge ratio of bracketing NIST 3120a measurements. This method also yields Ge concentration values based on the measured spike/sample ratio. The measurement uncertainty is reported as the internal 2σ standard error of the used sample blocks, or 2σ standard deviation of all NIST 3120a bracketing standard measurements within a given analytical session, whichever is higher.

3 RESULTS

3.1 Glacial Stream Chemistry

The measured major cation concentrations were low in all sampled streams (**Table 1**), in agreement with previous data collected at the end of the melt season in late August (Hindshaw et al., 2014; Andrews et al., 2018; Andrews and Jacobson, 2018; Hatton et al., 2019a). In particular, there was a clear distinction between the small Isunngua streams draining the edge of Isunnguata Sermia glacier, where Na and K concentrations ranged between 4–13 μmol/L, and the large rivers draining the Leverett-Russell glaciers, with Na and K ranging between 19–36 μmol/L (**Table 1**). Ca and Mg concentrations were more similar between the two localities, with 6–13 μmol/L Mg and 13–35 μmol/L Ca. Dissolved Ge and Si concentrations ranged between 12–46 pmol/L and 7–24 μmol/L, respectively, resulting in Ge/Si ratios of 0.9–2.2 μmol/mol (for comparison, global riverine average is 0.54 ± 0.10 μmol/mol; Froelich et al. (1992)). The Ge concentration in the large (Watson and Akuliarusiarsuup Kuua) rivers was twice that in the small Isunngua streams (avg. ± 2 s.d.: 37 ± 18 and 16 ± 9 μmol/mol, respectively). The large Watson River sample filtered 2 days after collection (JO-14) had slightly higher concentrations of all dissolved elements, which may reflect either some solute addition from sediments before filtration or a natural evolution toward higher concentrations at the end of the melt season since this sample was collected last, three days after the preceding Watson River sample.

3.2 Experimental Weathering

There are two potential complicating factors that are important to address. First, the solutions were not poisoned and it is therefore possible that some microbial growth took place during the two years of the experiment. However, the experiments were carried out in the dark, preventing the growth of any photosynthetic organisms. No change in sample appearance or odor was detected in any of the bottles during the experiment and we thus infer that any microbial growth in the experimental solutions was limited.

Second, the solution volume changed during the experiments due to sampling and potentially some evaporation. In total, sampling removed between 5 and 20% of the total initial solution volume by the end of the experiment. However, care was taken to subsample each solution with the sediment fully suspended, therefore keeping the sediment/water ratio constant. Based on the pre- and post-experiment volumes and taking into account the total subsampled volume, water mass balance was preserved within ±10–20%, with no systematic loss of water among the different samples. Finally, because the Isunngua stream samples had very low suspended sediment concentrations, they can effectively serve as control for any evaporative pre-concentration. The constant concentrations of conservative major cations in these samples therefore also indicate the lack of any evaporative water loss (see below).

During the lab experiment, some solute concentrations in the unfiltered stream samples continued to increase over the course of more than two years (**Figure 2**; **Tables 2**, **3**). Again, there was a clear distinction between the main river (AK, QK, and Watson) and the small Isunngua stream samples. For the main rivers, Na, K, and Mg concentrations increased slightly, by less than 10 μmol/L, to about 40–50, 25–30, and 14−20 μmol/L, respectively, over the course of the experiment (0–20% increase). Ca concentrations increased about two-fold, by 10 − 40 μmol/L to final values of ~ 60 − 70 μmol/L (**Figure 2**). Dissolved Si concentrations increased about 7-9-fold in a logarithmic fashion, reaching 130–230 μmol/L by the end of the experiment, more than any of the other analyzed solutes. In contrast, dissolved Ge concentrations increased only about two-fold, from 24–39 to ~70 pmol/L. For Isunngua streams, the major cation concentrations remained relatively constant throughout the experiment, with only Si concentrations showing a small increase from 7–18 to 26–37 μmol/L and Ge from 12–23 to 25–29 pmol/L.

Fe and Al concentrations in the main river samples showed a consistent decrease toward the end of the experiment, from ~12 to below 0.1–0.2 μmol/L (**Figures 3A**,**B**). Similarly, Mn concentrations decreased from ~100 to 60–70 nmol/L (**Figure 3C**). Although there are only a few data points available, Fe and Al concentrations in the Isunngua stream experiments appear similar to the main rivers, while Mn concentrations were much lower, ranging between 7–36 nmol/L after 50–190 days of reaction.

For the main rivers, Ge/Si ratios decreased significantly, from initial values of 1.5–1.9 to 0.4–0.6 μmol/mol by the end of the experiment (**Figure 3D**). In contrast, Isunngua stream Ge/Si remained relatively stable around 0.9–1.5 μmol/mol with the exception of JO-5, where initial Ge/Si of 2.2 decreased to 1.0 μmol/mol after 50 days of reaction.

Due to the low Ge concentrations, δ^{74}Ge composition could only be determined for the large Watson River sample that was filtered 2 days after collection (JO-14) and for the two other samples (QK and Watson rivers) after 470 days of reaction. The former was 0.86 ± 0.24‰, reported previously and lower than all other (non-glacial) rivers analyzed around the world to date (Baronas et al., 2017, Baronas et al., 2018), yet still higher than the 0.48 ~ 0.23‰ of the Watson River suspended load (**Figure 3E**). The two samples analyzed at the end of the experiment exhibited significantly higher δ^{74}Ge of 1.86 ± 0.28 and 2.24 ± 0.35‰, similar to non-glacial rivers elsewhere (Baronas et al., 2018).

3.3 Suspended Sediment Concentrations

Suspended sediment concentrations determined for three main river samples (JO-1, JO-12, and JO-13) at the end of the experiment were 0.6, 1.3, and 2.0 g/L, respectively, which is within the range of values previously measured (Wimpenny et al., 2010; Hindshaw et al., 2014; Hatton et al., 2019a). Suspended sediment concentrations were too low to reliably measure for any of the Isunngua streams and are estimated to be below 0.1 g/L.

4 DISCUSSION

4.1 Field Signatures

The chemical composition of the AK, QK, and Watson rivers, as well as of the Isunngua streams at similar locations to those sampled here, has been previously studied in detail by a number of researchers (e.g., Wimpenny et al., 2010, Wimpenny et al., 2011; Graly et al., 2014; Hindshaw et al., 2014, Hindshaw et al., 2019; Yde et al., 2014; Andrews and Jacobson, 2018; Hatton et al., 2019a). In general, the majority of weathering reactions are thought to occur in the subglacial environment, characterized by a large reactive mineral surface area due to glacial comminution and relatively short (but seasonally variable) water transit times, similar to many other glacial systems (Tranter and Wadham, 2014). More specifically, during the early melt season (May-June) the Leverett Glacier outlet appears to primarily drain distributed pockets of subglacial fluids which had been previously stored for months or longer

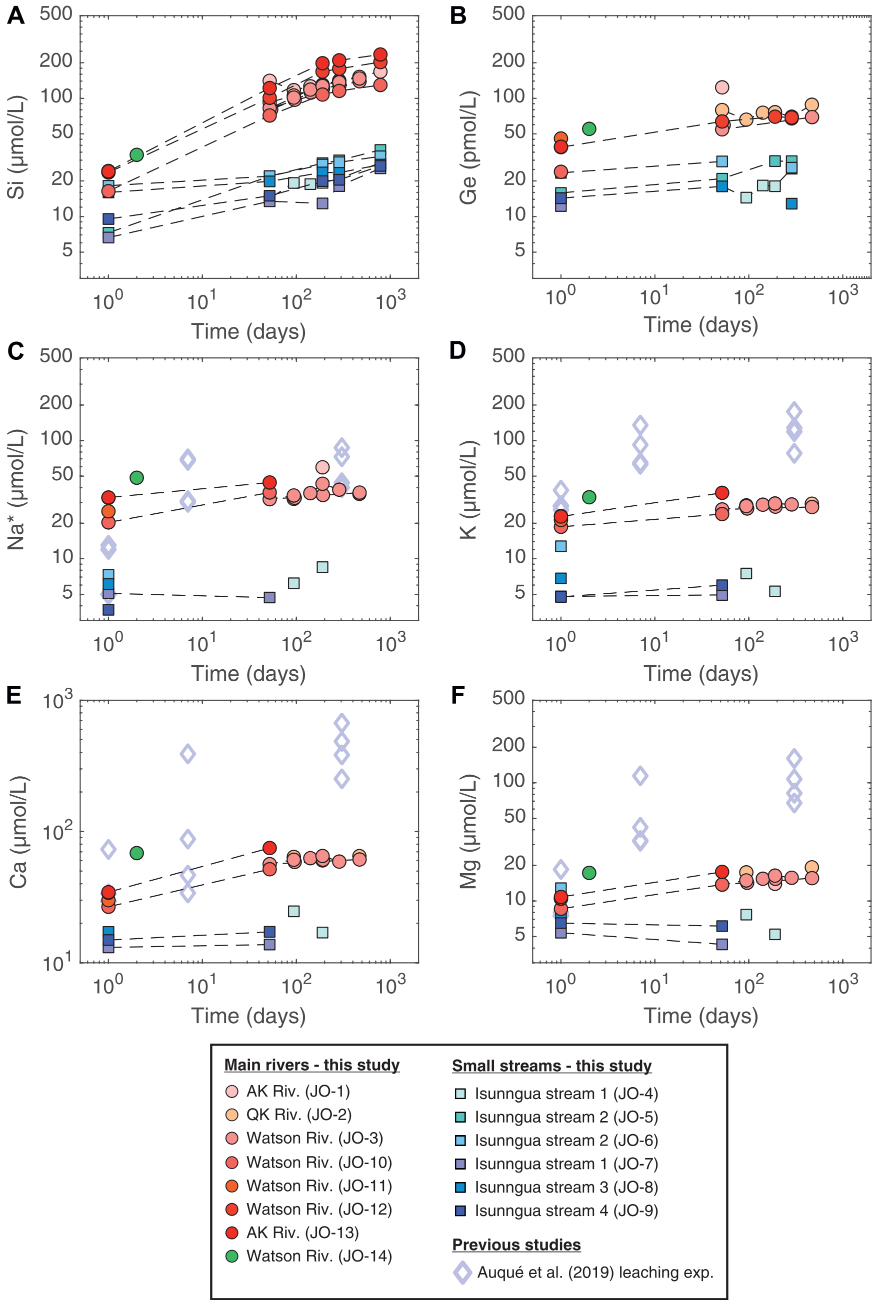

FIGURE 2 | Evolution of dissolved element concentrations during the course of the lab weathering experiment. Also shown are the results of Auqué et al. (2019), where Isunngua moraine till was leached using deionized water for up to 1 year but at a much higher sediment/water ratio equivalent to ~600 g/L suspended sediment concentration. Na* refers to Na concentrations corrected for cyclic salt inputs (Na* = Na–0.85 · Cl), where Cl concentrations were assumed to be equal to 3 and 0.5 μmol/L for main river and Isunngua stream samples, respectively, based on literature data (Wimpenny et al., 2010; Hindshaw et al., 2014; Hatton et al., 2019a; Deuerling et al., 2019).

(Chu et al., 2016) and thus exhibit relatively high solute concentrations (Bartholomew et al., 2011; Hindshaw et al., 2014; Hatton et al., 2019a). As melting and discharge increases through July-August, subglacial channels become established and connected, resulting in the efficient discharge of meltwater, which has only hours or days to interact with the subglacial bed (Chandler et al., 2013; Cowton et al., 2013; Lindbäck et al., 2015).

The lower concentrations of the small Isunngua streams draining the southern edge of Isunnguata Sermia can be readily explained by their smaller drainage basin and stream power, compared to the main rivers. The larger Watson River

TABLE 2 | River sediment weathering experiment data: main rivers (Akuliarusiarsuup Kuua (AK), Qinnguata Kuussua (QK), and Watson Rivers).

Sample ID	Subsample	Subsample date	Reaction time (days)	Ge (pmol/L)	Si (µmol/L)	Ge/Si (µmol/mol)	Na (µmol/L)	K (µmol/L)	Ca (µmol/L)	Mg (µmol/L)	SO_4 (µmol/L)	Al (µmol/L)	Fe (µmol/L)	Mn (nmol/L)	δ^{74}Ge (‰)
JO-1	Field	2014–08–19	1	–	–	–	–	–	–	–	–	–	–	–	–
	T-1	2014–10–10	52	124	141	0.88	–	–	–	–	–	–	–	–	–
	T-2	2014–11–21	94	–	117	–	–	–	–	–	–	–	–	–	–
	T-3	2015–01–07	141	–	126	–	–	–	–	–	–	–	–	–	–
	T-4	2015–02–25	190	–	131	–	62.4	29.3	60.2	14.0	16.5	1.1	0.04	95	–
	T-5	2015–06–01	286	68	142	0.48	–	–	–	–	–	–	–	–	–
	Final	2016–10–12	785	–	168	–	–	–	–	–	–	–	–	–	–
JO-2	Field	2014–08–19	1	–	–	–	–	–	–	–	–	–	–	–	–
	T-1	2014–10–10	52	80	92	0.86	–	–	–	–	–	5.1	1.1	126	–
	T-2	2014–11–21	94	66	106	0.62	35.1	28.3	64.0	17.5	19.2	2.0	0.21	91	–
	T-3	2015–01–07	141	76	118	0.64	–	–	–	–	–	2.6	0.39	73	–
	T-4	2015–02–25	190	76	130	0.59	–	–	–	–	–	–	–	–	–
	T-5	2015–06–01	286	70	138	0.51	–	–	–	–	–	0.89	0.05	53	–
	Final	2015–12–01	469	–	152	–	38.4	29.2	64.9	19.3	16.6	0.59	0.08	59	1.86 ± 0.28
JO-3A	Field	2014–08–19	1	–	–	–	–	–	–	–	–	–	–	–	–
	T-1	2014–10–10	54	59	80	0.74	–	–	–	–	–	1.7	0.30	107	–
	T-2	2014–11–21	96	–	97	–	35.8	26.7	58.7	14.3	17.9	0.90	0.07	100	–
	T-3	2015–01–07	143	–	112	–	–	–	–	–	–	1.4	0.15	91	–
	T-4	2015–02–25	192	–	121	–	37.6	27.6	61.0	15.4	17.0	0.99	0.08	82	–
	T-5	2015–06–01	288	–	129	–	–	–	–	–	–	0.08	–	73	–
	Final	2015–12–01	471	69	139	0.50	39.3	27.4	61.2	15.6	16.0	0.32	0.04	75	2.24 ± 0.35
JO-3B	Field	2014–08–19	1	--	--	–	–	–	–	–	–	–	–	–	–
	T-1	2014–10–10	52	55	82	0.66	34.9	26.2	56.4	13.8	15.7	0.37	0.05	–	–
	T-2	2014–11–21	94	–	101	–	37.3	27.9	61.0	14.9	24.6	1.1	0.08	–	–
	T-3	2015–01–07	141	–	119	–	38.9	28.7	62.6	15.4	16.8	1.7	0.15	–	–
	T-4	2015–02–25	190	–	127	–	46.1	29.3	65.1	16.4	17.4	0.79	0.04	–	–
	T-5	2015–06–01	286	–	137	–	41.4	28.8	59.0	15.7	16.5	0.54	0.01	–	–
	Final	2015–12–01	469	–	147	–	–	–	–	–	–	–	–	–	–
JO-10	Field	2014–08–23	1	24	16	1.46	23.3	18.6	26.7	8.6	–	–	–	–	–
	T-1	2014–10–10	52	–	72	–	36.4	23.9	51.6	13.8	15.4	1.5	0.24	164	–
	T-2	2015–02–25	190	–	108	–	–	–	–	–	–	–	–	–	–
	T-3	2015–06–01	286	–	115	–	–	–	–	–	–	–	–	–	–
	Final	2016–10–12	785	–	130	–	–	–	–	–	–	–	–	–	–
JO-12	Field	2014–08–24	1	39	24	1.63	35.8	23.0	34.2	10.5	–	1.9	0.90	87	–
	T-1	2014–10–10	52	64	101	0.63	–	–	–	–	–	–	–	–	–
	T-2	2015–02–25	190	70	168	0.42	–	–	–	–	–	–	–	–	–
	T-3	2015–06–01	286	69	178	0.39	–	–	–	–	–	–	–	–	–
	Final	2016–10–12	785	–	203	–	–	–	–	–	–	–	–	–	–
JO-13	Field	2014–08–24	1	39	24	1.62	36.0	22.8	34.5	10.8	–	–	–	–	–
	T-1	2014–10–10	52	–	122	–	47.2	36.1	74.9	17.6	27.5	1.1	0.14	171	–
	T-2	2015–02–25	190	–	198	–	–	–	–	–	–	–	–	–	–
	T-3	2015–06–01	286	–	210	–	–	–	–	–	–	–	–	–	–
	Final	2016–10–12	785	–	235	–	–	–	–	–	–	–	–	–	–
JO-14	Field	2014–08–29	2	55.1[a]	33.3[a]	1.66[a]	51.5[a]	33.1[a]	68.5	17.3[a]	29.0	8.5	4.1	104	0.86 ± 0.24[a]

[a] *Previously published in* Baronas et al. (2018).

TABLE 3 | River sediment weathering experiment data: small Isunngua streams.

Sample ID	Subsample	Subsample date	Reaction time (days)	Ge (pmol/L)	Si (μmol/L)	Ge/Si (μmol/mol)	Na (μmol/L)	K (μmol/L)	Ca (μmol/L)	Mg (μmol/L)	SO_4 (μmol/L)	Al (μmol/L)	Fe (μmol/L)	Mn (nmol/L)
JO-4	Field	2014–08–20	1	–	–	–	–	–	–	–	–	–	–	–
	T-1	2014–10–10	52	18	14	1.27	–	–	–	–	–	–	–	–
	T-2	2014–11–21	94	14	19	0.75	6.2	7.5	24.7	7.7	12.5	0.68	0.10	36
	T-3	2015–01–07	141	18	19	0.97	–	–	–	–	–	–	–	–
	T-4	2015–02–25	190	18	19	0.94	11.5	5.3	17.0	5.2	5.7	0.50	0.10	15
	T-5	2015–06–01	286	25	21	1.21	–	–	–	–	–	–	–	–
	Final	2016–10–12	785	–	28	–	–	–	–	–	–	–	–	–
JO-5	Field	2014–08–20	1	16	7	2.17	–	–	–	–	–	–	–	–
	T-1	2014–10–10	52	21	22	0.95	–	–	–	–	–	–	–	–
	T-2	2015–02–25	190	29	28	1.04	–	–	–	–	–	–	–	–
	T-3	2015–06–01	286	29	30	0.98	–	–	–	–	–	–	–	–
	Final	2016–10–12	785	–	37	–	–	–	–	–	–	–	–	–
JO-6	Field	2014–08–22	1	23	18	1.29	7.3	12.8	27.4	12.8	–	–	–	–
	T-1	2014–10–10	52	29	22	1.33	–	–	–	–	–	–	–	–
	T-2	2015–02–25	190	–	28	–	–	–	–	–	–	–	–	–
	T-3	2015–06–01	286	26	29	0.90	–	–	–	–	–	–	–	–
	Final	2016–10–12	785	–	32	–	–	–	–	–	–	–	–	–
JO-7	Field	2014–08–22	1	12	7	1.85	5.1	4.8	13.1	5.4	–	–	–	–
	T-1	2014–10–10	52	–	13	–	4.7	4.9	13.8	4.3	4.9	1.5	0.39	7
	T-2	2015–02–25	190	–	13	–	–	–	–	–	–	–	–	–
	T-3	2015–06–01	286	–	18	–	–	–	–	–	–	–	–	–
	Final	2016–10–12	785	–	26	–	–	–	–	–	–	–	–	–
JO-8	Field	2014–08–22	1	14	16	0.89	6.1	6.8	17.2	7.9	–	–	–	–
	T-1	2014–10–10	52	18	20	0.91	–	–	–	–	–	–	–	–
	T-2	2015–02–25	190	–	24	–	–	–	–	–	–	–	–	–
	T-3	2015–06–01	286	–	23	–	–	–	–	–	–	–	–	–
	Final	2016–10–12	785	–	28	–	–	–	–	–	–	–	–	–
JO-9	Field	2014–08–22	1	14	10	1.50	3.7	4.8	14.9	6.5	–	–	–	–
	T-1	2014–10–10	52	–	15	–	–	6.0	17.2	6.1	8.9	1.0	0.26	16
	T-2	2015–02–25	190	–	20	–	–	–	–	–	–	–	–	–
	T-3	2015–06–01	286	–	20	–	–	–	–	–	–	–	–	–
	Final	2016–10–12	785	–	27	–	–	–	–	–	–	–	–	–

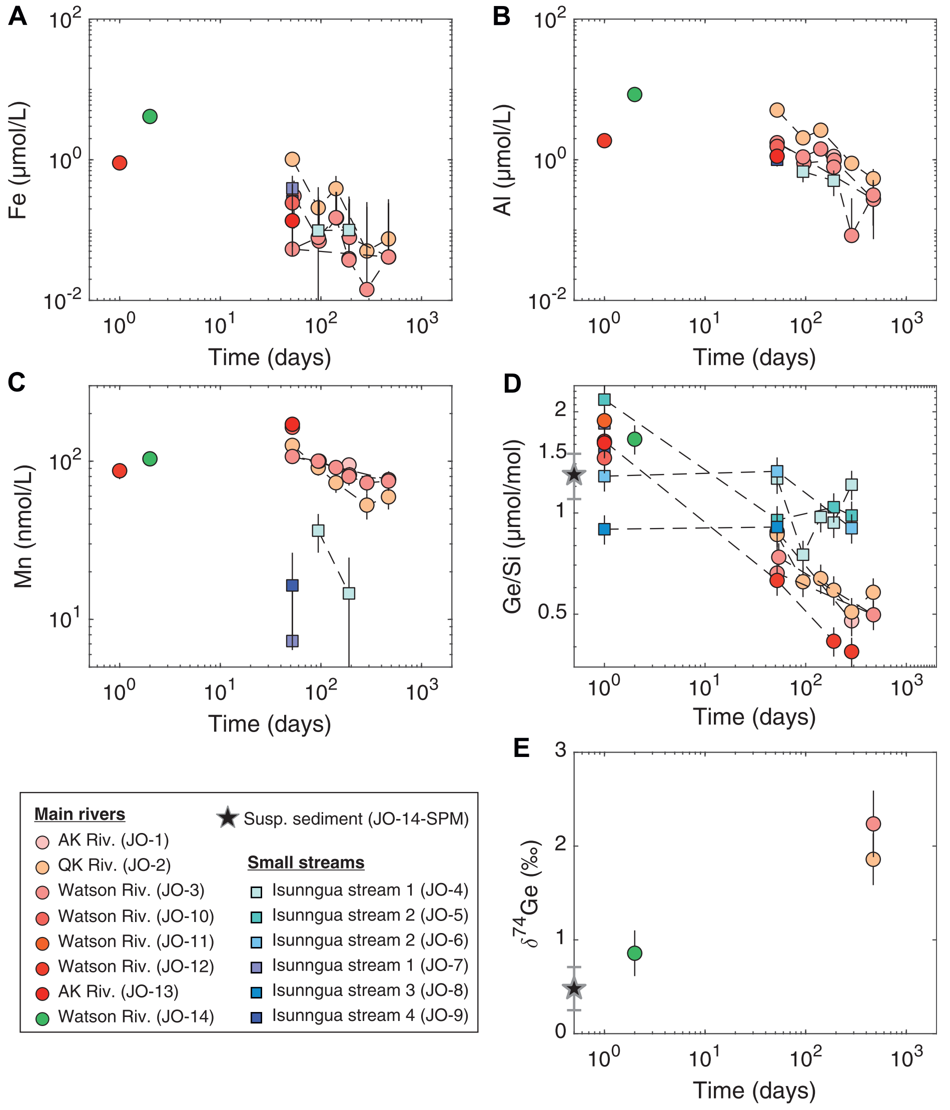

FIGURE 3 | Evolution of dissolved trace element concentrations, Ge/Si, and Ge isotope ratios during the course of lab weathering experiment. The Ge/Si and Ge isotope composition of the suspended sediment is shown as a black star at Time ≈ 0 in panels **(D)** and **(E)**.

catchment area can extend over ~12,000 km^2 under the Greenland Ice Sheet, with 1,000–2,000 m^3/s peak discharge (e.g., Lindbäck et al., 2015; Van As et al., 2017). In contrast, the Isunngua streams drain only 30–50 km^2 of the southern Isunnguata Sermia margin, with 10–20 m^3/s peak discharge (Rennermalm et al., 2013; Lindbäck et al., 2015), as most of the drainage from this glacier takes places through the Isortoq River, the main outlet to the west. The small marginal streams sampled here thus appear to discharge meltwater that had very little interaction with glacial till.

Sampled during the late melt season at the end of August, the AK, QK, and Watson rivers in this study primarily reflect the "efficient drainage," short water transit type fluids, as indicated by the low solute concentrations (**Table 1**). Once dissolved Na is corrected for cyclic salt inputs (see above), and assuming there is not significant Na supply from cation exchange with marine sedimentary rocks (Tipper et al., 2021), it can be assumed to come exclusively from the weathering of bedrock silicate minerals. Then, element-to-Na ratios can be used to assess the dissolution of different silicate and trace minerals and the precipitation of secondary phases (**Figure 4**). As noted in previous studies, the dissolved composition of the streams draining the Leverett and Russell glaciers is for the most part consistent with the dissolution of dominant gneissic bedrock minerals, such as plagioclase, K-feldspar, and hornblende, with some additional contribution of Ca from either trace carbonates or Ca-rich silicates [**Figure 4B**; Wimpenny et al. (2011); Hindshaw et al. (2014); Hindshaw et al. (2019)]. However, there is a significant non-stoichiometric enrichment in dissolved K (**Figure 4C**), consistent with the previously

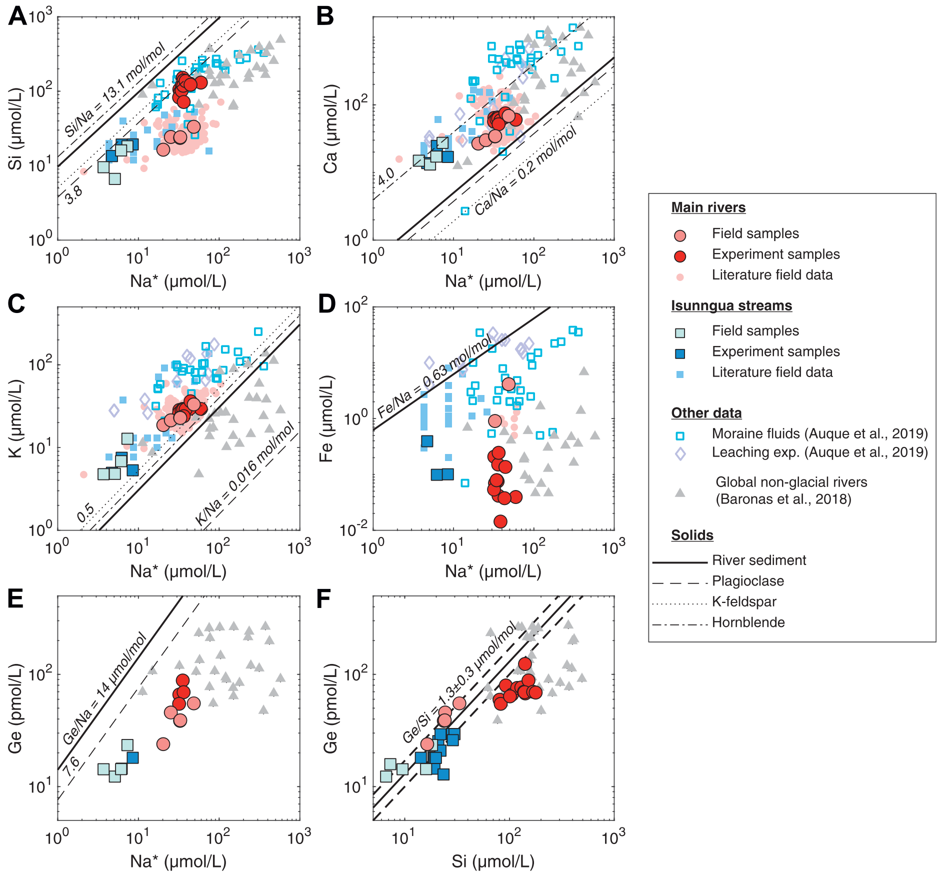

FIGURE 4 | Solute signatures of streams and dominant bedload minerals in southwest Greenland compared to experimental solutions and global rivers. Main (Akuliarusiarsuup Kuua, Qinnguata Kuussua, and Watson) river and Isunngua stream literature data from Wimpenny et al. (2010); Hindshaw et al. (2014); Andrews et al. (2018); Andrews and Jacobson (2018); Deuerling et al. (2019); Hatton et al. (2019a). River sediment and individual mineral compositions from Wimpenny et al. (2010) and Hindshaw et al. (2014), respectively. Na* refers to Na concentrations corrected for cyclic salt inputs (Na* = Na–0.85 · Cl). The solid and dashed lines in **(F)** show the Ge/Si and 2 S.D. uncertainty, respectively, of the Watson River suspended sediment, calculated from Ge concentration measured in this study and previously measured Si concentrations (**Table 1**).

proposed preferential leaching of glacially ground biotite in the Leverett catchment (Andrews and Jacobson, 2018; Auqué et al., 2019; Hindshaw et al., 2019). Since biotite and other micas typically exhibit higher Ge/Si ratios than other silicates (Mortlock and Froelich, 1987; Filippelli et al., 2000; Kurtz et al., 2002), their preferential weathering could result in elevated Ge/Si of the dissolved phase, as proposed previously for glacial streams in Alaska (Anders et al., 2003). However, there is no indication of this when the dissolved and the suspended sediment Ge/Si ratios are compared (**Figure 4F**), suggesting congruent weathering of silicates with regards to Ge/Si during weathering under the Greenland Ice Sheet.

In contrast to the major cations, we observed substantial depletion of dissolved Si and Fe in the field samples (**Figures 4A,D**), consistent with the subglacial precipitation of aSi (Hawkings et al., 2017; Hatton et al., 2019a; Urra et al., 2019) and Fe oxyhydroxide phases (Wimpenny et al., 2010; Hindshaw et al., 2014; Aciego et al., 2015; Stevenson et al., 2017; Auqué et al., 2019; Hawkings et al., 2020). Similarly to Si/Na*, Ge/Na* indicates Ge depletion, requiring uptake by secondary phases (**Figure 4E**). Again, the agreement between the solid and dissolved Ge/Si suggests that any uptake of these elements into secondary phases during subglacial weathering is likely congruent. This makes it unlikely that Si and Ge are taken up by aluminosilicate clays or Fe oxyhydroxides, which are known to lower Ge/Si in non-glacial streams (Froelich et al., 1992; Baronas et al., 2018). The phase removing Si and Ge from solution during initial subglacial weathering is thus most likely to be amorphous silica (aSi), which has been shown to control Si isotope dynamics under the Leverett Glacier and to represent the majority of Si exported from this watershed (Hawkings et al., 2018; Hatton et al., 2019a).

Although the subglacial formation mechanism of aSi is unknown, it likely involves either leaching or localized supersaturation at the surface of glacial till particles (Hawkings et al., 2017; Hatton et al., 2019b) which may be aided or even induced by freezing (Dietzel, 2005; Woronko and Hoch, 2011; Pokrovsky et al., 2013; Oelze et al., 2015; Alfredsson et al., 2016).

Possibly as a result of its unique formation mechanism, subglacial aSi has shown much weaker $\delta^{30}Si$ fractionation compared to most other secondary phases (Frings et al., 2016), with aSi only 0.1–0.2‰ lower than the silicate bedrock in Leverett Glacier outflow (Hawkings et al., 2018; Hatton et al., 2019a). Similarly, previous studies of aSi preserved in jasper and banded iron formation deposits suggest that there is limited Ge/Si fractionation during its inorganic precipitation (Grenne and Slack, 2003; Hamade et al., 2003; Delvigne et al., 2012), consistent with the lack of fractionation observed in our field samples. Although no direct measurements of $\delta^{74}Ge_{aSi}$ are available, given the strongly coupled fractionation of Ge/Si, δ^{30}Si, and δ^{74}Ge in world's rivers (Baronas et al., 2018), it is reasonable to expect that $\delta^{74}Ge_{aSi}$ is also similar to bedrock composition (as represented in our study by the Watson River SPM).

4.2 Experimental Weathering of Glacial River Sediments

The experimental setup did not aim to represent either the subglacial weathering environment (since riverine rock/water ratio is much lower), or the marine environment where the sediments are ultimately exported and deposited. Instead, the experiments offered a way to directly observe Ge/Si and δ^{74}Ge behavior during water-rock interaction in the absence of Ge and Si uptake by vegetation, unavoidable in most non-glacial catchments (Baronas et al., 2018). In addition, the Watson River suspended matter is composed primarily of recently produced proglacial till (Nelson et al., 2014; Harper et al., 2017; Overeem et al., 2017) and thus should primarily reflect local bedrock composition, with only a minor contribution from secondary aluminosilicate clays and Fe/Al-oxides (Wimpenny et al., 2010; Graly et al., 2016; Andrews and Jacobson, 2018; Auqué et al., 2019, but see Crompton et al. (2015)).

Importantly, by using aliquots of unfiltered river water, we allow continuity between the field-filtered and experimental samples and ensure that the dissolved composition of the dilute solutions is not dominated by cation exchange reactions or other artifacts associated with reacting lab-dried sediments with pure deionized water. This approach is distinct from previous weathering experiments of glacial till, which were designed to specifically simulate subglacial processes (Brown et al., 1996; Hodgkins et al., 1998; Brown et al., 2001; Auqué et al., 2019).

A direct comparison can be made with the results of the experiment performed by Auqué et al. (2019), who reacted deionized water with air-dried till collected from a moraine north of the Russell Glacier for up to 305 days at 5.5°C. Another key difference is the much higher sediment/water ratio in their experiment (570 g/L) compared to ours (<0.1–2.0 g/L). Despite the lower temperature, their cation release rates were much higher compared to ours, especially for Ca and Mg (**Figure 2**). This difference is most easily explained by the much higher sediment/water ratio and the rapid dissolution of secondary calcite and gypsum present in the moraine till (Auqué et al., 2019). The rapid cation exchange of dried sediments with deionized water is also likely to play a role during the early stage. Unfortunately, there were no dissolved Si or Ge concentrations reported for the Auqué et al. (2019) experiment, and we are therefore unable to assess how their different experimental parameters would influence the release of these elements.

4.2.1 Inferred Dissolution Reactions

In the absence of evaporation and biological effects, the evolution of solute concentrations during our weathering experiments (**Figures 2, 3**) should reflect the net effect of the dissolution and precipitation of a range of solid phases. Given the difference in physical conditions (higher temperature, access to oxygen, and longer water-rock interaction times, see **Section 4.3**) the dissolution-precipitation reactions during the experiment are likely to differ from those during subglacial weathering. Both the main river and the Isunngua stream samples started out enriched in K/Na* (and slightly in Ca/Na*) relative to the various solid phases (see discussion of field samples above). Throughout the experiment, the solute concentrations (incl. Na*) and ratios of the Isunngua samples remained relatively constant, which is not surprising given their very low SPM concentrations.

In the main river samples, an increase in Na* and K indicated the dissolution of a small amount of silicates, such as plagioclase (saturation index (SI) of −3.8 to −5.7) and K-feldspar (SI of −1.5 to −2.7), both dominant in the local bedrock (Hindshaw et al., 2014). The dissolved Ca/Na* increased slightly from around 1.1–1.6 mol/mol (**Figure 4B**), perhaps reflecting the dissolution of a small amount of trace calcite or garnet (Hindshaw et al., 2019). In contrast, K/Na* remained constant within uncertainty around 0.7 mol/mol (**Figure 4C**), which suggests negligible dissolution of biotite, consistent with a K-mica SI of 2.2–6.7.

Importantly, Si/Na* shows the largest change in the case of main river (AK, QK, and Watson) samples, increasing from values significantly below the mineral ratios at the beginning and approaching the mineral Si/Na by the end of the experiment (**Figure 4A**). Crucially, the *increase* in dissolved Si/Na* ratio varied between 4 and 33 mol/mol, often significantly higher than 4–5 mol/mol of the dominant orthogneiss rock, corrected for relatively unreactive quartz (Hindshaw et al., 2014). The excess Si added to solution is almost certainly due to the dissolution of highly reactive amorphous silica (undersaturated, SI = −1.1 to −1.6) previously formed in the subglacial environment (Hawkings et al., 2017; Hatton et al., 2019b). It was shown by Hatton et al. (2019a) that aSi is present in concentrations of up to 300 μmol/L in Leverett Glacier outflow and strongly impacts its dissolved Si dynamics, with an increased dissolution of aSi during mid-melt season in late June-July when subglacial waters with the longest residence times are being discharged. Over the duration of our experiment (470 or 785 days, depending on the sample), dissolved Si concentrations in main river samples increased by 113–235 μmol/L. For samples where suspended sediment concentrations were measured, this translated to a dissolution of 0.6–1.4 wt% SiO_2, in close agreement with the values of 0.3–1.4 wt% aSi determined for Leverett Glacier outflow using a Na_2CO_3 leaching technique (Hatton et al., 2019a).

Calculating the observed Si release rate during the experiment can potentially help further distinguish between the dissolution of aSi and primary silicate minerals. By assuming a sediment surface area typical of glacial till sediments [0.5–5 m^2/g, from Brantley et al. (1999)], we calculate Si dissolution rates in the range of $10^{-12} - 10^{-10}$ mol m^{-2} s^{-1} during the first few months, decreasing by about an order of magnitude to $10^{-13} - 10^{-11}$ mol m^{-2} s^{-1} by the end. These rates are consistent with the far-from-equilibrium rates determined in lab experiments of various freshly ground silicate minerals but significantly faster than rates determined in the field using soil profile data ($10^{-17} - 10^{-14}$ mol m^{-2} s^{-1}; White and Brantley (2003); Brantley and Olsen (2014)). This is despite the fact that dissolved Si at the end of the experiment approaches relatively high concentrations at which the precipitation of various secondary aluminosilicate clays is possible (kaolinite SI calculated between −1.2 and 4.5, depending on the pH). This could mean that the calculated rates are the lower limit estimate for gross dissolution. Although glacial environments are effective in producing reactive, freshly ground till from primary minerals, our samples were collected in outlet rivers and we expect the sediments to be subglacially pre-weathered to some degree, which should also lower their dissolution rate. Combined with the non-stoichiometric Si/Na* release discussed above, we therefore take the high Si release rates determined here as further evidence that Si is supplied to the solution primarily via the dissolution of aSi rather than crystalline silicate minerals. Indeed, the dissolution rates determined here agree very well with the 10^{-12} mol m^{-2} s^{-1} measured for the dissolution of pure aSi under very similar pH and temperature and conditions (Rimstidt et al., 2016). Importantly, the exact source of Si does not matter in our further consideration of Ge/Si and Ge isotope fractionation, as discussed below.

4.2.2 Ge/Si and Ge Isotope Ratio Evolution During the Experiment

There are two possible main interpretations of the evolution of dissolved Ge/Si and δ^{74}Ge over time: 1) simple addition via dissolution of a solid phase; and 2) addition coupled with removal via secondary phases. In the first case, the change in these ratios (**Figures 3D,E**) should reflect a mixing trend between the initial solution and the dissolving phase(s) supplying Ge. There was only a small increase in dissolved Ge concentrations over time (**Figure 2B**) which makes it difficult to calculate the composition of this putative source. In the cases where dissolved Ge detectably increased, the Ge/Si ratio added to solution ranged between 0.1 and 0.3 μmol/mol and δ^{74}Ge between 4.1 and 7.6‰. These values are very different from the Watson River suspended sediment composition (1.3 ± 0.3 μmol/mol and 0.48 ± 0.23‰) or any primary silicate minerals, which range between 0.5–6 μmol/mol and 0.4–0.8‰ (e.g., Mortlock and Froelich, 1987; Kurtz et al., 2002; Rouxel and Luais, 2017), thus ruling out silicates as the source of Ge (unless coupled with Ge removal to a secondary phase and associated fractionation; see the following section). It is theoretically possible that subglacially formed aSi is Ge-poor and isotopically heavy, as there is little data on Ge behavior during aSi formation (and no data on δ^{74}Ge), especially during glacial weathering. However, we deem this unlikely, given 1) the lack of Ge/Si and δ^{74}Ge fractionation in the field samples, as outlined above in **Section 4.1**; and 2) the fact that an overwhelming majority of secondary phases documented to date exhibit the opposite fractionation, i.e., high Ge/Si and low δ^{74}Ge (Murnane and Stallard, 1990; Froelich et al., 1992; Pokrovsky et al., 2014; Rouxel and Luais, 2017; Baronas et al., 2018; Qi et al., 2019; Baronas et al., 2020). Therefore, our preferred hypothesis is that the change in dissolved Ge/Si and δ^{74}Ge during the experiments reflects both the dissolution of aSi or silicates (or both) and Ge precipitation (or adsorption) coupled to isotopic fractionation.

4.2.3 Inferred Secondary Reactions and Ge Isotope Fractionation

Although it is difficult to discern whether any secondary phases precipitated during the weathering experiment, the decrease in Fe, Al, and Mn concentrations suggest that trace metals were scavenged from the solution, whether by precipitation of amorphous oxides, secondary clays, or by adsorption onto already present mineral surfaces. The amorphous $Al(OH)_3$ and $Fe(OH)_3$ were generally undersaturated (SI of −3.4–−1.1 and −1.1–2.2, respectively), while their ordered analogues of gibbsite and goethite were supersaturated (SI of −0.9–1.6 and 4.8–8.1, respectively, with negative values only at assumed pH = 9, see Methods). Wimpenny et al. (2010) and Hawkings et al. (2020) have shown that in west Greenland streams, the majority of Fe and Al in this size fraction are present in colloidal form (particles in the 10 kDa −0.2 μm size range). The experimental water sub-samples in this study were filtered through 0.2 μm pore size membrane and it is therefore possible that the measured decreasing concentrations of these metals reflect the flocculation of Fe and Al colloids into larger amorphous particles or their breakdown and the subsequent adsorption of Fe and Al onto existing particle surfaces or incorporation into forming aluminosilicate clays. Although we lack the data to determine the exact phase sequestering dissolved Ge, we speculate that adsorption to (or co-precipitation with) Fe oxyhydroxides is the most likely mechanism, based on the previously well documented adsorption and co-precipitation of Ge with Fe oxyhydroxides in a wide range of Earth surface environments (Burton et al., 1959; Bernstein, 1985; Bernstein and Waychunas, 1987; Mortlock and Froelich, 1987; Murnane et al., 1989; Anders et al., 2003; Pokrovsky et al., 2006; Baronas et al., 2018, Baronas et al., 2019), a behavior which is exploited in the Ge pre-concentration method used for isotope measurements (see Methods). It is therefore quite likely that dissolved Ge concentration and δ^{74}Ge composition is controlled by the same process that governs Fe (and possibly Al) concentrations.

Dissolved δ^{74}Ge increased significantly by the end of the experiment, from 0.86 ± 0.24 to 1.9–2.2‰ (**Table 2**; **Figure 3E**). These results are consistent with the broad negative correlation between Ge/Si and δ^{74}Ge in global river catchments, induced by Ge uptake into secondary weathering phases (Baronas et al., 2018). To quantitatively constrain δ^{74}Ge fractionation during the sediment weathering experiment, we use the following assumptions:

(1) The initial Ge and Si concentrations in the solution (i.e., in supraglacial melt water before rock-water

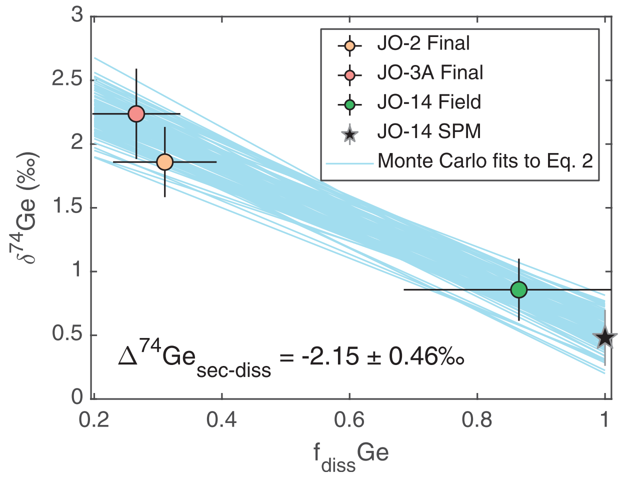

FIGURE 5 | Dissolved δ^{74}Ge as a function of dissolved Ge fraction remaining in solution (f_{diss}Ge). The blue lines show 100 examples of the 10,000 Monte Carlo linear regression fits incorporating uncertainty in both parameters. The slopes are equivalent to the fractionation factor $\Delta^{74}Ge_{sec-diss}$ (see **Eq. 2**) and the value shown is the mean ±2 S.D. of all Monte Carlo runs.

contact) were negligible. The dissolved Ge and Si in the initial unfiltered river water samples (at *t* = 1 day) used in the experiment were therefore taken to be derived from subglacial rock-water interaction that took place before sample collection.

(2) A negligible portion of Si released via the dissolution of aSi (or silicates) during the experiment was removed from solution by co-precipitation with secondary phases. This is reasonable, given the low dissolved Al and Fe concentrations compared with Si (**Figure 3**).

(3) Mineral dissolution released Ge into solution with a $Ge/Si_{dissolving}$ ratio of 1.6 ± 0.4 μmol/mol, calculated as the mean and standard deviation of all field-filtered river samples (**Table 1**), slightly higher than the 1.3 ± 0.3 μmol/mol of bulk sediment (**Figure 3D**), correcting for unreactive quartz. This $Ge/Si_{dissolving}$ value could be reflecting the dissolution of either aSi or primary silicate minerals. It has only a small effect on the calculated Ge isotope fractionation factor (see **Section 4.2.1**).

(4) The difference between measured Ge concentrations at the end of the experiment and those expected from aSi (or silicate) dissolution reflects the amount of Ge removed by secondary phase uptake (e.g., via incorporation into Fe oxyhydroxides). The fraction of Ge remaining in solution can then be calculated as:

$$f_{diss}Ge = \frac{Ge_{measured}}{Ge/Si_{dissolving} \cdot Si_{measured}} \tag{1}$$

where $Ge_{measured}$ and $Si_{measured}$ are the concentrations measured at the end of the weathering experiment ("Final" samples, **Table 2**).

The increase in δ^{74}Ge with time (coupled with relatively constant Ge concentrations) is most simply explained by a loss of isotopically light Ge from solution, while dissolution of aSi continues. Given the batch reactor setup and the long sediment-water interaction time, it is reasonable to assume that Ge removed from solution is able to isotopically equilibrate with dissolved Ge (especially if the removal mechanism is reversible adsorption to Fe oxyhydroxides), in which case Ge isotope fractionation can be described using the equilibrium (or "batch") isotope fractionation model:

$$\delta^{74}Ge_{diss} = \delta^{74}Ge_{primary} - \Delta^{74}Ge_{sec-diss} \cdot (1 - f_{diss}Ge) \tag{2}$$

where $\delta^{74}Ge_{primary}$ is the composition of the dissolving phase(s) (assumed to be equal to the Watson suspended load value of 0.48 ± 0.23‰; see **Sections 4.1**, **4.2.2**) and $\Delta^{74}Ge_{sec-diss}$ is the isotopic fractionation factor associated with Ge removal from solution. Using **Eq. 2** on the sediment weathering experimental data yields $\Delta^{74}Ge_{sec-diss}$ = −2.15 ± 0.46‰ (**Figure 5**), where the uncertainty (reported as 2 S.D.) is quantified using a Monte Carlo approach (implemented in MATLAB 2019b and supplied in the **Supplementary Material**) that repeats the fit of **Eq. 2** 10,000 times, taking into account analytical and propagated uncertainties in $\delta^{74}Ge_{diss}$ and f_{diss}Ge, respectively. This value is in good agreement with both the −1.7 ± 0.1‰ determined for experimental Ge adsorption onto pure goethite (Pokrovsky et al., 2014), as well as the −4.9 to −1.6 range of $\Delta^{74}Ge_{sec-diss}$ determined for global non-glacial rivers (Baronas et al., 2018). It is significantly larger than the $\Delta^{74}Ge_{sec-diss}$ of −0.3 ± 1.1‰, calculated as the difference between Watson River dissolved and SPM signatures and indicating the limited isotopic fractionation in the subglacial environment (Baronas et al., 2018).

4.3 Implications for Ge Isotope Behavior During Subglacial and Non-glacial Weathering

As discussed above, subglacial weathering results in less pronounced Ge uptake by secondary phases (although this may be masked to some degree by the incongruent weathering of Ge-rich silicate phases) and little to no fractionation of Ge isotopes, in contrast to the clear fractionation of both Ge/Si and δ^{74}Ge observed during the weathering experiment. Overall, the combination of field and experimental evidence published to date points to distinct Ge behavior during subglacial vs. non-glacial weathering, with the latter resulting in much more pronounced δ^{74}Ge fractionation (Baronas et al., 2018). As we infer above, this is likely the result of the distinct secondary phases dominating Ge uptake in each environment (aSi under the glaciers vs. Fe oxyhydroxides or aluminosilicate clays during the experiment and in natural non-glacial environments), which are in turn controlled by the distinct weathering regimes, and in particular the low temperatures, high rates of comminution, and relatively short water residence times in the subglacial environment.

While the role that water transit times play in the dynamics of chemical weathering is poorly understood, it has very important implications for our understanding of the relationship between weathering and climate (e.g., Maher and Chamberlain, 2014; Li, 2019; Torres and Baronas, 2021). Therefore, the possibility that dissolved δ^{74}Ge might be primarily controlled by rock-water interaction time and may help understand the kinetics of weathering is an intriguing prospect. It is well documented that groundwaters that are years, decades, and even millennia old form a substantial component of discharge in many non-glacial catchments (Jasechko, 2019). In contrast, the glacial river catchments sampled here are thought to store only small amounts of water interannually (Lindbäck et al., 2015; Van As et al., 2017), with any water stored over winter likely discharged next year (Chu et al., 2016). The contrast in δ^{74}Ge between glacial and non-glacial catchments, along with the increase in δ^{74}Ge during our experiment, provides support for the hypothesis that dissolved Ge isotopes are increasingly fractionated with prolonged rock-water reaction time.

An important caveat is that potential seasonal and spatial variations in δ^{74}Ge of glacial streams are unconstrained, given the single field data point (**Table 1**). However, this sample was collected during peak discharge in the late melt-season (Van As et al., 2017), dominated by the efficient drainage of recent meltwater. Given that the bulk of Watson River annual discharge and solute flux is comprised of such recent meltwater (Yde et al., 2014; Linhoff et al., 2017), our samples should thus provide a reasonable approximation of the average annual composition (also supported by the agreement with literature data in **Figures 4A–C**). In addition, a timeseries dataset of Alaskan glacial rivers shows that the highest (least fractionated) dissolved Ge/Si is encountered during peak melt-season (Mortlock and Froelich, 1987), consistent with our data in Greenland. Nevertheless, given the overall paucity of data, it remains an open question why δ^{74}Ge and Ge/Si remain unfractionated during subglacial weathering and how their behavior relates to different weathering reaction dynamics.

4.4 Implications for Amorphous Si Bioavailability

Our experimental results add to the growing evidence that the flux of amorphous Si from glacial landscapes is several times higher than that of dissolved silica (Hawkings et al., 2017, Hawkings et al., 2018; Hatton et al., 2019a; Hatton et al., 2019b). Importantly, the high Si release rates observed during our experiments under ambient 25°C temperature and circum-neutral pH conditions (see **Section 4.2.1** and **Figure 2**) indicate that this aSi is highly labile and thus likely an important source of dissolved silica in the offshore marine environment. Given the lower temperature but the higher ionic activity of seawater, aSi dissolution rates offshore are expected to be similar to our experiments (Kato and Kitano, 1968; Icenhower and Dove, 2000; Dove et al., 2008; Rimstidt et al., 2016). Our results therefore fully support the similar experimental data of Hawkings et al. (2017), as well as their prediction that aSi dissolution is a major source of dissolved Si in the Watson River estuary. Given that dissolved Si is an important nutrient for diatom growth in the region, the export of highly soluble aSi (along with other nutrients) by Greenland runoff is likely to play an important role as the offshore productivity and ecosystem dynamics shift with changing climate (Lawson et al., 2014; Hawkings et al., 2015; Tremblay et al., 2015; Arrigo et al., 2017; Hendry et al., 2019).

4.5 Implications for the Interpretation of Paleorecords

Lastly, our results suggest that δ^{74}Ge and Ge/Si signatures recorded in marine biogenic silica (diatom or sponge) deposits have the potential to reconstruct variations in (sub)glacial weathering over glacial-interglacial cycles. Given the substantial flux of glacial aSi, which may even rival total riverine dissolved silica flux during deglaciations (Hawkings et al., 2017, Hawkings et al., 2018), as well as its rapid dissolution rate [**Section 4.4**; Hawkings et al. (2017)], it may similarly provide a large and variable flux of dissolved Ge. In the case of Ge/Si and δ^{74}Ge, the continental weathering signal would first have to be deconvolved from the significant but poorly quantified fractionation during marine sediment authigenesis, which may vary with changes in temperature, detrital inputs, and/or shelf sediment Fe redox conditions (Hammond et al., 2004; Baronas et al., 2016, Baronas et al., 2017, Baronas et al., 2019).

Importantly, evidence to date suggests limited biological fractionation of δ^{74}Ge and Ge/Si by diatoms (e.g., Shemesh et al., 1989; Sutton et al., 2010; Rouxel and Luais, 2017) and constant, local temperature- and chemistry-independent, δ^{74}Ge fractionation by siliceous sponges (Guillermic et al., 2017). The relative lack of biological influence on δ^{74}Ge contrasts with δ^{30}Si, whose signatures in seawater and marine paleorecords are dominated by biological fractionation effects (e.g., Hendry and Brzezinski, 2014; Sutton et al., 2018). Indeed, a preliminary Southern Ocean diatom paleorecord indicates a decoupling of seawater δ^{74}Ge, Ge/Si, and δ^{30}Si signatures across the penultimate deglaciation (Mantoura, 2006; Rouxel and Luais, 2017). Although additional work is needed, this is an early indication that this multi-proxy combination may help constrain past variations in glacial Si export and other aspects of the coupled global Si-Ge cycle.

5 CONCLUSION

This study investigated Ge/Si and δ^{74}Ge signatures in southwest Greenland streams draining the Greenland Ice Sheet and during continued river sediment-water interaction in the laboratory for up to 2 years. In the Watson River and its tributaries draining the large subglacial catchment, both Ge and Si were depleted relative to dissolved Na, indicating removal into secondary phases during subglacial weathering. However, the dissolved Ge/Si and δ^{74}Ge signatures were close to the silicate parent mineral composition, indicating limited fractionation (and possibly some preferential weathering of Ge-rich minerals, such as biotite), in contrast to non-glacial rivers which typically exhibit fractionated composition (Baronas et al., 2018). Sediment weathering experiments resulted in a large increase in dissolved Si concentrations, a much smaller increase in dissolved Ge, a decrease in dissolved Ge/Si, and a significant increase in δ^{74}Ge.

We propose that a significant portion of Ge is incorporated into subglacially formed amorphous silica (aSi), resulting in minimal Ge/Si and δ^{74}Ge fractionation under the ice sheet. The formation and re-dissolution of aSi has been recently identified as the main control on δ^{30}Si in subglacial environments (Hawkings et al., 2018; Hatton et al., 2019a; Hatton et al., 2019b). During continued glacial till weathering in the laboratory lasting 470–785 days, both Si and Ge were released as aSi dissolved, and Ge was then incorporated into secondary phases. This resulted in significant fractionation of Ge/Si and δ^{74}Ge, bringing these signatures close to the values observed in non-glacial rivers. The change in dissolved δ^{74}Ge composition during the experiment was correlated with the estimated fraction of Ge removed from solution. Applying a simple batch (closed system equilibrium) model to the experimental data yielded a $\Delta^{74}\mathrm{Ge}_{\mathrm{sec-diss}}$ fractionation factor of −2.15 ± 0.46‰, consistent with previously determined values for experimental Ge adsorption onto Fe oxyhydroxide phases (Pokrovsky et al., 2014). These results directly demonstrate that the fractionated dissolved Ge/Si and Ge isotope signatures in rivers can be generated solely through weathering reactions in the absence of vegetation. The high aSi dissolution rate during our experiments also provides evidence that it is likely to be readily bioavailable, supporting the role of glacial discharge as an important source of dissolved silica to coastal marine biosilicifier communities.

DATA AVAILABILITY STATEMENT

The original contributions presented in the study are included in the article/**Supplementary Material**, further inquiries can be directed to the corresponding author.

AUTHOR CONTRIBUTIONS

JB designed the study. DH and LS obtained the funding. MB and LP collected the samples. JB and OR performed Ge isotope analyses. JB performed the experiments and modeling and wrote the article, with input from all co-authors.

FUNDING

Fieldwork was supported by NASA Cryosphere Program Grants NNX14AH93G and 80NSSC19K0942 to LS, managed by Thomas P. Wagner, Colene Haffke, and Thorsten Markus. Laboratory and analytical work was supported by United States NSF grants OCE 1061700 and 1260692 to DH. JB was also supported by an InterRidge research fellowship and a John Montagne Award from GSA Quaternary Geology and Geomorphology Division. Support to OR was provided by the Institut Carnot Ifremer EDROME and the LabexMer ANR-10-LABX-19–01.

ACKNOWLEDGMENTS

Field, logistics, and cargo support was provided by Polar Field Services. Josh West is thanked for allowing the experiment to continuously run and take up space in his incubator for 2 years. Yi Hou is thanked for help with Si concentration analyses at USC and Ed Tipper for support with ICP-AES analyses in Cambridge. We thank the reviewers for constructive comments that helped improve the manuscript.

SUPPLEMENTARY MATERIAL

The Supplementary Material for this article can be found online at: https://www.frontiersin.org/articles/10.3389/feart.2021.551900/full#supplementary-material.

REFERENCES

Aciego, S. M., Stevenson, E. I., and Arendt, C. A. (2015). Climate vs. geological controls on glacial meltwater micronutrient production in southern Greenland. *Earth Planet. Sci. Lett.* 424, 51–58. doi:10.1016/j.epsl.2015.05.017

Alfredsson, H., Clymans, W., Hugelius, G., Kuhry, P., and Conley, D. J. (2016). Estimated storage of amorphous silica in soils of the circum-Arctic tundra region. *Global Biogeochem. Cycles* 30, 479–500. doi:10.1002/2015GB005344

Anders, A. M., Sletten, R., Derry, L., and Hallet, B. (2003). Germanium/silicon ratios in the Copper River Basin, Alaska: weathering and partitioning in periglacial vs. glacial environments. *J. Geophys. Res.* 108, 6005. doi:10.1029/2003JF000026

Anderson, S. P. (2007). Biogeochemistry of glacial landscape systems. *Annu. Rev. Earth Planet. Sci.* 35, 375–399. doi:10.1146/annurev.earth.35.031306.140033

Anderson, S. P., Drever, J. I., and Humphrey, N. F. (1997). Chemical weathering in glacial environments. *Geology* 25, 399. doi:10.1130/0091-7613(1997)025¡0399:CWIGE¿2.3.CO;2

Andrews, M. G., and Jacobson, A. D. (2018). Controls on the solute geochemistry of subglacial discharge from the Russell Glacier, Greenland Ice Sheet determined by radiogenic and stable Sr isotope ratios. *Geochim. Cosmochim. Acta* 239, 312–329. doi:10.1016/j.gca.2018.08.004

Andrews, M. G., Jacobson, A. D., Osburn, M. R., and Flynn, T. M. (2018). Dissolved carbon dynamics in meltwaters from the Russell Glacier, Greenland ice sheet. *J. Geophys. Res.* 123, 2922–2940. doi:10.1029/2018JG004458

Arrigo, K. R., van Dijken, G. L., Castelao, R. M., Luo, H., Rennermalm, A. K., Tedesco, M., et al. (2017). Melting glaciers stimulate large summer phytoplankton blooms in southwest Greenland waters. *Geophys. Res. Lett.* 44, 6278–6285. doi:10.1002/2017GL073583

Auqué, L. F., Puigdomenech, I., Tullborg, E. L., Gimeno, M. J., Grodzinsky, K., and Hogmalm, K. J. (2019). Chemical weathering in a moraine at the ice sheet margin at Kangerlussuaq, western Greenland. *Arct. Antarct. Alp. Res.* 51, 440–459. doi:10.1080/15230430.2019.1660125

Baronas, J. J., Hammond, D. E., Berelson, W. M., McManus, J., and Severmann, S. (2016). Germanium-silicon fractionation in a river-influenced continental margin: the Northern Gulf of Mexico. *Geochim. Cosmochim. Acta* 178, 124–142. doi:10.1016/j.gca.2016.01.028

Baronas, J. J., Hammond, D. E., McManus, J., Wheat, C. G., and Siebert, C. (2017). A global Ge isotope budget. *Geochim. Cosmochim. Acta* 203, 265–283. doi:10.1016/j.gca.2017.01.008

Baronas, J. J., Hammond, D. E., Rouxel, O. J., and Monteverde, D. R. (2019). A first look at dissolved Ge isotopes in marine sediments. *Front. Earth Sci.* 7, 1–17. doi:10.3389/feart.2019.00162

Baronas, J. J., Torres, M. A., West, A. J., Rouxel, O. J., Georg, R. B., Bouchez, J., et al. (2018). Ge and Si isotope signatures in rivers: a quantitative multi-proxy approach. *Earth Planet. Sci. Lett.* 503, 194–215. doi:10.1016/j.epsl.2018.09.022

Baronas, J. J., West, A. J., Burton, K. W., Hammond, D. E., Opfergelt, S., Pogge von Strandmann, P. A. E., et al. (2020). Ge and Si isotope behavior during intense tropical weathering and ecosystem cycling. *Global Biogeochem. Cycles* 34. e2019GB006522. doi:10.1029/2019GB006522

Bartholomew, I., Nienow, P., Sole, A., Mair, D., Cowton, T., Palmer, S., et al. (2011). Supraglacial forcing of subglacial drainage in the ablation zone of the Greenland ice sheet. *Geophys. Res. Lett.* 38, 1–5. doi:10.1029/2011GL047063

Bernstein, L. (1985). Germanium geochemistry and mineralogy. *Geochim. Cosmochim. Acta* 49, 2409–2422. doi:10.1016/0016-7037(85)90241-8

Bernstein, L. R., and Waychunas, G. A. (1987). Germanium crystal chemistry in hematite and goethite from the Apex Mine, Utah, and some new data on germanium in aqueous solution and in stottite. *Geochim. Cosmochim. Acta* 51, 623–630. doi:10.1016/0016-7037(87)90074-3

Brantley, S. L., White, A. F., and Hodson, M. E. (1999). “Surface area of primary silicate minerals,” in *Growth, Dissolution and Pattern Formation in Geosystems*. Dordrecht: Springer, 291–326.

Brantley, S., and Olsen, A. (2014). “Reaction kinetics of primary rock-forming minerals under ambient conditions,” in *Treatise on Geochemistry*. 2nd Edn. Elsevier, 7, 69–113.

Brown, G. H. (2002). Glacier meltwater hydrochemistry. *Appl. Geochem.* 17, 855–883. doi:10.1016/S0883-2927(01)00123-8

Brown, G. H., Hubbard, B., and Seagren, A. G. (2001). Kinetics of solute acquisition from the dissolution of suspended sediment in subglacial channels. *Hydrol. Process.* 15, 3487–3497. doi:10.1002/hyp.1039

Brown, G. H., Tranter, M., and Sharp, M. J. (1996). Experimental investigations of the weathering of suspended sediment by alpine glacial meltwater. *Hydrol. Process.* 10, 579–597. doi:10.1002/(SICI)1099-1085(199604)10:4<579::AID-HYP393>3.0.CO;2-D

Burton, J., Culkin, F., and Riley, J. (1959). The abundances of gallium and germanium in terrestrial materials. *Geochim. Cosmochim. Acta* 16, 151–180. doi:10.1016/0016-7037(59)90052-3

Chandler, D. M., Wadham, J. L., Lis, G. P., Cowton, T., Sole, A., Bartholomew, I., et al. (2013). Evolution of the subglacial drainage system beneath the Greenland Ice Sheet revealed by tracers. *Nat. Geosci.* 6, 195–198. doi:10.1038/ngeo1737

Chillrud, S. N., Pedrozo, F., Temporetti, P., Planas, H., and Froelich, P. (1994). Chemical weathering of phosphate and germanium in glacial meltwater streams: effects of subglacial pyrite oxidation. *Limnol. Oceanogr.* 39, 1130–1140. doi:10.4319/lo.1994.39.5.1130

Chu, W., Schroeder, D. M., Seroussi, H., Creyts, T. T., Palmer, S. J., and Bell, R. E. (2016). Extensive winter subglacial water storage beneath the Greenland Ice Sheet. *Geophys. Res. Lett.* 43, 484–512. doi:10.1002/2016GL071538

Cornelis, J.-T., Delvaux, B., Georg, R., Lucas, Y., Ranger, J., and Opfergelt, S. (2011). Tracing the origin of dissolved silicon transferred from various soil-plant systems towards rivers: a review. *Biogeosciences* 8, 89–112. doi:10.5194/bg-8-89-2011

Cowton, T., Nienow, P., Sole, A., Wadham, J., Lis, G., Bartholomew, I., et al. (2013). Evolution of drainage system morphology at a land-terminating Greenlandic outlet glacier. *J. Geophys. Res. Earth Surf.* 118, 29–41. doi:10.1029/2012JF002540

Crompton, J. W., Flowers, G. E., Kirste, D., Hagedorn, B., and Sharp, M. J. (2015). Clay mineral precipitation and low silica in glacier meltwaters explored through reaction-path modelling. *J. Glaciol.* 61, 1061–1078. doi:10.3189/2015JoG15J051

Davison, B. J., Sole, A. J., Livingstone, S. J., Cowton, T. R., and Nienow, P. W. (2019). The influence of hydrology on the dynamics of land-terminating sectors of the Greenland ice sheet. *Front. Earth Sci.* 7, 1–24. doi:10.3389/feart.2019.00010

De La Rocha, C., Brzezinski, M., DeNiro, M., and Shemesh, A. (1998). Silicon-isotope composition of diatoms as an indicator of past oceanic change. *Nature* 395, 680–683.

Delvigne, C., Cardinal, D., Hofmann, A., and André, L. (2012). Stratigraphic changes of Ge/Si, REE+Y and silicon isotopes as insights into the deposition of a Mesoarchaean banded iron formation. *Earth Planet. Sci. Lett.* 355–356, 109–118. doi:10.1016/j.epsl.2012.07.035

Derry, L. A., Kurtz, A. C., Ziegler, K., and Chadwick, O. A. (2005). Biological control of terrestrial silica cycling and export fluxes to watersheds. *Nature* 433, 728–731. doi:10.1038/nature03299

Deuerling, K. M., Martin, J. B., Martin, E. E., Abermann, J., Myreng, S. M., Petersen, D., et al. (2019). Chemical weathering across the western foreland of the Greenland Ice Sheet. *Geochim. Cosmochim. Acta* 245, 426–440. doi:10.1016/j.gca.2018.11.025

Dietzel, M. (2005). Impact of cyclic freezing on precipitation of silica in Me-SiO2-H2O systems and geochemical implications for cryosoils and -sediments. *Chem. Geol.* 216, 79–88. doi:10.1016/j.chemgeo.2004.11.003

Dove, P. M., Han, N., Wallace, A. F., and De Yoreo, J. J. (2008). Kinetics of amorphous silica dissolution and the paradox of the silica polymorphs. *Proc. Natl. Acad. Sci.* 105, 9903–9908. doi:10.1073/pnas.0803798105

Dubnick, A., Wadham, J., Tranter, M., Sharp, M., Orwin, J., Barker, J., et al. (2017). Trickle or treat: the dynamics of nutrient export from polar glaciers. *Hydrol. Process.* 31, 1776–1789. doi:10.1002/hyp.11149

Engström, J., and Klint, K. E. S. (2014). Continental collision structures and post-orogenic geological history of the kangerlussuaq area in the southern part of the nagssugtoqidian orogen, central west Greenland. *Geosciences* 4, 316–334. doi:10.3390/geosciences4040316

Escoube, R., Rouxel, O. J., Edwards, K., Glazer, B., and Donard, O. F. X. (2015). Coupled Ge/Si and Ge isotope ratios as geochemical tracers of seafloor hydrothermal systems: case studies at Loihi Seamount and East Pacific Rise 950’N. *Geochim. Cosmochim. Acta* 167, 93–112. doi:10.1016/j.gca.2015.06.025

Escoube, R., Rouxel, O. J., Luais, B., Ponzevera, E., and Donard, O. F. (2012). An intercomparison study of the germanium isotope composition of geological reference materials. *Geostand. Geoanal. Res.* 36, 149–159. doi:10.1111/j.1751-908X.2011.00135.x

Filippelli, G., Carnahan, J., Derry, L., and Kurtz, A. (2000). Terrestrial paleorecords of Ge/Si cycling derived from lake diatoms. *Chem. Geol.* 168, 9–26. doi:10.1016/S0009-2541(00)00185-6

Frings, P. J., Clymans, W., Fontorbe, G., De La Rocha, C. L., and Conley, D. J. (2016). The continental Si cycle and its impact on the ocean Si isotope budget. *Chem. Geol.* 425, 12–36. doi:10.1016/j.chemgeo.2016.01.020

Froelich, P., Blanc, V., Mortlock, R., Chillrud, S., Dunstan, W., Udomkit, A., et al. (1992). River fluxes of dissolved silica to the ocean were higher during glacials: Ge/Si in diatoms, rivers, and oceans. *Paleoceanography* 7, 739–767. doi:10.1029/92PA02090

Froelich, P., Hambrick, G., Andreae, M., Mortlock, R., and Edmond, J. (1985). The geochemistry of inorganic germanium in natural waters. *J. Geophys. Res.* 90, 1133–1141. doi:10.1029/JC090iC01p01133

Georg, R., Reynolds, B., West, A., Burton, K., and Halliday, A. (2007). Silicon isotope variations accompanying basalt weathering in Iceland. *Earth Planet. Sci. Lett.* 261, 476–490. doi:10.1016/j.epsl.2007.07.004

Gerringa, L. J., Alderkamp, A. C., Laan, P., Thuróczy, C. E., De Baar, H. J., Mills, M. M., et al. (2012). Iron from melting glaciers fuels the phytoplankton blooms in Amundsen Sea (Southern Ocean): iron biogeochemistry. *Deep-Sea Res. Part II* 71–76, 16–31. doi:10.1016/j.dsr2.2012.03.007

Graly, J. A., Humphrey, N. F., and Harper, J. T. (2016). Chemical depletion of sediment under the Greenland ice sheet. *Earth Surf. Process. Landforms* 41, 1922–1936. doi:10.1002/esp.3960

Graly, J. a., Humphrey, N. F., Landowski, C. M., and Harper, J. T. (2014). Chemical weathering under the Greenland ice sheet. *Geology* 42, 551–554. doi:10.1130/G35370.1

Grenne, T., and Slack, J. F. (2003). Paleozoic and Mesozoic silica-rich seawater: evidence from hematitic chert (jasper) deposits. *Geology* 31, 319–322. doi:10.1130/0091-7613(2003)031<0319:PAMSRS>2.0.CO;2

Guillermic, M., Lalonde, S. V., Hendry, K. R., and Rouxel, O. J. (2017). The isotope composition of inorganic germanium in seawater and deep sea sponges. *Geochim. Cosmochim. Acta* 212, 99–118. doi:10.1016/j.gca.2017.06.011

Hamade, T., Konhauser, K. O., Raiswell, R., Goldsmith, S., and Morris, R. C. (2003). Using Ge/Si ratios to decouple iron and silica fluxes in Precambrian banded iron formations. *Geology* 31, 35. doi:10.1130/0091-7613(2003)031<0035:UGSRTD>2.0.CO;2

Hammond, D. E., McManus, J., and Berelson, W. M. (2004). Oceanic germanium/silicon ratios: evaluation of the potential overprint of temperature on weathering signals. *Paleoceanography* 19, PA2016. doi:10.1029/2003PA000940

Harper, J. T., Humphrey, N. F., Meierbachtol, T. W., Graly, J. A., and Fischer, U. H. (2017). Borehole measurements indicate hard bed conditions, Kangerlussuaq sector, western Greenland Ice Sheet. *J. Geophys. Res. Earth Surf.* 122, 1605–1618. doi:10.1002/2017JF004201

Hatton, J. E., Hendry, K. R., Hawkings, J. R., Wadham, J. L., Kohler, T. J., Stibal, M., et al. (2019a). Investigation of subglacial weathering under the Greenland Ice Sheet using silicon isotopes. *Geochim Cosmochim Acta* 247, 191–206. doi:10.1016/j.gca.2018.12.033

Hatton, J. E., Hendry, K. R., Hawkings, J. R., Wadham, J. L., Opfergelt, S., Kohler, T. J., et al. (2019b). Silicon isotopes in Arctic and sub-Arctic glacial meltwaters: the role of subglacial weathering in the silicon cycle. *Proc. R. Soc. A* 475, 20190098. doi:10.1098/rspa.2019.0098

Hawkings, J. R., Hatton, J. E., Hendry, K. R., de Souza, G. F., Wadham, J. L., Ivanovic, R., et al. (2018). The silicon cycle impacted by past ice sheets. *Nat. Commun.* 9, 1–10. doi:10.1038/s41467-018-05689-1

Hawkings, J. R., Skidmore, M. L., Wadham, J. L., Priscu, J. C., Morton, P. L., Hatton, J. E., et al. (2020). Enhanced trace element mobilization by Earth's ice sheets. *Proc. Natl. Acad. Sci.* 117, 202014378. doi:10.1073/pnas.2014378117

Hawkings, J. R., Wadham, J. L., Benning, L. G., Hendry, K. R., Tranter, M., Tedstone, A., et al. (2017). Ice sheets as a missing source of silica to the polar oceans. *Nat. Commun.* 8, 14198. doi:10.1038/ncomms14198

Hawkings, J. R., Wadham, J. L., Tranter, M., Lawson, E., Sole, A., Cowton, T., et al. (2015). The effect of warming climate on nutrient and solute export from the Greenland Ice Sheet. *Geochemical Perspect. Lett.* 1, 94–104. doi:10.7185/geochemlet.1510

Hawkings, J., Wadham, J., Tranter, M., Telling, J., Bagshaw, E., Beaton, A., et al. (2016). The Greenland Ice Sheet as a hot spot of phosphorus weathering and export in the Arctic. *Global Biogeochem. Cycles* 30, 191–210. doi:10.1002/2015GB005237

Hendry, K. R., and Brzezinski, M. a. (2014). Using silicon isotopes to understand the role of the Southern Ocean in modern and ancient biogeochemistry and climate. *Quat. Sci. Rev.* 89, 13–26. doi:10.1016/j.quascirev.2014.01.019

Hendry, K. R., Huvenne, V. A., Robinson, L. F., Annett, A., Badger, M., Jacobel, A. W., et al. (2019). The biogeochemical impact of glacial meltwater from Southwest Greenland. *Prog. Oceanogr.* 176, 102126. doi:10.1016/j.pocean.2019.102126

Hindshaw, R. S., Rickli, J., and Leuthold, J. (2019). Mg and Li stable isotope ratios of rocks, minerals, and water in an outlet glacier of the Greenland ice sheet. *Front. Earth Sci.* 7, 1–16. doi:10.3389/feart.2019.00316

Hindshaw, R. S., Rickli, J., Leuthold, J., Wadham, J., and Bourdon, B. (2014). Identifying weathering sources and processes in an outlet glacier of the Greenland Ice Sheet using Ca and Sr isotope ratios. *Geochim. Cosmochim. Acta* 145, 50–71. doi:10.1016/j.gca.2014.09.016

Hodgkins, R., Tranter, M., and Dowdeswell, J. A. (1998). The hydrochemistry of runoff from a "cold-based" glacier in the high Artic (Scott Turnerbreen, Svalbard). *Hydrol. Process.* 12, 87–103. doi:10.1002/(SICI)1099-1085(199801)12:1<87:AID-HYP565>3.0.CO;2-C

Icenhower, J. P., and Dove, P. M. (2000). The dissolution kinetics of amorphous silica into sodium chloride solutions: effects of temperature and ionic strength. *Geochim. Cosmochim. Acta* 64, 4193–4203. doi:10.1016/S0016-7037(00)00487-7

Jasechko, S. (2019). Global isotope hydrogeology—review. *Rev. Geophys.* 57, 835–965. doi:10.1029/2018RG000627

Jochum, K. P., Schuessler, J. A., Wang, X. H., Stoll, B., Weis, U., Müller, W. E., et al. (2017). Whole-Ocean changes in silica and Ge/Si ratios during the last deglacial deduced from long-lived giant glass sponges. *Geophys. Res. Lett.* 44, 555–611. doi:10.1002/2017GL073897

Kato, K., and Kitano, Y. (1968). Solubility and dissolution rate of amorphous silica in distilled and seawater at 20* C. *J. Oceanogr. Soc. Jpn.* 24, 147–152. doi:10.5928/kaiyou1942.24.147

Kurtz, A., Derry, L., and Chadwick, O. (2002). Germanium-silicon fractionation in the weathering environment. *Geochim. Cosmochim. Acta* 66, 1525–1537. doi:10.1016/S0016-7037(01)00869-9

Lawson, E. C., Wadham, J. L., Tranter, M., Stibal, M., Lis, G. P., Butler, C. E., et al. (2014). Greenland ice sheet exports labile organic carbon to the arctic oceans. *Biogeosciences* 11, 4015–4028. doi:10.5194/bg-11-4015-2014

Li, L. (2019). Watershed reactive transport. *Rev. Mineral. Geochem.* 85, 381–418. doi:10.2138/rmg.2018.85.13

Lindbäck, K., Pettersson, R., Hubbard, A. L., Doyle, S. H., Van As, D., Mikkelsen, A. B., et al. (2015). Subglacial water drainage, storage, and piracy beneath the Greenland ice sheet. *Geophys. Res. Lett.* 42, 7606–7614. doi:10.1002/2015GL065393

Linhoff, B. S., Charette, M. A., Nienow, P. W., Wadham, J. L., Tedstone, A. J., and Cowton, T. (2017). Utility of 222Rn as a passive tracer of subglacial distributed system drainage. *Earth Planet. Sci. Lett.* 462, 180–188. doi:10.1016/j.epsl.2016.12.039

Lugolobi, F., Kurtz, A. C., and Derry, L. A. (2010). Germanium-silicon fractionation in a tropical, granitic weathering environment. *Geochim. Cosmochim. Acta* 74, 1294–1308. doi:10.1016/j.gca.2009.11.027

Maher, K., and Chamberlain, C. P. (2014). Hydrologic regulation of chemical weathering and the geologic carbon cycle. *Science* 343, 1502–1504. doi:10.1126/science.1250770

Mantoura, S. C. (2006). Development and application of opal based paleoceanographic proxies. Ph.D. thesis. England (United Kingdom): University of Cambridge.

Meire, L., Meire, P., Struyf, E., Krawczyk, D. W., Arendt, K. E., Yde, J. C., et al. (2016). High export of dissolved silica from the Greenland Ice Sheet. *Geophys. Res. Lett.* 43, 9173–9182. doi:10.1002/2016GL070191

Mortlock, R., Charles, C., Froelich, P., Zibello, M., Saltzman, J., Hays, J., et al. (1991). Evidence for lower productivity in the Antarctic Ocean during the last glaciation. *Nature* 351, 220–223. doi:10.1038/351220a0

Mortlock, R., and Froelich, P. (1987). Continental weathering of germanium: Ge/Si in the global river discharge. *Geochim. Cosmochim. Acta* 51, 2075–2082. doi:10.1016/0016-7037(87)90257-2

Mortlock, R., and Froelich, P. (1996). Determination of germanium by isotope dilution-hydride generation inductively coupled plasma mass spectrometry. *Anal. Chim. Acta* 332, 277–284. doi:10.1016/0003-2670(96)00230-9

Mullin, J., and Riley, J. (1955). The colorimetric determination of silicate with special reference to sea and natural waters. *Anal. Chim. Acta* 12, 162–175. doi:10.1016/S0003-2670(00)87825-3

Murnane, R. J., Leslie, B., Hammond, D. E., and Stallard, R. F. (1989). Germanium geochemistry in the southern California borderlands. *Geochim. Cosmochim. Acta* 53, 2873–2882. doi:10.1016/0016-7037(89)90164-6

Murnane, R., and Stallard, R. (1990). Germanium and silicon in rivers of the Orinoco drainage basin. *Nature* 344, 749–752.

Nelson, A. H., Bierman, P. R., Shakun, J. D., and Rood, D. H. (2014). Using *in situ* cosmogenic 10Be to identify the source of sediment leaving Greenland. *Earth Surf. Process. Landforms* 39, 1087–1100. doi:10.1002/esp.3565

Oelze, M., von Blanckenburg, F., Bouchez, J., Hoellen, D., and Dietzel, M. (2015). The effect of Al on Si isotope fractionation investigated by silica precipitation experiments. *Chem. Geol.* 397, 94–105. doi:10.1016/j.chemgeo.2015.01.002

Opfergelt, S., Burton, K., Pogge von Strandmann, P., Gislason, S., and Halliday, A. (2013). Riverine silicon isotope variations in glaciated basaltic terrains: implications for the Si delivery to the ocean over glacial-interglacial intervals. *Earth Planet. Sci. Lett.* 369–370, 211–219. doi:10.1016/j.epsl.2013.03.025

Overeem, I., Hudson, B. D., Syvitski, J. P., Mikkelsen, A. B., Hasholt, B., Van Den Broeke, M. R., et al. (2017). Substantial export of suspended sediment to the global oceans from glacial erosion in Greenland. *Nat. Geosci.* 10, 859–863. doi:10.1038/NGEO3046

Parkhurst, D. L., and Appelo, C. (2013). "Description of input and examples for PHREEQC version 3: a computer program for speciation, batch-reaction, one-dimensional transport, and inverse geochemical calculations," in *Technical report*. Reston, VA: US Geological Survey, 497.

Pokrovsky, O., Pokrovski, G., Schott, J., and Galy, A. (2006). Experimental study of germanium adsorption on goethite and germanium coprecipitation with iron hydroxide: X-ray absorption fine structure and macroscopic characterization. *Geochim. Cosmochim. Acta* 70, 3325–3341. doi:10.1016/j.gca.2006.04.012

Pokrovsky, O. S., Galy, A., Schott, J., Pokrovski, G. S., and Mantoura, S. (2014). Germanium isotope fractionation during Ge adsorption on goethite and its coprecipitation with Fe oxy(hydr)oxides. *Geochim. Cosmochim. Acta* 131, 138–149. doi:10.1016/j.gca.2014.01.023

Pokrovsky, O. S., Reynolds, B. C., Prokushkin, A. S., Schott, J., and Viers, J. (2013). Silicon isotope variations in Central Siberian rivers during basalt weathering in permafrost-dominated larch forests. *Chem. Geol.* 355, 103–116. doi:10.1016/j.chemgeo.2013.07.016

Qi, H. W., Hu, R. Z., Jiang, K., Zhou, T., Liu, Y. F., and Xiong, Y. W. (2019). Germanium isotopes and Ge/Si fractionation under extreme tropical weathering of basalts from the Hainan Island, South China. *Geochim. Cosmochim. Acta* 253, 249–266. doi:10.1016/j.gca.2019.03.022

Raiswell, R., Tranter, M., Benning, L. G., Siegert, M., De'ath, R., Huybrechts, P., et al. (2006). Contributions from glacially derived sediment to the global iron (oxyhydr)oxide cycle: implications for iron delivery to the oceans. *Geochim. Cosmochim. Acta* 70, 2765–2780. doi:10.1016/j.gca.2005.12.027

Rennermalm, A. K., Smith, L. C., Chu, V. W., Box, J. E., Forster, R. R., Van Den Broeke, M. R., et al. (2013). Evidence of meltwater retention within the Greenland ice sheet. *Cryosphere* 7, 1433–1445. doi:10.5194/tc-7-1433-2013

Rickli, J., Hindshaw, R. S., Leuthold, J., Wadham, J. L., Burton, K. W., and Vance, D. (2017). Impact of glacial activity on the weathering of Hf isotopes – observations from Southwest Greenland. *Geochim. Cosmochim. Acta* 215, 295–316. doi:10.1016/j.gca.2017.08.005

Rimstidt, J. D., Zhang, Y., and Zhu, C. (2016). Rate equations for sodium catalyzed amorphous silica dissolution. *Geochim. Cosmochim. Acta* 195, 120–125. doi:10.1016/j.gca.2016.09.020

Rouxel, O. J., Galy, A., and Elderfield, H. (2006). Germanium isotopic variations in igneous rocks and marine sediments. *Geochim. Cosmochim. Acta* 70, 3387–3400. doi:10.1016/j.gca.2006.04.025

Rouxel, O. J., and Luais, B. (2017). Germanium isotope geochemistry. *Rev. Mineral. Geochem.* 82, 601–656. doi:10.2138/rmg.2017.82.14

Shemesh, A., Mortlock, R. A., and Froelich, P. N. (1989). Late cenozoic Ge/Si record of marine biogenic opal: implications for variations of riverine fluxes to the ocean. *Paleoceanography* 4, 221–234. doi:10.1029/PA004i003p00221

Siebert, C., Nägler, T., and Kramers, J. (2001). Determination of molybdenum isotope fractionation by double-spike multicollector inductively coupled plasma mass spectrometry. *Geochem. Geophys. Geosyst.* 2, 2000GC000124. doi:10.1029/2000GC000124

Smeets, P. C., Kuipers Munneke, P., van As, D., van den Broeke, M. R., Boot, W., Oerlemans, H., et al. (2018). The K-transect in west Greenland: automatic weather station data (1993–2016). *Arct. Antarct. Alp. Res.* 50, S100002. doi:10.1080/15230430.2017.1420954

Smith, L. C., Chu, V. W., Yang, K., Gleason, C. J., Pitcher, L. H., Rennermalm, A. K., et al. (2015). Efficient meltwater drainage through supraglacial streams and rivers on the southwest Greenland ice sheet. *Proc. Natl. Acad. Sci. U.S.A.* 112, 1001–1006. doi:10.1073/pnas.1413024112

Stevenson, E. I., Fantle, M. S., Das, S. B., Williams, H. M., and Aciego, S. M. (2017). The iron isotopic composition of subglacial streams draining the Greenland ice sheet. *Geochim. Cosmochim. Acta* 213, 237–254. doi:10.1016/j.gca.2017.06.002

Sutton, J., Ellwood, M. J., Maher, W. A., and Croot, P. L. (2010). Oceanic distribution of inorganic germanium relative to silicon: germanium discrimination by diatoms. *Global Biogeochem. Cycles* 24, GB2017. doi:10.1029/2009GB003689

Sutton, J. N., André, L., Cardinal, D., Conley, D. J., de Souza, G. F., Dean, J., et al. (2018). A review of the stable isotope bio-geochemistry of the global silicon cycle and its associated trace elements. *Front. Earth Sci.* 5, 112. doi:10.3389/feart.2017.00112

Tipper, E. T., Stevenson, E. I., Alcock, V., Knight, A. C. G., Baronas, J. J., Hilton, R. G., et al. (2021). Global silicate weathering flux overestimated because of sediment–water cation exchange. *Proc. Natl. Acad. Sci.* 118, e2016430118. doi:10.1073/pnas.2016430118

Torres, M. A., and Baronas, J. J. (2021). Modulation of riverine concentration–discharge relationships by changes in the shape of the water transit time distribution. *Global Biogeochem. Cycles* 35. e2020GB006694. doi:10.1029/2020GB006694

Torres, M. A., Moosdorf, N., Hartmann, J., Adkins, J. F., and West, A. J. (2017). Glacial weathering, sulfide oxidation, and global carbon cycle feedbacks. *Proc. Natl. Acad. Sci.* 114, 8716–8721. doi:10.1073/pnas.1702953114

Tranter, M., and Wadham, J. L. (2014). "Geochemical weathering in glacial and proglacial environments," in *Treatise on Geochemistry*. 2nd Edn. Elsevier, 7, 157–173.

Tremblay, J. E., Anderson, L. G., Matrai, P., Coupel, P., Bélanger, S., Michel, C., et al. (2015). Global and regional drivers of nutrient supply, primary production and CO2 drawdown in the changing Arctic Ocean. *Prog. Oceanogr.* 139, 171–196. doi:10.1016/j.pocean.2015.08.009

Urra, A., Wadham, J., Hawkings, J. R., Telling, J., Hatton, J. E., Yde, J. C., et al. (2019). Weathering dynamics under contrasting Greenland ice sheet catchments. *Front. Earth Sci.* 7, 299. doi:10.3389/feart.2019.00299

Van As, D., Mikkelsen, A. B., Nielsen, M. H., Box, J. E., Liljedahl, L. C., Lindbäck, K., et al. (2017). Hypsometric amplification and routing moderation of Greenland ice sheet meltwater release. *Cryosphere* 11, 1371–1386. doi:10.5194/tc-11-1371-2017

Van Gool, J. A., Connelly, J. N., Marker, M., and Mengel, F. C. (2002). The nagssugtoqidian orogen of West Greenland: tectonic evolution and regional correlations from a west Greenland perspective. *Can. J. Earth Sci.* 39, 665–686. doi:10.1139/e02-027

Vick-Majors, T. J., Michaud, A. B., Skidmore, M. L., Turetta, C., Barbante, C., Christner, B. C., et al. (2020). Biogeochemical connectivity between freshwater ecosystems beneath the west antarctic ice sheet and the sub-ice marine environment. *Global Biogeochem. Cycles* 34, e2019GB006446. doi:10.1029/2019GB006446

White, A. F., and Brantley, S. L. (2003). The effect of time on the weathering of silicate minerals: why do weathering rates differ in the laboratory and field?. *Chem. Geol.* 202, 479–506. doi:10.1016/j.chemgeo.2003.03.001

Wimpenny, J., Burton, K. W., James, R. H., Gannoun, A., Mokadem, F., and Gíslason, S. R. (2011). The behaviour of magnesium and its isotopes during glacial weathering in an ancient shield terrain in West Greenland. *Earth Planet. Sci. Lett.* 304, 260–269. doi:10.1016/j.epsl.2011.02.008

Wimpenny, J., James, R. H., Burton, K. W., Gannoun, A., Mokadem, F., and Gíslason, S. R. (2010). Glacial effects on weathering processes: new insights from the elemental and lithium isotopic composition of West Greenland rivers. *Earth Planet. Sci. Lett.* 290, 427–437. doi:10.1016/j.epsl.2009.12.042

Woronko, B., and Hoch, M. (2011). The development of frost-weathering microstructures on sand-sized quartz grains: examples from Poland and Mongolia. *Permafr. Periglac. Process.* 22, 214–227. doi:10.1002/ppp.725

Yde, J. C., Finster, K. W., Raiswell, R., Steffensen, J. P., Heinemeier, J., Olsen, J., et al. (2010). Basal ice microbiology at the margin of the Greenland ice sheet. *Ann. Glaciol.* 51, 71–79. doi:10.3189/172756411795931976

Yde, J. C., Knudsen, N. T., Hasholt, B., and Mikkelsen, A. B. (2014). Meltwater chemistry and solute export from a Greenland ice sheet catchment, Watson river, west Greenland. *J. Hydrol.* 519, 2165–2179. doi:10.1016/j.jhydrol.2014.10.018

Conflict of Interest: The authors declare that the research was conducted in the absence of any commercial or financial relationships that could be construed as a potential conflict of interest.

Advantages of publishing in Frontiers

OPEN ACCESS
Articles are free to read
for greatest visibility
and readership

FAST PUBLICATION
Around 90 days
from submission
to decision

HIGH QUALITY PEER-REVIEW
Rigorous, collaborative,
and constructive
peer-review

TRANSPARENT PEER-REVIEW
Editors and reviewers
acknowledged by name
on published articles

Frontiers
Avenue du Tribunal-Fédéral 34
1005 Lausanne | Switzerland

Visit us: www.frontiersin.org
Contact us: frontiersin.org/about/contact

REPRODUCIBILITY OF RESEARCH
Support open data
and methods to enhance
research reproducibility

DIGITAL PUBLISHING
Articles designed
for optimal readership
across devices

FOLLOW US
@frontiersin

IMPACT METRICS
Advanced article metrics
track visibility across
digital media

EXTENSIVE PROMOTION
Marketing
and promotion
of impactful research

LOOP RESEARCH NETWORK
Our network
increases your
article's readership